

Spontaneous Symmetry Breaking Transport

From Anomalous Response to Chiral Separation

Dissertation

zur Erlangung des Doktorgrades
an der Fakultät für Physik
der Universität Bielefeld

vorgelegt von

David Speer
am
01. März 2011

begutachtet durch

Prof. Dr. Peter Reimann
Prof. Dr. Jürgen Schnack

Abstract

We consider the dynamics of Brownian particles exposed to symmetric periodic potentials and driven out of equilibrium by symmetric driving forces at several examples. For any non-zero temperature, the average velocity vanishes but there may be dynamical states of sustained transport spontaneously breaking the symmetry in the deterministic limit, named spontaneous symmetry breaking transport. If the symmetry of the dynamics is broken by a small perturbation, e.g. a constant bias force, the particle mobility may be in practically any direction, even in the direction opposite to the bias force. Changing only a scalar parameter of the dynamics, e.g. the amplitude or frequency of the symmetric driving force, the particle can be directed into almost any direction. Without a constant bias force, the diffusion coefficient of the particle diverges in the deterministic limit. In more than one (spatial) dimension, diffusion is highly anisotropic, and the direction of fast diffusion can be adjusted by a scalar parameter of the dynamics, e.g. the amplitude of the symmetric driving force. Our examples are (i) the dynamics of an underdamped Brownian particle in a one dimensional periodic potential, published in [1, 2] and verified experimentally in [3], (ii) the dynamics of an overdamped Brownian particle in a two dimensional square lattice, published in [4], and (iii) the dynamics of two interacting Brownian particles, i.e. a dimer, in a one dimensional periodic potential. Lastly, we show how lattice potentials can be exploited to sort molecules that differ only by their chirality, published in [5]. Using spontaneous breaking of chiral symmetry, the two chiral partners can be directed into orthogonal directions under the influence of a constant bias force in a symmetry direction of the lattice and into opposite directions if a periodic driving force is applied.

printed on permanent paper ∞ ISO 9706

Contents

1	Introduction	4
2	Symmetries and transport	10
2.1	Introduction	10
2.2	Discrete symmetries	12
2.3	Spatial symmetries of a square lattice	14
2.4	Symmetries of a periodic driving force	14
2.5	Some examples of spatio-temporal symmetries	15
2.5.1	Spatially one dimensional dynamics	15
2.5.2	Spatially two dimensional dynamics	16
2.5.3	Rigid bodies in two dimensional potentials and chirality	18
2.6	Symmetry breaking bifurcations	20
2.7	Spontaneous symmetry breaking transport (SSBT)	23
2.8	Summary and conclusion	26
3	Spatially one dimensional dynamics	27
3.1	Introduction	27
3.2	Preprint of [1]	29
3.3	Preprint of [2]	35
3.4	Mechanism of absolute negative mobility	50
3.5	Preprint of [3]	53
3.6	Experimental realization	57
3.7	Graphics processing unit (GPU) programming	62
3.8	Summary	63
3.9	Appendix	65
3.9.1	Phase diagrams	65
3.9.2	Brook+ example	68
4	Spatially two dimensional dynamics	70
4.1	Introduction	70
4.2	Preprint of [4]	74
4.3	Model	78
4.4	Numerical treatment of the potentials	80
4.5	Choice of parameters	81
4.6	Symmetries	82
4.7	Rotated coordinate frame	83

4.8	Spontaneous symmetry breaking for $\alpha = 45^\circ$	84
4.9	SSBT for $\alpha = 45^\circ$	89
4.9.1	Limiting cases	90
4.9.2	Repetitive tongue structure	91
4.9.3	Comparison with the dynamics of Josephson junctions	92
4.9.4	Period 1 SSBT orbits	93
4.9.5	Period 2 SSBT orbits	95
4.10	Creation of SSBT at $\alpha = 45^\circ$	97
4.10.1	Disappearance of the unbounded attractor	101
4.10.2	Other tongues	101
4.10.3	Spontaneous symmetry breaking transport	102
4.11	Consequences at $\alpha = 45^\circ$	102
4.11.1	Anisotropic Diffusion	102
4.11.2	Absolute negative mobility	105
4.12	Breaking S_{xy} Symmetry	110
4.13	Choice of parameters	111
4.14	Transition from $\alpha = 45^\circ$ at fixed frequency	112
4.15	SSBT for $\alpha \neq 45^\circ$	116
4.15.1	Description of color palettes in the phase diagrams	116
4.15.2	SSBT in the a - α plane of parameter space at $\vec{F} = 0$	118
4.15.3	SSBT in the Ω - a plane of parameter space at $\vec{F} = 0$	122
4.16	Broken S_0 symmetry: all symmetries are broken	123
4.16.1	$\vec{F} \neq 0$ in the a - α plane of parameter space	123
4.17	Quasiperiodic transport at $\vec{F} \neq 0$	124
4.18	Summary of transport properties at $\Gamma = 0$	127
4.19	Noise effects	129
4.20	Rotating the bias force	133
4.21	Directing Brownian motion	134
4.22	Directing Diffusion	136
4.23	Some possible experimental realizations	139
4.24	Summary and outlook	143
4.25	Appendix	145
4.25.1	Bessel function approximation	145
4.25.2	Creation of SSBT at other values of Ω	146
4.25.3	Spatially 1D dynamics	148
4.25.4	Phase space structure of transport	151
4.25.5	Creation of SSBT at $\alpha = 54^\circ$	153
4.25.6	The applicability of the theory from [1, 2] at large Γ	156
4.25.7	Stochastic differential equation solver	159
4.25.8	Coupled Josephson junctions	161
4.25.9	Supplementary figures	163
5	Quenched disorder	166
5.1	Introduction	166
5.2	Modelling quenched disorder	167
5.3	Analogy to thermal fluctuations	168

5.4	The Golosov effect: trapping events	169
5.5	Averaging in the disordered dynamics	172
5.6	Effect of quenched disorder on phase-locked SSBT attractors	174
5.6.1	Deterministic phase diagram	174
5.6.2	Disorder effects	175
5.6.3	Escape rates	175
5.6.4	Quenched disorder induced absolute negative mobility	178
5.6.5	Thermal fluctuations and quenched disorder	180
5.7	Summary and outlook on inertia effects	182
6	Dimers in one dimension	184
6.1	Introduction	184
6.2	Model	185
6.3	Convex interaction potentials	187
6.4	Non-convex interaction potentials	189
6.5	Identical monomers - symmetric dimers	190
6.5.1	Bound interaction potentials	191
6.5.2	Mechanism of SSBT	194
6.5.3	Consequences of SSBT	195
6.5.4	Unbounded interaction potentials	197
6.5.5	Uncoupled dynamics	198
6.5.6	Interplay of coupled dynamics and uncoupled dynamics	198
6.6	Asymmetric dimers	200
6.7	Conclusions	202
7	Chiral separation	204
7.1	Preprint of [5]	206
7.2	Equations of motion of a rigid body	210
7.3	Setup	212
7.4	“Long” molecules	215
7.5	Spontaneous symmetry breaking transport leading to chiral separation .	218
7.6	180° chiral separation by an asymmetric periodic drive	222
7.6.1	$\alpha = 45^\circ$	222
7.6.2	$\alpha \neq 45^\circ$	224
7.7	Symmetric periodic drive	225
7.7.1	Directing Brownian motion	225
7.7.2	Diffusive separation	226
7.7.3	180° separation by absolute transverse mobility	228
7.8	Differently shaped molecules and large triangles	231
7.9	Small molecules and locally flat potentials	232
7.10	Rotation	239
7.11	Proof of principle experiment	243
7.12	Generalizations, further experimental realizations	245
8	Conclusion	247

Chapter 1

Introduction

The advances in the understanding, observation, and control of micrometer scale physics [6] and, from a different point of view, in the understanding and modeling of superconductivity [7], have lead to great interest in the transport properties of Brownian particles [8], see [9–11] for a few reviews. In this work we will show that the transport direction of Brownian particles can be controlled by making use of dynamical states of stationary directed transport spontaneously breaking a symmetry of the dynamics, *spontaneous symmetry breaking transport (SSBT)*. Our central results cover three exemplary Brownian particle dynamics and have been published in [1–5], of which we include preprints¹ in the respective chapters, i.e. [1–3] in chapter 3, [4] in chapter 4, and [5] in chapter 7.

We begin with a short outline of our work, followed by a more detailed introduction. The three main parts of this work, chapter 3, chapter 4, and chapter 7, can be read separately and use the notations of the respective publications. Chapter 2 gives a formal introduction to the role of symmetries in the dynamics of Brownian particles and an outlook of how our methods can be generalized beyond the examples which we consider in this work. Our first example is an underdamped² Brownian particle in a one dimensional symmetric potential. Our main results are summarized in the brief account [1], and [2] and chapter 3 provide further details. The main effect predicted in [1], *absolute negative mobility*, has been measured experimentally in the context of Josephson junctions [3]. Moving beyond the restrictions of spatially one dimensional dynamics in chapter 4 (summarized in [4]), we will consider the overdamped³ dynamics of a Brownian particle in a two dimensional periodic potential as our second example, generalize our results to weakly disordered potentials in chapter 5, and consider the special case of two interacting Brownian particles in spatially one dimensional overdamped dynamics in chapter 6. Lastly, we will turn to chiral symmetry of rigid molecules and show how a chiral molecule can be separated from its chiral partner molecule⁴ in chapter 7 (summarized in [5]).

A key question is how the transport properties of Brownian particles can be controlled by an experimentalist, e.g. to separate the different species of Brownian particles in a mixture. While the direct and individual manipulation and observation of Brownian

¹The preprints are largely identical to the printed articles. The latter can be obtained via the publishers.

²I.e., its mass cannot be neglected.

³The mass of the particle is negligible compared to the friction forces.

⁴i.e. the molecule which is its mirror image

particles by an experimentalist has become possible per se⁵, it is not feasible on a larger scale which is what is often necessary in quantitative experiments, drug research and manufacturing, or biological processes.

If the dynamics of a Brownian particle are spatially asymmetric⁶ and far from thermodynamic equilibrium, directed transport is the generic result according to Curie's principle⁷, even if the asymmetry is unbiased. Such dynamics are referred to as *Brownian motors* or *ratchets*⁸, and current reversals of ratchets, i.e. the inversion of the transport direction in dependence of some parameter, are one possible tool to control transport, in particular in the context of particle sorting [9, 10]. Then, the difference between two species of particles in a mixture can be considered as such a parametric variation, and the different particle species can be made to move into opposite directions.

The current vanishes exactly in spatially symmetric and ergodic dynamics. If the symmetry is broken by a weak perturbation, a non-zero current is the generic result. If the perturbation is inverted, that current is inverted as well, and weakly perturbed symmetric dynamics are always “close” to a current reversal. In that sense, symmetric dynamics are possibly in an advantageous state to control the transport direction of Brownian particles, e.g. for the purpose of particle sorting. The question is to what extend an experimentalist can control the direction of the symmetry breaking perturbation, if and how fast particles are transported due to this perturbation, and, in a sorting experiment, whether the different species of particles react differently to changes of that perturbation. We will focus on the conceptually simplest symmetry breaking perturbation, a constant bias force, and occasionally remark on more general perturbations. In chapter 7, we will also consider the chirality of molecules as a symmetry breaking perturbation. The naive expectation is that different particle species will be dragged into the same or almost the same direction by a constant bias force and particle sorting would be rather inefficient. Indeed, in linear dynamics this is exactly the case. For particles on a structured surface⁹ subjected only to a constant bias force, the angle between that force and the transport direction, the *deflection angle*, is limited by the symmetry properties of the surface [4, 5, 18–20]. E.g., the deflection angle has to be smaller than 45° for a point particle on a surface with square lattice symmetry¹⁰, and thermodynamic stability requires the deflection angle to be smaller than 90° if the dynamics are in thermodynamic equilibrium without the bias force. The angles between the transport directions of different particle species on the same substrate are limited by the maximum deflection angle and are typically much smaller, see e.g. [18, 21] for a few theoretical investigations and [22–28] for some experiments. We will overcome these limitations by making use of SSBT.

⁵See, e.g., [6, 12, 13]

⁶I.e. the dynamics are not the same if viewed through a mirror. We will formally discuss this matter in chapter 2.

⁷We will discuss Curie's principle [14] in more detail in chapter 2.

⁸See [10] for a review, [15] for an experimental proof using colloids, and [16, 17] for experiments in the context of superconducting interference devices.

⁹I.e. the dynamics are spatially two dimensional.

¹⁰Trivially, deflection angles of almost 90° can be achieved if there is a hard wall on the surface, and the bias force is almost orthogonal to that wall. This is the limit of small bias forces and small noise strengths of a general (rectangular) lattice with different potential barrier heights for the lattice directions. But then, due to the “trivial” nature of the deflection, different particle species will have very similar transport directions, and this limit is not of much use for particle sorting.

A simple, but nonergodic and otherwise useless, example of SSBT is that of a single particle moving without friction and stochastic fluctuations in a spatially symmetric potential of finite height and depth. If its initial momentum is sufficiently large, it will continue to move forever, i.e. it is in a dynamical state of stationary directed transport. While the dynamics of that particle are globally¹¹ symmetric, i.e. it is impossible to distinguish from its mirror image, the high initial momentum state spontaneously breaks this symmetry, i.e. it carries SSBT. Stationary transport is ruled out in thermodynamic equilibrium¹². While there are countless ways of driving a thermodynamic system out of equilibrium, we will focus on deterministic driving forces throughout this work. We will consider non-interacting¹³ classical particles for which ergodicity breaking is possible only in the deterministic limit, i.e. in the absence of stochastic fluctuations¹⁴. We will show [1–5] that if SSBT is present in the deterministic part of the dissipative dynamics of a Brownian particle, the transport properties of the noisy (and thus ergodic) dynamics can be controlled via the interplay of SSBT, a weak symmetry breaking perturbation, and thermal noise. In particular, this nonlinear interplay lifts the linear connection between the “preferred” direction¹⁵ implied by a constant bias force and the resulting transport direction of Brownian particles.

In other words, SSBT may lead to directed transport against an applied bias force. For small bias forces, this counterintuitive behavior has come to be known as *absolute negative mobility*¹⁶ (ANM) or *negative absolute resistance* (or conductance) when referring to the charge carriers in electrical devices.

In the latter context, ANM was discovered experimentally as a purely quantum mechanical effect more than 30 years ago in a sample of bulk GaAs [30, 31] and later in semiconductor heterostructures [32], Semiconductor super lattices [33]¹⁷, and charge density waves [35]. ANM of classical particles has probably been measured first indirectly and “accidentally” during the 1980’s investigation of chaos in microwave irradiated Josephson junctions in e.g. [36, 37]¹⁸ as negative absolute resistance of a Josephson junction but went largely unnoticed at the time. Much later, the phenomenon gained much theoretical attention for classical particles. One of the first theoretical demonstrations, [38], used a model of interacting Brownian particles. For certain parameters, this model also exhibits a spontaneous ratchet effect in the thermodynamic limit of an infinite number of particles similar to [29], in which case “anomalous hysteresis” [38] is found. Further

¹¹In the sense that all available configurations of the particle are considered.

¹²Our example of a single particle does not equilibrate.

¹³A very small number of interacting particles will be considered in chapter 6.

¹⁴For an infinite number of interacting classical particles in a symmetric system, [29] shows that *spontaneous symmetry breaking* leads to a spontaneous breaking of ergodicity and thus to directed transport. Nonanalyticities, e.g. a divergent potential barrier, may also be a cause of ergodicity breaking but we will not consider this case.

¹⁵In so far as such a direction is given. E.g., a parametric asymmetry of the potential [10] and chirality [5] of a molecule do not lead to a clearly defined “preferred” direction.

¹⁶The mobility is the slope of the response curve, i.e. the current in dependence of the applied force. Absolute refers to the zero bias (force) mobility.

¹⁷It is interesting to note that SSBT accompanies ANM in that context, see also [34].

¹⁸The dynamics of small Josephson junctions can be mapped onto the dynamics of a classical particle in a washboard potential [7], and absolute negative resistance of a Josephson junction translates into ANM of a classical particle in a washboard potential. See [2, 3] and chapter 3 for a more detailed discussion.

models were put forth in [39–44] and [44] shows that no more than 3 interacting particles are needed to get ANM. The mechanism of ANM in [38] is that, for certain parameter values, the symmetry breaking bias force stabilizes the part of phase space responsible for the (spontaneous) ratchet effect that leads to an uphill current, i.e. against the bias force, and the mechanism is, in that sense, rather similar to the one described in the preceding paragraph. [43] shows ANM in a random walk model penalizing larger jumps in the spirit of Parrondo’s game [45, 46]. This “high velocity penalty” introduces a fundamentally different mechanism of ANM. Moving the “high velocity penalty” into a two dimensional surface structure, ANM of a single classical particle subjected to a deterministic driving force and a potential geometry that forces the particle on a meandering path was first shown as a noise induced effect in [47–50]¹⁹. Another variant is to move the “high velocity penalty” into an internal state variable, allowing for an otherwise one dimensional dynamics [56, 57], or to the transition rate between two ratchet dynamics of opposite directions [58], which we will revisit in chapter 6. [47] paved the way for a direct experimental proof for colloids in a microfluidic device [59–61] which allowed ANM to be applied to particle sorting [62]: one species of colloids shows ANM while the other does not. Hence, the different particles are transported into opposite directions and separated (see also [52] for a recent review).

ANM of a single classical particle moving in a simple one dimensional periodic potential and subjected to symmetric driving forces and equilibrium thermodynamic fluctuations was discovered theoretically²⁰ by [63], and independently at the same time by the author [1, 2], see chapter 3. These dynamics can be mapped onto the dynamics of a Josephson junction modeled in the resistively and capacitively shunted junction (RCSJ) model [7, 64, 65], allowing for the immediate experimental realization presented in [3]. For these dynamics, an intuitive explanation for the effect is given in [1, 2], see chapter 3. Using the interplay of deterministic and stochastic dynamics, various further astonishing effects could be facilitated, such as noise induced ANM (NANM) (either with positive mobility [1, 2] or vanishing mobility [63] in the deterministic limit) or normal zero bias mobility, but the particle moves uphill for a certain interval of non-zero bias forces [1, 2].

The main requirements of the effects put forth in [1–3, 63] are a three dimensional phase space, broken thermodynamic equilibrium and nonlinearity, as shown in [1, 2]. The general idea of SSBT induced ANM can be extended to the overdamped dynamics of two interacting Brownian particles in a one dimensional periodic potential, as we will show in chapter 6, and to the overdamped dynamics of a periodically driven Brownian particle in a two dimensional potential, as we will show in chapter 4 for a perfectly periodic potential and in chapter 5 for an almost periodic (weakly disordered) potential. Lifting the restriction of transport in only one spatial dimension allows for a much richer response behavior and for more promising applications. Due to the nonlinear interplay of the pe-

¹⁹See [51, 52] for reviews. Furthermore, [53, 54] show that non-equilibrium random fluctuations induce ANM of a single classical particle in meandering geometries, and [55] extends the idea put forth in [47] by using the shape of the particles to get a suitable trapping mechanism penalizing large bias forces.

²⁰As has been mentioned above, due to the general nature of the effect it was already contained in much earlier works, but has gone largely unnoticed. Furthermore, [56, 57] show ANM in the spatially one dimensional overdamped dynamics of a single Brownian particle with an additional fluctuating internal state variable, that can also be considered as a non-equilibrium noise source. Both approaches can be considered as simplifications of more complex dynamics. In particular, the non-equilibrium noise used in [57] is not completely unlike an extremely simplified model of the inertia forces.

riodic drive, the bias force, the periodic potential, and noise, the transport direction of the Brownian particle depends on almost all scalar parameters in a nontrivial way. This allows us to direct the Brownian particle into almost any direction by changing only a single scalar quantity, e.g. the amplitude of the periodic drive, and not changing any inherent direction of the dynamics, coined “directing Brownian motion” in [4]. Furthermore, this “sensitive” dependence of the transport direction on the system parameters is ideally suited for particle sorting. The differences between different particle species can be considered as such system parameters, and it is thus possible to sort more than two different particle species simultaneously in the same device by “directing” each species into a different direction. In dynamics in which transport is restricted to a narrow channel or one dimension, this is possible only by making use of multiple sorting stages²¹, or one has to use differences in the absolute migration velocities of the particle species, see e.g. [67, 68].

Lastly, we will turn to chiral symmetry. A molecule which is not identical to its image in any planar mirror is called *chiral*. Typically, a chiral molecule and its chiral partner (i.e. its mirror image) have rather similar physical properties, e.g. mass, charge, volume, spectral properties or dissociation energy, but their biological or pharmaceutical properties may be very different. E.g., a specific chiral molecule may have a medical use, while its mirror image is toxic [69, 70]. Several methods of separation employing a chiral selector, i.e. an ingredient which is not identical to its mirror image, have been put forth [70–74]. Due to the effort involved in finding a suitable chiral selector for a given molecule, chiral selector free methods are desirable. Several methods employing hydrodynamic flows have been put forth theoretically [67, 68, 75–79], and some have been verified experimentally [80–83] for natural and artificial chiral objects of sizes from centimeters to micrometers. A different method is to use an achiral structure for chiral separation [84, 85] and to make use of the different interactions of the chiral partners with the achiral structure. The advantage is that one structure may be used to sort many chemically different but physically (i.e. volume, mass, etc.) similar molecules. To that end, we will show that a tilted periodic potential (i.e. subjected to a constant bias force) may be used for highly efficient chiral separation [5], see chapter 7. In the generic case of the tilted potential having no symmetries, we will make use of the different deflection angles of the chiral partners. If the potential is reflection symmetric across a line, and the bias force responsible for the tilt is parallel to that line, the tilted potential remains reflection symmetric across that line. Transport of achiral molecules perpendicular to that line spontaneously breaks this symmetry (SSBT). Considering the chirality of a chiral molecule as a symmetry breaking perturbation, we will make use of SSBT to achieve highly efficient chiral separation, with the transport directions of the chiral partners being orthogonal. Adding a time dependent driving force, the separation efficiency can be enhanced further, and the chiral partners can be made to move into opposite directions even for rather large noise strengths. Alternatively, diffusive separation can be achieved with each chiral partner diffusing very fast along one direction and very slowly in the orthogonal direction, and the directions of fast diffusion are orthogonal for the chiral partners. A proof of principle

²¹ E.g., in the Anselmetti lab of Bielefeld University three different species of colloids could be separated in the same ratchet device using an ac electrophoresis generated potential [6] and multiple sorting stages. During each stage, one species is made to move into one direction, while the other species move into the opposite direction, and thus the species can be separated [66].

experiment has been conducted successfully in the Anselmetti lab of Bielefeld University [86] (see chapter 7).

Chapter 2

Symmetries and transport

This chapter gives a formal introduction to discrete symmetries of (random) dynamical systems describing the dynamics of Brownian particles and tries to give a unifying view on the remainder of this work. After an introduction, we will formally define the governing equations in section 2.2 and give examples of the symmetries encountered in this work in sections 2.3-2.5. Some of the main consequences of symmetries in dynamical systems will be discussed in sections 2.6-2.7. In section 2.8, we give an overview of how the considered symmetries are used in this work.

2.1 Introduction

Symmetries are ubiquitous in physical theories. Often, symmetries simplify calculations dramatically. In nature all symmetries are typically broken but often weakly. E.g. to obtain the theory of solid state physics, heavy use of lattice symmetries is made while typical solid molecules contain numerous impurities. But the volume of these impurities is typically negligible compared to the volume of the body considered, and the symmetric theory describes most of the physics of the solid body correctly.

We are interested in the influence of symmetries on the transport properties of Brownian particles. If the particle dynamics are symmetric, i.e. there is some symmetry transformation¹ which leaves the dynamics invariant, it is intuitively clear that any particle trajectory has the same probability as its image under the symmetry. In an ergodic dynamics² the average transport velocity of the particle has to be invariant under the symmetry, i.e. its component “transverse”³ to the symmetry has to vanish. Reflection symmetry through a point is the most dramatic example, leading to an exactly vanishing average velocity.

Conversely, if there is no symmetry in the dynamics, Curie’s principle [14] states “that if a certain phenomenon is not ruled out by symmetries, then it will occur” [10] implies

¹e.g. a reflection or a rotation

²For a definition in the context of chaotic maps see e.g. p. 56 of [87] and pp. 299-300 of [87] for a further discussion. For our purposes, the additive Wiener process [88, 89] will always provide ergodicity in the sense that the corresponding Fokker-Planck equation [90, 91] will have a unique attractor for normalized initial conditions.

³i.e. the components that are not invariant under the symmetry

that a broken symmetry leads to a non-zero current⁴ “transverse” to that symmetry⁵. This phenomenon has been extensively studied in the context of ratchets⁶ [10].

Thermodynamic equilibrium requires all transport currents to vanish [10]. Weakly perturbed thermodynamic equilibrium can be treated within linear response theory [90] and the second law of thermodynamics and thermodynamic stability put severe restrictions on the transport properties of such dynamics. Namely, the current in response to an externally applied force has to be in the direction of that force⁷ and the non-equilibrium current in response to a weak and bounded driving force of zero mean vanishes in linear order [10].

To avoid that restriction, we will consider far from thermodynamic equilibrium conditions provided by periodic driving forces throughout this work except for some parts of chapter 7. We will consider dynamics with weakly perturbed symmetries, and try to understand their transport properties from the unperturbed dynamics. Usually, it is much easier to understand the transport properties of the symmetric dynamics, and our hope is that this approach allows us to control the transport properties of the perturbed dynamics. E.g., one application is particle sorting. Without symmetry, the dynamics of different particle species will be, simply, different, but without additional knowledge no conclusion can be drawn about the transport velocities and, in particular, their directions (directions of the average velocities). In some cases [5], it turns out that without fine tuning of the dynamics, the transport properties of not too different particle species will be rather similar without using symmetries (e.g., see Fig. 1 of [5] and figure 7.15), but if symmetries can be used, the dynamics become highly selective (Fig. 2 of [5]). If the dynamics have a symmetry, one knows that the transport velocities transverse to the symmetry of all particle species will be zero. If the symmetry is weakly broken (perturbed), the transport velocities will be non-zero in general, and will be different for all particle species. If we construct our dynamics such that the transport direction depends sensitively on the parameters (i.e. particle species), different particle species can be transported into different directions, allowing for simultaneous sorting. It turns out that spontaneous symmetry breaking transport is a convenient way of creating such a situation.

Our tool of choice for breaking the symmetry will be an applied constant bias force. In principle, our results can be carried over to more general perturbations, see e.g. [92–95] for a hint in that direction. The advantage of a constant bias force is its simplicity, and its clearly defined direction, setting naive expectations. The response of an equilibrium system to a constant bias force is given by linear response theory to be in the direction of that force (see above). In the limit of very large bias forces, the response current will again be in the direction of the bias force. An illustration of some possible response behaviors can be found in [51].

The dynamics of a Brownian particle can be described by a Langevin, or stochastic

⁴An ensemble of Brownian particles with some average velocity generates a current (of Brownian particles). We will use the terms “current” and “average velocity” (of Brownian particles) equivalently.

⁵unless there is some other symmetry at work, such as thermal equilibrium

⁶a device that generates a current from zero mean driving forces or fluctuations.

⁷In higher dimensions, the scalar product between the force and the current has to be positive, i.e. the mobility tensor has to be positive (semi-)definite.

differential equation (SDE)⁸ [88–90] and can be written as

$$\frac{d\vec{q}(t)}{dt} = \dot{\vec{q}}(t) = \vec{Q}(\vec{q}(t), t) + D\vec{\xi}(t). \quad (2.1)$$

$\vec{q}(t)$ with components $q_i(t) = \vec{q}(t) \cdot \vec{e}_i$, $i = 1 \dots N$ ⁹ describes the state of the particle, e.g. the particle position. The state $\vec{q}(t)$ moves in the vector field $\vec{Q}(\vec{q}, t)$ (sufficiently smooth). D is the (constant) diffusion matrix ($N \times N$ constant matrix over \mathbb{R}) and $\vec{\xi}(t)$ is a N dimensional stochastic (Wiener-) process modeling the thermal noise to which the particle is subjected. We have restricted ourselves to additive noise by choosing D constant, and will restrict ourselves to Gaussian processes $\vec{\xi}(t)$ with $\langle \xi_i(t) \xi_j(s) \rangle = \delta_{ij} \delta(t - s)$ ¹⁰. While that restriction is not necessary, we will keep it for simplicity, as that case will be the only one relevant to this work. Each pair (\vec{q}, t) describes one state of our dynamics, and *phase space* is the $N + 1$ dimensional Euclidean space of the (\vec{q}, t) for a non-autonomous ($\vec{Q}(\vec{q}, t)$ depends explicitly on time) equation and, dropping time for an autonomous equation, it is N dimensional in that case.

2.2 Discrete symmetries

Euclidean symmetries can be divided into translations and orthogonal transformations. A brief discussion of symmetries and their consequences can be found in e.g. [97]. We will write a Euclidean symmetry as $S = (\hat{S}, \vec{L}), (s_t, T_S)$ with the real $N \times N$ orthogonal matrix \hat{S} and \vec{L} being the spatial part of the symmetry, and the numbers T_S and $s_t = \pm 1$ are the temporal part of the symmetry. The symmetry S acts on phase space vectors as

$$S(\vec{q}, t) = (\hat{S}\vec{q} + \vec{L}, s_t t + T_S) \quad (2.2)$$

which also defines its action on *trajectories* $(\vec{q}(t), t)$, where $\vec{q}(t)$ is a solution of (2.1) and thus its action on solutions of (2.1).

We will consider only dissipative dynamical systems in which time inversion, $s_t = -1$, induces a change of stability and will not be of further relevance. Therefore we set

$$s_t = +1 \quad (2.3)$$

henceforth. When discussing Hamiltonian dynamics and one dimensional overdamped dynamics we will comment briefly on time inversion symmetry.

We call (2.1) S symmetric if

$$\vec{Q}(\hat{S}\vec{q} + \vec{L}, t + T_S) = \hat{S}\vec{Q}(\vec{q}, t) \quad (2.4)$$

and

$$\hat{S}\vec{\xi}(t - T_S) \doteq \vec{\xi}(t) \quad (2.5)$$

⁸We will ignore the differences, and refer to both equivalently.

⁹ \vec{e}_i is the unit vector along the usual lines [96]. Throughout this work, we will refer to the components of a vector \vec{q} with indices, i.e. $q_i = \vec{q} \cdot \vec{e}_i$ with the usual (Euclidean) scalar product of vectors in \mathbb{R}^N . We will refer to the components of vectors on the plane also with indices x/y in the natural way.

¹⁰The average is meant to be over all realizations of the noise process, and the δ 's are to be interpreted in the usual way [90].

with (2.5) meaning that all statistical properties of these processes are identical, i.e. the resulting SDE's are identical. In particular, this means that the realization of the stochastic process $\vec{\xi}(t)$ has the same statistical weight as the realization $\hat{S}\vec{\xi}(t - T_S)$ [10, 98].

All symmetries (including the identity¹¹) of a given equation (2.1) form a mathematical group [96, 99–102], i.e. combinations of symmetries will be symmetries again (and the identity is a symmetry).

In the deterministic case $D = 0$, the consequence of (2.4) is that if we have a particular solution $\vec{q}(t)$ satisfying the S symmetric equation (2.1), we get

$$\vec{q}_S(t) := \hat{S}\vec{q}(t - T_S) + \vec{L} \quad (2.6)$$

also satisfying (2.1), i.e. $\vec{q}_S(t)$ is another solution, which we call the S *symmetry partner* of $\vec{q}(t)$, or, depending on the context, *the image of $\vec{q}(t)$ under S* . If

$$\vec{q}(t) = \vec{q}_S(t) \quad (2.7)$$

both partners are identical, and we will call $\vec{q}(t)$ S symmetric. Otherwise, there will be up to $m_S \in \mathbb{N} \cup \infty$ symmetry partners with m_S being the smallest number (or infinity) for which $S^{m_S} = 1$, and we will call $q(t)$ a *spontaneous symmetry breaking* solution.

If (2.1) furthermore satisfies (2.5), each trajectory of (2.1), belonging to a particular realization of the stochastic process, and its S symmetry partner, belonging to the realization $\hat{S}\vec{\xi}(t - T_S)$ of the stochastic process, will have equal weight [10, 98].

For our purposes, the main consequence of the symmetry partner solutions is that averages will satisfy the symmetry. In particular, the average (transport) velocity (or current)

$$\vec{v} := \left\langle \dot{\vec{q}} \right\rangle_{\vec{\xi}(t), t, \vec{q}(t_0)} = \lim_{t \rightarrow \infty} \frac{\vec{q}(t) - \vec{q}(t_0)}{t - t_0} \quad (2.8)$$

(where the average is over time, initial conditions and all realizations of the stochastic process, and the second equality due to ergodicity) will satisfy the symmetry since for each trajectory¹² contributing to that average, its symmetry partner contributes with the same weight but inversed (under the symmetry) contribution¹³ [10]:

$$\hat{S}\vec{v} = \vec{v}. \quad (2.9)$$

This is the formal way of saying that currents transverse to the symmetry vanish. \vec{v} is an eigenvector of \hat{S} to the eigenvalue 1 (we ignore the trivial case of $\vec{v} = 0$). A special kind of current not captured in this picture are vortex currents. See e.g. [97] for a discussion thereof.

Tacitly requiring (2.5) from now on, we furthermore focus on the deterministic part of (2.1) when discussing the symmetry properties of (2.1).

¹¹Which we write as 1 irrespective of the set it operates on.

¹²We will refer to specific solutions of (2.1) as trajectories.

¹³Alternatively, one can consider the distributions directly, and thus the corresponding Fokker-Planck equation [90, 91]. Discrete symmetries translate into symmetries of the Fokker-Planck equation, with supersymmetry [98] being an exception.

2.3 Spatial symmetries of a square lattice

The main types of spatial symmetries considered in this work will be reflection symmetries, possibly combined with translations of time. Our main examples in spatially two dimensional dynamics will be the symmetries of a square lattice (mapping the lattice onto itself), i.e. those of a force field $\vec{F}(\vec{r}) = -\nabla U(\vec{r})$ being the gradient of a potential with square lattice symmetry [103] and $\vec{q} = \vec{r} = (x, y)$ ¹⁴. If each lattice site (i.e. the “atoms” of the lattice) satisfies these symmetries, the system will be symmetric with respect to these symmetries. For the potential this results in

$$U(\hat{S}\vec{r} + \vec{L}) = U(\vec{r}). \quad (2.10)$$

We will call such a potential (spatially) (\hat{S}, \vec{L}) symmetric, or short \hat{S} ¹⁵ symmetric, and the derived force field $-\nabla U(\vec{r})$ (spatially) \hat{S} symmetric. The motion of a particle moving in such a potential is described by a SDE of the form (2.1) according to Newton’s law and the fluctuation dissipation theorem [90].

	\hat{S}_x	\hat{S}_y	\hat{S}_{xy}	$\hat{S}_0 = \hat{S}_x \circ \hat{S}_y$	$\hat{S}_{\frac{\pi}{2}} = \hat{S}_y \circ \hat{S}_{xy}$
$\hat{S}\vec{r}$	$(x, -y)$	$(-x, y)$	(y, x)	$(-x, -y)$	$(-y, x)$
m_S	2	2	2	2	4
$\vec{v} = (v_x, v_y)$	$v_y = 0$	$v_x = 0$	$v_x = v_y$	$\vec{v} = 0$	$\vec{v} = 0$

Table 2.1: Some linear symmetries of a two dimensional square lattice, their action on $(\vec{r}) = (x, y)$, m_S of the implied symmetry of the dynamics, and their consequences for the average velocity when no other forces are at work. The coordinate frame is chosen such that $\vec{L} = 0$ [100].

These linear symmetries have a severe impact on the average velocity (2.8), as shown in table 2.3. On the other hand, if the dynamics are such that all relevant symmetries are broken, Curie’s principle implies that, in general, the affected component of \vec{v} will not be zero under non-equilibrium conditions [10].

Furthermore, we have translational symmetries of the lattice, each shifting one component of \vec{q} by the lattice spacing in that direction. Note that unless we restrict our dynamics (e.g. to a torus¹⁶) a symmetry consisting only of a translation, i.e. $S = \left((1, \vec{L}), (1, 0)\right)$, has $m_S = \infty$.

2.4 Symmetries of a periodic driving force

We will consider the special case of rocking and pulsating driving forces, i.e. we restrict $\vec{Q}(\vec{q}, t)$ to be of the form

$$\vec{Q}(\vec{r}, t) = b(t) \cdot \vec{Q}(\vec{r}) + \vec{A}(t). \quad (2.11)$$

¹⁴Note that we will consider all components of $\vec{q} = \vec{r}$ to be spatial coordinates, and the symmetries affecting all components, i.e. we consider overdamped dynamics. Generalizations to non-spatial components of \vec{q} (e.g. inertial dynamics) or symmetries not affecting all components are obvious.

¹⁵If we can, we will choose the coordinate systems such that $L = 0$ [10].

¹⁶I.e., we consider some components of \vec{q} modulo some period. Geometrically, the resulting phase space is a torus, which we will call our unit cell. We will tacitly do so if the dynamics are periodic unless otherwise noted, or specifically referring to parts of phase space outside the unit cell.

$\vec{A}(t)$ is called a rocking drive, $b(t) \cdot \vec{Q}(\vec{r})$ is called a pulsating, or flashing, potential, and we will call $b(t)$ a (scalar) pulsating drive for short. Note that we use the same symbol \vec{Q} for both vector fields since the number of the arguments is sufficient to differentiate both. If the vector field $\vec{Q}(\vec{r})$ is (spatially) (\hat{S}, \vec{L}) symmetric, $b(t)$ does not affect this symmetry but $\vec{A}(t)$ may affect the symmetry. If

$$\hat{S}\vec{A}(t) = \vec{A}(t), \quad (2.12)$$

i.e. $\vec{A}(t)$ is in the 1 eigenspace of \hat{S} (for all t), the dynamics are $S = ((\hat{S}, \vec{L}), (1, 0))$ symmetric. If $\vec{A}(t)$ is not in the 1 eigenspace of \hat{S} , (2.4) can only be satisfied by the choice of $(1, T_S)$ to be such that

$$\hat{S}\vec{A}(t) = \vec{A}(t + T_S). \quad (2.13)$$

This in turn requires that

$$\hat{S}b(t)\vec{Q}(\vec{r}) = b(t + T_S)\vec{Q}(\hat{S}\vec{r} + \vec{L}), \quad (2.14)$$

i.e. the time shifts of the pulsating drive and the rocking drive can not be chosen independently, putting a restriction on a simultaneously rocking and pulsating potential (or allowing for another way of breaking symmetry).

Without further specifying $\vec{A}(t)$, we cannot go into more detail than (2.13)-(2.14). Therefore, we will focus on a few examples. A purely rocking drive with synchronized components, i.e. $b(t) = 1$ and $\vec{A}(t) = \vec{A}a(t)$ with the direction \vec{A} and the real valued drive protocol $a(t)$, is symmetric if either $\hat{S}\vec{A} = \vec{A}$, i.e. above discussed situation and (2.12), or $\hat{S}\vec{A} = -\vec{A}$ and $a(t + T_S) = -a(t)$ due to orthogonality of \hat{S} . From the latter it follows that $a(t + 2T_S) = a(t)$, i.e. $\vec{A}(t) = \vec{A}(t + 2T_S)$ is periodic with period $T = 2T_S$. Symmetries of both kinds will be discussed in chapters throughout this work, see e.g. [4].

Another important example is that of a periodic symmetric elliptic drive, breaking vorticity symmetry [97] in general. Then the symmetry \hat{S} may cycle through the components of $\vec{A}(t)$, with T_S compensating. Consider a two dimensional dynamics with $b(t) = 1$, $T_S = \frac{T}{4}$, $\hat{S}_{\frac{\pi}{2}}$. Then, $\vec{Q}(\hat{S}_{\frac{\pi}{2}}\vec{r}) = \hat{S}_{\frac{\pi}{2}}\vec{Q}(\vec{r})$ and $A_1(t + T) = A_1(t) = -A_1(t + \frac{T}{2}) = A_2(t + \frac{T}{4}) = -A_2(t + \frac{T}{4} + \frac{T}{2})$. This situation is considered in e.g. [104] and a hexagonal lattice symmetry is considered in [105–107].

2.5 Some examples of spatio-temporal symmetries

2.5.1 Spatially one dimensional dynamics

First, we will discuss the spatially one dimensional inertial dynamics of a point particle with mass M , coordinate x and velocity \dot{x} moving in the pulsating force field $F(x) = -b(t)U'(x)$ of a periodic and symmetric potential $U(x) = U(-x)$ ¹⁷, subjected to a rocking drive $A(t)$, friction force $-\eta\dot{x}$ and Gaussian white noise $\xi(t)$. The dynamics are given by (2.1) and setting $\vec{q}(t) = (x(t), \dot{x}(t))$, $\vec{Q}(\vec{q}, t) = \left(\dot{x}, \frac{-\eta\dot{x} + b(t) \cdot U'(x) + A(t)}{M}\right)$ and $D = \text{diag}\left(0, M^{-1}\sqrt{2\Gamma}\right)$ ¹⁸. The only spatial symmetry leading to a vanishing current is

¹⁷We have set possible shifts L to zero by our choice of the coordinate system [10].

¹⁸I.e. $\text{diag}(d_1, d_2, \dots, d_N)_{ij} = \delta_{ij}d_i$.

$\hat{S}_0(x, \dot{x}) = (-x, -\dot{x})$. The associated symmetry transformation is

$$S_0(x, \dot{x}, t) = (-x, -\dot{x}, t + \frac{T}{2}) \quad (2.15)$$

with $A(t + T) = A(t) = -A(t + \frac{T}{2})$ and either

$$U(x) = U(-x) \text{ and } b(t + \frac{T}{2}) = b(t) \quad (2.16)$$

or

$$U(x) = -U(-x) \text{ and } b(t + \frac{T}{2}) = -b(t) = -b(t + T), \quad (2.17)$$

and if $A(t) = 0 \forall t$, there is no requirement to $b(t)$.

In the two limits $M = 0$ or $\eta = 0$ of the particle dynamics, $s_t = -1$ symmetries can be applied, but care has to be taken. For simplicity we consider only $b(t) = 1$. In overdamped dynamics ($M = 0$), supersymmetry [97, 98], i.e. $s_t = -1$, $U(x) = -U(x + \frac{L}{2})$ and $A(-t) = -A(t)$, leads to a vanishing current but that result cannot be extended to higher dimensions, as the time reflection induces a change of stability. Only the low dimensional phase space of a one dimensional dynamics makes the symmetry work [108]. In the Hamiltonian limit $\eta = 0$, a symmetry with $s_t = -1$ requiring $\vec{A}(-t) = \vec{A}(t + T_S)$ is at work, leading to a vanishing current [97, 108–110] for a certain part of phase space.

2.5.2 Spatially two dimensional dynamics

Our second example are the overdamped dynamics of a point particle in a square lattice potential $U(\vec{r})$ with symmetries as shown in table 2.3, and driven out of equilibrium by a rocking drive $\vec{A}(t)$. The dynamics are given by (2.1) and setting $\vec{q}(t) = \vec{r}(t) = (x(t), y(t))$ to be the particle coordinate at time t , $\vec{Q}(\vec{q}, t) = -\vec{\nabla}U(\vec{q}) + \vec{A}(t)$ and $D = \text{diag}(\sqrt{2\Gamma}, \sqrt{2\Gamma})$. Our discussion can be extended to a pulsating potential or inertia forces along the lines of section 2.5.1. Geometrically, \hat{S}_x , \hat{S}_y and \hat{S}_{xy} correspond to reflections across lines, the x axis, the y axis and the separatrix $x = y$ respectively. \hat{S}_0 is a point reflection through the origin and $\hat{S}_{\frac{\pi}{2}}$ is a rotation by 90° . If the periodic drive respects these symmetries as discussed in section 2.4, we get the symmetries of the particle dynamics. Some examples are shown in table 2.2.

	S_x	S_y	S_{xy}
$S(x, y, t)$	$(x, -y, t + T_S)$	$(-x, y, t + T_S)$	$(y, x, t + T_S)$
m_S	2	2	2
$\vec{v} = (v_x, v_y)$	$v_y = 0$	$v_x = 0$	$v_x = v_y \frac{T}{2}$
$A_x(t + T_S)$	$A_x(t)$	$-A_x(t)$	$A_y(t)$
$A_y(t + T_S)$	$-A_y(t)$	$A_y(t)$	$A_x(t)$
T_S	$\frac{T}{2}$	$\frac{T}{2}$	$\frac{T}{2}$

	S_0	$S_{\frac{\pi}{2}}$
$S(x, y, t)$	$(-x, -y, t + \frac{T}{2})$	$(-y, x, t + \frac{T}{4})$
m_S	2	4
$\vec{v} = (v_x, v_y)$	$\vec{v} = 0$	$\vec{v} = 0$
$A_x(t + T_S)$	$A_x(t)$	$-A_y(t)$
$A_y(t + T_S)$	$-A_y(t)$	$A_x(t)$
T_S	$\frac{T}{2}$	$\frac{T}{4}$

Table 2.2: Some symmetries of an overdamped particle moving in a two dimensional square lattice potential and subjected to a rocking drive $\vec{A}(t)$. The symmetries are shown in table 2.3, their action on a phase space vector $(\vec{r}, t) = (x, y, t)$, m_S , the constraint put on the average velocity $\vec{v} = (v_x, v_y)$, the requirements on the rocking drive $\vec{A}(t) = (A_x(t), A_y(t))$ for a symmetry to be at work, and the value of T_S with respect to the period T of the rocking drive. Note that T_S may be zero if the rocking drive satisfies (2.12). In all other cases, the presence of the symmetry implies periodicity.

2.5.3 Rigid bodies in two dimensional potentials and chirality

Our last example are the dynamics of rigid bodies (molecules) on a symmetric surface. We consider a molecule to be an ensemble of N different point particles (monomers) coupled to each other via suitable interaction potentials depending only on the distance of the monomers, and of which the limit of stiff coupling is taken. The interaction potential is invariant under all Euclidean transformations affecting all monomers equally, and the symmetries of the potential will be symmetries of the equations of motion along the lines of section 2.2 before we take the limit of stiff coupling. That limit is singular in that the interaction potential may have several equilibrium configurations. This corresponds to a specific molecule having different possible configurations, between which switches are extremely rare under the assumed circumstances. Therefore, not all Euclidean symmetries of the potential “survive” the limit of rigid coupling. Only those symmetries of the potential that map the chosen equilibrium configuration onto itself will be symmetries of the rigid molecule dynamics.

Reflection symmetries are of special interest in that context. Rigid molecules which are identical to their image in a mirror, i.e. there is a true reflection symmetry¹⁹ which maps the molecule onto itself, are called *achiral*. Molecules that are not identical to their images in any mirror are called *chiral* [5, 111–113]. These symmetries are of particular importance in biology, chemistry and medicine [69, 70].

The overdamped dynamics of a rigid molecule consisting of N monomers with friction coefficients γ_i and positions \vec{x}_i in a two dimensional potential (i.e. constrained to two spatial dimensions) can be described by one vector \vec{X} being a suitable linear combination of the N monomer positions \vec{x}_i and one angle ϕ [114] forming a three dimensional phase space with elements $\vec{q} = (\vec{X}, \phi)$. For the dynamics of the rigid molecule only the symmetries of this reduced description are relevant. They follow along the same lines as in section 2.2, i.e. (2.4). Defining [5, 67, 68, 79] (see chapter 7):

$$\vec{X}(t) = \sum_{i=1}^N \frac{\gamma_i}{\gamma} \vec{x}_i(t) \quad (2.18)$$

$$\vec{y}_i(t) = \vec{x}_i(t) - \vec{X}(t) = \mathbf{O}(\phi(t)) \vec{y}_i(0) \quad (2.19)$$

with $\phi(t) = \phi_i(t) - \phi_i(0) = \text{atan} \left(\frac{y_{iy}(t)}{y_{ix}(t)} \right) - \phi_i(0) \forall i \in [1, N]$, $\gamma = \sum_{i=1}^N \gamma_i$, $\gamma_\phi = \sum_{i=1}^N \gamma_i \vec{y}_i^2$ and $\mathbf{O}(\phi) = \begin{pmatrix} \cos(\phi) & -\sin(\phi) \\ \sin(\phi) & \cos(\phi) \end{pmatrix}$, our equations of motion read

$$\dot{\vec{X}}(t) = \frac{\sum_{i=1}^N \vec{F}(\vec{x}_i(t), t)}{\gamma} + \vec{\zeta}(t), \quad (2.20)$$

$$\dot{\phi}(t) = \frac{\vec{e}_z \cdot \sum_{i=1}^N \vec{y}_i(t) \times \vec{F}(\vec{x}_i(t), t)}{\gamma_\phi} + \zeta_\phi(t). \quad (2.21)$$

We have temporarily embedded the vectors in three dimensions to get a short notation for (2.21). The $(\vec{\zeta}, \zeta_\phi)$ are independent Gaussian white noises (see chapter 7), the $\vec{y}_i(0)$, $i \in [1, N]$, define the reference configuration and $\phi(t)$ is the rotation angle with respect to

¹⁹The symmetry cannot be represented by a combination of other symmetries not involving a reflection.

the reference configuration. Together with (2.18)-(2.19), the right hand sides of (2.20)-(2.21) define $\vec{Q}(\vec{q}, t)$. Our analysis applies equally to different choices of $\vec{X}(t)$, as long as $\vec{X}(t)$ is not changed by permutation of “identical” monomers, which we will define below. The choice of the reference configuration $(\vec{y}_i(0))$, $i \in [1, N]$ is arbitrary, but once made, we have to keep it fixed.

To identify the symmetries of a rigid molecule in a potential, we proceed as follows. Mathematically, the set of monomer coordinates can be interpreted as an unordered set of colored points $\{(\vec{x}_i, a_i)\}$ [113], the color being the physical properties of the monomers (i.e. mass, friction coefficient (shape), charge etc.). Using that approach, one can identify the symmetries of the rigid molecule in free space, i.e. all (spatial) Euclidean transformations (affecting only the coordinates of the colored points) which map the set of colored points onto itself. These transformations map the given equilibrium configuration of the non-stiff interaction potential onto itself, up to permutations of identical monomers. Choosing a suitable coordinate frame of the free molecule and assuming bounded molecules in two dimensions, these symmetries applied to the reduced description by $\vec{q} = (\vec{X}, \phi)$ yield symmetries of the dynamics.

If the free molecule has a rotation symmetry by an angle θ , $\mathbf{O}(\theta)$, we get translational symmetry of the ϕ coordinate:

$$\vec{Q}(\vec{X}, \phi + \theta) = \vec{Q}(\vec{X}, \phi) \quad (2.22)$$

by directly inserting the rotated molecule configuration $\mathbf{O}(\theta)\vec{x}_i$ in (2.20)-(2.21).

If the potential has a rotation symmetry $\hat{S} = \mathbf{O}(\theta_S)$, i.e. $\hat{S}\vec{F}(\vec{x}, t) = \vec{F}(\hat{S}\vec{x} + \vec{L}, t + T_S)$, we get a rotation symmetry of the rigid molecule dynamics. Applying \hat{S} yields a new valid configuration of the rigid molecule, i.e. $\hat{S}\mathbf{O}(\phi)\vec{y}_i = \mathbf{O}(\phi + \theta_S)\vec{y}_i$. Inserting $\hat{S}\vec{x}_i$ into (2.18)-(2.21), we get the symmetry S' of the rigid molecule dynamics (which is induced by the rotation \hat{S} along with the translations L and T_S):

$$S'((\vec{X}, \phi), t) = ((\hat{S}\vec{X} + \vec{L}, \phi + \theta_S), t + T_S), \quad (2.23)$$

and S' satisfies (2.2) for $\vec{Q}(\vec{q}, t)$ as defined by (2.18)-(2.21).

Next, we consider a reflection symmetry of the potential. It is sufficient to consider \hat{S}_x , i.e. $\vec{F}(\hat{S}_x\vec{x} + \vec{L}, t + T_S) = \hat{S}_x\vec{F}(\vec{x}, t)$ is reflection symmetric across the x axis. All other reflection symmetries of $\vec{F}(\vec{x})$ can be constructed from \hat{S}_x using rotations and translations. Applying the symmetry to the monomer positions, we can construct the new phase space vector if $\hat{S}_x\mathbf{O}(\phi)\vec{y}_i(0) = \mathbf{O}(\phi')\vec{y}_{i'}(0)$ with a new angle ϕ' and a permutation of the indices on the right hand side respecting color, i.e. $a_i = a_{i'}$, which requires the free rigid molecule to have a reflection symmetry. Assuming that reflection symmetry to be a reflection across the x axis without loss of generality²⁰, we obtain from basic planar geometry $\phi' = -\phi$. A reflection across an arbitrary line passing through the origin can be written as $\hat{S} = \mathbf{O}(\theta_S)\hat{S}_x\mathbf{O}(-\theta_S)$ where θ_S is the angle enclosed by the reflection line and the x axis. We get for a general (spatial) reflection symmetry \hat{S} of $\vec{F}(\vec{x})$

$$S'((\vec{X}, \phi), t) = ((\hat{S}\vec{X} + \vec{L}, 2 \cdot \theta_S - \phi), t + T_S) \quad (2.24)$$

²⁰In other words, we fix the reference configuration.

as the induced symmetry of the rigid molecule satisfying (2.2) because the reflection inverts the sign of the cross product in (2.21). Moreover, we get for its spatial part

$$\hat{S}'(\vec{X}, \phi) = (\hat{S}\vec{X}, -\phi), \quad (2.25)$$

which is of interest in particular for the average velocity (see below).

Thus, in a two dimensional potential with the symmetries as shown in table 2.3, the dynamics of an achiral molecule is reflection symmetric with respect to (the symmetries induced by) \hat{S}_x , \hat{S}_y and \hat{S}_{xy} (in the sense of the spatial symmetry applied to all monomers, followed by some suitable Euclidean symmetry not involving any reflections across lines), while that of a chiral molecule is not. Note that the dynamics will still be symmetric with respect to the reflection across a point \hat{S}_0 or the rotation $\hat{S}_{\frac{\pi}{2}}$ and combinations thereof (again to be understood in the sense outlined above).

A crucial observation is that a reflection maps a chiral molecule onto its mirror image, i.e. symmetry (or chiral) partner. Therefore, if the potential has a reflection symmetry, the dynamics of a chiral molecule and its partner will be mirror images of each other. This applies in particular to their average velocities. In the overdamped dynamics (with obvious generalizations to finite mass dynamics) of an achiral rigid molecule in a potential having a reflection symmetry \hat{S} , we get

$$\hat{S}'\vec{v} = \vec{v} \quad (2.26)$$

for its average velocity $\vec{v} = (v_x, v_y, v_\phi)$ with $v_{x/y} = \langle \dot{X}_{x/y} \rangle$ and the average angular velocity $v_\phi = \langle \dot{\phi} \rangle$. In particular, this means that the average angular velocity has to vanish. Considering a chiral molecule and its symmetry partner and denoting their average velocities as $\vec{v}_{L/R}$ ²¹, we get

$$\hat{S}'\vec{v}_L = \vec{v}_R, \quad (2.27)$$

i.e. the symmetry maps the average velocities of the chiral partners onto each other. Using this property, the transport properties of chiral molecules can be controlled [5, 67] (see chapter 7).

2.6 Symmetry breaking bifurcations

An important consequence of symmetries in the noise free $D = 0$ dynamics are *symmetry breaking bifurcations* [100, 115]. Let $\vec{Q}_\mu(\vec{q}, t)$ depend sufficiently smoothly on a parameter μ and have a symmetry S with $m_S = 2$ for all values of μ . Let $\vec{q}_\mu(t) = \vec{q}_\mu(T_q + t)$ be a S symmetric and stable²² periodic solution (periodic orbit) of (2.1), and thus a stable fixed point of the T_q -stroboscopic map Θ_{T_q} ²³. A common bifurcation occurring in such dynamical systems is a symmetry breaking bifurcation [87, 115]. At $\mu = 0$, $\vec{q}_\mu(t)$

²¹I.e. \vec{v}_L is the average velocity of the molecule described by $\{(\vec{x}_i, a_i)\}$ and \vec{v}_R that of the molecule described by $\{(\hat{S}\vec{x}_i, a_i)\}$.

²²I.e. a trajectory starting sufficiently close to the periodic orbit converges to the periodic orbit for sufficiently long times.

²³The stroboscopic map (or time T map) Θ_T is the map (derived from the vector field) that iterates time by T , i.e. $\Theta_T(\vec{q}, t_0) = \vec{q}(T + t_0)$ with $\vec{q}(t_0) = \vec{q}$ being the trajectory with initial condition \vec{q} at time

undergoes a change of stability (becoming unstable) by one of its Floquet multipliers²⁴ crossing the unit circle (or equivalently for the Lyapunov exponents [87]). Simultaneously a pair of new solutions of (2.1), \vec{q}_\pm , springs into existence for $\mu > 0$ with opposite stability properties (i.e. stable) and *spontaneously breaking S symmetry*, i.e. $\vec{q}_-(t)$ is the image of $\vec{q}_+(t)$ under S and $\vec{q}_-(t) \neq \vec{q}_+(t)$. This situation is called a (supercritical) *pitchfork bifurcation* [115] or *symmetry breaking bifurcation*. If the pair of symmetry breaking orbits exists already for $\mu \leq 0$ (but unstable) and “vanishes” for $\mu > 0$, the bifurcation is called *subcritical*, and can lead to hysteresis if there is another stable branch²⁵ of the bifurcation connected to the symmetry breaking unstable branches via saddle node bifurcations, see [115] or figure 4.7(b1) for an example. Note that in higher dimensions the stability properties discussed need only to apply to one direction in phase space, i.e. one eigenspace of the Floquet operator. Considering the whole spectrum of the Floquet operator, the solutions considered may well be all linearly unstable in another direction, and thus unstable.

An important consequence of spontaneous symmetry breaking is that if one of the spontaneous symmetry breaking objects undergoes some change (i.e. bifurcation), its symmetry partner(s) will undergo the same change. E.g., if a spontaneous symmetry breaking attractor²⁶ collides with a spontaneous symmetry breaking periodic orbit, its

t_0 . By choosing a different starting time, different stroboscopic mappings are obtained. Unless otherwise noted, we will always refer to the $t_0 = 0$ map and drop the t_0 dependence. In a periodically driven system, i.e. if $\vec{Q}(\vec{q}, t + T) = \vec{Q}(\vec{q}, t)$, we will refer to the natural stroboscopic map as $\Theta = \Theta_T$.

The stroboscopic map is a special (and very convenient) case of a Poincaré map [87, 115]. We will consider more general Poincaré maps only for autonomous (i.e. time independent) vector fields. To define a Poincaré map, one needs a $N - 1$ dimensional manifold M (the Poincaré surface of section) transverse to the vector field, i.e. the vector field is nowhere tangent to M . The Poincaré map maps each point \vec{q} on M to the next intersection of the trajectory passing through \vec{q} with M .

Thus, the dynamics of a continuous time differential equation are equivalent to the dynamics of an invertible map of lower dimension.

²⁴For an exhaustive treatment see [116]. The Floquet multipliers are the eigenvalues of the Jacobian $\frac{d\Theta_{T_q}}{d\vec{q}} \Big|_{\vec{q}}$ (Floquet operator), where \vec{q} is the fixed point of Θ_{T_q} corresponding to the periodic orbit (thus the Floquet multipliers are the Lyapunov numbers of the stroboscopic map). A periodic orbit is stable iff all Floquet multipliers are in the interior of the unit circle and unstable if at least one Floquet multiplier is outside. If a Floquet multiplier is on the unit circle, the orbit is marginally stable in that direction, i.e. critical, which is the case at a bifurcation. The same applies to a fixed point of a general (invertible) map instead of the stroboscopic map, but different names are used then, see [87].

²⁵We call the family of periodic orbits $(\mu, q_\mu(t))$ a branch of the bifurcation. E.g. at the symmetry breaking bifurcation two new branches due to $\vec{q}_\pm(t)$ are created. Considering the stroboscopic map, and possibly phase space reduced to a torus, each branch corresponds to curves $(\mu, \vec{q}_\mu(t_0 + n \cdot T))$. If $\vec{q}_\mu(t)$ are periodic orbits with period T , i.e. fixed points of the stroboscopic map, it corresponds to only one curve. Period two fixed points of the stroboscopic map (i.e. fixed points of the two times iterated stroboscopic map Θ^2) correspond to two curves, and so forth for orbits of higher periodicity. Non periodic orbits result in an infinite number of curves, and thus more or less complicated structures. In particular, the invariant measure on a chaotic attractor (see below) is usually approximated by the density of the curves in phase space [87]. Plotting only one component of the branches versus one parameter, one obtains the usual bifurcation diagrams [117], see e.g. figure 4.7.

²⁶An attractor [87, 115, 118] is a closed invariant set \mathcal{A} (i.e. for each $(\vec{q}, t) \in \mathcal{A}$, the trajectory passing through (\vec{q}, t) is contained in \mathcal{A} for later and earlier times), which is contained in an open and absorbing subset of phase space \mathcal{U} (i.e. $\mathcal{A} \subset \mathcal{U}$, and for each $(\vec{q}, t) \in \mathcal{U}$, the trajectory passing through (\vec{q}, t) is contained in \mathcal{U} for later times), and \mathcal{A} attracts all trajectories in \mathcal{U} , i.e. $\lim_{t \rightarrow \infty} \text{distance}((\vec{q}(t), t), \mathcal{A}) = 0$ for all trajectories passing through \mathcal{U} , and the distance is the Euclidean distance [119, 120]. The largest

symmetry partner(s) will collide with the symmetry partner(s) of that periodic orbit. If that periodic orbit is symmetric, all the symmetry partners of the spontaneous symmetry breaking attractor will collide with the same periodic orbit, resulting in an *attractor merging crisis* (or its reverse):

Let \mathcal{A}_\pm be S symmetry breaking (chaotic²⁷ attractors of $\vec{Q}_\mu(\vec{q}, t)$ at $\mu < 0$, i.e. $S\mathcal{A}_+ = \mathcal{A}_-$ in the sense that each orbit $\vec{q}_+(t)$ on \mathcal{A}_+ is mapped onto an orbit $\vec{q}_-(t)$ on \mathcal{A}_- . At $\mu = 0$ let both attractors undergo boundary crises²⁸ simultaneously (as both attractors are each other's image under the action of S this is always the case) such that the basin of attraction of \mathcal{A}_- can be reached from \mathcal{A}_+ (and vice versa due to symmetry), and no other "new" regions of phase space except for the unstable manifolds connecting both attractors become accessible. Then both attractors form a "new" S symmetric chaotic attractor for $\mu > 0$ [87, 115, 123, 124]. See figure 4.7(b5) for an example. We will call the reverse bifurcation also an attractor merging crisis. Again, in higher dimensions (at least 3, which is always the case in this work) the same consideration applies if the attractors have another "unstable" direction (i.e. an unstable manifold) not involved in the bifurcation, and the objects may be chaotic repellers²⁹ (with the basins of attraction replaced by the sticky regions [126]).

[127] shows that under certain circumstances, i.e. spatially one dimensional inertial dynamics of a particle subjected to a periodic driving force, a symmetry breaking bifurcation may be a necessary prerequisite for period doubling bifurcations, and thus for the Feigenbaum transition to chaos [121, 122].

For symmetries with higher m_S , these bifurcations will involve "more" symmetry breaking branching solutions/attractors. We will not consider this situation in more detail, but this may be important in the understanding of the transport properties of dynamics with such symmetries, e.g. [104–107].

Spontaneous symmetry breaking in itself may be used for separation purposes if the spontaneous symmetry breaking attractors have spatial coordinates differing enough to allow for separation. See [79] for an idea in that direction in the context of chiral separation.

of all such sets is the *basin of attraction* of \mathcal{A} .

²⁷For a thorough discussion of chaotic attractors, see e.g. [87, 115, 118]. For our purposes, a chaotic attractor is non-periodic and contains an infinite number of periodic orbits, the dynamics on the attractor are given by the unstable manifolds of these periodic orbits and trajectories on the attractor have positive Lyapunov exponents [87] (i.e. two trajectories starting with almost identical initial conditions diverge). The chaotic attractors considered in this work are usually generated from a Feigenbaum or period doubling cascade [121, 122] at some point in their "lives", but may contain additional structures due to further bifurcations.

²⁸I.e. the attractor touches its basin of attraction [87].

²⁹E.g., if a chaotic attractor undergoes a boundary crisis, typical trajectories on the attractor will leave the attractor, but there may be differently created chaotic repellers. The resulting *repelling* phase space object is called a chaotic repeller, and the associated behaviour is called *transient chaos*. One important property is that the lifetime of *chaotic transients*, i.e. the average time trajectories spend on the chaotic repeller before leaving it, scales like $\tau_{\text{transient}} \propto (\mu - \mu_c)^{-h}$, where μ is a system parameter, μ_c is the value at which the chaotic repeller is created from a boundary crisis, and h is a scaling exponent, typically larger than $\frac{1}{2}$ [87, 123–126]. For a review, see [126].

2.7 Spontaneous symmetry breaking transport (SSBT)

For our purposes, the absence of transport currents in any other direction than the 1 eigenspace of a symmetry, cf. (2.9), is the most important consequence of that symmetry. Restricting ourselves to the directions orthogonal to the 1 eigenspace of the symmetry S (or rather, the 1 eigenspace of its spatial part \hat{S}) with $m_S = 2$ for simplicity, without noise individual orbits (and attractors) may carry transport transverse to the symmetry (i.e. a non-zero average velocity \vec{v} not in the 1 eigenspace of the symmetry). But they will always come as symmetry related pairs (each being the other's image under S) with

$$\vec{v}_+ = \hat{S}\vec{v}_- , \quad (2.28)$$

where we have used the $+/$ sign to differentiate between the symmetry partners. Thus we have *spontaneous symmetry breaking transporting attractors*, called *SSBT attractors* for short. One immediate consequence is that SSBT attractors enhance diffusion³⁰. Thermal noise averages over the pair of SSBT attractors. For small noise strengths this leads to a strongly enhanced diffusion because noisy trajectories will alternate between both attractors, and the diffusion coefficient diverges in the deterministic limit. If the SSBT attractors vanish at some bifurcations and their remains are correctly connected³¹, unbiased³² deterministic diffusion is found in the deterministic dynamics, with the deterministic diffusion coefficient scaling with the distance from the bifurcation [123, 130–136].

The simplest, but somewhat trivial, example of SSBT can be found in the Hamiltonian dynamics of a particle in free space. The dynamics are S_0 symmetric. If the particle has an initial velocity, its orbit will be transporting. Applying S_0 yields the orbit of the particle with opposite initial velocity, and we have a pair of SSBT orbits. Actually the same will still occur if a suitable periodic potential and drive are added in a less trivial manner, see e.g. [110]. Another well known and well studied example are zero crossing Shapiro steps [137], corresponding to periodic (or phase-locked³³) orbits of a

³⁰Trajectories for different realizations of the noise process and/or initial conditions are different, such that for sufficiently large times (we consider only one dimension or component) the Einstein relation $\langle (q(t) - \langle q(t) \rangle)^2 \rangle = 2D^*t$ holds [8, 90, 128] with the non-zero diffusion coefficient D^* . Anomalous diffusion refers similar relations with different algebraic relations [129]. Due to deterministic chaos, D^* may already be non-zero in the absence of noise, resulting in *deterministic diffusion*, cf section 4.11.1 and section 4.22.

³¹They may be connected via the unstable manifolds of some periodic orbits that are part of the attractors and allow trajectories to escape from the (former) attractors. Furthermore, the remains of the SSBT attractors have to be part of the resulting attractor. The simplest such situation is a pair of chaotic SSBT attractors colliding via a symmetric unstable periodic orbit in an attractor merging crisis, see section 2.6. Other scenarios may involve transient chaotic objects connecting the former SSBT attractors or the former SSBT attractors merging with another chaotic attractor. E.g. two periodic attractors vanishing through tangent bifurcations and merging with a previously existing chaotic repeller leads to intermittency [87]. If the periodic orbits are SSBT attractors, the resulting chaotic attractor will give rise to deterministic diffusion.

³²If the resulting attractor is not symmetric, biased deterministic diffusion results.

³³An attractor is called phase-locked if there are T^*, l, \vec{L}^* such that

$$\left| \vec{q}(j \cdot T^* - t_0) - \vec{q}(t_0) - j \cdot \vec{L}^* \right| < l \quad (2.29)$$

for all $j \in \mathbb{N}$, and all trajectories $\vec{q}(t)$ on the attractor. E.g., a transporting period 1 orbit that advances an integer number of spatial periods (in each component of the position) in each temporal period of a

particle in a one dimensional periodic and symmetric potential subjected to a periodic and symmetric drive, i.e. the same situation as considered in e.g. [110] but in the presence of dissipation. Zero crossing Shapiro steps can be used to “create” various intriguing transport phenomena connected with *absolute negative mobility* [1, 63], see chapters 3-6. A third example is a long and narrow molecule (rod-like) with a reflection symmetry in a two dimensional periodic egg carton (e.g. see figure 4.1(b)) potential. The potential is S_x , S_y and S_{xy} symmetric, and the molecule is preferably aligned with the x or y axes³⁴. If the molecule is subjected to a constant weak bias force³⁵ breaking S_x and S_y symmetry but leaving the dynamics S_{xy} invariant, the molecule will move into a direction which has a positive scalar product with the direction of the bias force. If the bias force is weak enough, the molecule will remain aligned with the potential and move in the x or the y direction, depending on its initial configuration. As a result, we get a pair of SSBT attractors. Basically the same idea can be applied to less trivial molecules to sort chiral molecules [5], see chapter 7. Lastly, SSBT can arise as a spontaneous ratchet effect. [38] shows that an infinite number of interacting particles under non-equilibrium conditions may undergo a phase transition into a state of broken symmetry that leads to a spontaneous current, see also [29, 38–44], [138] show that a granular gas subjected to shaking may undergo a phase transition again leading to a state of spontaneously broken symmetry, which can be used to generate a spontaneous ratchet effect, and [139] show theoretically and [140] experimentally that a symmetric non-equilibrium driving force leads to a state of spontaneously broken symmetry of two pendula, or nanomechanical electron shuttles driven by a symmetric ac voltage in the experiment, which results in a spontaneous dc current across the device containing the pendula. q

To use SSBT to achieve “transport phenomena”, one usually breaks the symmetry S that is broken by SSBT by a small perturbation. Otherwise, the transport velocity will be zero, in which case one can use the less direct approach of diffusive sorting, which again relies on SSBT, see e.g. section 4.22 and section 7.7.2. In the case of a point particle in a potential the perturbation may be a small (constant) tilt of the potential (force) but also a parametric asymmetry of the potential. In the case of an extended body (i.e. the example of the rod-like molecules) this may be a parametric asymmetry of the molecule breaking its reflection symmetry. We now consider the family of dynamical systems implied by $\vec{Q}_\mu(\vec{q}, t)$, sufficiently smooth in μ . Let $\vec{Q}_0(\vec{q}, t)$ have a symmetry S (again with $m_S = 2$, but generalizations are obvious) that is broken for $\mu > 0$, i.e. $\vec{Q}_\mu(\vec{q}, t)$, $\mu > 0$ are not S symmetric. Moreover, we assume a pair of SSBT (or more generally spontaneous symmetry breaking) attractors³⁶ \mathcal{A}_\pm (as above) at $\mu = 0$. At $\mu = 0$ we have $S\mathcal{A}_\pm = \mathcal{A}_\mp$. If the situation at $\mu = 0$ is structurally stable, i.e. typical, we get

$$S\mathcal{A}_\pm \approx \mathcal{A}_\mp \quad (2.30)$$

time (with period T) and space (with period \vec{L}) periodic dynamical system is phase-locked with $T^* = T$ and $\frac{L_i^*}{L_i} \in \mathbb{Z}$ and each component of the average velocity is an integer multiple of the corresponding component of the fundamental velocity: $v_i = n \frac{L_i}{T}$, n integer. If that periodic orbit undergoes a period doubling cascade, the result will be a phase-locked chaotic attractor with $T^* = T$ and $\frac{L_i^*}{L_i} \in \mathbb{Z}$ [137]. The same applies with regard to well chosen Poincaré surfaces of sections in autonomous dynamics, see chapter 7.

³⁴Imagine a rod in an egg carton.

³⁵I.e. a tilt of the potential.

³⁶Generalizations to other (e.g. not stable) objects are obvious.

for $0 < \mu \ll 1$. This is to be interpreted in the sense that for sufficiently small μ each perturbed attractor can be obtained from the attractor at $\mu = 0$ by Taylor expansion in μ . For almost all initial conditions, orbits on both attractors will be rather “similar” either directly, in the case of periodic attractors, or statistically for non-periodic attractors. Moreover, all smooth properties of the attractors (i.e. smooth functions of all external parameters, such as the coordinate $\vec{q}(t^*)$ of some specific orbit at some specific time t^* on the attractor or the pseudopotential depth of attractors³⁷) will vary continuously under changes of μ until a bifurcation occurs. This applies particularly to discrete properties of the attractors (such as the periodicity of periodic orbits, or the average velocity in case of phase-locked orbits) which will be identical even for $\mu > 0$.

If $\vec{Q}_\mu(\vec{q}, t)$ additionally depends on some more external parameters, and calling the whole space of parameters the *parameter space*, the regions in parameter space in which the symmetry related pair of attractors undergoes bifurcations will be “similar”. We consider only one additional parameter for simplicity. We define the set (region) of parameter space enclosed by the set of parameters at which the attractors undergo bifurcations that change their stability to unstable, or where they vanish, their *region of existence* which we denote $\mathcal{G}_\pm(\mu)$ for the two attractors. At $\mu = 0$ the sets will be identical for both attractors, $\mathcal{G}_+(0) = \mathcal{G}_-(0) = \mathcal{G}_0$, and we assume \mathcal{G}_0 to be an interval. For small $\mu > 0$, the borders of $\mathcal{G}_\pm(\mu)$ will be lines in parameter space with different slopes. Around the borders of \mathcal{G}_0 , and for $\mu > 0$, typically there will be regions of parameter space in which only one of the symmetry partners³⁸ is stable. See figures 3.1 and 7.4 for examples. By choosing the “right” border, one can choose between the attractors. Assuming the solutions of the SDE to be dominated by these attractors for weak thermal noise, the transport behavior can be controlled.

In the example of a point particle in a periodic potential, one can choose between transport directions in the direction orthogonal to the 1 eigenspace of S . μ introduces some “preferred” direction in the system (such as a constant tilt of the potential), and the transport properties of the system will be dominated by the interplay of SSBT and μ , which may lead to nontrivial response behavior [1, 2, 4, 63, 92, 93]. In a similar context, SSBT of an infinite number of interacting point particles has been reported in e.g. [38, 40–44, 138] as a phase transition, again with concomitant nontrivial response behavior. Concerning the example chiral rod-like molecules, one can choose a border of \mathcal{G}_0 such that one chiral molecule is transported in the x direction and its mirror image in the y direction leading to separation [5] if μ is the chirality inducing “asymmetry”. That way, SSBT can be exploited to create a sensitive dependence of the transport properties on the system parameters (e.g. particle properties) needed for separation purposes. These considerations can be extended to the unstable objects left behind by the attractors outside their regions of existence. Typically, the escape times from these objects scale with the distance from the region of existence of the attractor [126, 146, 147], allowing for a similar treatment as above, see e.g. [2], Sec. V D.

³⁷The pseudopotential depth V_A is discussed in e.g. [141–145]. Basically, the mean escape time τ_{esc} from an attractor perturbed by a small amount of thermal noise of strength Γ scales like $\tau_{esc} \sim e^{\frac{V_A}{\Gamma}}$, i.e. it follows the same law as the escape of a particle from a potential well would. There are different models for the prefactor [144]. See also [2] for an investigation in the context of SSBT attractors.

³⁸Strictly speaking, the attractors are only symmetry partners at $\mu = 0$. We will call the two attractors symmetry partners also for $\mu > 0$, tacitly referring to their “similarity”, as discussed in this section.

2.8 Summary and conclusion

We have formally introduced symmetries in ordinary and stochastic differential equations and identified the simple symmetries relevant to this work, mainly those of a square lattice and a rocking drive. Considering different symmetry classes, the results of the remainder of this work can be extended in the same framework to other dynamics. SSBT attractors, i.e. a pair³⁹ of attractors carrying currents of opposite signs with respect to a symmetry⁴⁰ may be used to control the transport of Brownian particles. Without perturbing the symmetry, the enhancement of diffusion due to SSBT attractors can be used to sort particles. Weakly perturbing the symmetry, and thus “choosing” one of the SSBT attractors, the different particle species can be transported into opposite directions with respect to the symmetry. Due to the nonlinear interplay of SSBT, the perturbation and noise, the outcome of this interplay is nontrivial and can lead to an unexpected response behavior. The determination of this outcome in some special cases is the aim of this work.

In chapter 3 we will consider the dynamics of an inertial Brownian particle in a S_0 symmetric spatially one dimensional potential subjected to appropriate driving forces. Using SSBT, various absolute negative mobility related “unexpected” response behaviors of the particle can be explained [1–3]. In chapters 4–5 we consider the overdamped dynamics of a Brownian particle in a two dimensional symmetric square lattice potential and subjected to appropriate driving forces. Due to spontaneous symmetry breaking and SSBT, the particle can be directed into almost any direction, or an ensemble of different particles can be sorted simultaneously [4]. In chapter 6 we consider the dynamics of two coupled overdamped particles in a spatially one dimensional S_0 symmetric potential driven by a symmetric drive. We will show that SSBT can be used to generate the same “unexpected” response behaviors as discussed in chapter 3. In chapter 7 we consider the dynamics of chiral molecules in a two dimensional square lattice potential and show that SSBT can be used to separate the chiral partners, either by breaking all symmetries or by using diffusion enhancement in the presence of S_0 symmetry [5].

³⁹or more

⁴⁰in the sense that the symmetry maps the current of one attractor onto that of the other

Chapter 3

Spatially one dimensional dynamics

In this chapter we discuss spontaneous symmetry breaking transport (SSBT) in spatially one dimensional dynamics, starting with a brief introduction to SSBT of underdamped¹ Brownian particles. The main results are summarized in the brief account [1] and the long account [2], of which we include preprints² in sections 3.2-3.3. In section 3.4 we review the mechanism leading to SSBT induced absolute negative mobility (ANM) and its relation to the Bessel function approximation of Shapiro steps³. [137]. The effects predicted theoretically in [1] have been realized experimentally and published in [3], which we preprint in section 3.5. In section 3.6 we will discuss the method with which we have fitted the experimental data to the theoretical model and review in detail the mechanism which gives rise to ANM (or negative absolute resistance) in the experiment. We close this chapter by a brief discussion of how the fitting of experimental data to a theoretical model in [3] could be done in less than a minute instead of several days without much effort using a graphics processing unit (GPU) (section 3.7).

3.1 Introduction

Recently, anomalous transport behavior⁴, namely a Brownian particle moves uphill against an applied bias force in spatially one dimensional dynamics, has been found and explained by the presence of SSBT in the zero bias (symmetric) dynamics [1, 63]. This discovery has led to a series of publications [2, 148–150], has been demonstrated experimentally in [3], and has enabled the discovery of closely related effects due to colored noise [151], superimposed ratchet effects [92–95] or the same effects in a different system (i.e. a different potential) [94]. In spatially one dimensional dissipative systems SSBT has been known for a long time in the field of Josephson junctions [152] and has been explained within the picture of a single particle moving in a rocked washboard potential [153] onto which the dynamics of a Josephson junction can be mapped within the

¹I.e. the particle dynamics include inertia effects.

²The preprints are largely identical to the printed articles. The latter can be obtained via the publishers.

³ In short, Shapiro steps correspond to a single particle in a periodic potential synchronizing with an externally applied periodic driving force via the nonlinearity of the potential, resulting in the particle current v taking a rational value when appropriately normalized to the period of the drive and the period of the potential.

⁴See [51] for a review of some non-equilibrium response behaviors defying “linear” expectations.

RCSJ (resistively and capacitively shunted junction) model under certain circumstances [7, 64, 65]. In that field SSBT is more commonly known as zero crossing⁵ Shapiro steps [154] and has been particularly useful for zero bias voltage standards [137, 155].

In short, Shapiro steps correspond to a single particle in a periodic potential synchronizing with an externally applied periodic driving force via the nonlinearity of the potential, resulting in the particle current v taking a rational value when appropriately normalized, i.e.

$$v = \langle \dot{x} \rangle = \lim_{t \rightarrow \infty} \frac{1}{t} \int_{t_0}^t \dot{x}(t') dt' = \frac{n}{m} \frac{L}{\tau} \quad (3.1)$$

with L the period of the potential, τ the period of the periodic drive $n \in \mathbb{Z}$ and $m \in \mathbb{N} \setminus \{0\}$.

As has been detailed in chapter 2, if the potential and the drive are symmetric (and the dynamics are thus S_0 symmetric), zero crossing Shapiro steps are always found in pairs carrying currents of opposite signs. Upon perturbing the symmetry, the result is determined by the interplay of the perturbation, noise and the Shapiro steps and is thus influenced by the nonlinearity and broken thermal equilibrium, allowing for counterintuitive transport behavior not found in simpler (linear or equilibrium) dynamics. Our results are summarized in the following publications, the brief account [1] and a more detailed account [2]. In particular, the understanding of the remainder of this chapter requires the reading of [2], we will adopt the notation of [2] and refer to the model described by (1)-(2) of [2] throughout this chapter.

⁵Shapiro steps show up as regions of constant non-zero voltage in the current-voltage characteristics of Josephson junctions. In that picture the (bias) current corresponds to an applied bias force and the voltage to the average velocity. Hence, zero crossing means that a Shapiro step crosses the zero bias axis.

3.2 Preprint of [1]

D. Speer, R. Eichhorn, and P. Reimann, EPL **79**, 10005 (2007),
Copyright (2007) by EPLA

epl draft

Brownian motion: Anomalous response due to noisy chaos

D. SPEER, R. EICHHORN and P. REIMANN

Universität Bielefeld, Fakultät für Physik, 33615 Bielefeld, Germany

PACS 05.45.-a – Nonlinear Dynamics and nonlinear dynamical systems

PACS 05.40.-a – Fluctuation phenomena, random processes, noise, and Brownian motion

PACS 05.60.-k – Transport processes

Abstract. – We predict three different, quite unusual transport properties of an underdamped Brownian particle in the form of current and force of opposite signs. Their origin is a subtle interplay between the stability of coexisting attractors, noise induced metastability, and transient chaos. Numerical simulations are complemented by intuitive explanations of the basic mechanism and analytical approximations.

Introduction. – Due to thermodynamic stability conditions, when a system at thermal equilibrium is perturbed by an externally applied static force, it is bound to respond with a current whose direction is in accordance with that of the force. Things change drastically for systems far from equilibrium. For example, already an unperturbed non-equilibrium system may exhibit a current due to some kind of thermal ratchet effect [1]. Another example is given by unperturbed non-equilibrium systems without current (usually due to certain symmetry properties), which respond to a static bias with a permanent net transport opposite in direction to that of the bias. Such a quite astonishing anomalous response behavior has so far been experimentally observed in bulk GaAs [2], semiconductor heterostructures [3], and structured microfluidic systems [4]. On the theoretical side, investigations are based on dissipative quantum mechanical models [5], classical many particle systems [6], as well as single classical particle dynamics in more than one dimension [7,8], see also [9] for a recent review.

In our present Letter, we theoretically predict three closely related anomalous transport properties for a single Brownian particle in one dimension: (i) A dc-bias of either sign (but not too large modulus) generates a particle current of the opposite sign. (ii) For small dc-bias, the particle current is as usual, but changes sign upon increasing the bias, before returning to normal for even larger bias. (iii) For a given dc-bias, the behavior is as usual for low temperatures, but upon increasing the temperature, first turns anomalous and later again normal. Moreover, we show that such a system represents in a certain sense a “minimal model” and at the same time is

straightforward to realize experimentally. Upon completion of our present work, the above effect (i) has also been reported by Machura et al. in Ref. [10] (see also footnote [22] therein). While the qualitative findings in [10] agree with ours, the underlying physical mechanisms are quite different in the two cases. Moreover, quantitatively the effect is considerably more pronounced in our case. In other words, our present work is complementary to [10] in that a new physical mechanism for the above effect (i) is identified, and two additional new effects (ii) and (iii) are reported.

Model. – Our working model describes the Brownian motion of a particle $x(t)$ with mass M and friction coefficient η in a *symmetric, periodic* potential $V(x) = V(x+L) = V(-x)$,

$$M \ddot{x}(t) = -\eta \dot{x}(t) - V'(x(t)) + f(t) + F + \sqrt{2\eta T} \xi(t), \quad (1)$$

where $f(t) = f(t+\tau) = -f(t+\tau/2)$ is a *periodic, unbiased* driving, F a dc-bias, and the δ -correlated Gaussian noise $\xi(t)$ models thermal fluctuations with temperature T [11]. The quantity of main interest is the time and ensemble averaged velocity

$$v := \frac{\tau}{L} \left\langle \lim_{t \rightarrow \infty} \frac{1}{t} \int_0^t dt' \dot{x}(t') \right\rangle. \quad (2)$$

We mainly focus on the simplest example of harmonic $V(x)$ and $f(t)$ in dimensionless units such that

$$M = 1, \quad V(x) = -\cos x, \quad f(t) = A \sin(\omega t). \quad (3)$$

This very model is of relevance in many different contexts, such as Josephson junctions, superionic conductors,

charge density waves, fluxons, phase and mode locking [11] etc. and has been extensively studied with respect to noisy chaos and phase-locking [12, 13], stochastic resonance [14], escape processes [15] etc. An even much larger literature exists on special limits (vanishing M , η , T , f etc.) or generalizations (non-harmonic V or f , 2-dim. systems etc.) of the model (1,3), addressing various aspects of ratchet effects [1, 16, 17] and diffusive transport [11], to name but two examples.

Basic properties. – Assuming $\eta, T > 0$, the dynamics (1,3) is ergodic and hence the velocity (2) independent of initial conditions. For symmetry reasons, it follows that $F \mapsto -F$ implies $v \mapsto -v$, in particular $v = 0$ for $F = 0$. Our main objective is to find velocities v opposite to the bias F , equivalent to opposite signs of average current and voltage in a Josephson junction. To appreciate that such a behavior is indeed quite remarkable, we first show that every term in (1,3) is indispensable and thus the *model is minimal*. (i) Due to ergodicity, the time average in (2) actually makes the ensemble average superfluous. It follows that $v = (\tau/L) \lim_{t \rightarrow \infty} x(t)/t$, independent of $x(0)$ and independent of the particular realization of the noise $\xi(t)$. Next, consider two solutions $x_1(t)$ and $x_2(t)$ with $M = 0$, identical seeds $x_1(0) = x_2(0)$ and identical realizations of the noise $\xi(t)$, but with different bias, say $F_1 > F_2$. Whenever $x_1(t) = x_2(t)$ it follows from (1) that $\eta[\dot{x}_1(t) - \dot{x}_2(t)] = F_1 - F_2 > 0$. Hence, $x_1(t) \geq x_2(t)$ for all t and hence $v_1 \geq v_2$. Since $v = 0$ for $F = 0$ we find that v and F cannot have opposite signs in the absence of the *inertia term* $M\ddot{x}(t)$ in (1). (ii) Since $v = 0$ for $F = 0$, Newton's second law might seem to imply a positive acceleration and hence $v > 0$ whenever $F > 0$, and similarly for $F < 0$. However, this argument tacitly assumes that one may simply superimpose the effects of those forces which are already present when $F = 0$ with the effect of an additional finite F . This is only correct for a linear dynamics, i.e. without the *potential force* $-V'(x)$ in (1), and then readily yields for the velocity (2) the result $v = (\tau/L)(F/\eta)$. (iii) v opposite to F might seem incompatible with thermodynamic stability criteria or the second law of thermodynamics. However, this objection does not apply for systems *out of equilibrium* [18]. The latter is guaranteed in (1) by the *periodic driving* $f(t)$. (iv) Omitting the $-\eta\dot{x}(t)$ in (1) is equivalent to the limit $\eta \rightarrow 0$ with ηT kept fixed. But whenever $T \rightarrow \infty$, the effect of the potential force $-V'(x)$ is negligible, implying according to (ii) that $v = (\tau/L)(F/\eta)$. Hence $v/F \rightarrow \infty$ without the *dissipative term* $-\eta\dot{x}(t)$ in (1).

Numerical results and intuitive explanation. – Next we show that the model (1,3) indeed can give rise to v opposite to F . In view of the above high- T argument (iv), we can focus on *small temperatures*. Moreover, one readily sees that v opposite to F is impossible for very small and large frequencies ω . Our detailed analysis shows that the lower limit is about 0.01 and the upper limit about 2 and that for our purposes *the optimal choice*

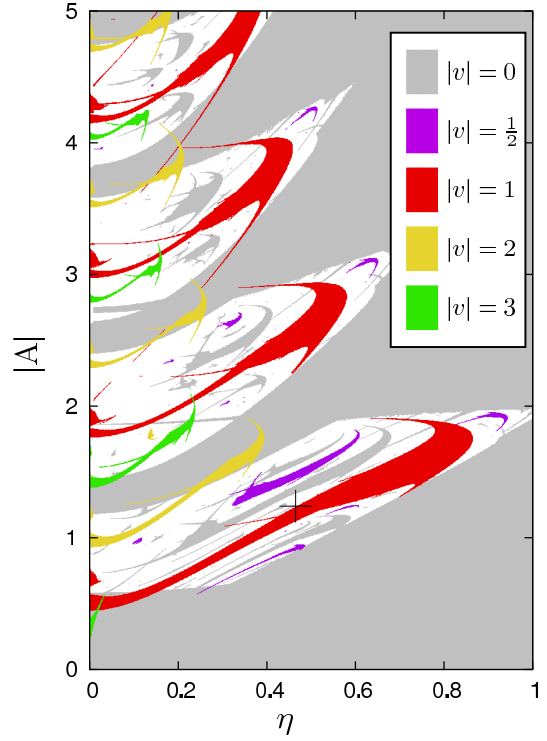


Fig. 1: Velocity v from (2) for various driving amplitudes A and friction coefficients η , obtained by numerical solutions of (1,3) with $F = 0$, $T = 0$, $\omega = 0.6$, and sampling many different initial conditions. Colors: periodic and phase-locked aperiodic attractors for a few dominating rational v -values. White: all remaining cases. The black cross represents $\eta = 0.465$, $A = 1.24$.

is around $\omega = 0.6$. Focusing first on the unbiased ($F = 0$), deterministic ($T = 0$) case, the two remaining parameters are A and η . In general, analytical progress is still fairly hopeless [13], but numerical solutions are readily available. As usual [13, 16], we find that for large times t those solutions $x(t)$ either converge towards a periodic attractor or maintain an aperiodic behavior, depending on A , η , and the initial conditions. In the case of a periodic attractor, a rational velocity $v = n/m$ results in (2). An aperiodic solution $x(t)$ may either be: (i) phase-locked aperiodic, i.e. it still proceeds by n elementary spatial cells during m time-periods, but with an aperiodic behavior within the elementary cell, or (ii) non-phase-locked aperiodic. Fig. 1 summarizes our numerical findings. Note that for symmetry reasons every solution with $v \neq 0$ has a coexisting twin brother with opposite v . Further, v is invariant under $A \mapsto -A$. For asymptotically small and large A , only solutions with $v = 0$ survive. In agreement with the well known Hamiltonian ($\eta \rightarrow 0$) and overdamped ($\eta \rightarrow \infty$) limits [17], small η bring along a whole mess of coexisting attractors with different velocities, while for moderate-to-

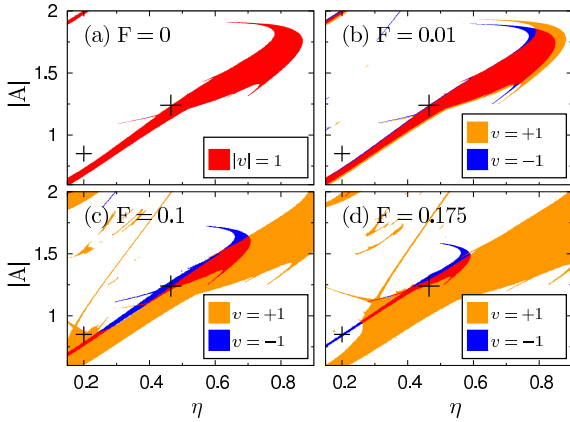


Fig. 2: (a) Magnification of the lowest red stripe in Fig. 1. The small black cross represents $\eta = 0.2$, $A = 0.85$. (b)-(d): Same but for $F > 0$. Red indicates coexistence of $v = 1$ and $v = -1$.

larger η one finds a unique $|v|$ in most cases.

Fig. 2 illustrates how the degeneracy between $v = 1$ and $v = -1$ is lifted by the bias F . To gain further insight we note that a solution with a given velocity $|v| = 1$ will dissipate on average less energy when η is decreased. Now, consider any border point in Fig. 2a where the $|v| = 1$ solutions ceases to exist when η is decreased (e.g. the larger black cross). But now, instead of decreasing η we apply a small positive bias $F > 0$. Then a solution with positive velocity $v = 1$ gains energy on the average, which is basically equivalent to saying it dissipates less, and hence ceases to exist. In other words, the border of the orange region moves into the direction of increasing η upon increasing F , at least for sufficiently small F (later, non-linear corrections take over). Analogous arguments hold for any border in Fig. 2, thus explaining why the orange and blue regions move to the right and left, respectively, upon increasing F . For any such border point in (a) which turns blue in (b)-(d) we thus expect a *velocity v opposite to the bias F*. By inspection of Fig. 2, one furthermore sees that the parameters corresponding to the larger black cross are *optimal* in the sense that they remain within the blue region for the largest interval of F -values.

For this parameter set, additional details are provided by Fig. 3. At least for $F > 0.01$, the deterministic velocities (blue) are readily understood from the above discussion, and similarly for the corresponding attractors (red), being either of periodic or phase-locked aperiodic type. While at most two velocities coexist, there are three coexisting period doubling bifurcation cascades. Each starts with a period-one attractor (via tangent bifurcation) and ends with a crisis, i.e. a collision of a chaotic attractor with an unstable periodic orbit [19]. The remnant “ghost” of the chaotic attractor after the crisis is a chaotic repeller [20]. Finally, the regime $F < 0.01$ can be understood by the fact that the larger black cross in Fig. 2a is

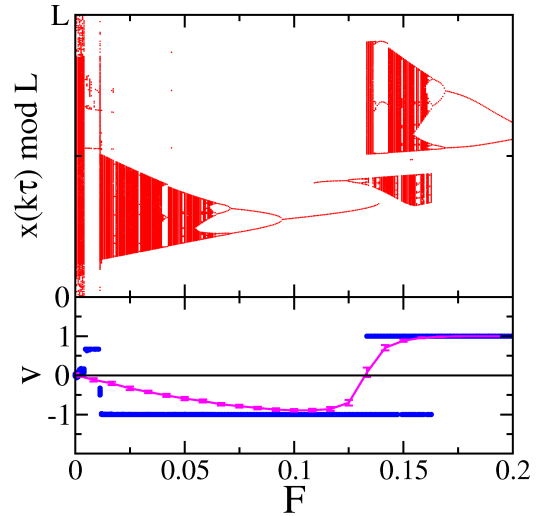


Fig. 3: Attractors (red) and velocities (blue) versus bias F from numerical solutions of (1,3) with $T = 0$, $\omega = 0.6$, $\eta = 0.465$, $A = 1.24$ and sampling many different initial conditions. For any given F , the red dots represent $x(k\tau)$ modulo L (stroboscopic map of the reduced spatial dynamics) for sufficiently large k to omit initial transients. In addition, the numerically determined velocity v from (2) for $T = 0.001$ is indicated by the purple symbols with error bars. Since $F \leftrightarrow -F$ implies $v \mapsto -v$, negative F are omitted.

actually not exactly at the border but rather slightly outside of the red region. The resulting attractors in Fig. 3 consist of two “vertical red stripes”, corresponding to non-phase-locked aperiodic attractors, separated by a small periodic window with $v = 2/3$. Within this small window an analogous scenario as for $F > 0.01$ develops, whose details are beyond the resolution of Fig. 3.

Noise effects. – Next we address the effect of thermal noise with finite temperatures T in (1). As mentioned already, as far as transport opposite to an external bias is concerned, we can focus on small T . The first main consequence of any finite T is that any deterministic attractor turns metastable, and due to the noise induced transitions between them the dynamics is always ergodic and hence the velocity (2) independent of the initial condition. While in the deterministic case the unstable periodic orbits and chaotic repellers play no role with respect to the velocity (2), in the presence of noise they are back in the game during the transitions between the attractors. Essentially, the velocity (2) will thus be the average over the individual velocities of all the attractors and repellers, weighted with their respective dwelling times. Accordingly, the main qualitative effect of the noise in Fig. 3 is averaging between coexisting velocities and washing out the fine details.

To illustrate these qualitative arguments in more detail, we next compare numerical results for finite T step by step

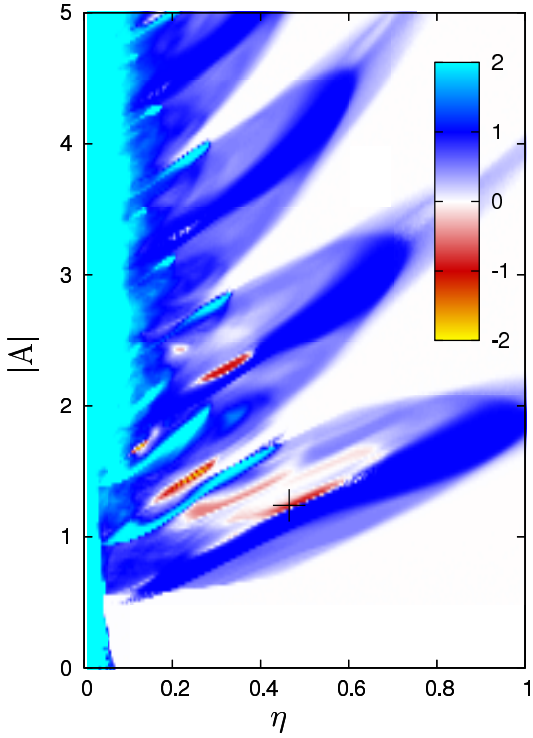


Fig. 4: Same as Fig. 1 but for $T = 0.001$ and $F = 0.1$. The value of the velocity v from (2) is independent of initial conditions and indicated by the coloring.

with our above findings for $T = 0$. Fig. 4 is the analog of Fig. 1 but for finite temperature T and bias F (for $F = 0$ one always has $v = 0$ due to symmetry and ergodicity). Apparently, the periodic and phase-locked aperiodic solutions with $v = 0$ (grey in Fig. 1) are quite robust against some noise and bias (white in Fig. 4). For the periodic and phase-locked aperiodic solutions with finite v (colored in Fig. 1) the symmetry breaking $F > 0$ in most cases leads to a dominance of the solutions with positive v (orange in Fig. 2, blue in Fig. 4) but also substantial regions with v opposite to F (red in Fig. 4) survive at the upper borders of some colored stripes in Fig. 1. The quite notable positive velocities v within the lowest stripe in Fig. 4 and the negative velocities at the upper border of this stripe are obviously the noisy traces of the orange and blue regions in Fig. 2c, and similarly for the other stripes in Fig. 4.

The main conclusion from Fig. 4 is that net motion against the bias F indeed can survive in the presence of noise. In fact, for any given friction η between 0.1 and 0.65 there exists an interval of amplitudes A with significant v opposite to F according to Fig. 4! Furthermore, comparison of the red islands in Fig. 4 suggests that there are parameter values (η, A) whose motion against F is even somewhat faster and more robust than the one indicated by the larger black cross. Its actual quantitative robust-

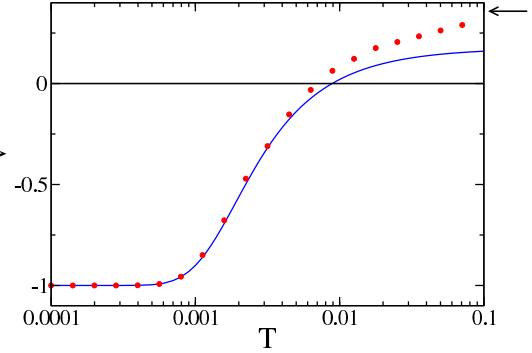


Fig. 5: Red: Velocity v from (2) versus temperature T by numerically solving (1,3) with $F = 0.1$, $\omega = 0.6$, $\eta = 0.465$, $A = 1.24$. Blue: Analytical approximation (4,5). Arrow: Analytical asymptotics $v = (\tau/L)(F/\eta) \simeq 0.358$ for $T \rightarrow \infty$.

ness against bias and noise is shown in Figs. 3 and 5. Hence we expect that by further optimizing parameters, one possibly may be able to improve the maximal F in Fig. 3 and also the maximal T in Fig. 5 with v opposite to F by a factor of 2-3, but not much beyond that. Fig. 4 furthermore suggests that periodic attractors of low period are more stable against noise than those of high period and phase-locked aperiodic solutions.

It is well known that weak noise leads to rare escapes from deterministic attractors and that also the deterministically irrelevant unstable periodic orbits and chaotic repellers play an important role in such processes [11–15, 20]. For the parameter set of Fig. 5 we have analyzed in more detail the transitions between the deterministic period-one attractor with $v = -1$ (see Fig. 3) and the dominating chaotic repeller, being the remnant “ghost” of the nearby chaotic attractor. Focusing on small $T \lesssim 0.001$, we found that these transitions can be described very well in terms of escape rates k_a and k_r from the periodic orbit and the repeller, respectively, of the form

$$k_a \simeq 0.14 \cdot \exp\{-0.0034/T\}, \quad k_r \simeq 0.081. \quad (4)$$

Moreover, we found that the numerical solutions are very well characterized by a velocity of $v_r \simeq 0.88$ within the realm of the chaotic repeller, while for the periodic attractor, as expected, one finds $v_a \simeq -1$. The velocity (2) can thus be approximated by averaging over v_r and v_a with weights proportional to the inverse escape rates (dwelling times),

$$v \simeq [v_r k_r^{-1} + v_a k_a^{-1}] / [k_r^{-1} + k_a^{-1}]. \quad (5)$$

The agreement with the numerical results in Fig. 5 is remarkably good even at rather high T .

Further anomalous response properties. — From our so far insights we can readily predict two further remarkable transport properties of the system (1,3). First, consider the small black crosses in Fig. 2. For weak bias

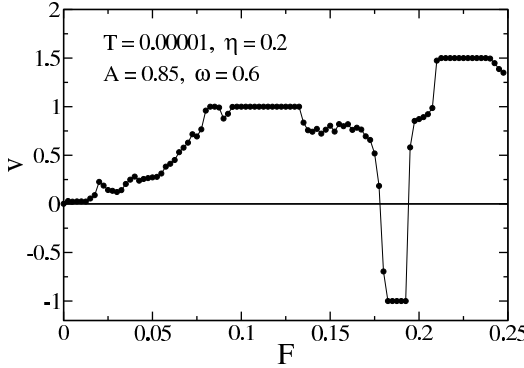


Fig. 6: Velocity v from (2) by numerically solving (1,3) for the indicated parameters.

F we are somewhere in the white or grey domain of Fig. 1 and hence a velocity v of the same sign as F is expected. Around $F = 0.1$ the small black cross in Fig. 2c enters a bulge of the orange area which is “moving upwards” as a function of F , while in Fig. 2d the blue stripe takes over. The corresponding quite unusual behavior v as a function of the bias F is nicely confirmed by Fig. 6: For small $F > 0$, the velocity is positive, then turns negative upon increasing F , and finally returns to positive.

Second, we focus on the small periodic window around $F = 0.008$ in Fig. 3. Similarly as in (4,5), one has a competition between this deterministic attractor with $v_a \simeq 2/3$ and a chaotic repeller with $v_r \simeq -1$. As confirmed by Fig. 7, for small T the attractor wins ($v > 0$), then the repeller takes over ($v < 0$), and finally the large- T asymptotics $v = (\tau/L)(F/\eta) \simeq 0.028$ is approached.

Experimental realizations and conclusions. – In conclusion, we have unraveled in Figs. 3,6,7 three rather astonishing transport properties of the stochastic dynamics (1,3). An immediate experimental realization is provided by way of the Stewart-McCumber model [13,21] for the phase difference φ across a Josephson junction with capacity C , resistance R , and critical current I_c , equivalent to the dimensionless form (1,3) via the well known relations [13,21] $\varphi(t/\omega_p) = x(t)$, $I(t/\omega_p) = I_c[f(t) + F]$, $\eta = (RC\omega_p)^{-1}$, $T = C(\omega_p/I_c)^2 k_B T^*$. Here, $I(t)$ is the external current, $\omega_p := (2\pi I_c/\Phi_0 C)^{1/2}$ the plasma frequency, $\Phi_0 := h/2e$ the flux quantum, and $k_B T^*$ the thermal energy. The voltage across the junction is given by the second Josephson-relation $U(t) = \Phi_0 \dot{\varphi}(t)/2\pi$ [13,21] and hence its average via (2) by $\langle U \rangle = (I_c/C)(\omega/\omega_p^2)v$.

For instance, our predictions from Fig. 3 can be realized by a Josephson junction with resistance $R \approx 0.2 \Omega$, capacity $C \approx 250 \text{ pF}$, critical current $I_c \approx 180 \mu\text{A}$, temperature $T \approx 4.2 \text{ K}$, driven by an ac-current of frequency 28 GHz and amplitude 220 μA . The minimum of v in Fig. 3 will correspond to a dc bias of about 20 μA with a resulting average voltage of about $-10 \mu\text{V}$. Such an experiment [22] is

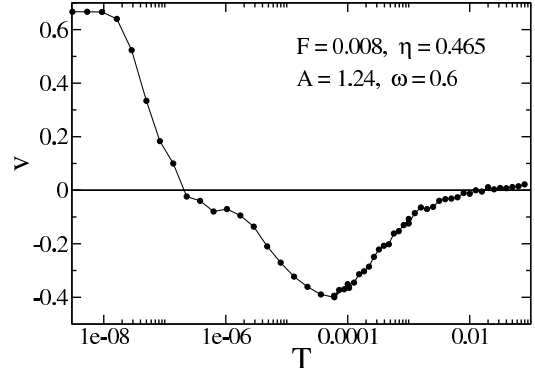


Fig. 7: Same as Fig. 5, but for $F = 0.008$.

presently under construction in the group of Dieter Kölle and Reinhold Kleiner in Tübingen (Germany) within a joint project with the present authors.

Further experimental realization may be cold atoms in resonance with laser induced optical lattices [23] and the diffusion of single molecules on atomically clean crystal surfaces [24]. In such systems, the bias F and/or the driving $f(t)$ in (1) may also be substituted [25] by suitable “traveling-wave potentials” in place of the static $V(x)$.

Apart from their fundamental interest [2,3,18] such effects may be applied for particle sorting [4], stabilization of unstable states, and making work (transport) available upon request [8].

Finally, the basic physical mechanism as identified in our discussion of Figs. 1-3 is clearly quite robust against a large variety of modifications and generalizations of the dynamics (1,3). The only indispensable prerequisites are deterministic chaos, phase locking, and the symmetry properties. For example, we have found similar effects for various non-harmonic $V(x)$ and $f(t)$ in (1) and also when the “periodically rocking force field” $-V'(x) + f(t)$ in (1) is replaced by a “pulsating field” of the form $-V'(x)[1+f(t)]$. More details will be presented elsewhere.

This work was supported by Deutsche Forschungsgemeinschaft under SFB 613, RE 1344/3-1, and RE1344/5-1

REFERENCES

- [1] LINKE, H. (SPECIAL ISSUE GUEST EDITOR), *Appl. Phys. A*, **75** (2002) 167-352; REIMANN P., *Phys. Rep.*, **361** (2002) 57; KLAFTER J. and URBAKH M. (SPECIAL ISSUE GUEST EDITORS), *J. Phys.: Condens. Matter*, **17** (2005) S3661-4024;
- [2] BANIS T. J., PARSHELYUNAS I. V. and POZHELA Y. K., *Sov. Phys. Semicond.*, **5** (1972) 1727.
- [3] KEAY B. J., ZEUNER S., ALLEN S. J., MARANOWSKI K. D., GOSSARD A. C., BHATTACHARYA U. and RODWELL M. J. W., *Phys. Rev. Lett.*, **75** (1995) 4102.

[4] ROS A., EICHHORN R., REGTMEIER J., DUONG T. T., REIMANN P. and ANSELMETTI D., *Nature*, **436** (2005) 928.

[5] PAVLOVICH V. V. and EPSTEIN E. M., *Sov. Phys. Semicond.*, **10** (1976) 1196; AGUADO R. and PLATERO G., *Phys. Rev. B*, **55** (1997) 12860; HARTMANN L., GRIFONI M. and HÄNGGI P., *Europhys. Lett.*, **38** (1997) 497; GOYCHIK I. and MAY V., *Phys. Lett. A*, **238** (1998) 59.

[6] REIMANN P., KAWAI R., VAN DEN BROECK C. and HÄNGGI P., *Europhys. Lett.*, **45** (1999) 545; MANGIONI S. E., DEZA R. R. and WIO H. S., *Phys. Rev. E*, **63** (041115) 2001; CLEUREN B. and VAN DEN BROECK C., *Europhys. Lett.*, **54** (2001) 1.

[7] EICHHORN R., REIMANN. P. and HÄNGGI P., *Phys. Rev. Lett.*, **88** (2002) 190601; JIMÉNEZ DE CISNEROS B, REIMANN P. and PARRONDO J. M. R, *Europhys. Lett.*, **64** (2003) 599; EICHHORN R. and REIMANN P., *Europhys. Lett.*, **69** (2005) 517.

[8] CLEUREN B. and VAN DEN BROECK C., *Phys. Rev. E*, **65** (2002) 030101(R).

[9] EICHHORN R., REIMANN P., CLEUREN B. and VAN DEN BROECK C., *Chaos*, **15** (2005) 026113.

[10] MACHURA L., KOSTUR M., TALKNER P., LUCZKA J. and HÄNGGI P., *Phys. Rev. Lett.*, **98** (2007) 040601.

[11] RISKEN H., *The Fokker-Planck Equation* (Springer, Berlin) 1984.

[12] IANSITI M., HU Q., WESTERVELT R. M. and TINKHAM M., *Phys. Rev. Lett.*, **55** (1985) 746.

[13] KAUTZ R. L., *J. Appl. Phys.*, **52** (1981) 3528; *Rep. Prog. Phys.*, **59** (1996) 935.

[14] MARCHESONI F., *Phys. Lett. A*, **231** (1997) 61.

[15] JUNG P. and HÄNGGI P., *Ber. Bunsenges. Phys. Chem.*, **95** (1991) 411; JUNG P., *Phys. Rep.*, **234** (1993) 175; BORROMEI M., COSTANTINI G. and MARCHESONI F., *Phys. Rev. Lett.*, **82** (1999) 2820. YU Y. and HAN S., **91** (2003) 127003.

[16] BREYMAYER H.-J., *Appl. Phys. A*, **33** (1984) 1; JUNG P., KISSNER J. G. and HÄNGGI P., *Phys. Rev. Lett.*, **76** (1996) 3436; MATEOS J. L., **84** (2000) 258.

[17] SCHANZ H., DITTRICH T. and KETZMERICK R., *Phys. Rev. E*, **71** (2005) 026228; DENISOV S., FLACH S. and HÄNGGI P., *Europhys. Lett.*, **74** (2006) 588; AJDARI A., MUKAMEL D., PELITI L. and PROST J., *J. Phys. I France*, **4** (1994) 1551.

[18] ZIA R. K. P., PRAESTGAARD E. L. and O. G. MOURITSEN, *Am. J. Phys.*, **70** (2002) 384.

[19] GREBOGI C., OTT E. and YORKE J. A., *Phys. Rev. Lett.*, **48** (1982) 1507.

[20] T. TÉL, *Directions in Chaos*, edited by BAI-LIN H., Vol. **3** (World Scientific, Singapore) 1990.

[21] LIKHAREV K. K., *Dynamics of Josephson Junctions and Circuits* (Gordon and Breach, Philadelphia) 1986.

[22] STERK A., KLEINER R. and KOELLE D., *Phys. Rev. Lett.*, **95** (2005) 177006; BECK M., GOLDOBIN E., NEUHAUS M., SIEGEL M., KLEINER R. and KOELLE D., *Phys. Rev. Lett.*, **95** (2005) 090603.

[23] GRYNBERG G. and ROBILLARD C., *Phys. Rep.*, **35** (2001) 335; GOMMERS R., BERGAMINI S. and RENZONI F., *Phys. Rev. Lett.*, **95** (2005) 073003.

[24] AZZOZ M., KREUZER H. J. and SHEGELSKI M. R. A., *Phys. Rev. B*, **66** (2002) 125403; ANTCAZAK G. and EHRLICH G., **71** (2005) 115422.

[25] BORROMEI M. and MARCHESONI F., *Phys. Lett. A*, **249** (1998) 199; VAN DEN BROECK C., *Europhys. Lett.*, **46** (1999) 1.

3.3 Preprint of [2]

D. Speer, R. Eichhorn, and P. Reimann, Physical Review E **76**, 051110 (2007),
Copyright (2007) by the American Physical Society

Transient chaos induces anomalous transport properties of an underdamped Brownian particle

David Speer, Ralf Eichhorn, and Peter Reimann
Universität Bielefeld, Fakultät für Physik, 33615 Bielefeld, Germany

For an underdamped Brownian particle in a one-dimensional periodic potential we theoretically predict three unusual transport properties: (i) A static bias force (of either sign) generates an average particle motion in the opposite direction. (ii) A small bias leads to a particle transport in the direction of the bias, but upon increasing the bias the particle velocity reverses direction. (iii) For a given bias force, the particle motion follows the direction of the force for low temperatures, but upon increasing the temperature reverses its direction. The considered model is shown to be minimal for the occurrence of these phenomena. A detailed analysis of its deterministic properties and the influence of thermal noise is carried out with numerical simulations that are complemented by analytical approximations. Intuitive explanations of the basic mechanism behind the three effects are provided; their origin is attributed to a subtle interplay between the stability of coexisting attractors, noise induced metastability, and transient chaos. An experimental system for the realization of the predicted effects is given within the Stewart-McCumber model for Josephson junctions. Suitable parameter values for which these effects can be observed are quite realistic experimentally.

PACS numbers: 05.45.-a, 05.40.-a, 05.60.-k

I. INTRODUCTION

The interplay of non-linearity and (thermal) noise in non-equilibrium systems often gives rise to quite unusual emerging properties, in the sense that they might seem at first glance to contradict physical intuition or every-day experience. Prominent examples are the stabilization of transient chaos by noise [1, 2], ratchet effects [3], stochastic resonance [4], enhancement of diffusion [5], and noise suppression by noise [6], to name but a few. In many cases, such unusual properties can be revealed by considering the “characteristics” of the system in form of a response to an external perturbation.

Here, we predict three anomalous transport properties of a single Brownian particle in one dimension by studying its response to an external static bias force:

(i) In the absence of the bias the symmetry of the system rules out any systematic transport. When perturbing the system by a static force of either sign (but not too large modulus) the result is an average motion with velocity of just the opposite sign. This quite astonishing response behavior is referred to as “absolute negative mobility”, see [7] for a recent review. For single Brownian particles, it has been theoretically studied so far in two dimensional structured systems [8] or by including an “internal” degree of freedom [9]. Experimentally, it has been observed for charged Brownian particles in structured microfluidic devices [10], and due to quantum effects in a sample of bulk GaAs [11] and in semiconductor heterostructures [12]. In the latter two cases one also speaks of “absolute negative conductance”. For a more detailed account of the quite extensive literature (mainly theoretical) we refer to [7].

(ii) For small bias forces, the transport direction is as usual, i.e. in the direction of the bias. However, upon increasing the bias the transport velocity suddenly changes sign and switches to the direction opposite to the exter-

nal force, before returning to normal for even larger bias forces. To our knowledge, such a paradoxical non-linear response has so far only been reported in the theoretical studies [13] of single Brownian particles confined to two-dimensional meandering structures.

(iii) For a given bias force, the transport behavior is as usual for low temperatures, but upon raising the temperature, first turns anomalous and later again normal. In other words, by increasing the random fluctuations due to thermal noise the transport velocity can be reversed to be opposite to the bias, in contradiction to our intuitive expectation that an increase of noise would support the downhill motion in the direction of the bias.

With the present work we continue and provide the details of our brief account [14] on the existence of the above described transport phenomena (i)-(iii) in a one-dimensional dynamics of a Brownian particle for which inertial effects play a dominant role. An independent, closely related investigation of the above effect (i) has recently been published in Ref. [15]. While the qualitative findings therein agree with ours, the underlying physical mechanisms are fundamentally different in the two cases, as detailed in Sec. V.D below. Moreover, our approach to analyze the observed effects is complementary to the one from Ref. [15], admitting additional insight into the underlying physical mechanisms.

The paper is organized as follows: In Section II we introduce our model and the observable of main interest, namely the average particle velocity. In Section III basic properties of our model are discussed: It is shown that this model is minimal for the occurrence of the above described effects (i)-(iii), in particular a no-go theorem is mathematically proven for the case of overdamped one-dimensional systems. Focusing on the above effect (i), Section IV contains a detailed analysis of the deterministic properties of the model. The observed chaotic behavior in the deep non-linear regime does not admit

a quantitative analytical treatment. Instead, numerical simulations are complemented by intuitive explanations of the basic physical mechanism behind the occurrence of absolute negative mobility. Noise effects due to finite temperatures are thoroughly discussed in Section V and analytical approximations for the average particle velocity are provided that agree well with the numerical simulations. After this detailed analysis of absolute negative mobility, the occurrence of the other two phenomena (ii) and (iii) in our model follows quite naturally and is easily understood, as described in Section VI. In Section VII, Josephson junctions with the property that they can be well modeled by the so-called RCSJ or Stewart-McCumber model are considered as a concrete experimental system to which our theoretical predictions apply. Suitable parameter values for which the effects (i)-(iii) can be observed are quite realistic experimentally. Finally, we conclude and discuss our results with Section VII.

II. MODEL

Our working model consists in the one-dimensional dynamics of a Brownian particle with coordinate $x(t)$, mass M , and friction coefficient η [16],

$$M \ddot{x}(t) = -\eta \dot{x}(t) - V'(x(t)) + f(t) + F + \sqrt{2\eta T} \xi(t) \quad (1)$$

where $V(x) = V(x+L) = V(-x)$ is a *spatially symmetric*, L -periodic potential, $f(t) = -f(t+\tau/2)$ is a *temporally symmetric*, τ -periodic driving, F is a dc-bias, and thermal fluctuations are modeled as usual by unbiased, δ -correlated Gaussian noise $\xi(t)$ with units of the temperature T such that Boltzmann's constant equals one. Furthermore, we focus on the simplest example, namely purely harmonic potentials $V(x)$ and drivings $f(t)$, and we adopt dimensionless units of time, length, and mass such that

$$M = 1, \quad V(x) = -\cos x, \quad f(t) = A \sin(\omega t) \quad (2)$$

i.e. $L = 2\pi$ and $\tau = 2\pi/\omega$. More general models will be briefly addressed at the end of the paper.

Driven Brownian motion in a periodic potential is of relevance in many different contexts, such as atomic friction, fluxons in semiconductors, superionic conductors, Josephson junctions, charge density waves, phase and mode locking phenomena, intracellular transport, neural activity, and so on, see e.g. Ref. [16, 17] and references therein. The corresponding minimal model (1), (2) has been extensively studied e.g. from the viewpoints of noisy chaos and phase locking [18–22], resonance activation [23, 24], stochastic resonance [25], and escape processes [26–28]. An even much larger literature is available if one also includes slight modifications (e.g. non-harmonic V or f), generalizations (e.g. two-dim. models), or special limits (vanishing M , η , T , f etc.) of the basic model (1), (2), addressing various aspects of ratchet

effects [3b, 29, 30] and diffusive transport [16, 17], to name but two examples.

The observable of foremost interest in (1), (2) will be the time and ensemble averaged particle velocity

$$v := \frac{\tau}{L} \left\langle \lim_{t \rightarrow \infty} \frac{1}{t} \int_0^t dt' \dot{x}(t') \right\rangle \quad (3)$$

expressed as a dimensionless multiple of the spatial and temporal periods L and τ . The ensemble average is indicated by $\langle \cdot \rangle$ and the time average ensures independence of initial transients and of the τ -periodic oscillations imposed by the driving $f(t)$ in (1).

III. BASIC PROPERTIES, MINIMAL MODEL, NO-GO THEOREM

The dynamics (1), (2) is ergodic for any finite noise strength ηT and hence the velocity (3) unique (independent of initial conditions). For symmetry reasons, it follows that $F \mapsto -F$ implies $v \mapsto -v$, in particular $v = 0$ for $F = 0$. As mentioned at the beginning, our main objective will be to find situations with opposite signs of F and v . To appreciate that such a behavior is indeed quite astonishing, we first give three arguments which – at first glance – seem to prohibit it altogether.

First, according to Newton's second law, when increasing the force from $F = 0$ to a finite value one should always expect a finite acceleration in the same direction and hence a change of the velocity from $v = 0$ to a finite value of the same sign. This argument, however, is no longer conclusive for a *non-linear* dynamics: one cannot simply superimpose the effects of those forces which are already present when $F = 0$ with the effect of an additional finite F . Indeed there is one non-linear term in (1), (2), namely $-V'(x)$.

Second, one might object that a velocity v opposite to a dc-force F contradicts thermodynamic stability criteria, the principle of Le Châtelier, and ultimately the second law of thermodynamics. Again, such an argument is no longer conclusive for systems *out of equilibrium* [32]. The latter is guaranteed in (1) by the periodic driving $f(t)$.

Third, let us consider any one-dimensional stochastic dynamics of the form

$$\dot{x}(t) = h(x(t), t) + F + g(x(t), t) \xi(t) \quad (4)$$

whose solutions $x(t)$ are almost certainly ergodic and continuous. Furthermore, let us define v as in (3) but without the prefactor τ/L . For ergodicity reasons, the time average is equivalent to the ensemble average, hence the latter is in fact superfluous. It follows that $v = \lim_{t \rightarrow \infty} x(t)/t$, independent of $x(0)$ and independent of the particular realization of the noise $\xi(t)$ [3b]. Next, consider two solutions $x_1(t)$ and $x_2(t)$ of (4) with identical seeds $x_1(0) = x_2(0)$ and identical realizations of the noise $\xi(t)$, but with different dc-bias F , say $F_1 > F_2$. Then, for any t with the property $x_1(t) = x_2(t)$ it follows

from (4) that $\dot{x}_1(t) - \dot{x}_2(t) = F_1 - F_2 > 0$. Exploiting continuity, we can infer that $x_1(t) \geq x_2(t)$ for all t and hence $v_1 \geq v_2$ [33]. In other words, v is a monotonically increasing function of F , implying the following *no-go theorem*: v and F cannot have opposite signs for any continuous, ergodic dynamics of the form (4) with $v = 0$ for $F = 0$. In a special case, namely for t -independent h and constant g in (4), the same conclusion has been reached in a completely different way in Ref. [34]. For our purposes, the above generalization for t -dependent h in (4) is indispensable. Namely, by comparison with (2) we now can rigorously rule out opposite signs of v and F in the absence of the *inertia term* $M\ddot{x}(t)$ in (1) (overdamped limit).

Omitting the *dissipative term* $-\eta\dot{x}(t)$ in (1) is equivalent to the limit $\eta \rightarrow 0$ with ηT kept fixed, i.e. a system coupled to an infinitely hot bath. Then, the effect of the potential force $-V'(x(t))$ is negligible. As seen above, this excludes v opposite to F .

As we will see later, without the last term in (1), v opposite to F is still possible but this may now depend on the choice of the initial conditions. Apart from that, we can conclude that every single term in (1) is indispensable. In this sense *the model (1), (2) is minimal*.

It remains to be shown that this minimal model indeed can give rise to net motion against the average force [35]. In general, the dynamics (1), (2) exhibits an extremely rich behavior as a function of its parameters η , A , ω , F , T . A general overview is provided, e.g., by Refs. [20–22]. Our objective is not such a systematic exploration but rather to unravel the above mentioned anomalous transport behavior.

Such a behavior can readily be ruled out for very small and large frequencies ω : Below some lower limit an adiabatic approximation becomes valid [36], and beyond some upper limit an approximation by means of Bessel functions holds [22]; absolute negative mobility is ruled out within the range of validity of both approximations. Our detailed analysis shows that the lower limit is about 0.01, and the upper limit about 2, and that

$$\omega = 0.6 \quad (5)$$

is close to the optimal choice, see also the following discussion. Moreover, as already mentioned before, for large temperatures T the effects of the potential force $-V'(x)$ in (1) become negligible. The remaining linear dynamics (1) is readily solved, yielding for the velocity (3) the result

$$v \rightarrow \frac{\tau}{L} \frac{F}{\eta} \quad \text{for } T \rightarrow \infty \quad (6)$$

in the direction of F . Hence, we can focus on the low temperature regime.

IV. DETERMINISTIC BEHAVIOR

Starting with the unbiased dissipative dynamics (1), (2) in the deterministic limit (i.e. $F = 0$, $\eta > 0$, $T = 0$),

the remaining control parameters are A and η . In general, analytical progress is still fairly hopeless [20–22], but numerical solutions are readily available. As usual [20–22, 29], one finds that those deterministic solutions of the dissipative dynamics (1), (2) either converge towards a periodic attractor [37] or maintain an aperiodic behavior in the long time limit, depending on the choice of A , η , and the initial conditions.

In the case of a periodic attractor, the resulting average velocity (3) is of the form $v = n/m$ with integers n and m , indicating that the periodic attractor proceeds by n spatial periods L of the potential $V(x)$ during m time-periods τ of the driving $f(t)$ in (1). In the aperiodic case we distinguish between: (i) Phase locked aperiodic: the long time solution still proceeds by n elementary spatial cells during m time-periods, but with an aperiodic behavior of the reduced dynamics within the elementary cell $[0, L]$ [38]; (ii) Non-phase locked aperiodic [39].

A. Numerical findings

The colors in Fig. 1 summarize our numerical findings for a few dominating n/m -ratios, including both periodic and phase locked aperiodic attractors. The remaining white regions refer to non-phase locked attractors [41]. For symmetry reasons, every solution with $v \neq 0$ has a coexisting twin brother with opposite v . Further, v is invariant under $A \mapsto -A$. In agreement with what one would have expected, for very small and large amplitudes A , only solutions with $v = 0$ survive. Also in agreement with the well known behavior in the Hamiltonian ($\eta \rightarrow 0$) and overdamped ($\eta \rightarrow \infty$) limits, for weak (but finite) dissipation η one typically finds a whole mess of coexisting attractors with different velocities v by probing different seeds [30], while for larger η the asymptotic velocity is in most cases unique apart from the above mentioned degeneracies due to symmetry [42]. Such a situation with unique velocity is, for instance, observed in the (η, A) regions around the two black crosses in Fig. 1, which indicate the parameter values we study in more detail below, see (7) and (12).

A magnification of the lowest red stripe in Fig. 1 is reproduced in Fig. 2a, while in Figs. 2b-d the effect of a finite static bias F in (1) is illustrated. As mentioned above, the red region in Fig. 2a comprises coexisting solutions for $F = 0$ with either $v = 1$ or $v = -1$. This degeneracy is lifted by gradually increasing F , and hence the regions with $v = 1$ and $v = -1$ in Figs. 2b-d start to diverge. Focusing on any point at the border of the colored region in Fig. 2a (an example is indicated by the larger black cross), there is a well defined local “speed” at which the two border-lines with $v = 1$ and $v = -1$ in Figs. 2b-d start to move apart upon increasing F . For any such border point (η, A) which turns blue in Figs. 2b-d (e.g. the larger black cross) we thus expect a *velocity* $|v| = 1$ *opposite to the static bias* F , at least for not too large $|F|$.

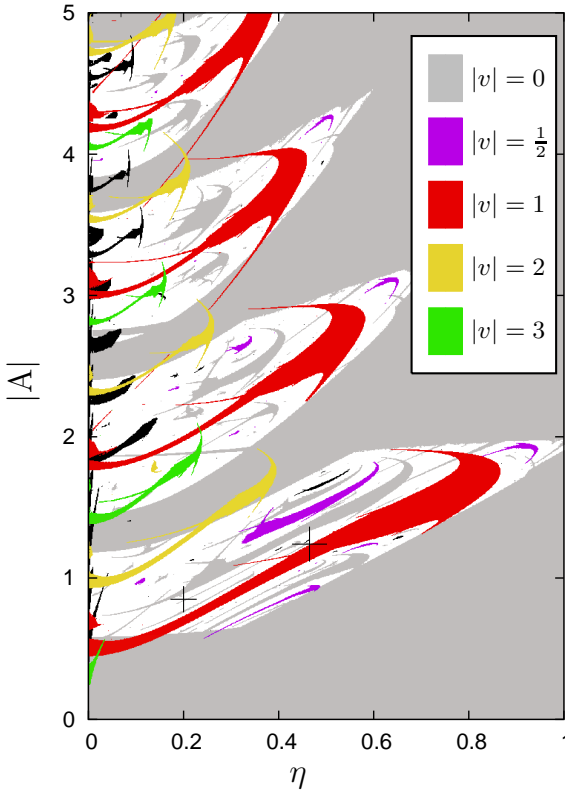


FIG. 1: (Color) Regions in the (η, A) plane with periodic and phase locked aperiodic attractors of the unbiased, deterministic, dissipative dynamics (1), (2), (5), i.e. $F = 0$, $T = 0$, $\eta > 0$, $\omega = 0.6$, obtained by numerical integration sampling many different initial conditions. Colors: average velocity v from (3) on these attractors for a few dominating rational v -values. Black: other rational v -values. White: no phase locked attractors have been found. Overlapping of regions with different colors typically indicates coexistence of attractors. The larger black cross represents (7) and the smaller one (12).

B. Basic physical mechanism

The way in which the two regions with $v = 1$ and $v = -1$ in Fig. 2 move apart and deform upon variation of the bias F can be qualitatively understood by means of the following two intuitive arguments. First, it is quite clear that for sufficiently large F any net motion in the opposite direction will finally become impossible. This basically explains why the blue region in Fig. 2 shrinks and finally disappears upon increasing F , while the orange region grows (at least for not too large F ; later it disappears as well). Second, it is plausible that for any fixed amplitude A , a solution with a given velocity $|v| = 1$ will dissipate on average less energy when η is decreased. Now, consider any border point in Fig. 2a

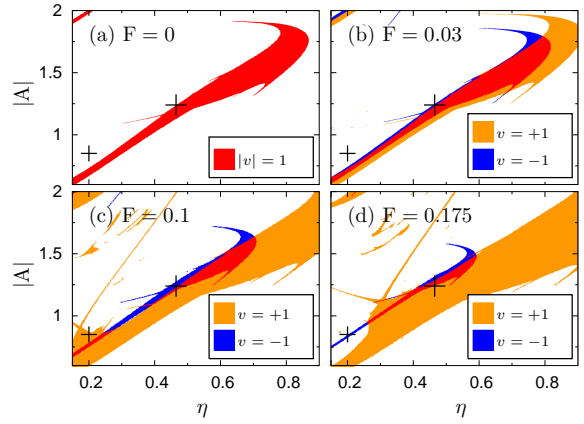


FIG. 2: (Color) (a) Magnification of the lowest red stripe in Fig. 1. The large black cross represents (7), the small one (12). (b)-(d): Same but for $F > 0$. Periodic and phase locked aperiodic attractors with $v = 1$ are indicated in orange and those with $v = -1$ in blue, yielding red in the coexistence regions. Apart from this degeneracy due to symmetry (see also main text), the asymptotic velocities $v = \pm 1$ are unique, i.e. independent of initial conditions [41].

(e.g. the larger black cross) where the $|v| = 1$ solutions cease to exist when η is decreased. But now, instead of decreasing η we apply a small positive bias $F > 0$. Along the same lines, a solution with positive velocity $v = 1$ gains energy on the average, which is basically equivalent to saying it dissipates less. Therefore we expect that this solution ceases to exist. While not rigorous, this argument explains why for any given A -value the border under consideration moves into the direction of increasing η upon increasing F , at least for sufficiently small F (later, non-linear corrections take over). Analogous arguments hold for any border point of the orange and blue regions in Fig. 2, thus explaining why they move to the right and left, respectively, upon increasing F . By inspection of Fig. 2, one furthermore sees that the parameter choice indicated by the larger black cross, i.e.

$$\eta = 0.465 \quad A = 1.24, \quad (7)$$

is optimal in the sense that it remains within the blue region for the largest interval of F -values.

C. Bifurcation diagrams

A more detailed illustration of the above reasoning is provided by Fig. 3. The panels (a)-(d) correspond to horizontal sections through the larger black cross in the corresponding panel of Fig. 2. The red dots in Fig. 3a-d are a common way of visualizing attractors of a nonlinear dynamics [22]. These bifurcation diagrams reveal the two qualitatively different dynamical situations already clas-

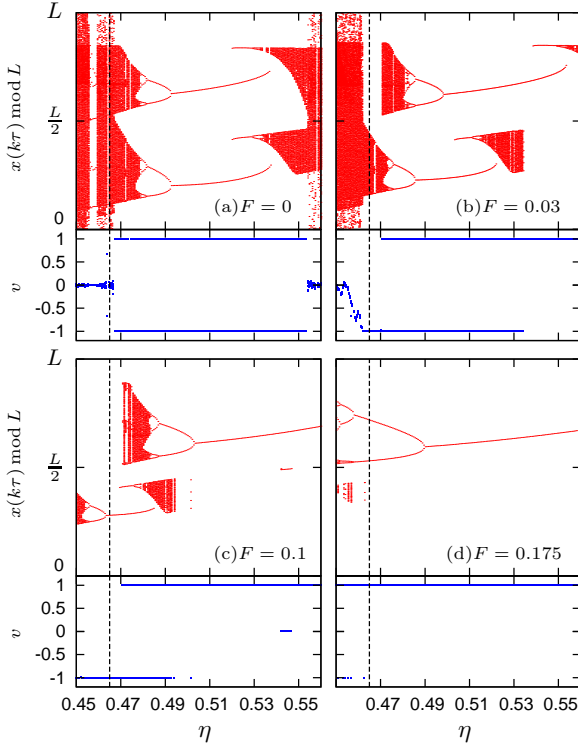


FIG. 3: (Color online) Bifurcation diagrams of attractors (red) [37] and concomitant velocities (blue) versus damping strength η from numerical solutions of the deterministic dissipative dynamics (1)-(3) with $T = 0$, $\omega = 0.6$, $A = 1.24$ and the same values of the static bias F as in Fig. 2. For any given η and F , the red dots represent $x(k\tau)$ modulo L (stroboscopic map of the reduced spatial dynamics) for a set of sufficiently large integers k such that initial transients have died out. The dashed line at $\eta = 0.465$ correspond to the larger black cross in Fig. 2. Coexistence of different velocities v implies coexistence of attractors, but not vice versa.

sified above. The vertical red stripes that cover the whole spatial period L correspond to non-phase locked aperiodic attractors, whereas the period-doubling cascades to chaos and the periodic windows comprise phase locked aperiodic and periodic attractors.

The large window without non-phase locked aperiodic attractors in each panel corresponds to the colored region along the horizontal sections in Figs. 2a-d. Focusing on Fig. 3a, we find $v = 0$ in the entire non-phase locked regime and within most of the small periodic windows. Within the large window, the phase locked solution with velocity $v = 1$ and its symmetry partner with $v = -1$ are each generated by two attractors. All four attractors are born out of tangent bifurcations, coexist in a small η range around $\eta \approx 0.53$ (in which they are connected by an unstable invariant set in phase space), and are destroyed by way of crisis [22, 45] after evolving through a

period doubling route to chaos. In particular, four phase-locked attractors coexist around $\eta \approx 0.53$, but only two velocities $v = 1$ and $v = -1$ are observed. Note that in the stroboscopic map in Fig. 3a the actual symmetry of the $v = 1$ and $v = -1$ solutions would be recovered after shifting the stroboscopic times for one of them by $\tau/2$.

For $F > 0$ (Figs. 3b-d) the symmetry of the period doubling cascades is broken, especially their birth (tangent bifurcations) and death (crises) points along the η -axis no longer coincide. As a consequence, a gap is opening up at the lower end of the phase locked regime (small η -values), where only solutions with $v = -1$ remain possible, whereas the formerly coexisting solution with $v = 1$ has lost stability and turned into a chaotic repeller [1]. An analogous gap opens up at the upper crises. Since one is dealing with either a periodic attractor or phase locked aperiodic solutions within the entire phase locked regime, structural stability implies that the time- and space-periodicities n and m do not change and hence the velocities $v = n/m$ indeed keep their values ± 1 upon changing F . In contrast, the velocity v within the η -regimes with non-phase locked aperiodic attractors is expected to depend continuously on the bias F and hence in general no longer vanishes for finite F .

The situation within the small windows is analogous to that in the large one, but beyond the resolution of Fig. 3. A very small periodic window containing $v = \pm 2/3$ phase locked attractors is located in Fig. 3a at $\eta \approx 0.464$ just left to the dashed line, but is beyond the resolution of Fig. 3a. It gives rise to another anomalous transport behavior as detailed in Sec VI.

In the same vein, the results for $T = 0$ in Fig. 4 can be readily understood by observing that they basically amount to a cut through Figs. 3a-d along the dashed line (fixed $\eta = 0.465$). The fact that the parameters in (7) do not exactly hit the border line in Fig. 2a (see also Fig. 3a) explains why v does not immediately jump to -1 for $F > 0$. A nice illustration of three coexisting attractors but only two velocities $v = 1$ and $v = -1$ is visible around $F = 0.13$ in Fig. 4.

According to our above explanations of Figs. 2-4, the simplest case of net motion opposite to the bias F is exemplified by the specific parameter choice (7) and $F = 0.1$. In this case, there is a unique attractor of the deterministic dynamics (1), (2), (5), consisting of a period $m = 1$ orbit whose time evolution is illustrated by the 9 snapshots in Fig. 5. Apparently, the delicately tuned up and down tilting of the total potential prevents the particle from running downhill and even stabilizes the periodic uphill motion against arbitrary perturbations of finite duration!

Basically, the solution in Fig. 5 advances by one spatial period during the first half time-period and remains within the same spatial period in the second half time-period. The same rough behavior applies for all the solutions within the lowest red stripe in Fig. 1. Likewise, the solutions within the next red stripe in Fig. 1 advance by 2 spatial periods during one half time-period and then

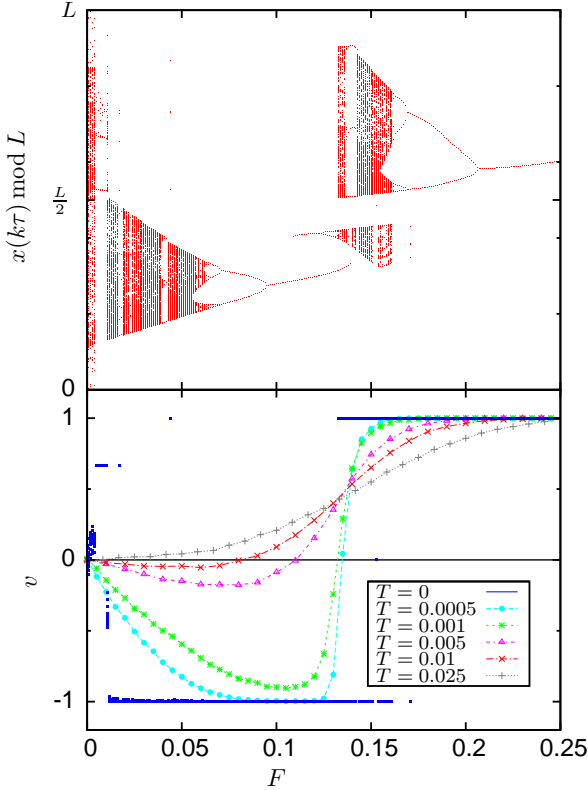


FIG. 4: (Color online) Same as Fig. 3a, but keeping $\eta = 0.465$ fixed and instead varying F . In addition, the numerically determined velocity v from (3) for various T is indicated in the lower part. The numerical uncertainty is of the order of the symbol size. The connecting lines serve as guides to the eye. Since $F \mapsto -F$ implies $v \mapsto -v$, negative F are omitted.

move back by one spatial period during the second half time-period, and so on: in each red stripe the solutions advance by n and then return by $n - 1$ spatial periods, resulting in $|v| = 1$ in all cases, and similarly for the other colored stripes in Fig. 1.

Besides the “main” stripe of the lowest red region in Fig. 1 there are many very fine additional filaments emanating from this main stripe, see also Fig. 2a (the one to the lower left of the larger black cross is relatively well visible, most of the others are at or below the resolution of the numerics or the figures). With increasing F the corresponding orange filaments in Fig. 2 start to grow and move somewhat. Some of the small periodic windows in Figs. 3 and 4 can be traced back to such filaments. If a filament crosses a part of one of the other main stripes with a different color in Fig. 1, there are several coexisting $|v|$ -values. As announced above, the measure of parameter values (η, A) for which this is the case, is quite small for moderate-to-large η . Moreover, only the solutions within the main stripes are reasonably robust against parameter changes and perturbations e.g.

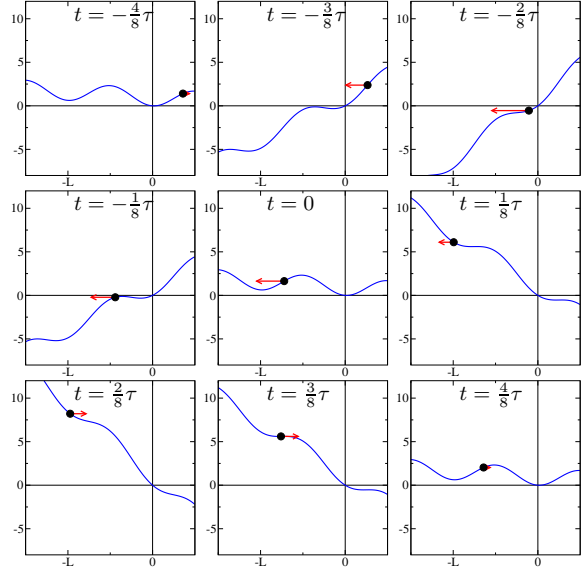


FIG. 5: (Color online) Time evolution of the unique attractor of the deterministic dynamics (1), (2) with $T = 0$, $\omega = 0.6$, $A = 1.24$, $\eta = 0.465$ (cf. Eqs. (5) and (7)), and $F = 0.1$. The black dots and red arrows indicate position and velocity of the stable period-one orbit $x(t)$ at 9 time instances during one driving period. The blue curves represent the instantaneous total potential $V(x) - x[f(t) + F] + 1$ according to (1), (2).

by weak noise.

V. NOISE EFFECTS

Next we address the effect of thermal noise with finite temperatures T in (1). As mentioned at the end of Sec. III, we can focus on small T . The first main consequence of any finite T is that any deterministic attractor turns metastable, and due to the noise induced transitions between them the dynamics is always ergodic and hence the velocity (3) independent of the initial condition. While in the deterministic case the unstable periodic orbits and chaotic repellers play no role with respect to the velocity (3), in the presence of noise they are back in the game during the transitions between the attractors. Essentially, the velocity (3) will thus be the average over the individual velocities of all the attractors and repellers, weighted according to their “lifetimes” [46].

To illustrate these qualitative arguments in more detail, we next compare numerical results for finite T step by step with our above findings for $T = 0$. Fig. 6 is the analog of Fig. 1 but for finite temperature T and bias F [47]. Apparently, the periodic and phase locked aperiodic solutions with $v = 0$ (grey in Fig. 1) are quite robust against some noise and bias (white in Fig. 6). For the periodic and phase locked aperiodic solutions with finite v

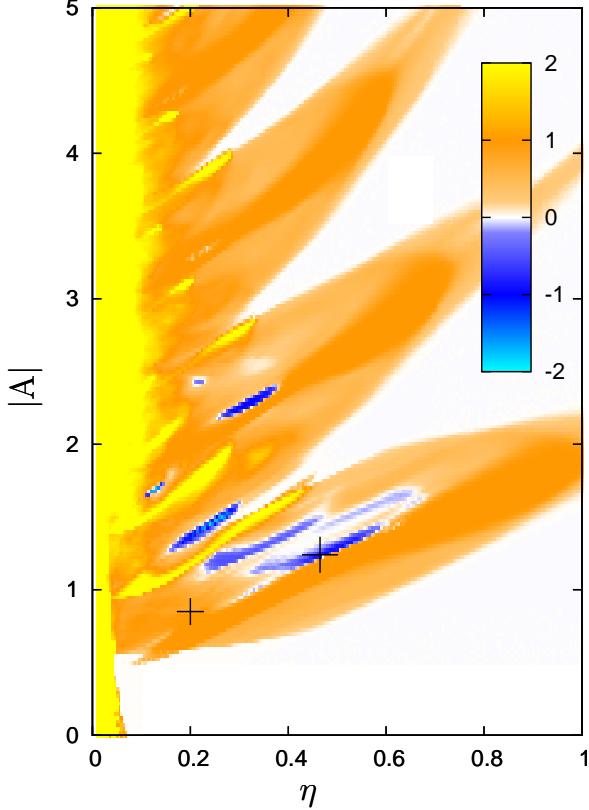


FIG. 6: (Color) Same as Fig. 1 but for $T = 0.001$ and $F = 0.1$. The value of the velocity v from (3) is independent of initial conditions and indicated by the coloring.

(colored in Fig. 1) the symmetry breaking $F > 0$ in most cases leads to a dominance of the solutions with positive v (orange in Figs. 2 and 6) but also substantial regions with v opposite to F (blue in Figs. 2 and 6) survive at the upper borders of some colored stripes in Fig. 1. The quite notable positive velocities v within the lowest stripe in Fig. 6 and the negative velocities at the upper border of this stripe are obviously the noisy traces of the orange and blue regions in Fig. 2c, and similarly for the other stripes in Fig. 6.

The main conclusion from Fig. 6 is that net motion against the bias F indeed can survive in the presence of noise. In fact, for any given friction η between 0.1 and 0.65 there exists an interval of amplitudes A with significant v opposite to F according to Fig. 6! Furthermore, comparison of the blue islands in Fig. 6 suggests that there are parameter values (η, A) whose motion against F is even somewhat faster and more robust than the one indicated by the larger black cross, however with a more complicated deterministic motion than the one in Fig. 5. Its actual quantitative robustness against bias and noise is shown in Figs. 4 and 7. Hence, we expect that by optimizing parameters, one may be able to further improve

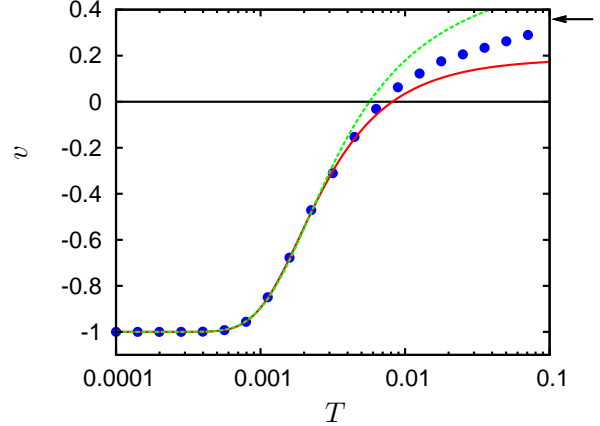


FIG. 7: (Color online) Symbols: Average velocity v from (3) versus temperature T from numerical solutions of (1), (2), (5) with parameter values (7) (labeled by the larger black cross in Figs. 1, 2, 6), and with bias $F = 0.1$. The numerical uncertainty is smaller than the symbol size. Red solid line: analytic approximation (8), (10), (11); green dashed line: analytic approximation (9)-(11), with velocities $v_+ = 0.88$ and $v_- = -1$, cf. Fig. 9. Arrow: analytical asymptotics $v \rightarrow 0.358$ for $T \rightarrow \infty$ according to (6).

the maximal F in Fig. 4 and the maximal T in Fig. 7 with v opposite to F , see Sec. VB below. Comparison of Figs. 1 and 6 furthermore suggests that periodic attractors of low period are more stable against noise than those of high period and phase locked aperiodic solutions.

A. Analytic approximation

The noisy counterpart of the deterministic, period-one solution from Fig. 5 is depicted in Fig. 8. According to Fig. 8a, roughly speaking, the trajectory seems to switch randomly between pieces with a negative slope v_- and pieces with a positive slope v_+ . Those with v_- are almost perfectly periodic and indeed practically coincide with the deterministic period-one orbit and hence one readily understands that $v_- = -1$. Those with v_+ have an aperiodic fine structure which can be naturally understood as the fingerprint of the underlying chaotic repeller, see the above discussion of Fig. 3. Contrary to the naive first guess $v_+ \approx 1$, the average velocity of long lived transients on the repeller is found to be $v_+ \approx 0.88$, cf. Fig. 8b. In other words, the chaotic repeller does not strictly maintain the velocity of the former attractor, and in fact there does not seem to be any reason why it should do so.

We have analyzed the above noisy transitions between the period-one attractor and the chaotic repeller by extensive numerical simulations for a number of temperatures T between 2.5×10^{-3} and 6.7×10^{-4} . We found that they can be described very well in terms of escape

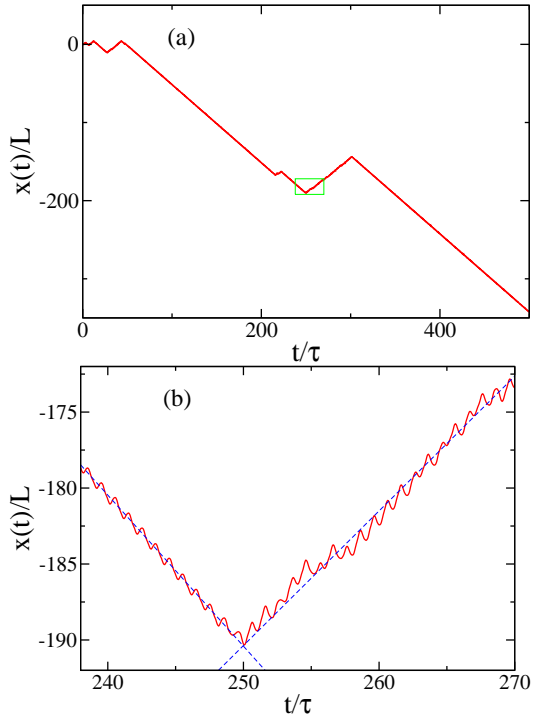


FIG. 8: (Color online) Typical numerical solution $x(t)$ of the dynamics (1), (2), (5), with parameter values (7) (labeled by the larger black cross in Figs. 1, 2, 6), and with $T = 0.001$ and $F = 0.1$. (a) Global behavior. (b) Magnification of the green window in (a). Dashed: straight lines with slopes $v_+ = 0.88$ and $v_- = -1$.

rates k_- and k_+ from the periodic orbit and the repeller, respectively [46]. Thus, we adopt a two state Markov model for the system with the states being the attractor ('-' state) and the repeller ('+' state). Asymptotically, the escape rates are given by the inverse lifetimes of the states. In principle, these could be determined from the average (temporal) length of the uninterrupted $v = -1$ ($v \approx 0.88$, respectively)-segments of the noisy trajectory, cf. Fig. 8. The length of these segments is expected to follow an exponential distribution for sufficiently long segments, and the average lifetimes can be obtained from the exponents of the cumulative distribution functions. However, the numerical determination of the time instant at which the motion switches from one state to the other turned out to be ambiguous when based only on the particle position $x(t)$. It is more convenient to use a well-defined set in the (x, v) phase space that represents the '-' state with motion on or close to the phase locked attractor, and to track when the trajectory leaves this set and enters its complement, corresponding to the '+' state on the repeller.

This approach is illustrated with Fig. 9. The crosses represent the stroboscopic signature of the $v = -1$ at-

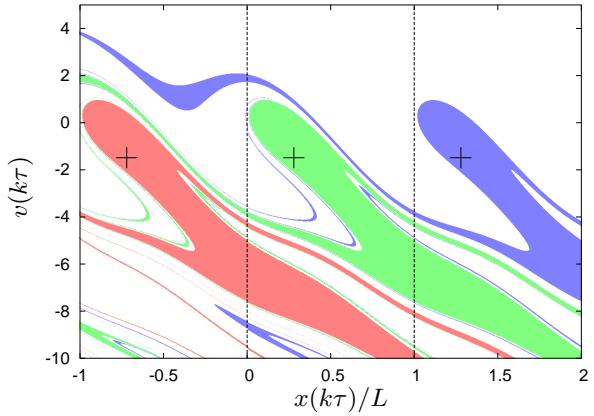


FIG. 9: (Color) Stroboscopic representation of the phase-locked periodic attractor with $v = -1$ (black crosses), whose time evolution is illustrated in Fig. 5, shown within three spatial periods of the full (x, v) phase space (indicated by the dashed lines) for three consecutive driving periods. The colored regions represent the synchronous basin of attraction of the attractor (see main text) also for these three driving periods. The right cross and blue region correspond to the first, the middle cross and green region to the second, and the left cross and red region to the third driving period. This picture can be periodically repeated to the right and to the left to obtain the attractor and its synchronous basin of attraction for previous and later driving periods, respectively. The synchronous basins of attraction of all these periods have filaments that extend into the shown part of the phase space, and if one included them, they would completely cover the white region.

tractor for three successive driving periods, i.e. if the trajectory starts on the rightmost cross in Fig. 9, it is located on the middle cross one period later, and on the left cross another period later. A deterministic solution ($T = 0$) starting from any other point in the phase plane [48] (irrespective of its color) is eventually attracted to this periodic trajectory. The colored regions consist of those trajectories in phase space that, while converging to the attractor, move "synchronously" with a trajectory on that attractor, i.e. a point from the blue region jumps to the green region and then to the red region during two successive driving periods. We term this subset of the total basin of attraction the "synchronous basin of attraction", and use it to define the set in phase space that represents the '-' state of the noisy dynamics in the following way. A noisy trajectory switches from the '+' state to the '-' state when entering the blue part of the synchronous basin of attraction within the rightmost spatial period of Fig. 9 (or the green part within the middle period, or the red part within the left period, etc.), and remains in the '-' state until it leaves the synchronous basin of attraction of the associated attractor [22]. Consequently, a trajectory in the '-' state moves uphill against the force $F > 0$ with $v = -1$ exactly like a

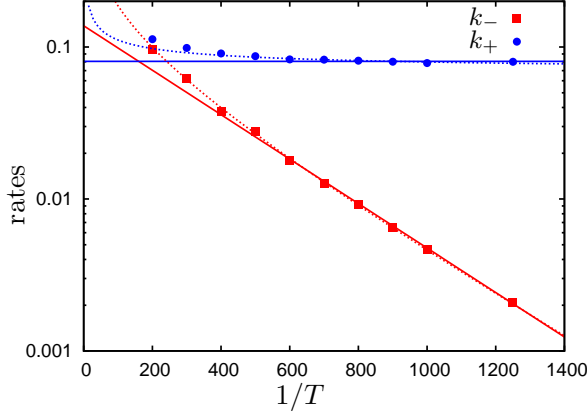


FIG. 10: (Color online) Arrhenius plot of the escape rates k_- and k_+ from the attractor (red squares) and the repeller (blue dots), respectively. Remaining parameter values: same as in Figs. 5, 7-9. The statistical uncertainties are of the order of the symbol sizes. The solid lines represent the data fits (8), the dashed lines show (9). All fits are based only on the escape rates for temperatures $T \lesssim 0.0025$, because in this temperature range the description of the noisy trajectories in terms of transitions between the '+' and '−' state with respective escape rates k_+ and k_- is expected to be valid, as is self-consistently concluded from the obtained values in the exponents of (8) and (9).

trajectory on that attractor (and would continue to do so if the noise source is switched off). The behavior in the complementary '+' state is characterized by a downhill motion close to the chaotic repeller resulting in $v \approx 0.88$.

Based on this definition of the '+' and '−' states, the average lifetime of the attractor is calculated from the average time it takes a trajectory, initialized on the attractor [49], to leave the synchronous basin of attraction for the first time. The average lifetime of the repeller is determined from an ensemble method [1], which basically estimates the exponential part of the decay into the '−' state of a population of trajectories being initialized close to the repeller in the '+' state.

The temperature dependence of the resulting escape rates is shown in Fig. 10. The escape rate k_- from the attractor (red squares) is found to be well described by an Arrhenius law [22], whereas the escape rate k_+ from the repeller (blue dots) is found to be roughly temperature independent (cf. solid lines in Fig. 10):

$$k_- = 0.14 \exp(-0.0034/T), \quad k_+ = 0.081. \quad (8)$$

These approximations can be improved by taking into account the temperature dependence of the pre-factor in the Arrhenius law of k_- [50], and by heuristically including a lowest order temperature dependence of k_+ of the form \sqrt{T} , yielding (cf. dashed lines in Fig. 10)

$$k_- = 2.5\sqrt{T} \exp(-0.0028/T), \quad k_+ = 0.07 + 0.46\sqrt{T}. \quad (9)$$

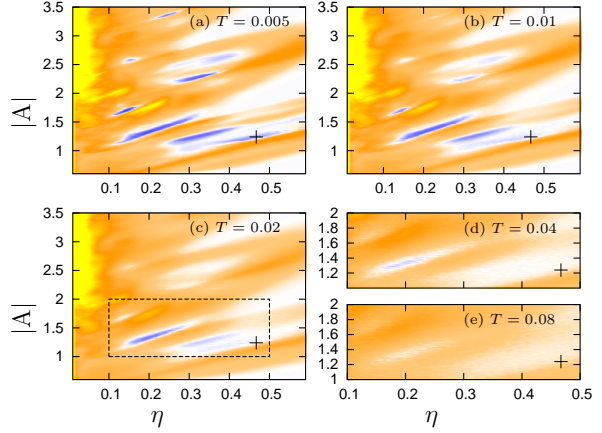


FIG. 11: (Color) Same as Fig. 6, but for $F = 0.05$ and various T ; blue indicates negative velocities with transport against the bias (see color panel in Fig. 6). (d) and (e) represent magnifications of the dashed box in (c), but for higher temperatures. Negative average velocities can still be observed for $T = 0.04$. The black cross represents the parameter values (7).

Both, the Arrhenius form of k_- and the approximate T -independence of k_+ are quite plausible, while the quantitative details are clearly beyond the analytical realm.

Next, the probabilities p_- and p_+ to be in the '−' state on the attractor and the '+' state on the repeller, respectively, will be approximately proportional to the inverse escape rates (lifetimes) and normalized, i.e.

$$p_{\pm} = \frac{k_{\pm}^{-1}}{k_+^{-1} + k_-^{-1}}. \quad (10)$$

Finally, this suggests to approximate the velocity v by the average over the velocities v_{\pm} associated with attractor and repeller, weighted with the respective probabilities p_{\pm} ,

$$v \simeq v_+ p_+ + v_- p_-. \quad (11)$$

The agreement with the numerical results in Fig. 7 is remarkably good even at rather high T , where the rate theory is expected to fail. Surprisingly, the more sophisticated form (9) of the escape rates shows no notable improvement as compared to the less precise representation (8). The reason is that by (8) both, k_- and k_+ , are underestimated for larger T (see Fig. 10) so that the respective errors compensate in (10).

B. Maximal temperature and bias

Next, we address the question: What is the maximally achievable temperature which still supports net motion

against the applied bias, and similarly, what is the maximally achievable bias?

Figure 7 shows that the attracting properties of the periodic $v = -1$ orbit are overruled by thermal noise effects if T becomes large, so that finally the average velocity is in the direction of the bias F . Although it is clear from the discussion of Eq. (6) that for high enough temperatures T transport is always (i.e. for any values of the other parameters in (1)) in the direction of F , the quantitative details of the temperature region with v opposite to F depend on the specific properties of all attractors and repellers present, and thus on the specific parameter values in (1), (2). For our choice (7), e.g., we see from Fig. 4 (lower part) that a smaller bias F (still $F > 0$) allows for larger T with an average motion against the bias. A more comprehensive picture of this observation is presented with Fig. 11, showing that part of Fig. 6, which contains the blue regions with average velocities opposite to F , for smaller bias but larger temperatures. From Fig. 11(d) we see that transport against the bias is possible even for temperatures as high as $T = 0.04$ for optimized values of η and A .

One might conjecture that the temperature range with v opposite to F becomes largest for $F \rightarrow 0$. This is, however, not generally true, because the stability of the present attractors can change considerably with decreasing F , and even new attractors or repellers with other T -specific properties can come into play and dominate the transport behavior. Indeed the parameter values (7) constitute an example for such a situation, as discussed in detail in Sec. VI below.

From a complementary point of view, we may expect that the strength of the bias F at which the negative average velocity finally becomes positive and then follows the direction of F can be larger for smaller temperatures T . Although we could find (numerically) transport against the bias for forces up to $F = 0.32$ at $T = 4 \times 10^{-5}$, a general statement is not possible in the same sense as above.

C. Speedy uphill motion

In comparison with purely noise-induced negative mobilities as studied in [7–9, 13, 15], the maximal velocities against the external bias observed here are considerably larger (typically at least by one order of magnitude). As detailed above, this is due to the fact that for not too large temperatures the noisy dynamics (1) is governed by the presence of phase locked attractors with deterministic transport in the direction opposite to the bias. Accordingly, the effect can readily be accelerated by exploiting phase locked attractors with higher velocities $|v|$, see Fig. 1. As an example, we consider $n/m = 3$ by choosing the parameter values given in Fig. 12. These values are located at the upper border of the green region in Fig. 1 around $\eta \approx 0 \dots 0.23$ and $A \approx 1.5 \dots 1.8$, which indicates the existence of a symmetric pair of period-one

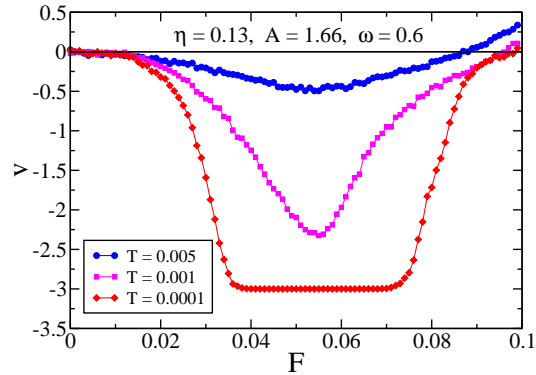


FIG. 12: (Color online) Average velocity v for the given parameter values and for various temperatures, obtained from numerical simulations of (1), (2). The indicated values for η and A are located at the upper border of a green region in Fig. 1 with deterministic transport velocities $|v| = 3$.

attractors with $|v| = 3$. Hence, transport against the bias F occurs by the same mechanism as illustrated with Fig. 2 for the $|v| = 1$ attractors. The resulting speedy uphill motion is depicted in Fig. 12 for various temperatures T . Surprisingly, it is comparably robust against noise and only little less stable with respect to increasing bias forces F as the slower uphill motion in Fig. 7.

In principle, unlimited acceleration of the uphill transport seems to be possible by using attractors with even higher deterministic velocities $|v|$. In practice, however, this is limited by the fact that such attractors are typically located at smaller η -values in coexistence with other attractors, and only exist in rather small parameter regions.

D. Non-transporting attractors and comparison with Ref. [15]

Non-transporting phase locked deterministic solutions with $v = 0$ typically exist over large parameter ranges (see, e.g., the grey region in Fig. 1). If there is a parameter region, in which such a non-transporting solution coexists with a symmetric pair of transporting attractors at $F = 0$, then absolute negative mobility can occur for suitable parameter values at the border of that region by the same mechanism as detailed in Fig. 2. The only qualitative difference to Fig. 2 is that the white background would be grey, indicating the coexisting $v = 0$ attractor. This situation is exemplified by Fig. 13 for some finite bias $F > 0$ (compare to Fig. 2c); suitable parameter values are located in the blue region, indicating the existence of a transporting attractor with $v = -1/2$. Correspondingly, the noisy trajectories at small temperatures T switch between three different states, since the uphill and downhill transporting ‘-’ and ‘+’ states are

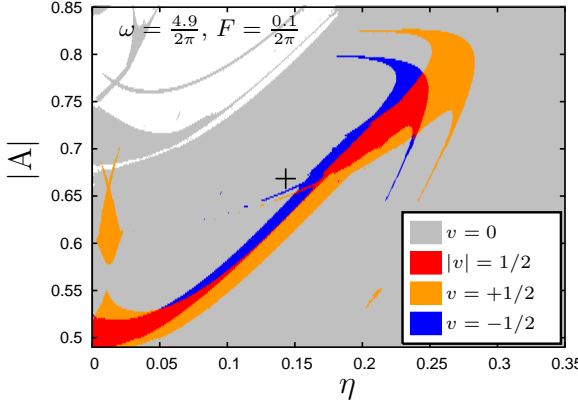


FIG. 13: (Color) Same as Fig. 2, but for the case of coexisting $v = 0$ and $v = \pm \frac{1}{2}$ attractors. The indicated cross and the chosen frequency ω and bias force F represent the parameter values used in Figs. 1 and 2 of Ref. [15]; a vertical section through the cross corresponds to Fig. 1(a) therein. (Note that the units used by us and in Ref. [15] differ by some factors of 2π .)

now complemented by a non-transporting '0' state. As a main consequence, the achievable velocities v opposite to F are slowed down considerably.

In contrast to the above situation, the parameter values indicated by the black cross in Fig. 13 are never reached by the blue region for any bias $F > 0$ (nor by the orange and red regions). Nevertheless, absolute negative mobility can occur by another, different mechanism: Obviously, at $T = 0$ we find $v = 0$, because the non-transporting solution is globally attractive. At small temperatures T , however, the dynamics is governed not only by the stable $v = 0$ orbit but also by two repellers that emerge from the $v = -1/2$ and $v = 1/2$ attractors due to crises occurring at the border lines of their stability regions (the blue and orange region in Fig. 13). Since the escape time from a repeller scales with the distance from the crisis according to some power law [51], and since the black cross in Fig. 13 for $F > 0$ is closer to the blue than to the orange region, the major contribution of the chaotic repellers to the noisy trajectories comes from the repeller with negative $v \approx -1/2$. As a result, an average velocity v opposite to the bias F is observed for small temperatures T .

The above explanations represent our announced complementary intuitive insight into the basic physical mechanism behind the effect of "absolute negative mobility induced by thermal equilibrium fluctuations", recently reported by Machura *et al.* [15]. While the latter effect *per se* is qualitatively very similar to the one discussed in the previous Section of our present paper (see also Ref. [14] and footnote [22] in Ref. [15]), the underlying basic physical mechanism is thus quite different. Moreover, qualitatively the maximally achievable velocities are sub-

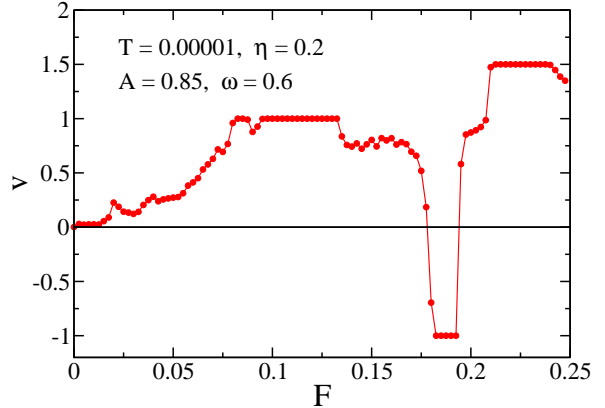


FIG. 14: (Color online) Symbols: Numerically determined velocity v from (3) for (1), (2) with parameters as indicated in the plot. The numerical uncertainty is smaller than the symbol size. The red line is a guide to the eye.

stantially smaller: In our units, the maximal velocity v opposite to a negative bias F reported by Machura *et al.* [15] is about $v = 0.017$, and our more detailed numerical analysis of the parameter range from Fig. 13 indicates that one indeed can hardly do better.

In summary, the distinct feature of the effect reported in Ref. [15] is that it is purely noise induced, while the effect at the main focus of Ref. [14] and our present study has the advantage of producing much larger velocities.

VI. FURTHER ANOMALOUS TRANSPORT PROPERTIES

Our so far understanding of the system (1), (2) allows us to readily predict further remarkable transport properties. Two examples are discussed in the following.

First, we consider the small black cross in Fig. 2 at

$$\eta = 0.2 \quad A = 0.85. \quad (12)$$

For small bias F we are somewhere in the white or grey domains of Fig. 1. Around $F = 0.1$ the small black cross in Fig. 2c penetrates a bulge of the orange area which is "moving upwards" as a function of F . Hence, a velocity v of the same sign as F is expected. At the still larger F -value in Fig. 2d, the small black cross has left the orange bulge again and now instead is hit by the blue stripe, so that we expect a velocity v opposite to F . The corresponding prediction for the velocity v as a function of the bias F is nicely confirmed by the numerical simulations in Fig. 14. For small bias, the velocity direction is as usual, but changes sign upon increasing the bias, before returning to normal for even larger F [52].

Second, we focus on the small periodic window around $F = 0.007$ in Fig. 4. This window represents an attractor with a unique deterministic velocity $v = 2/3$ in the

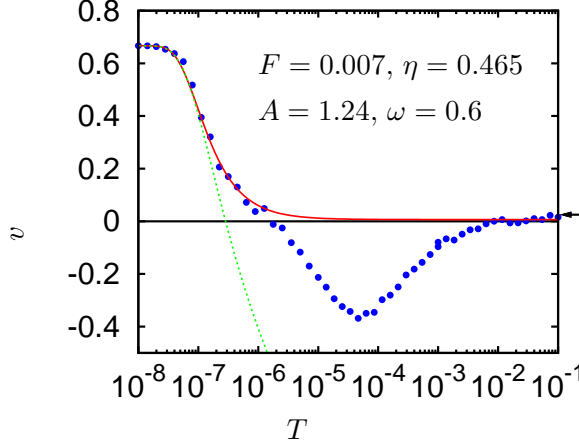


FIG. 15: (Color online) Same as Fig. 7, but for $F = 0.007$. Lines: approximation (10)-(11) with $v_+ = 2/3$, $v_- = -1$, and $k_+ = 0.024 \exp(-1.35 \times 10^{-7}/T)$, $k_- = 0.036$ (red solid line), $k_- = 0.038 - 6.6\sqrt{T} k_+ = 63\sqrt{T} \exp(-1.1 \times 10^{-7}/T)$, (green dashed line).

direction of the bias F . The reason for the appearance of this attractor at small bias forces is that the parameter values (7) indicated by the larger black cross in Figs. 1 are not exactly located at the upper border of the red stripe but somewhat above. The $v = -1$ attractor contained in this red region and emerging from it in blue in Fig. 2 reaches the larger black cross only at $F \approx 0.012$ (cf. Fig. 4); for smaller F it turns into a chaotic repeller. Similarly as in (8)-(11), one thus has a competition between the deterministic attractor with $v_+ = 2/3$ and this chaotic repeller with $v_- \approx -1$. As confirmed by Fig. 15, for small T the attractor with $v \simeq 2/3$ wins, then the repeller with $v \simeq -1$ takes over, and finally the usual large- T asymptotics $v = (\tau/L)(F/\eta) \simeq 0.028$ according to (6) is approached. Therefore, the response behavior for the bias force around $F = 0.007$ is as usual in the direction of F for low temperatures, but upon increasing the temperature first turns opposite to F , and then switches again to normal. Note that of the temperatures $T > 0$ shown in Fig. 4 only the largest one falls into the ranges with positive v at $F \approx 0.007$.

VII. ABSOLUTE NEGATIVE CONDUCTANCE IN A JOSEPHSON JUNCTION

As a concrete experimental example of the predicted absolute negative mobility we consider the Stewart-McCumber or RCSJ (resistively and capacitively shunted junction) model [22, 31] for the phase difference φ across a Josephson junction with capacity C , resistance R , critical current I_c (maximal Josephson current), and externally imposed current $I(t)$. Within this model, the φ

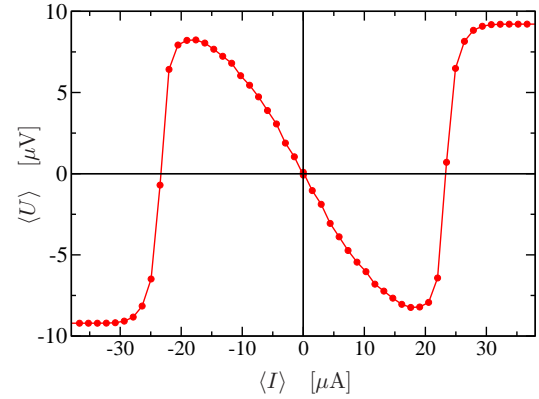


FIG. 16: (Color online) Same data as the green symbols in Fig. 4 but presented according to the Stewart-McCumber model (1), (2), (13), (14) for a Josephson junction with resistance $R \approx 0.2 \Omega$, capacity $C \approx 250 \text{ pF}$, critical current $I_c \approx 180 \mu\text{A}$, temperature $T \approx 4.2 \text{ K}$, driven by an ac-current of frequency 28 GHz and amplitude 220 μA .

dynamics is governed by the dimensionless equations (1), (2) via the identifications

$$\begin{aligned} \varphi(t/\omega_p) &= x(t), \quad I(t/\omega_p) = I_c [f(t) + F], \\ \eta &= (RC\omega_p)^{-1}, \quad T = C(\omega_p/I_c)^2 k_B T^*, \end{aligned} \quad (13)$$

where $\omega_p := (2\pi I_c/\Phi_0 C)^{1/2}$ is the plasma frequency, $\Phi_0 := h/2e$ the flux quantum, and $k_B T^*$ the thermal energy.

As far as the RCSJ model is concerned [22, 31], the voltage $U(t)$ across the junction is given by $\Phi_0 \dot{\varphi}(t)/2\pi$ (second Josephson-relation) and hence its average according to (3), (13) by

$$\langle U \rangle = \frac{I_c}{C} \frac{\omega}{\omega_p^2} v \quad (14)$$

Hence, absolute negative mobility for a Brownian particle (1), (2) corresponds to absolute negative conductance in a Josephson junction, characterized by a dc-component of the current $I(t)$ in (13) with sign opposite to average voltage in (14).

Using the relations (13),(14), our predictions from Fig. 4 can be realized by a Josephson junction with resistance $R \approx 0.2 \Omega$, capacity $C \approx 250 \text{ pF}$, critical current $I_c \approx 180 \mu\text{A}$, temperature $T \approx 4.2 \text{ K}$, driven by an ac-current of frequency 28 GHz and amplitude 220 μA . The theoretically predicted I-V curve is shown in Fig. 16.

Additionally, by varying the AC amplitude, noisy I-V characteristics corresponding to bifurcation diagrams in the A direction should be accessible using the same junction. We remark that it is not necessary to hit the given parameters exactly as can be inferred from Fig. 6. Parameter values as exemplified in Fig. 16 are quite realistic and the resulting voltages $\langle U \rangle$ easily detectable.

Such an experiment [54] is presently under construction in the group of Dieter Kölle and Reinhold Kleiner in Tübingen (Germany). In fact, the effect might have already been implicitly observed (without further discussion or explanation) in the experimental work [55].

VIII. SUMMARY AND CONCLUSIONS

In conclusion, we have unraveled in Figs. 4,14,15 three rather astonishing transport properties of the one dimensional stochastic dynamics (1), (2): (i) a transport opposite to the static bias F (absolute negative mobility, Fig. 4), (ii) anomalous non-linear response in form of a average particle velocity that follows the direction of F for small F , but switches direction upon increasing F (Fig. 14), and (iii) a reversal of the transport direction from normal to anomalous at a fixed bias force F but for increasing temperature T (Fig. 15).

Apart from our own brief account [14] on such phenomena and the independent discovery of effect (i) by Machura *et al.* [15] (see Sec. V.D), further preliminary hints to the existence of effects (i) and (ii) in a one dimensional model (1), and an experimental trace of effect (i) are also implicitly contained already in the previously existing literature on Josephson junctions (see [35, 52, 55]). These findings are, however, not further discussed or explained in those works, because their focus is on other (dynamical) aspects of Josephson junctions. In fact, these “accidental” observations of the above effects (i), (ii) point to their remarkably common occurrence in dynamical systems like (1), as demonstrated by our present paper.

The above effects (i)-(iii) are observed for system parameters that are all of the order of magnitude of unity. This fact makes analytical studies extremely difficult; for instance, a perturbational approach becomes completely impossible. Accordingly, our detailed analysis of the model (1), (2), its deterministic limit, and the effects of noise due to finite temperatures relies on extensive numerical simulations. An important exception is our strict proof using mathematical and physical arguments that the model (1) is minimal, in the sense that any of the terms in (1) is indispensable for the occurrence of the above phenomena.

Based on the numerical findings, we were able to develop a simple intuitive physical picture for the mechanism behind the observed response phenomena. Their occurrence is traced back to a subtle interplay of deterministic phase locked attractors, transient chaos on chaotic repellers and noise-induced metastability of these dynamical “states”. The latter has been shown to be well

described by a simple rate-theoretical approach (see Section V.A).

Apart from their fundamental interest [11, 12, 32] the effects (i)-(iii) may be applied for particle sorting [10], stabilization of unstable states, and making work (transport) available upon request [7]. For instance, one can see from Fig. 6 that particles with different friction coefficients (e.g. due to different sizes) can easily be guided into opposite directions by a suitable choice of the driving amplitude A .

As an experimental realization of the predicted effects we propose resistively and capacitively shunted Josephson junctions. Their dynamical behavior is characterized by the RCSJ- or Stewart-McCumber model which is mathematically equivalent to our model (1), (2). Suitable parameter values for which the above effects are predicted to occur are quite realistic experimentally.

Further experimental realization may be cold atoms in resonance with laser induced optical lattices [56, 57] and diffusion of single atoms and molecules on atomically clean crystal surfaces [58–60]. In such systems, the bias F and/or the driving $f(t)$ in (1) may also be substituted [61] by suitable “traveling-wave potentials” (pump) in place of the static $V(x)$. More precisely, $-V'(x(t)) + f(t) + F$ in (1) is replaced by $-V'(x(t) - v_0 t - g(t))$, with average velocity v_0 and superimposed sinusoidal oscillations $g(t)$. Indeed, for the transformed variable $y(t) := x(t) - v_0 t - g(t)$ one readily recovers [61] the original dynamics (1) with $F = -\eta v_0$ and a suitably chosen A in (2). The effects predicted in the present work would result in averaged velocities that are considerably faster than the traveling velocity v_0 of the “entraining” potential, so that the particle is “running ahead” of the traveling-wave potential.

Finally, the basic physical mechanism as identified in our discussion of Figs. 1-3 is clearly quite robust against a large variety of modifications and generalizations of the dynamics (1), (2). The only indispensable prerequisites are deterministic chaos, phase locking, and the symmetry properties $V(-x) = V(x)$ and $f(t + \tau/2) = -f(t)$. For example, we have found similar effects for various non-harmonic $V(x)$ and $f(t)$ in (1) and also when the “periodically rocking force field” $-V'(x) + f(t)$ in (1) is replaced by a “pulsating field” of the form $-V'(x)[1 + f(t)]$.

Acknowledgements

We thank T. Tél, D. Kölle, R. Kleiner, and P. Talkner for stimulating discussions. This work was supported by Deutsche Forschungsgemeinschaft under SFB 613, RE 1344/3-1, and RE1344/5-1

[1] For a review see T. Tél in *Directions in Chaos*, edited by Hao Bai-Lin, (World Scientific, Singapore, 1990), Vol. 3.

[2] M. Franaszek, Phys. Rev. A **44**, 4065 (1991); P. Reimann, J. Stat. Phys. **82**, 1467 (1996).

[3] a) E. R. Kay, D. A. Leigh, and F. Zerbetto *Angew. Chem. Int. Ed.* **46**, 72 (2007); b) P. Reimann, *Phys. Rep.* **361**, 57 (2002); c) H. Linke (special issue guest editor), *Appl. Phys. A* **75** 167, (2002); d) J. Klafter J. and M. Urbakh (special issue guest editors), *J. Phys.: Condens. Matter* **17**, S3661 (2005).

[4] K. Wiesenfeld, F. Moss, *Nature* **373**, 33 (1995); L. Gamaitoni, P. Hänggi, P. Jung, F. Marchesoni, *Rev. Mod. Phys.* **70**, 223 (1998).

[5] Hu Gang, A. Daffertshofer, H. Haken, *Phys. Rev. Lett.* **76**, 4874 (1996); G. Costantini and F. Marchesoni, *Europhys. Lett.* **48**, 491 (1999); P. Reimann, C. Van den Broeck, H. Linke, P. Hänggi, J. M. Rubi, and A. Pérez-Madrid, *Phys. Rev. Lett.* **87**, 010602 (2001).

[6] J. M. G. Vilar, J. M. Rubi, *Phys. Rev. Lett.* **86**, 950 (2001); Y. Seol, K. Visscher, and D. B. Walton, *Phys. Rev. Lett.* **93**, 160602 (2004).

[7] R. Eichhorn, P. Reimann, B. Cleuren, and C. Van den Broeck, *Chaos* **15**, 026113 (2005).

[8] R. Eichhorn, P. Reimann, P. Hänggi, *Phys. Rev. Lett.* **88**, 190601 (2002); *Phys. Rev. E* **66**, 066132 (2002); B. Cleuren, C. Van den Broeck, *Phys. Rev. E* **67**, 055101(R) (2003); R. Eichhorn and P. Reimann, *Europhys. Lett.* **69**, 517 (2005).

[9] B. Cleuren and C. Van den Broeck, *Phys. Rev. E* **65**, 030101(R) (2002); B. Jiménez de Cisneros, P. Reimann, and J. M. R. Parrondo, *Europhys. Lett.* **64**, 599 (2003).

[10] A. Ros *et al.*, *Nature* **436**, 928 (2005); R. Eichhorn *et al.*, *Eur. Phys. J. Special Topics* **143**, 159 (2007); J. Regtmeier *et al.*, *Eur. Phys. J. E* **22**, 335 (2007); J. Regtmeier *et al.*, *J. Sep. Sci.*, in press.

[11] T. J. Banis, I. V. Parsheleyunas, and Y. K. Pozhela, *Sov. Phys. Semicond.* **5**, 1727 (1972).

[12] B. J. Keay *et al.*, *Phys. Rev. Lett.* **75**, 4102 (1995).

[13] R. Eichhorn, P. Reimann, and P. Hänggi, *Physica A* **325**, 101 (2003); R. Eichhorn and P. Reimann, *Phys. Rev. E* **70**, 035106(R) (2004).

[14] D. Speer, R. Eichhorn, and P. Reimann, *EPL* **79**, 10005 (2007).

[15] L. Machura, M. Kostur, P. Talkner, J. Luczka, and P. Hänggi, *Phys. Rev. Lett.* **98**, 040601 (2007).

[16] H. Risken, *The Fokker-Planck Equation* (Springer, Berlin, 1984).

[17] M. Borromeo and F. Marchesoni, *Phys. Rev. Lett.* **84**, 203 (2000); P. Reimann, C. Van den Broeck, H. Linke, P. Hänggi, J. M. Rubi, and A. Pérez-Madrid, *Phys. Rev. E* **65**, 031104 (2002).

[18] E. G. Gwinn and R. M. Westervelt, *Phys. Rev. Lett.* **54**, 1613 (1985).

[19] M. Iansiti, Q. Hu, R. M. Westervelt, and M. Tinkham, *Phys. Rev. Lett.* **55**, 746 (1985).

[20] R. L. Kautz, *J. Appl. Phys.* **52**, 3528 (1981).

[21] R. L. Kautz and R. Monaco, *J. Appl. Phys.* **57**, 875 (1985).

[22] R. L. Kautz, *Rep. Prog. Phys.* **59**, 935 (1996).

[23] P. Jung, *Phys. Rep.* **234**, 175 (1993).

[24] Y. Yu and S. Han, *Phys. Rev. Lett.* **91**, 127003 (2003).

[25] F. Marchesoni, *Phys. Lett. A* **231**, 61 (1997).

[26] R. L. Kautz, *Phys. Lett. A* **125**, 315 (1987).

[27] P. Jung and P. Hänggi, *Ber. Bunsenges. Phys. Chem.* **95**, 311 (1991).

[28] M. Borromeo, G. Costantini, and F. Marchesoni, *Phys. Rev. Lett.* **82**, 2820 (1999).

[29] H.-J. Breymayer, *Appl. Phys. A* **33**, 1 (1984); P. Jung, J. G. Kissner, and P. Hänggi, *Phys. Rev. Lett.* **76**, 3436 (1996); J. L. Mateos, *ibid.* **84**, 258 (2000); J. L. Mateos, *Acta Physica Polonica B* **32**, 307 (2001); J. L. Mateos, *Physica A* **325**, 92 (2003); M. Barbi and M. Salerno, *Phys. Rev. E* **62**, 1988 (2000); C. M. Arizmendi, F. Family, and A. L. Salas-Brito, *Phys. Rev. E* **63**, 061104 (2001); M. Borromeo, G. Costantini, and F. Marchesoni, *Phys. Rev. E* **65**, 041110 (2002); W. S. Son, I. Kim, Y. J. Park, and C. M. Kim, *Phys. Rev. E* **68**, 067201 (2003); F. Marchesoni, S. Savel'ev, and F. Nori, *Phys. Rev. E* **73**, 021102 (2006); M. Kostur, L. Machura, P. Hänggi, J. Luczka, and P. Talkner, *Physica A* **371**, 20 (2006).

[30] H. Schanz, T. Dittrich, and R. Ketzmerick, *Phys. Rev. E* **71**, 026228 (2005); S. Denisov, S. Flach, and P. Hänggi, *Europhys. Lett.* **74**, 588 (2006);

[31] W. C. Steward, *Appl. Phys. Lett.* **12**, 277 (1968); D. E. McCumber, *Appl. Phys.* **39**, 3113 (1968); K. K. Likharev, *Dynamics of Josephson Junctions and Circuits* (Gordon and Breach, Philadelphia, 1986); W. Buckel and R. Kleiner, *Superconductivity: Fundamentals and Applications* (Wiley-VHC, Berlin, 2004).

[32] R. K. P. Zia, E. L. Praestgaard, and O. G. Mouritsen, *Am. J. Phys.* **70**, 384 (2002).

[33] We remark that g and h containing δ -spikes or a shot noise $\xi(t)$ would lead to discontinuous $x(t)$ and hence spoil the argument.

[34] G. A. Cecchi, M. O. Magnasco, *Phys. Rev. Lett.* **76**, 1968 (1996).

[35] A first hint along this line is implicitly buried in three papers by Kautz, namely in Fig. 4 of [20], Fig. 3a of [21], and Figs. 13c, 25b of [22]. A second hint comes from the recent works [30] on the Hamiltonian limit $\eta \rightarrow 0$ in (1), implying the existence of deterministic solutions running against the force F for suitably chosen initial conditions. Investigating and optimizing their stability against dissipation and noise (finite η) could have been an alternative starting point of our present work, but in fact our approach was different.

[36] C. Chi and C. Vanneste, *Phys. Rev. B* **42**, 9875 (1990).

[37] We use the term “attractor” both for a stable, “attracting” orbit $x(t)$ of the dynamics and for the thereby sampled “attracting set” in phase space. In the latter case we tacitly consider the reduced version of the spatially periodic dynamics (1), i.e. x and $x + L$ are identified as far as the attracting set is concerned.

[38] Such a solution may be either chaotic or of non-chaotic, aperiodic type (Feigenbaum attractor).

[39] Such a solution may be either chaotic or quasiperiodic. The former case is closely related with deterministic diffusion [40]. The latter case is possible only for finite bias F for the specific deterministic dynamics (1), (2), see Sect. 5 in [22].

[40] H. Fujisaka and S. Grossmann, *Z. Phys. B* **48**, 261 (1982); T. Geisel and J. Nierwetberg, *Phys. Rev. Lett.* **48**, 7 (1982); M. Schell, S. Fraser, and R. Kapral, *Phys. Rev. A* **26**, 504 (1982).

[41] Other phase locked attractors (with different velocities), which have not been found by our numerical method due to the finite grid resolution in η and A and the limited number of random initial conditions sampled, either have very small basins of attraction and/or exist only in very small regions of the (η, A) parameter space. The same applies for non-phase locked attractors that may coexist with phase locked attractors in the considered parameter

region.

[42] For $M = T = 0$ in (1), the velocity (3) must be unique, see [43] and Sect. 5.3.2 in [3b], though one may still have coexisting attractors [44].

[43] A. Ajdari, D. Mukamel, L. Peliti, and J. Prost, *J. Phys. I France* **4**, 1551 (1994).

[44] R. Bartussek, P. Hänggi, and J. G. Kissner, *Europhys. Lett.* **28**, 459 (1994).

[45] C. Grebogi, E. Ott, and J. A. Yorke, *Phys. Rev. Lett.* **48**, 1507 (1982); R. L. Kautz, *J. Appl. Phys.* **62**, 198 (1987)

[46] F. T. Arecchi, R. Badii, and A. Politi, *Phys. Rev. A* **32**, 402 (1985); R. L. Kautz, *J. Appl. Phys.* **58**, 424 (1985); P. Reimann, R. Müller, and P. Talkner, *Phys. Rev. E* **49**, 3670 (1994).

[47] For $T > 0$ and $F = 0$ one always has $v = 0$ due to symmetry and ergodicity.

[48] In the sense that points located exactly on an unstable trajectory have measure zero, and that the basins of attraction of possibly coexisting attractors have negligible measure (see remark [41]).

[49] This implicitly assumes that the escape rate is independent of the initial condition in the synchronous basin of attraction, which is well justified for small temperatures. Regions of the synchronous basin of attraction close to its borders or very far from the attractor, which might lead to a different escape rate have small statistical weights and can be neglected.

[50] J. Lehmann, P. Reimann, P. Hänggi, *Phys. Rev. Lett.* **84**, 1639 (2000); *Phys. Rev. E* **62**, 6282 (2000).

[51] J. C. Sommerer, *Phys. Lett. A* **176**, 85 (1993).

[52] A first theoretical hint for the occurrence of this effect in the closely related Stewart-McCumber model for Josephson junctions (see Sec. VII) has been observed in Fig. 8 of [53], however, without any further discussion or explanation.

[53] D. C. Cronemeyer, C. C. Chi, A. Davidson, and N. F. Pedersen, *Phys. Rev. B* **31**, 2667 (1985).

[54] A. Sterck, R. Kleiner, and D. Koelle, *Phys. Rev. Lett.* **95**, 177006 (2005); M. Beck *et al.*, *Phys. Rev. Lett.* **95**, 090603 (2005).

[55] N. F. Pedersen, O. H. Soerensen, B. Dueholm, and J. Mygind, *J. Low. Temp. Phys.* **38**, 1 (1980).

[56] G. Grynberg and C. Robilliard, *Phys. Rep.* **35**, 335 (2001).

[57] R. Gommers, S. Bergamini, and F. Renzoni, *Phys. Rev. Lett.* **95**, 073003 (2005).

[58] T. Ala-Nissila, R. Ferrando, and S. C. Ying, *Advances in Physics* **51**, 949 (2002).

[59] M. Azzouz, H. J. Kreuzer, and M. R. A. Shegelski, *Phys. Rev. B* **66**, 125403 (2002).

[60] G. Antczak and G. Ehrlich, *Phys. Rev. B* **71**, 115422 (2005).

[61] M. Borromeo and F. Marchesoni, *Phys. Lett. A* **249**, 199 (1998); C. Van den Broeck, *Europhys. Lett.* **46**, 1 (1999). R. Landauer and M. Büttiker, *Physica Scripta* **T9**, 155 (1985); L. P. Faucheu, G. Stolovitzky, A. Libchaber, *Phys. Rev. E* **51** (1995) 5239; V. I. Talyanskii, J. M. Shilton, M. Pepper, C. G. Smith, C. J. B. Ford, E. H. Linfield, D. A. Ritchie, G. A. C. Jones, *Phys. Rev. B* **56** (1997) 15180; C. Rocke, S. Zimmermann, A. Wixforth, J. P. Kotthaus, G. Böhm, G. Weimann, *Phys. Rev. Lett.* **78** (1997) 4099.

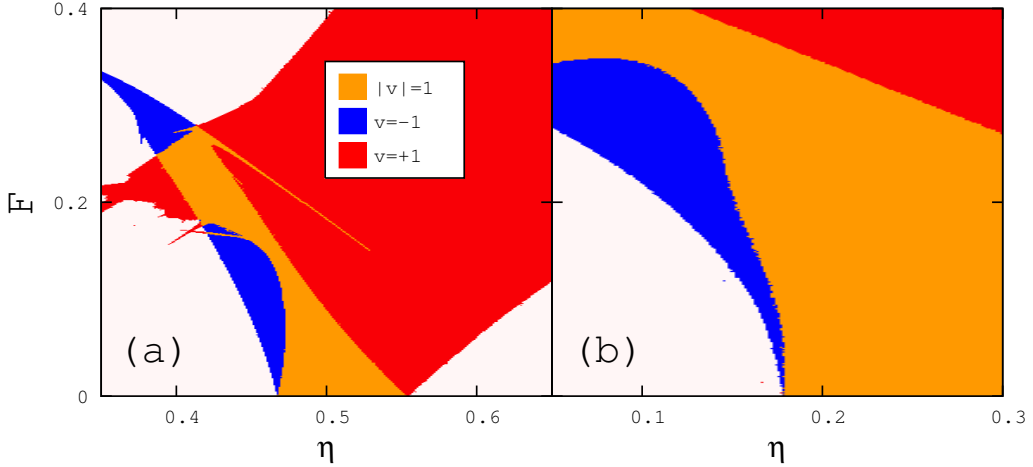


Figure 3.1: Phase diagram at $T = 0$ as described in [2] (figure 2) for (a) the dynamics described by (1)-(2) of [2] and $\omega = 0.6$, $T = 0$ and $A = 1.24$, the colors being identical to figure 2 of [2] and (b) for a particle with coordinate $x(t)$ in a pulsating potential obeying $\ddot{x}(t) + \eta\dot{x}(t) + \sin(0.7t)\sin(x(t)) = F$. All phase diagrams in this chapter have been calculated along the lines of section 3.9.1.

3.4 Mechanism of absolute negative mobility

The mechanism leading to ANM has been described in [1, 2], see section IV.B of [2]. Complementary to [1, 2], the intuitive argument can be beautifully illustrated by the phase diagram figure 3.1 showing the regions of existence of the involved attractors in the η - F plane of parameter space for two different dynamics. The argument can be further explained by the relevant work contributions. For simplicity, we consider a pair of period 1 SSBT attractors with average velocities $v_{\pm} = \pm 1$ (cf. (3) of [2]) and $\dot{x}_{\pm}(t) = \pm \frac{L}{2\pi}\omega + \zeta_{\pm}(t)$. When the particle starts at $x_{0\pm}$ at time $t_{0\pm}$ and advances one length unit in the corresponding transport direction, the work contribution of the dissipation (at zero temperature [156]) is

$$W_{\pm}^{\eta} = -\eta \int_{x_{0\pm}}^{x_{0\pm} \pm L} \dot{x}_{\pm}(t) dx_{\pm}(t) = -\eta\omega \frac{L^2}{2\pi} - \eta \int_{t_{0\pm}}^{t_{0\pm} + \frac{2\pi}{\Omega}} \zeta_{\pm}^2(t) dt, \quad (3.2)$$

and the contribution of the bias force is

$$W_{\pm}^F = \pm FL. \quad (3.3)$$

An increase of F can be compensated for by a decrease of η for the attractor transporting against the bias force, and an increase of η for the symmetry partner, if the change of second term in (3.2) and that of all remaining work contributions could be neglected. The second term in (3.2) can increase or decrease when any parameter of the dynamics is changed, and the same applies to the work performed by the potential and the periodic drive. Essentially, these contributions depend on the shape of the trajectory, i.e. $\zeta_{\pm}(t)$, and if that were to remain constant when F and η are varied, the intuitive explanation would be exact. Furthermore, the argument is supported by the so called Bessel function approximation [137, 157], cf. (3.5), and the relation between F and η implied by the

argument becomes exact for the attractor carrying transport in the direction of the bias force for large F because $v = \frac{F}{\eta}$ for $F \gg 1$ and all other parameters of order 1. Lastly, it can be extended to phase-locked chaotic attractors when a longer time interval is considered, and the argument can be extended to the drive frequency because a change of the drive frequency has the same effect as a change of the friction coefficient in (3.2) due to phase-locking, see also section 4.11.2. Hence, we expect the region of existence of the attractor transporting against the bias force to move towards smaller η when F is increased, and that of its symmetry partner to move towards larger η . We have found this argument to be surprisingly well satisfied for the dynamics considered in figure 3.1 for many different parameters.

A particularly noteworthy feature of SSBT of underdamped particles in spatially one dimensional periodic potentials subjected to a sinusoidal periodic rocking drive is that the dynamics can be well approximated by the so called Bessel function approximation [137, 154]. The approximation works for large frequencies ω and drive amplitudes A by making the ansatz

$$x(t) = x_0 + n\omega t + \frac{A}{\omega\sqrt{\omega^2 + \eta^2}} \sin\left(\omega t + \tan\left(\frac{\eta}{\omega}\right)\right), \quad (3.4)$$

inserting (3.4) into the equations of motion and expanding everything into a Fourier series. One obtains that the regions of existence of Shapiro steps of order n , i.e. with $v = n\omega$ and period 1, are given by Bessel functions:

$$|F - \eta\omega n| \leq \left| J_n \left(\frac{A}{\omega\sqrt{\omega^2 + \eta^2}} \right) \right|. \quad (3.5)$$

The borders of the regions of existence given by this approximation can be shown [137] to be saddle node bifurcations, and there are no borders towards smaller η within the approximation, and the 3.5 is in line with the intuitive argument discussed above with respect to the movement of the SSBT parameter regions.

Upon decreasing the frequency towards the “nonlinear regime” [137, 158] (see e.g. figure 27 of [137] and figure 3 of [158]), these Bessel function shaped regions of existence (and the associated Shapiro steps being called Bessel function Shapiro step) develop a resonance like instability at their center leading to a period doubling cascade to a chaotic attractor and the subsequent destruction of that attractor via a boundary crisis [137]. Exactly at this instability, ANM is found close to the regime of validity of the Bessel function approximation [1, 2, 157]. Even for parameters “deep” in the nonlinear regime far from the validity of the Bessel function approximation, the regions of existence of SSBT (and, more generally, phase-locked attractors) keep some of the features of the Bessel function form, most notably the saddle node bifurcation close to the border given by the approximation (see figure 3 of [158]).

Due to the very general nature of the approximation, basically relying only on Fourier expanding the equations of motion in the drive frequency, this locking mechanism is of a very general nature, and hence can be found also for differently shaped potentials [4], drive forces [159–161], overdamped particles [7, 162, 163] and higher dimensions [4, 7, 17, 164, 165], while the associated analytical computations usually cannot be carried out due to the added complexity. In particular, we have found a very similar behavior,

including the remains of Bessel function shaped regions of existence of SSBT attractors, for an overdamped particle in a two dimensional periodic and symmetric potential, see [4] and chapter 4.

3.5 Preprint of [3]

J. Nagel, D. Speer, T. Gaber, A. Sterck, R. Eichhorn, P. Reimann, K. Ilin, M. Siegel, D. Koelle, and R. Kleiner, Physical Review Letters **100**, 217001 (2008),
 Copyright (2008) by the American Physical Society

Observation of negative absolute resistance in a Josephson junction

J. Nagel,¹ D. Speer,² T. Gaber,¹ A. Sterck,¹ R. Eichhorn,²
 P. Reimann,² K. Ilin,³ M. Siegel,³ D. Koelle,¹ and R. Kleiner^{1,*}

¹Physikalisches Institut – Experimentalphysik II and Center for Collective Quantum Phenomena and their Applications, Universität Tübingen, Auf der Morgenstelle 14, D-72076 Tübingen, Germany

²Fakultät für Physik, Universität Bielefeld, 33615 Bielefeld, Germany

³Institut für Mikro- und Nanoelektronische Systeme, Universität Karlsruhe (TH), Hertzstraße 16, D-76187 Karlsruhe, Germany

(Dated: May 9, 2011)

We experimentally demonstrate the occurrence of negative absolute resistance (NAR) up to about -1Ω in response to an externally applied dc current for a shunted Nb-Al/AlO_x-Nb Josephson junction, exposed to a microwave current at frequencies in the GHz range. The realization (or not) of NAR depends crucially on the amplitude of the applied microwave current. Theoretically, the system is described by means of the resistively and capacitively shunted junction model in terms of a moderately damped, classical Brownian particle dynamics in a one-dimensional potential. We find excellent agreement of the experimental results with numerical simulations of the model.

PACS numbers: 05.45.-a, 05.40.-a, 05.60.Cd, 74.50.+r

When a static force is applied to a system consisting of mobile particles, these particles usually move in the direction of the force, i. e., they show positive mobility, which leads to, e. g., a positive conductance or resistance in electrical systems. Also well known is the fact that such a system can exhibit regions of negative differential mobility/resistance [1–6]. However, the absolute mobility/resistance usually remains positive. The opposite response, i. e., a motion against the static force is termed negative absolute mobility or negative absolute resistance (NAR). This is clearly a quite counter intuitive effect which, at first glance, might seem even to be in conflict with Newton’s laws and thermodynamic principles [7]. Yet, nonlinear systems being driven far from equilibrium can indeed exhibit not only a negative differential resistance but also a NAR effect. Unambiguous and convincing experimental observations of NAR are still quite scarce, involving systems consisting of electrons in a sample of bulk GaAs [8], electrons in semiconductor heterostructures [9], electrons in low dimensional conductors [10], and charged Brownian particles in structured microfluidic devices [11]. Apart from the low dimensional conductors, the system was always driven out of equilibrium by means of an ac driving force and then its response to an externally applied static perturbation was studied. On the theoretical side, a considerably larger literature is available, most notably on different types of semiconductors and semiconductor heterostructures [7]. In all those cases (except [11]) NAR is based on purely quantum mechanical effects which cannot be transferred into the realm of classical physics. For classical systems, a first theoretical demonstration of the effect was provided in the context of a spatially periodic and symmetric model system of interacting Brownian particles, sub-

jected to multiplicative white noise [12]. While each of the different ingredients of the model is quite realistic in itself, their combined realization in an experimental system seems difficult. In particular, the main physical mechanism is based on collective effects of at least three interacting particles [13]. An entirely different mechanism was later on suggested theoretically for a realistic, classical model dynamics of a single Brownian particle in a suitably tailored, two-dimensional potential landscape in Ref. [14] and subsequently realized experimentally in Refs. [11, 15]. As a first application of NAR, the separation of different particle species has been realized in Ref. [16]. While the underlying basic physical mechanism still requires at least two spatial dimensions, very recently, NAR has been analyzed and predicted theoretically to occur also in the simplest possible case of a single Brownian particle dynamics in one dimension [17, 18]. More precisely, two basically different physical mechanisms capable of generating NAR in such systems have been unraveled, namely a purely noise induced effect in Ref. [17] and a transient chaos induced effect in Refs. [18]. In both cases, an experimental realization by means of a Josephson junction subjected to suitable dc and ac currents has been proposed. In this Letter we show that a moderately damped Josephson junction being driven by microwaves indeed shows NAR of the type predicted in Refs. [18]. A first hint along these lines can be found in Fig. 13 of [19], although without further explanation or discussion and no direct reference to the resistively and capacitively shunted junction model.

To model the Josephson junction we use the resistively and capacitively shunted junction model [20, 21]. It describes the equation of motion for the difference δ of the phases of the superconducting order parameter in the two electrodes

$$I = \frac{\Phi_0}{2\pi} C \ddot{\delta} + \frac{\Phi_0}{2\pi R} \dot{\delta} + I_0 \sin \delta + I_N . \quad (1)$$

*Electronic address: kleiner@uni-tuebingen.de

Here, C , R , and I_0 denote the junction capacitance, resistance and maximum Josephson current, respectively, dots indicate time-derivatives, Φ_0 is the magnetic flux quantum, and $I = I_{dc} + I_{ac} \sin(\omega t)$ is the total current applied to the junction, consisting of a dc and a high frequency ac component. The first term on the right hand side of Eq. (1) describes the displacement current $C\dot{U}$, where U is the voltage across the junction, and has been rewritten in terms of $\dot{\delta}$ using the Josephson relation $\dot{\delta} = 2\pi U/\Phi_0$. The second term describes the current through the resistor R , the third term the Josephson current, and the last term the noise current arising from Nyquist noise in the resistor. Its spectral power density is assumed to be white with $S_I(f) = 4k_B T/R$, where T is the temperature and k_B Boltzmann's constant. The model (1) implicitly assumes that magnetic fields created by circulating supercurrents can be neglected (short junction limit). This holds when the lateral junction dimensions are below about $4\lambda_J$, where $\lambda_J = (\Phi_0/4\pi\mu_0 j_0 \lambda_L)^{1/2}$ is the Josephson length in terms of the critical current density j_0 , the London penetration depth λ_L , and the magnetic permeability μ_0 .

By integrating Eq. (1) one obtains δ and, by time averaging, the dc voltage $V = \Phi_0 \langle \dot{\delta} \rangle / 2\pi$ across the junction. This is the main observable of our present work, which is measured when recording $V(I_{dc})$, the current voltage characteristics (IVC). For numerical simulations, (1) can be rewritten in dimensionless units by normalizing currents to I_0 , voltages to $I_0 R$, times to $t_c = \Phi_0 / (2\pi I_0 R)$, and hence frequencies to $f_c = I_0 R / \Phi_0$, yielding

$$i = \beta_c \ddot{\delta} + \dot{\delta} + \sin \delta + i_N, \quad (2)$$

where $i = i_{dc} + i_{ac} \sin(\tau f/f_c)$ is the normalized applied current, $\tau = t/t_c$ the normalized time, $\beta_c = (f_c/f_{pl})^2 = 2\pi I_0 R^2 C / \Phi_0$ the Stewart-McCumber parameter, $f_{pl} = (I_0 / (2\pi\Phi_0 C))^{1/2}$ the Josephson plasma frequency, and i_N the normalized noise current with spectral density $S_i(f/f_c) = 4\Gamma$ and noise parameter $\Gamma = 2\pi k_B T / I_0 \Phi_0$.

In a nutshell, the basic ingredients of NAR as predicted in [18] are as follows. The unperturbed deterministic dynamics (Eq. (2) with $i_{dc} = 0$ and $i_N = 0$) exhibits two symmetric attractors, carrying currents of opposite signs (zero crossing Shapiro steps). When an external perturbation in the form of a static bias i_{dc} is applied, a subtle interplay of this bias force and the dissipation leads to a destabilization of that attractor, whose current points into the same direction as the applied bias. Its remnant is a strange repeller, exhibiting transient chaos, hence the name “transient chaos induced NAR” coined in [18]. The actual realization of NAR along these lines requires a careful choice of model parameters in (2) within the general regime of frequencies f comparable to f_{pl} and values of β_c roughly between 1 and 100. To obtain precise quantitative results, we have solved Eq. (2) numerically for various such parameter values by integrating and averaging over typically $5 \cdot 10^3$ periods of the ac current.

For experiments, which were performed at $T = 4.2$ K, we used circular Nb-Al/AlO_x-Nb Josephson junctions

with an area of $200 \mu\text{m}^2$, cf. upper left inset in Fig. 1(a). The junctions were shunted by a AuPd strip with resistance $R = 1.27 \Omega$ and integrated in a coplanar waveguide. We denote the critical current I_c as the maximum dc current for which $V = 0$. In general, I_c is a function of I_{ac} and fluctuations. By measuring $I_c(I_{ac} = 0)$ and matching it with simulations we determined $I_0 = 197 \mu\text{A}$, yielding $I_0 R = 250 \mu\text{V}$, $f_c = 121 \text{ GHz}$ and $\Gamma = 9 \cdot 10^{-4}$. The Josephson length is about $40 \mu\text{m}$, i. e., well above the $16 \mu\text{m}$ diameter of our junctions assuring the short junction limit. The design value of the capacitance was 8.24 pF , yielding $f_{pl} = 43 \text{ GHz}$, and $\beta_c = 7.9$. The actual value used in the simulations shown below is somewhat smaller, namely $\beta_c = 7.7$, reproducing particularly well the hysteretic IVC in the absence of microwaves. The transport measurements have been performed with a standard four terminal method, using filtered leads. Microwaves between 8 and 35 GHz, with variable output power P_m , were applied through a semirigid cable that was capacitively coupled to the 50Ω coplanar waveguide. The samples were electromagnetically shielded and surrounded by a cryoperm shield, to reduce static magnetic fields.

Given I_0 , R , C , T and I_{dc} , all relevant model parameters are fixed, with the exception of the (frequency dependent) coupling factor between the microwave amplitude $\sqrt{P_m}$ applied from the source and the amplitude I_{ac} of the ac current induced across the junction. We have fixed this factor by comparing the measured dependence of $I_c(\sqrt{P_m})$ with the calculated curve $I_c(I_{ac})$, as shown in the right inset of Fig. 1, for a microwave frequency of 19 GHz ($f/f_c \approx 0.16$). The experimental and theoretical curves are in good agreement. In particular, the main side maxima can be found, both in experiment and simulation. By adjusting the position of these maxima, we obtain a coupling factor $I_{ac}/\sqrt{P_m}(19 \text{ GHz}) = 1.0 \text{ mA}/\sqrt{\text{mW}}$.

Figure 1(a) shows IVCs under $f = 19$ GHz microwave irradiation at three values of I_{ac} . In the absence of microwaves (black line) the IVC is hysteretic, exhibiting a critical current of $195 \mu\text{A}$ and a return current of $100 \mu\text{A}$ (black arrows). When the microwave field is applied, the hysteresis decreases with increasing I_{ac} , and step-like features appear on the IVC. At $P_m = 194 \mu\text{W}$ ($I_{ac} = 435 \mu\text{A}$; magenta line), we observe NAR with a resistance of -1.07Ω , occurring in an interval $|I_{dc}| \leq 20 \mu\text{A}$ (i. e., approximately 10 % of I_0). When I_{ac} is increased to $P_m = 253 \mu\text{W}$ ($I_{ac} = 497 \mu\text{A}$; green line) the NAR has disappeared. However, centered on a voltage which corresponds to the first Shapiro step ($V_1 = \Phi_0 f \approx 39 \mu\text{V}$), regions of negative differential resistance appear. In Fig. 1(b) measured and simulated IVCs for the two microwave amplitudes $435 \mu\text{A}$ and $497 \mu\text{A}$ are compared. For the former case, which is recorded at the microwave amplitude where the maximum NAR has been observed, the agreement between the experimental and the theoretical curve is nearly perfect. For the latter case some small differences can be seen, although the agreement is

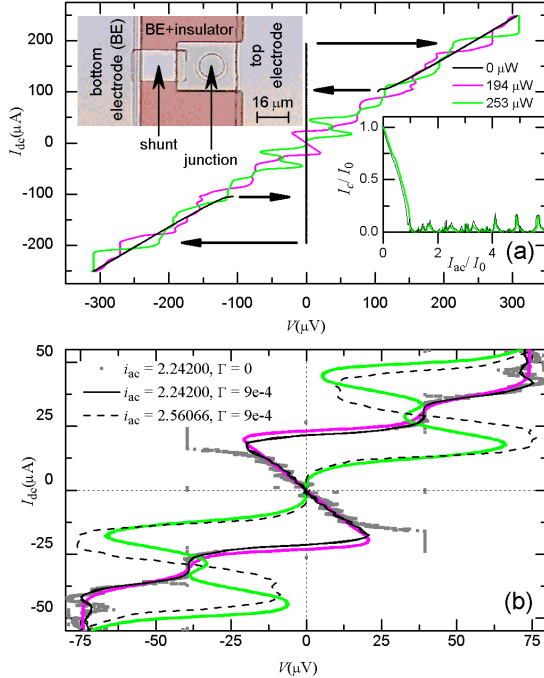


FIG. 1: Current voltage characteristics (IVC) of the Josephson junction at 4.2K in a 19 GHz microwave field. (a): at 3 levels of applied microwave power (0 μ W, 194 μ W and 253 μ W) showing the effect of negative absolute resistance at 194 μ W ($I_{dc} = 435 \mu$ A) and of negative differential resistance at 253 μ W ($I_{dc} = 497 \mu$ A). Left inset: image of the Josephson junction. Right inset: measured (thick green) and calculated (thin black) dependence of the critical current I_c on the microwave current amplitude I_{ac} . (b): enlargement of the measured IVCs for 194 μ W and 253 μ W, together with the simulated IVCs, cf. legend.

still very good. To demonstrate the origin of the NAR, the grey curve in Fig. 1(b) shows a simulated IVC for $i_{ac} = 2.24200 \mu$ A and $\Gamma = 0$, i. e., for the noise-free case. The curve shows $n = -1$ Shapiro steps to be the cause of NAR, clearly revealing its nature to be of the type discussed in [18].

Figure 2 compares in more detail the measured and calculated dependence of V on I_{dc} and on I_{ac} , for two frequencies (8 GHz and 19 GHz). For $f = 8$ GHz, the comparison between measured $I_c(\sqrt{P_m})$ and simulated $I_c(I_{ac})$ curves yields a coupling factor $I_{ac}/\sqrt{P_m}(8 \text{ GHz}) = 0.33 \text{ mA}/\sqrt{\text{mW}}$. In the graphs, V is normalized to $\Phi_0 f$, yielding an integer value n for the n -th Shapiro step. Again, the agreement between theory and experiment is very good. There are at least five I_{ac} intervals where NAR appears at $f = 8$ GHz, and three such intervals at $f = 19$ GHz. Within those regimes, the resistance at $I_{dc} = 0$ reaches values up to about -1Ω . In the case of $f = 8$ GHz, the NAR persists up to values of

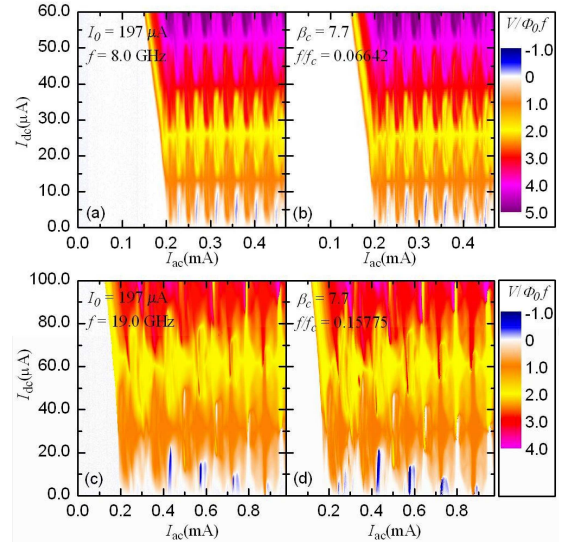


FIG. 2: Contour plot of the normalized dc voltage $V/\Phi_0 f$ across the junction as a function of dc current I_{dc} and microwave current amplitude I_{ac} . (a) $f = 8$ GHz, experiment; (b) $f = 8$ GHz, simulation; (c) $f = 19$ GHz, experiment; (d) $f = 19$ GHz, simulation. For symmetry reasons, $I_{dc} \leftrightarrow -I_{dc}$ implies $V \leftrightarrow -V$, hence negative I_{dc} values are not shown. Blue areas indicate NAR.

$|I_{dc}| \approx 10 \mu$ A, for all values of I_{ac} for which NAR shows up. In contrast, for $f = 19$ GHz, the I_{dc} interval for NAR decreases with increasing I_{ac} . When we increased the frequency further to 35 GHz, hysteretic Shapiro steps appeared on the IVC, crossing the voltage axis ($I_{dc} = 0$). As a consequence, NAR ceases to exist both in the experiment and the simulations.

In a second series of experiments we applied a magnetic field B parallel to the junction plane in order to tune (decrease) its Josephson current I_0 , making it a B dependent function $I_0(B)$ [22]. Thus all I_0 -dependent parameters entering the normalized equation (2) acquire a B -dependence, in particular i , β_c , f/f_c , and Γ . Figure 3 shows a comparison of the measured and calculated dependence of the resistance upon I_{ac} and $I_0(B)$. Again, we find excellent agreement between measurement and theory. Blue regions indicate NAR. Their most remarkable feature is that the values of I_{ac} , for which NAR appears, practically do not depend on I_0 . Furthermore, we find that the NAR value can be tuned by I_0 via an applied magnetic field. For our junction parameters we find a maximum NAR at $I_0 \approx (0.4 \dots 0.6)I_0(B = 0)$, which is increasing with I_{ac} .

In conclusion, we have observed negative absolute resistance (NAR) of up to about -1Ω in a shunted Nb-Al/AlO_x-Nb Josephson junction device subjected to microwaves. To clearly see the effect, a careful choice of parameters is required, but still the range of suitable

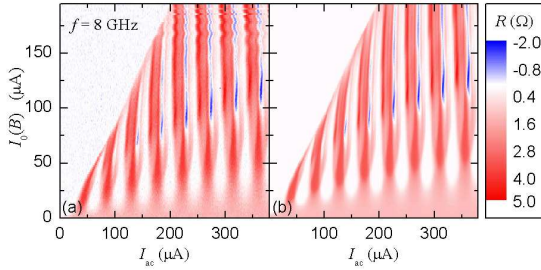


FIG. 3: (a) Contour plot of the experimentally measured resistance $R := V(I = 5 \mu\text{A})/5 \mu\text{A}$ as a function of the Josephson current $I_0(B)$ and of the microwave amplitude I_{ac} . I_0 has been varied by applying a magnetic field to the junction. Graph (b) shows the corresponding simulated plot. For both graphs parameters at $B = 0$ are the same as in Fig. 2(a),(b).

parameters is quite large. In all cases, we obtain very good agreement with theoretical simulations of the resistively and capacitively shunted junction model. Furthermore a closer inspection of the corresponding

model dynamics reveals that the relevant physical mechanism is of the transient chaos induced NAR type from [18]. The similarity between our Fig. 1 and Fig. 2 in [9] suggests that with respect to NAR, purely quantum mechanical band structure and energy quantization effects may be imitated by inertia effects in a purely classical, one dimensional noisy dynamics. Moreover, our Fig. 3 exhibits many features which are quite similar to the corresponding plots in [18], while the intuitive explanation of the almost vertical stripe-pattern in Fig. 3 remains as an open problem. As an application, our present work opens the intriguing perspective of a new resistor-type electronic element which is tunable between positive and negative resistance via an easily accessible external control parameter, e. g., the amplitude of an ac driving or an externally applied magnetic field in the mT range.

This work was supported by the Deutsche Forschungsgemeinschaft (Grants No. KO 1303/7-1, RE 1344/5-1, and SFB 613).

[1] S. R. White and M. Barma, *J. Phys. A* **17**, 2995 (1984).
[2] G. A. Griess and P. Serwer, *Biopolymers* **29**, 1863 (1990).
[3] V. Balakrishnan and C. Van den Broeck, *Physica A* **217**, 1 (1995).
[4] G. A. Cecchi and M. O. Magnasco, *Phys. Rev. Lett.* **76**, 1968 (1996).
[5] G. W. Slater, H. L. Guo, and G. I. Nixon, *Phys. Rev. Lett.* **78**, 1170 (1997).
[6] R. K. P. Zia, E. L. Praestgaard, and O. G. Mouritsen, *Am. J. Phys.* **70**, 384 (2002).
[7] For a review see R. Eichhorn, P. Reimann, B. Cleuren, and C. Van den Broeck, *Chaos* **15**, 026113 (2005).
[8] T. J. Banys, I. V. Parshevunas, and Y. K. Pozhela, *Sov. Phys. Semicond.* **5**, 1727 (1972).
[9] B. J. Keay, S. Zeuner, Jr. S. J. Allen, K. D. Maranowski, A. C. Gossard, U. Bhattacharya, and M. J. W. Rodwell, *Phys. Rev. Lett.* **75**, 4102 (1995).
[10] H. S. J. van der Zant, E. Slot, S. V. Zaitsev-Zotov, and S. N. Artemenko, *Phys. Rev. Lett.* **87**, 126401 (2001).
[11] A. Ros, R. Eichhorn, J. Regtmeier, T. T. Duong, P. Reimann, and D. Anselmetti, *Nature* **436**, 928 (2005).
[12] P. Reimann, R. Kawai, C. Van den Broeck, and P. Hänggi, *Europhys. Lett.* **45**, 545 (1999).
[13] C. Van den Broeck, B. Cleuren, R. Kawai, and M. Kam-bon, *Int. J. Mod. Phys. C* **13**, 1195 (2002).
[14] R. Eichhorn, P. Reimann, and P. Hänggi, *Phys. Rev. Lett.* **88**, 190601 (2002); *Phys. Rev. E* **66**, 066132 (2002); *Physica A* **325**.
[15] R. Eichhorn, A. Ros, J. Regtmeier, T. Tu Duong, P. Reimann, and D. Anselmetti, *Eur. Phys. J. Spec. Top.* **143**, 159 (2007); J. Regtmeier, S. Grauwin, R. Eichhorn, P. Reimann, D. Anselmetti, and R. Ros, *J. Sep. Sci.* **30**, 1461 (2007).
[16] J. Regtmeier, R. Eichhorn, T.T. Duong, P. Reimann, D. Anselmetti, and R. Ros, *Eur. Phys. J. E* **22**, 335 (2007).
[17] L. Machura, M. Kostur, P. Talkner, J. Luczka, and P. Hänggi, *Phys. Rev. Lett.* **98**, 040601 (2007).
[18] D. Speer, R. Eichhorn, and P. Reimann, *Europhys. Lett.* **79**, 10005 (2007); *Phys. Rev. E* **76**, 051110 (2007).
[19] N. F. Pedersen, O. H. Soerensen, B. Dueholm, J. Mygind, *J. Low. Temp. Phys.* **38**, 1 (1980).
[20] W. C. Stewart, *Appl. Phys. Lett.* **12**, 277 (1968).
[21] D.E. McCumber, *J. Appl. Phys.* **39**, 3113 (1968).
[22] A. Barone and G. Paterno, *Physics and Application of the Josephson Effect*, John Wiley and Sons, New York, 1982.

3.6 Experimental realization

Supplementary to [3], in this section we will summarize earlier hints to ANM or its electrical pendant negative absolute resistance (NAR) in Josephson junctions and briefly discuss further experimental realizations in real pendula. Then we will discuss one of the most striking features of [3], the excellent agreement between the theoretical model and the experiment.

Since the ANM effect is of a very general nature and expected to be found in almost any Josephson junction operating in the chaotic regime around zero bias, it is not surprising that ANM, or rather its electrical pendant, negative absolute resistance (NAR) has already been measured prior to [3]. The first hints along these lines are found in Fig. 13 of [36] and Fig. 12(c) and 14(c) of [37], but without further discussion of NAR. Also without further discussion, early theoretical studies (Fig. 4 of [166], Fig. 3(a) of [167] and Figs. 13(c) and 25(b) of [137]) point towards the occurrence of NAR, although they lack the inclusion of noise and are thus less conclusive than the experiments.

Another line of possible experimental realization of the ANM effects of rather fundamental nature are real pendula, i.e. a mass, or “bob”, connected via a stiff rod to a pivot in a constant (gravitational) force field. In that context, the displacement of the bob, described by the angle between its current position and its equilibrium position, takes the role of the particle coordinate, and the resulting potential is a cosine potential. Its undamped dynamics are described by equations equivalent to (1)-(2) of [2] with $\eta = 0$ (and possibly, see below, a different driving force), and ANM translates into an average angular velocity opposed to an (average) torque applied to the pendulum. In the literature, various methods to provide the necessary driving forces are described, the most promising using magnetic fields [168, 169], leading to equations equivalent (up to noise and friction) to those studied in [1, 2], or an oscillating pivot [170, 171], leading to equations similar to those used to obtain figure 3.1(b). Two other variants would be to use a rotating pivot coupling via friction to the pendulum, or to put a permanent magnet on the bob and another onto a rotating disc such that the magnet drives the bob whenever it comes close to the bob. Using a symmetric protocol for the rotation of the disc, or two counter-rotating discs, the driving would be symmetric. An essential difference lies in fluctuations and friction. Depending on the construction of the apparatus, fluctuations are negligible, but ANM can be observed in that case, if one considers parameters for which there is only one attractor. In general, the friction forces due to the pivot will be different from the model of damping considered in this work. Using magnetic fields [169], the same friction forces as considered in [1, 2] can be realized. Furthermore, there seems to be no reason why another type of friction should not yield the same ANM effects. While probably practically useless otherwise, such an experiment may serve as a beautifully simple and direct demonstration of ANM. E.g., if a mass is connected via a string to the pivot, it exerts a torque due to gravitation to the pendulum, and hence would be lifted up by the pendulum⁶.

Our main contribution to the work [3] lies in the theoretical analysis of NAR, some simulations, and in carrying out some of the simulations leading to the high precision of the RCSJ model parameters as found in [3], and thus the similarity between theory and experiment. We will first comment on the latter, and close this section with a

⁶This idea is due to Peter Reimann.

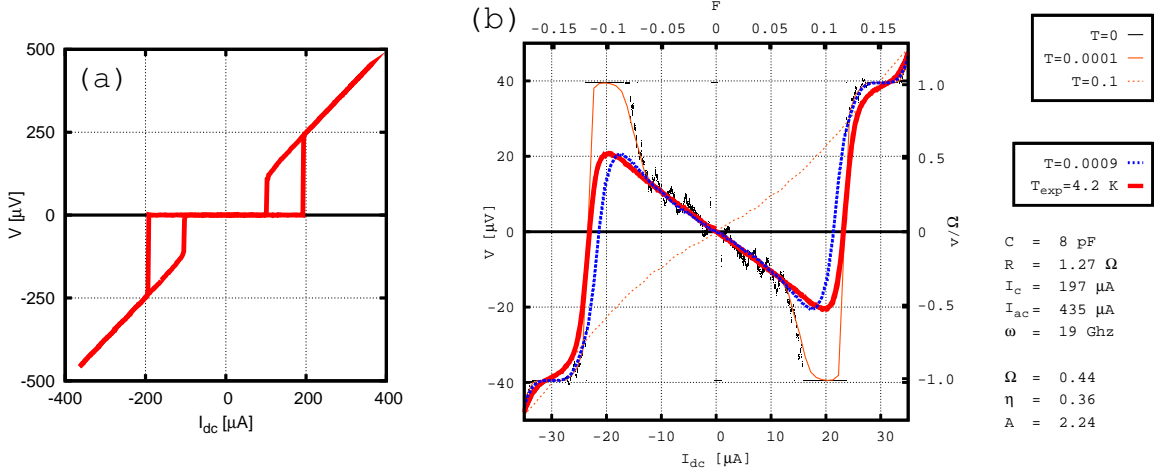


Figure 3.2: (a) current voltage characteristic of the junction considered in [3], cf. Fig. 1 of [3]. (b) the same as in (a) but $194\mu\text{W}$ microwave current is applied, and simulation results are shown. The simulation parameters are shown in panel (b), and the experimental data was provided by Joachim Nagel, Universität Tübingen.

more detailed theoretical discussion of the NAR effect. Basically, most of the parameters employed in the RCSJ model [7, 64, 65], namely (1) and (2) of [3], can be calculated from the design parameters of the Josephson junction, with the capacitance C given by the junction geometry and material parameters, the resistance R given by the material parameters of the shunt resistor and the temperature given by the cooling (liquid He). The critical current I_0 is not given by the design with sufficient precision but can be calculated from measured current voltage characteristics without microwave irradiation, see e.g. figure 3.2(a) and the black line of figure 1a of [3]. The measurement is performed by increasing the dc current from zero until the junction jumps to a non-zero voltage state, corresponding to subjecting a particle in a sinusoidal potential with barrier heights of $2 \cdot I_0$ to an increasing bias force, and then measuring the critical bias force at which the particle starts moving. By matching the obtained current voltage characteristic with a simulation taking into account noise, the critical current is obtained [3]. Moreover, the slope of the resistive portion of the current voltage characteristic is proportional to the resistance R of the model, the difference between the measured value and the design value being minimal.

The coupling factor $\frac{I_{ac}}{\sqrt{P_m}}$ connecting the irradiated microwave power to the ac bias current to which the junction is subjected cannot be easily estimated from the employed junction design and varies with frequency, it being dependent on how the microwaves propagate through the junction design. By matching measurements at various microwave powers with simulations at various ac bias amplitudes, this factor can be obtained. One way is to measure the critical current $I_c(\sqrt{P_m})$ (i.e. the dc current at which the junction switches from the zero voltage state to a non-zero voltage state) in the presence of microwave irradiation [7], see the lower right inset of figure 1a of [3]. To obtain an even better estimate, we have calculated figure 3.3, i.e. we have simulated figure 2 of [3] for various values of the McCumber parameter $\beta_C = \frac{2\pi I_0 R^2 C}{\Phi_0}$ and coupling factor, and computed the difference between the measured and simulated voltages, simply using the sum over all absolute differences of voltages at all considered data points. With all other

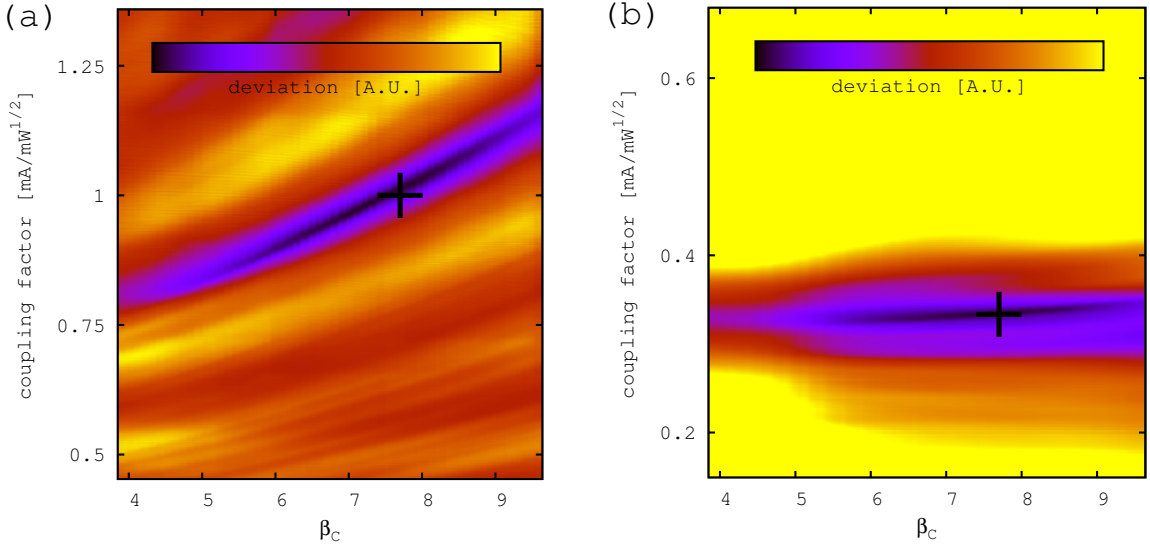


Figure 3.3: Deviation between simulations and experiment for (a) $f = 19\text{GHz}$ and (b) $f = 8\text{GHz}$, obtained by comparing the voltage measured in the experiment with simulated voltages in the experimentally easily accessible $I_{ac} - I_{dc}$ plane of parameter space, i.e. figure 2 of [3]. The remaining model parameters are fixed by figure 3.2(a) as $R = 1.27\Omega$, $I_0 = 197\mu\text{A}$ and $T = 4.2\text{ K}$ by design (He cooling). Thus β_c is proportional to the junction capacitance C . The crosses indicate the parameters used in [3]. The experimental data was provided by Joachim Nagel, Universität Tübingen.

parameters fixed β_c is proportional to the junction capacitance, and thus particle mass. The figure implies that the actual choice of the value of β_c is not critical, while the value of the coupling factor can be obtained rather precisely. The actual values were chosen close to the design parameters of the junction while reproducing the features of interest in figure 2 of [3] satisfactorily, in particular the regions of NAR. The quality of the fit could be further enhanced by using a different weighting, i.e. cost function [172].

As can be seen from figure 3.2(b) and in particular from figures 2 and 3 of [3], the final agreement between theory and experiment is striking. To further elucidate the mechanism behind NAR as found in figure 1b of [3] and figure 3.2(b), we calculate the deterministic (i.e. $T = 0$ in (1)-(2) of [2]) phase diagram for the model parameters describing the junction used in [3]. This diagram, figure 3.4, is the equivalent of figure 2 of [2] with some added information. In the units of [2] the drive frequency is $\omega = 0.43774$ and thus comparable to the frequency used in [2]. The regions of existence of the relevant attractors have a very similar shape as in figure 2 of [2], and the ‘‘movement’’ of the attractors upon switching on the bias current (bias force) is likewise very similar. Thus the mechanism is indeed the same as discussed in [2].

The model parameters corresponding to the simulated curve (dashed blue line) and matching the measured curve (thick red line) in the units of [2] are $\omega = 0.43774$, $\eta = 0.36$ and $A = 2.242$. The actual parameters considered in figure 3.2(b) are slightly outside the main region of SSBT at zero bias current(force) directly on one of the filaments of the region of existence of the SSBT attractors, around which a region of deterministic chaos is found, as in [2] (where the final choice of parameters, i.e. $\eta = 0.465$ and $A = 1.24$, is in the chaotic region, but that difference is minor). This can be seen particularly

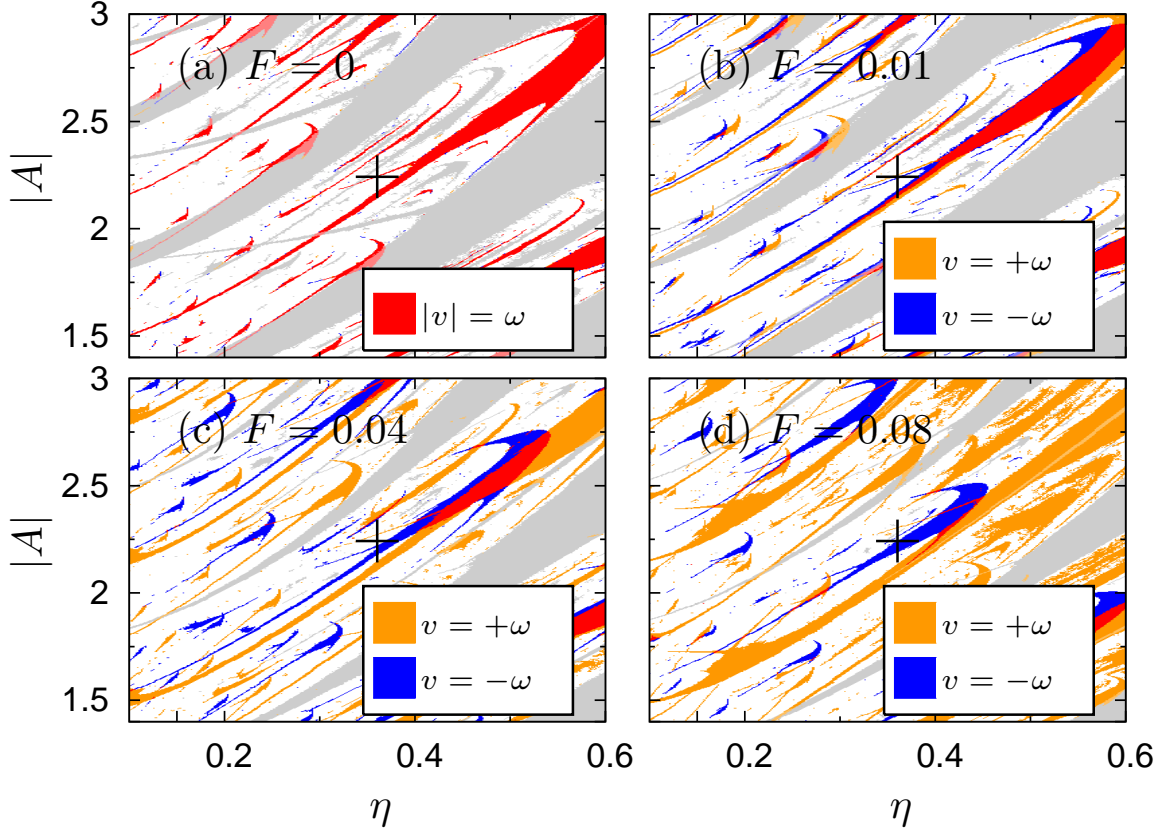


Figure 3.4: Deterministic $T = 0$ phase diagram for the dynamics (1)-(2) of [2]. Additionally to the equivalent information shown in Fig. 2 of [2], parameter regions of non-transporting attractors are shown in grey, coexistence of transporting phase-locked attractors with non-transporting attractors by desaturation of the color of the phase-locked attractor (rarely seen), and transporting phase-locked attractors of all velocities are shown, not just $|v| = \omega$. The parameters are $\omega = 0.43774$ and F is indicated in the panels. The parameters indicated by the cross correspond to the set of parameters (except F) used to obtain the grey curve in figure 1b of [3], i.e. $\beta_c = 7.7$ and $f_c = 121$ GHz. The other simulations corresponding to $f = 19$ Ghz in [3] are calculated for the same parameters, but $T = 0.0009$ and possibly different ac and dc currents (forces).

well from the black points in figure 3.2(b) showing the simulated deterministic behavior. At zero bias force (dc current) (and also for very small bias forces) the particle current (voltage) locks to $v = \omega$, i.e. on the filament of the SSBT attractor (see figure 3.4) or, in other words, on the broken Shapiro step. For slightly larger bias currents the junction is in a chaotic state, the current being dominated by periodic windows of the chaotic attractor appearing, vanishing or almost appearing (i.e. appearing for slightly different parameter values than those considered) and thus influencing the current on the chaotic attractor [87, 124–126, 146]. Globally, the dominating influence is from the main SSBT attractors becoming stable around $I_{dc} \approx 20\mu\text{A}$ (or $F \approx 0.1$), having a much larger weight in the ergodic chaotic attractor due to their greater stability⁷ than minor periodic

⁷E.g., the pseudopotential depths scale with the distance from the birth and death points of the attractors, and are very small for minor periodic windows with a very small size in parameter space.

windows. For slightly different parameter values, i.e. outside the filament, the junction is in a (deterministic) diffusive chaotic state at zero bias and the current is zero, but the phase diffuses chaotically (result not shown). These features are washed out by the addition of noise (solid orange line in figure 3.2(b)), and thus the difference is rather of academic nature. Finally, hypothetically increasing the noise strength by several orders of magnitude, NAR vanishes as expected (dashed orange line in figure 3.2(b)).

Lastly, we turn to the other anomalous transport properties predicted in [1, 2, 63]. First, noise induced NAR is probably found for at least some parameters considered in [3], e.g. take figure 3.2(b) and consider the part of the black curve where it is barely positive for small positive bias currents around $I_{dc} \approx 1.5\mu\text{A}$. Thus, if the parameters used to obtain the black curve were the exact parameters describing the junction, NAR would clearly be noise induced. But even if that is not the case, slightly different parameters will yield similar curves, or even non-transporting or positive current carrying periodic windows and NAR would be noise induced. But in contrast to [63], non-transporting attractors with appreciably large regions of existence are practically never found close to the SSBT attractors leading to NAR. Compare figure 3.4 with figure 13 of [2] describing the situation as found in [63]: the SSBT attractors actually coexist with a non-transporting attractor, whose region of existence is much larger than those of the SSBT attractors (or the attractors into which they evolve upon breaking the symmetry). Considering the noise induced NAR effect described by figure 15 of [2], a similar conclusion applies. While the parameters considered in, e.g., figure 2 of [3], do indeed show the effect (e.g. see the black points in figure 3.2(b)) for sufficiently low temperatures, such temperatures are inaccessible to the experiment as conducted in [3]. Furthermore, it is not possible to change the temperature during the experiment, and even if the experimental apparatus would allow doing so, a change in the temperature leads to a change in the junction parameters, most notably the critical current [7], thus making an experiment revealing noise induced NAR very difficult. One way of getting around this would be to use a magnetic field reducing the critical current [3, 7]. In properly scaled units, and upon adjusting the dc current, microwave amplitude and frequency accordingly, one could effectively lower the noise strength in the rescaled dynamics without changing any other parameter. Such a measurement would be possible in theory but the difficulties involved in changing the microwave frequency in particular would make it rather difficult, notwithstanding that noise induced ANM is not found theoretically for the junction parameters and noise strengths considered. Finally, from a practical point of view, the effect would rather be magnetic field induced ANM since the absolute temperature is not actually changed during such an experiment. Turning to the effect described by figure 14 of [2], i.e. a positive voltage for a small dc bias current turning into a negative voltage for a larger dc bias current, the effect as described in [2] cannot be found in the experiment of [3] due to the temperature (or rather the noise strength) being too large. Some of the regions of NAR shown in figure 2 of [3] have a rather complex shape or are tilted in the I_{ac} - I_{dc} plane of parameter space, even at the temperature considered. Naively, the effect predicted by figure 14 of [2] is realized for these parts of parameter space, since there are regions of small bias forces in which the voltage is positive, and the NAR region is reached for larger bias forces. But the observed positive voltages for small bias forces are very small and below the experimental precision of [3]. The simulations do indeed show that the effect described by figure 14 of [2] is found, and, judging from the very good

agreement between theory and experiment, we conclude that this effect may be realized in [3], but at vanishing amplitude, i.e. in the same sense as noise induced ANM.

3.7 Graphics processing unit (GPU) programming

The processing time to obtain the fits of the experimental data to the RCSJ model, i.e. figure 3.3, could be significantly decreased by using graphics processing units (GPUs) [173–175]. Thus, the method seems to be well suited for a simple (single machine) real time Josephson junction characterization without much effort. The computing time to obtain one panel of figure 3.3 in double precision arithmetics is about 7 days using a single thread on a contemporary Intel Q6600 processor (CPU) running at 2.4 Ghz without further optimization. This can be easily reduced by parallelization. We have found that using an ATI Radeon 3850 graphics processor (GPU), costing less than 50 Euros at the time of writing, and doing the calculations in single precision arithmetics⁸ this time can be shortened by a factor of about $\frac{1}{180}$ (see figure 3.5). To that end, a slightly different but relatively easy to use programming model, Brook+ [176], has to be used, see figure 3.6 for the main code used to generate figure 3.5. [173] have found that using a faster GPU with the CUDA [177] programming model, this factor can be improved to almost $\frac{1}{700}$ ⁹. Using the most advanced GPUs available at the time of writing, e.g. an ATI Radeon 5970, costing less than 500 Euros at the time of writing, we estimate this factor to be of the order of about $\frac{1}{2000}$ ¹⁰. Thus, the processing time can be reduced to several minutes without further optimizing the calculations and to less than a minute with such optimizations¹¹. This in turn would make a very convenient tool for experimentalists whenever such a high precision in the model parameters is needed.

As an example of how to employ a GPU for calculations, we have recalculated part of Fig 4. of [2] (see figure 3.5 for details) and measured the runtime on an otherwise idle system. The GPU used to obtain figure 3.5 is capable of performing roughly 320 mathematical operations in parallel, but that number may be less for more complex operations [176]. To show the simplicity of the code, we have included the main routines used to generate figure 3.5 on the GPU, which have not been optimized in any kind. The SDE solver algorithm employed is taken from [180], while the very simple method to generate random numbers is taken from [173].

⁸As [173] point out, these are sufficient for the noisy calculations. If possible, using double precision arithmetics reduces the GPUs performance by a factor of $\frac{1}{2}-\frac{1}{8}$ [176, 177], depending on the architecture, while the CPU is not affected, since it performs the computations at 80 bits anyhow [178].

⁹[173] use a comparable CPU.

¹⁰The ATI Radeon 3850 is rated at 427 GFLOPS and the ATI Radeon 5970 is rated at 4640 GFLOPS single precision [179]. While these theoretical numbers do not necessarily translate into application performance [173], they may serve as an indication of relative performance when comparing similar devices and applications.

¹¹As we were not time constrained, we have used a very high resolution in the figures, which is not necessary. Reducing that, and possibly using a minimization algorithm to find the minimum, should reduce computation time dramatically without much effort. We have used a much smaller value than necessary for the integration step size $h = 0.003\frac{2\pi}{\Omega}$ in the (2,3)rd order stochastic Runge-Kutta algorithm employed [180, 181] to be on the safe side and used the same sample size to calculate the averages at each grid point.

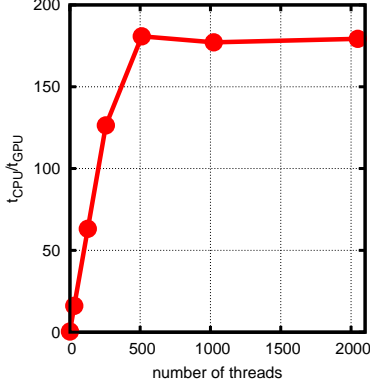


Figure 3.5: Total runtime t_{CPU} of a single thread on the CPU compared to the runtime t_{GPU} of many (as indicated on the axis) threads on the GPU taken to compute part of the green line of Fig. 4 of [2], i.e. solving the system (1)-(2) of [2], but only one trajectory of length $2000T$ is used at each data point. The total computation time is about 3 seconds on the GPU for 2048 threads. The CPU calculation has been performed only for 32 data points to reduce overhead (i.e. the equivalent of 32 threads), and then extrapolated.

3.8 Summary

We have shown that SSBT induced ANM is a common feature of spatially one dimensional inertial dynamics far from thermal equilibrium and exhibiting deterministic chaos. The mechanism behind ANM, the competition between SSBT induced transport without bias force and the applied bias force, has been detailed, and we have given a heuristic prediction for the parameters at which ANM can be found. Our predictions have been verified experimentally with excellent agreement between theory and experiment if the model parameters are calculated with sufficient precision, and we have shown a method of obtaining the parameters quickly and without much effort. This method might be of use in future experiments requiring a precise knowledge of the model parameters. The required computing time can be drastically reduced using a GPU, and that idea can be extended to different problems which are computationally limited by algebraic operations and light on memory access.

As hinted at by figure 3.1 and various further publications [92–95, 150, 151] considering other potentials, drive forces or noise sources, the mechanism is of a very general nature and can be expected to be found in various other dynamics considering particles in a nonlinear potential and subjected to a non-equilibrium drive, the main requirement being the presence of SSBT. SSBT of underdamped particles and the mechanism which gives rise to it is well known [137, 152, 153, 155]. The overdamped dynamics of a single particle on a two dimensional, symmetric and periodic surface meets the same requirements, i.e. a three dimensional phase space, nonlinearity and non-equilibrium. Two spatial dimensions allow for a richer transport behavior, making the dynamics even more interesting. This applies also to underdamped particles in two spatial dimensions [182–184] but their dynamics are of less interest from a fundamental point of view since they are not minimal, and the mechanism would be a trivial extension in the limit of separable dynamics. Moreover, in many important experimental systems, e.g. biological systems, microfluidic devices and vortices in superconductors, the dynamics are overdamped. In overdamped single particle

dynamics, SSBT has not yet been investigated in detail, and there are only a few hints throughout recent literature [104–106, 185] to our knowledge. Furthermore, it is well known that SSBT, or zero crossing Shapiro steps, are not found for Josephson junctions operating in the overdamped regime [137] (in which case the low dimension of phase space rules out SSBT), and we will deal with overdamped super conducting interference devices (SQUIDS) in chapter 6. We will show that SSBT and all effects derived from SSBT can be found for suitable spatially two dimensional dynamics in chapter 4 and that the added spatial dimensions allows for a much better control of the transport properties.

3.9 Appendix

3.9.1 Phase diagrams

Basically, phase diagrams are two parameter bifurcation diagrams showing some property of the dynamics encoded in color. Typically, phase diagrams are most useful if there are sufficiently large (compared to the section of parameter space shown) regions throughout which that property is constant, i.e. there are phases. Basically, the phase diagrams in the theory of phase transitions and critical phenomena have a very similar meaning.

Unless otherwise noted, the phase diagrams in this work show some property of the average velocity of attractors. We restrict ourselves to nondiffusive attractors, since it is difficult to tell a (chaotic) transient from a diffusive (chaotic) attractor. We consider a trajectory to be “on” a nondiffusive attractor, if it satisfies (2.29) with certain tolerances, as discussed in the next paragraph. Thus, if the trajectory is cut into a number of segments of a certain length (in time) each, the average velocity, calculated for each segment separately, does not depend on the segment within the numerical tolerances defined below. Periodic and phase-locked attractors [137], cf. footnote 33 of section 2.7, are prime examples, but we have also found certain quasiperiodic attractors, cf. section 4.17, to fall into this category within the numerical tolerances defined below.

Numerical protocol

Numerically, the phase diagrams are obtained as follows. A (rectangular) grid in parameter space is chosen. At each grid point, a certain number N_{seed} (typically about 10) of random initial seeds in phase space are drawn according to a uniform distribution (with some parts of phase space corresponding to unphysical initial conditions possibly excluded). For each seed, it is determined whether the seed lies in the basin of attraction of a stable periodic orbit (periodic attractor) as follows. Each seed is iterated up to $i_{max} \gtrsim 300$ under Θ (i.e. its images under Θ^i , $i, i_{max} \in \mathbb{N}$, $0 < i < i_{max}$ are calculated). We determine if a periodic attractor is reached by directly checking for periodicity of the stroboscopic map Θ . To that end, periodicity is assumed if an image of the initial seed is mapped onto itself (possibly shifted in each component by some integer multiple of the corresponding spatial period) by some iterate Θ^m (with $m \leq 32$ in most cases) of the stroboscopic map in the sense that the point and its image are in a small ball, typically of radius $\epsilon \lesssim 10^{-3}$ times the spatial period. It is then checked if the images of the point under Θ^{m+j} of the point are again mapped into the same ball for $1 < j < 5$, to avoid unstable periodic orbits.

Once a periodic orbit is found, it is saved, and no further iterates of Θ are computed. At each grid point (in parameter space) neighboring those of the initial seed, we check for the presence of the same periodic orbit (smoothly distorted due to the change of parameters), using the phase space coordinates of the periodic orbits as initial conditions (seeds) [117]. In other words, we “follow” the evolution of the periodic orbit upon changing the system parameters. If a periodic orbit is found and has the same average velocity \vec{v}_{po} (up to some numerical tolerance of order 0.01), the new orbit is saved, and the same procedure is repeated for each grid point at which the periodic orbit is found. (Note that we allow for different periodicities, i.e. we ignore period changing bifurcations not affecting transport, since we want to follow period doubling cascades.)

If no periodic orbit is found for a neighboring grid point, we check if a nondiffusive attractor has been created as follows. As initial condition the known (but for different parameters) periodic orbit is chosen and iterated by $\Theta^{k,j}$ with k, j integers, and typically $k \gtrsim 16$ and $1 \leq j \leq 8$. If (2.29) is satisfied with $T^* = k \cdot T$ for each j considered, $l = 2L$ (with L being the spatial period, which we assume to be identical for all components of the phase space vector) and $\vec{L}^* = k \cdot \vec{v}_{po}$, then the last coordinate thus obtained is assumed to lie “on” a nondiffusive attractor. If, for at least one j , (2.29) is not satisfied, the seed is discarded. If a nondiffusive attractor is found, it is again “followed”, as described above.

If the initial seed is not mapped onto a periodic orbit (according to above described procedure) after i_{max} iterations of Θ , it is tested whether a nondiffusive attractor has been found as described above. If the trajectory is found to be nondiffusive, the attractor is “followed” as described above.

After cycling through the whole grid each grid point is assigned a color as described in the text. If no nondiffusive attractor is found, i.e. the grid point is “empty”, it is left white.

Coarse grid and fine grid

To increase the resolution of the figures without increasing the computation time by the same magnitude, we use 2 differently spaced grids of parameter space. Practically all the computation time is spent in computing the iterates of Θ , and most of these have to be calculated for random seeds corresponding to long chaotic transients or in the basins of attraction of chaotic attractors. In particular, the “following” of periodic attractors is computationally rather “cheap”, since (if the grid is sufficiently fine) the initial condition is already close to the attractor. Random seeds are drawn only on a “coarse” grid, which is a subset of a “fine” grid, on which nondiffusive attractors are followed. Typically we choose grid spacings such that the “coarse” grid has 4 times the spacing of the “fine” grid, i.e. has only $\frac{1}{16}$ th of the “fine” grid points, of which there are typically more than 100000.

Consequences for chapter 3

Concerning the dynamics (1)-(2) of [2] considered in chapter 3, the method outlined above yields the regions of existence of phase-locked attractors created from periodic orbits quite well. Directly considering solutions of (1)-(2) of [2], we have found this to be the typical transport behavior in the sense that for the dominant part of parameter space, transport is dominated by such attractors, except for the white regions in the phase diagrams, which contain diffusive chaotic attractors in most cases. The average velocity of trajectories on these attractors varies (more or less) continuously with changes of parameters in the sense that there are no “large” jumps (until further bifurcations/crises occur [2]), but the weight according to the invariant density [87] of the different parts of the attractor changes. Without a more detailed investigation, it is not possible to determine whether such behavior corresponds to a chaotic transient or a chaotic attractor, and of what nature that attractor is.

Consequences for chapters 4-6

By directly evaluating representative trajectories, we have found a similar behavior for the models considered in chapters 4-6, i.e. (4.9), (5.1) and (6.11) (all considered without noise or disorder) with one exception. When the symmetry is broken, i.e. $\vec{F} \neq 0$ in (4.9), (5.1) or (6.11), quasiperiodic attractors are found for certain parameters, as discussed in section 4.17. We have found the quasiperiodic attractors to be nondiffusive within our numerical tolerances (as discussed above), and they are shown in the phase diagrams.

Consequences for chapter 7

The same as for chapters 4-6 applies to the quasiperiodic attractors found in the dynamics (2)-(4) of [5] in the presence of a symmetric drive, cf. section 7.46, but they show up already without a bias force. Without a time dependent driving force, the (noise free) autonomous dynamics discussed in chapter 7, i.e. (2)-(4) of [5], are treated slightly differently. Instead of the stroboscopic section, three (approximate) Poincaré surfaces of section are used simultaneously along the lines of [117]: $X_x = 0$, $X_y = 0$ and $\phi = 0$, and for each of the induced maps the same procedure as for the stroboscopic mapping Θ (see above) is used to detect nondiffusive transporting attractors. Furthermore, bounded attractors are detected as fixed points of the dynamics if, at the given precision of the solver, the solution does not change within one iteration of the solver. In practice, a trajectory is iterated until it crosses any of the above discussed Poincaré surfaces of section, it is found to end on a fixed point of the dynamics or a time of typically more than 250 (in the units of chapter 7) has elapsed (in which case the trajectory is discarded). If it crosses any of the above discussed Poincaré surfaces of section, one iterate of the associated map is calculated, and the trajectory is continued. Since, in the units used in chapter 7, the average velocity of periodic attractors is not constant when a parameter is changed, we do not require the average velocity to remain so when “following” nondiffusive attractors as outlined above.

Discussion

Due to the various tolerances used (e.g. i_{max} , ϵ , l , precision of the ordinary differential equation solver, basically rkqs with $\text{eps} = 10^{-7}$ of [186], grid spacing), the lines of bifurcations at which the attractors are created or vanish are not calculated accurately [117]. At the resolutions and figure sizes in this work, these numerical errors are negligible for the figures shown in this work, but may become visible upon magnification. At system parameters not corresponding to bifurcations, the dynamics are structurally stable, i.e. a small change in some parameter does not invoke a qualitative change of the dynamics. Since (in two dimensional diagrams) the lines (or points) at which bifurcations occur have measure zero, practically all system parameters considered yield structurally stable dynamics, and our method is sufficiently accurate (typically more than 3 digits for the parameters at which bifurcations occur, which is usually beyond the resolution of the figures).

Moreover, not all attractors are found due to the limited number of initial conditions and the limited grid resolution. If a random seed drawn at the grid point (i, j) (in parameter space) has a probability $0 \leq p(i, j) \leq 1$ of being in the basin of attraction of one

specific attractor (taking into account finite integration time, tolerances etc. as outlined above), the total probability of drawing at least one initial condition in the basin of attraction of that attractor is $p = N_{seed} \sum_{i,j} p(i,j)$. Attractors of interest to this work (i.e. sufficiently robust against thermal noise and other perturbations), typically have basins of attraction occupying rather large fractions of phase space (say one tenth or more), and regions of existence (non-zero $p(i,j)$) occupying a non-negligible part of parameter space (typically more than 50 points of the coarse grid). Therefore, the probability of finding such attractors is practically one with our method, and, once found at one point, the whole (connected component of the) region of existence of the attractor is typically found. Conversely, “smaller” attractors (either smaller basins of attraction or smaller regions of existence) are not found, but that is no problem since these attractors can be neglected for the noise strengths considered in this work.

Furthermore, it is possible that transients show up as nondiffusive attractors according to the method outlined above due to the numerical tolerances employed. Typically, the resultant “impostor attractor” is found only at very few and isolated grid points unless the transient is particularly long lived, which typically happens only around the lines of bifurcations creating the transient. Thus, such transients show up only as a slightly too large region of existence of the corresponding attractor. We have verified our main conclusions by directly evaluating trajectories, and, more importantly, by applying thermal noise.

3.9.2 Brook+ example

```

double test(unsigned int tmax, unsigned int N)
{
    // accounting
    int k;
    double elap;
    timeval st, et;

    // streams
    ::brook::Stream<float2> x(1,&N);
    ::brook::Stream<float2> ox(1,&N);
    ::brook::Stream<float> varianz(1,&N);
    ::brook::Stream<unsigned int>
        rng_state(1,&N);
    ::brook::Stream<float4> sysparms(1,&N);
    ::brook::Stream<unsigned int>
        orng_state(1,&N);

    // local variables
    float2 *input_x=new float2[N];
    float2 *input_ox=new float2[N];
    float *input_varianz=new float[N];
    float4 *input_sysparms=new float4[N];
    unsigned int *input_rng_state=
        new unsigned int[N];
    unsigned int *input_orng_state=
        new unsigned int[N];
    float input_h;
    float input_t;
    float input_tmax;

    // start time measurement
    gettimeofday(&st, 0);
    srand ( time(NULL) );

    // initialize local variables
    input_h=0.01f;
    input_t=0.0f;
    input_tmax=((float)tmax)*6.28/0.6;
    for (int k=0;k<N;k++) {
        input_orng_state[k]=rand()%99999999;
        input_sysparms[k].x=-0.465f;
        input_sysparms[k].y=0.6f;
        input_sysparms[k].z=1.24f;
        input_sysparms[k].w=0.0f+(float)k
            /(float)N*0.2f;
        input_x[k].x=0.0f;
        input_x[k].y=0.0f;
        input_rng_state[k]=input_orng_state[k];
        input_varianz[k]=sqrt(-0.001f*2.0f*
            input_sysparms[k].x*3.0f*input_h);
    }

    // move local data to the GPU
    x.read(input_x);
    sysparms.read(input_sysparms);
    varianz.read(input_varianz);
    rng_state.read(input_rng_state);

    // run the calculation on the GPU
    srk_jos(input_h,input_t,input_tmax,
        varianz,sysparms,x,
        rng_state,ox,orng_state);

    // read result from GPU
    ox.write(input_ox,0);
    orng_state.write(input_orng_state,0);

    // final time
    gettimeofday(&et, 0);
    elap=(double)((et.tv_sec-st.tv_sec)
        +0.000001*(double)(et.tv_usec-st.tv_usec));
    delete [] input_x;
    delete [] input_ox;
    delete [] input_varianz;
    delete [] input_sysparms;
    delete [] input_rng_state;
    delete [] input_orng_state;
    return elap;
}

kernel void srk_jos(float ext_h, float ext_t,
    float ext_tmax, float ext_varianz<>,
    float4 ext_sysparms<>, float2 ext_x<>,
    unsigned int ext_rng_state<>,
    out float2 ext_ox<>,
    out unsigned int ext_orng_state<>)
{
    float
    unsigned int rng_state;
    float h,t,tmax,tc,twoPI,T,theta1,theta2,
        h23,h16,h12,h14,stmp,varianz;
    float4 sysparms;
    float2 H2,H3,A1,dx,xc,x;
    // SDE solver constants
    h=ext_h; h23=0.666667f*h; h16=0.166667f*h;
    h12=0.5f*h; h14=0.25f*h;
    // local variables
    rng_state = ext_rng_state;
    tmax=ext_tmax-h; t=ext_t; x=ext_x;
    sysparms=ext_sysparms;
    varianz=ext_varianz;
    twoPI=2.0f*3.141592653589793f;
    T=twoPI/sysparms.y;
    // xc and tc count the number of spatial and
    // temporal periods
    xc=x; tc=0.0f;

    while (t+tc<tmax) {
        // account for periodicity
        if (x.x>twoPI) {
            x.x=x.x-twoPI; xc.x=xc.x+twoPI;
        }
        if (x.x<-twoPI) {
            x.x=x.x+twoPI; xc.x=xc.x-twoPI;
        }
        if (t>T) {
            t=0.0f; tc=tc+T;
        }
        // calculate 3 point distributet RVs
        rng_state = rng_state ^ (rng_state >> 13);
        rng_state = rng_state ^ (rng_state << 17);
        rng_state = rng_state ^ (rng_state >> 5);
        theta1 = ((float)rng_state)/4294967296.0f;
        if (theta1<0.666667f) theta1=0.0f;
        else {
            if (theta1<0.833333f) theta1=varianz;
            else theta1=-varianz;
        }
        rng_state = rng_state ^ (rng_state >> 13);
        rng_state = rng_state ^ (rng_state << 17);
        rng_state = rng_state ^ (rng_state >> 5);
        theta2 = ((float)rng_state)/4294967296.0f;
        if (theta2<0.666667f) theta2=0.0f;
        else {
            if (theta2<0.833333f) theta2=varianz;
            else theta2=-varianz;
        }
        // SDE solver step
        stmp=sysparms.z*sin(sysparms.y*t)
            +sysparms.w;
        dx.x=x.y;
        dx.y=sysparms.x*x.y-sin(x.x)+stmp;

        H2.x=x.x+h23*dx.x; H2.y=x.y+h23*dx.y;
        stmp=sysparms.z*sin(sysparms.y
            *(t+0.66667f*h))+sysparms.w;
        A1.x=H2.y;
        A1.y=sysparms.x*H2.y-sin(H2.x)+stmp;

        H3.x=x.x+h16*dx.x+h12*A1.x;
        H3.y=x.y+h16*dx.y+h12*A1.y+theta2;
        x.x=x.x+h14*(dx.x+A1.x);
        x.y=x.y+h14*(dx.y+A1.y);

        A1.x=H3.y;
        A1.y=sysparms.x*H3.y-sin(H3.x)+stmp;
        x.x=x.x+h12*(dx.x+A1.x);
        x.y=x.y+h12*(dx.y+A1.y)+theta2;

        t=t+h;
    }
    // return result
    ext_ox=x+xc;
    ext_orng_state=rng_state;
}

```

Figure 3.6: Main part of the C/Brook+ code used to generate figure 3.5. The same code, only with the float4 and float2 variables replaced by float variables has been used for the CPU calculation.

Chapter 4

Spatially two dimensional dynamics

In this chapter we will show that spontaneous symmetry breaking transport (SSBT) can be used to direct a Brownian particle on a surface into almost any direction. Our main result is summarized in the short publication [4], of which a preprint¹ is included in section 4.2 to give an overview. The remainder of this chapter is devoted to a thorough investigation of the effects summarized in [4]. The results of chapters 5 and 6 are derived from the results presented in this chapter.

In section 4.1, we summarize the main result of chapter 3 and give an overview of previous efforts to understand and control the transport properties of Brownian particles on two dimensional surfaces. The mechanism which gives rise to SSBT in spatially two dimensional overdamped dynamics will be unraveled in the simplest case when the drive is in a symmetry direction of the lattice in sections 4.8-4.10.3. The consequences of SSBT in that simple case, i.e. absolute negative mobility (ANM) and anisotropic deterministic diffusion, will be discussed in section 4.11. In sections 4.12-4.15, we show how SSBT is created when the drive is not in a symmetry direction of the lattice and investigate its consequences in sections 4.17-4.22, culminating in “directing Brownian motion” on a periodic surface.

4.1 Introduction

It is well known that spontaneous symmetry breaking transport (SSBT) is a common feature of simple underdamped dynamics in one or more dimensions when either a rocking [1, 109, 110, 137, 154] or pulsating drive [157, 187, 188] is applied. In Hamiltonian dynamics, a high starting velocity induces sustained transport, see e.g. [110]. Including friction, this question becomes more complicated [137]. Recently, it was shown independently by the author [1, 2] and Machura et al. [63] that SSBT can be exploited to achieve various novel transport phenomena: ANM and various noise induced ANM effects [1–3, 63, 92–95, 148–151, 157], see chapter 3. The general idea of these effects is that the direction of transport is controlled by the competition of the direction induced by a constant bias force (or any other symmetry breaking term introduced into the equations of motion) and the pair of transport directions given by a pair (or more) of SSBT attractors, see section 2.7. Thus, the intuitive idea of an average transport in a “preferred” direction,

¹The preprint is largely identical to the printed article which can be obtained via the American Physical Society.

given for instance by a constant bias force, is no longer valid, and the opposite can be the “normal” behavior for certain parameters (not too far from the symmetric case).

In general, the exploitation of SSBT to achieve “interesting” transport phenomena seems to be coupled to the occurrence of chaos in simple 1D underdamped dynamics [1, 2, 63, 137, 157]. While chaos is not a necessary companion of SSBT [137, 157], see also section 6.6, the occurrence of SSBT requires the ingredients for the occurrence of chaos: a 3 dimensional phase space and nonlinearity [1, 2]. In the dynamics considered in [1, 2], the coordinates are the particle position, velocity and time. The Poincare-Bendixon-Theorem [118] excludes chaos in two dimensional dynamical systems, so three dimensional systems are “minimal” for the occurrence of chaos, as is nonlinearity [87, 115, 118]. The exploitation of SSBT to achieve “interesting” transport phenomena in [1, 2, 63] made use of instabilities linked to chaos. Thus, SSBT and chaos are coupled in the sense that they occur in the same class of systems.

A natural question to ask is whether ANM and SSBT can be found for a single overdamped particle in a two dimensional periodic and symmetric potential and driven out of equilibrium by a symmetric and periodic driving force. The dynamics of the particle are described by a two dimensional non-autonomous differential equation, and thus, with regard to chaos, the same effects as for the inertial dynamics of a single particle in a one dimensional periodic potential can be expected. The idea is to “replace” the inertial forces by a second spatial dimension. But then, there is no simple mechanism of SSBT, as there is no term in the dynamics which can store directed “energy” in an obvious manner, like the momentum in inertial (or Hamiltonian) dynamics. In the absence of other forces, the only mechanism of “energy” storage is the particle coordinate. If the particle sits on the descending flank of a potential barrier (or equivalently in the basin of attraction of a potential well), it has “directed” energy. But due to the periodic nature of the potential it is not possible to draw a curve (i.e. a particle trajectory) through the potential only through regions of the potential with a positive scalar product of the force field (i.e. the gradient of the potential) and one fixed direction. Thus, the case of a purely unidirectional “energy” storage such as inertia in the high initial velocity case of Hamiltonian dynamics is not possible.

The added spatial dimension allows for a much richer transport behavior. First, the response of the particle to a dc bias force or, more generally, a symmetry breaking perturbation can now be, in principle, a current in any direction, i.e. the particle may be *deflected* from the direction of the bias force and the angle between the bias force and the average velocity of the particle is called the *deflection angle*. Throughout the literature, deflection angles of up to 90° are reported: deflection angles of less than 45° are reported for Brownian particles on a square lattice driven only by a constant bias force, see e.g. [23–25, 28, 189–192] (experimentally) and [18–21, 26, 27, 193, 194] (theoretically). A deflection angle of 45° cannot be achieved, and the limit is approached for small bias forces and temperatures [20]. Another variant is to replace the symmetric potential with a ratchet potential, resulting in a geometric ratchet [195–201]. The particle is deflected from the direction of the bias force due to the asymmetry of the potential, and deflection angles of less than 90° are possible². Applying a constant bias force and a (time) periodic

²Trivially, if a Brownian particle is made to slide along a “wall”, a deflection angle of almost 90° can be reached. The same applies to symmetric rectangular lattices in the limit of small noise and bias forces along the same lines as in [20].

circular drive to Brownian particles in a square lattice potential, deflection angles of 90° are reported in [104, 202, 203] and termed “absolute transverse mobility”. For interacting particles, a spontaneous deflection of the particles even if the dc drive is in a symmetry direction of the lattice, i.e. the deflection spontaneously breaks a reflection symmetry of the dynamics, is reported in [204–207]. That deflection is similar to the SSBT effect discussed for extended and structured molecules in chapter 7. Lastly including inertia effects in a spatially two dimensional dynamics, it is clear that ANM can be observed if one embeds the system considered in chapter 3 [1, 2] in two dimensions. Thus, already for separable dynamics³ a wide variety of deflection angles can be obtained easily. Therefore, we will not pursue this direction in detail. Previous studies in this direction have focused on broken symmetry, i.e. ratchet effects [183, 208], or considered the small driving force limit and separable dynamics [184].

Second, without a symmetry breaking perturbation, the particle will diffuse, i.e. an initially sharply localized distribution of particles will cover a certain area after some time has elapsed. The rate at which the distribution widens is a powerful tool to control the particle in one spatial dimension [22, 105, 209–219]. Adding a second direction, the particle may exhibit *anisotropic diffusion*, i.e. the particle distribution will be elliptical, making diffusion a much more powerful tool than in one spatial dimension.

With regard to SSBT and ANM, a recent series of papers [104–106, 185, 202, 203, 220] considers the overdamped dynamics of a single particle in a symmetric two dimensional potential and driven by a circular symmetric AC drive. [105, 106, 185, 220] consider a potential with hexagonal symmetry and report SSBT, both experimentally and theoretically, but do not study the particle mobility⁴. Since SSBT is found, the experiment [105, 106, 185, 220] is a good candidate to test our findings [4] experimentally. [104, 202, 203] consider square lattice potentials and report diffusive delocalized motion but not SSBT. Including a dc bias force [104] contains a hint that the average particle current might have been against the dc drive but remains inconclusive⁵. Furthermore, [104, 202, 203] show several realizations of differential negative mobility, i.e. an increase of the bias force leads to a decrease of the particle current, while that current is still in the direction of the bias force. From [221] we conclude that the same results can be obtained for many interacting particles subjected to periodic pinning potentials and a circular ac drive. Differential negative mobility (and ANM as a special case) can already be observed for single spherical (or non-spherical) particles subjected to thermal noise in a trapping, or meandering, geometry [47–50, 53–55, 222]⁶. In spatially one dimensional dynamics, SSBT of interacting overdamped particles is reported in the limit of infinitely many particles in e.g. [29, 38–44] where a non-equilibrium phase transition in the thermodynamic limit leads to SSBT and ANM. In some of these models, ANM can be found for as few as three interacting Brownian particles [43, 44]. Likewise, SSBT of a

³I.e. the equations of motion can be separated into two independent equations, each equation describing the movement of one component of the particle position.

⁴i.e. the change of the particle current (average velocity) when a constant bias force is applied

⁵Figs. 6 and 10 in [104] might contain a realization of ANM, but the data is obtained (cf. sec. II of [104]) by starting with zero dc bias and then slowly increasing the bias force to the first data point, and from there to the second and so forth. Effectively, only a single deterministic particle trajectory is generated and the curve may depend on the initial condition. Due to the reported presence of deterministic diffusion, and thus an unbounded attractor, ANM might be observed in the system considered in [104].

⁶experimentally realized in [3, 52, 59–62]

granular gas, i.e. interacting hard sphere particles, is reported in [138], but the mobility is not studied. Using a linear periodic driving force but introducing an asymmetry, various ratchet effects can be realized in spatially two dimensional dynamics, e.g. [223–236] (drive parallel to the direction of transport) and [234, 237–239] (drive orthogonal to the direction of transport), see [10, 11] for reviews. Common to all these studies is that one reflection symmetry of the dynamics remains intact, such that transport breaking this symmetry is ruled out.

We will consider the simplest possible situation of a single overdamped Brownian particle subjected to a periodic rocking driving force in a periodic potential: the simplest possible scenario for SSBT and ANM in overdamped dynamics: due to the low dimensional phase space of one dimensional overdamped dynamics, SSBT is ruled out, and the no-go theorem from [1, 2] rules out ANM. As mentioned above, we include a preprint of our publication [4] as a summary of our findings.

4.2 Preprint of [4]

D. Speer, R. Eichhorn, and P. Reimann, Physical Review Letters **102**, 124101 (2009),
 Copyright (2009) by the American Physical Society

Directing Brownian motion on a periodic surface

David Speer¹, Ralf Eichhorn^{1,2}, and Peter Reimann¹

¹Universität Bielefeld, Fakultät für Physik, 33615 Bielefeld, Germany

²NORDITA, Roslagstullsbacken 23, 10691 Stockholm, Sweden

We consider an overdamped Brownian particle, exposed to a two-dimensional, square lattice potential and a rectangular ac-drive. Depending on the driving amplitude, the linear response to a weak dc-force along a lattice symmetry axis consist in a mobility in basically any direction. In particular, motion exactly opposite to the applied dc-force may arise. Upon changing the angle of the dc-force relatively to the square lattice, the particle motion remains predominantly opposite to the dc-force. The basic physical mechanism consists in a spontaneous symmetry breaking of the unbiased deterministic particle dynamics.

PACS numbers: 05.45.-a, 05.60.-k, 05.40.-a

Brownian particle dynamics in two-dimensional periodic potential landscapes arise in a large variety of different contexts. Examples include driven vortex lattices [1–3], surface diffusion [4], a ring of several Josephson junctions [5], colloidal particles or globular DNA in structured microfluidic devices [6, 7] and in optical [8, 9] or magnetic [10] lattices, enzymatic reaction cycles driving molecular motors [11], nanoscale friction [12] and superlubricity [13]. They have recently attracted considerable theoretical [1, 14] and experimental [8] interest for particle sorting in two-dimensional periodic structures with the help of an externally applied dc-force, whose angle relatively to the periodic potential can be parametrically changed. The key point is that the resulting particle velocity may exhibit a different direction than the applied dc-force and that the deflection angle may be different for different particle species. While the deflection angles between force and velocity remain bounded to relatively small values, our present system will lead to (practically) arbitrary deflection angles.

A second recent series of papers [2, 10] considers the same system but in the presence of an additional circular ac-drive. Deflection angles up to 90° (absolute transverse mobility) have been found in [2], while [10] reports transporting orbits in the absence of a dc-drive. A related variant is to replace the circular by a more common, linear ac-drive, but now breaking the time-space symmetry by choosing a bi-harmonic driving signal [3], and focusing on the low friction regime [15]. The setup we will consider here is related but simpler: a standard ac-drive without any concomitant space-time symmetry breaking and negligible inertia effects.

Unbiased far from equilibrium dynamics of a Brownian particle, responding to a dc-force by a directed transport opposite to that force, have been extensively investigated under the label “absolute negative mobility” (ANM) [7, 16]. Our present work represents the natural extension, namely an unbiased far from equilibrium system admitting an easily controllable linear response into (practically) any direction relative to the dc-force, including ANM as a special case.

We consider the following 2d Langevin dynamics of a

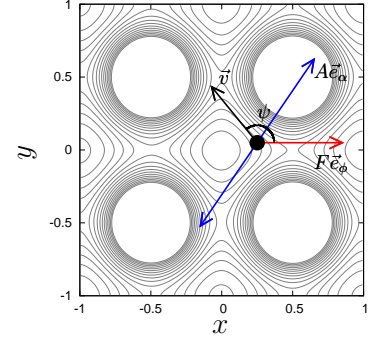


FIG. 1: Schematic illustration of our model (1). The contour lines represent the potential $U(\vec{r})$ with a cut-off for better visualization (white discs). The double arrow indicates the ac-drive $A(t)\vec{e}_\alpha$, one arrow the dc-bias $F\vec{e}_\phi$, and another arrow the particle velocity (2). The particle is sketched by the black dot. The angle ψ quantifies the “deflection” of \vec{v} from $F\vec{e}_\phi$.

Brownian particle with coordinates $\vec{r} = x\vec{e}_x + y\vec{e}_y$:

$$\dot{\vec{r}}(t) = A(t)\vec{e}_\alpha + F\vec{e}_\phi - \nabla U(\vec{r}(t)) + \sqrt{2\Gamma} \vec{\xi}(t). \quad (1)$$

Thus, inertia effects are neglected (overdamped dynamics), and the friction coefficient is absorbed into the time unit. As illustrated with Fig. 1, $A(t)$ is the ac-driving signal along the direction $\vec{e}_\alpha := (\cos \alpha, \sin \alpha)$, and analogously for the dc-bias $F\vec{e}_\phi$. The periodic potential is represented by $U(\vec{r})$ and thermal fluctuations of temperature Γ are modeled by the two delta-correlated, Gaussian noise components of $\vec{\xi}(t)$. We focus on the particularly simple rectangular driving $A(t) = a \text{sign}\{\cos(\Omega t)\}$ with amplitude a and period $T = 2\pi/\Omega$. We verified that a sinusoidal $A(t)$ leaves all our main findings qualitatively unchanged and expect the same for even more general $A(t)$. Further, we focus on the potential $U(\vec{r}) = \sum \tilde{U}(\vec{r} + Ln\vec{e}_x + Lm\vec{e}_y)$ with $r := |\vec{r}|$, $\tilde{U}(\vec{r}) = u \exp\{-r/\lambda\}/r$, and $u, \lambda > 0$. In other words, we consider a square lattice of repulsive Yukawa potentials, a standard choice for screened charges [2]. Again, we expect that our results remain qualitatively unchanged for

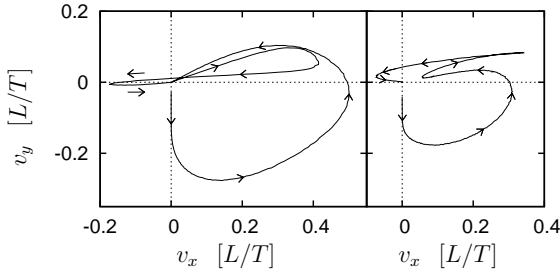


FIG. 2: Velocity (2) from numerical simulations of (1) for $\alpha = 0.15 \cdot 360^\circ = 54^\circ$, $a \in [4.3, 8]$, $\phi = 0^\circ$, $F = 0.03$, $\Omega = 4.3$, $\Gamma = 2.2 \cdot 10^{-4}$ (left) and $\Gamma = 6.7 \cdot 10^{-4}$ (right). Shown is the parametric dependence of the velocity components v_x, v_y on the ac-amplitude a in units of L/T ($L = 1$, $T = 2\pi/\Omega$). Arrows indicate increasing a -values. Upon further decreasing F , a close to linear response behavior of \vec{v} results (not shown).

more general $\tilde{U}(\vec{r})$, modelling e.g. pinned vortices [1], optical tweezers [8, 9], or magnetic bubbles [10], and we have explicitly verified this for Gaussian shaped repulsive and attractive potentials. Without loss of generality we choose length and time units with $L = 1$ and $u = 1$. Regarding λ , we obtained practically indistinguishable results for all $\lambda \geq 4$, variations by a few percent down to $\lambda \approx 1$, and notable quantitative but no qualitative differences at least down to $\lambda \approx 0.1$. In the following we focus on the representative example $\lambda = 4$.

The observable of main interest will be the time-averaged particle velocity

$$\vec{v} = v_x \vec{e}_x + v_y \vec{e}_y := \lim_{t \rightarrow \infty} \frac{1}{t} \int_0^\infty dt' \dot{\vec{r}}(t') . \quad (2)$$

being independent of the seed $\vec{r}(0)$ and the realization of $\vec{\xi}(t)$ in (1) for any $\Gamma > 0$ due to ergodicity reasons.

Generally speaking, the periodic potential, the ac-drive and the dc-bias in (1) give rise to several ‘‘competing directions’’, whose net effect on the velocity \vec{v} from (2) is far from obvious. For zero bias F , the ac-forcing still keeps the system off equilibrium but any non-zero velocity \vec{v} is prohibited by symmetries [17]. Our first objective is the linear response of \vec{v} to a weak dc-bias along the x -axis, cf. Fig. 1. Our findings in Fig. 2 exhibit a quite intriguing behavior. Keeping all ‘‘competing directions’’ fixed and solely changing the ac-amplitude by 40%, almost any direction of \vec{v} may arise, even motion exactly opposite to the applied dc-bias (ANM).

Next, we focus on a set of parameters close to the occurrence of ANM in Fig. 2 and now ask for the response of \vec{v} upon changing the direction of the dc-bias. Again, the results in Fig. 3 are quite non-trivial, the most remarkable feature being that the projection of the velocity along the dc-bias is mostly negative, i.e. the particle motion remains predominantly opposite to the dc-force ($90^\circ < \psi < 270^\circ$). Similarly as in Fig. 2, the effect is particularly striking for small noise strengths Γ , and vanishes for $\Gamma \gtrsim 10^{-3}$.

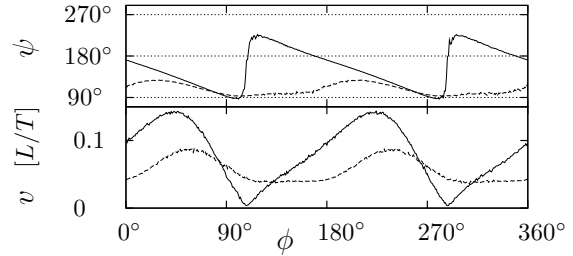


FIG. 3: Deflection angle ψ (see Fig. 1) and velocity $v := |\vec{v}|$ versus ‘‘dc-directionality’’ ϕ (see (1)) for the same system as in Fig. 2 but with $a = 7.4$, and $\Gamma = 4.4 \cdot 10^{-4}$ (solid), $\Gamma = 6.7 \cdot 10^{-4}$ (dashed).

To better understand these findings we first focus on the deterministic dynamics ($\Gamma = 0$) in the simplest case when the ac-drive and the dc-bias are parallel and acting along one of the main symmetry axes of the periodic potential. Regarding the $(1, 0)$ direction, i.e. $\phi = \alpha = 0^\circ$, the lines $y = n/2$ constitute invariant sets of the deterministic dynamics (1), stable for odd and unstable for even n . Thus, the particle motion is confined between two neighboring such lines and generically is attracted by the one with odd n for large times. Further, the velocity (2) necessarily must follow the direction of the dc-force, i.e. $\psi = 0^\circ$, and, in particular, vanishes for $F = 0$. This qualitative behavior remains unchanged in the presence of noise ($\Gamma > 0$). Analogous conclusions hold for the $(0, 1)$ lattice direction.

Turning to the $(1, 1)$ direction, i.e. $\phi = \alpha = 45^\circ$, the lines $x - y = n$ now constitute invariant sets of the deterministic dynamics (1) due to its invariance under $S_1 : (x, y) \mapsto (y, x)$. Again, the particle motion must remain confined between two adjacent such lines, implying for the velocity (2) that $\psi = 0^\circ$ and hence $v_x = v_y$. But now, the motion on the invariant lines may change its stability properties upon variation of a system parameter, and additional non-trivial attractors, not contained in any of the invariant lines, may arise. A typical example is shown in Fig. 4. We see that – depending on the driving amplitude a and possibly also on the seed $\vec{r}(0)$ – the orbit $\vec{r}(t)$ approaches a periodic or a chaotic long time behavior. The concomitant velocity (2) is still well defined but – in contrast to the noisy case $\Gamma > 0$ – now may depend on the initial condition $\vec{r}(0)$. The ‘‘central’’ straight line in the bifurcation diagram for $a < 3.22$ belongs to all the periodic attractors on the invariant sets $x - y = n$, exemplified by (a) in the upper inset of Fig. 4, and giving rise to a vanishing average velocity. At $a \approx 3.09$ we observe the appearance of an additional pair of non-transporting ($\vec{v} = 0$) periodic attractors, spontaneously breaking S_1 as well as the second symmetry $S_2 : (x, y) \mapsto (-x, -y)$ of (1), but still maintaining (up to translations) $S_1 \circ S_2 : (x, y) \mapsto (-y, -x)$, see (b) in Fig. 4. Thus, there are now three coexisting attractors within every unit cell of the periodic potential, one of

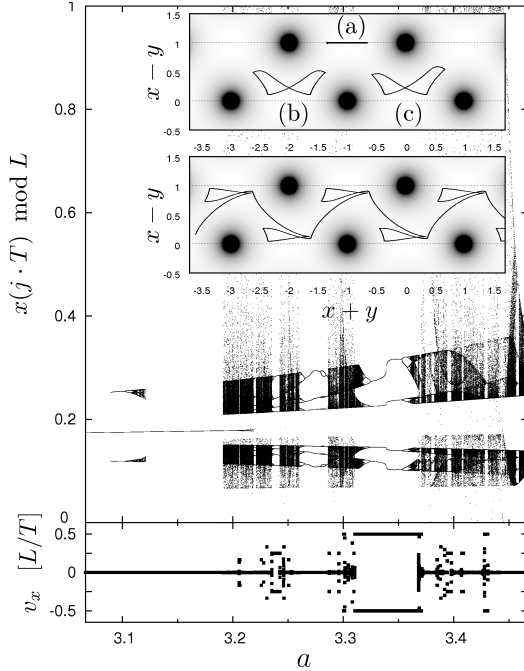


FIG. 4: Upper part: Bifurcation diagram for the unbiased ($F = 0$) deterministic ($\Gamma = 0$) dynamics (1) with $\alpha = 45^\circ$, $\Omega = 3$, and varying a . Shown is a stroboscopic representation of the attractors, governing the long-time behavior, by plotting $x(jT)$ modulo L ($L = 1$), i.e. the reduced x -component at multiples j of the driving period $T = 2\pi/\Omega$, for several different seeds $\vec{r}(0)$ after initial transients have died out. Lower part: Corresponding x -component of the average velocity (2) in units of L/T . Upper inset: Stable periodic orbits (attractors) for $a = 3.1$ (a and b) and for $a = 3.107$ (c). Dotted: invariant sets $x - y = n$. Black “clouds” and “discs” represent the potential $U(\vec{r})$, corresponding to Fig. 1 after a 45° rotation. Lower inset: stable period-2 transporting orbit for $a = 3.33$.

type (a), the others of type (b) and its image under S_1 . At $a \approx 3.102$ the pair of type (b) attractors exhibits a pitchfork bifurcation, which spontaneously breaks the $S_1 \circ S_2$ symmetry (symmetry breaking bifurcation [18]), resulting in four distinct, non-transporting attractors per unit cell. One of them is exemplified with (c) in Fig. 4, its three “brothers” follow as mirror images with respect to the closest $x - y = n$ and/or $x + y = n$ lines. Upon further increasing a , a period doubling route to chaos follows, which would be impossible without the preceding symmetry breaking bifurcation [18]. The corresponding attractors loose stability by way of a crisis at $a \approx 3.12$. They reappear beyond $a \approx 3.19$ as “chaotic bands”, interrupted by “periodic windows”. Some of these windows exhibit attractors corresponding to phase-locked *transporting* orbits. The symmetry breaking bifurcation at $a \approx 3.102$ is pivotal for such transporting orbits: Since there is no systematic force ($F = 0$), which could fa-

vor motion in one or the other direction, *spontaneous symmetry breaking* of all symmetries involving S_2 is an indispensable prerequisite for transporting orbits. The simplest and most prominent example arises within the periodic window at $a \approx 3.33$, exhibiting two attractors between any pair of adjacent $x - y = n$ lines. One such orbit is exemplified in the lower inset of Fig. 4, its “twin brother” follows as mirror image with respect to any $x + y = n$ line. Apparently, this orbit arises by continuing the deformation of orbit (b), which leads to (c) even further, and rewiring one of its “arms” into the neighboring unit cell. The latter operation cannot be realized by a continuous deformation and hence one might guess that this somehow happens within the “gap” in the bifurcation diagram between $a \approx 3.12$ and $a \approx 3.19$.

Due to the $S_1 \circ S_2$ symmetry at $F = 0$, oppositely transporting orbits co-exist and are stable within exactly the same range of the other system parameters. Applying a force $F \neq 0$, however, breaks the symmetry and hence the existence regions of the two orbits in parameter space no longer coincide. Closer inspection of how these regions change shape and size reveals that there are, for not too large $|F|$, parameter values, where *the only stable orbit is the one which transports against the dc-bias F* . In other words, we recover yet another example of “pure” ANM ($\psi = 180^\circ$) [7, 16], which furthermore turns out to survive even in the presence of (sufficiently weak) noise ($\Gamma > 0$).

We finally address the case of arbitrary (but fixed) orientations of the external forcings. Without loss of generality we restrict ourselves to $0 < \alpha < 90^\circ$ but admit arbitrary ϕ . For such general driving directions the deterministic dynamics (1) is not restricted any more by simple invariant sets. Rather, by means of extensive computer simulations we have found that transporting particle motion is created in a way very similar to the case exemplified above with Fig. 4, and typically “locks” to one of the three main symmetry axes $(1, 0)$, $(0, 1)$ or $(1, 1)$, depending on amplitude and frequency of the ac-drive. In particular, for $F = 0$, symmetry dictates the *co-existence of transport into opposite directions* for either of these basic orientations. Applying a (not too large) dc-bias $F \vec{e}_\phi$ along a direction that is generally different from the one of the ac-drive, $\phi \neq \alpha$, has two main effects: First, this co-existence is lifted, yielding parameter regions where only one transporting direction out of the 6 different possible directions is stable. Second, new transport directions around the orientation of the bias force become accessible that follow a similar “locking scheme” as in [14] upon variation of a system parameter.

In other words, systematically changing, say, the driving amplitude a leads to “jumps” in the deterministic transport direction where – due to the time-dependent ac-drive – also transport with velocity components opposite to the bias force occurs, in marked contrast to previous findings in [14]. The main effect of (weak) thermal noise is to “interpolate” between neighboring deterministic directions, resulting in the smooth behavior shown

in Fig. 2: transport in virtually any direction but with emphasis on directions around the orientation of the dc-bias. Similarly, the variations of the deflection angle ψ observed in Fig. 3 result from a basically unchanged orientation of \vec{v} into the “negative” $(1, 0)$ direction as long as the dc-bias has a non-vanishing component in the “positive” $(1, 0)$ direction (i.e. $-90^\circ \lesssim \phi \lesssim 90^\circ$) and a quick transition into the opposite situation when the dc-orientation ϕ moves into the complementary regime between 90° and 270° . In any case, too large noise strengths Γ basically override the effects of the periodic potential and the system tends to return to the trivial behavior in the absence of the periodic potential.

In conclusion, several quite astonishing linear response transport phenomena of a very simple and general non-equilibrium system have been observed and understood

to the extent that an efficient and systematic search of pertinent parameter regions becomes easily feasible. The system is minimal in so far as any further reduction or simplification unavoidably rules out one of the indispensable prerequisites, most notably the occurrence of spontaneous symmetry breaking and chaos in the deterministic limit. On the other hand, the effects are robust against a large variety of modifications and amendments of the model and hence should be realizable in several different experimental systems [5–10] for instance for particle sorting purposes.

We thank J. Nagel, D. Koelle, and R. Kleiner for fruitful discussions. This work was supported by Deutsche Forschungsgemeinschaft under SFB 613 and RE1344/4-1

- [1] C. Reichhardt and F. Nori, Phys. Rev. Lett. **82**, 414 (1999); B. Y. Zhu, F. Marchesoni, V. V. Moshchalkov, and F. Nori, Phys. Rev. B **68**, 014514 (2003).
- [2] C. Reichhardt, C. J. Olson, and M. B. Hastings, Phys. Rev. Lett. **89**, 024101 (2002); C. Reichhardt and C. J. Olson Reichhardt, Phys. Rev. E **68**, 046102 (2003).
- [3] S. Ooi, S. Savel'ev, M. B. Gaifullin, T. Mochiku, K. Hirata, and F. Nori, Phys. Rev. Lett. **99**, 207003 (2007).
- [4] J. L. Vega, R. Guantes, and S. Miret-Artés, J. Phys. Condens. Matter **14**, 6193 (2002); S. Miret-Artés and E. Pollak, J. Phys. Condens. Matter **17**, S4133 (2005).
- [5] U. Geigenmüller, J. Appl. Phys. **80**, 3934 (1996); A. Sterck, S. Weiss, and D. Koelle, Appl. Phys. A **75**, 253 (2002).
- [6] C.-F. Chou et al., PNAS **23**, 13762 (1999); R. L. Huang et al., Nature Biotech. **20**, 1048 (2002); Science **304**, 987 (2004); M. Baba et al., Appl. Phys. Lett. **83**, 1468 (2003); E. B. Cummings and A. K. Singh, Anal. Chem. **75**, 4724 (2003); J. Regtmeier et al., Anal. Chem. **79**, 3925 (2007).
- [7] A. Ros et al., Nature **436**, 928 (2005); J. Regtmeier et al., J. Sep. Sci. **30**, 1461 (2007); Eur. Phys. J. E **22**, 335 (2007).
- [8] P. T. Korda, M. B. Taylor, and D. G. Grier, Phys. Rev. Lett. **89**, 128301 (2002); M. P. MacDonald, G. C. Spalding, and K. Dholakia, Nature **426**, 421 (2003); P. Tierno, A. Soba, T. H. Johansen, and F. Sagués, Appl. Phys. Lett. **93**, 214102 (2008).
- [9] K. Mangold, P. Leiderer, and C. Bechinger, Phys. Rev. Lett. **90**, 158302 (2003); S. Beil et al., Europhys. Lett. **73**, 450 (2006).
- [10] P. Tierno, T. H. Johansen, and T. M. Fischer, Phys. Rev. Lett. **99**, 038303 (2007); A. Soba, P. Tierno, T. M. Fischer, and F. Sagués, Phys. Rev. E **77**, 060401 (2008).
- [11] M. O. Magnasco, Phys. Rev. Lett. **72**, 2656 (1994); P. Reimann Phys. Rep. **361**, 57 (2002).
- [12] R. Prioli, A. M. F. Rivas, F. L. Freire Jr., and A. O. Caride, Appl. Phys. A **76**, 565 (2003); P. Reimann and M. Evstigneev, New J. Phys. **7**, 25 (2005).
- [13] M. Dienwiebel et al., Phys. Rev. Lett. **92**, 126101 (2004); G. S. Verhoeven, M. Dienwiebel, and J. W. M. Frenken, Phys. Rev. B **70**, 165418 (2004).
- [14] A. Gopinathan and D. G. Grier, Phys. Rev. Lett. **92**, 130602 (2004); C. Reichhardt and C. J. Olson Reichhardt, Phys. Rev. E **69**, 041405 (2004); M. Pelton, K. Ladavac, and D. G. Grier, Phys. Rev. E **70**, 031108 (2004); A. M. Lacasta, J. M. Sancho, A. H. Romero, and K. Lindenbergh, Phys. Rev. Lett. **94**, 160601 (2005); J. P. Gleeson, J. M. Sancho, A. M. Lacasta, and K. Lindenbergh, Phys. Rev. E **73**, 041102 (2006).
- [15] R. Guantes and S. Miret-Artés, Phys. Rev. E **67**, 046212 (2003); S. Sengupta, R. Guantes, S. Miret-Artés, and P. Hänggi, Physics A **338**, 406 (2004).
- [16] R. Eichhorn, P. Reimann, and P. Hänggi, Phys. Rev. Lett. **88**, 190601 (2002); Phys. Rev. E **66**, 066132 (2002); B. Cleuren and C. Van den Broeck, Phys. Rev. E **67**, 055101(R) (2003); L. Machura, M. Kostur, P. Talkner, J. Luczka, and P. Hänggi, Phys. Rev. Lett. **98**, 040601 (2007); M. Kostur, L. Machura, P. Talkner, P. Hänggi, and J. Luczka, Phys. Rev. B **77**, 104509 (2008); D. Speer, R. Eichhorn, and P. Reimann, EPL **79**, 10005 (2007); Phys. Rev. E **76**, 051110 (2007); J. Nagel, et al. Phys. Rev. Lett. **100**, 217001 (2008).
- [17] S. Denisov, Y. Zolotaryuk, S. Flach, and O. Yevtushenko, Phys. Rev. Lett. **100**, 224102 (2008).
- [18] J. W. Swift and K. Wiesenfeld, Phys. Rev. Lett. **52**, 705 (1984).

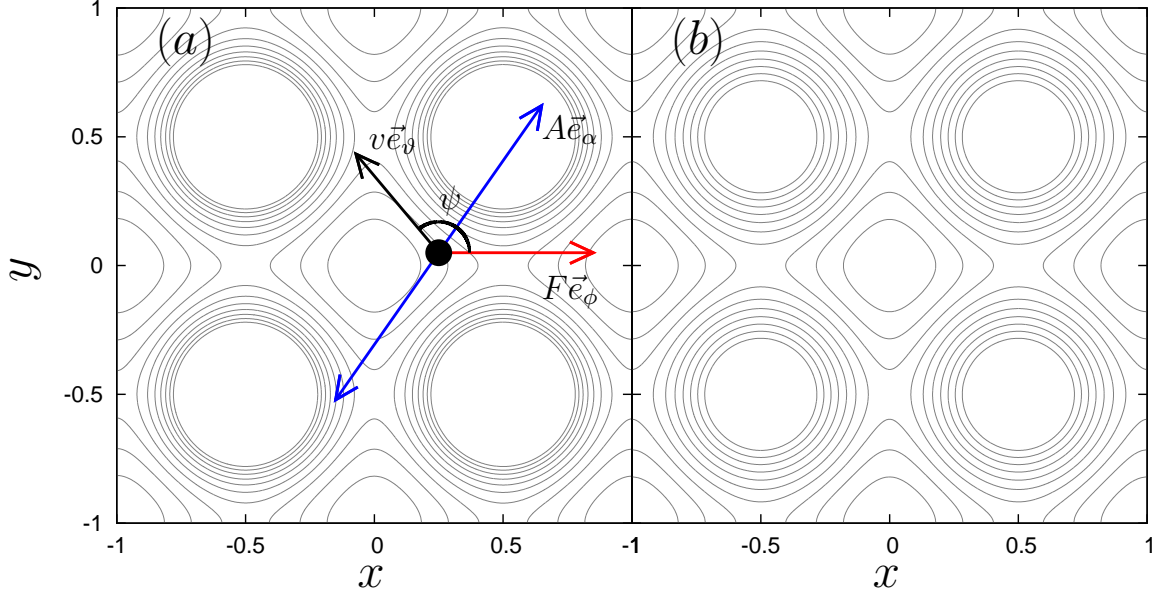


Figure 4.1: (a) Yukawa and (b) Gauss square lattice potential with $L_x = L_y = 1$ represented by equipotential lines, i.e. (4.2) with (a) (4.3) and (b) (4.4). The parameters are $\lambda = 4$ (a) and $u = 10$ and $\sigma = \frac{1}{4}$ (b). In panel (a) the relevant vectors are shown, namely, the average velocity $\vec{v} = v\vec{e}_\phi$ (black), the constant bias force $\vec{F} = F\vec{e}_\phi$ (red) and the deflection angle ψ (i.e. the angle enclosed by \vec{F} and \vec{v}). The periodic driving force is indicated by a blue double arrow $\vec{A} = A\vec{e}_\alpha$.

4.3 Model

As a simple and representative example we choose the Langevin dynamics of the position coordinate $\vec{r}(t) = (x(t), y(t))$ of a single overdamped Brownian particle interacting with a periodic potential $U(\vec{r})$, a rocking drive $\vec{A}(t)$, a constant bias force $\vec{F} = F\vec{e}_\phi$ ⁷ and two dimensional Gaussian white noise $\vec{\xi}(t)$ of strength Γ :

$$\eta \dot{\vec{r}}(t) = \vec{A}(t) + \vec{F} - \vec{\nabla}U(\vec{r}(t)) + \sqrt{2\eta\Gamma}\vec{\xi}(t) \quad (4.1)$$

with $\langle \xi_i(t)\xi_j(s) \rangle = \delta_{ij}\delta(t-s)$.

Normalization factors of the potential can be absorbed into the friction coefficient η , which can in turn be absorbed into the time unit. Specifically, we set

$$U(x, y) = \sum_{n,m} \tilde{U} \left(x + \left(n + \frac{1}{2} \right) \cdot L, y + \left(m + \frac{1}{2} \right) \cdot L \right) \quad (4.2)$$

and choose the sample potentials \tilde{U} to be

$$\tilde{U}_{\text{Yukawa}}(x, y) = \frac{\exp(-\frac{r}{\lambda})}{r} \quad (4.3)$$

⁷ \vec{e}_ϕ is the unit vector enclosing the angle ϕ with the x axis, i.e. in the direction of ϕ . Likewise, we will denote the unit vectors in the x/y direction as $\vec{e}_{x/y}$.

(Yukawa potential, a standard model for screened charges [202, 203, 240, 241]) with $r = |\vec{r}|$ and $\lambda > 0$, or, occasionally,

$$\tilde{U}_{\text{gauss}}(x, y) = u \cdot \sigma \cdot \exp\left(-\frac{r^2}{2\sigma^2}\right) \quad (4.4)$$

(Gauss potential, a standard model for optical traps [23, 24, 28, 189, 191, 242]) with $\sigma > 0$ and $u \neq 0$. The prefactor σ ensures that the gradient has the maximum value $|\vec{\nabla}\tilde{U}(\sigma\vec{e}_\nu)| = u \cdot \exp\left(-\frac{1}{2}\right)$ with ν being an arbitrary direction. This choice turns out to be convenient when comparing different values of σ . It is important that due to the rotational symmetry of (4.3) and (4.4) the force due to a single lattice site is also rotationally symmetric and thus depends only on the distance r from the lattice site. Otherwise, the total potential would have different symmetry properties. Both potentials turn out to yield qualitatively similar results if certain conditions are met, see figure 4.40 and figure 4.4.

As normalization, we set

$$L = L_x = L_y = 1 \quad (4.5)$$

from now on, but will refer to the lattice period as L occasionally. For the driving force we write

$$\vec{A}(t) = \vec{e}_\alpha \cdot a \cdot \tilde{f}(t) \quad (4.6)$$

with the *drive protocol* $\tilde{f}(t)$, the *drive amplitude* a and the *drive direction* α . We will use only periodic drive protocols with period T and frequency $\Omega = \frac{2\pi}{T}$. For the drive protocol we will choose a square wave in most cases:

$$\tilde{f}_{\text{square}}(t) = \text{sign}(-\sin(\Omega \cdot t)) \quad (4.7)$$

and, in a few cases, a sine wave protocol

$$\tilde{f}_{\text{sine}}(t) = -\sin(\Omega \cdot t). \quad (4.8)$$

Our “standard” model reads

$$\dot{\vec{r}}(t) = \vec{e}_\alpha \cdot a \cdot \text{sign}(-\sin(\Omega \cdot t)) + F\vec{e}_\phi - \vec{\nabla}\tilde{U}_{\text{Yukawa}}(\vec{r}(t)) + \sqrt{2\Gamma}\vec{\xi}(t) \quad (4.9)$$

and our central observable will be the time- and ensemble averaged dimensionless velocity,

$$\vec{v} = v\vec{e}_\vartheta = \frac{T}{L} \lim_{t \rightarrow \infty} \frac{1}{t} \int_0^\infty dt' \dot{\vec{r}}(t'), \quad (4.10)$$

taking values of $\frac{n}{m}$ with $n \in \mathbb{Z}$ and $m \in \mathbb{N} \setminus \{0\}$ for periodic, and thus also for phase-locked solutions. Our notation is largely the same as in [4], except for the normalization of the average velocity, a shift of the potential and in the drive protocol.

(4.7) turns out to be advantageous in overdamped dynamics, as, for sufficiently large drive amplitudes a , it prevents the particle from relaxing towards the potential minima in the low frequency limit $\Omega \rightarrow 0$. In contrast, any smooth drive protocol respecting S_0 symmetry, e.g. (4.8), allows the particle to relax towards a potential minimum if the frequency is sufficiently low. This results in trajectories with different initial conditions getting very close when they relax towards the minima, resulting in narrow basins of

attraction. Usually, this yields a low noise resistance, i.e. pseudopotential depth [2, 141, 144, 243] of the attractor, since already a small noise kick may put a noisy trajectory on the attractor outside the attractor's basin of attraction. This is particularly relevant in the presence of symmetry induced bistability.

The square wave drive (4.7) introduces a discontinuity into the dynamics. This may have significant effects on the dynamics. In particular, it may lead to deterministic chaos in a non-autonomous one dimensional ordinary differential equation of the same class as considered here but without S_0 symmetry [244]. Without the discontinuity, chaos is excluded in such dynamics [118]. We have verified that our results are qualitatively unchanged if the discontinuity is lifted by using the sine drive protocol (4.8), see in particular figure 4.31 and figure 4.41, see also section 4.6.

4.4 Numerical treatment of the potentials

With regard to our choice of λ and σ in (4.4) and (4.3) (see section 4.5), it is clear that the numerical computation of (4.2) is prohibitively expensive. First, a numerical cutoff has to be introduced, i.e. the sum is computed only for a finite number of terms (see also footnote 5 of section 5.2). We keep only the terms from the neighborhood of the elementary cell that the particle is in up to a certain radius (more precisely all lattice sites with a Chebyshev distance⁸ from the elementary cell the particle is in equal to or less than that radius). For (4.3), we have found the sum to converge if about 20 neighboring grid sites are taken into account, in the sense that there are no discernible differences, at the resolution of the figures, if the attractors shown in (e.g.) figure 4.7 are computed for different radii. To avoid the computation of the sum in each step of the solver, we compute the force field on an equally spaced rectangular grid and use bilinear interpolation [186]. To that end, we have found the numerics to converge already if the grid has a resolution higher than 100×100 , in the sense that there are no discernible differences, at the resolution of the figures, if the attractors shown in (e.g.) figure 4.7 are computed. When calculating unstable periodic orbits with large Floquet multipliers, the nonanalyticities introduced by the bilinear interpolation result in some problems at certain combinations of the system parameters, numerical tolerances and grid sizes, which can be avoided by varying the system parameters⁹. If the computations are done

⁸The Chebyshev distance of two points \vec{a}, \vec{b} in \mathbb{R}^N is $\max_i |a_i - b_i|$.

⁹To calculate the stroboscopic map Θ used to obtain unstable periodic orbits of the dynamics we have used the rk4 ODE solver from [186] with $h = 10^{-3}$ since the rkqs algorithm from [186] yielded worse results (even for much smaller values of ϵ), possibly due to the interplay of the minimization scheme, the adaptive step size control and the interpolated force field. Convergence of the minimization scheme is assumed if the residual is sufficiently small, i.e. $|\Theta(\vec{r}_{fp}) - \vec{r}_{fp}| < 10^{-6}$, and we have found our results to be robust if the residual is either increased or decreased by more than one order of magnitude. We have found the minimization scheme to fail to converge for some combinations of bifurcation parameter values and grids from which the force field is interpolated, even if the residual is increased by two orders of magnitude. This is due to the nonanalyticities of the bilinearly interpolated force field. We have found that decreasing the grid spacing (and thus increasing the resolution of the force field interpolation) does not solve the problem satisfactorily but considering more values of the bifurcation parameter does. To find all unstable periodic orbits, we use a very high resolution grid in the bifurcation parameter. To follow unstable periodic orbits (in the same sense as following stable periodic orbits in phase diagrams) we have not used equally spaced values of the bifurcation parameter but vary the spacing at each increase of the bifurcation parameter until the minimization scheme converges or a maximum/minimum step width of

on a normal processor (CPU) with a sufficiently large on chip cache, we have found the method to be sufficiently fast for our purposes. For large grid sizes, and possibly for large noise strengths, we have found a significant increase of the computation time. The first can be attributed to the grid becoming too large for the on chip caches of the CPU, while the latter may be attributed to the data prefetch algorithms of the CPU working less efficiently for noisy trajectories. The situation would be much different if the computations were to be done on a GPU. Then, the frequent memory accesses would be prohibitively expensive due to the much smaller on chip caches, and the large number of threads competing for the caches. In that case a summation technique (see footnote 5 of section 5.2) would yield better results. With regard to the Gauss potential, a similar conclusion applies, only that the radii of the neighborhood taken into account may be much smaller. We have found the method to have converged for radii larger than 4 for $\sigma = 0.25$ (and possibly smaller, depending on the choice of σ) in the same sense as above.

4.5 Choice of parameters

From now one, we will consider the case of no noise and no bias force

$$\Gamma = 0 \text{ and } \vec{F} = 0 \quad (4.11)$$

unless otherwise noted, i.e. S_0 symmetric deterministic dynamics, and try to show how SSBT is created. To begin, we fix the free parameters σ in (4.4) and λ in (4.3). For $\lambda \rightarrow 0$ the potential using (4.3) becomes flat, the dynamics become linear and SSBT is ruled out. For $\lambda \rightarrow \infty$ the potential converges to that generated by a square lattice of electric charges and SSBT is not ruled out. Thus, we expect a good choice of λ to be $\lambda \gg 1$. The treatment of that case involves some subtleties, which we avoid by choosing

$$\lambda = 4 \quad (4.12)$$

unless otherwise noted. For larger λ we found no significant differences in the dynamics. A slightly different line of reasoning applies to (4.4) with respect to σ . For both $\sigma = 0$ and $\sigma \rightarrow \infty$ the potential becomes flat, and we do not expect SSBT. Thus, there should be an “ideal” choice in between. We expect it to be somewhat less than the lattice period L since this yields a potential without flat parts, while the depth of the potential wells is reduced for $\sigma > L$. Unless otherwise noted, we choose

$$\sigma = 0.25 \text{ and } u = 10 \quad (4.13)$$

from now on since this choice closely matches our choice of λ in (4.3), see figure 4.40.

the bifurcation parameter is reached. To further improve these calculations for unstable periodic orbits with unfavorable Floquet multipliers we estimate the phase space coordinate of the unstable periodic orbit at each new value of the bifurcation parameter from the known phase space coordinates of the unstable periodic orbit at the previous values of the bifurcation parameter according to the method described in [117], i.e. extrapolation. This method allows larger steps in the bifurcation parameter to be taken and reduces computation time.

4.6 Symmetries

A general treatment of the possible symmetries of the dynamics is found in chapter 2. The square lattice Gauss and Yukawa potentials are \hat{S}_0 , \hat{S}_{xy} , \hat{S}_x , \hat{S}_y and $\hat{S}_{\frac{\pi}{2}}$ symmetric (see (4.14)-(4.17) and table 2.3). Due to the symmetry of the potential, it is sufficient to consider $\alpha \in [0^\circ, 45^\circ]$, since the whole interval $[0^\circ, 360^\circ]$ is contained in the image of $[0^\circ, 45^\circ]$ under the action of suitable combinations of the lattice symmetries. Note that removal (by considering a potential of lower symmetry) of any one of these symmetries is enough to change this.

Together with the symmetry properties of the periodic drive, the spatial symmetries of the potential imply symmetries of the dynamics. As in chapter 2, we use the same symbols for the symmetries of the non-autonomous dynamics, but without the hats. Furthermore, we usually do not specify the action of these symmetries on time, tacitly assuming their actions to be along the lines of section 2.4. The main symmetries considered in this chapter are (cf. section 2.4):

$$S_0 : (x, y, t) \rightarrow \left(-x, -y, t + \frac{T}{2} \right) \quad (4.14)$$

$$S_{xy} : (x, y, t) \rightarrow (y, x, t) \quad (4.15)$$

$$S_x : (x, y, t) \rightarrow (x, -y, t) \quad (4.16)$$

$$S_y : (x, y, t) \rightarrow (-x, y, t) . \quad (4.17)$$

We will write all other symmetries as combinations of these symmetries. Furthermore, we define the lattice shift symmetries as

$$S_{L_x} : (x, y, t) \rightarrow (x + 1, y, t) \quad (4.18)$$

$$S_{L_y} : (x, y, t) \rightarrow (x, y + 1, t) \quad (4.19)$$

and use the same symbols but with hats for their restrictions on the spatial coordinates (x, y) .

For $F = 0$, S_0 symmetry is always at work. $\alpha = 0^\circ$ breaks S_y ¹⁰ and S_{xy} symmetry, but the dynamics remain S_x symmetric. This implies that the lines $(x, \frac{n}{2})$, $x \in \mathbb{R}$, $n \in \mathbb{Z}$ are invariant manifolds (of the dynamics)¹¹. In our case, they are stable for n even and unstable for n odd, as can be readily inferred from eqs. (4.2)-(4.4) and figure 4.1. These invariant manifolds are linear subspaces, and the dynamics on to the linear subspaces can be described by a one dimensional non-autonomous ordinary differential equation describing the overdamped dynamics of a point particle in a one dimensional S_0 symmetric and periodic potential. Hence, all results with respect to deterministic spatially one dimensional overdamped dynamics apply after initial transients have died out, and SSBT and ANM can be ruled out due to the low dimensional nature of the attracting manifold¹².

¹⁰as defined by (4.17). If the temporal part is defined as in (4.14) (i.e. time is shifted by $\frac{T}{2}$), another symmetry is derived, but that symmetry does not imply the presence of invariant manifolds of the dynamics.

¹¹Meaning that a trajectory that has at least one common point with the invariant manifold is necessarily a part of the invariant manifold.

¹²Since there is only one spatial degree of freedom, SSBT solutions would have to cross, which is not possible, and the no-go theorem from [2] rules out ANM.

As discussed at the end of section 4.3, [244] have shown that the discontinuous forcing (4.7) can lead to chaos in the (driven) overdamped dynamics of a point particle, and thus in the dynamics on the attracting manifold of (4.9) for $\vec{F} \parallel \vec{A}(t) \forall t$ and $\alpha = 0^\circ$. By extensive numerical simulations, we have verified that there are no chaotic attractors in the dynamics on that attracting manifold if $\vec{F} = 0$. Therefore, the result due to [244] might require broken S_0 symmetry.

For $\alpha = 45^\circ$, the only remaining symmetry is S_{xy} (and S_0). The lines

$$W_n = (x + n, x), x \in \mathbb{R} n \in \mathbb{Z} \quad (4.20)$$

are invariant manifolds, and the dynamics are restricted to “transport channels” confined by adjacent invariant manifolds W_n, W_{n+1} ¹³. Since potential minima and maxima alternate along the invariant manifolds, the attractor of the deterministic dynamics is not necessarily contained in a linear invariant subspace. Thus, SSBT is not ruled out a priori¹⁴. The main consequence of the presence of the invariant manifolds W_n is that trajectories are restricted to “transporting channels” between two of these manifolds, since, without noise, no trajectory on one of these invariant manifolds can leave the manifold, nor can any trajectory started outside any of these invariant manifolds ever enter any of these manifolds. Thus, the average velocity \vec{v} of all attractors has to be zero orthogonal to the bisectrix, i.e. SSBT with respect to S_{xy} is ruled out, see section 2.7. This makes the treatment of $\alpha = 45^\circ$ simpler than that of more general choices of α and we set¹⁵

$$\alpha = 45^\circ \quad (4.21)$$

for now. For all other values of α between 0° and 45° , the only remaining symmetry is S_0 and there is no restriction on the average velocity and SSBT attractors with transport in practically any direction are possible. This case is most complex and will be treated later.

4.7 Rotated coordinate frame

For $\alpha = 45^\circ$, we use a rotated (and stretched) coordinate frame in which the invariant manifolds $W_n, n \in \mathbb{Z}$ are parallel to the coordinate axes for convenience:

$$\tilde{x} = x + y \quad (4.22)$$

$$\tilde{y} = x - y. \quad (4.23)$$

The new unit cell is $(\tilde{x}, \tilde{y}) \in [-1, 1] \times [-1, 1]$. This unit cell can be subdivided by the invariant manifold W_0 (i.e. $\tilde{y} = 0$) into a lower half $[-1, 1] \times [-1, 0]$ and an upper half

¹³Whenever referring to the W_n from now on, we tacitly require n to be integer.

¹⁴Yet, under similar conditions, we have not found SSBT. For the potential $U(x, y) = u \cdot (\cos(2\pi \cdot x) \cdot \cos(2\pi \cdot y) + \cos(2\pi \cdot x) + \cos(2\pi \cdot y))$ and a driving force in arbitrary direction and of either form (4.8) or (4.7) we did not find SSBT despite exhaustive numerical search. The same applies to the potential $U(x, y) = u \cdot \cos(2\pi \cdot x) \cdot \cos(2\pi \cdot y) + y^2$ irrespective of the drive protocol used and the latter can be explained by “Middleton’s no-passing rule”, see chapter 6.

¹⁵Note that the same argument applies to $\alpha = 0^\circ$, but that case is of no interest, as discussed above.

$[-1, 1] \times [0, 1]$, i.e. phase space is separable, as was argued in section 4.6. S_{xy} maps one half onto the other, and the dynamics in both halves are equivalent. We will use

$$[-1, 1] \times [0, 1] \quad (4.24)$$

as our unit cell for $\alpha = 45^\circ$. The following applies only to the interior of our unit cell. We replace \hat{S}_{xy} with

$$\hat{\tilde{S}}_{xy} := \hat{S}_{L_x} \circ \hat{S}_{xy} : (\tilde{x}, \tilde{y}) \rightarrow (\tilde{x} + 1, -\tilde{y} + 1), \quad (4.25)$$

which maps the ‘‘transport channel’’, i.e. $[-\infty, +\infty] \times (0, 1)$, onto itself. Likewise, we replace \hat{S}_0 by

$$\hat{\tilde{S}}_0 := \hat{S}_{xy} \circ \hat{S}_0 : (\tilde{x}, \tilde{y}) \rightarrow (-\tilde{x}, \tilde{y}) \quad (4.26)$$

which maps the unit cell $(\tilde{x}, \tilde{y}) \in (-1, 1) \times (-1, 1)$ onto itself and leaves each ‘‘transport channel’’ invariant. Note that we have assigned the ‘‘lower’’ part of the invariant manifold $[-1, 1] \times \{0\}$ to the unit cell for completeness. On the invariant manifold, we continue to use the ‘‘unrotated’’ symmetry group $\{\hat{S}_{xy}, \hat{S}_0\}$ since $\hat{\tilde{S}}_{xy}$ maps one invariant manifold onto another. The unit cell is separable, i.e. there exists no trajectory leading from one of the invariant manifolds W_n (cf. (4.20)) into the interior. Therefore it is valid to consider two different symmetry groups for its components.

4.8 Spontaneous symmetry breaking for $\alpha = 45^\circ$

We now turn to $\alpha = 45^\circ$ as the simplest possible scenario for SSBT in (4.9). The remaining parameters are the drive amplitude a and frequency Ω . Transporting solutions of (4.9) necessarily break \tilde{S}_0 symmetry and all (combined) symmetries containing S_0 . Therefore, we begin our discussion of SSBT by considering the symmetry properties of (spatially) *bounded*¹⁶ (non-transporting) periodic attractors of (4.9).

For large drive frequencies $\Omega \gg 1$, the particle is expected to show regular behavior under certain circumstances. The drive power $\frac{a}{\Omega}$ is a more convenient way to characterize the drive properties for large frequencies. At fixed drive power $\frac{a}{\Omega}$, the oscillation amplitude of a free particle subjected to the periodic drive remains constant. For large frequencies $\Omega > 10$, the general structure of the symmetry properties of periodic attractors is (see figure 4.2(b)):

1. For very small drive power $\frac{a}{\Omega}$, there are only symmetric attractors living on the invariant manifold W_0 and respecting both symmetries S_0 and S_{xy} since small oscillations around the potential minima are symmetric (see section 4.10). An example of such an orbit at $\Omega = 10$ is shown in figure 4.3(a) (dashed).
2. Upon increasing the drive power, there is a symmetry breaking bifurcation¹⁷ creating (a pair of) \tilde{S}_0 but not \tilde{S}_{xy} symmetric attractors. An example of this pair of

¹⁶Meaning that the attractor, projected onto the (spatial) coordinate space, i.e. the x - y plane, is bounded. In turn, trajectories on the attractors have zero average velocity.

¹⁷This bifurcation is equivalent to the bifurcation (b_1) discussed in figure 4.7, with the direction of the symmetry breaking branches inverted, i.e. in the direction of increasing drive power.

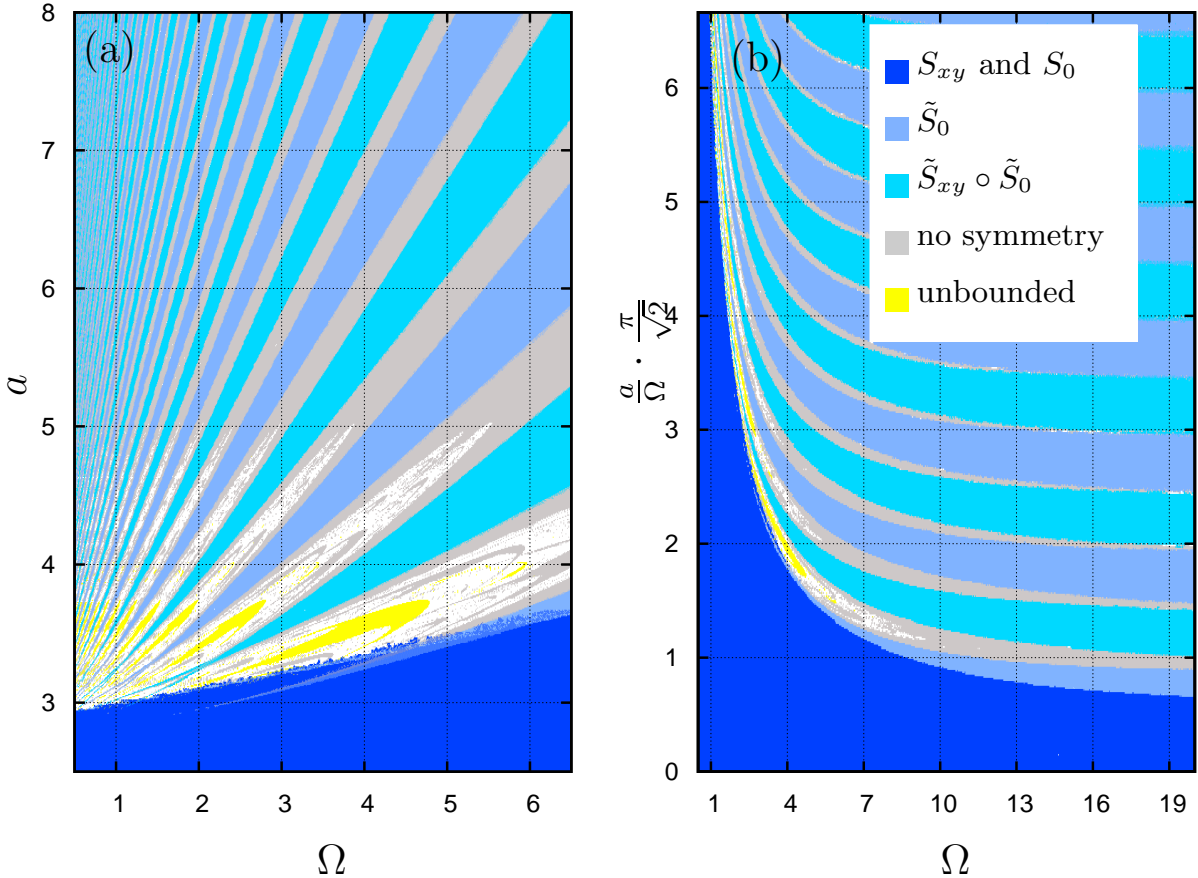


Figure 4.2: (Symmetry-) Phase diagram for the deterministic dynamics (4.9) with $\vec{F} = 0$, $\Gamma = 0$ and $\alpha = 45^\circ$. Shown are the symmetry properties, encoded in colors according to the legend in (b), of non-transporting (bounded) periodic attractors of (4.1). Regions of existence of unbounded (see text) periodic attractors are also shown and will be discussed in more detail in section 4.9, see also figure 4.4. White regions correspond to non-periodic attractors. Coexistence of different symmetry classes are shown by shading of the two corresponding colors. (a) shows the Ω - a plane of parameter space, see also figure 4.4(a). In (b) the rescaled drive amplitude $\frac{a}{\Omega}$ proportional to the asymptotic oscillation amplitude has been used instead of the drive amplitude a . The figure has been obtained by the same method as described in section 3.9.1, i.e. figure 3.1, but only periodic attractors are shown. The grid resolution is 800×800 grid points, and the absolute numerical tolerance of the Runge-Kutta algorithm with adaptive step size control, rkqs of [186], is $\epsilon = 5 \cdot 10^{-7}$ with all components of the solution being weighed equally.

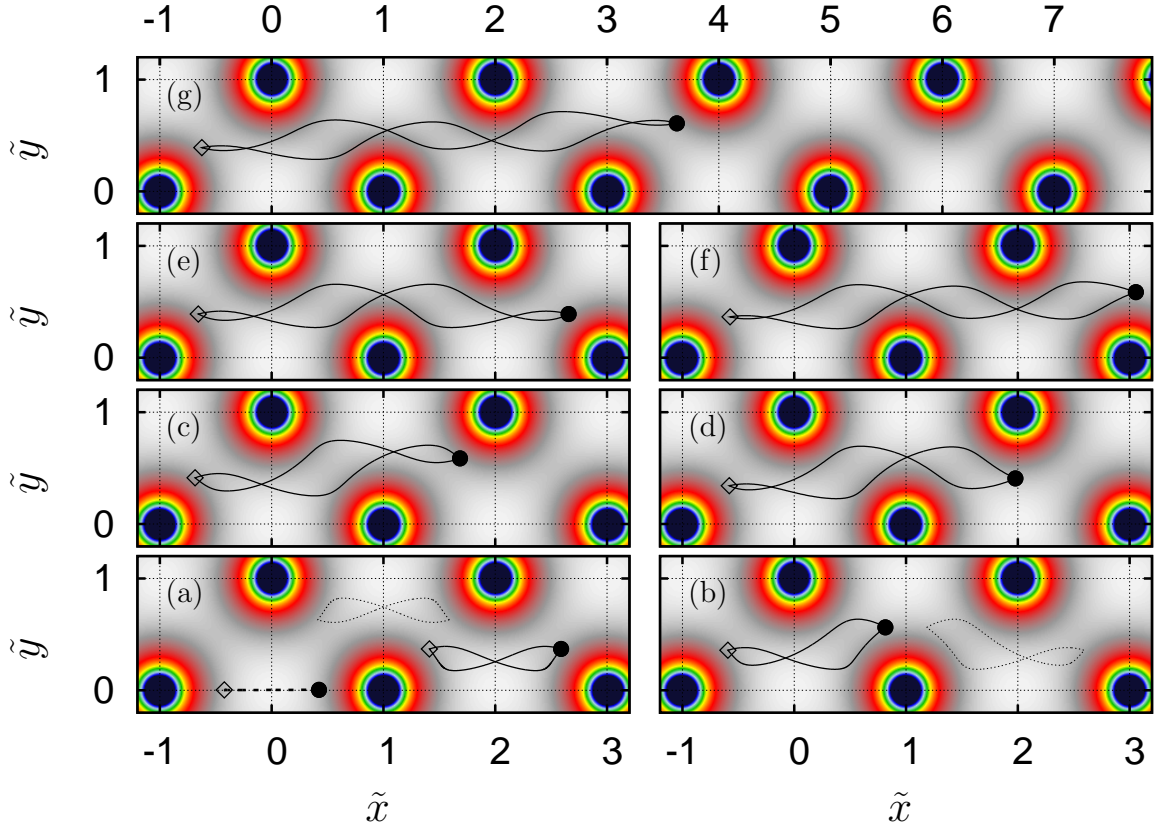


Figure 4.3: Stable periodic orbits (attractors) of the deterministic dynamics (4.9) with all parameters as in figure 4.2, $\Omega = 10$ and various values of the drive power $\frac{a}{\Omega}$: (a) $\frac{a}{\Omega} = 0.35$ (dashed-dotted), $\frac{a}{\Omega} = 0.4$ (solid and dashed, the dashed orbit is the (shifted) image of the solid orbit under \hat{S}_{xy}); (b) $\frac{a}{\Omega} = 0.45$ (solid and dashed, the dashed orbit is the (shifted) image of the solid orbit under $\hat{S}_{xy} \circ \hat{S}_0$); (c) $\frac{a}{\Omega} = 0.65$; (d) $\frac{a}{\Omega} = 0.7$; (e) $\frac{a}{\Omega} = 0.85$; (f) $\frac{a}{\Omega} = 0.925$; (g) $\frac{a}{\Omega} = 1.05$. The particle positions when the drive changes sign are marked by the symbols, and the distance of the symbols is the oscillation amplitude. Note that we show not only the unit cell, and thus some of the symmetric orbits have to be shifted before they are really mapped onto themselves by their symmetry. The same applies to all further trajectories shown in this work. The same numerical scheme has been used as in figure 4.2 and will be used for all other deterministic trajectories shown in this work.

attractors is shown in figure 4.3(a) (solid and dotted). The drive power value at which this bifurcation occurs converges to $\frac{a}{\Omega} \frac{\pi}{\sqrt{2}} \approx 0.56$ for very large frequencies¹⁸.

3. At drive power $\frac{a}{\Omega} \frac{\pi}{\sqrt{2}} \approx 0.96$, there is a further symmetry breaking bifurcation creating 4 nonsymmetric attractors. Two of them are shown in figure 4.3(b). The other two follow by applying \tilde{S}_{xy} to the orbits. For slightly larger drive power ($\mathcal{O}(\frac{1}{\Omega})$), a symmetry restoring bifurcation follows, creating $\tilde{S}_{xy} \circ \tilde{S}_0$ symmetric attractors (see figure 4.3(c)). The distance of these bifurcations shrinks to 0 as $\frac{1}{\Omega}$. We have found a width of less than 0.01 at $\Omega = 80$.
4. The bifurcations discussed in 3 repeat in inverse order at drive power $\frac{a}{\Omega} \frac{\pi}{\sqrt{2}} \approx 1.35$. Nonsymmetric attractors (see figure 4.3(d)) are created in a symmetry breaking bifurcation and destroyed in a symmetry restoring bifurcation for a slightly larger value of drive power (again, $\mathcal{O}(\frac{1}{\Omega})$), creating \tilde{S}_0 symmetric attractors, see figure 4.3(e). For larger drive powers, the widths of the regions of existence of nonsymmetric attractors are even smaller.
5. The \tilde{S}_0 symmetric attractors undergo the same bifurcation as described above in 3 at $\frac{a}{\Omega} \frac{\pi}{\sqrt{2}} \approx 1.99$ (see figure 4.3(f)), while the then created $\tilde{S}_{xy} \circ \tilde{S}_0$ symmetric attractors (see figure 4.3(g)) undergo the same bifurcation as described above in 4 at $\frac{a}{\Omega} \frac{\pi}{\sqrt{2}} \approx 2.4$. In other words, the bifurcations repeat periodically in $\frac{a}{\Omega} \frac{\pi}{\sqrt{2}}$ with a period of approximately 1.

This regular structure at large drive frequencies and amplitudes can be justified by an analytical approximation based on a Fourier series expansion of (4.9) and its solution. In section 4.25.1 we give a sketch of how the approximation can be obtained, but do not go into details. The approximation yields that increasing the drive power $\frac{a}{\Omega}$ by $\frac{\sqrt{2}}{\pi}$, the oscillation amplitude¹⁹ of non-transporting periodic orbits increases by exactly the spacing of minima on the invariant manifolds (4.20) in the drive direction (i.e. $(\Delta\tilde{x}, \Delta\tilde{y}) = (\pm 2, 0)$ in figure 4.3). This is shown in figure 4.3. Compare in particular (a) with (e), and (c) with (g). Thus, such an increase in the oscillation amplitude corresponds to one additional potential maximum and one additional potential minimum (counting only those on the “lower” invariant manifold $\tilde{y} = 0$) passed during each drive period, and the total number of potential minima and maxima passed during each drive period increases by two (counting both equally).

For smaller frequencies, this regular structure is broken up and the symmetry breaking bifurcations occur at larger drive power for lower frequencies, indicating that the particle no longer follows the drive as a free particle would. Thus, the stripes (of regions of existence of symmetric attractors) are “bend upwards” in figure 4.2(b). Moreover, the widths of the stripes of regions of existence of nonsymmetric periodic attractors grow

¹⁸The rate of convergence is $\frac{1}{\Omega}$. This rate of convergence basically applies to all critical values of the drive power $\frac{a}{\Omega}$ discussed below. It has been obtained numerically and its being independent of frequency for asymptotically large frequencies will be justified later by an analytical approximation. Furthermore, our numerics failed for frequencies larger than $\Omega = 80$ yielding a precision less than 0.02 in the asymptotic values given below. With that in mind, we omit the $\mathcal{O}(\frac{1}{\Omega})$ correction henceforth.

¹⁹We define the oscillation amplitude as the distance between the turning points of the orbits in the \tilde{x} direction, i.e. $|\tilde{x}(0) - \tilde{x}(\frac{T}{2})|$. The turning points points are also marked in figure 4.3.

for smaller frequencies (in the $\frac{a}{\Omega}$ direction) at the expense of the width of the stripes of symmetric attractors.

Most importantly, for $\Omega \lesssim 10$ regions of existence of non-periodic attractors emerge in the stripes of nonsymmetric attractors. These chaotic attractors are created via period doubling cascades [87, 115, 121, 122] and will be discussed below in section 4.9. By the argument due to [127], period doubling bifurcations, and thus chaos created by that mechanism, can only occur for the nonsymmetric attractors, except in very special cases. In short, the argument is that by using S_0 , the stroboscopic map Θ^{20} can be written as the square of another map, $\tilde{\Theta}_{S_0}$. Using the $\frac{T}{2}$ propagator $\Theta_{T/2}(\vec{r}_0) = \vec{r}(\frac{T}{2})$, where $\vec{r}(t)$ is the trajectory passing through \vec{r}_0 at time 0, i.e. $\vec{r}(0) = \vec{r}_0$, we write

$$\Theta = \left(\hat{S}_0 \Theta_{T/2} \right)^2 = \tilde{\Theta}_{S_0}^2, \quad (4.27)$$

and likewise for $S_{xy} \circ S_0$ ²¹.

Symmetric (with respect to either of these symmetries) periodic orbits are then fixed points of $\tilde{\Theta}_{S_0}$. A symmetry breaking bifurcation means a period doubling bifurcation of that map. In turn, a period doubling bifurcation (with respect to Θ) of the symmetric orbit means a period quadrupling bifurcation of $\tilde{\Theta}_{S_0}$. This is a two-parameter bifurcation [127, 245], a highly special situation as argued in [127]. In other words, the manifold of parameter space in which the bifurcation occurs has two dimensions less than parameter space. For dynamics in which there is a restriction on the phase space volume contraction rate, and thereby a restriction on the Floquet multipliers, such as those considered in e.g. [1, 2], this period quadrupling can even be ruled out completely [127].

Within these regions of non-periodic attractors, *unbounded*²² (including SSBT) attractors are found for $\Omega \lesssim 6$. The drive power $\frac{a}{\Omega}$ is not a convenient parameter for small frequencies, and we use the drive amplitude a from now on. Figure 4.2(a) shows an enlargement of the regions of existence of unbounded periodic attractors found in figure 4.2(b). From figure 4.2(a) it is clear that they are found only in the regions of non-periodic attractors, which in turn are found only in the regions of nonsymmetric attractors, as has been detailed above.

The structure of non-periodic and unbounded attractors will be further discussed in section 4.9, and the mechanism by which they are created will be discussed in more detail in section 4.10.

²⁰The stroboscopic map (or time T map) Θ is the map that iterates time by T , i.e. $\Theta(\vec{r}_0) = \vec{r}(T)$ with $\vec{r}(0) = \vec{r}_0$ being the trajectory with initial condition \vec{r}_0 at time 0, see footnote 23 of section 2.6.

²¹In detail (see [127]), the calculation is as follows. Defining the propagator $P_{t_0}^{t_1} : \mathbb{R}^2 \rightarrow \mathbb{R}^2 : \vec{r} \rightarrow \vec{r}(t_1)$, where $\vec{r}(t)$ is the trajectory passing through \vec{r} at time t_0 , i.e. $\vec{r}(t_0) = \vec{r}$, the stroboscopic map can be written as $\Theta = P_{T/2}^T \circ P_0^{T/2}$. In S_0 symmetric (and likewise in $S_{xy} \circ S_0$ symmetric dynamics with S_0 replaced by $S_{xy} \circ S_0$), for each trajectory $\vec{r}(t)$ there is another trajectory $\tilde{\vec{r}}(t) = S_0 \vec{r}(t) = \hat{S}_0 \vec{r}(t + \frac{T}{2})$. Using such a pair of trajectories, we get $P_0^{T/2} \hat{S}_0 \vec{r}(\frac{T}{2}) = P_0^{T/2} \tilde{\vec{r}}(0) = \tilde{\vec{r}}(\frac{T}{2}) = \hat{S}_0 \vec{r}(T) = \hat{S}_0 P_{T/2}^T \vec{r}(\frac{T}{2})$ and thus $P_{T/2}^T = \hat{S}_0^{-1} P_0^{T/2} \hat{S}_0$, where $\hat{S}_0^{-1} = \hat{S}_0$ denotes the inverse of \hat{S}_0 . (4.27) follows immediately.

²²In the literal sense. An unbounded attractor, projected into the x - y plane (spatial coordinates) does not fit into any ball of finite radius. Transporting attractors are the prime examples. Our second important example are chaotic diffusive attractors, on which the average velocity is zero, but individual trajectories are unbounded.

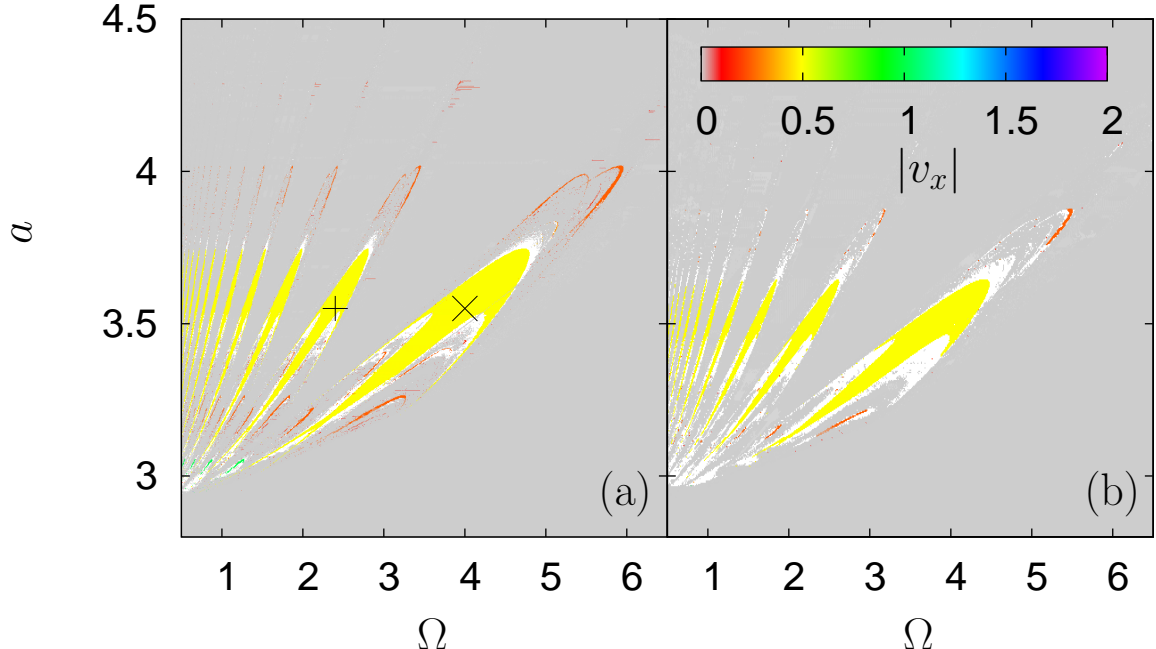


Figure 4.4: Phase diagram for the dynamics (4.1) with $\vec{F} = 0$, $\Gamma = 0$, drive protocol (4.7) with $\alpha = 45^\circ$ and potentials (4.3) (a) and (4.4) (b). Shown are regions of parameter space in which phase-locked attractors are found. Their transporting velocities are indicated by colors, see the legend. Non-transporting attractors are displayed in grey. White regions correspond to regions where no phase-locked attractors have been found. Note that due to $\alpha = 45^\circ$, one has $v_x = v_y$. The figure, as well as all following phase diagrams, has been obtained by the same method as described in section 3.9.1, i.e. figure 3.1. The grid resolution is at least 400×400 grid points for all phase diagrams, and the absolute numerical tolerance of the Runge-Kutta algorithm with adaptive step size control, rkqs of [186], is less than $\epsilon = 5 \cdot 10^{-7}$ with all components of the solution being weighed equally.

4.9 SSBT for $\alpha = 45^\circ$

We will now discuss the above mentioned regions of unbounded attractors. Our numerical findings are summarized in figure 4.4.

First, due to the similarity between the potentials, see figure 4.1, there is no significant difference between (4.3) and (4.4), as can be seen from figure 4.4. In particular, the divergence of (4.3) and the area around it is of no relevance since this region of phase space is not accessible to deterministic trajectories unless initiated in it. We will henceforth focus on (4.3) and figure 4.1(a).

Phase locked SSBT attractors exist for $\Omega \lesssim 6$, and a values roughly between 3 and 4. Their parameter regions²³, shown as colors indicating their average velocity in figure 4.4, are isolated from each other, and are surrounded predominantly by grey areas, corresponding to bounded attractors, or, less frequently, white areas, corresponding to unbounded diffusive attractors. We have found most of the latter to belong to unbounded \tilde{S}_0 symmetric diffusive chaotic attractors²⁴ by looking at representative trajectories.

²³or region of existence, i.e. the region of parameter space, in which they exist

²⁴i.e. chaotic attractors leading to unbiased deterministic diffusion, see section 4.11.1

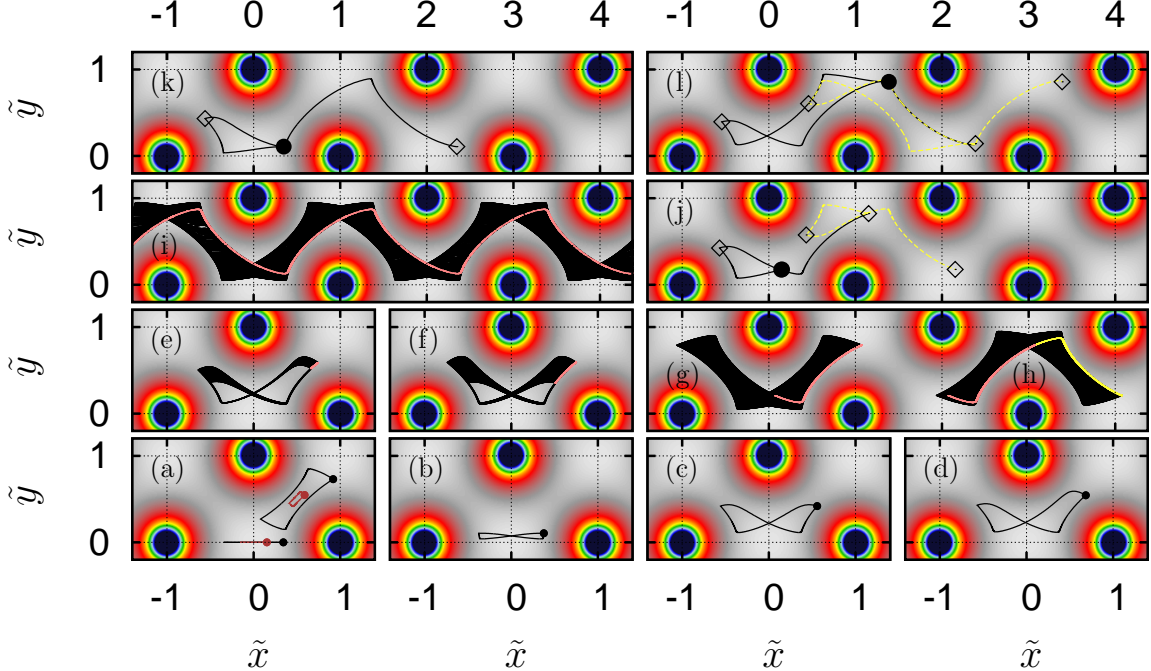


Figure 4.5: Trajectories for the same dynamics as considered in figure 4.4(a) for (a): $\Omega = 6.99$, $a = 1$ (red) and $\Omega = 4.01$, $a = 3$ (black); (b)-(j): $\Omega = 4$ and $a = 3.22$ (b), 3.25(c), 3.29(d), 3.303(e), 3.304(f), 3.383(g), 3.383(h), 3.384(i), 3.41(j); (k) $\Omega = 1.85$ and $a = 4.58$; (l) $\Omega = 2$ and $a = 3.41$. The particle coordinate at $t = nT$, $n \in \mathbb{N}$ is indicated by a filled circle in (a)-(d) and as red dots in (e)-(i) with the exception of (h). In (h), the shifted coordinate at $t = nT$ of the trajectory shown in (g) is shown by the red line, and the coordinate at $t = nT$ of the black trajectory in (h) is shown by the yellow line. In (j)-(l) the particle coordinate at $t = \frac{n}{2}T$, $n \in \mathbb{N} \setminus \{0\}$ is indicated by black diamonds and the particle coordinate at $t = 0$ by a black circle. Furthermore, the particle trajectory is drawn as a black line for $t \in [0, T]$ and as a dashed yellow line for $t \in [T, 2T]$. (e)-(i) show chaotic attractors, and the filled black areas show the projection of the attractors while the colors lines show their images under Θ .

In contrast to [1, 2], section 4.10 and chapter 6, most of the SSBT regions in parameter space contain attractors with $|v| = 0.5$ transport, and are either period 2 attractors, or attractors which are created via period doubling from period 2 attractors, see figure 4.5(g) for an example periodic orbit. Period 1 SSBT attractors with $|v| = 1$ are also found, but their concomitant parameter region is much smaller. Their apparent absence in figure 4.1(b) is due to the resolution of the figure.

4.9.1 Limiting cases

We have not found SSBT outside the region of the a - Ω plane shown in figure 4.4, except for $\Omega \rightarrow 0$. This can be explained by the need for a three dimensional phase space: we can discard most limiting cases for a and Ω . For $a = 0$, $\Omega = 0$ or $\frac{\Omega}{a} \rightarrow \infty$ there is no time-dependence and phase space is two dimensional. $a \rightarrow \infty$ will be treated in section

4.9.3 and rules out SSBT according to (4.28) if the gradient of the potential is bounded²⁵.

The last limiting case is that of $0 < \Omega \ll 1$. Then SSBT occurs just as for $\Omega \approx 1$, see section 4.9.2. The basic mechanism of SSBT is unchanged, see section 4.9.5 and occurs within the part of the drive period just before the drive changes sign. The parameter space region occupied by each individual SSBT attractor shrinks with $\Omega \rightarrow 0$. Due to this, noise resistivity of these attractors is usually smaller than for intermediate frequencies. Even for the smooth drive protocol (4.8), we have found SSBT for $\Omega = 0.01$. At that frequency, the particle will always relax *almost* into a local minimum when the drive changes sign. This in turns seems to make SSBT impossible as long as there is only one minimum, as trajectories would then cross in that minimum. Since the particle does not exactly relax to the minimum, trajectories do not actually cross, but come *very* close. The noise resistance of these SSBT attractors is extremely small and they are of no interest.

4.9.2 Repetitive tongue structure

The (yellow) regions of existence of the main $|v_x| = 0.5$ SSBT attractors are “tongue”-shaped in the Ω - a plane. A higher drive frequency requires a larger drive amplitude to achieve SSBT and each tongue is tilted to the right. Basically, each tongue can be interpreted as a periodic window²⁶ of a diffusive chaotic attractor. The main periodic orbit of this windows has period 2, and is terminated either by tangent bifurcations or period doubling cascades ending in chaotic crises. The diffusive chaotic attractor largely occupies the white areas around the yellow tongues, but its region of existence extends beyond into the grey area (bounded attractors), as can be inferred from e.g. figure 4.7. Around each tongue, further windows of “smaller” (in the sense that their parameter region has smaller volume) SSBT attractors carrying different average velocities are found.

Basically, all $|v_x| = 0.5$ tongues to the left (e.g. the second, counting from the right, marked with a '+') are tilted and distorted copies of the rightmost tongue (marked with a 'x'). The chief difference is that during each half period of the periodic drive, the particle travels a larger distance in the instantaneous direction of the driving force (which it then travels back during the second half-period of the drive). In effect the average transport velocity is not changed, see figure 4.5(j) and figure 4.5(l) for an illustration. The orbit in figure 4.5(j) corresponds to the rightmost tongue and the orbit in figure 4.5(l) belongs to the second $v_x = 0.5$ tongue.

Essentially, the isolated and repeated appearance of SSBT parameter regions can be explained from the nonlinear synchronization of the periodic potential and the periodic drive leading to phase-locking. An intuitive explanation for this can be given by looking directly at the shape of the periodic SSBT orbits, which we will do in sections 4.9.4-4.9.5, and a more complicated explanation can be given by comparison with the dynamics of Josephson junctions, i.e. (1)-(2) of [2], see section 4.9.3.

²⁵In case of (4.3), the potential (and its derivative) is unbounded. Thus, one cannot rule out SSBT for arbitrarily large drive amplitudes. In our extensive numerical simulations, we found only bounded periodic oscillations. A likely explanation for this behavior is that trajectories are straight lines away from the part of the potential with large gradients of magnitude a . Going to a bounded potential yielding equivalent dynamics removes the problem.

²⁶Periodic windows correspond to a stable periodic orbit “suddenly” appearing in the complicated structure of a chaotic attractor after a system parameter is varied and then somehow loosing stability when that parameter is varied further [115, 246].

4.9.3 Comparison with the dynamics of Josephson junctions

The shape and structure of each SSBT parameter region in figure 4.4(a) features a striking resemblance to those found in the dynamics of Josephson junctions, i.e. (1)-(2) of [2], see chapter 3 and fig. 1 of [2], if one replaces Ω in figure 4.4(a) with the friction strength η , which is tantamount to writing (4.9) in the rescaled time $t' = \Omega \cdot t$. In that context, the synchronization can be explained by a Fourier series expansion of the equations of motion [137, 157]. The main differences are as follows. First, unbounded diffusive attractors occupy a smaller fraction of parameter space in figure 4.4(a) and are replaced by non-transporting attractors or coexist with non-transporting attractors. Second, SSBT is absent above a certain threshold value of the drive amplitude a in figure 4.4(a) and, third, the dominant SSBT attractors found in figure 4.4(a) correspond to period 2 windows²⁷, while in [1, 2] attractors from period 1 windows are dominant, see sections 4.9.4-4.9.5 for a more detailed discussion.

In chapter 3 and [137], it was argued that the general structure of the main windows follows from a Fourier expansion in the drive frequency of the equations of motion, (1)-(2) of [2], called the Bessel function approximation. The approximation is valid in several limiting cases [137], $a, \Omega \gg 1$ with $\frac{a}{\Omega} = \mathcal{O}(1)$ being of interest to us. Such an approximation is more problematic for (4.9): in order to get SSBT in [1, 2, 137, 157] at high frequencies, the friction coefficient has to be sufficiently small. The principal equation of the Bessel function approximation is the lowest order (constant) term of the Fourier expansion and is obtained by averaging over the equation of motion, i.e. (4.9). Substituting $t' = \Omega t$ and dividing (4.9) by a in order to get a “finite” coefficient for the derivative and then averaging over time, one obtains

$$\frac{\Omega}{a} \left\langle \dot{\vec{r}} \right\rangle = \frac{1}{a} \left\langle -\vec{\nabla} U(\vec{r}) \right\rangle. \quad (4.28)$$

For $a \gg 1$ and $\vec{v} \neq 0$, SSBT is ruled out, in contrast to [2, 137] and, in the regime where the Bessel function approximation can be expected to be valid, SSBT is ruled out in (4.9). Another hint towards the inapplicability of a Bessel function approximation is the shape of the regions of existence of SSBT attractors, cf. figure 4.4. Comparing with the shapes of the SSBT parameter regions found in [1, 2, 137], we find that the shape of the regions in figure 4.4(a) corresponds to tongues with unstable centers, so called “broken” *Shapiro steps*²⁸, which are found only in the chaotic regime, where the Bessel function approximation fails [137]. Since we have no adjustable parameter left to “reach” a regime where the Bessel function approximation becomes valid, the approximation cannot be extended.

Yet, it is reasonable to expect some features of this regular structure to survive, and the main features of the main SSBT parameter regions in figure 4.4(a) can be understood from the Bessel function approximation. First, the Bessel function approximation leads to isolated and, with decreasing (and properly scaled) drive power, periodically repeated SSBT regions, cf. (3.5), explaining the repeated structure of SSBT regions in figure 4.4(a). Second, the Bessel function approximation gives one set of boundary curves by an appropriate Bessel function, cf. section 3.4 and (3.5). These boundaries correspond to

²⁷They are created from period 2 orbits by period doubling cascades.

²⁸Cf. footnote 3 of chapter 3.

saddle node bifurcations. A second border emerges when the drive frequency is decreased by the appearance of deterministic chaos in the dynamics, namely by a period doubling cascade of the attractor culminating in a chaotic boundary crisis after which either an unbounded symmetric attractor is left behind, or another attractor, which had been in existence independently [1, 2, 137], takes over.

In figure 4.4, this general structure is recovered. This is most easily seen by the largest region of existence of SSBT attractors (tongue) (marked with a 'x'). The large Ω part of its region of existence is bounded on both sides (with respect to a) by saddle node bifurcations, the interval of a values for which the attractor exists is unbroken, and there is no period doubling (see for example $\Omega = 4.5$, figure 4.11). When Ω is decreased, the interval of a values for which the attractor exists becomes "broken", see figure 4.7. This instability is due to a period doubling cascade to chaos and a chaotic crisis, as in [1, 2, 137]. For even smaller frequencies, the orbits involved in the saddle node bifurcations both become unstable in another direction of phase space, and no SSBT attractor is found for these frequencies in figure 4.4. The relevant orbits are still present, but with different stability properties²⁹.

In effect, the so called Bessel function Shapiro step [137, 154] becomes unstable in its center [1, 2, 137]. This, see the white regions in figure 4.4, results in a diffusive chaotic attractor, occupying the center of the former Shapiro step if there are no other stable structures. For certain drive frequencies, this attractor in turn has periodic windows, in which the center of the former Shapiro step reappears, as seen in figure 4.4 and Fig. 1 in [1, 2]. For small frequencies, only these parts of the SSBT attractor remain, as in [1, 2].

4.9.4 Period 1 SSBT orbits

An interesting feature in figure 4.4 are $|v_x| = 1$ SSBT attractors (green), which correspond to period 1 windows of the diffusive chaotic attractor. They can be found³⁰ for small frequencies $\Omega < 1.3$ and $a \approx 3$, break \tilde{S}_{xy} in addition to \tilde{S}_0 , and their regions of existence are much smaller than those of the $|v_x| = 0.5$ attractors. An example orbit is shown in figure 4.5(k). We will now discuss the shape of the $|v_x| = 1$ period 1 orbits, which is much simpler than the shape of the dominant $|v_x| = 0.5$ period 2 orbits.

At $t = 0$ (when the drive changes sign to be in the negative \tilde{x} direction), the particle starts on the trajectory of a particle subjected only to a constant bias force in the $+\tilde{x}$ direction, more or less at the point where it is closest to the invariant manifold $\tilde{y} = 0$ and also close to the potential maximum at $(\tilde{x}, \tilde{y}) = (1, 0)$. Due to the potential minimum at $(\tilde{x}, \tilde{y}) = (0, 0)$, the invariant manifold $\tilde{y} = 0$ is attracting at first, and the particle relaxes towards the invariant manifold. Once the particle passes the saddle point where the invariant manifold becomes repulsive (in the \tilde{y} direction), the particle travels around the potential maximum at $(\tilde{x}, \tilde{y}) = (-1, 0)$. Since the particle starts close to the invariant manifold $\tilde{y} = 0$, it is slow while travelling around the potential maximum and does not get around the potential maximum before the drive changes its direction.

This behavior is the origin of transport. Due to the relaxation towards the invariant manifold $\tilde{y} = 0$, the particle gets so close to it that it spends the remainder of the first half period of the drive travelling slowly around the potential maximum at $(\tilde{x}, \tilde{y}) = (-1, 0)$.

²⁹I.e. the Floquet multiplier not involved in the saddle node bifurcation becomes greater than one.

³⁰Their apparent absence in panel (b) is due to the resolution of the figure.

When the drive changes sign, the particle is far away from the invariant manifold $\tilde{y} = 0$ (in figure 4.5(k), the particle is actually close to $\tilde{y} = 0.5$) and quickly “relaxes” to the path of a particle subjected only to a constant bias force (in the $+\tilde{x}$ direction). At the end of the drive period, the particle arrives at its initial position but shifted by 2 length units in the $+\tilde{x}$ direction and the orbit continues periodically.

Construction of period 1 SSBT orbits

In principle, a SSBT orbit could be constructed according to this mechanism for other potentials of the same lattice type and symmetry. First, one has to choose a constant bias force for which unbounded solutions exist. One then picks a suitable initial condition on the orbit that a particle travels on if subjected to a constant positive bias force (i.e. in the $+\tilde{x}$ direction). This initial condition has to be so that the particle relaxes towards one of the invariant manifolds (4.20), without loss of generality $\tilde{y} = 0$, upon being subjected to a negative instantaneous force from the drive during the first half period, is slowed down when “travelling” around the next potential maximum, and the first half period of the drive has to be long enough that the particle is sufficiently far from the invariant manifold $\tilde{y} = 0$ when the drive changes sign. Then, the particle does not relax too far towards the potential minimum. Instead, it relaxes towards the orbit of a depinned particle subjected to a constant bias force of same value as the instantaneous drive. Once it reaches its shifted initial condition, one sets this time as the end of the “second” half period of the drive “protocol”.

The issue is that the half periods of the drive have to be of the same length. Both can be made arbitrarily long by letting the particle travel on the constant bias force paths. But in order to match the lengths of both half periods of the drive, these times cannot be varied smoothly due to the requirements to the particle positions described above. This explains the repetitive appearance and disappearance of these orbits in figure 4.4. With decreasing frequency, the path travels a larger distance during each half period of the drive, and the lengths of these segments have to be matched with the periodicity of the potential. In fact, this matching is rather subtle as is shown by the small size of the regions of existence of period 1 SSBT attractors in figure 4.4.

Moreover, for each fixed potential geometry, there is an upper limit of how close to the invariant manifold (4.20) the particle can relax from the constant bias force trajectory when the drive changes sign. Thus, there is a maximum a value for which this mechanism of SSBT can work, and, for the same reason, the maximum average velocity is bounded. In fact, we have not found periodic orbits with $|v_x| > 1$ in figure 4.4, but that may be due to the resolution of the figure.

In comparison with [2, 137], i.e. the case of one spatial dimension with inertial forces, these inertial forces have now been substituted by the second spatial dimension in a nontrivial manner. A particle with inertial dynamics “stores” energy in its momentum when it is accelerated. Then, if a force opposite to that momentum is applied to the particle, that momentum is depleted first, and the particle does not change its direction instantaneously. Here, loosely speaking, the \tilde{y} component of the particle position takes this role, but it cannot store “directed” momentum. Instead, if the particle is close to the middle of the elementary cell, $\tilde{y} = 0.5$, and a (sufficiently large) force is applied to the particle, the particle will be transported relatively quickly into the next elementary cell,

and its “instantaneous mobility” in the \tilde{x} direction is “high”, i.e. the particle reacts to a force in the \tilde{x} direction by moving quickly into the direction of that force. In contrast, if the particle is close to the invariant manifold $\tilde{y} = 0$ and a force is applied to the particle, the particle has to travel around the potential maxima towards $\tilde{y} = 0.5$ first, thereby “depleting” \tilde{y} , before it can reach the next elementary cell, and its “instantaneous mobility” in the \tilde{x} direction is “low”. In that sense, the dynamics are somewhat related to particle transport and diffusion in confining geometries [47, 55, 247–251] in which the “instantaneous” particle mobility in the one direction depends on the other coordinate(s) of the particle. and

4.9.5 Period 2 SSBT orbits

Having understood the shape of the $|v_x| = 1$ period 1 orbits, we now turn to the shape and structure of the $|v_x| = 0.5$ period 2 orbits found in the yellow tongues in figure 4.4. As seen from figure 4.5(j), the orbit consists of two parts, each a full drive period long. The second part (shown in yellow) can be obtained from the first part by application of $\hat{\tilde{S}}_{xy}$ since the orbit is a fixed point of $\hat{\tilde{S}}_{xy} \circ \Theta$ on the torus³¹. Therefore, it is sufficient to discuss only the first (black in figure 4.5(j)) part of the orbit.

The first part of the orbit appears to be just another version of the period 1 orbit in figure 4.5(k) which has been cut during the second half period of the drive: the particle starts close to the invariant manifold $\tilde{y} = 0$, relaxes towards $\tilde{y} = 0$ and travels slowly around the next maximum at $(\tilde{x}, \tilde{y}) = (-1, 0)$. When the drive changes sign, the particle relaxes onto the constant bias force trajectory corresponding to the instantaneous direction of the drive ($+\tilde{x}$). When the particle has reached the image under $\hat{\tilde{S}}_{xy}$ of its starting position, the drive changes sign before the orbit has traveled a full elementary cell. This is where the orbit differs from the period 1 orbit (apart from “minor” shifts). Due to $\hat{\tilde{S}}_{xy}$ symmetry, this is repeated in the second drive period, and the particle ends on its starting position shifted by spatial period of the rotated coordinate frame since $\hat{\tilde{S}}_{xy}^2(\tilde{x}, \tilde{y}) = (\tilde{x} + 2, \tilde{y})$, see also (4.30).

Comparing with the period 1 orbit, it becomes apparent why the period 2 orbit has greater regions of existence, i.e. is more robust against variations of the parameters. In the case of the period 1 orbit, the particle has to travel ≈ 2 length units in one half period of the drive, which requires a certain amount of drive power. But this higher drive power means that the particle has to relax closer to the invariant manifold $\tilde{y} = 0$ during the first half period of the drive (when the drive is in the $-\tilde{x}$ direction) to be slowed down long enough. On the period 2 orbit, the particle has to travel only ≈ 1 length unit during one half period of the drive, and the drive power may be significantly lower. First, this is why period 2 orbits can be found for much smaller drive power than period 1 orbits. Second, and more importantly, the closer to the invariant manifold the particle has to be, the more subtle the matching of the different parts of the periodic orbit becomes.

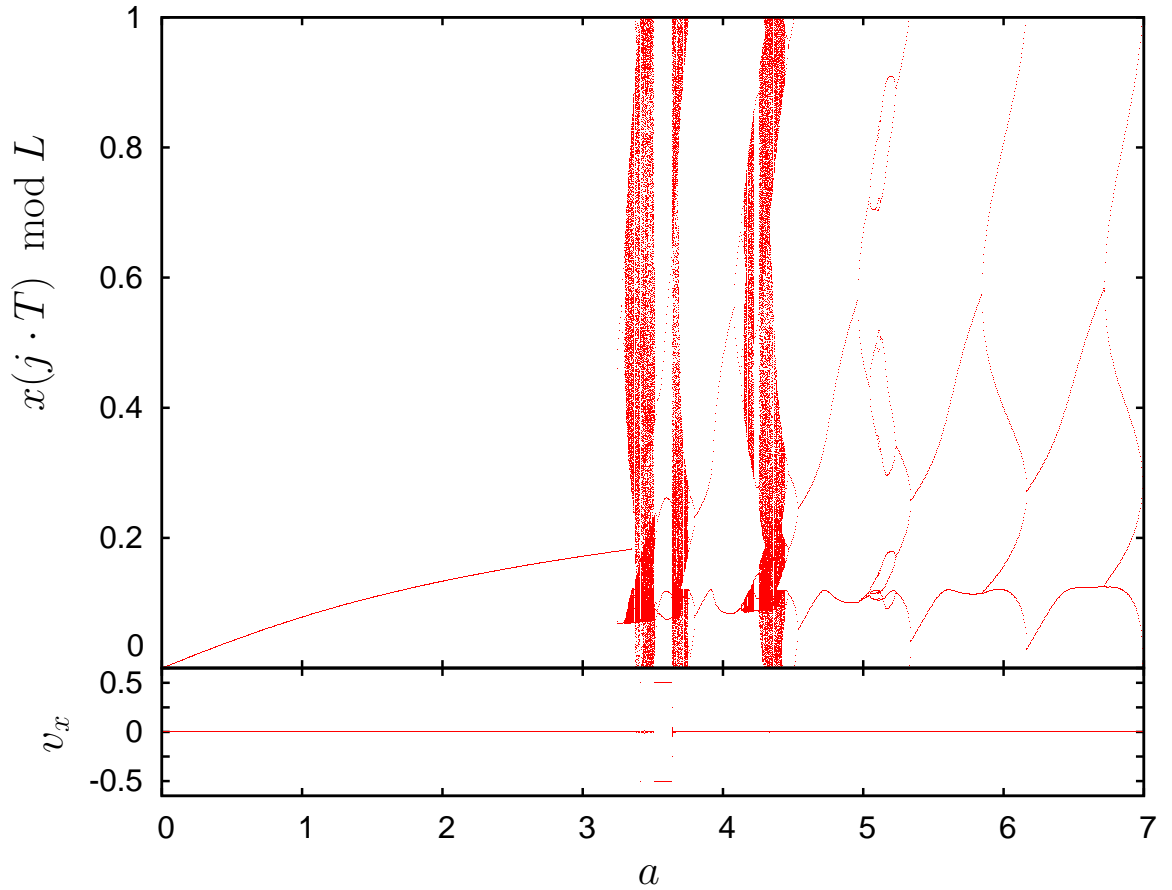


Figure 4.6: Bifurcation diagram for the same dynamics as considered in figure 4.4(a) and $\Omega = 4$, i.e. a vertical cut through figure 4.4(a). The upper panel shows the x component of the stroboscopic map Θ of attractors reduced to a torus, and the lower panel shows their average velocities. The figure has been obtained by integrating the equation of motion for a sufficiently long time (such that initial transients have died out) at least 25 times (for each parameter value considered) with uniformly distributed random initial conditions, and then plotting the final 50 stroboscopic images of each trajectory as indicated by the axis label. Furthermore, periodic orbits have been detected and followed according to the same method used to obtain the phase diagrams, see figure 4.2. See also Fig. 3 of [2] and Fig. 4 of [4], and the corresponding explanations.

4.10 Creation of SSBT at $\alpha = 45^\circ$

We now analyze the structure of figure 4.4(a) in more detail by means of a bifurcation analysis. We choose

$$\Omega = 4 \quad (4.29)$$

as a convenient choice for this analysis. A comparison with the analysis in [4], at a less convenient frequency, can be found in section 4.25.2.

First, consider figure 4.6 corresponding to a vertical cut through figure 4.4(a) at $\Omega = 4$ for a large set of a values, in particular starting at $a = 0$ and showing only attractors. There are only non-transporting and bounded attractors for $a \notin [3.38, 4.35]$. For $a \in [3.38, 4.35]$ (see also figure 4.7 for an enlargement of this region) there are unbounded (diffusive chaotic) attractors of 0 net average velocity and SSBT attractors as periodic windows of these unbounded attractors. The SSBT attractors are almost always phase-locked, and most are even periodic.

For $a < 3.24$ there is only one periodic, S_0 and S_{xy} symmetric non-transporting attractor living on the invariant manifolds (4.20). We will treat this attractor in more detail below. For $a \gtrsim 5.35$ there is only a \tilde{S}_0 symmetric attractor coexisting with its image under \tilde{S}_{xy} . As a is increased further, these attractors undergo a \tilde{S}_0 symmetry breaking bifurcations at $a \approx 5.85$, and a nonsymmetric bounded periodic attractor and its 3 images under $\{\tilde{S}_0, \tilde{S}_{xy}\}$ is created. These nonsymmetric attractors undergo \tilde{S}_0 symmetry restoring bifurcations at $a \approx 6.17$, and \tilde{S}_0 symmetric bounded periodic attractor is created. This process repeats periodically upon further increasing a , as has been discussed in section 4.8. Transporting attractors are found in figure 4.6 between $3.38 < a < 3.68$, though more transporting attractors exist as periodic windows of the unbounded attractors, especially around $a \approx 4.3$, corresponding to the second (marked with a '+') tongue in figure 4.4, section 4.9.2. Their regions of existence are smaller than the resolution of figure 4.6, and therefore these SSBT attractors are of no further interest here.

We now turn to a detailed analysis of the creation of SSBT attractors. For $a = 0$ there is only the force of the potential (4.2) acting on the particle. Thus, the particle will relax to the minimum corresponding to its initial position. This is located at $(\tilde{x}, \tilde{y}) = (0, 0)$ (the minimum at $(1, 1)$ belongs to the lower part of the next elementary cell and is equivalent due to symmetry). There are no other minima in the elementary cell, and all minima lie on of the invariant manifolds (4.20).

Upon switching on the drive, the particle starts to oscillate around the minimum. This oscillation is restricted to the invariant manifold $\tilde{y} = 0$ for sufficiently small a and grows in amplitude when a is increased, see figure 4.5(a). Once the oscillations become large enough, the behavior changes. This is shown in more detail in figure 4.7, in which some of the important bifurcation are marked as (b_1-b_5) . We will henceforth refer to these bifurcations often as figure 4.7(b₁)-(b₅). At $a \approx 3.34$ (see figure 4.7(b₁)) the periodic attractor loses stability in a symmetry breaking bifurcation [115], see section 2.6. The oscillations on the invariant manifold $\tilde{y} = 0$ have become unstable since the amplitude has become large enough for the trajectory to reach regions of the potential where the invariant manifold $\tilde{y} = 0$ is repulsive already for $a = 0$ ³².

³¹Therefore, the orbit has to break that symmetry before it can undergo period doubling as discussed in section 4.8.

³²At $a = 0$ the vector field component orthogonal to the invariant manifold, $\tilde{y} = 0$ without loss of

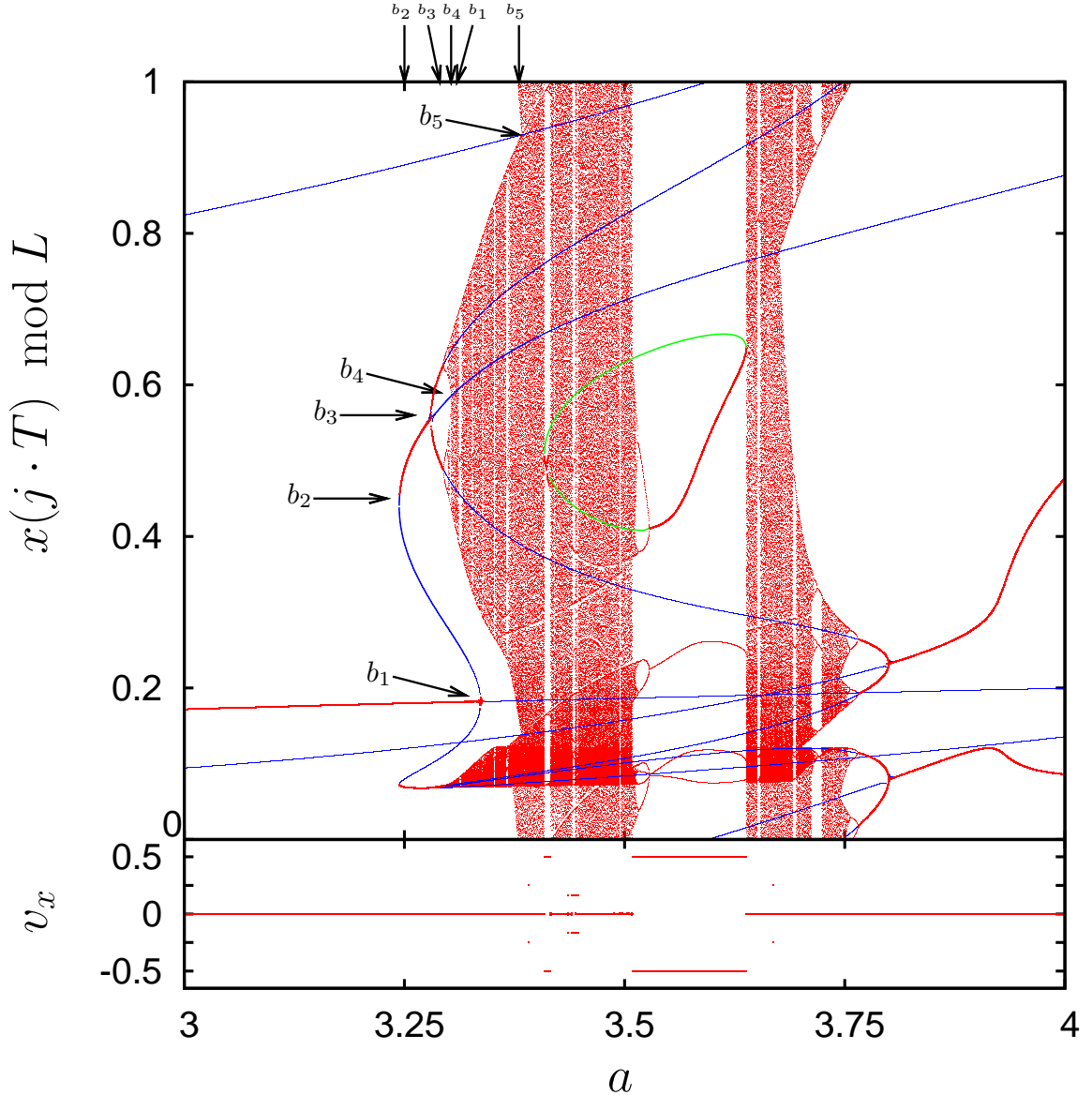


Figure 4.7: Bifurcation diagram for the same dynamics as considered in figure 4.4(a) and $\Omega = 4$, i.e. a vertical cut through figure 4.4(a). The red dots are identical to figure 4.6, the blue lines show all unstable periodic orbits of period 1, and the green lines show two selected unstable transporting period 2 orbits. The unstable periodic orbits have been obtained by finding the fixpoints of the stroboscopic map (or its iterates) [117] using the hybrids minimization algorithm from [252] for 10000 randomly chosen initial conditions (for each parameter value considered), and a much higher resolution in the bifurcation parameter than used for the attractors. For more details see footnote 9 of section 4.10.

This bifurcation creates a pair of \tilde{S}_{xy} symmetry breaking unstable periodic orbits, see figure 4.5(b). As can be seen from figure 4.7(b₁), the orbits start close the invariant manifold $\tilde{y} = 0$ at the bifurcation and then move away from the invariant manifold $\tilde{y} = 0$. Due to the direction of the bifurcation, the orbits exist for smaller values of a , i.e. “prior” to their point of creation in the chosen arbitrary parameterization of the bifurcation diagram. At $a \approx 3.24$ these “new” orbits become stable in a tangent bifurcation, see figure 4.7(b₂). One of these stable periodic orbits is shown in figure 4.5(c). At $a \approx 3.28$, these stable branches undergo \tilde{S}_0 symmetry breaking bifurcations, see figure 4.7(b₃), creating four stable periodic orbits, which are related to each other by the symmetry group $\{\tilde{S}_0, \tilde{S}_{xy}\}$. An example of one of these orbits is shown in figure 4.5(d).

The \tilde{S}_0 symmetry breaking bifurcation is the prerequisite for the following period doubling bifurcation starting at $a \approx 3.29$ and thus chaos, as has been discussed in section 4.8. After the first period doubling, the attractor undergoes a period doubling cascade, and at the accumulation point of the period doubling cascade a chaotic attractor is created [87, 121, 122]. An example is shown in figure 4.5(e). As before, all four attractors are obtained by application of the symmetry group.

At $a \approx 3.3$ (figure 4.7(b₄)) each pair of \tilde{S}_0 symmetry breaking attractors collides in an attractor merging crisis [115]. Both chaotic attractors, each belonging to one of the branches created at the bifurcation (b₃), collide simultaneously with the unstable branch of the bifurcation (b₃), and thus both attractors collide³³. The result is a (pair) of globally \tilde{S}_0 symmetric bounded chaotic attractors. One of them is shown in figure 4.5(f).

Upon further increasing a , the attractor “grows” and deforms, and in particular the amplitude of oscillations grows further, see figure 4.5(g). At $a \approx 3.38$ (see figure 4.7(b₅)), the attractor has grown such that it touches its image under \tilde{S}_{xy} , and, due to \tilde{S}_0 symmetry, also its image under $\tilde{S}_0 \circ \tilde{S}_{xy}$, see figure 4.5(h). Since the set in phase space where the attractors touch at the bifurcation belongs to neither attractor but is part of the union of both attractor’s basin boundaries, it is invariant under the dynamics. Usually such sets are periodic orbits, as is the case here. It is the unstable periodic orbit which oscillates around the saddle connecting two adjacent minima in the same transport channel of the potential. An example of this orbit is shown in figure 4.5(a) for two different values of a , and it is traced from $a = 0$ to the bifurcation (b₅) in figure 4.8.

Thus, it is now possible for trajectories, initiated on the (former) attractor, to reach the images (under \tilde{S}_{xy} or $\tilde{S}_0 \circ \tilde{S}_{xy}$) of the (former) attractor, and, likewise, trajectories initiated on one of the images (under \tilde{S}_{xy} or $\tilde{S}_0 \circ \tilde{S}_{xy}$) of the (former) attractor to reach the (former) attractor. Simultaneously, due to \tilde{S}_{xy} symmetry, each image (under \tilde{S}_{xy}) of the (former) attractor touches its image (under \tilde{S}_{xy}), and likewise for $\tilde{S}_0 \circ \tilde{S}_{xy}$. Since

$$\hat{\tilde{S}}_{xy}^2(\tilde{x}, \tilde{y}) = (\tilde{x} + 2, \tilde{y}), \quad (4.30)$$

the attractor becomes an unbounded \tilde{S}_{xy} and \tilde{S}_0 symmetric chaotic attractor consisting

generality, is pointing toward the invariant manifold $\tilde{y} = 0$ around the minimum and is thus attracting and repulsive around the maximum(divergence). Once oscillations on the invariant manifold $\tilde{y} = 0$ reach this point they do not become unstable immediately, since the attracting part around the minimum will still dominate if the drive frequency Ω is not too small. This happens once the combination of time spent on the repulsive part of the invariant manifold $\tilde{y} = 0$ and strength of repulsion dominates.

³³I.e. each of the 4 attractors collides with its image under \tilde{S}_0 .

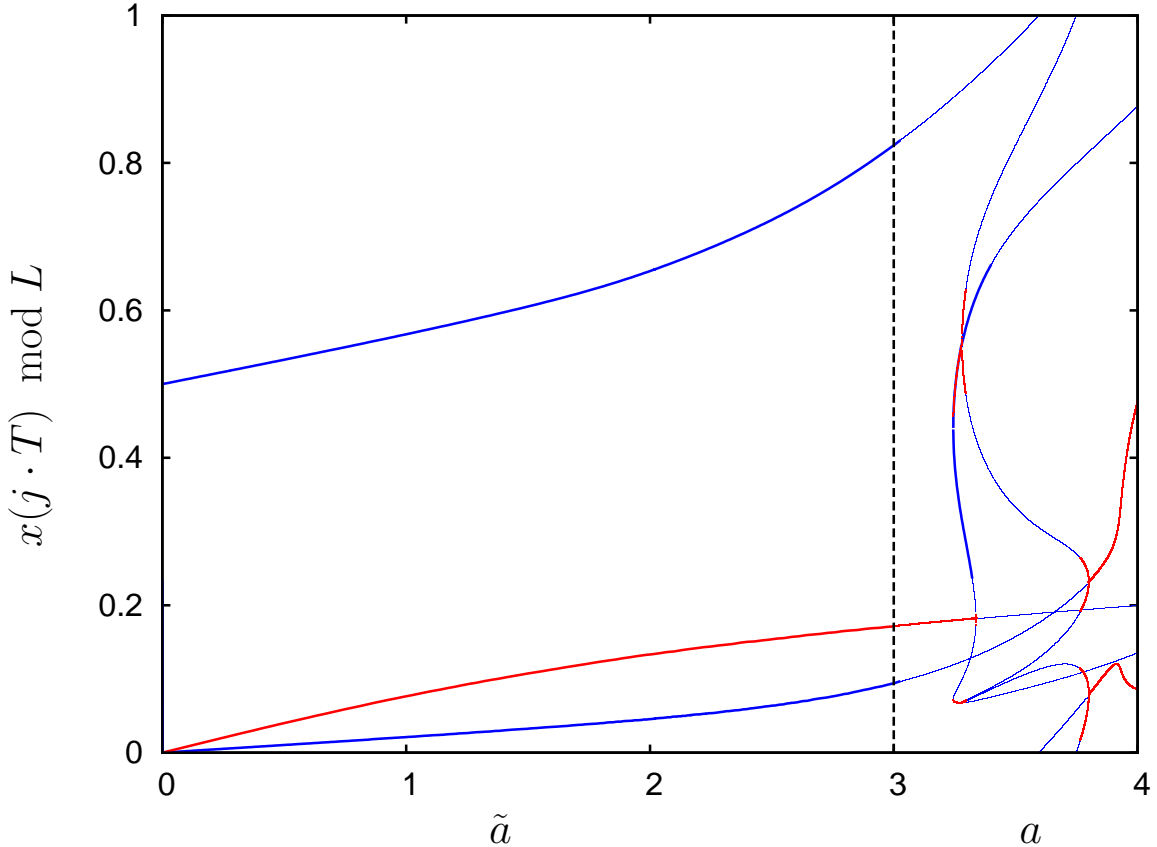


Figure 4.8: Bifurcation diagram for the same dynamics as considered in figure 4.4(a) and $\Omega = 4$ for $a > 3$ (see below) showing all period 1 orbits, obtained by the same method as described in figure 4.7. Stable orbits are shown as red lines, and unstable orbits are shown as blue lines. Furthermore, the part of the bifurcation diagram left of the vertical dashed line ($a = 3$) considers a different curve in parameter space as bifurcation parameter: $(a, \Omega)(\tilde{a}) = \left(\tilde{a}, 4 + (4 - 7) \frac{\tanh(3\tilde{a} - 6) - 1}{2}\right)$, which starts at $(a, \Omega)(0) = (0, 7)$ and ends at $(a, \Omega)(3) = (3, 4)$ (for all practical purposes). The reason is as follows: The Floquet multipliers z can be written as $z = e^{\frac{2\pi}{\Omega}c}$ with c being the Floquet exponent. Around $a \gtrsim 0$, all period 1 orbits will oscillate around potential equilibria. Thus, the Floquet exponents will be proportional to the curvature of the potential (which is of the order of 10 for the unstable directions of the saddles) and the period of the drive, T . This follows from expanding the potential around the equilibrium and calculating the orbits and their stability properties analytically. At $\Omega = 4$, the Floquet exponents of unstable periodic orbits can thus be estimated to be around 15, yielding $z \approx e^{15}$ for the Floquet multipliers, i.e. the unstable orbits cannot be calculated numerically.

of all the copies of the attractor and their images under \tilde{S}_{xy} merged, see figure 4.5(i),

Thus, the whole attractor shown in figure 4.5(i) is created from the “evolution” of only two periodic orbits, the one oscillating around the minimum, the one oscillating around the saddle, and their images under the symmetry transformations. Conversely, this route to the creation of an unbounded attractor can be ruled out if the conditions are different. For instance, if no saddle exists, or no potential minima in the case of a locally flat potential. Moreover, in the case of more complex potentials, the creation of SSBT has likewise to follow a different route. In that sense, the case considered here is the simplest for the creation of SSBT in two dimensional overdamped single particle dynamics.

4.10.1 Disappearance of the unbounded attractor

Upon further increasing a , the unbounded attractor vanishes at $a \approx 3.67$ in a reverse attractor merging crisis, leaving behind two bounded chaotic attractors³⁴, which are again related to each other through \tilde{S}_{xy} symmetry. These attractors undergo a reverse period doubling cascade when a is increased further, terminating at $a \approx 3.8$ in two periodic (period 1) attractors (of which each is the other’s image under \tilde{S}_{xy}). The main point is that the process of the disappearance of the unbounded attractor is the same as its creation, and no unbounded chaotic repeller is left behind in phase space. This conclusion is further supported by figure 4.35(d).

4.10.2 Other tongues

Continuing our examination of the evolution of the periodic (period 1) attractors created at $a \approx 3.8$ (and discussed above), we see that through a similar process an unbounded chaotic attractor is created at $a \approx 4.3$, see figure 4.6 and also figure 4.4 (the orange “specks” in figure 4.4 around $\Omega = 4$ and $a \approx 4.3$ correspond to periodic windows of this attractor). This attractor disappears at $a \approx 4.33$ through the same mechanism as detailed above, leaving behind two periodic (period 1) bounded attractors at $a \approx 4.54$. Upon further increasing a , these attractors undergo period doubling bifurcations (up to period 4), followed by reverse period doubling bifurcations and thus develop a “bubble” at $a \approx 5.1$ in the bifurcation diagram. Upon changing some other system parameter, e.g. for a lower frequency, these bubbles can undergo period doubling cascades to form another chaotic attractor.

According to figure 4.4 and figure 4.2(b), the unbounded attractor at $a \approx 4.3$ can be associated with the second (counting from right) $|v_x| = 0.5$ main region of SSBT by following the line defined by slope of the tongue in the Ω - a plane of parameter space in figure 4.4. This line corresponds to the symmetry breaking bifurcation leading to the region of nonsymmetric attractors in which the SSBT attractors are found, see figure 4.2(b). Likewise, the bubbles around $a \approx 5.1$ can be associated with the third main SSBT attractor in figure 4.4 or the corresponding stripe of nonsymmetric attractors in figure 4.2 by the same argument.

³⁴Note that these bounded attractors extend into the neighboring elementary cell, as do their basins of attraction.

Again, this can be attributed to the argument found in [127]: the symmetry-breaking bifurcation, i.e. the presence of nonsymmetric periodic orbits is a prerequisite to period doubling bifurcations. Thus bubbles, chaotic attractors (such that are created from a period doubling cascade) and finally SSBT can only occur in the stripes of nonsymmetric attractors in figure 4.2.

4.10.3 Spontaneous symmetry breaking transport

It is crucial to observe that while the unbounded attractor in total is \tilde{S}_0 symmetric, i.e. the image under \tilde{S}_0 of each orbit on the attractor is part of the attractor, this is not true for individual orbits of finite time on the attractor. I.e. the attractor is globally \tilde{S}_0 symmetric, but not locally (in time).

For instance, if the particle “travels” from the part of the attractor corresponding to figure 4.5(g) to the part of the attractor corresponding to the image under \tilde{S}_{xy} of the first part, this part of the orbit certainly breaks \tilde{S}_0 symmetry in a transporting manner, as the particle has then been “spontaneously” transported.

Usually, orbits on the attractor shown in figure 4.5(i) consist of very long orbits on parts of the attractor corresponding to those shown in figure 4.5(g)-(h) and short transits to new parts of the attractor. When such transits occur, and in which direction, depends sensitively on the initial conditions. The attractor is chaotic diffusive, transporting with zero net average velocity.

This attractor has periodic windows. Some of these are non-transporting windows, but there are also transporting periodic windows, i.e. Shapiro steps, such as the large periodic window around $a \approx 3.6$ in figure 4.7. Considering that the attractor already contains short “transporting” orbits spontaneously breaking \tilde{S}_0 symmetry for finite time intervals, the existence of these windows seems likely.

The structure of the simplest of such periodic windows, found for larger frequencies, always follows the same scheme: a periodic orbit is “created” from a tangent bifurcation on each side of the window, see for instance figure 4.11(a) for an example at $\Omega = 4.5$. For smaller frequencies, the periodic windows are more complex. The periodic orbits undergo period doubling cascades ending in chaotic crises in the center of the windows, and thus merge with the underlying chaotic attractor. This is the case for the “main” periodic window in figure 4.7 around $a \approx 3.6$. Its full extend is illustrated by plotting also the periodic orbit for values of a where it is unstable, and its companion unstable periodic orbit. Furthermore, the periodic orbits need not be stable at the tangent bifurcations at the borders of the windows. This structure corresponds to the situation already described in [1, 2, 137, 157] and chapter 3. In particular, the instability of the Shapiro steps in their centers was used in [1–3] to get ANM.

4.11 Consequences at $\alpha = 45^\circ$

4.11.1 Anisotropic Diffusion

As can be seen from figure 4.7, at $\Gamma = 0$ the average velocity depends on initial conditions and is not a smooth function of parameters (e.g. the SSBT windows in figure 4.7). This

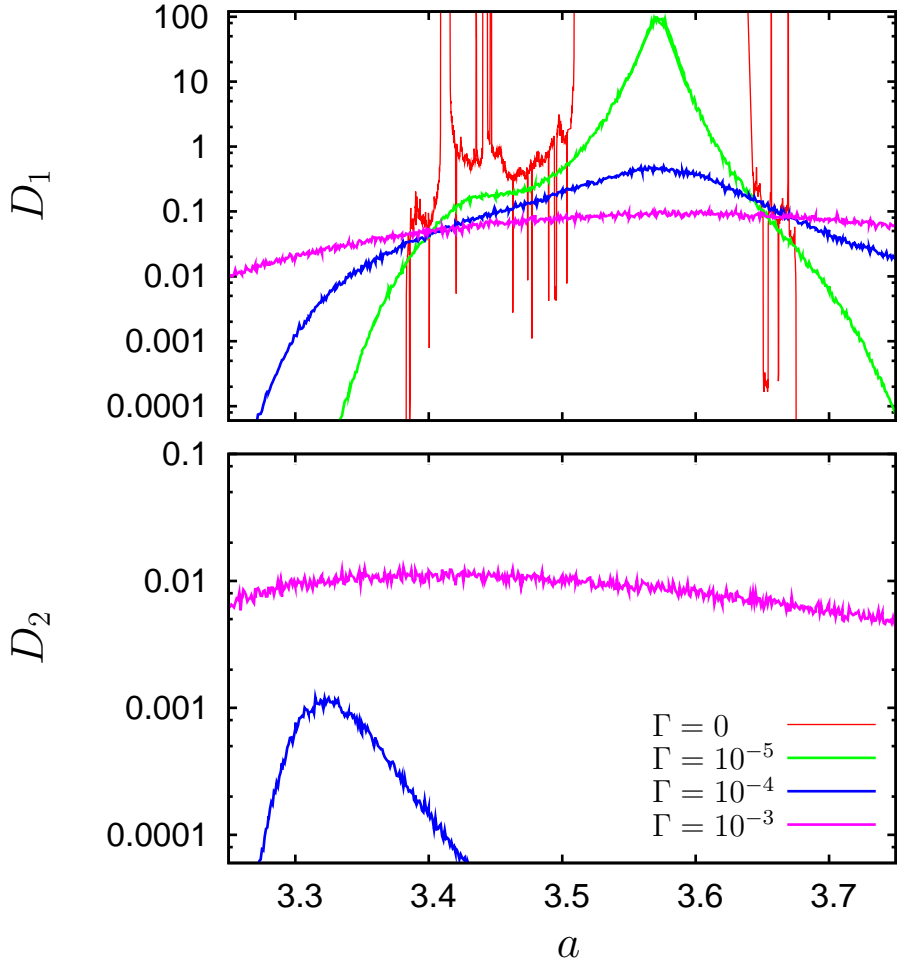


Figure 4.9: Diffusion coefficients D_1 and D_2 as defined in (4.32) for the dynamics (4.9) with $\vec{F} = 0$, $\alpha = 45^\circ$, $\Omega = 4$ and various Γ as indicated in the legend. The diffusion coefficients have been obtained from a sample of 500 trajectories of length 5000 drive periods each. The plotting range has been restricted since smaller values of $D_{1/2}$ are not correctly obtained from our sample size, and the divergence of the red line has been cut off. In particular, $D_{1/2} = 0$ unless the curve obviously leaves the plotting area for larger values. The (larger) wiggles of the $\Gamma = 0$ curve are due to periodic windows, as discussed in the text, but of no further relevance, and the small wiggles of all curves are due to the statistical uncertainty due to our limited sample. $\vartheta_D = 45^\circ$, as defined in (4.32), within the precision of our data for all parameters considered.

has consequences for the diffusion matrix

$$\mathbf{D} = \lim_{t \rightarrow \infty} \frac{1}{2t} \begin{pmatrix} \langle (x(t) - x(0))^2 \rangle & \langle (x(t) - x(0))(y(t) - y(0)) \rangle \\ \langle (x(t) - x(0))(y(t) - y(0)) \rangle & \langle (y(t) - y(0))^2 \rangle \end{pmatrix} \quad (4.31)$$

$$= \mathbf{O}_{\vartheta_D} \begin{pmatrix} D_1 & 0 \\ 0 & D_2 \end{pmatrix} \mathbf{O}_{-\vartheta_D} \quad (4.32)$$

of the S_0 symmetric dynamics with the rotation matrix $\mathbf{O}_{\vartheta_D} = \begin{pmatrix} \cos(\vartheta_D) & -\sin(\vartheta_D) \\ \sin(\vartheta_D) & \cos(\vartheta_D) \end{pmatrix}$, the diffusion coefficients (eigenvalues) $D_1 > D_2$ and the main diffusion direction ϑ_D being the direction of the eigenvector of \mathbf{D} to the eigenvalue D_1 . If the diffusion coefficients are different, there is a *direction of strong diffusion*, and diffusion is *anisotropic*. SSBT corresponds to ballistic directed transport. Thus, at $\Gamma = 0$, the main diffusion direction will be the direction of SSBT and $D_1 = \infty$ (also at $\alpha \neq 45^\circ$). Due to S_{xy} symmetry, the diffusion matrix has to be invariant under \hat{S}_{xy} , and thus $\vartheta_D \in \{45^\circ, 135^\circ, 225^\circ, 315^\circ\}$, where the latter two orientations are equivalent to the former two. At the borders (in parameter space) of SSBT there is an algebraic divergence of the diffusion coefficient related to crisis induced intermittency [123–126, 146, 253–255] leading to deterministic diffusion, which has been studied extensively for one dimensional maps as model systems [130, 131, 133, 134, 256–258], note in particular [131] discussing a very similar scenario for the creation of SSBT in the climbing sine map. Deterministic diffusion in continuous dynamical systems is discussed in particular with respect to Josephson junctions in [132, 133, 135–137] and the Hamiltonian case is discussed in, e.g. [259–262]. The critical exponents of the escape times of the intermittent chaotic repellers are expected to be $\pm \frac{1}{2}$ depending on the scenario considered [135], from which the scaling of the diffusion coefficient follows [126]. In the presence of (weak) noise, the eigenvalues of \mathbf{D} are always finite, but the divergence can still be observed as a sharp increase of the diffusion coefficient for sufficiently small noise strengths. For arbitrarily large noise strengths, diffusion is isotropic since the potential can be neglected. Therefore, the expected effect of noise on SSBT dominated deterministic diffusion is that the larger diffusion coefficient shrinks and that the smaller diffusion coefficient grows but, due to the complexity of the dynamics, deviations from this behavior can be expected.

Figure 4.9 summarizes the (unbiased) diffusion properties of the dynamics (4.9) at $\alpha = 45^\circ$ and $\Omega = 4$. For all parameter values considered, we have found $\vartheta_D = 45^\circ$ within the precision of our data, and the \tilde{x} direction is always the main diffusion direction. We consider $\Gamma = 0$ first, i.e. the red curve in the upper panel of figure 4.9. Due to the invariant manifolds W_n , we have $D_2 = 0$ and $\vartheta = 45^\circ$ strictly. There is no diffusion outside the region of existence of the unbounded diffusive chaotic object behind SSBT, starting at $a \approx 3.38$ and ending at $a \approx 3.67$. In the parameter range of the unbounded diffusive chaotic attractor, D_1 takes a non-zero and finite value (deterministic diffusion) and varies continuously (with a) except at bifurcations. At the borders of each SSBT periodic window of the attractor, there is a power law divergence of D_1 , and $D_1 = 0$ in periodic windows of bounded attractors [132, 133, 135–137]. Diffusion is highly anisotropic when D_1 is large. For small, but non-zero, noise strengths Γ , both diffusion coefficients are always finite, non-zero, and loosely follow their deterministic values except around the bifurcations and divergences, but D_2 remains unmeasurably small for $\Gamma < 10^{-4}$ (and our sample size). Moreover, the onset of diffusion (i.e. non-zero values of D_1 in the

upper panel of figure 4.9) is shifted away from the chaotic crises creating the unbounded attractor, leading to diffusion outside the parameter region of deterministic diffusion. For larger noise strengths, the deterministic behavior is smoothed out. An interesting feature of the lower panel is the peak of D_2 for $\Gamma = 10^{-4}$ around $a \approx 3.33$. For these a values, the deterministic attractors looks like the attractors shown in figure 4.5(e)-(h), and diffusion orthogonal to the invariant manifolds W_n is particularly effective before the onset of deterministic diffusion parallel to the invariant manifolds W_n at $a \approx 3.38$. At $\Gamma = 0.001$, D_1 remains almost constant throughout the a interval considered but is still quite far from its asymptotic large noise value (of 0.01)³⁵. The diffusion anisotropy can, in principle, be used for separation, e.g. along the lines of [105, 106, 185, 220].

4.11.2 Absolute negative mobility

A second remarkable consequence of SSBT is that due to the presence of SSBT, the dynamics already have some (here two) “preferential” directions, namely the transport directions of the pair of SSBT attractors. The introduction of another “preferential” direction into the dynamics, in the simplest case by adding a constant bias force $\vec{F} = F\vec{e}_\phi$, $F \geq 0$, leads to a “competition” of all the “preferential” directions. Here, we consider only $\phi = 45^\circ$ or $\phi = 225^\circ$, i.e. a perturbation which breaks S_0 but leaves S_{xy} intact. Thus, the invariant manifolds W_n remain, and, without noise, transport remains restricted to the transporting channels.

The result of the “competition” between the SSBT attractors and the bias force is not clear unless one of the competing directions dominates in an obvious manner, e.g. if the bias force is large. *The direction of transport is decoupled from the direction implied by symmetry breaking perturbations because of SSBT.* This applies also to other perturbations than a constant bias force, e.g. to ratchet potentials or an asymmetry of the periodic drive if considered as a symmetry breaking perturbation, see [92–95] for a hint in that direction. The consequence may be transport against the bias force and is called *absolute negative mobility* (ANM) [10, 11, 51].

While there is no general rule stating which SSBT attractor will survive a constant bias force, an intuitive argument was given in [1, 2] and section 3.4 using that the work done by the bias force can be compensated for by a change of the work done by the dissipation. The intuitive argument can be applied to the overdamped dynamics (4.9). First, we have absorbed the friction coefficient η of the dynamics (4.1) into the time unit to get the dynamics (4.9). Thus, multiplying η in (4.1) by some factor is the same as to multiply the frequency Ω in (4.9) by the same factor, and we can replace the label of the horizontal axis in figure 4.12 by η and use the argument from section 3.4. Second, a change of the drive frequency has the same effect on the relevant work contribution as a change of the friction coefficient for a phase-locked trajectory, cf. (3.2), because the average velocity increases when the frequency is increased.

Thus, *to increase the constant bias force $F\vec{e}_{45^\circ}$ can be compensated for by a decrease of the frequency Ω for a phase-locked attractor transporting against the bias force, and an increase of Ω for its symmetry partner.* When a bias force $F\vec{e}_{45^\circ}$ is applied to the dynamics (4.9), the parameter regions of the attractors transporting against the bias force should move towards smaller frequencies, and those of their symmetry partners should

³⁵ $D_1 \approx \Gamma$ is reached around $\Gamma = 1$ for the parameters considered.

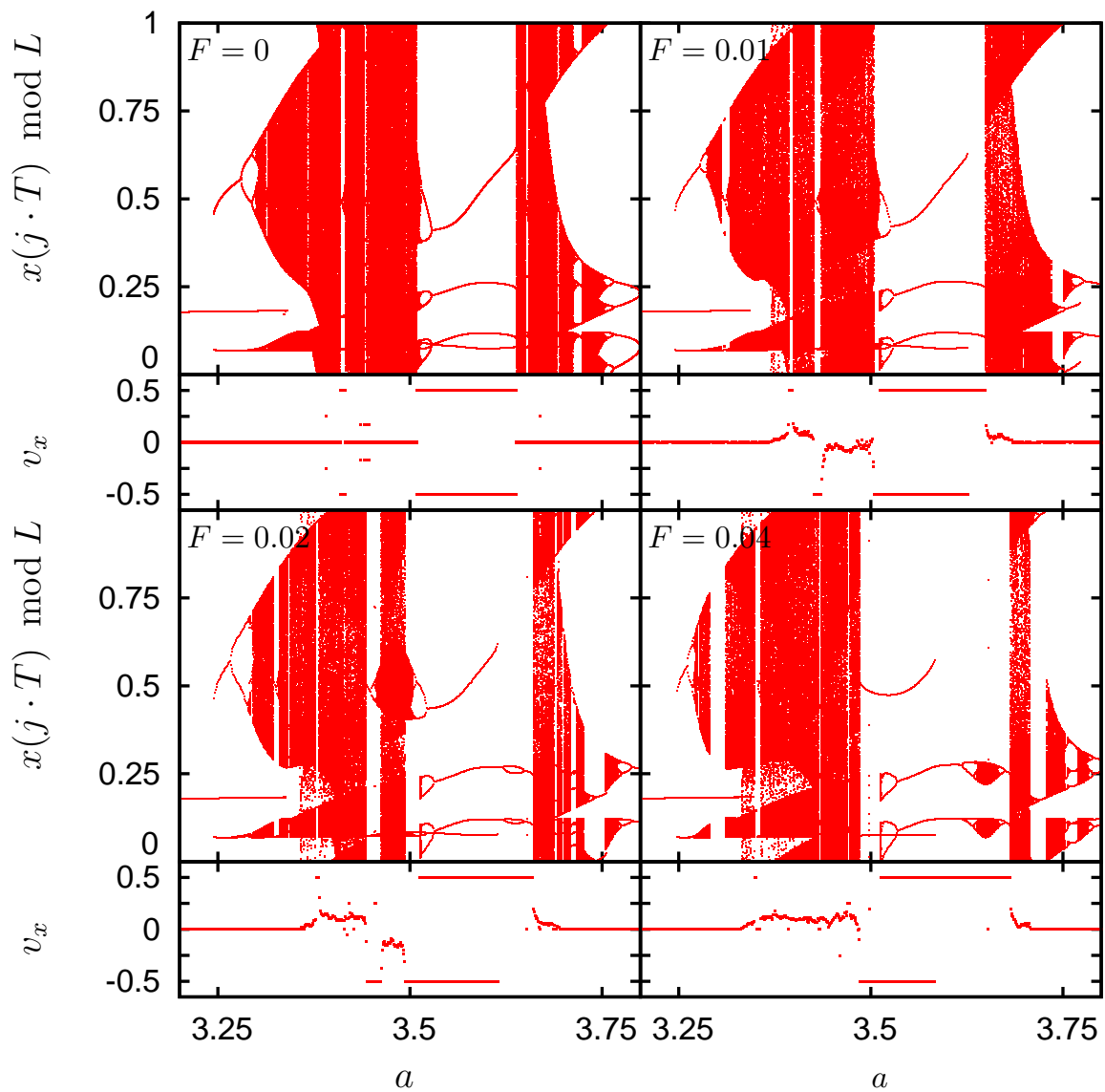


Figure 4.10: Bifurcation diagram, calculated for the same parameters and dynamics and drawn along the same lines as figure 4.7. Only the values of the bias force $\vec{F} = F\vec{e}_x$ are different, as indicated in the panels.

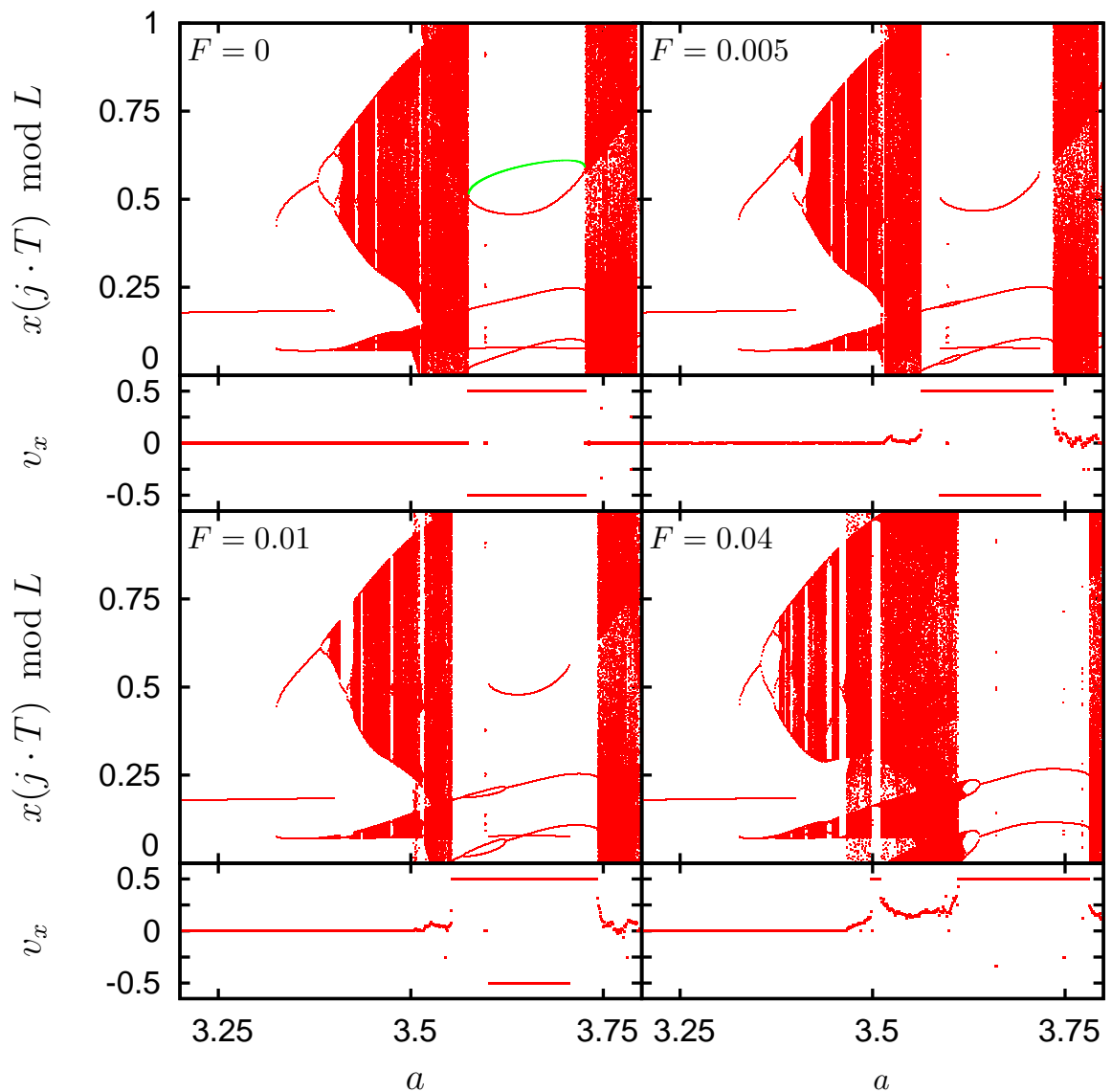


Figure 4.11: Bifurcation diagram at $\Omega = 4.5$, various $\vec{F} = F\vec{e}_x$ as indicated in the panels, and otherwise calculated for the same dynamics and parameters and drawn along the same lines as figure 4.7.

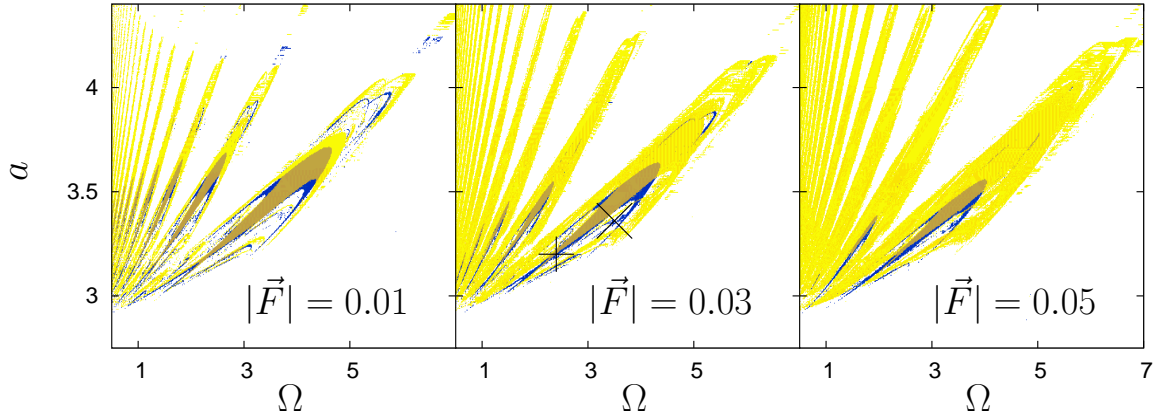


Figure 4.12: Phase diagram for the deterministic $\Gamma = 0$ dynamics (4.9) and \vec{F} as indicated in the panels. Shown are regions of parameter space in which spontaneous symmetry breaking nondiffusive transporting attractors are found. Their transport direction is shown by colors. Yellow corresponds to $\vartheta = 45^\circ$ and blue to $\vartheta = 225^\circ$. Coexistence of both transport directions is shown by shading, yielding ochre. White regions contain no (found) no phase-locked attractors. Note that due to $\alpha = 45^\circ$, only $\vartheta = 45^\circ$ and $\vartheta = 225^\circ$ are possible.

move towards larger frequencies. Simultaneously, the parameter regions of attractors transporting in the direction of the bias force should grow since, for very large bias forces, only these should survive, and the parameter regions of attractors transporting against the bias force should shrink. If the parameter regions of the pair of SSBT attractors has a border towards smaller Ω at $F = 0$, the attractor transporting against the bias force is expected to move into that “empty” region when the force is switched on and to be the only one stable of the two attractors in that region for $F > 0$. Hence, we expect to find ANM at these borders. This is the case for the large frequency parts of the SSBT tongues shown in figure 4.12 but not for their small frequency parts. In addition to this movement of the parameter regions in the Ω direction (of parameter space) when the bias force is switched on, the parameter regions of attractors transporting in the direction of the bias force move “quickly” towards larger drive amplitudes a , and the parameter regions of attractors transporting against the bias force move towards smaller a . The work contribution of the periodic drive to the energy balance of phase-locked (periodic) transporting solutions, upon which our intuitive argument relies, is not unidirectional [110], and we are unable to extend our argument to the drive amplitude a ³⁶. In fact, this very “fast” movement³⁷ of the regions of existence in the a direction (of parameter space) seems to be special to $\alpha = 45^\circ$, and if $\alpha \neq 45^\circ$ the movement in the a direction is much “slower”, cf. figure 4.18, and the same is true for the dynamics considered in chapter 6.

Another argument as to where ANM can be expected to occur in figure 4.12 can be obtained from the analogy of the tongue structure of figure 4.4 with the Bessel function Shapiro steps observed in [1–3, 157] (see section 4.9.3). At the borders of the regions of

³⁶This would be possible by taking into account the specific shape of the transporting solutions, but this would be highly specific to the situation considered here.

³⁷In that context, slow and fast are to be interpreted as the speed at which the parameter regions move when F is increased, i.e. is interpreted as the “time” variable of that movement.

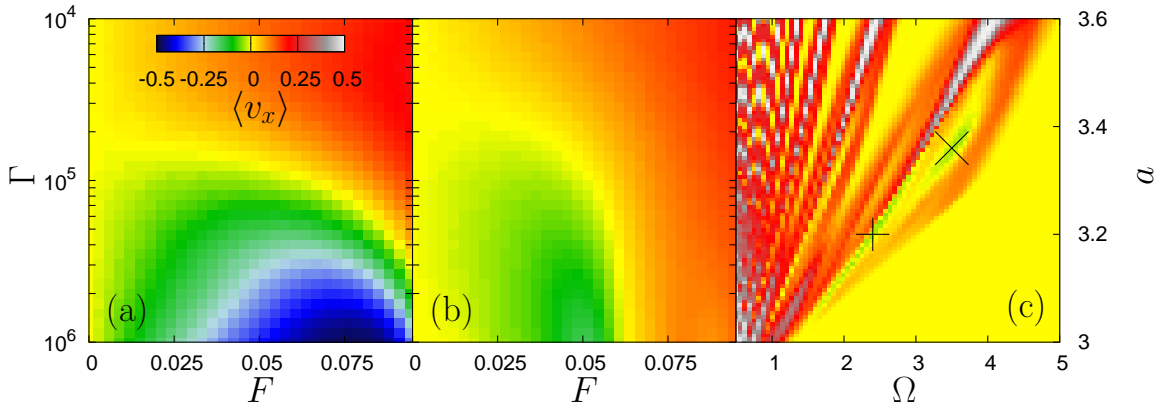


Figure 4.13: Average transport velocity, encoded in colors according to the legend shown in (a). The same dynamics are considered as in figure 4.12, but (a) $\Omega = 2.4$ and $a = 3.2$ (corresponding to the $+$ in right panel), (b) $\Omega = 3.5$ and $a = 3.36$ (corresponding to the \times in the right panel), and (c) $\vec{F} = 0.03\vec{e}_{45^\circ}$ and $\Gamma = 10^{-5}$. The averages have been computed from 50 trajectories of length $10000T$ numerically calculated with a step size $h = 0.01 \approx 0.004T$ in the second order stochastic Runge-Kutta scheme, see section 4.25.7 for more details. All numerically obtained averages over the solutions of SDE's are calculated with the same method and similar parameters in the following.

existence of the Shapiro steps (tongues of SSBT attractors) given by the Bessel function approximation, the approximation excludes ANM, cf. (3.5). When the frequency is decreased, the Bessel function structure of the Shapiro step is destroyed, and the Shapiro steps undergoes a period doubling instability first at its center [137]. There is a hint [3, 157] that ANM occurs at this instability. The large frequency part of each tongue in figure 4.4(a) and figure 4.12 corresponds to the remnants of the Bessel function Shapiro step, as was argued in section 4.9.3. At $\Omega = 4.5$, the tongue (Shapiro step) has no instability in its center, and there is no deterministic ANM, cf. figure 4.11. Conversely, at $\Omega = 4$ the tongue (Shapiro step) is terminated $a \approx 3.51$ by a chaotic crisis, and reappears at $a \approx 3.41$ by the same mechanism. At both chaotic crises, ANM is found for $F > 0$, cf. figure 4.10.

We now turn to the effect of thermal noise, i.e. $\Gamma > 0$, on SSBT induced ANM. Thermal noise smoothes out the deterministic SSBT and suppresses ANM [1, 2]. Nonetheless, the interplay of noise, SSBT attractors and other attractors may lead to some quite interesting phenomena [1, 2, 63] where noise even seems to induce ANM at first glance [63], though the mechanism behind ANM is deterministic [2]. Given the right choice of parameters, both variants of noise induced ANM, cf. Fig. 3 of [63] and Fig. 15 of [2], will occur here as well. Therefore, we do not show these phenomena explicitly, but restrict ourselves to a brief analysis of the noise resistivity of ANM as encountered here. Figure 4.13 shows a summary of our findings. The numerical method used to solve the SDE (4.9) is due to [181] and described in section 4.25.7.

Panel (c) shows the results of our simulation with a noise strength of $\Gamma = 10^{-5}$ and $|F| = 0.03$ corresponding otherwise to the $\Gamma = 0$ case shown in the middle panel of figure 4.12. ANM (i.e. blue areas) can only be found at some of the places which figure 4.12 suggests, most notably at the lower (with respect to a) edge of the stable part of

the largest SSBT attractor (indicated by a '+' in panel (c)), but also in the diffusively chaotic regime close to the top end of the tongue-shaped region of existence of the SSBT attractor, marked with a '×' in panel (c).

At the noise strength considered here, the effectiveness of deterministic ANM is very low. The noise induced escape time from attractors (and thus their statistical weight upon averaging) scales like $\sim e^{V_A/\Gamma}$ for small noise strengths [1, 2, 137, 137, 141–143, 143–145, 243, 243, 263, 264]. If the noise strength Γ and the pseudopotential depth V_A are of similar magnitude, noise induced escape from the attractor occurs within a few drive periods, and the attractor no longer contributes significantly to the average velocity. The results is that not all “blue” regions from figure 4.12 show up in figure 4.13(c). For the two representative choices of parameters indicated in figure 4.13(c), a more detailed analysis of the effects of noise and bias force on ANM is presented in figure 4.13(a) ('+') and figure 4.13(b) ('×').

At the parameters considered in panel (a) of figure 4.13, ANM is induced by the periodic attractor carrying transport against the bias force. At low noise strengths Γ , the average velocity is significantly larger than if ANM is due to a diffusive chaotic attractor as considered in figure 4.13(b), and ANM survives for larger bias forces. In both cases, the noise strength at which ANM vanishes is comparable. The larger current at low noise strengths in figure 4.13(a) is due to the fact that transport is more effective. Trajectories in this regime mostly consist of parts closely resembling trajectories on the SSBT attractor responsible for ANM interrupted by short bursts into other regions of phase space. These bursts are suppressed exponentially as $\Gamma \rightarrow 0$. In contrast, trajectories in the diffusive chaotic regime close to the regions of existence of SSBT attractors spent most of their time on the chaotic repellers due to the (unstable) SSBT attractors and switch intermittently between them [1, 2, 126, 253, 256]. The parts carrying transport against the direction of the force are due to the remnant of the SSBT attractor transporting against the bias force, i.e. the ANM attractor, and have a similar, but not necessarily identical [2], average velocity as trajectories on the attractor. Most parts of the trajectory not on the repeller due to the ANM attractor carry transport in the direction of the bias force and reduce the effectiveness of transport.

In conclusion, ANM is sustained up to noise strengths of order $\Gamma \approx 10^{-5}$ and bias forces of order $F \approx 10^{-1}$. Typical pseudopotential depths of SSBT attractors carrying transport against the bias force will be of the same magnitude, i.e. of order 10^{-5} [1, 2]. Thus, noise resistivity is about 2-3 orders of magnitude lower compared to [1, 2]. Part of this can be attributed to the fact that the potential barrier separating adjacent potential minima considered here is about $\frac{1}{4}$ as that considered in [1, 2]. Second, trajectories get rather close to the invariant manifolds W_n and thus to their S_{xy} symmetry partners living on the other side of W_n . This may lead to a low pseudopotential depth. For smooth drive protocols this effect is even more pronounced, as discussed section 4.3. This is lifted for $\alpha \neq 45^\circ$, and as we will see in section 4.19, the noise resistivity will be larger by an order of magnitude then.

4.12 Breaking S_{xy} Symmetry

As of yet, we have considered the drive to be such that (4.9) is S_{xy} symmetric. The chief reason for doing so was the simplicity due to the main consequence of S_{xy} symmetry:

the transport direction is fixed up to its sign. This makes the discussion of SSBT and its creation clearer because there are fewer “independent”, i.e. not related by symmetry, objects in phase space (attractors, repellers etc.) to be considered.

As has been noted above, it is conceivable that the symmetry leads to a lower noise resistivity (lower pseudopotential depth) of SSBT attractors. Moreover, the restriction of the transport direction allows no new effects beyond those possible in the dynamics considered in [1, 2, 63] to be found except for anisotropic diffusion. Rather, our findings so far strengthen the claim of [1, 2] that a three dimensional phase space, S_0 symmetry, and chaos are the main ingredients for SSBT induced ANM. With respect to a single particle in a periodic potential driven out of equilibrium by a deterministic driving force, we have now covered the two main classes of systems by rather generic and minimal examples.

We now turn break S_{xy} by letting $\alpha \neq 45^\circ$ to find “new” effects which are not possible in one spatial dimension. The particle may now travel into *any* direction on the surface. Our main object is to control the transport properties of the particle. This has now become more fruitful, as any direction is available, but also more complicated for the same reason.

By setting ϕ into some direction with a sufficiently large force, one can direct the particle into any desired direction. But our archetypical application is to sort different species of particles. With just a constant force in some direction, it is natural to expect all different species of particles experiencing that force to be transported into a similar direction. This is just what happens and in geometries such as considered here, the deflection angle, i.e. the angle between the transport direction of the particle and the bias force, is restricted to be smaller than 45° [18–20]. Similarly, the angle between the transport directions of different particle species is restricted. For a notable exception for *extended* objects with an internal structure see [5] and chapter 7. Our goal is to be able to steer the particle into any direction without “rotating” any inherent direction of the dynamics, coined *directing Brownian motion* in [4].

4.13 Choice of parameters

Parameter space has more dimensions now, as neither α nor ϕ are fixed any more. From figure 4.4 it is apparent that the choice of the drive frequency Ω does not affect the appearance of SSBT significantly as long as the frequency is not too high: there is always a matching drive amplitude a for which a SSBT attractor can be found. We choose $\Omega = 4$ fixed at first and vary only the drive amplitude a . In the S_0 symmetric case $\vec{F} = F\vec{e}_\phi = 0$, the remaining parameter is α , while in the case with the bias force, F and ϕ come into play. The primary role of the bias force is to break S_0 symmetry. For bias forces of sufficiently small absolute value F , the response of the system will be linear in the force for almost all parameters³⁸. Thus, we restrict ourselves to a few appropriately chosen directions of the bias force in the following. The most interesting directions of bias force seem to be

³⁸This is no contradiction to the nonlinearity of the dynamics. In particular, with noise, there are no nonanalyticities in the average velocity as a function of any parameter, and we can Taylor expand. The Jacobian of the average velocity as a function of the bias force is called the mobility tensor. Effectively, we will estimate this Jacobian.

1. the coordinate axes: $\phi = 0^\circ, 90^\circ$
2. the bisectrix: $\phi = 45^\circ$
3. the direction of the periodic drive: $\phi = \alpha$.

The latter case may be particularly important in systems where both bias forces are generated from the same source. While changing the absolute value of the bias force may lead to remarkable results [1, 2], here we will focus on the regime of small bias forces.

4.14 Transition from $\alpha = 45^\circ$ at fixed frequency

We consider the case of $\vec{F} = 0$ and $\Omega = 4$ as noted above. We first choose a fixed drive amplitude $a = 3.55$ which lies near the center of the main periodic SSBT window found in figure 4.7 at $\alpha = 45^\circ$. With all other parameters fixed, we lift S_{xy} symmetry by varying the direction of the periodic drive α and obtain figure 4.14: the SSBT attractors “survive” up to $\alpha \approx 45.3^\circ$. Then, the unbounded chaotic attractor reappears followed by another smaller periodic SSBT window at $\alpha \approx 45.4^\circ$. Even though the symmetry itself is no longer in effect, the periodic windows visible in figure 4.14 still satisfy the transport restriction imposed by S_{xy} symmetry, i.e. $v_x = v_y$. The same applies to diffusion on the unbounded chaotic attractor which replaces the periodic windows after they terminate in boundary crises. I.e. while trajectories may cross the lines W_n ³⁹, no net transport results for the unbounded chaotic attractor. This may be astonishing at first glance, but the chaotic attractor can only carry transport across the line W_n once a connection via the unstable manifold of some unstable periodic orbit part of the attractor (or a more complex combination thereof) crossing the former invariant manifold of the dynamics and connecting to the copy of the attractor⁴⁰ on the other side of the former invariant manifold of the dynamics is formed. Apparently, for the unstable periodic orbits forming the backbone of the chaotic attractor, this does not happen for the parameters considered here⁴¹.

At $\alpha \approx 45.57$, the unbounded chaotic attractor suddenly shrinks (indicated by the arrow in figure 4.14) and undergoes a backwards-oriented attractor merging crises (i.e. an attractor “separation” crisis). Apart from the lifted \tilde{S}_{xy} symmetry and the direction with respect to the bifurcation parameter, this is the “same” bifurcation as the bifurcation/crisis (b_5) in figure 4.8 in the following sense. In figure 4.8(b_5), the bounded attractor \mathcal{A} collides with the attractor $\tilde{\mathcal{A}} = \tilde{S}_{xy}\mathcal{A}$, such that trajectories initiated on \mathcal{A} can reach $\tilde{\mathcal{A}}$, i.e. \mathcal{A} is “connected” to $\tilde{\mathcal{A}}$. Simultaneously, $\tilde{\mathcal{A}}$ collides with the attractor $\tilde{S}_{xy}\mathcal{A}$, but that

³⁹Until now, these lines were called “invariant manifolds” W_n , (4.20). But for $\alpha \neq 45^\circ$, they are no longer invariant.

⁴⁰Again, a more complex scenario involving other transient objects in phase space is possible.

⁴¹Note that the unstable periodic orbit oscillating around the potential minimum crosses the lines W_n for any $\alpha \neq 45^\circ$. For $\alpha = 45^\circ$, the lines W_n constitute its inset (stable manifolds). Therefore, it cannot be part of the chaotic attractor in that case. But if it does not lie in the phase space region occupied by the chaotic attractor, no net transport across the former invariant manifold of the dynamics results for the chaotic attractor. The situation where, for some reason, this orbit is part of the chaotic attractor in the sense that the outset of one of the unstable periodic orbits of the chaotic attractor touches the inset of this orbit seems to be highly exceptional, and more importantly structurally unstable, e.g. of weight 0 in parameter space.

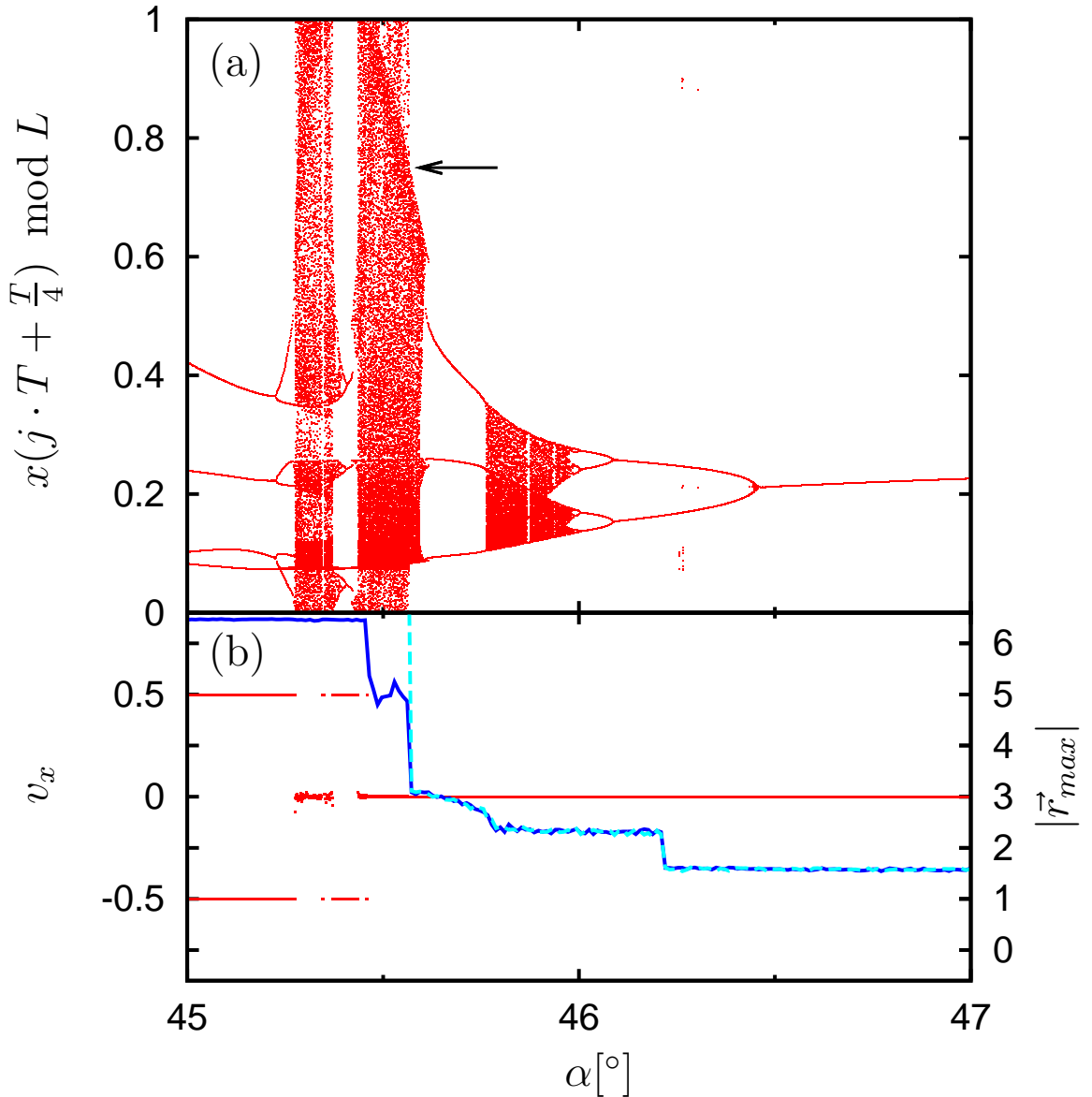


Figure 4.14: (a) Bifurcation diagram as in figure 4.6 with α as bifurcation parameter and fixed $\Omega = 4$, $a = 3.55$ and $F = 0$. While $\alpha \neq 45^\circ$ breaks S_{xy} symmetry, we have found only attractors for which $v_x = v_y$, and thus it is sufficient to show only the v_x component of the average velocity in panel (b), in units of the unrotated coordinate frame. Additionally, in panel (b) the maximum transient length (4.33) is shown (right scale) for $n = 6$ (solid blue line) and $n = 20$ (dashed cyan line) and 5000 random initial seeds have been used to approximate the maximum in (4.33). Please note that we show $|\vec{r}_{max}|(n)$ in units of the rotated coordinate frame. This incurs a stretching by a factor of $\sqrt{2}$, compared to the original coordinate frame.

attractor is the copy of \mathcal{A} in the next elementary cell due to (4.30), and an unbounded attractor is formed⁴². If \tilde{S}_{xy} symmetry is lifted by a small perturbation, the two crises in figure 4.8(b₅) no longer occur simultaneously. Therefore, when α is increased from 45° in figure 4.14, one of the above discussed connections is lifted first, and that happens at $\alpha \approx 45.57$. The second connection is lifted “later”, at $\alpha \approx 46.1^\circ$ but that is not visible from the upper panel of figure 4.14, since that panel shows only attractors.

To that end, we consider the *maximum transient length*

$$|\vec{r}_{max}|(n) = \max_{\vec{r}_0, \vec{r}(t_0) = \vec{r}_0} |\vec{r}(nT) - \vec{r}(t_0)|, n \text{ integer} \quad (4.33)$$

where $\vec{r}(t)$ is the trajectory passing through \vec{r}_0 at time t_0 . $|\vec{r}_{max}|(n)$ measures the maximum Euclidean distance any trajectory can cover in the given time $n \cdot T$. Ideally, we would consider $|\vec{r}_{max}| = \lim_{n \rightarrow \infty} |\vec{r}_{max}|(n)$ if the limit exists (see below). Then, if there is a transporting periodic orbit or an unbounded attractor or repeller, $|\vec{r}_{max}| = \infty$, and the speed of the divergence depends on the average velocity of transporting attractors or on the properties of the unbounded attractor. Conversely, if there is only a bounded period 1 attractor, or a bounded attractor on which the dynamics are ergodic, $|\vec{r}_{max}|$ will be the largest possible Euclidean distance of any point on the attractor to any point on the basin boundary. If there is more than one attractor, $|\vec{r}_{max}|$ will take the largest possible value for all attractors. If there is an attractor on which the dynamics are different, e.g. a periodic orbit of higher periodicity, $|\vec{r}_{max}|(n)$ may fail to converge for $n \rightarrow \infty$. Numerically, we will choose a fixed n , and will not observe that effect. Furthermore, if the starting time is varied, the shape of the attractors and their basins of attraction changes, affecting $|\vec{r}_{max}|(n)$, but we avoid this in our numerics by always setting $t_0 = 0$. We have found $|\vec{r}_{max}|$ to be well approximated by $|\vec{r}_{max}|(n)$ for $n \geq 6$, unless unbounded objects/attractors are present, cf. figure 4.14. Whenever $|\vec{r}_{max}|$, thus obtained, changes abruptly we expect a qualitative change of the dynamics, i.e. a bifurcation, but it is clear that not all bifurcations can be found that way. One possible way to gain further insight using the same calculation is to replace $\vec{r}(nT) - \vec{r}(t_0)$ in (4.33) by a suitable scalar product, e.g. $\vec{e}_x \cdot (\vec{r}(nT) - \vec{r}(t_0))$, which is shown in figure 4.43 for $\vec{e}_{\tilde{x}}$, $\vec{e}_{\tilde{y}}$, \vec{e}_x and \vec{e}_y .

The crises of \mathcal{A} and $\tilde{\mathcal{A}}$ discussed above should be observable as discontinuous changes of $|\vec{r}_{max}|$, unless another phase space structure leads to a larger transient length. The maximum transient length $|\vec{r}_{max}|(n)$, calculated for two different n , is shown in the lower panel of figure 4.14. The crisis at $\alpha \approx 45.57$ is observable as a sharp decrease of $|\vec{r}_{max}|$. Then, $|\vec{r}_{max}|$ varies smoothly due to the deformation of the attractor, which is of no interest to us, and at $\alpha \approx 46.1^\circ$ $|\vec{r}_{max}|$ decreases sharply due to the second crisis discussed above or, rather, due to the rearrangement of the involved periodic orbits and their invariant manifolds.

This claim is further supported by figure 4.15(a). We now consider the a - α plane of parameter space at fixed frequency $\Omega = 4$ and show $|\vec{r}_{max}|$. The region of existence of unbounded attractors are red in figure 4.15(a), corresponding to large maximum transient lengths which we have cut off at 3 length units of the rotated coordinate frame. The regions of existence of the unbounded attractors behind SSBT at $\alpha = 45^\circ$ correspond the triangular red region in figure 4.15(a) that contains the '◊', i.e. around $\alpha = 45^\circ$

⁴²Due to \tilde{S}_0 symmetry, even more crises occur at the same time, as discussed in section 4.10, but these are not important here.

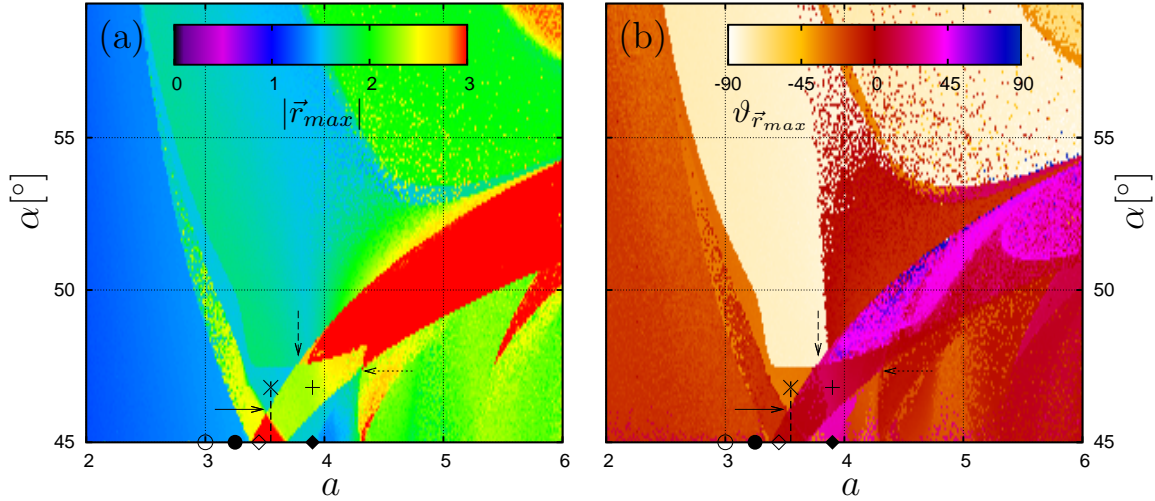


Figure 4.15: (a) Maximum transient length (4.33) for $n = 12$ and 5000 random initial seeds, cf. figure 4.14, for the same dynamics as considered in figure 4.14. $|\vec{r}_{max}|$ is encoded in colors, and the color palette has been cut off after 3 length units in the rotated coordinate frame. (b) The angle enclosed by the vector \vec{r}_{max} , corresponding to $|\vec{r}_{max}|$ in (a), and the \tilde{x} axis, encoded in colors. Due to S_0 symmetry, only a half circle of directions is shown and coexistence with transients of the opposite direction (i.e. other half of the circle) tacitly assumed. Note that we have shown the angle with respect to the rotated coordinate frame for ease of comparison. In both panels, the symbols correspond to the parameters shown in figure 4.35. The dashed line indicates the parameters considered in figure 4.14. A slightly different representation, allowing for further insight is shown in figure 4.43.

and $a = 3.5$. At $\alpha = 45^\circ$, the left (i.e. towards decreasing a) border of the red triangle is the bifurcation/crisis (b_5) in figure 4.8 which splits into two branches of crises upon lifting S_{xy} symmetry, and the right border is analogous. Thus, there are two “arms” with somewhat larger $|\vec{r}_{max}| \gtrsim 2$ projecting out from the sides of the red triangle, and their borders correspond to one of the bifurcations/crises discussed above. The direction of the connection intact within each arm can be best seen from figure 4.43(c)-(d).

Of interest is the right arm towards larger a . We will discuss its properties only briefly, and a more detailed account can be found in section 4.25.4. The right arm of the red triangle meets other lines of jumps of $|\vec{r}_{max}|$ at two points of interest. At $\alpha = 45^\circ$, there is another region of SSBT around $a \approx 4.3$, cf. figure 4.6. It is not well resolved in figure 4.15(a), but the areas of larger $|\vec{r}_{max}| \gtrsim 2$ belonging to it are visible, and their borders are lines of bifurcations analogous to the borders of the arms of the red triangle containing the ‘ \diamond ’. At the first point of interest, marked by the dotted arrow in figure 4.15(a), the lower border of the right arm meets that area of larger $|\vec{r}_{max}|$, and $|\vec{r}_{max}|$ suddenly increases around this point. Since both connections meeting at that point connect regions of phase space which are not separated by any of the lines W_n (n integer), the unbounded object found in that region is unbounded only in the \tilde{x} direction as indicated by $\vartheta_{\vec{r}_{max}} = 0^\circ$ ($\vartheta_{\vec{r}_{max}}$ is the angle enclosed by \vec{r}_{max} and the \tilde{x} axis and shown in panel (b) of figure 4.15). We have found SSBT with transport in the \tilde{x} direction in that parameter region.

At the second point of interest, marked with a dashed arrow in figure 4.15, the upper border of the right arm of the red triangle meets another line where $|\vec{r}_{max}|$ changes sharply. That line can be traced back to $\alpha = 90^\circ$, see figure 4.31, and can be explained as follows. At $\alpha = 90^\circ$ and small a , the particle oscillates around the potential minima on a bounded period 1 orbit. When a is increased, that period 1 orbit interchanges stability with the saddle separating it from its copy in the next elementary cell (in the y direction) in a degenerate pitchfork bifurcation at a critical a value [162, 163]⁴³. When α is decreased from 90° , that degeneracy is lifted and there are two lines of bifurcations similar to the situation encountered at $\alpha = 45^\circ$ discussed above. When one of these lines meets the right arm of the red triangle, $|\vec{r}_{max}|$ increases abruptly, and even more importantly, $\vartheta_{\vec{r}_{max}}$ changes to almost 45° , i.e. \vec{r}_{max} is now in the x direction. We have found SSBT in the x direction in that parameter region. A more detailed account can be found in section 4.25.3 and section 4.25.4.

In summary, we have shown that unbounded attractors at $\alpha \neq 45^\circ$ are, in a sense, a consequence of unbounded attractors at $\alpha = 45^\circ$. When the phase space objects due to which unbounded attractors are found at $\alpha = 45^\circ$ “meet” phase space objects with different symmetry properties, the resulting unbounded attractors are no longer restricted by either symmetry properties.

4.15 SSBT for $\alpha \neq 45^\circ$

4.15.1 Description of color palettes in the phase diagrams

We start with a technical digression. As all transport directions are now possible, the visualization of regions of existence of attractors can no longer show the full information available due to the limitations of printing on paper. We show only the transport direction of the attractors and indicate coexistence of attractors with different transport directions. Even that can lead to very confusing phase diagrams. Therefore, we have chosen parameters such that the phase diagrams are rather clear.

In order to show regions of coexistence of attractors with different transport directions, we use different approaches:

1. Coexisting attractors with opposite transport directions are the most common case due to S_0 symmetry, since we are considering the case of rather small bias forces. We use the colors shown in the color palette in figure 4.16(a) for coexistence of attractors with opposite transport directions.
2. Coexistence of transporting attractors with non-translating attractors is very common at $\vec{F} = 0$. In that case, we show coexistence of a pair of transporting attractors and a non-translating attractor by the same tonality as in the palette in figure 4.16(a) but of a lighter shade.
3. For $F > 0$, all transport directions are possible and shown by the color palette in figure 4.16(b). Coexistence of pairs of attractors with opposite transport directions is assigned the corresponding color from the palette in figure 4.16(a). Most regions

⁴³We have found the same behavior as [162, 163] for the dynamics on the attracting manifold of the dynamics (4.9) for $\alpha = 90^\circ$.

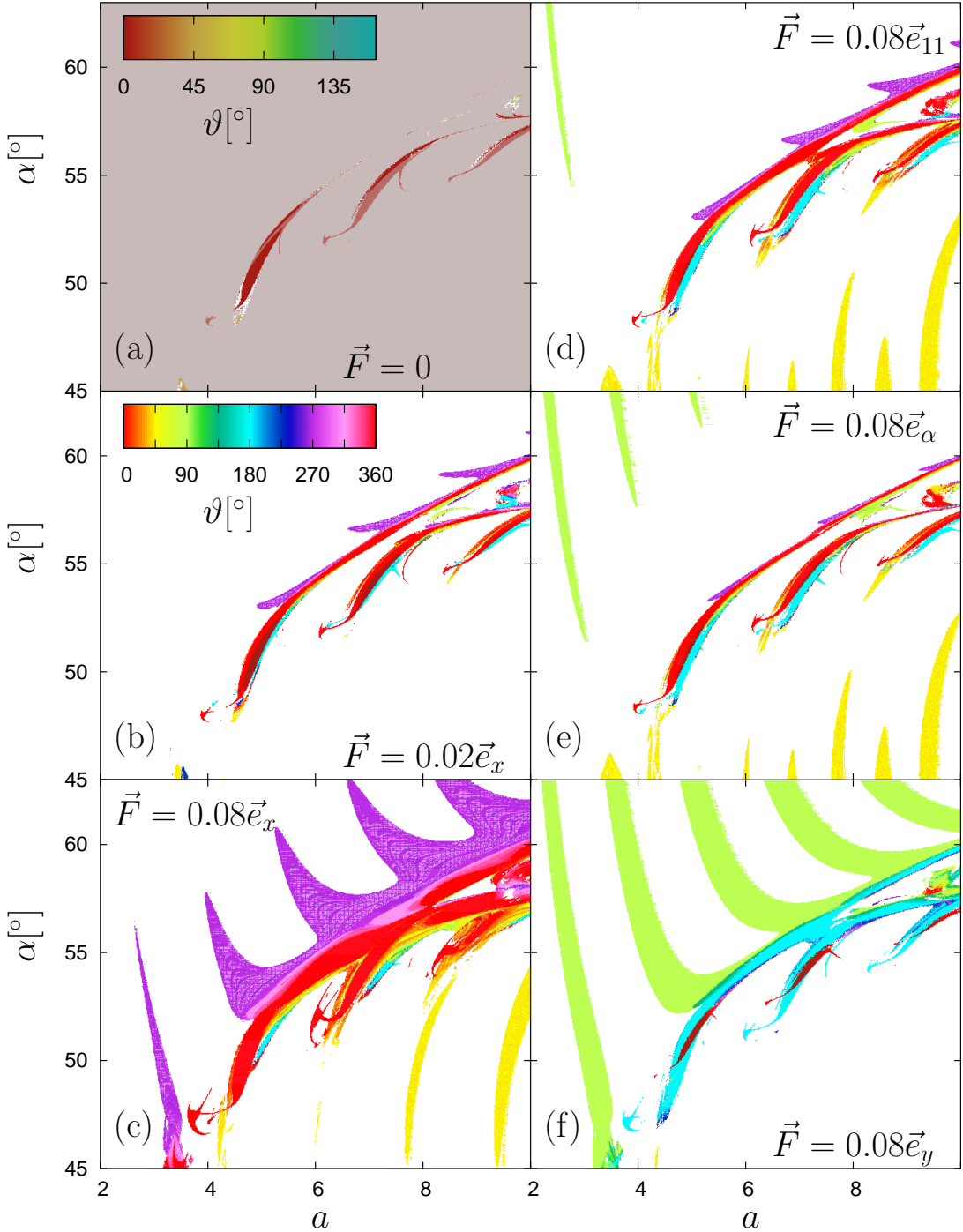


Figure 4.16: Deterministic $\Gamma = 0$ phase diagrams for the dynamics (4.9) with $\Omega = 4$ and \vec{F} as indicated in the panels. As in figure 4.12, only the direction of phase-locked attractors is shown by colors, as indicated by the color palettes. For a detailed description of the palettes and colors, see section 4.15.1. Panels (b)-(f) will be discussed in section 4.16. Some of the attractors visible only in panels (b)-(f) are quasiperiodic, cf. section 4.17. The white specks in their regions of existence are due to their complicated structure not being completely captured by our method of calculating the phase diagrams, cf. section 3.9.1. The same applies to all following deterministic phase diagrams with $\vec{F} \neq 0$.

of existence of non-transporting attractors shrink with $|\vec{F}| > 0$. The phase diagrams become too complicated if non-transporting attractors are shown, and we do not show non-transporting attractors for $\vec{F} \neq 0$. The case of attractors with different, but not anti parallel, transport directions is shown by a checkerboard pattern corresponding to the two transport directions. Due to the high resolution of the figures this pattern blends into a “mix” color to the eye, which is the best we could achieve. This case is extremely rare, as discussed in the text (below).

4.15.2 SSBT in the a - α plane of parameter space at $\vec{F} = 0$

First, consider figure 4.16(a) for $\Omega = 4$ and $\vec{F} = 0$. Shown is the phase diagram, i.e. regions of existence of phase-locked transporting attractors and non-transporting attractors. Since the diagram extends to $\alpha = 45^\circ$ and $\Omega = 4$, it can be compared to figure 4.7, which is a horizontal cut through figure 4.16(a) at $\alpha = 45^\circ$, and also to figure 4.14, which is a vertical cut through figure 4.16(a) at $a = 3.55$.

At $a \approx 3.5$ the SSBT attractors found at $\alpha = 45^\circ$ are recovered and shown in yellow. As discussed in section 4.14, lifting S_{xy} symmetry destroys the attractors, but the phase space structures left behind are involved in the creation of “new” SSBT attractors at $\alpha \gtrsim 48^\circ$. Most of these “new” SSBT attractors carry transport in the $(1,0)$ direction⁴⁴ (exceptions are, e.g., the attractors carrying transport in the $(1,1)$ direction).

Furthermore, transporting windows with transport in the $(0, 1)$ direction are found for e.g. $\alpha \approx 57^\circ$ and $a \approx 8$. Their regions of existence are very small and hard to make out in figure 4.16(a). These attractors are also found for the other values of Ω considered below in figure 4.17 with similar properties. Their existence can be explained from symmetry arguments: at $\alpha = 90^\circ$, transport is restricted to the $(0,1)$ direction due to S_x symmetry (even if there are no transporting attractors in that case). For α approaching 90° , S_x symmetry gradually takes over, leading to transport in the $(0,1)$ direction. Due to their small weight in parameter space, these transporting windows are of no further interest here, and we focus on the large periodic windows with transport in the $(1,0)$ direction. The first begins at $\alpha \approx 49^\circ$ and $a \approx 4.5$ and extends to $\alpha \approx 55^\circ$ and $a \approx 6$ ⁴⁵ but has a maximum width of about $\Delta a \approx 0.25$ in the a direction for fixed α and about $\Delta \alpha \approx 1^\circ$ in the α direction for fixed a . The transporting periodic window appearing already at $\alpha \approx 48^\circ$ and $a \approx 4$ is part of this large window, but the connecting filament is either unstable, beyond the resolution of figure 4.16(a) or exists only for different parameter values⁴⁶. This can be inferred, e.g., from the other transporting periodic windows with larger oscillation amplitude having a stable filament in the corresponding part or from the large window with transport in the direction of the applied bias force in figure 4.16(d).

This transporting periodic window is significantly larger (in parameter space) than the one responsible for SSBT at $\alpha = 45^\circ$. It can be expected to be more robust against random perturbations (such as noise or quenched disorder) and is more interesting to

⁴⁴We refer to the lattice direction by (n,m) , meaning the direction of $n \cdot \vec{e}_x + m \cdot \vec{e}_y$.

⁴⁵A filament of the periodic window extends even further in both directions but with negligible widths in either direction. This filament is due to the periodic orbits forming the window being part of the whole chaotic repeller occupying the portion of phase space outlined in figure 4.15.

⁴⁶I.e. the two parts of the region of existence of the attractor are connected in the full parameter space.

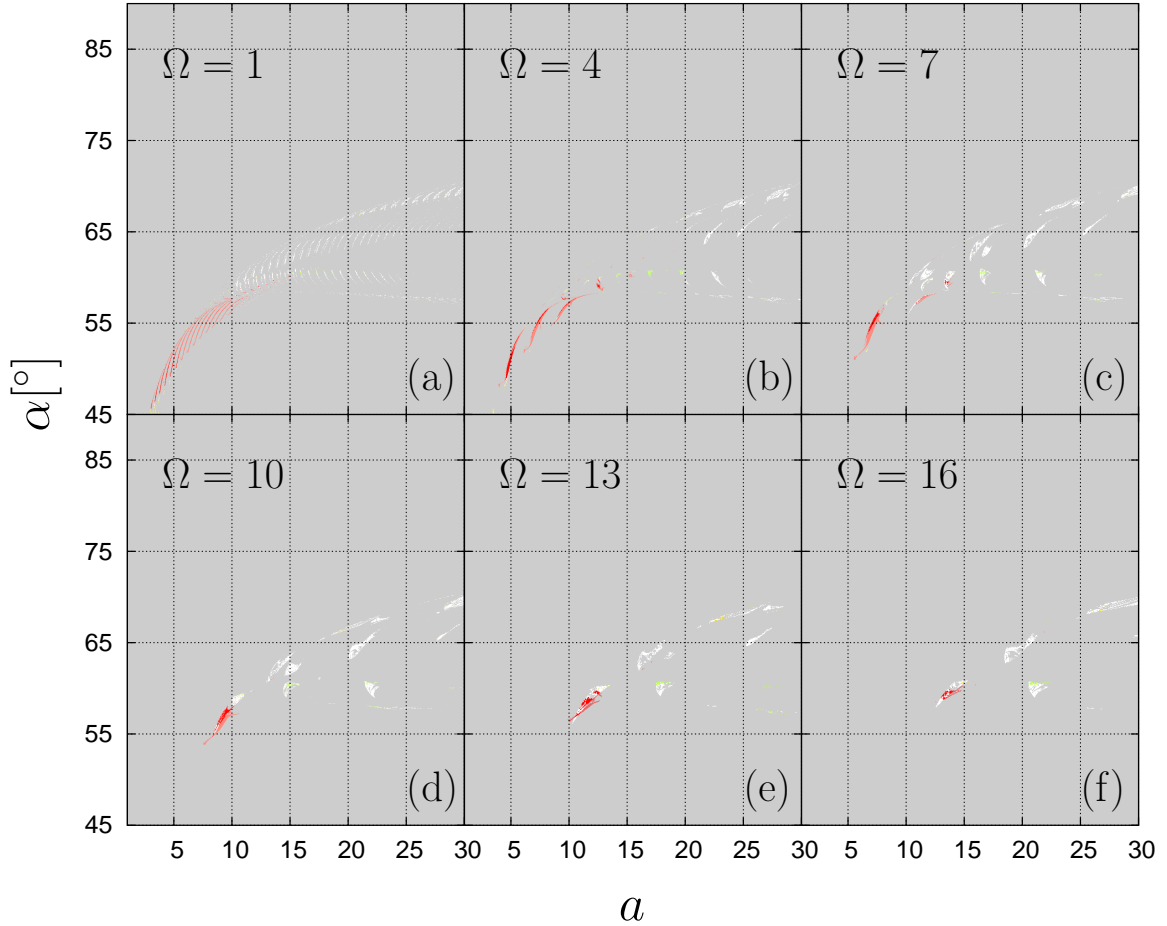


Figure 4.17: a - α plane phase diagrams for various Ω as indicated in the panels and for the same dynamics as in figure 4.16(a). The color palette is the same as used in figure 4.16(a).

study from a practical point of view.

Further copies of this transporting periodic window appear for larger a , and the values of α for which they appear increase for larger a . There are a total of 3 large periodic windows. This repeated occurrence is due to the same locking effect as described in section 4.9.2, see also figure 4.5. As can be seen from figure 4.17(b) further islands of unbounded attractors (corresponding to white regions in figure 4.17(b)) appear after the third large window. Usually, the white regions contain transporting periodic windows, but these windows are beyond the resolution of figure 4.17(b).

In general, the overall size (or weight) in parameter space of the transporting windows decreases with increasing oscillation amplitude of the periodic orbits. I.e. the “first” transporting periodic window seems to be best suited from a practical point of view. This observation is also largely supported by figure 4.17 considering other values of Ω . For larger Ω , the size of the transporting periodic windows largely decreases, especially for the ones with larger oscillation amplitude as can be seen from figure 4.4, where the number of transporting “tongues” encountered by varying a at fixed drive frequency Ω decreases with increasing drive frequency, see also figure 4.18. The islands of diffusive attractors encountered in figure 4.17 can be explained from figure 4.2. At fixed (not

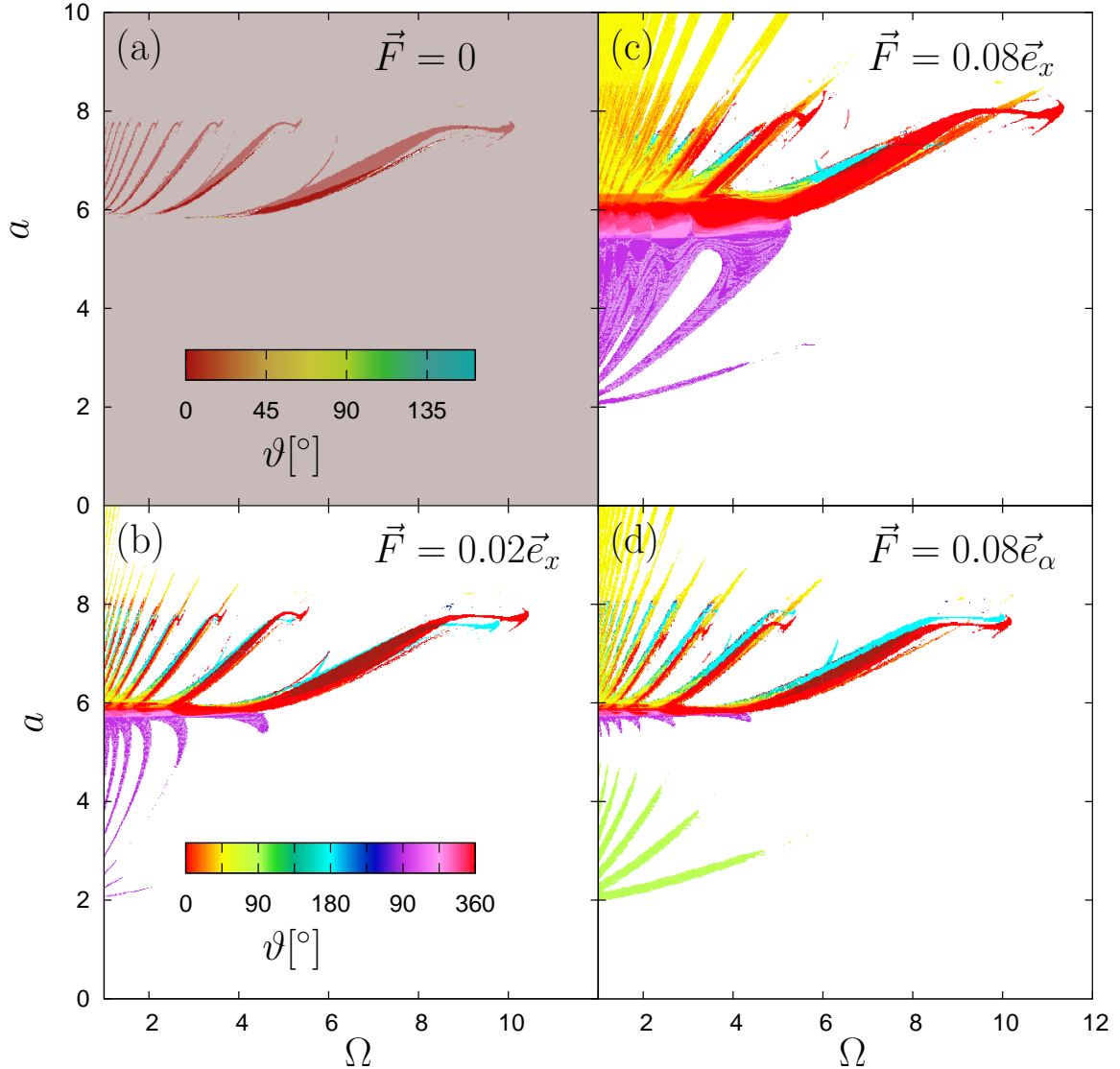


Figure 4.18: Phase diagram for $\alpha = 54^\circ$ and various \vec{F} (as indicated in the panels) in the Ω - a plane of parameter space and otherwise the same dynamics as in figure 4.16. As in figure 4.16, non-transporting attractors are shown in (a) and are not shown in (b)-(d), see section 4.15.1.

too large) frequency, regions of attractors with broken S_0 symmetry are encountered repeatedly when increasing a , and these regions may contain chaos as was argued in section 4.8.

In turn, for the smallest drive frequency considered in figure 4.17, $\Omega = 1$, the size of the transporting islands is also significantly decreased, while their number has increased significantly. Again, comparing with figure 4.4, this behavior is expected. Therefore, there is an “optimum” value of Ω somewhere between 1 and 10 for SSBT.

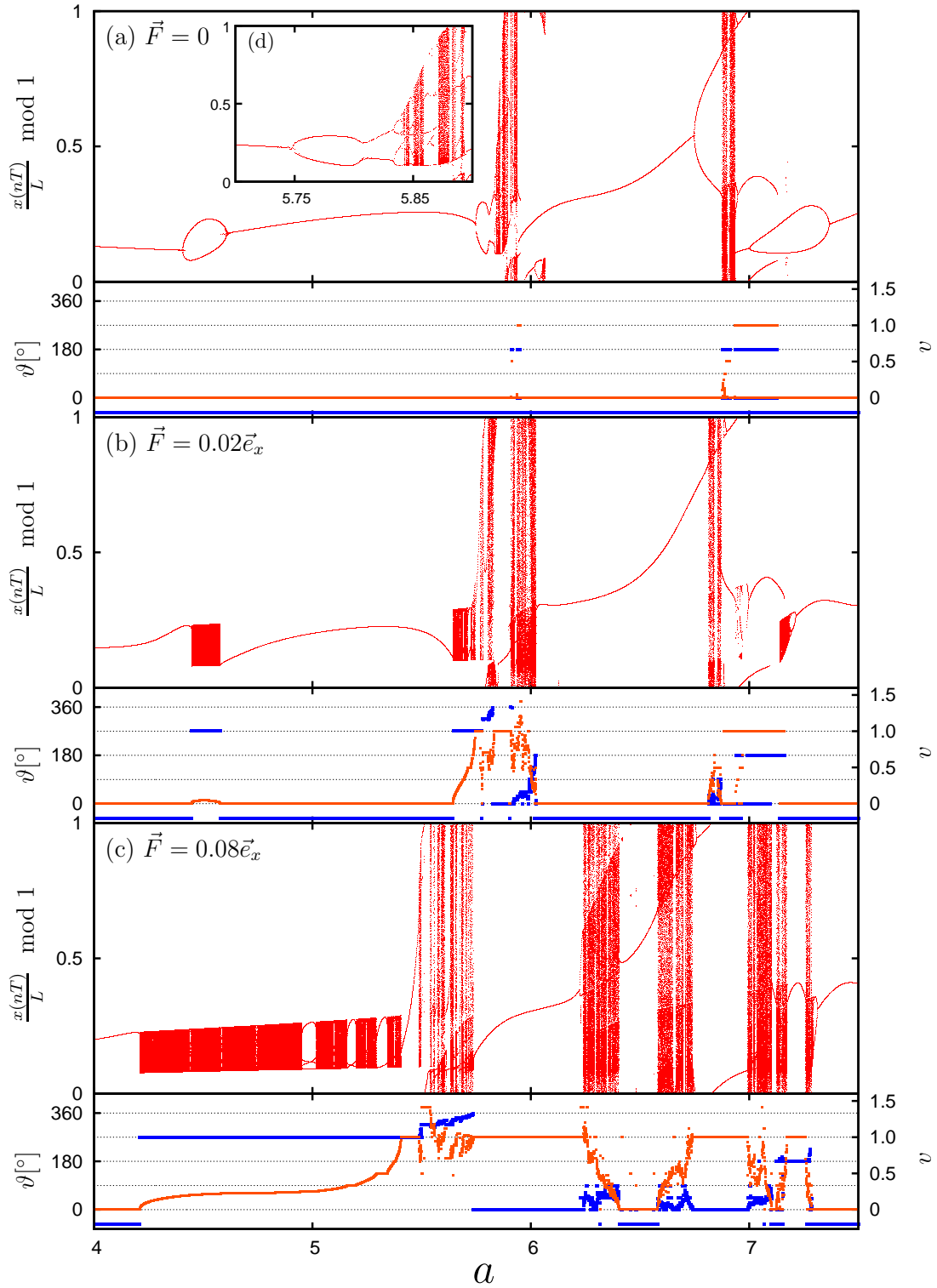


Figure 4.19: Bifurcation diagram of the dynamics (4.9) with $\alpha = 54^\circ$, $\Omega = 4$ and \vec{F} as indicated in the panels, showing only attractors obtained and drawn by the same method as described under figure 4.16. Each panel is subdivided into an upper part showing the asymptotic large-time stroboscopic section of the dynamics and a lower part showing the average transport velocity $\vec{v} = v \vec{e}_\vartheta$. ϑ is shown in blue and v in red. The inset (d) shows an enlargement of the upper part of panel (a).

4.15.3 SSBT in the Ω - a plane of parameter space at $\vec{F} = 0$

From figure 4.17 we infer that practically any $\alpha \in [48^\circ, 58^\circ]$ yields SSBT on a large transporting window for a suitably chosen value of the drive amplitude a . We focus on

$$\alpha = 54^\circ \quad (4.34)$$

to further investigate the role of the drive frequency Ω . The result is found in figure 4.18. The structure encountered is again similar to that found in figure 4.4. The largest (connected) regions of existence of SSBT attractors is found for the largest frequencies considered (SSBT is not found for larger frequencies), and slightly shrunken and distorted copies of this SSBT region are found for smaller Ω . These regions always extend from $a \approx 6$ to $a \approx 8$, and beyond these values of a SSBT is not found. All SSBT attractors found carry transport in the $(1, 0)$ direction. Other directions are not expected since our choice of α is such that it is smaller than the value for which attractors carrying transport in the $(0, 1)$ direction are found but also quite far from the symmetric case $\alpha = 45^\circ$, for which attractors carrying transport in the $(1, 1)$ direction are expected.

We show the nature of SSBT at $\alpha = 54^\circ$ in more detail in figure 4.19(a). Around $a \approx 4.5$ there is a symmetry-breaking “bubble”, which will be discussed below in section 4.17. The first main window of SSBT attractors is encountered at $a \approx 5.93$. The process which leads to its creation is discussed in more detail in section 4.25.5.

For small values of a , there is a S_0 symmetric periodic orbit (see figure 4.37(a) for an equivalent orbit at slightly different frequency) which undergoes a symmetry breaking bifurcation at $a \approx 5.75$, yielding a pair of nonsymmetric, non-transporting periodic orbits (see figure 4.37(b)). These non-transporting orbits undergo a period doubling cascade with accumulation point around $a \approx 5.842$, where a nonsymmetric bounded chaotic attractor (see figure 4.37(c)) is created. It merges with its symmetry partner in an attractor merging crisis around $a \approx 5.844$, yielding a symmetric bounded chaotic attractor (see figure 4.37(d)). At $a \approx 5.87$ an unbounded (in all directions) chaotic attractor is found. This attractor carries diffusion into “all” directions in the sense that any elementary cell on the lattice can be reached from any other. The argument that this should indeed be the case since there is no restricting symmetry does not always hold in the deterministic limit, see section 4.14. We will discuss this in the appendix (section 4.25.5).

A second (and larger) main window of SSBT is located at $a \approx 6.93$. It is interesting to note that the main $|v| = 1$ window is preceded by (in the sense that one finds for smaller values of a) a period adding sequence of SSBT orbits yielding a staircase-like structure in the average velocity with average velocities of values $|v| = \frac{1}{n}$. That sequence begins at $a \approx 6.9$ and is visible only as a few non-zero and non-integer values of v in figure 4.19(a). Moreover, the window is terminated by a saddle node bifurcation for larger a . Since the SSBT window coexists with a non-transporting attractor, this does not yield a diffusive chaotic attractor but a chaotic repeller of that nature. At this border of the window ANM is encountered, see section 4.16 and figure 4.19(b).

From figure 4.18 it follows that the largest (the “rightmost”) region of SSBT attractors is the “best” choice for studying SSBT due to its expected robustness against changes of parameters or random fluctuations (see figure 4.24 for a demonstration of this fact). This would imply a choice of

$$\Omega \approx 6 \quad (4.35)$$

to choose parameters close to the center⁴⁷ of this region and to avoid coexistence with other (non-transporting) attractors. This choice is ideal for just achieving SSBT and related effects (namely ANM and deterministic diffusion) but not for “directing Brownian motion”, see below.

4.16 Broken S_0 symmetry: all symmetries are broken

As has been discussed in section 4.11, $\vec{F} = 0$ implies that the average particle velocity will be zero in the presence of thermal fluctuations. Therefore the control of the transport properties is limited to using diffusion properties, cf. section 4.11.1 and section 4.22.

Breaking S_0 symmetry by letting

$$\vec{F} = F\vec{e}_\phi \neq 0 \quad (4.36)$$

from now on provides a more direct approach to control the transport properties of the particle.

4.16.1 $\vec{F} \neq 0$ in the a - α plane of parameter space

For reasons which will become apparent in the following paragraph, we stay with our previous choice

$$\Omega = 4. \quad (4.37)$$

Since $\Omega = 4$ is not too different from $\Omega = 6$, the differences with respect to robustness against random perturbations turn out to be only a factor of about 2, leaving room for optimization.

As has been discussed in section 4.13, we limit our investigation to a few representative directions for the bias force, namely $\vec{F} \parallel \vec{e}_x$, $\vec{F} \parallel \vec{e}_y$, $\vec{F} \parallel \vec{e}_{45^\circ}$ and $\vec{F} \parallel \vec{e}_\alpha$. We consider a small bias forces $F = 0.02$ only in (one of) the directions of SSBT, and a somewhat larger force $F = 0.08$ in all directions considered. The latter choice removes most of the coexistence of attractors with different transport directions, making the diagrams readable. We start with $\vec{F} = 0.02\vec{e}_x$ found in figure 4.16(b).

First, lifting S_0 symmetry separates the regions of existence of coexisting SSBT attractors of opposite transport velocities yielding red (transport in the direction of the bias force) and blue (transport against the bias force) regions. The movement of the regions of existence in the Ω direction is just as predicted by the intuitive argument discussed in section 4.11.2, i.e. the regions of existence of SSBT attractors transporting against the bias force move towards smaller Ω , and the regions of existence of their symmetry partners move towards larger Ω . Simultaneously, the regions of existence of the former move towards smaller a , and those of the latter towards larger a , but the “speed” of that

⁴⁷At the borders of the regions of existence of SSBT attractors, their pseudopotential depth vanishes. We therefore expect the center of the regions of SSBT attractors to be the best choice with respect to their stability. While instabilities of Shapiro steps (and thus SSBT attractors) have also been found in the center of the steps (regions of existence) [137], this effect was found at the transition from the regular regime to the chaotic regime, while we are considering parameters “deep” in the chaotic regime, where the center of the former Shapiro step has already undergone this instability, see section 4.9.3 and section 4.11.2.

movement (with respect to F) is rather slow. Since the parameter regions of SSBT have borders towards smaller Ω at $F = 0$, ANM is found at those borders, see figure 4.37(h) for an example orbit at $\Omega = 4$, $a = 5.95$. The regions of existence of $\vartheta = 45^\circ$ attractors separate likewise. Simultaneously, the regions of existence of attractors with transport in the direction of the bias force grow, while the regions of existence of attractors with transport against the bias force shrink.

Second, in the region of parameter space where deterministic chaos is found for $\vec{F} = 0$, which largely coincides with the region of $|\vec{r}_{max}| > 3$ in figure 4.15, “new” attractors emerge from periodic windows becoming stable and/or growing. Apparently, their transport directions are influenced by, but in general not equal to, the transport directions of other large transporting windows in their vicinity. Individually, these “new” attractors have rather small regions of existence, in particular for smaller bias forces \vec{F} , but allow for deterministic transport with many “new” directions.

Third, regions of existence of “new” attractors with completely different properties, and in particular new transport directions, emerge in parameter regions in which neither chaos nor unbounded objects are found for $\vec{F} = 0$. All these “new” attractors are created at parameter values close to the remains of S_0 symmetry breaking bifurcations which become avoided bifurcations for broken S_0 symmetry [115]. The attractors are non-periodic and we will discuss their properties in the following section.

4.17 Quasiperiodic transport at $\vec{F} \neq 0$

There are two main types of these “new” attractors, both quasiperiodic⁴⁸ but differing by their transport direction. The first emerge around the symmetry-breaking bifurcations in the S_{xy} symmetric case close to $\alpha = 45^\circ$ and reach out towards $\alpha > 45^\circ$ carrying $\vartheta = 45^\circ$ transport (or $\vartheta = 315^\circ$ for \vec{F} with opposite sign). Their properties are similar to those of the second type, which we will discuss now.

The second type emerges around the S_0 symmetry breaking bifurcations at $\alpha = 90^\circ$ continued towards $45^\circ < \alpha < 90^\circ$, see figure 4.15. These attractors are first found close to the regions of existence of the SSBT attractors discussed above (section 4.10) at the borders towards smaller drive amplitudes a (and thus at the borders of the regions of existence of the unbounded objects discussed in section 4.14). Most of the attractors carry exactly $\vartheta = 90^\circ$ transport. The case of other \vec{F} , in particular $\vec{F} \parallel \vec{e}_y$ will be discussed below. Upon closer inspection, there is a more or less smooth transition of their transport direction where their regions of existence meet those of the SSBT attractors. As can be seen from figure 4.19, the absolute values of their transport velocities varies smoothly with the drive amplitude a . This is due to the quasiperiodic nature of the attractors differing significantly from that of the phase-locked SSBT attractors considered so far.

These new transporting attractors are analyzed in detail in figure 4.20 using the representative example of the attractor existing for the smallest a value around $a \approx 2.8$ for $\Omega = 4$ in figure 4.16(c). At $a = 0$ and for each value of \vec{F} , there are only three periodic orbits: the one oscillating around the potential minimum and the orbits oscillating around the saddles. Already at $\vec{F} = 0$, the two saddles in the elementary cell (we are now considering the unrotated elementary cell and the coordinates x and

⁴⁸ Trajectories on the attractors never close on the torus, but the attractors are not chaotic [115].

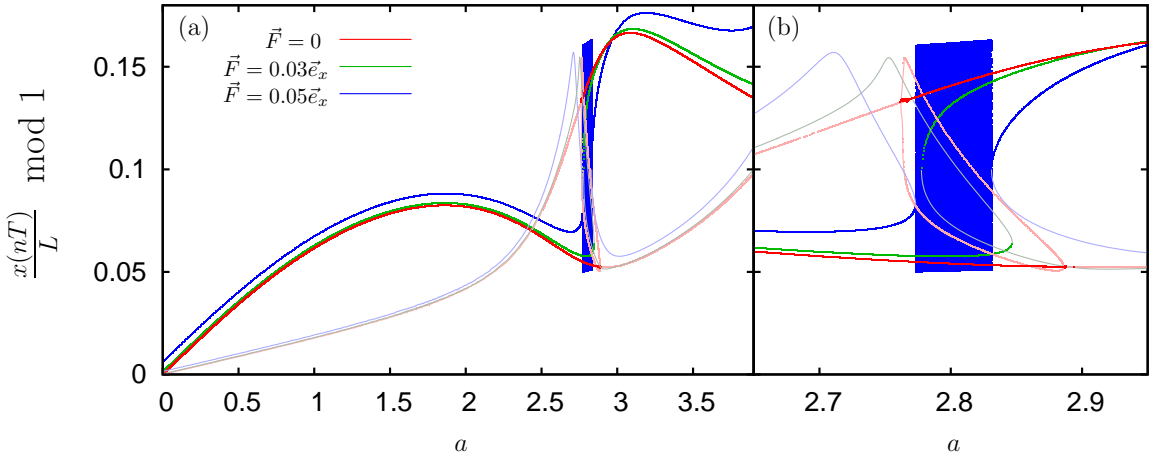


Figure 4.20: Bifurcation diagram of the deterministic $\Gamma = 0$ dynamics (4.9) for $\alpha = 54^\circ$, $\Omega = 4$ and various \vec{F} , see legend. Shown are both attractors and unstable period 1 orbits, obtained and drawn according to the same method as outlined under figure 4.7. The unstable periodic orbits are drawn in lighter colors. (b) shows a magnified view of the region of interest in (a). Since the figure shows only a part of phase space (in the x -direction), one unstable periodic orbit is missing, see text. Apart from this orbit, all unstable periodic orbits (found) are shown. For $a < 2.5$, the unstable periodic orbit oscillating around the saddle has been obtained using the method described under figure 4.8, starting at $a = 0$, $\Omega = 7$ and ending at $a = 2.5$, $\Omega = 4$.

y) are not equivalent, and the unstable periodic orbits oscillating around these saddles are not equivalent. In figure 4.20, we show only the unstable orbit oscillating around the saddle at $(x, y) = (0, 0.5)$. The other saddle $(x, y) = (0.5, 0.0)$ is not contained in the window of phase space shown in the figure. Since the orbit oscillating around the saddle $(x, y) = (0.5, 0.0)$ is isolated from the other periodic orbits considered here, it is not relevant to the discussion⁴⁹. With that in mind, the other (stable) periodic orbit found around $a = 0$ in figure 4.20 is the one oscillating around the potential minimum.

For $\vec{F} = 0$, at $a \approx 2.76$ and $a \approx 2.89$ there are pitchfork bifurcations. At the latter, the orbit oscillating around the potential minimum (see figure 4.21(a)) undergoes a backwards-oriented pitchfork bifurcation, becoming unstable for larger a and creating two branches of S_0 symmetry breaking unstable periodic orbits. These branches are connected to the former pitchfork bifurcation, where the unstable periodic orbit oscillating around the saddle (see figure 4.21(b)) becomes stable for larger a . In figure 4.19(a) the same situation is found at $a \approx 4.4$ and $a \approx 4.6$ with the directions of the (symmetry-breaking) pitchfork bifurcations reversed⁵⁰. Thus, a “bubble” with broken S_0 symmetry is created, unstable in figure 4.20 and stable in figure 4.19(a).

⁴⁹We were unable to find it using our simple numerical methods for $\Omega = 4$ due to its Floquet multipliers being too large. Moreover, using the method described under figure 4.8 we were also unable to find it, indicating that it is not involved in any bifurcation changing its stability within the parameter ranges considered in figure 4.20. Since the bifurcations we are considering here are “complete” in the sense of all branches being present, we conclude that the orbit is not involved in any of them.

⁵⁰In figure 4.19(a), two periodic orbits also “exchange” roles/stability. These changes of symmetry and stability can be attributed to the same reasons as discussed in section 4.8.

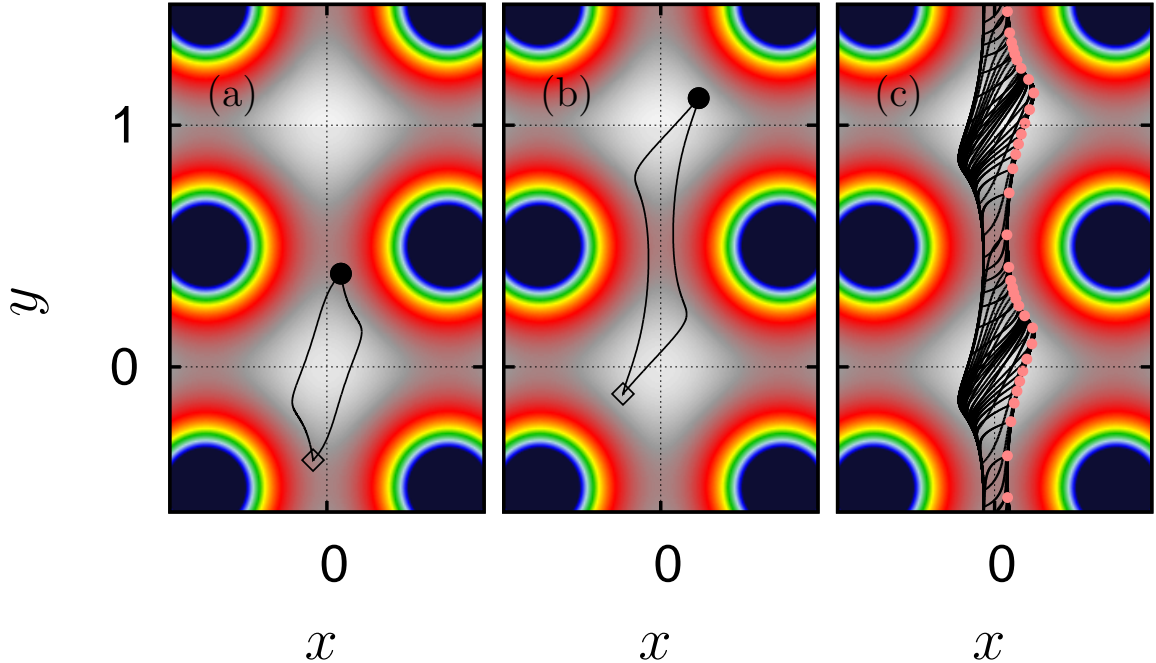


Figure 4.21: Periodic orbits (a)-(b) and quasiperiodic orbit (c) corresponding to the parameters and dynamics considered in figure 4.20 except for $\vec{F} = 0$, $a = 2.7$ (a), $\vec{F} = 0$, $a = 2.9$ (b) and $a = 2.8$, $\vec{F} = 0.05\vec{e}_x$ (c). In panels (a) and (b) the turning points of the orbits (i.e. the times when the periodic drive changes sign) are marked by a filled circle (drive protocol becomes negative) and an open diamond (drive protocol becomes positive). In panel (c), only one turning point (drive protocol becomes negative) is marked by red points, indicating the attractor's shape under the stroboscopic section. Moreover, only a part of the orbit is drawn in full phase space (not reduced to the torus).

For $\vec{F} \neq 0$ the pitchfork bifurcations become “avoided” pitchfork bifurcations (see the green curve in figure 4.20) [115]. This means that the subcritical pitchfork bifurcation becomes a tangent bifurcation where the stable orbit collides with one of the (formerly symmetry breaking⁵¹) unstable orbits, and the other (formerly symmetry breaking) unstable orbit is no longer “involved” in this bifurcation. It is now “directly” connected to the other remaining periodic orbit, the (formerly symmetric) unstable periodic orbit created in the pitchfork bifurcation, see the green curve in figure 4.20 and also [115] for a beautiful illustration. In our case, the unstable periodic orbit “uninvolved” in the tangent bifurcation is connected to the other avoided pitchfork bifurcation, which transforms likewise.

These tangent bifurcations “move” upon increasing the bias force. In particular, the avoided pitchfork bifurcation involving the orbit oscillating around the potential minimum occurs for smaller values of a , while the other avoided pitchfork bifurcation occurs for larger values of a . Thus, at first the a values at which they occur move towards each other for increasing bias force modulus. At $\vec{F} \approx 0.03\vec{e}_x$ they are almost identical. Beyond this “critical” value of the force, the tangent bifurcations exchange places in the bifurcation diagram. This leaves a “hole” in the bifurcation diagram without periodic orbits (in the

⁵¹With $|\vec{F}| \neq 0$ there is no S_0 symmetry any longer and thus there are no symmetric orbits.

phase space region formerly occupied by the orbits considered so far). Since the orbits involved are connected to each other via their invariant manifolds forming an invariant circle (see below), this is an infinite period bifurcation [115], creating a quasi-periodic attractor, see figure 4.21(c) for the corresponding orbit.

The bifurcation creating transport can be explained by considering the spatially periodic structure of the equations. Let us consider one of the pairs of stable and unstable periodic orbits creating the infinite period bifurcation, e.g. set $a = 2.75$ fixed, increase the modulus of $\vec{F} = F\vec{e}_x$ and consider the “lower” branch of the two bifurcations. The structure of the infinite period bifurcation implies that, prior to the bifurcation, the unstable manifold of the unstable periodic orbit is directly connected to the stable manifold of the stable periodic orbit. Here, we have to be careful with winding numbers on the torus or, in other words, to which copy of the stable periodic orbit in which elementary cell the two halves of unstable manifolds are connected. In our case, the unstable periodic orbit oscillating around the saddle at $(x, y) = (0, 0.5)$ is the separatrix separating the basins of attraction of the stable periodic orbits oscillating around the minima at $(x, y) = (0, 0)$ and $(x, y) = (0, 1)$. One half of its unstable manifold connects to the stable periodic orbit oscillating around $(x, y) = (0, 0)$, and the other half connects to the copy of that stable periodic orbit oscillating around $(x, y) = (0, 1)$. If the stable and the unstable periodic orbit annihilate in a tangent bifurcation, they leave behind their connected (un)stable manifolds creating the quasiperiodic transporting attractor. We have verified this structure [117] for representative parameter choices for this system (not shown) .

In particular, this explains the structurally stable transport direction of the attractor far from the region of existence of SSBT attractors, although the modulus of its transport velocity is not structurally stable. Basically, this structure is similar to the one encountered for only a constant bias force, but in that case one deals with fixed points of the dynamics instead of periodic orbits [214, 215].

Upon further increasing the bias force (but keeping its direction), the size of these attractors in parameter space grows as can be expected from the direction in parameter space into which the responsible avoided symmetry breaking bifurcations move for increasing bias forces.

Letting $\vec{F} \rightarrow -\vec{F}$, the transport direction of the quasiperiodic attractors is reflected at the origin, i.e. changes sign. As has been argued above, the transport direction will be parallel to \vec{e}_y in certain regions of parameter space. Therefore, one interval of bias forces can be associated with $\vartheta = 90^\circ$ transport and another interval, which follows upon reflection at the origin, with $\vartheta = 270^\circ$ transport. This is shown in figure 4.22 and accounts for the $\vartheta = 90^\circ$ attractors found for $\vec{F} = 0.08\vec{e}_{45^\circ}$, $\vec{F} = 0.08\vec{e}_y$ and $\vec{F} = 0.08\vec{e}_\alpha$, since at $\alpha \neq 45^\circ$ there is no symmetry restricting the values of α at which the transport current is inverted. In fact, this angle varies with α , and it is fixed only at $\alpha = 45^\circ$. Lastly, the quasiperiodic attractors turn out to be remarkably robust against a rotation of the bias force $\vec{F} = F\vec{e}_\phi$, cf. figure 4.22. E.g., the $\vartheta = 90^\circ$ attractor (light green in figure 4.22) survives beyond $\phi = 180^\circ$ for certain a values, i.e. $\vec{e}_\vartheta \cdot \vec{F} < 0$.

4.18 Summary of transport properties at $\Gamma = 0$

Putting things together, with all symmetries broken we have an abundance of attractors transporting in practically all directions, depending on the choice of system parameters.

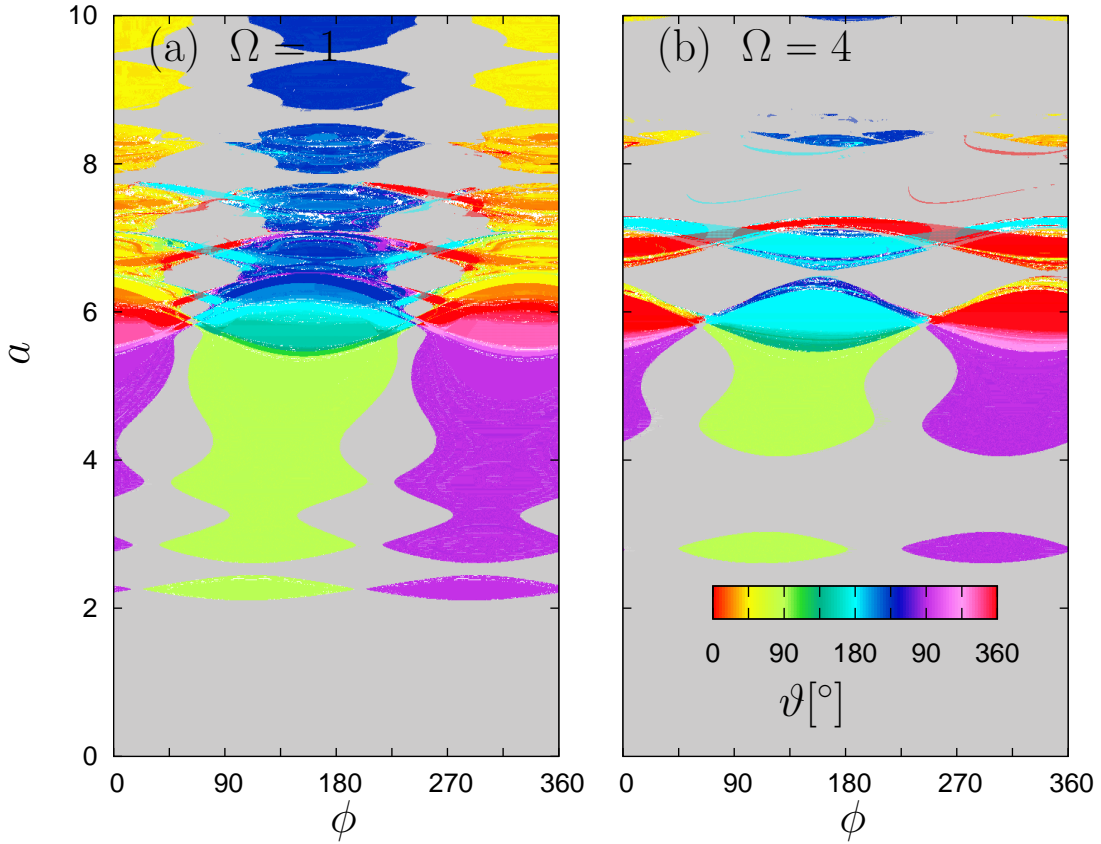


Figure 4.22: Deterministic $\Gamma = 0$ phase diagrams for the dynamics (4.9) with $\alpha = 54^\circ$, Ω as indicated in the panels and $\vec{F} = 0.08\vec{e}_\phi$. The transport direction of transporting attractors is encoded in colors, cf. the legend in (b), and non-transporting attractors are shown as grey. In case of coexistence of transporting and non-transporting attractors, only the transporting attractor is shown. $\phi \in [180^\circ, 360^\circ]$ can be obtained from $\phi \in [0^\circ, 180^\circ]$ due to S_0 symmetry.

The interplay of the periodic potential and the periodic drive leads to pairs of SSBT attractors with opposite transport directions, carrying transport parallel to the (1,1) and (1,0) directions. A second consequence of this interplay are symmetry breaking bifurcations. The interplay of the symmetry breaking bifurcations and an applied bias force leads to quasiperiodic attractors carrying transport parallel to the (0,1) and (1,1) directions, depending on the direction of the applied bias force. Where the regions of existence of these attractors meet those of other attractors, the interplay of the competing transport directions leads to an even richer spectrum. A crucial observation is that the transport direction can be rotated without rotating anything in the system. E.g. choosing Ω fixed, say $\Omega = 4$, and varying the drive amplitude with all parameters fixed (i.e. a horizontal line in figure 4.18(c)), attractors carrying transport into most directions are encountered in the sense that for each direction on the surface an attractor carrying transport into a direction that differs only by a few degrees is encountered, the only exception being the $\vartheta = 275^\circ$ direction. In turn, this allows a particle to be *directed* along a surface, but except for a few discrete directions given by phase-locked and quasiperiodic attractors with large parameter regions, the transport direction of the particle depends

sensitively on the choice of system parameters. Thus, it is rather difficult to direct a specific particle species into a specific direction unless that direction is “special”, but the mechanism of directing the particle is highly sensitive to different particle species. As we will see in the next section, the former limitation is mitigated by thermal noise.

4.19 Noise effects

So far, we have been considering the deterministic dynamics, $\Gamma = 0$. Adding noise leads to a plethora of new effects such as diffusion [8, 128], stabilization of transient chaos [147, 265], suppression of deterministic diffusion [258], ANM related effects [1, 2, 63, 151], and, most importantly for our purposes, noise induced escape from deterministic attractors [1, 2, 137, 141, 144, 263, 264], to name but a few. The latter has effects both beneficial and detrimental to our purpose, namely *directing Brownian motion*.

Noise induced escape destabilizes attractors. In the deterministic case, once a trajectory has reached an attractor, it will stay there indefinitely. In the presence of noise, it will leave that attractor after a time, visiting other regions of phase space. For the transport of a particle “living” on such a trajectory, this means that its average velocity will be the time average over the (deterministic) average velocities of all regions of phase space it visits and thus, due to ergodicity, the average over all points of phase space, each weighed with its weight [90, 91]. First, and detrimental to our purpose, this usually reduces the average velocity in the presence of transporting attractors because the symmetry breaking perturbation is small. In the systems and parameters considered here, i.e. for small bias forces, transporting attractors or the unstable objects which are created upon their destruction are the regions of phase space with the largest (deterministic) average velocities out of those regions of phase space with appreciable weight. For $\Gamma \rightarrow \infty$, the average velocity will be $\vec{v} = \vec{F}$ [10], which is much smaller than the (deterministic) average velocities due to SSBT.

Second, noise induced metastability smoothes the average velocity as a function of a system parameter. In the deterministic case, this function is usually discontinuous due to bifurcations and even multi-valued due to coexistence of attractors⁵². Noise induced transitions between deterministic attractors lift this by ergodic averaging over phase space [10, 90]. For the purpose of *directing* a particle on a surface this is crucial from a practical point of view. In the deterministic case, a very small change in some parameter can lead to a completely different transport velocity or even trap the particle on a non-transporting attractor. Thus, control of the particle might then become impossible in an experiment. Therefore, noise is an essential ingredient for *directing* Brownian motion, but only in the right quantity: we have briefly addressed the effects of noise in section 4.11.2 to estimate the noise strength at which ANM effects vanish at $\alpha = 45^\circ$ and found this to be of order $\Gamma \approx 10^{-5}$. As has already been hinted at in section 4.11.2, considering $\alpha \neq 45^\circ$ we expect the noise resistivity to increase, but there remains a threshold at which ANM and related effects vanish and their transport directions become inaccessible.

⁵²One can try to associate a statistical weight to attractors in the noise free case. If the limit $\Gamma \rightarrow 0$, e.g. of the average velocity, is well behaved, one can define a single valued function in the noise free case and a probability density (statistical weight) of phase space. But one then has a statistical description of a nonergodic dynamics, which needs further interpretation.

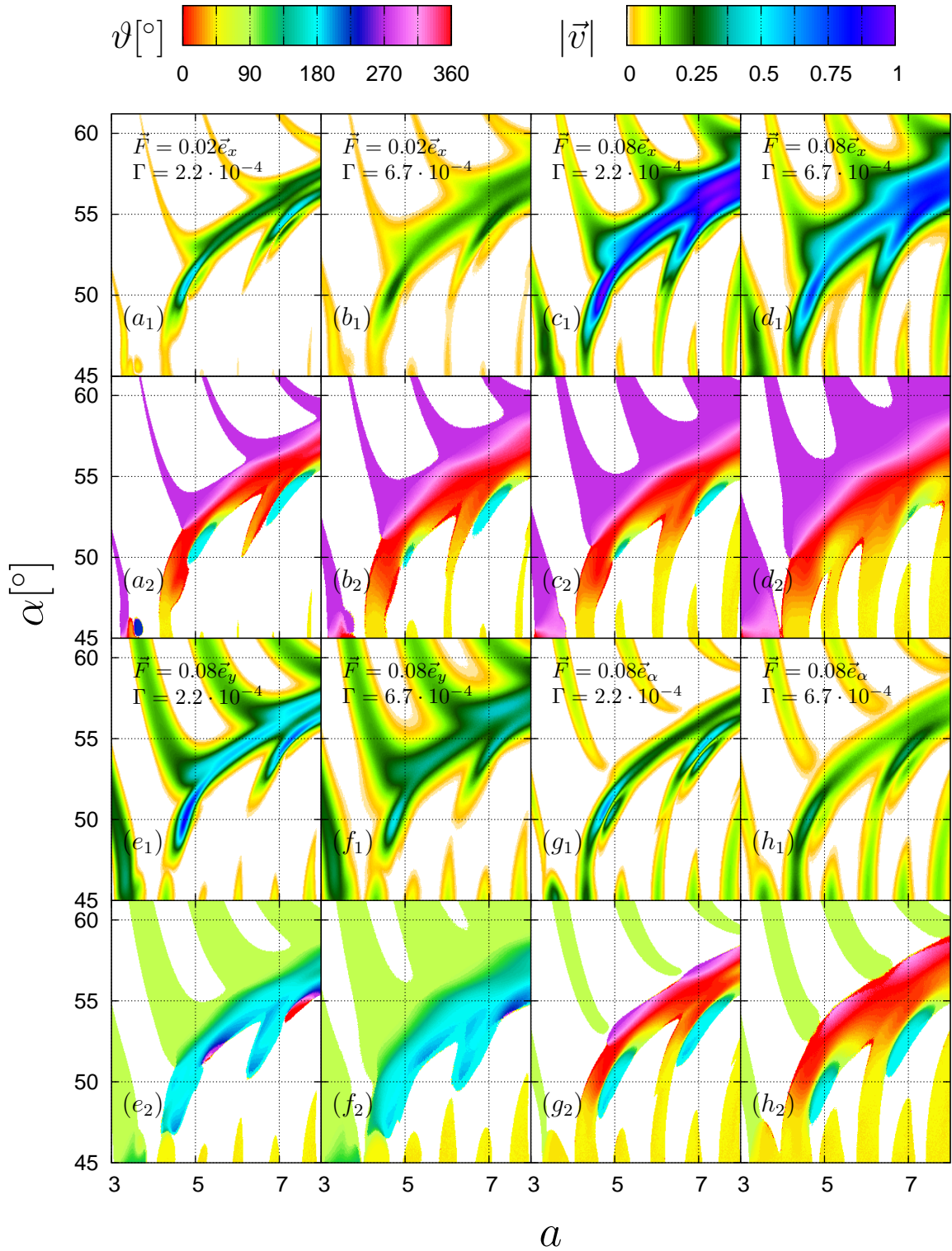


Figure 4.23: Dimensionless average velocity $\vec{v} = |\vec{v}| \vec{e}_\vartheta$ for the dynamics (4.9), $\Omega = 4$ and remaining parameters as indicated in the figure. ϑ is shown in the lower rows (subscripts 2), and v in the upper rows (subscripts 1). The palette for $|\vec{v}|$ has been cut off. If $|\vec{v}| < 0.008$, corresponding to a displacement of less than 400 elementary cells for the single trajectory used to obtain the averages, white is displayed for ϑ and $|\vec{v}|$. If $|\vec{v}| > 1$, the palette above figure 4.24 is used.

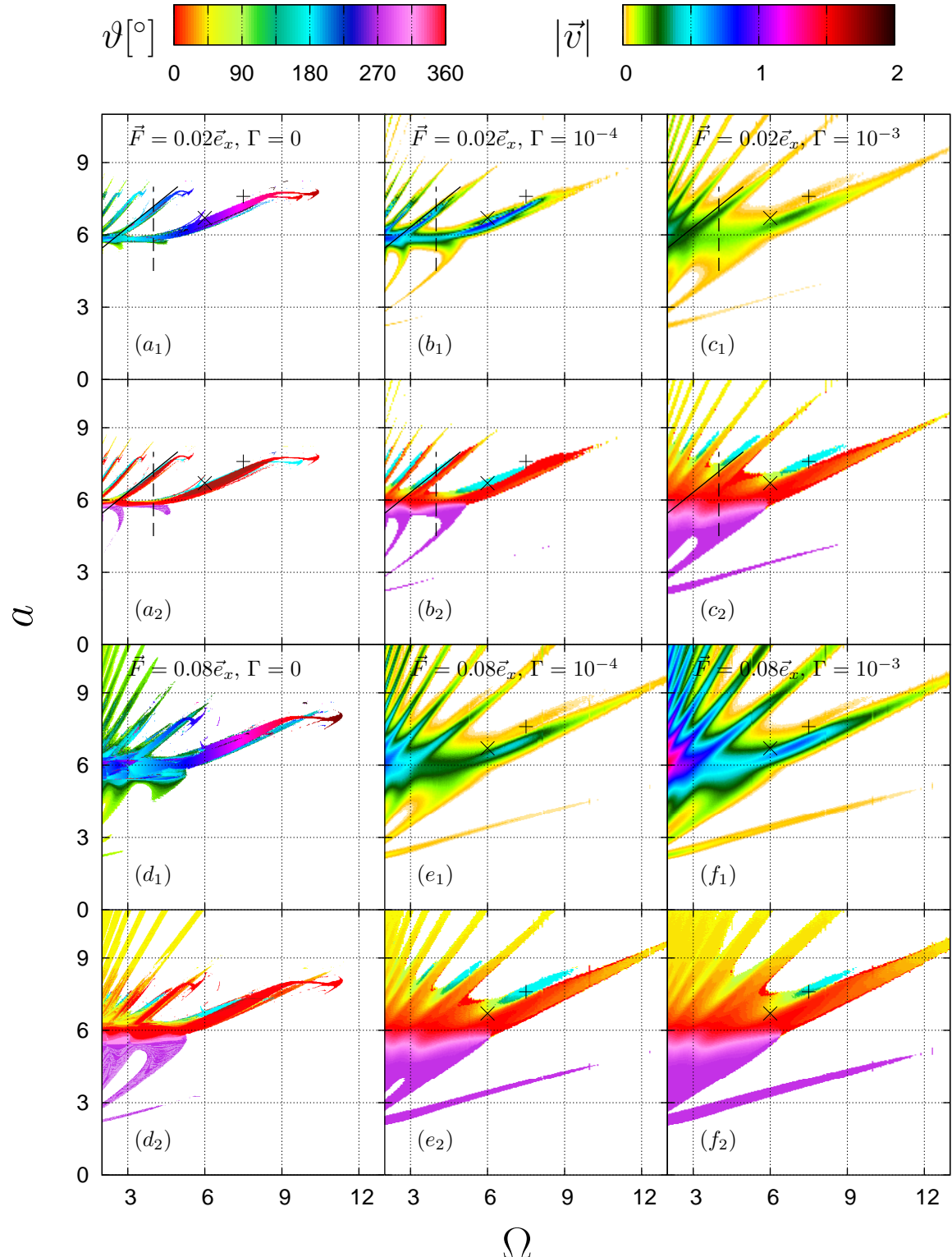


Figure 4.24: Dimensionless average velocity $\vec{v} = |\vec{v}| \vec{e}_\vartheta$ for the dynamics (4.9), $\alpha = 54^\circ$ and remaining parameters as indicated in the figure. ϑ is shown in the lower rows (subscripts 2), and $|\vec{v}|$ in the upper rows (subscripts 1). If $|\vec{v}| < 0.01$, corresponding to a displacement of less than 200 elementary cells for the single trajectory used to obtain the averages, white is displayed for ϑ and $|\vec{v}|$.

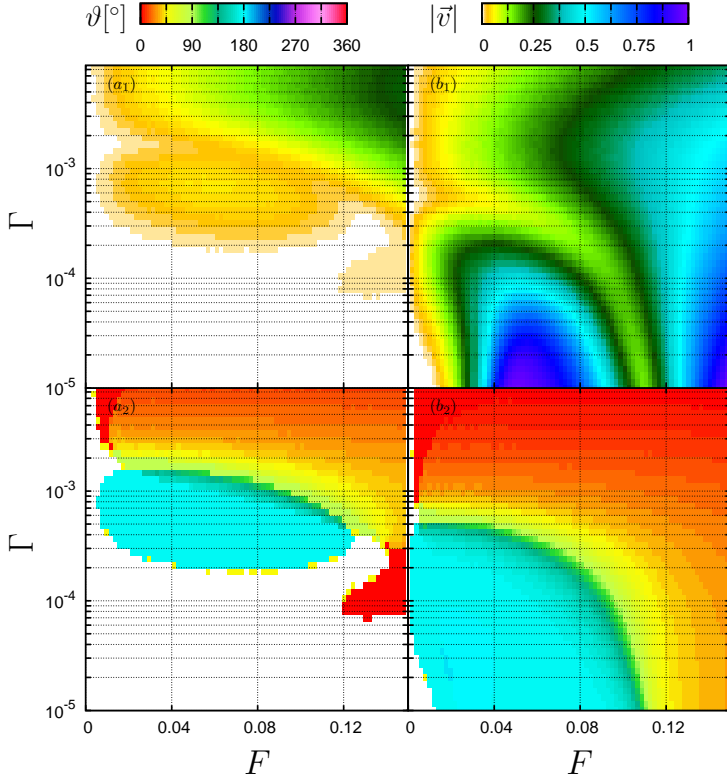


Figure 4.25: Dimensionless average velocity $\vec{v} = |\vec{v}| \vec{e}_\vartheta$ for the dynamics (4.9), $\alpha = 54^\circ$, $\vec{F} = F \vec{e}_x$, (a) $\Omega = 7.5$, $a = 7.6$ (corresponding to the '+' in figure 4.24) and (b) $\Omega = 6$, $a = 6.7$ (corresponding to the 'x' in figure 4.24). ϑ is shown in the lower rows (subscripts 2), and $|\vec{v}|$ in the upper rows (subscripts 1). If $|\vec{v}| < 0.008$, corresponding to a displacement of less than 3200 elementary cells for the single trajectory used to obtain the averages, white is displayed for ϑ and $|\vec{v}|$.

Figures 4.23, 4.24 and 4.25 summarize of our findings. Figure 4.25 shows the maximum noise strengths and bias forces possible for two representative choices of parameters exhibiting ANM (see the symbols in figure 4.24). The maximum noise strengths for which ANM is supported are of the order $\Gamma \approx 10^{-3}$, that is two orders of magnitude larger than for $\alpha = 45^\circ$. The maximum bias forces against which transport is supported, also called load forces, are of similar magnitude at $F \approx 0.1$, compared to $\alpha = 45^\circ$. Figures 4.23 and 4.24 are analogs of figures 4.16 and 4.18 showing the modulus of the average velocity $|\vec{v}|$ and its direction ϑ in separate panels as indicated by the color palettes and the captions. For completeness, the results for $\Gamma = 0$ are repeated in figure 4.24, and moreover $|\vec{v}|$ at $\Gamma = 0$ is included, which is not shown in figure 4.18.

Due to the destabilization of non-transporting attractors and the associated increase of the statistical weights of deterministically transient regions in phase space, the regions in parameter space with measurable transport velocities grow. Basically, this is the same effect as is behind noise induced ANM discussed in [63] and [1, 2], see therein for a brute force quantitative analysis in terms of pseudopotentials for a representative example. The difference lies in the transport properties of the deterministic repellers and attractors involved. In short, if the deterministic attractor vanishes by means of some bifurcation, it leaves behind an unstable object in phase space, the nature of which depends on the

particular bifurcation. Here, these objects are chaotic repellers, but also the traces of periodic orbits prior to their birth in tangent bifurcations [115, 253, 254, 266]⁵³. Due to noise, these regions of phase space become accessible and gain a positive statistical weight and thus influence the average transport velocity. Therefore, these effects are most pronounced in regions of phase space where there are only non-transporting deterministic attractors.

Thus, the effect of noise on attractors carrying transport against the bias force is as follows. These attractors are SSBT attractors, S_0 symmetry is only weakly broken and their regions of existence are always close to the regions of existence of their symmetry partners (i.e. their images under S_0 at $\vec{F} = 0$). In regions of parameter space for which only attractors carrying transport against the bias force exist, the remains of the attractors carrying transport in the direction of the bias force (e.g. chaotic repellers) gain statistical weight due to noise, and the average velocity is reduced or even inverted, as was discussed in [1, 2]. But simultaneously, upon increasing the noise strength regions in parameter space neighboring the regions of existence of the deterministic attractors acquire their transport properties. Due to this mechanism, upon increasing the noise strength, the regions of parameter space exhibiting transport against the applied bias force move into regions of parameter space previously exhibiting no transport. This effect has been discussed in [63] and termed “noise induced absolute negative mobility”. For a unified notation, we term this effect noise induced ANM (NANM). As an example consider the parameters

$$\Omega = 7.5 \text{ and } a = 7.6, \quad (4.38)$$

and a vertical line through figure 4.25(a). Comparing with [2, 63], the fraction of parameter space occupied by non-transporting attractors is much larger in the overdamped dynamics considered here, and NANM is much more common in overdamped dynamics. It is particularly noteworthy that through the movement of ANM regions, NANM survives for larger noise strengths than “normal” ANM, as exemplified in figure 4.25, and also visible in figure 4.24, but the concomitant average velocity is very small in modulus.

4.20 Rotating the bias force

We have addressed the effect of different directions of the constant bias force briefly in the discussion of figures 4.16, 4.18, 4.23, 4.24 and in particular 4.22. Applying S_0 , the bias force is rotated by 180° . Therefore, each attractor moves in parameter space upon rotating the bias force such that its S_0 symmetry partner takes its place after a 180° rotation, see figure 4.22. This is most easily seen for the pairs of SSBT attractors, but also applies to the quasiperiodic attractors which only exist for broken S_0 symmetry, as has been discussed in section 4.17. Choosing a point in parameter space minus the direction of the bias force ϕ , the transport direction is determined by the attractors “visiting” this point in parameter space upon changing ϕ . As an example we select parameters which correspond to a SSBT attractor leading to ANM at $\phi = 0^\circ$ and rotate

⁵³I.e., we are referring to the region of phase space involved in the regular (laminar) parts of intermittent chaos, only that we do not require that their stable manifolds be connected to the unstable manifolds of a chaotic attractor. Therefore we do not require deterministic intermittency, but intermittency is induced by noise.

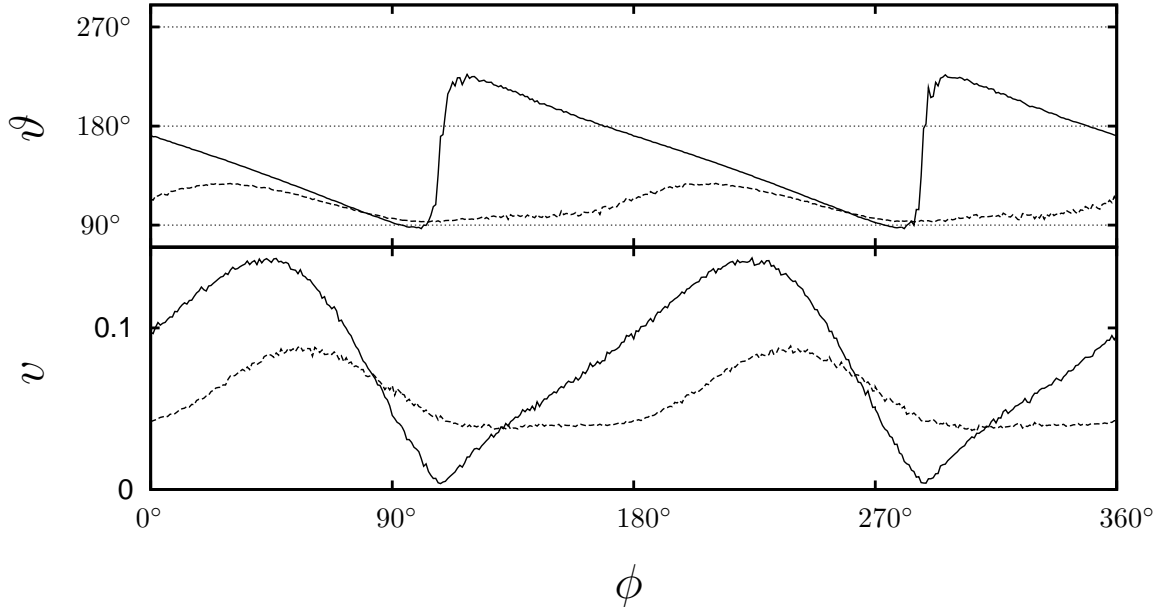


Figure 4.26: Average velocity $\vec{v} = v\vec{e}_\vartheta$ (upper panel: ϑ , lower panel: v) for the dynamics (4.9) with $\alpha = 54^\circ$, $\Omega = 4.3$, $a = 7.4$, $\vec{F} = 0.03\vec{e}_\phi$, $\Gamma = 4.4 \cdot 10^{-4}$ (solid lines) and $\Gamma = 6.7 \cdot 10^{-4}$ (dashed lines).

the bias force in figure 4.26. For the smaller noise strength considered in figure 4.26, the direction of transport remains largely in the negative x direction until the bias force points in the y direction. For ϕ slightly larger than 90° , the transport direction quickly changes to the positive x direction, remains so until ϕ passes 270° , and then changes again to be in the negative x direction due to symmetry reasons. In turn, the deflection angle ϑ shows a linear dependency on ϕ , varying between 90° and 270° , and jumps at the inversion points. Deterministically, the modulus of the transport velocity vanishes around the inversion points due to non-transporting attractors. With noise, it becomes very small at the inversion points. For the larger noise strength considered in figure 4.26, the effect is washed out, with the deflection angle no longer reaching 180° , but staying close to 90° . In turn, the modulus of the average velocity is larger around the inversion points due to noise induced transport, and smaller in between due to (SSBT induced) phase-locked transport being destabilized. Figure 4.26 is a horizontal (constant a) cut through the ANM region of a figure analogous to figure 4.22 but at a slightly different frequency.

4.21 Directing Brownian motion

We are now ready to understand the mechanism behind the control of the transport direction of a Brownian particle discussed in [4]. The interplay of SSBT attractors, symmetry breaking bifurcations and an applied (symmetry breaking) bias force leads to deterministic phase space structures allowing transport into most of the main directions of the lattice by selecting a suitable combination of frequency Ω and amplitude a of the periodic drive at fixed angles α and ϕ , cf. 4.16 and 4.18. Moreover, the spectrum of available transport directions remains almost complete if one of the remaining parameters is fixed,

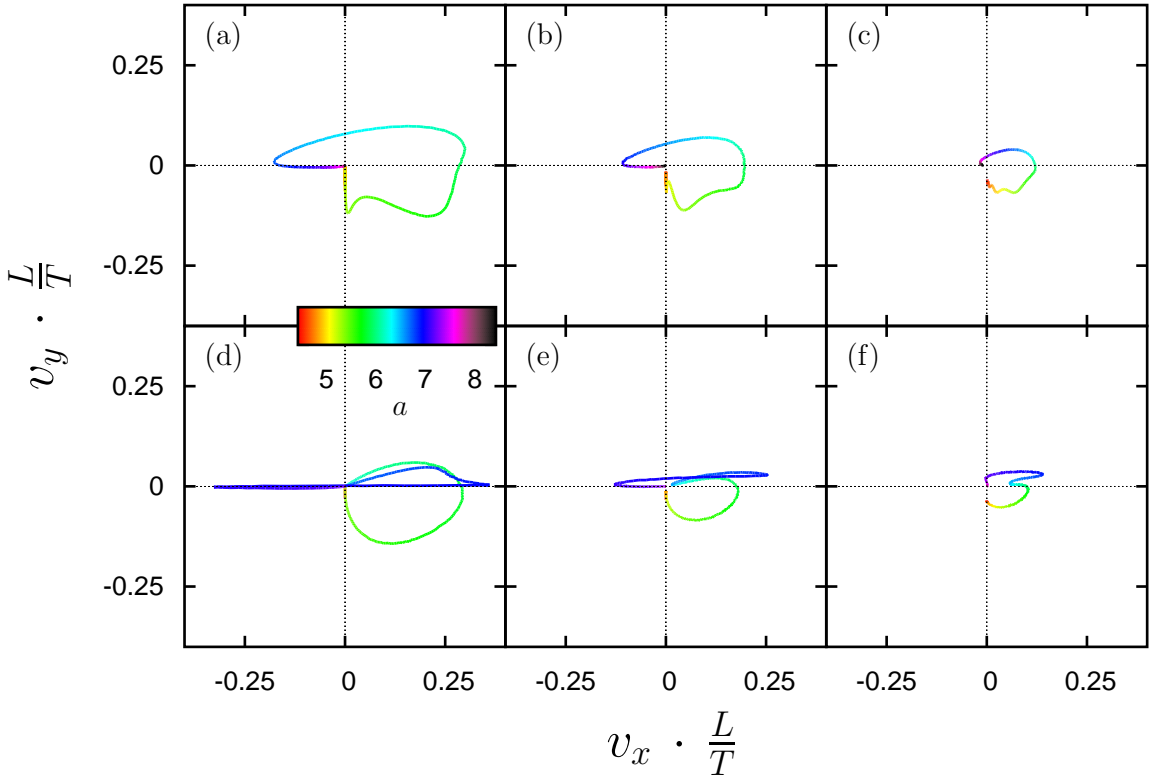


Figure 4.27: “Response spectrum”, i.e. both components of the average velocity $\vec{v} = (v_x, v_y)$ in dependence of some parameter, a , for the dynamics (4.9) with $\alpha = 54^\circ$ and $\Omega = 4$. The upper row, (a)-(c), shows $\vec{v}(a)$ for $a \in [4.5 : 8]$ as indicated by the color of the lines, see legend, and (a) $\Gamma = 10^{-4}$, (b) $\Gamma = 3 \cdot 10^{-4}$ and (c) $\Gamma = 10^{-3}$. The lower row, (d)-(f), shows $\vec{v}(a, \Omega(a))$ for $a \in [4.5 : 9]$ as indicated by the color of the lines, see legend, and (a) $\Gamma = 10^{-4}$, (b) $\Gamma = 3 \cdot 10^{-4}$ and (c) $\Gamma = 10^{-3}$. $\Omega(a)$ parameterizes the solid line in figure 4.24(a)-(c).

e.g. the drive frequency. By adding noise, the discontinuous behavior of the transport velocity is smoothed, and “new” transport directions become available through the noise induced averaging over all deterministic directions. We call the set of all directions that are available if a parameter of the dynamics is varied the response spectrum. Choosing the drive amplitude as a parameter, we get the response spectrum shown in figure 4.27, of which panels (d)-(f) show the same information as Fig. 2 of [4], except for different parameters being used.

The most remarkable feature of figure 4.27 is the presence of practically all transport directions, “selectable” without changing any inherent direction of the model. Previous studies in this line, cf. section 4.1, have been restricted to deflection angles of less than 90° , i.e. “absolute transverse mobility”, and hence the resultant response spectra were incomplete.

Upon closer inspection of the dependence of the transport direction on the particular choice of a in figure 4.27, i.e. the color of the line, it is evident that the most interesting part of the spectrum, where transport is against the applied bias force, corresponds only to a small set of a values. This can be explained from figure 4.18, in which panels (d)-(f) of figure 4.27 correspond to the vertical dashed line. The a values for which transport

against the bias force results correspond to the narrow “blue” stripes. In practice this sharp dependence may be a limitation. By giving up the simplicity of varying only one parameter, this limitation can be lifted. E.g., if Ω and a are varied simultaneously such that they trace a line passing longitudinally through the “blue stripe” in the a - Ω plane, the response spectrum as shown in figure 4.27(a)-(c) is obtained. Apart from the smoother dependence of the transport direction on the control parameter, the numerous current reversals observed as crossings of the $v_x = 0$ or $v_y = 0$ axes in figure 4.27(d)-(f) are lifted, and the response spectrum takes a more “circular” form. But this choice of varying the system parameters is artificial, may be much harder to realize experimentally and does not fit directly into the picture of different particle species corresponding to a different value of the control parameter⁵⁴.

4.22 Directing Diffusion

Another remarkable consequence of SSBT is deterministic anisotropic diffusion, as was already discussed in section 4.11.1 for $\alpha = 45^\circ$. We limit our discussion to unbiased diffusion, i.e.

$$\vec{F} = 0 \quad (4.39)$$

in this section. Due to SSBT, diffusion can be arbitrarily large in the sense that one eigenvalue of the diffusion tensor \mathbf{D} , (4.32), diverges with $\Gamma \rightarrow 0$, and diffusion is stronger in the direction of the corresponding eigenvector of the diffusion tensor, i.e. diffusion is anisotropic. At $\alpha = 45^\circ$, the diffusion tensor (4.32) was restricted by \tilde{S}_{xy} symmetry, and one of its eigenvectors had to be parallel to \vec{e}_{45° . That restriction is lifted when S_{xy} symmetry is broken by $\alpha \neq 45^\circ$, and we choose

$$\alpha = 54^\circ \quad (4.40)$$

since we have already explored this value in detail, cf. figure 4.18 and figure 4.24. The main features of interest are

1. For a between 6 and 8, SSBT attractors transporting parallel to the x axis alternate with bounded attractors, which are replaced by attractors transporting parallel \vec{e}_{45° for $\vec{F} \neq 0$.
2. For certain a values between 2 and 6 and $\vec{F} \neq 0$ there are quasiperiodic attractors transporting parallel to the y axis.

Arbitrarily strong anisotropic diffusion parallel to the x axis will be the result of the SSBT attractors and works along the same lines as discussed in section 4.11.1. The attractors

⁵⁴E.g., particles that differ by their radii, and thus friction coefficients, correspond to different values of Ω in the dynamics (4.9). If they furthermore differ by their interaction with the periodic drive, both parameters a and Ω are different for the particles. Another variant are particles that differ in their interaction with the periodic potential, i.e. their differences can be encoded into a prefactor \tilde{u} before the $\vec{\nabla} \tilde{U}_{\text{Yukawa}}(\vec{r}(t))$ term in (4.9). \tilde{u} can be absorbed into the units of the drive amplitude and the unit of time, and in the units of (4.9), one gets $\Omega(u) = \frac{\Omega_0}{\tilde{u}}$, $a(u) = \frac{a_0}{\tilde{u}}$, $F(u) = \frac{F_0}{\tilde{u}}$ and $\Gamma(u) = \frac{\Gamma_0}{\tilde{u}}$ where the parameters with subscript 0 are the parameters before \tilde{u} is absorbed. Hence, the parameters in the units of (4.9) of such particles lie on lines passing through the origin of the a - Ω plane and their response spectra will be more akin to panels (a)-(c) than (d)-(f) of figure 4.27.

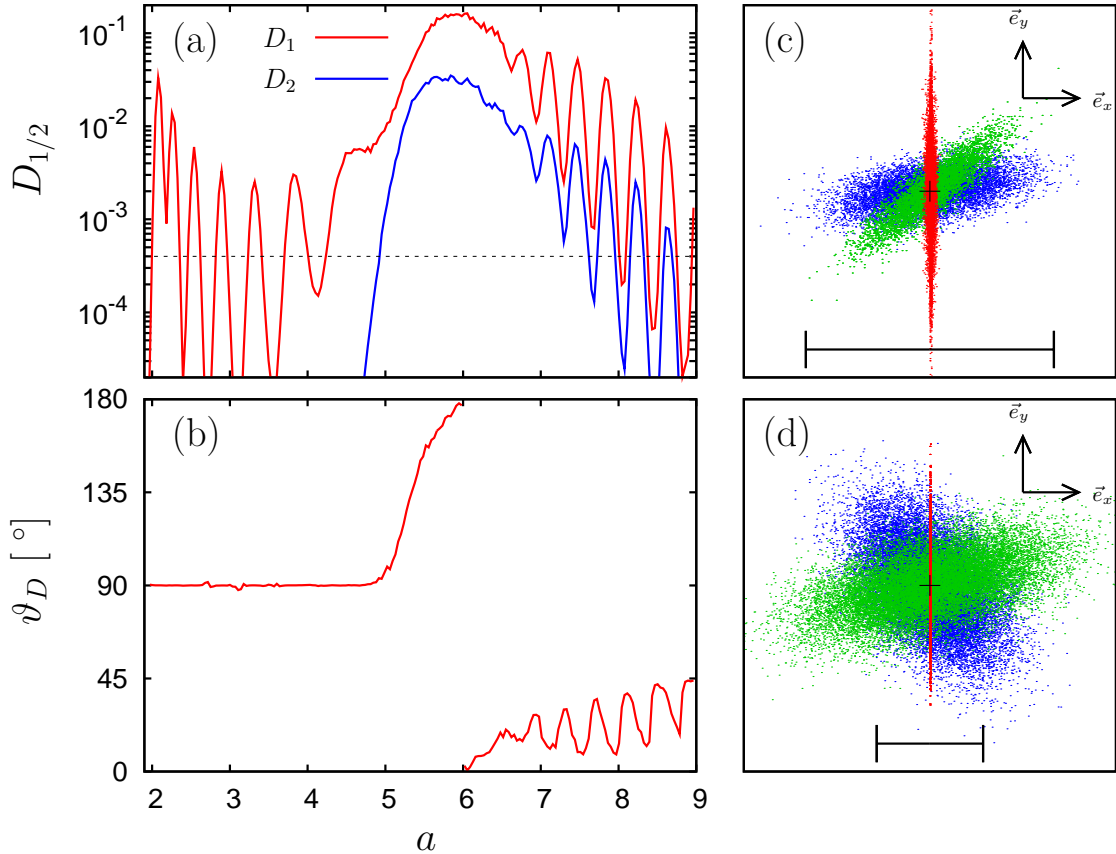


Figure 4.28: (a) Diffusion coefficients D_1 and D_2 as defined in (4.32) for the dynamics (4.9) with $\vec{F} = 0$, $\alpha = 54^\circ$, $\Omega = 1$ and $\Gamma = 4 \cdot 10^{-4}$. The diffusion coefficients have been obtained from a sample of 750 trajectories of length 15000 drive periods each. The plotting range has been restricted since smaller values of $D_{1/2}$ are not correctly obtained from our sample size, i.e. $D_{1/2} = 0$ if the curve is not visible. The rate of free diffusion, Γ , is shown as a dashed line. (b) ϑ_D , as defined in (4.32), for the same dynamics as in (a). (c) Sample particle distributions for the same dynamics as in (a) and (red) $a = 4.74$; (blue) $a = 7.94$; (green) $a = 8.58$. (d) Same as in (c) but different scale and (red) $a = 2.08$; (blue) $a = 5.3$; (green) $a = 6.73$. In (c)-(d), the positions at time $15000 \cdot T$ of 10000 particles initialized at the origin are shown, the origin is indicated by the black cross and a length of 100 elementary cells is indicated by the bar.

transporting parallel to the y axis and parallel to \vec{e}_{45° are similar⁵⁵, and quasiperiodic transport parallel to the y axis with broken S_0 symmetry has been investigated in detail in section 4.17. With respect to diffusion, it is akin to the diffusion of overdamped particles in one dimensional dynamics subjected to periodic driving forces [267–269] or a dc driving force [214, 215]. In that context, for small but non-zero noise strengths, diffusion can be significantly stronger than free diffusion at the same noise strength when the dynamics are close to a deterministic bifurcation affecting the particle velocity. In short, and slightly oversimplifying, the mechanism of stronger diffusion is that the noise has to work only a little to overcome a dynamical bottleneck and achieve a significant change of the particle position due to the instability of the dynamics at the bifurcation. In effect, for the parameters for which quasiperiodic transport is expected for $0 < |\vec{F}| \ll 1$, we can expect diffusion to be much stronger parallel to the y axis, i.e. anisotropic, and to be enhanced in comparison with pure thermal diffusion at the considered noise strength. We have verified both behaviors (numerically), arbitrarily strong anisotropic diffusion in the SSBT regime for $\Gamma \rightarrow 0$, and enhanced, by several orders of magnitude (depending on the noise strength and parameters), anisotropic diffusion in the other two cases.

In the spirit of “directing Brownian motion”, a remarkable consequence is that the direction of strong diffusion, i.e. the direction of the eigenvector belonging to the (much) larger eigenvalue of \mathbf{D} , can be selected by changing only the drive amplitude a (or another parameter, cf. figure 4.18 and figure 4.24). The two mechanisms of diffusion are very different. Diffusion due to SSBT is most effective at $\Gamma = 0$, while diffusion due to quasiperiodic transport is absent at $\Gamma = 0$ and most efficient at some optimum value of Γ . The difficulty is to choose the remaining parameters, i.e. Γ , Ω and a such that both mechanisms work reasonably, and, for practical purposes, result in comparable diffusion coefficients.

We have found $\Gamma = 4 \cdot 10^{-4}$ and $\Omega = 1$ to be a convenient choice for that purpose⁵⁶. The spectrum of diffusion behavior thus obtained is shown in figure 4.28. Roughly, there are three regimes. For small values of a , diffusion with $\vartheta_D = 90^\circ$ is found for certain a values and D_2 is always practically zero. The maximum D_1 values are about one order of magnitude smaller than in the other two regimes. When a approaches the region of deterministic SSBT, both diffusion coefficients increase significantly and ϑ_D “rotates” to $\vartheta_D \approx 0^\circ$. At the lower border of the deterministic SSBT region, around $a \approx 6$, the largest values of D_1 are found. The third regime, starting at $a \approx 6.5$, corresponds to the parameter range where deterministic SSBT regions and bounded attractors, or, with a

⁵⁵We have verified $\vartheta = 45^\circ$ transport to be created along the same lines as the quasiperiodic transport discussed in section 4.17, i.e. at $\vec{F} = 0$ there is a pitchfork bifurcation of a non-transporting periodic orbit, which splits into two tangent bifurcations (avoided pitchfork bifurcations [115]) when $\vec{F} \neq 0$. The tangent bifurcations “move” apart when the modulus of \vec{F} is increased, and at a “critical” \vec{F} value, a “gap” between the tangent bifurcations is created. In that gap, a non-periodic attractor with a continuously varying (with the bifurcation parameter) average velocity locked to $\vartheta = 45^\circ$ is found. We have not investigated whether that attractor is quasiperiodic or chaotic, since we do not believe that to be essential. Since the mechanism of its creation is the same as in section 4.17, we believe it to be quasiperiodic.

⁵⁶If a larger value of Ω is chosen, the $\vartheta = 45^\circ$ transporting regime is less pronounced, but the SSBT with $\vartheta = 0^\circ$ is more pronounced, cf. figure 4.18, and similar results can be obtained. We have not investigated smaller values of Ω . For other values of Γ , $10^{-4} < \Gamma < 10^{-3}$, we have obtained qualitatively similar results.

non-zero bias force, attractors with transport parallel to \vec{e}_{45° , alternate with increasing a . Thus, ϑ_D oscillates roughly between 0° and 45° and the diffusion coefficients oscillate likewise. Since SSBT is not found for $a > 8$, the oscillations of ϑ_D no longer reach 0° for larger a values. The deterministic pattern of symmetry breaking bifurcations, as shown in figure 4.2, is behind the oscillations of the properties of \mathbf{D} for $a > 8$.

Figure 4.28(a)-(b) enables us to choose a few exemplary a values such that each corresponds to a different direction of diffusion, and the magnitudes of the concomitant D_1 values are comparable. The result is found in figure 4.28(c)-(d). An immediate application would be to “direct” particles by diffusion, similar to section 4.21. Without changing any inherent direction of the dynamics, the interplay of the deterministic directions and noise enables us to control the direction of strong diffusion. In an experiment with a finite sample size, the particle distributions shown in figure 4.28(c)-(d) would mean that, depending on the a value, the different particle species would leave the sample at different places, i.e. are separated. If different particle species have (significantly) different diffusion coefficients, they can also be separated since the “faster” particle species will leave the sample (by diffusion) much earlier than the first.

According to figure 4.18 and figure 4.24, diffusive separation along the lines of this section is not restricted to particles that “differ” in their values of a .

Lastly, an interesting diffusion behavior can be constructed if the potential is not \hat{S}_{xy} symmetric such that the potential barrier orthogonal to the direction of SSBT is smaller than parallel to the direction of SSBT. At large noise strengths, and often when no SSBT is present, diffusion will then be enhanced along the lower potential barriers. Conversely, at low noise strengths and in the presence of SSBT, diffusion will be enhanced along to the direction of SSBT. In effect, the preferred direction of diffusion changes with temperature, but also with other system parameters affecting SSBT. Such behavior can be exploited for sorting purposes along similar lines as discussed in this section. We have verified this for a suitable model⁵⁷ and have indeed found the effect as expected.

4.23 Some possible experimental realizations

First, our conclusions are of a general nature and apply to various overdamped⁵⁸ dynamics of Brownian particles on periodic and symmetric (or slightly asymmetric) surfaces subjected to periodic and symmetric (or slightly asymmetric) driving forces. Such dynamics are given by, e.g., vortices in superconducting films with pinning sites [223–228], possibly making use of multiple vortex layers [230, 231], atoms on crystalline surfaces [182, 183, 208, 270], optical lattices [18, 23–25, 27, 28, 189, 190, 271–276], motor proteins (see chapter 6), magnetic potentials subjected to periodic magnetic fields [105, 106, 185, 218, 220, 277], rings of several Josephson junctions [107, 278, 279], colloids or DNA in microfluidic devices [280, 281] (square lattice geometries), [25, 61, 62, 282, 283] (symmetric lattices of lower symmetry), see also [4, 5] for further examples. We will con-

⁵⁷We have considered $U(x, y) = \cos(x) \cos(y) + \kappa_{xx} \cdot \cos(x) + \kappa_y \cdot \cos(y)$ and a sine drive protocol. For $\kappa_x < \kappa_y$, the potential is not \hat{S}_{xy} symmetric, the potential barrier in the y direction is lower than in the x direction, and the dynamics exhibit SSBT transverse to the x direction for $\alpha = 45^\circ$.

⁵⁸Preliminary results indicate that dynamics with inertia yield similar results, and nothing else is to be expected. In particular, SSBT seems to be somewhat more robust in not overdamped dynamics due to the inherent locking mechanism, see chapter 3.

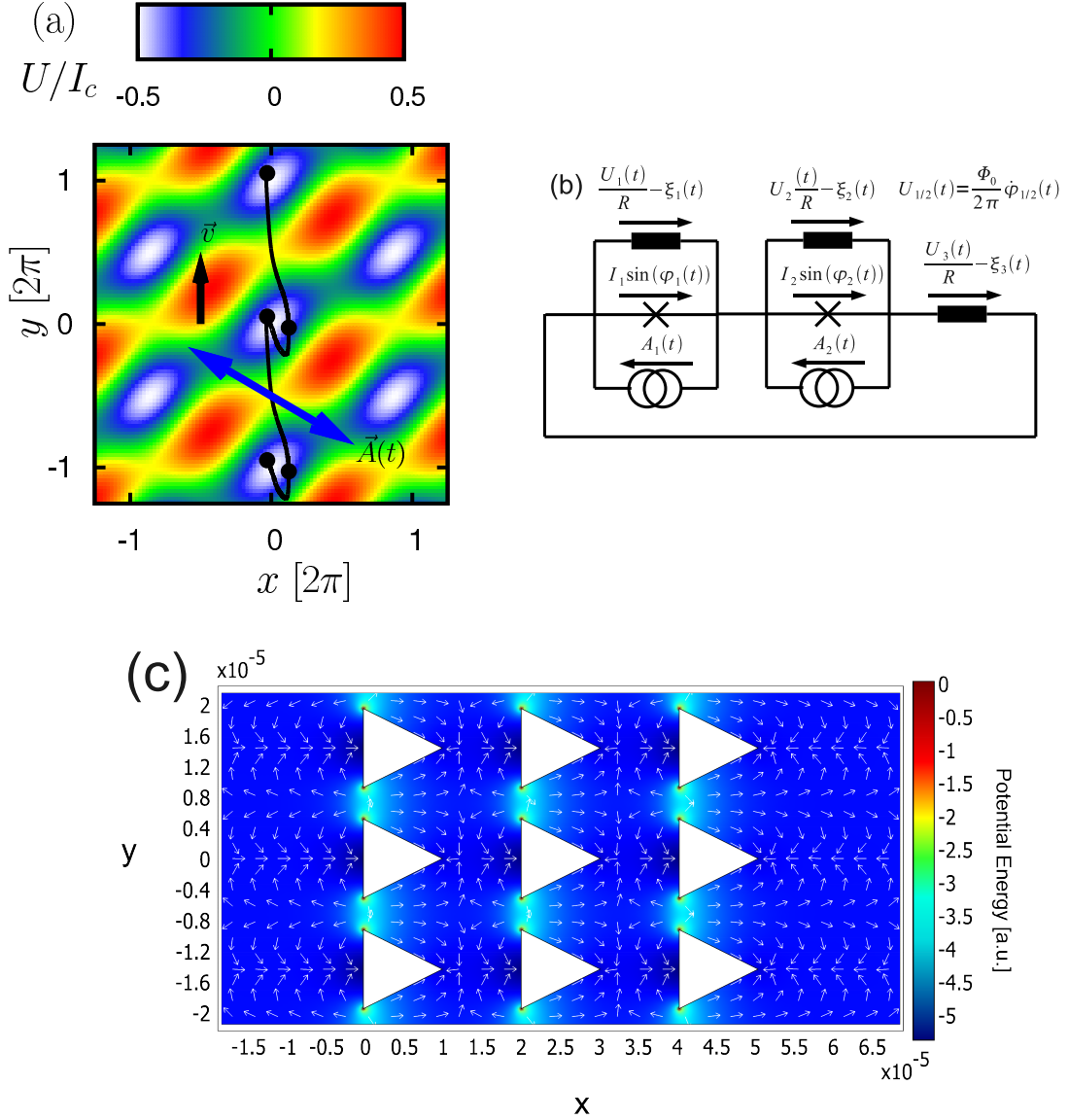


Figure 4.29: (a) Potential (4.68) for $I_2 = 2I_1$ normalized to $I_c = 286 \mu\text{A}$. The direction of the sinusoidal drive is indicated by the blue double arrow. A sample SSBT trajectory on a period 1 attractor is shown in black for 2 periods of the periodic drive. The time instants at which the drive changes sign are indicated by black dots, and the direction of the average velocity is indicated by the black arrow. (b) equivalent circuit of two resistively coupled Josephson junctions with negligible capacitances modeled in the RSJ model. The junction critical currents are $I_{1/2}$, the phase differences of the superconducting phases $\varphi_{1/2}(t)$ and the voltage drops across the junctions are $U_{1/2}(t)$. All resistors have resistance R , and the noise due to the resistors is denoted as $\xi_i(t)$. The bias currents are denoted as $A_{1/2}(t)$. The currents through each element of the circuit are indicated by their symbols and an arrow indicating the direction of a positive current. (c) Sample dielectrophoretic potential in an asymmetric microfluidic post array. x and y are given in meters. The figure was provided by Lukas Bogunovic, Universität Bielefeld [66].

sider two example realizations in more detail in the following: microfluidic devices and coupled Josephson junctions.

Microfluidic devices

In microfluidic devices, post arrays and dielectrophoresis (due to high frequency ac electric fields) may be used to generate suitable potentials [62, 66, 280]. An example dielectrophoretic potential generated by an ac field⁵⁹ in an asymmetric device is shown in figure 4.29(c) [66]. The advantage is that electrophoresis and electroosmosis [6] are averaged out due to the high ac frequency. Superimposing a slowly varying electric field or a hydrodynamic flow, the required periodic driving force could be generated. In the shown device, the driving would be parallel to the x axis. We have shown that if the drive is in a symmetry direction of the lattice, the observed SSBT induced effects are weaker than if the drive is in not in a symmetry direction. In an appropriate symmetric device, a more general direction of the drive can be obtained by tilting the lattice during the design process as in [86]. While such a setup would be far from the simple model considered in this work, we expect SSBT to be found in such a device if thermal fluctuations are sufficiently small compared to the dielectrophoretic potential. E.g., in such a device, an ensemble of different particles could be sorted simultaneously⁶⁰ (cf. figure 4.27 and figure 4.18, different particle species could have different sizes, polarizabilities etc., resulting in various ways of sampling through parameter space, e.g. figure 4.18) or ANM of particles could be observed. The main requirement is that diffusion is sufficiently weak, i.e. dielectrophoretic trapping has to be so strong that diffusion is completely suppressed on the time scale of the drive providing the ac driving of the particle.

Magnetic bubble lattices

SSBT has been observed experimentally for magnetic beads in a symmetric magnetic bubble lattice potential [105, 106, 185, 220] for a circular driving force and hexagonal lattice symmetry. Introducing an asymmetry into such dynamics, simultaneous one stage separation of more than two particle species should be possible, and if that asymmetry is a bias force, ANM should be observable for suitable parameters.

Coupled Josephson junctions

The dynamics of a superconducting ring containing three resistively shunted Josephson junctions can be mapped onto the dynamics of an overdamped particle in a hexagonal lattice [107], i.e. a similar system. We have observed SSBT and ANM for these dynamics. The model can be simplified by removing one of the junctions but keeping its resistor, yielding two resistively coupled Josephson junctions [278, 279], see figure 4.29(c) for an illustration of the setup. Using the same mapping as in [107], the dynamics of the resistively coupled junctions can be mapped onto that of an overdamped particle in a

⁵⁹The form of the potential does not depend on the frequency of the ac field, while the absolute values do [6]. Experimentally, the situation is more complicated. E.g. different particles with different polarizability properties “see” different potentials, depending on the ac frequency [6, 66].

⁶⁰Using ratchet effects, different particle species were sorted in the same device, but slightly differently, see footnote 21 in chapter 1.

symmetric oblique lattice (parallelogram lattice). Again, we have found SSBT and ANM for these dynamics. As an example, we show the potential for two Josephson junctions with different critical currents in figure 4.29(a), together with a sample period 1 SSBT orbit. The equations of motion can be derived from the equivalent circuit shown in figure 4.29(b), see section 4.25.8.

In an experiment, one major difficulty in building such a device is the direction of the driving force. To control the direction of the driving force, the two junctions have to be fed with different ac currents, i.e. microwaves, which is experimentally difficult [284]. The simplest setup yielding SSBT with reasonably large regions of stability in parameter space (that we have found) is if the second junction is fed with the same signal as the first junction, but its phase shifted by one half period. The microwave signal could be generated from one microwave source coupled with opposite polarities to each junction. In that case, the dynamics are very similar to the dynamics considered throughout this chapter, and we therefore do not show the results in detail. The sizes of the regions of existence of SSBT and ANM attractors are comparable to the dynamics (4.9)⁶¹, but their symmetry properties are somewhat different due to the reduced lattice symmetry. The same applies to the observed noise resistivities. We have neglected the correlations between the components of the noise process, but we do not expect significant differences if the correlations are accounted for.

From the transformations (4.67), one readily obtains the relation between the particle mobility and the current voltage behavior of the junctions⁶². One main result is that a negative scalar product of bias force and average particle velocity, which is typical for ANM (see figure 4.26), implies a negative scalar product of the vectors of the bias currents $\vec{I}_{dc} = (I_{dc,1}, I_{dc,2})$ ⁶³ and the voltage drops $\vec{U} = \langle (U_1(t), U_2(t)) \rangle$ across the junctions, i.e. negative absolute resistance (see [3] and chapter 3). E.g., for the parameters corresponding to the SSBT solution shown in figure 4.29(a), the voltage drop across the second junction is zero, and the first junction operates on a zero crossing Shapiro step. First, if a bias current is applied to the first junction (and the remaining parameters are suitable, e.g. at the right border of the regions of existence of the SSBT attractors), the voltage drop across the junction and the bias current will have opposite signs, and the same conclusions as in [3] apply to the junction. The circuit may be used as a resistor which can be “switched” between positive and negative resistance by adjusting an easily accessible external control parameter (e.g. the frequency or amplitude of the microwave signal or an externally applied magnetic field) [3]. Moreover, due to the two dimensional

⁶¹The shape of the regions of existence is rather similar to those found for two interacting overdamped particles, see chapter 6, figure 6.2.

⁶²The bias force applied to the overdamped particle is, cf. section 4.25.8, $\vec{F} = B_{AI} \vec{I}_{dc}$ (B_{AI} is defined in section 4.25.8, $\vec{I}_{dc} = (I_{dc,1}, I_{dc,2})$, and $I_{dc,1/2}$ are constant bias currents added to $A_{1/2}(t)$). We write the average particle velocity as $\vec{v} = \langle (\dot{x}, \dot{y}) \rangle$ (i.e. as (4.10), but without the normalization) and the vector of the voltage drop across the junctions is $\vec{U} = \langle (U_1(t), U_2(t)) \rangle$ (note that \vec{U} has nothing to do with the potential U , but we use the same letter for both). Thus,

$$\vec{I} \cdot \vec{U} = (B_{AI}^{-1} \vec{F}) \cdot (B_{r\varphi} \vec{v}) = \vec{F} \cdot (B_{AI}^{-1 t} B_{r\varphi}^{-1} \vec{v}) = 2 \vec{F} \cdot \vec{v}. \quad (4.41)$$

Using (4.41), the zero bias resistance and the zero bias mobility are found to be similar [96, 102], with $B_{AI}^{-1} = \frac{1}{2} B_{r\varphi}^t$ being the change of basis matrix.

⁶³ $I_{dc,1/2}$ are constant bias currents added to $A_{1/2}(t)$.

nature of the device, it would effectively act as two such resistors. Depending on the external parameters, either junction may be a positive or a negative resistor⁶⁴. Second, without the coupling there are no zero crossing Shapiro steps [1], which are used in zero bias voltage standards [155]. Hence, (arrays of) capacitively shunted junctions (i.e. junctions with a nonnegligible capacitance) are used in [137, 155]. “Our” device would allow resistively shunted junctions with negligible capacitances to be used in a zero bias voltage standard.

We can estimate the parameters for the ring similar as in [1, 3]. The parameters of figure 4.29(a) are $t_C = \frac{3\Phi_0}{2\pi RI_c}$, $f = \frac{1}{4t_c}$, $A_1(t)/I_c = 0.813 \sin(ft) = -A_2(t)/I_c$, $\frac{I_1+I_2}{I_c} = 1$, $\frac{I_1}{I_2} = 0.5$, and a noise strength of $\Gamma \sim 2 \cdot 10^{-4}$ is needed to obtain reasonable results. For a liquid Helium cooled junction operating at 4.2 K and irradiated by $f = 10$ Ghz microwaves, the sum of the critical currents is $I_c = \frac{k_B T}{\Gamma} \cdot \frac{2\pi}{3\Phi_0} \approx 286 \mu\text{A}$. For the resistors, we obtain $R = \frac{3\Phi_0}{2\pi I_c} 4f \approx 0.13 \frac{\text{V}}{\text{A}}$ (Ohm). The junction capacitances have to be sufficiently small to reach the overdamped operating regime. For a desired McCumber parameter [3] smaller than 0.1, the capacitances have to be smaller than 6 pF. The ring inductance would have to be as small as possible, smaller than 1 pH. Comparing with [3, 285], it should be possible to realize such a setup with similar methods.

4.24 Summary and outlook

We have shown that SSBT can be found in the spatially two dimensional overdamped dynamics of Brownian particles. Thus, the ANM related effects discussed in [1, 2] can indeed be realized in a spatially two dimensional but overdamped dynamics. To that end, the necessary degree of freedom, inertia, can be replaced by a second spatial coordinate. This leads to the natural extension of absolute negative mobility, “directing Brownian motion” on a surface, which allows a particle to be steered into almost any direction on a periodic surface by controlling only a scalar quantity, i.e. without rotating any inherent direction of the model. Another application is to sort more than two different species of particles simultaneously in one stage on the same substrate. Spontaneous symmetry breaking in the unbiased dynamics is the root of these effects, leading to transport locked to discrete directions in the form of SSBT and quasiperiodic transport together with an applied bias force. Both transport mechanisms lead to transport directions independent of the applied bias force up to a sign. Thermal noise averages between these competing directions and leads to a smooth response spectrum (\vec{v} as a function of some suitable system parameter) containing almost any direction. We have unraveled the mechanisms leading to SSBT at arbitrary angles of the periodic driving force and to locked quasiperiodic transport. Which transport mechanism is at work for a given set of system parameters, and its direction, depends on all parameters in a nontrivial manner. Transport into almost any direction can be achieved by selecting a suitable transport region in parameter space and varying only one parameter.

In addition to the results presented in this chapter, we have found SSBT to be robust against variations of the form of the drive, the potential and the inclusion of inertia forces.

⁶⁴To obtain suitable junction parameters, a more exhaustive search of parameter space would be necessary. We have obtained the described situation when both junctions were driven in a more general direction, i.e. the drive direction of the particle is not in a lattice direction.

In that case, the mechanism leading to SSBT in the one dimensional dynamics can be carried over to the spatially two dimensional dynamics, trivially so if the drive is parallel to a stable linear invariant manifold. If the drive is not in such a “trivial” direction, preliminary results show that the interplay between the different mechanisms leading to SSBT leads to a similarly rich dynamics, and that the picture remains qualitatively the same.

Dynamics with different symmetry properties, in particular other lattice symmetries, offer intriguing new possibilities. E.g. the hexagonal symmetry considered in [105, 106, 185, 220] leads to SSBT with all six lattice directions, which might further improve the control of the particle. While the structure of transporting attractors will be different for different symmetries, we expect our results to be robust in that case. Another important generalization of our model are ratchets with weakly perturbed symmetry. In that context, we expect the interplay of SSBT and locked quasiperiodic attractors with the ratchet symmetry breaking to allow for “directing Brownian motion” in a similar manner.

The spatially one dimensional overdamped dynamics of two coupled particles can be considered as a generalization of our model in the sense that the symmetry of one coordinate, the distance of the particles, is reduced because it is no longer periodic, but the phase space dimension remains the same. In particular, the experimentally important dynamics of an ac SQUID (a superconducting ring containing two Josephson junctions) modeled by the resistively shunted junction (RSJ) model [285] fall into this category. These dynamics will be discussed in chapter 6. Quenched disorder is another generalization, the most dramatic consequence being disorder induced absolute negative mobility, see chapter 5.

4.25 Appendix

4.25.1 Bessel function approximation

We have carried out the approximation only for a cosine drive protocol, since that is easier than for a square wave drive protocol (see below on how to extend the approximation). Moreover, we have used the potential

$$U(x, y) = \cos(x) \cos(y) + \kappa (\cos(x) + \cos(y)) \quad (4.42)$$

which corresponds to keeping only the lowest order terms of the Fourier sum of the potential (4.2) (see [193, 286] for similar simplifications with respect to the periodic potential) since the computations cannot be done reasonably for the Yukawa or Gauss square lattice potential considered in the remainder of this chapter. Thus, the equations of motion are

$$\dot{\vec{r}}(t) = -\vec{\nabla}U(\vec{r}(t)) + a\sqrt{2}\vec{e}_{45^\circ} \cos(\Omega t) \quad (4.43)$$

Basically, the idea is to expand all terms in (4.43) in Fourier series, which is the extension of the Bessel function approximation discussed in 3 and [137]. If either a , Ω or both are large compared to the forces due to the periodic potential, the latter can be treated as a small perturbation in the Fourier expansion. Using the properties of the trigonometric functions involved, namely [287]

$$\sin(a - b \sin(\phi)) = \sum_{k=-\infty}^{+\infty} J_k(b) \sin(a - k\phi) \quad (4.44)$$

$$\cos(a - b \sin(\varphi)) = \sum_{k=-\infty}^{+\infty} J_k(b) \cos(a - k\varphi), \quad (4.45)$$

the corrections to the free oscillation of the particle due to the potential can be calculated if a and Ω are large and $\frac{a}{\Omega} = \mathcal{O}(1)$. The resulting approximate solution takes the form

$$\frac{x(t) + y(t)}{2} = z_1 + \frac{a}{\Omega} \sin(\Omega t) \quad (4.46)$$

$$\frac{x(t) - y(t)}{2} = z_2 \quad (4.47)$$

and (4.46)-(4.47) inserted in to the equation of motion (4.43) yield

$$0 = \sin(z_1) \left(J_0 \left(2 \frac{a}{\Omega} \right) \cos(z_1) + \kappa J_0 \left(\frac{a}{\Omega} \right) \cos(z_2) \right) \quad (4.48)$$

$$0 = \sin(z_2) \left(\cos(z_2) + \kappa J_0 \left(\frac{a}{\Omega} \right) \cos(z_1) \right) \quad (4.49)$$

after averaging over one drive period. Solving (4.48)-(4.49) is straightforward and yields a number of solutions with different symmetry properties. Using the same approximation to calculate the stability properties of the obtained solutions along the lines of [137], i.e. to approximate the Floquet operator, the structure of the equivalent of figure 4.2 for the potential (4.42) can be obtained. In particular, the parameter values of symmetry breaking bifurcations can be obtained, but the (complicated and not shown) equations

have to be solved numerically. At a few example values of κ and Ω , we have verified that the approximation and the numerics agree well.

The approximation can be extended to the square wave drive protocol used here. For brevity, we only estimate the oscillation amplitude \tilde{a} of the approximate solution. We do not account for the different potential here since it does not affect the oscillation amplitude. The approximate solution will then take the form

$$\tilde{x}(t) = x(t) + y(t) = \tilde{x}_0 + \frac{a}{\Omega\pi} \frac{4}{\sqrt{2}} \sum_{k \text{ odd}} \frac{\cos(k\Omega t)}{k^2} \quad (4.50)$$

$$\tilde{y}(t) = x(t) - y(t) = \tilde{y}_0 \quad (4.51)$$

using the Fourier expression of the square wave drive $\text{sgn}(\sin(\Omega t)) = \frac{4}{\pi} \sum_{k \text{ odd}} \frac{\sin(k\Omega t)}{k}$. The oscillation amplitude follows by using $\sum_{k \text{ odd}} \frac{1}{k^2} = \frac{\pi^2}{8}$ [288] (S. 254) as $\tilde{a} = \pi\sqrt{2}\frac{a}{\Omega}$. This can also be obtained by directly integrating the equation of motion of a free particle subjected to a square wave drive yielding the same, but above expressions are useful to carry out the full approximation in the case of a square wave drive protocol. Similarly, the approximation can be extended to arbitrary potentials by extending the potential in a Fourier series.

Lastly, if a is not large, the small oscillations of the particle can be calculated directly by linearizing the force around the potential equilibria.

4.25.2 Creation of SSBT at other values of Ω

The choice of $\Omega = 4$ in section 4.10 is particularly convenient, as the objects involved are stable, and the direction of the bifurcations is such that the process follows the “natural” pattern of creation of new orbits upon increasing a , except for the bifurcation shown in figure 4.7(b_1). For different values of parameters, most notably lower frequencies, this is not the case. I.e. there is no reason why the periodic orbits created at the bifurcation figure 4.7(b_1) need to become stable at any point, nor does the unbounded chaotic object created from these need to be an attractor. Thus, if a chaotic repeller is created, SSBT may occur just as in the case discussed above. But it is much more difficult to analyze the structure of the process in detail due to the unstable nature of the objects involved.

If one chooses different parameters, one gets bifurcation diagrams like the one found in Fig. 4 of [4] for $\Omega = 4.5$, reproduced in figure 4.30. In that case, the bounded attractor loses stability at $\Omega \approx 3.12$ colliding with the orbit corresponding to the one created by the pitchfork bifurcation shown in figure 4.7(b_1). Its remnant is a chaotic repeller [126], having the same properties except for a “leak” through which trajectories escape the object (to periodic orbits on the invariant manifolds (4.20) in this case). At $a \approx 3.2$, the repeller re-collides with the same unstable periodic orbit and the attractor “reappears”. Knowing the underlying mechanism, it is clear what happens in that case.

For clarity, we have reproduced⁶⁵ the chaotic repeller in figure 4.30 (green), along with the relevant unstable periodic orbits (blue). Basically, the mechanism of the creation of

⁶⁵ For the reconstruction of the chaotic repeller, we have used the following method, similar to the method described in [126]. A large (1500) number of trajectories is started close to the chaotic repeller. Specifically, we have initiated the trajectories close to an unstable periodic orbit, which is supposed to be part⁶⁶ of the chaotic repeller (here we have used a cube with sides of length 0.005 centered on the orbit). Of these we show the particle positions at the time instant defined by the stroboscopic map used in the

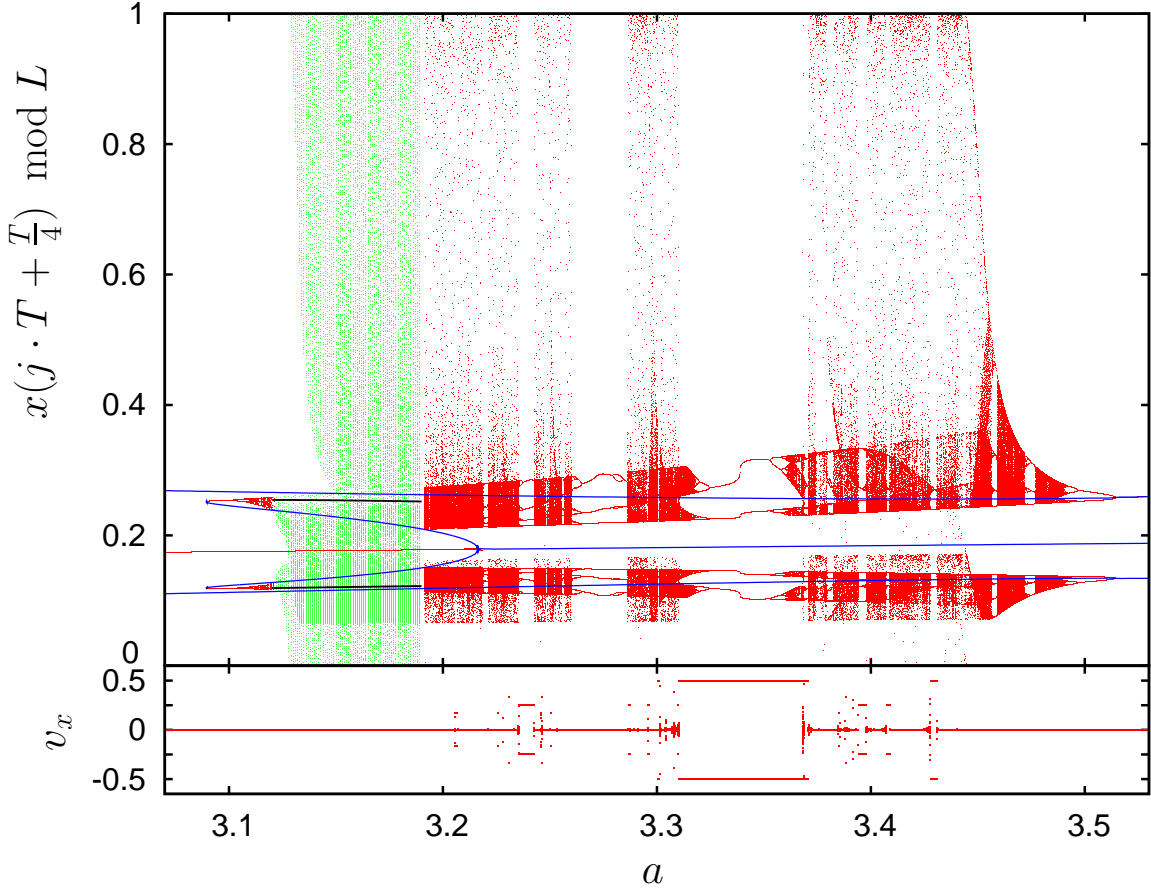


Figure 4.30: Bifurcation diagram showing attractors (red), selected unstable periodic orbits (blue) and two selected chaotic repellers (green). The attractors and unstable periodic orbits have been calculated as in figure 4.7, and the chaotic repeller according to footnote 65 of section 4.25.2. Shown are the particle positions during the first 3 consecutive drive periods of 1500 trajectories starting close (within a cube of length 0.005) to an unstable periodic orbit (shown in black), which is “part” of the chaotic repeller. The unstable periodic orbit is shown in grey. It is “created” at the S_0 symmetry breaking bifurcation at $a \approx 3.1$, corresponding to the bifurcation (b_3) in figure 4.7.

SSBT is the same as for $\Omega = 4$. All relevant bifurcations are recovered, to which the ones involving the “creation” and “destruction” of the chaotic repeller (green) are added. Please note that the weight of phase space is not correctly reproduced by the method used to calculate the repeller. Thus, the vertical frequency of (green) dots in figure 4.30 does not correspond to the weight of the corresponding portion of phase space. In the other parts of the figure, there is a “loose” correspondence. Therefore, the vertical frequencies of dots do not match for the representations of the attractor and the repeller in figure 4.30.

bifurcation diagram until the trajectories have left the repeller. For simplicity (and since our result is largely unaffected), we have used trajectories of a fixed and short length of a few drive periods ($3T$). While the method reproduces the portion of phase-space occupied by the repeller, the weight (i.e. the frequency of visits by the trajectories) of these regions is not correctly reproduced since the choice of the periodic orbit and the length of the trajectories is arbitrary.

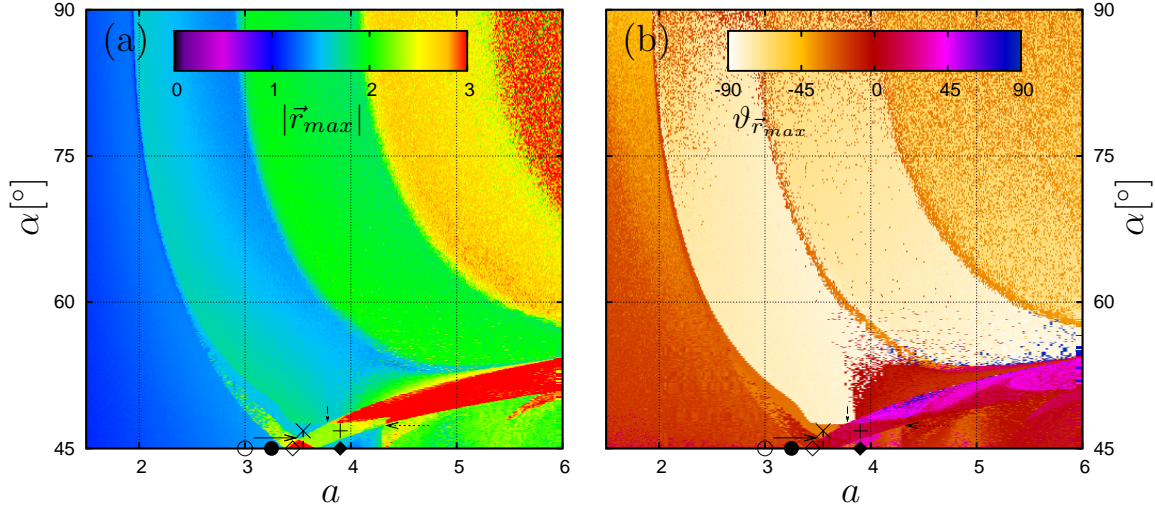


Figure 4.31: (a) maximum transient length $|\vec{r}_{max}|$ and (b) angle $\vartheta_{\vec{r}_{max}}$ obtained for the same dynamics and by the same method as in figure 4.15. A larger region of parameter space is shown.

4.25.3 Spatially 1D dynamics

This section is complementary to section 4.14. To understand the nature of the “meeting point” of the right arm of larger $|\vec{r}_{max}|$ belonging to the red triangle in figure 4.15 and the “critical” line coming from $\alpha = 90^\circ$, marked by a dashed arrow in figure 4.15, we have to digress towards $\alpha = 90^\circ$. The extension of figure 4.15 to $\alpha = 90^\circ$ is shown in figure 4.31

First, we consider the dynamics on the attracting invariant manifold $x = 0$ (and its copies due to the periodicity of the potential) of the dynamics (4.9) with $\alpha = 90^\circ$. In short, the behavior is as follows: for small drive amplitudes a , the particle oscillates around the minima with increasing oscillation amplitudes for increasing drive amplitudes. The corresponding periodic attractors are separated by unstable periodic orbits corresponding to S_0 symmetric oscillations around the saddles of the potential. I.e. there is one stable period 1 attractor and an unstable period 1 orbit, both S_0 symmetric. At some critical a value, the oscillations around the minima and the oscillations around the saddle exchange stability via a possibly degenerated pitchfork (symmetry breaking) bifurcation [162, 163] without changing periodicity. Upon further increasing the drive amplitude, this exchange of stability is reversed in another possibly degenerated pitchfork bifurcation. This process repeats ad infinitum. The corresponding oscillations simply grow in amplitude just as in the cases considered before. A detailed analysis including analytical proofs is found in [162, 163] for a similar system. We have found the same qualitative behavior for the system (4.9). In particular, the bifurcations are degenerated within the precision of our numerics. Since degenerate pitchfork bifurcations are limiting cases of ordinary pitchfork bifurcations, we do not further consider this particularity of the dynamics.

The crucial point is that due to these bifurcations, when embedded in the full three dimensional phase space of (4.9), the unstable manifolds of some periodic orbits are connected to other periodic orbits in different elementary cells. We will call this configuration of the unstable manifold henceforth a *connection*. We consider the first of these

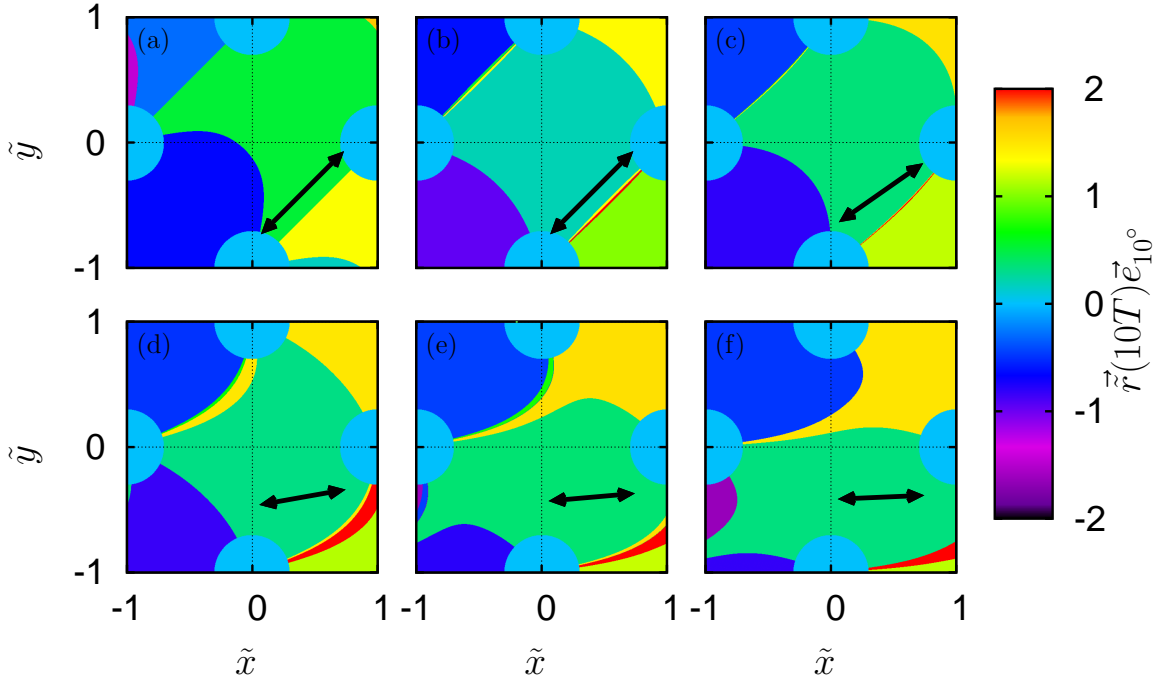


Figure 4.32: Basins of attraction of non-transporting period 1 attractors for the dynamics (4.9) at $\Omega = 4$, $\vec{F} = 0$, (a) $\alpha = 90^\circ$, $a = 1.9$, (b) $\alpha = 90^\circ$, $a = 2.2$, (c) $\alpha = 80^\circ$, $a = 2.55$, (d) $\alpha = 55^\circ$, $a = 3.05$, (e) $\alpha = 50^\circ$, $a = 3.55$ and (f) $\alpha = 47.43^\circ$, $a = 3.55$. The basins of attraction are displayed by colors representing the scalar product of the final particle coordinate after 10 drive periods with a suitably chosen vector (i.e. one not invariant under any symmetry), see the legend. The black double arrow indicates the direction of the periodic drive.

bifurcations, i.e. the one occurring for the smallest drive amplitude at $a \approx 1.95$ (and $\alpha = 90^\circ$). Prior to the bifurcation, the basins of attraction have roughly the form of distorted squares, see figure 4.32(a), and are the continuation to $a > 0$ of the basins of attraction of the potential wells at $a = 0$ which are exactly squares. Due to the periodic drive, the squares are distorted to the forms found in figure 4.32(a)⁶⁷.

After the bifurcation, the basins of attraction of each copy of the periodic attractor extend into the area of neighboring copies by a narrow stripe along the invariant manifold $x = 0$. Due to the singularity of the potential (4.3), we have not calculated the basins of attraction close to the singularity, where we expect these stripes to be connected to the main part of the basin of attraction. We infer this by comparison with the dynamics in the potential (4.4) which is very similar (see figure 4.4 and figure 4.42) and for which the corresponding basins of attraction are shown in figure 4.33. Using this system at a larger frequency to reduce the phase space volume contraction of the stroboscopic map used, the exact location of basin boundaries can be obtained, in particular the connectedness of the basins of attraction, see figure 4.34⁶⁸. Therefore, this bifurcation leads to a pair

⁶⁷Note that the squares are rotated since we are using the rotated coordinate frame in figure 4.32.

⁶⁸At the frequency used in figure 4.33, the stroboscopic map is strongly dissipative, and most initial conditions are mapped to the periodic attractor (within numerical precision) by one iteration of the map. This, together with the symmetry of the system, leads to the fixed point of the map corresponding to

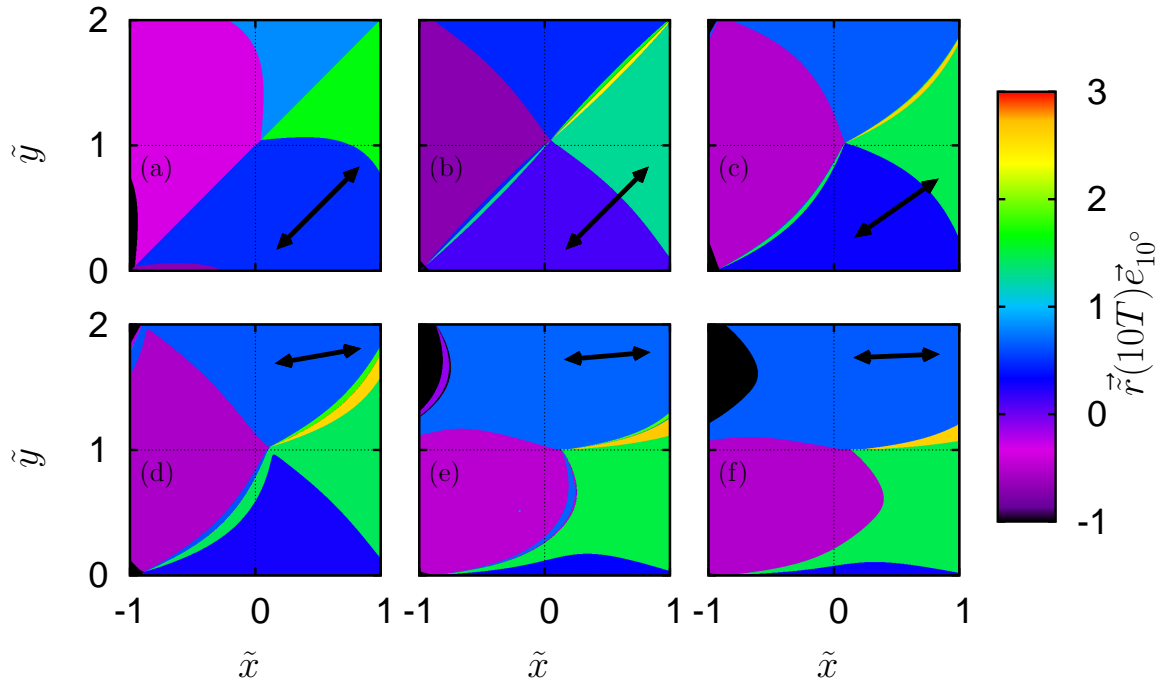


Figure 4.33: Basins of attraction of non-transporting period 1 attractors for the same dynamics as (4.9), but the potential (4.4) ($\sigma = 0.25$, $u = 1$) at $\Omega = 0.3$, $\vec{F} = 0$, (a) $\alpha = 90^\circ$, $a = 0.178$, (b) $\alpha = 90^\circ$, $a = 0.189$, (c) $\alpha = 60^\circ$, $a = 0.25$, (d) $\alpha = 60^\circ$, $a = 0.33$, (e) $\alpha = 47^\circ$, $a = 0.33$ and (f) $\alpha = 46.3^\circ$, $a = 0.33$. The basins of attraction are displayed as in figure 4.32, see also the legend. The black double arrow indicates the direction of the periodic drive.

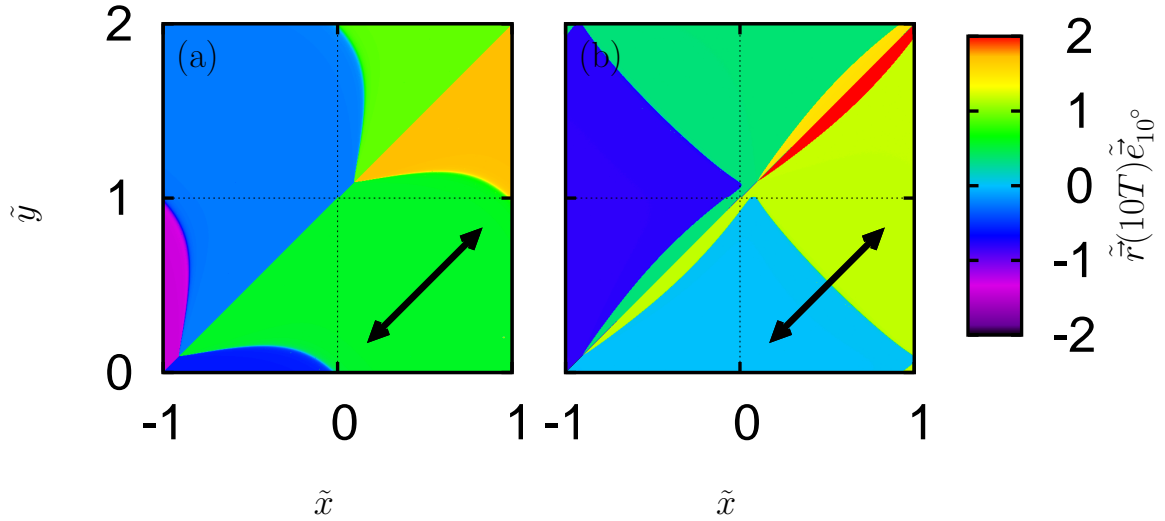


Figure 4.34: Basins of attraction of non-transporting period 1 attractors for the same dynamics as (4.9), but the potential (4.4) ($\sigma = 0.25$, $u = 1$) at $\Omega = 1$, $\vec{F} = 0$, $\alpha = 90^\circ$, (a) $a = 0.35$ and (b) $a = 0.36$. The basins of attraction are displayed as in figure 4.32, see also the legend. The black double arrow indicates the direction of the periodic drive.

of connections forming between different elementary cells (of the unrotated coordinate frame). Again, there are two connections due to symmetry, S_y symmetry in this case. These connections are different from the connections considered so far in that there is no deterministic chaos found in phase space⁶⁹.

Upon breaking S_y symmetry by letting $\alpha < 90^\circ$, the degeneracy of the pitchfork bifurcation is lifted and avoided nondegenerate pitchfork bifurcations result [115, 162, 163]. Then, there are two bifurcations leading to connections for two different a values, each corresponding to one connection, as has been discussed above. We now focus on the second of these lines, found at slightly larger a values than the first. At the “meeting point” marked by a dashed arrow in figure 4.15, this line meets the border of the “right” arm projecting out of the “red triangle” of SSBT at $\alpha = 45^\circ$. The transients now have a direction of $\vartheta_{\vec{r}_{max}} \approx 45^\circ$, i.e. are in the x direction. As can be inferred by comparison with figure 4.16, SSBT in the x direction is found within this region of “large transients” which is particularly important for applications.

4.25.4 Phase space structure of transport

This section is complementary to section 4.14 and contains a more detailed analysis of the phase space structure in the parameter space regions responsible for SSBT and the connection of SSBT at $\alpha = 45^\circ$ and $\alpha \neq 45^\circ$. We start with figure 4.35 which shows the elementary cell of the rotated coordinate frame for various representative parameters indicated by symbols in figure 4.15. For each initial condition (seed), the distance of the start point and the end point of a finite-time trajectory initiated at this seed is shown. The time (length of the trajectories) is 3 drive periods T . The distance is shown in colors. Black (apart from the regions around the potential maxima) corresponds to small distances close to 0. The distance is exactly zero if the trajectory is initiated on a non-transporting periodic orbit with a period of which 3 is a multiple. By considering the portions of phase space which are “smoothly” connected in these plots (i.e. the color varies smoothly), the basins of attraction of the attractors are obtained. Moreover, the smoothness of these colors indicates the nature of phase space. Transient chaos is indicated by a wildly varying and fractal structure, and regions of phase space which are transported into other elementary cells are shown by colors corresponding to larger distances.

First, we first consider $\alpha = 45^\circ$ to obtain a picture of “known” phase space to compare with. Figure 4.35(a) corresponds to $\alpha = 45^\circ$ and $a = 3$, for which there is only a \tilde{S}_{xy} and \tilde{S}_0 symmetric attractor, see figure 4.7. There are 2 points in the plot corresponding to 0 distance, but the second is just the image of the first under \tilde{S}_{xy} and lies in the “other half” of the elementary cell (the upper border $\tilde{y} = 1$ is not part of the elementary cell).

the unstable periodic orbit oscillating on the potential hill appearing to have 4 invariant manifolds, 2 of which do not really belong to the fixed point, as can be inferred from figure 4.34. Therefore, the basin boundaries formed by these invariant manifolds could not be calculated reliably due to the limited resolution of the numerics, in particular the bilinear interpolation used for the force field. At a larger frequency the dissipativeness, i.e. volume contraction, of the map is reduced, lifting these problems.

⁶⁹Note that we have not shown that any of the connections is tied to deterministic chaos. But the periodic orbits involved in the connections considered so far are “parts” of chaotic attractors or repellers, and therefore it is possible that their presence already implies chaos, e.g. their invariant feature tangles or similar features of deterministic chaos [118].

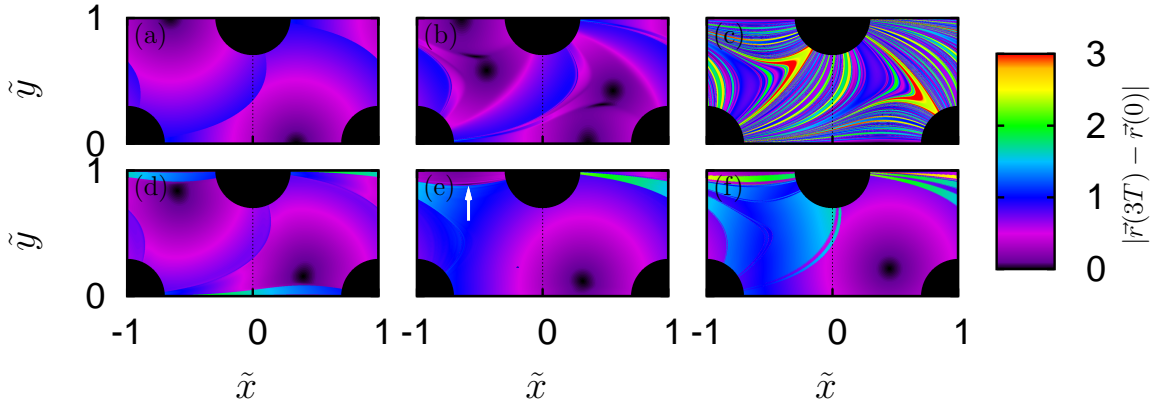


Figure 4.35: Distance $|\vec{r}(3T) - \vec{r}(0)|$ of the particle position after 3 drive periods T from its initial condition encoded in colors and for the same dynamics as considered in figure 4.15. The color palette is the same as in figure 4.15. The regions immediately around the potential maxima are painted in black, as there the forces due to the potential gradient are so large that this region of phase space is inaccessible for trajectories starting anywhere else. Parameters are the same as in figure 4.15, except for a and α : (a) $a = 3.0$, $\alpha = 45^\circ$ (empty circle), (b) $a = 3.25$, $\alpha = 45^\circ$ (filled circle), (c) $a = 3.45$, $\alpha = 45^\circ$ (empty diamond), (d) $a = 3.9$, $\alpha = 45^\circ$ (filled diamond), (e) $a = 3.55$, $\alpha = 46.8^\circ$ (plus) and (f) $a = 3.9$, $\alpha = 46.8^\circ$ (cross). The symbols in brackets correspond to the symbols in figure 4.15.

The basins of attraction of both attractors are clearly separated by a separatrix and have a “regular” structure.

Upon increasing a with $\alpha = 45^\circ$ fixed, a pair of \tilde{S}_{xy} symmetry breaking attractors is created, see again figure 4.7. They are shown in figure 4.35(b) for $a = 3.25$. The unstable periodic orbit, whose invariant manifolds form the separatrix separating these attractors is also visible as a “flat” black region on the separatrix. In figure 4.35(b), phase space has obtained a more complicated structure than in figure 4.35(a), but we have not found (upon magnification) fractal structures, e.g. sensitive dependence on initial conditions on a subset of phase space with non-zero measure.

At $a = 3.45$ (and $\alpha = 45^\circ$), an unbounded chaotic attractor exists, and phase space has a fractal structure, as shown in figure 4.35(c). As has been detailed in section 4.10, upon further increasing a , this chaotic attractor disappears by a mechanism similar to its creation. Figure 4.35(d), corresponding to $a = 3.9$, shows that no chaotic repeller is left behind when the unbounded chaotic attractor is destroyed, as already argued in section 4.10. There are two (again being each others images under \tilde{S}_{xy}) period 1 periodic attractors. Their basins of attraction have a smooth structure, and there is no sensitive dependence on initial conditions. In contrast to the case of $a < 3.3$ (i.e. panels (a) and (b)), the basins of attraction extend into the neighboring elementary cell, as can be seen by the “green” regions in figure 4.35(d).

Having an overview of phase space structures at $\alpha = 45^\circ$, we turn to the representative case of $\alpha = 46.8^\circ$. First, we consider $a = 3.55$ (figure 4.35(e)) corresponding to a maximum transient length smaller than 2 according to figure 4.15. Superficially, phase space has the same structure as for $a = 3.9$ and $\alpha = 45^\circ$. But in striking contrast, there is only one periodic attractor since \tilde{S}_{xy} symmetry has been broken. There are no

fractal structures, but the basin of attraction of the attractor extends into the neighboring elementary cells. Upon closer inspection, the image of the periodic attractor under \tilde{S}_{xy} is visible as an unstable periodic orbit in the plot, marked by a white arrow.

The second important case is encountered at $a = 3.9$ (and $\alpha = 46.8^\circ$) in the regime of larger maximum transient lengths greater than 2 length units. As seen from figure 4.35(f), the phase space structure is still rather similar compared to figure 4.35(e) with a single period 1 attractor. One major difference is that basin boundaries extend even beyond the neighboring elementary cell, e.g. trajectories starting around $\tilde{x} \approx 0.5$ and $\tilde{y} \approx 0.99$ are transported 2.5 length units until they reach the attractor two elementary cells away. While impossible to see in figure 4.35(f), most of the apparent basin boundaries seen in figure 4.35(f) contain a cantor like substructure of further basins of attraction of different attractors in different elementary cells that is robust against changes of the parameters controlling the numerical precision. We have found similar phase space structures for other sets of parameters corresponding to the area of larger maximum transient lengths greater than 2 in figure 4.15.

4.25.5 Creation of SSBT at $\alpha = 54^\circ$

We have argued in section 4.14 that the unbounded attractor leading to SSBT at $\alpha \neq 45^\circ$ is directly related to the unbounded attractor leading to SSBT at $\alpha = 45^\circ$. We will now analyze the creation of the unbounded attractor at $\alpha = 54^\circ$ analogous to our analysis in section 4.10, i.e. start at small a and show the relevant bifurcations when a is increased. We fix the frequency for this paragraph only at

$$\Omega = 3.8 \quad (4.52)$$

for convenience (e.g. at $\Omega = 4$ some of the orbits involved are unstable and the bifurcations occur in a different order with respect to a , complicating the analysis). The result is found in figure 4.36 showing the bifurcation diagram and figure 4.37 showing selected orbits.

Figure 4.36 shows only a values of interest. Except where otherwise noted, the bifurcations are most easily seen in the upper panel (a) of figure 4.36. For $a < 5.78$, the bifurcation diagram is largely equivalent to the one found for $\Omega = 4$, see figure 4.19. Our analysis starts with the S_0 symmetric periodic orbit at $a = 5.785$, cf. figure 4.37(a), corresponding to the symmetric orbit shown in figure 4.5(c). The orbit undergoes a S_0 symmetry breaking bifurcation at $a \approx 5.79$ yielding the orbit shown in figure 4.37(b). This orbit undergoes a period doubling cascade accumulating into a S_0 symmetry breaking bounded chaotic attractor at $a \approx 5.834$ (see figure 4.37(c) for an orbit on the attractor). This attractor merges with its image under S_0 at $a \approx 5.835$ forming a S_0 symmetric bounded chaotic attractor (see figure 4.37(d)). Now, the crucial bifurcation is this attractor merging with its image under S_{Ly} at $a \approx 5.844$, forming a chaotic attractor which is unbounded in the y direction and bounded in the x direction, see figure 4.37(f) for a representative orbit on the attractor. The symmetric orbit with which the attractors collide is the orbit oscillating around the saddle of the potential separating the two merging attractors, see figure 4.37(e). We have again used the same method as in figure 4.8 to verify that this orbit is indeed isomorphic to the periodic orbit created from the saddle of the potential at $a = 0$. As will be discussed below (see section 4.16), this orbit

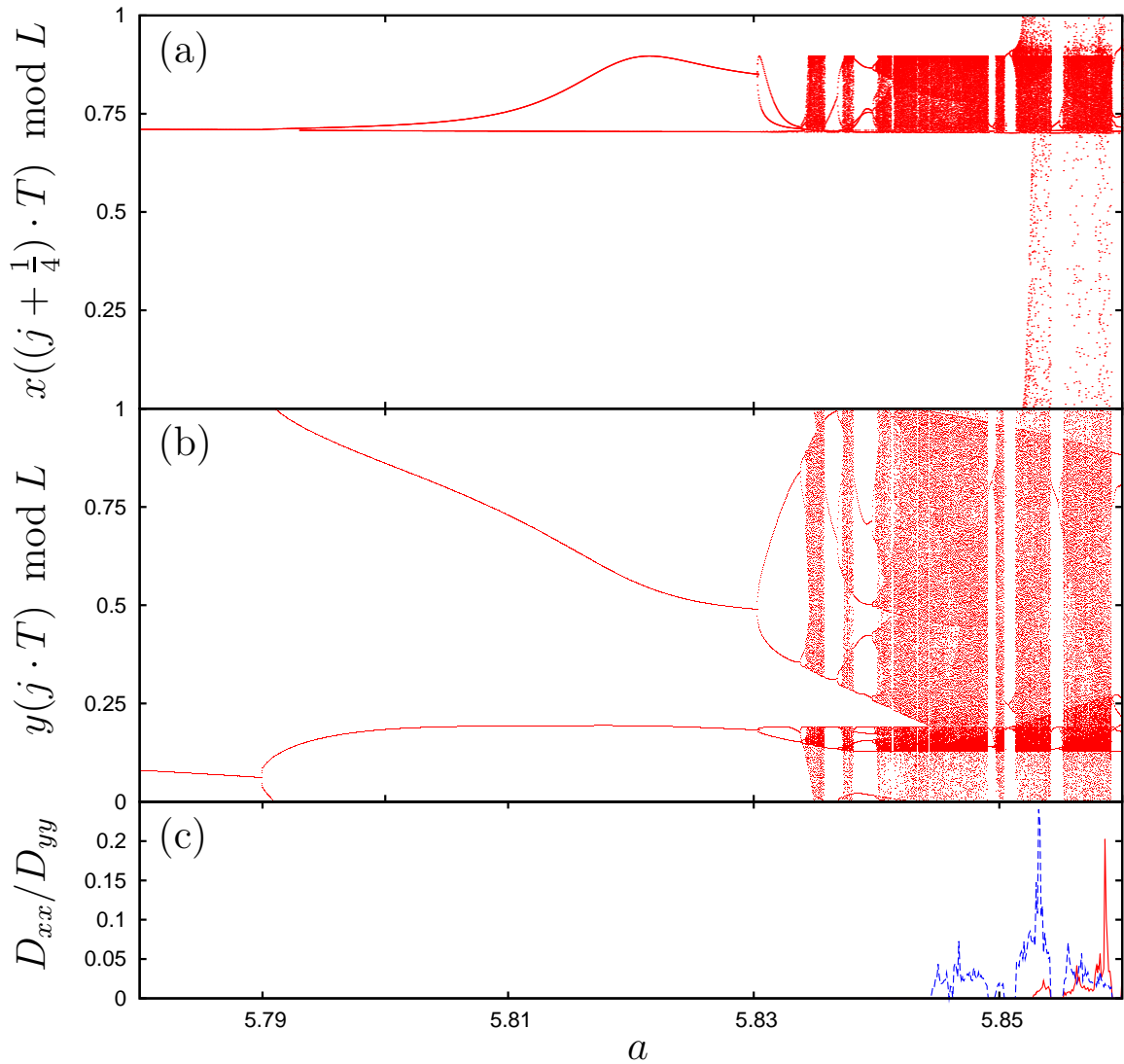


Figure 4.36: Bifurcation diagram of the deterministic $\Gamma = 0$ dynamics (4.9) with $\alpha = 54^\circ$, $\Omega = 3.8$ and $\vec{F} = 0$ showing only attractors obtained and drawn by the same method as described under figure 4.16. Panels (a) and (b) show one component of the stroboscopic map each, with the phases of the stroboscopic maps chosen differently, see the labels on the y axes. (c) shows, componentwise, the normalized mean squared displacement after $t = 20000$ drive periods, i.e., according to (4.32), $D_{xx/yy} = \vec{e}_{x/y}^t \cdot \mathbf{D} \cdot \vec{e}_{x/y}$. The red (solid) line corresponds to the x component, and the blue (dashed) line to the y component.

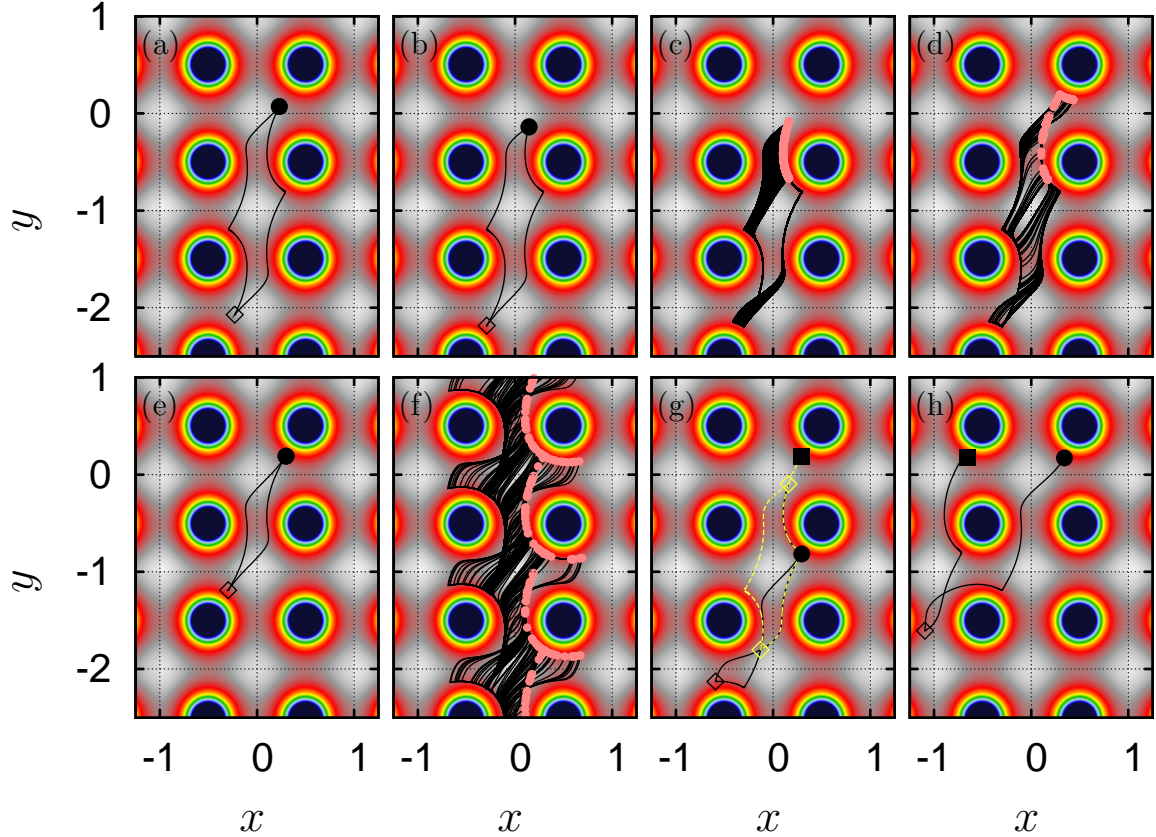


Figure 4.37: Trajectories of the deterministic $\Gamma = 0$ dynamics (4.9), corresponding to the parameters chosen in figure 4.36 (except for (h) corresponding to figure 4.19) and $a = 5.785$ (a), $a = 5.8$ (b), $a = 5.8347$ (c), $a = 5.8354$ (d), $a = 5.84445$ (e), $a = 5.845$ (f), $a = 5.85322$ (g) and $\Omega = 4$, $a = 5.95$ (h). In all panels except for (f), the turning points of the orbits (i.e. the times when the periodic drive changes sign) are marked by a filled circle (drive protocol becomes negative) and an open diamond (drive protocol becomes positive). In panel (f), only one turning point (drive protocol becomes negative) is marked by red points, indicating the attractor's shape under the stroboscopic map. To mark the end points of the orbits (g) and (h), a filled circle has been drawn at the start point of the orbit, and a filled square marks the end point of the orbit. Furthermore, the period 2 orbit (g) has been drawn in 2 colors, the first drive period in black and the second drive period in yellow (dashed).

also becomes stable for certain a values smaller than those considered in figure 4.36 and is involved in other symmetry breaking bifurcations.

The result of this bifurcation is (anisotropic) deterministic diffusion, as can be inferred from the elements of \mathbf{D} , cf. (4.32), corresponding to diffusion along the coordinate axes shown in the lowest panel (c) of figure 4.36. The mean squared displacement of the x component of the particle position remains 0, and there is no deterministic diffusion in the x direction. An example of a resulting SSBT periodic (period 2) orbit is shown in figure 4.37(g). Since the attractor is unbounded only in the y direction, the SSBT orbit is transporting into the y direction.

At $a \approx 5.85$, this attractor has a non-transporting period 1 window. The periodic orbits constituting the window are S_0 symmetry breaking. Therefore, there are two orbits, each being the other's image under S_0 . The orbits undergo a period doubling cascade, and the resulting chaotic attractor merges again with the former chaotic attractor. But, as can be seen from the x component of the stroboscopic section, cf. figure 4.36(b), the attractor now grows in the x component, collides (merges) with its image under S_{L_x} and creates an unbounded (in both components) chaotic attractor. The particle now diffuses over the whole lattice. This attractor allows for diffusion into "all" directions, as can also be seen from the mean squared displacement of the x component, see figure 4.36(c) (blue curve).

Upon changing the remaining parameters (e.g. Ω or α), the bifurcations move in parameter space, exchange order (with respect to a) and new bifurcations occur. In particular, the latter merging crisis can actually occur for smaller a than the former. This happens mostly for larger Ω , creating an unbounded attractor (in all directions). Moreover, depending on the chosen frequency (or other parameters), these merging crises occur while the chaotic object is unstable creating a chaotic unbounded repeller.

4.25.6 The applicability of the theory from [1, 2] at large Γ

Here, we are often considering ratios of noise strength Γ to pseudopotential depth V_A that are large compared to the ratios for which the quantitative theory from [1, 2] is applicable. E.g. for the attractor behind ANM in figure 4.25(b), the pseudopotential depth can be calculated along the lines outlined in [2] to be $V_A \approx 1.48 \cdot 10^{-5}$, and we are considering noise strengths larger by one or two orders of magnitude. A quantitative agreement is only to be expected if the ratios $\frac{V_A}{\Gamma}$ are sufficiently small. While it is possible to improve the approximation by including a non-equilibrium prefactor, see [2, 144, 263], the basic requirements remains that Γ should not be larger than V_A . In some cases even the unstable objects in phase space involved are different, as we are not only considering chaotic repellers, but more general phase space structures that allow a particle to move from one elementary cell to the next.

Yet, the qualitative picture remains the same, as we will show below. Denoting the particle position after the time T , when initialized at \vec{r}_0 for the particular realization $\vec{\xi}(t)$ of the Wiener process $\vec{r}(\vec{r}_0, T, \vec{\xi}(t))$, we consider the noisy displacement map ("shifted" stroboscopic section):

$$\Theta(\vec{r}_0, \vec{\xi}(t)) = \vec{r}(\vec{r}_0, T, \vec{\xi}(t)) - \vec{r}_0 \quad (4.53)$$

depending on the particular realization of the Wiener process and its mean value when

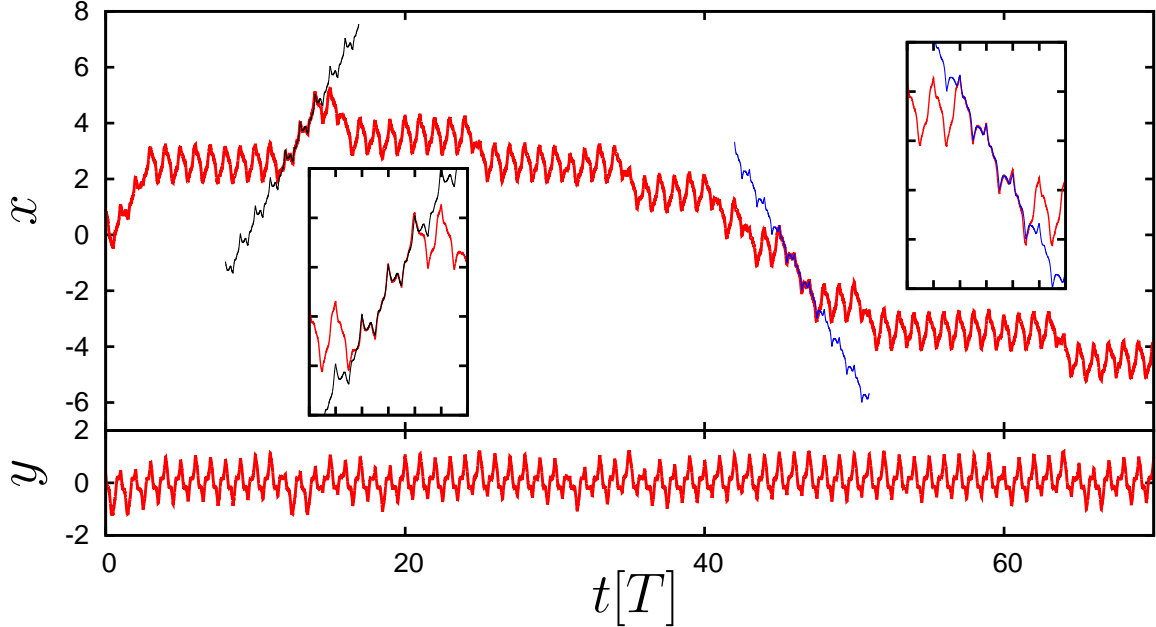


Figure 4.38: Typical noisy trajectory (red line) of the dynamics considered in figure 4.25(a), i.e. $\Omega = 7.5$, $a = 7.6$, $\alpha = 54^\circ$, $\vec{F} = 0.04\vec{e}_x$ and $\Gamma = 7 \cdot 10^{-4}$. The upper panel shows the x component, and the lower panel shows the y component. The black line corresponds to a trajectory on the deterministic attractor (stable period 1 orbit) carrying $\vec{v} = 1.0 \cdot \vec{e}_x$ transport at $a = 7.21$, and the blue line corresponds to its symmetry partner carrying $\vec{v} = -1.0 \cdot \vec{e}_x$ transport at $a = 7.21$. The insets are enlargements of the main trajectories.

averaged over all realizations of the Wiener process $\xi(t)$

$$\langle \Theta \rangle(\vec{r}_0) = \langle \vec{r}(\vec{r}_0, T) \rangle_{\xi(t)} - \vec{r}_0. \quad (4.54)$$

The average velocity then follows as

$$\langle \vec{v} \rangle = \frac{1}{T} \int_{\text{unit cell}} p(\vec{r}_0) \langle \Theta \rangle(\vec{r}_0) d\vec{r}_0 \quad (4.55)$$

with the stationary distribution $p(\vec{r}_0)$ on the torus [10], which we assume to exist. At sufficiently small noise strengths, $p(\vec{r}_0)$ is strongly peaked at regions of phase space containing attractors and only these regions contribute in (4.55). As an example, we consider the particularly relevant case of a deterministic attractor carrying no transport coexisting with two unstable objects carrying transport parallel and anti parallel to the direction of the applied bias force. These unstable objects need not be chaotic repellers, or even unstable periodic orbits, but can be more general transient objects such as what is left behind by a periodic orbit annihilated in a tangent bifurcation⁷⁰ (the latter is the case

⁷⁰In the presence of strong noise it is irrelevant whether one considers parameters prior to the annihilation of a periodic orbit or after with respect to (4.55). Without noise, (4.53) vanishes at a periodic orbit, or is of the form (nL, mL) for transporting periodic orbits. Thus, upon further iteration of (4.53) deterministically transporting trajectories are generated. After a periodic orbit disappears through a tangent bifurcation, (4.53) no longer vanishes (or is (nL, mL)), but retains a finite (but small, scaling

for the object behind (N)ANM in figure 4.25(a), as we will see below, cf. figure 4.38). Due to the ergodic nature of the dynamics in the presence of noise, $p(\vec{r}_0)$ will have a non-zero value for almost all \vec{r}_0 , and the unstable objects contribute in (4.55) with their weights. The weights, but also the effectiveness of transport, expressed by the average displacement in (4.54), scale with the distance from the (possibly) stable objects to which the transient objects are due [125, 146, 147, 258]. In particular, in the case of system parameters close to a region of existence of a pair of SSBT attractors carrying transport into opposite directions, the object closer to its region of stability (in parameter space) is likely to dominate over the other object. Superimposed over this competition is the transport due to an applied bias force. At very large noise strengths it yields $\langle \vec{v} \rangle = \vec{F}$ and cannot be due to one of the deterministic objects considered so far. The last contribution to (4.55) is due to the assumed deterministic attractor carrying no transport and leads, in general, to a reduction of (4.55) in modulus. The interplay of these four contributions to (4.55) determines transport in our simple picture. In particular, the only contribution leading to transport against an applied bias force is the one due to the object associated with the SSBT attractor carrying transport against the bias force. By comparing with e.g. [2], the basic mechanism is quite similar. As an example, we consider the noisy dynamics corresponding to figure 4.25(a) at $F = 0.04$ and $\Gamma = 7 \cdot 10^{-4}$ as shown in figure 4.38. In that case, deterministic phase space has only one attractor, a period 1 non-transporting orbit. As can be deduced from figures 4.18 and 4.24, for slightly smaller values of a , deterministic transporting attractors exist. At $a = 7.21$, there is a pair of period one orbits carrying $v = 1$ transport parallel and anti parallel to \vec{e}_x . The orbits are destroyed in tangent bifurcations at $a \approx 7.3425$ for the orbit carrying transport in the direction of the bias force, and $a \approx 7.36$ for the one carrying transport against the bias force. For $a \gtrsim 7.36$, the only attractor is the non-transporting period 1 orbit. At $a = 7.6$, we have calculated its pseudopotential depth as $V_A \approx 4 \cdot 10^{-4}$, i.e. at the noise strength considered, noise induced escape is very frequent, and escape times are of order T .

A typical noisy trajectory consists of longer parts where the particle oscillates on the deterministic period 1 orbit (or rather, close to it). When the particle leaves the attractor, it either travels in the negative or positive \vec{e}_x direction. Two of the longer of these transporting parts of the trajectory are compared to the transporting periodic orbits existing at $a = 7.21$ in figure 4.38, see the insets, and found to be practically identical. The shorter transporting bursts seem to be comparable in shape with the longer ones. We conclude that these transporting bursts are due to the transporting periodic orbits existing at $a = 7.21$, or rather what is left of them at $a = 7.6$, and the qualitative picture is the same as considered in [63] and [2]. A quantitative analysis along the lines of [1, 2] does not seem to be useful, since the NANM effect is most pronounced for relatively large noise strengths, i.e. $\frac{V_A}{\Gamma} \approx 0.57$. Therefore, the escape rate from the non-transporting attractor will, in general, not follow the Arrhenius law used in [1, 2]. Furthermore, the lifetimes of the two transient states are of the order of 1 drive period, in which case the assumption of a Markov model becomes doubtful.

with the distance from the bifurcation in parameter space) value in a neighborhood of the periodic orbit. But in the presence of strong noise no deterministic transporting trajectories are generated at all: some trajectories really reach a neighborhood of the periodic orbit again after one drive period has elapsed, but (almost) none reach it exactly, while others end up in entirely different regions of phase space. It is therefore irrelevant whether (4.53) vanishes exactly or is small but non-zero.

4.25.7 Stochastic differential equation solver

We have used the scheme given by Table 5.3 of [181], a stochastic Runge-Kutta algorithm, to obtain a weak solution of the SDE (4.1), which we write in this section as

$$\dot{\vec{r}}(t) = \vec{F}(\vec{r}(t), t) + \sqrt{2\Gamma}\vec{\xi}(t) \quad (4.56)$$

for brevity. $\vec{\xi}(t)$ is an N dimensional Wiener process, and $\vec{r}(t)$ are N dimensional vectors. The scheme converges in the weak sense with order 2 [89, 181] and deterministically (i.e. without noise) with order 3 [181, 186]. This improves the accuracy when only small noise strengths are considered. Simplified to our needs, i.e. additive noise, the scheme is as follows. The numerical approximation is calculated for the times $t_n = t_0 + h \cdot n$ and denoted by \vec{Y}_n , i.e. \vec{Y}_n approximates $\vec{r}(t_n)$. The support sites to calculate the numerical approximation at time t_{n+1} are given by

$$\vec{H}_1 = \vec{Y}_n \quad (4.57)$$

$$\vec{H}_2 = \vec{Y}_n + \frac{2}{3}\vec{F}(\vec{H}_1, t_n) \cdot h \quad (4.58)$$

$$\vec{H}_3 = \vec{Y}_n + \frac{1}{6}\vec{F}(\vec{H}_1, t_n) \cdot h + \frac{1}{2}\vec{F}(\vec{H}_2, t_n + \frac{2}{3}h) \cdot h + \sqrt{2\Gamma}\vec{\Xi}_n, \quad (4.59)$$

and the numerical approximation at time t_{n+1} is given by

$$\vec{Y}_{n+1} = \vec{Y}_n + \frac{1}{4}\vec{F}(\vec{H}_1, t_n)h + \frac{1}{4}\vec{F}(\vec{H}_2, t_n + \frac{2}{3}h)h + \frac{1}{2}\vec{F}(\vec{H}_3, t_n + \frac{2}{3}h)h + \sqrt{2\Gamma}\vec{\Xi}_n, \quad (4.60)$$

where the $\vec{\Xi}_n$ are independent 3 point distributed random variables with independent components, and each component is distributed according to

$$\text{Prob} \left\{ \vec{\Xi}_n \cdot \vec{e}_i = \sqrt{3 \cdot h} \right\} = \frac{1}{6}; \text{ Prob} \left\{ \vec{\Xi}_n \cdot \vec{e}_i = -\sqrt{3 \cdot h} \right\} = \frac{1}{6}; \text{ Prob} \left\{ \vec{\Xi}_n \cdot \vec{e}_i = 0 \right\} = \frac{2}{3}. \quad (4.61)$$

For not too large frequencies, we have found the method to converge around $h \lesssim 0.01$ in the sense that at the resolutions of the figures and the sample size the result of the computation does not change systematically or significantly upon further decreasing h , i.e. varies within statistical errors, see figure 4.39. As reference, we have found the results for $h = 0.01$ to be comparable in above described sense to those obtained with an extrapolated weak Euler-Maruyama scheme [89], see figure 4.39. Note that the extrapolation is feasible only if the statistical errors are sufficiently small, i.e. the sample sizes are large enough. Since the computation of each of the data points with highest precision in figure 4.39 takes about 30 hours of single threaded computation time, such sample sizes are not feasible on a larger scale. The typical sample sizes used to obtain averages in this work are at least one order of magnitude smaller than those used in figure 4.39 due to the limited computation time. For such sample sizes, and the resulting precision, the method converges in above described sense for somewhat larger values of h . We have used $h \lesssim 0.01$ throughout this work. As evident from figure 4.39, we would need about an order of magnitude more computation time to obtain the same precision using the Euler-Majurama scheme at the smaller noise strengths considered.

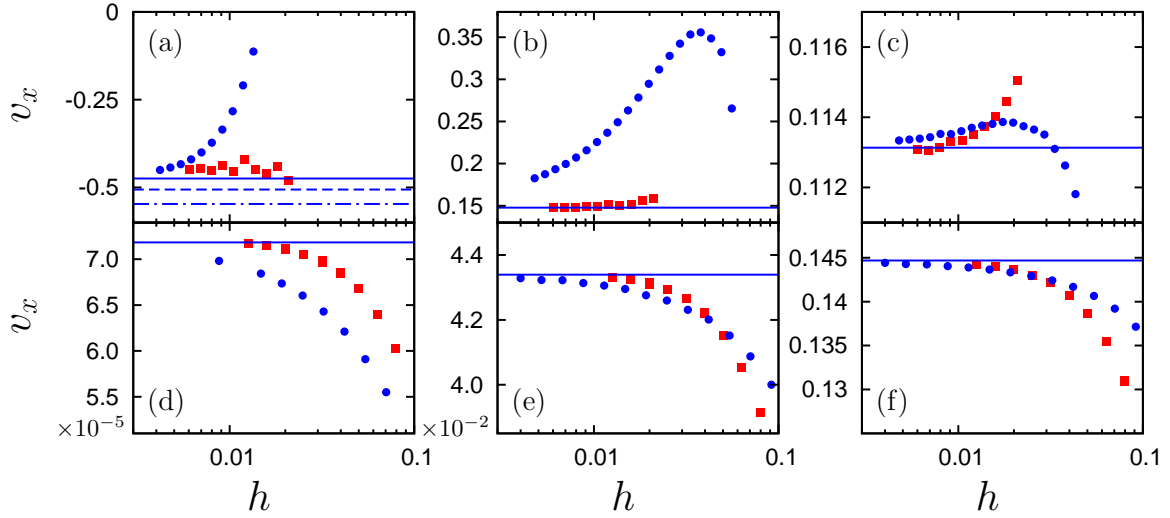


Figure 4.39: Convergence (with respect to the step width h) of the algorithm discussed in section 4.25.7 (red symbols) compared to that of the weak Euler-Majurama scheme [89] with $\frac{h}{4}$ (blue symbols), and thus incurring comparable (slightly higher) numerical costs. Shown are numerical approximations of the x component of the average velocity in dependence of h for the dynamics (4.9) with $\lambda = 4$, $\Omega = 6$, $a = 6.7$, $\alpha = 54^\circ$, $\vec{F} = 0.05\vec{e}_x$, (a) $\Gamma = 10^{-4}$, (b) $\Gamma = 10^{-3}$ and (c) $\Gamma = 10^{-2}$. The averages have been obtained by averaging 25000 trajectories of length $10000T$ for different realizations of the stochastic process. The symbol sizes are of the order of 3 times the (estimated) standard deviation of the mean average velocity. Furthermore, the two last obtained (smallest h) data points for the weak Euler-Majurama scheme have been extrapolated to $h = 0$, and the concomitant average is indicated by the blue lines. In (a), the weak Euler-Majurama scheme fails to converge in the given precision, as indicated by the blue lines, showing the extrapolation result for the three last obtained pairs of data points (the pair for largest h corresponding to the dashed-dotted lines, the next to the dashed line, and the last to the solid line as in the other panels), exhibiting a systematic drift, which, within the precision of the figure, is absent from the other panels. In (d)-(f) the corresponding autonomous $a = 0$ dynamics are considered with $T = 1$, $\vec{F} = 1.4\vec{e}_x$, (d) $\Gamma = 10^{-3}$, (e) $\Gamma = 3 \cdot 10^{-3}$ and (f) $\Gamma = 7 \cdot 10^{-3}$. In panel (d), 10000 trajectories of length 100000 time units have been used to compute the averages, and in panels (e)-(f) the same number of trajectories, but of length 10000 time units. The blue lines correspond to linear extrapolations of the last four data points obtained for the Euler-Maruyama scheme. Note the scaling of v_x in panels (d) and (e).

4.25.8 Coupled Josephson junctions

In this section, we derive the equations of motion of the coupled Josephson junctions shown in figure 4.29(b). Using Kirchhoff's law for the current flowing from the first junction to the second junction, one obtains

$$I_1 \sin(\varphi_1(t)) + \frac{\Phi_0}{2\pi R} \dot{\varphi}_1(t) - A_1(t) - \xi_1(t) = I_2 \sin(\varphi_2(t)) + \frac{\Phi_0}{2\pi R} \dot{\varphi}_2(t) - A_2(t) - \xi_2(t), \quad (4.62)$$

where we have introduced the phase differences of the superconducting phases of the junctions $\varphi_{1/2}$ [7] with critical currents $I_{1/2}$, the shunt resistance R , the externally applied currents $A_{1/2}(t)$, the magnetic flux quantum Φ_0 and the noise currents due to the shunt resistors $\xi_{1/2}(t)$ with $\langle \xi_i(t) \xi_j(s) \rangle = \delta_{ij} \delta(t-s) \frac{2k_B T_K}{R}$. k_B is Boltzmann's constant and T_K is the temperature in Kelvin. The currents through the junctions are given by Josephson's equations [7].

Applying Kirchhoff's law to the current from the second junction flowing through the single (third) resistor, we get

$$\frac{U_3(t)}{R} - \xi_3(t) = I_2 \sin(\varphi_2(t)) + \frac{\Phi_0}{2\pi R} \dot{\varphi}_2(t) - A_2(t) - \xi_2(t). \quad (4.63)$$

Using the fact that the voltage drop across the whole device has to be zero, i.e. $U_1(t) + U_2(t) + U_3(t) = 0$, together with Josephson's equations for the voltage drops across the junctions,

$$\frac{\Phi_0}{2\pi R} (\dot{\varphi}_1(t) + \dot{\varphi}_2(t)) = - \left(I_2 \sin(\varphi_2(t)) + \frac{\Phi_0}{2\pi R} \dot{\varphi}_2(t) - A_2(t) - \xi_2(t) + \xi_3(t) \right) \quad (4.64)$$

follows. A similar device is studied in e.g. [135]. The equations of motion of the two phases follow from simple algebraic manipulations:

$$\begin{aligned} 3 \frac{\Phi_0}{2\pi R} \dot{\varphi}_1(t) &= I_2 \sin(\varphi_2(t)) - 2I_1 \sin(\varphi_1(t)) + 2A_1(t) - A_2(t) \\ &+ 2\xi_1(t) - \xi_2(t) + \xi_3(t) \end{aligned} \quad (4.65)$$

$$\begin{aligned} 3 \frac{\Phi_0}{2\pi R} \dot{\varphi}_2(t) &= I_1 \sin(\varphi_1(t)) - 2I_2 \sin(\varphi_2(t)) + 2A_2(t) - A_1(t) \\ &+ 2\xi_2(t) - \xi_1(t) + \xi_3(t). \end{aligned} \quad (4.66)$$

Applying [107]

$$\begin{pmatrix} x(t) \\ y(t) \end{pmatrix} = \underbrace{\begin{pmatrix} 0 & \frac{\sqrt{3}}{2} \\ 1 & \frac{1}{2} \end{pmatrix}}_{B_{r\varphi}} \begin{pmatrix} \varphi_1(t) \\ \varphi_2(t) \end{pmatrix} \quad \begin{pmatrix} A_x(t) \\ A_y(t) \end{pmatrix} = \underbrace{\begin{pmatrix} -\frac{1}{2\sqrt{3}} & \frac{1}{\sqrt{3}} \\ \frac{1}{2} & 0 \end{pmatrix}}_{B_{AI} = \frac{1}{2} (B_{r\varphi}^{-1})^t} \begin{pmatrix} A_1(t) \\ A_2(t) \end{pmatrix}, \quad (4.67)$$

the dynamics are equivalent to that of an overdamped particle with damping coefficient $\frac{\Phi_0}{R}$ moving in the periodic potential

$$U(x, y) = -\frac{I_1}{2} \cos \left(y - \frac{x}{\sqrt{3}} \right) - \frac{I_2}{2} \cos \left(\frac{2}{\sqrt{3}} x \right), \quad (4.68)$$

and subjected to a rocking driving force $(A_x(t), A_y(t))$, and the noise transforms like the bias currents. The components of the resulting noise process are not uncorrelated, e.g. if one transforms the dynamics to a Fokker-Planck equation. See figure 4.29(a) for an illustration of the potential for $I_2 = 2 \cdot I_1$.

4.25.9 Supplementary figures

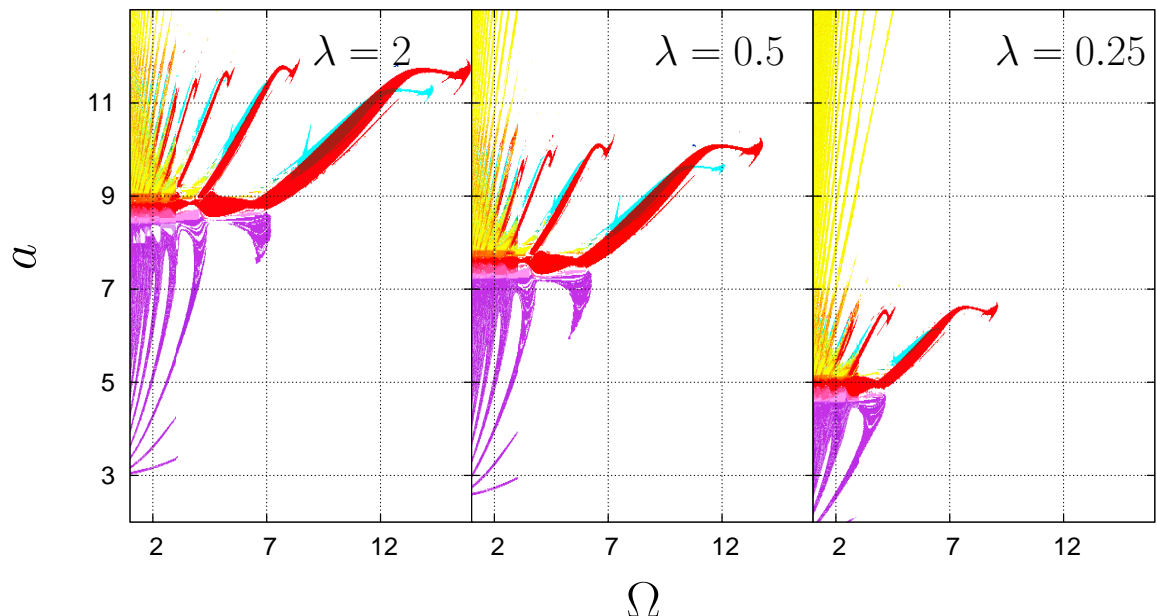


Figure 4.40: The same phase diagram for the same dynamics and parameters as shown in figure 4.18(b), except for λ , as indicated in the panels.

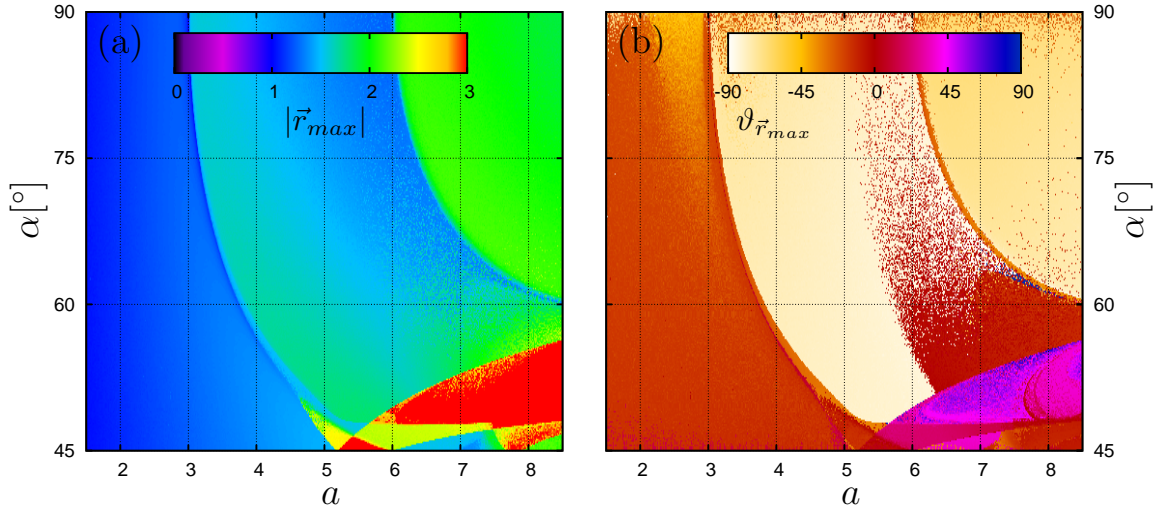


Figure 4.41: (a) $|\vec{r}_{max}|$ and (b) angle $\vartheta_{\vec{r}_{max}}$ obtained by the same method for the same dynamics and parameters as in figure 4.31, except for the drive. A sine drive (4.8) has been used instead of the square wave drive (4.7). We have chosen a different frequency, $\Omega = 6.5$, to match the different drive protocols such that we are considering an equivalent part of the phase diagram at $\alpha = 45^\circ$, $\Gamma = 0$, i.e. figure 4.4.

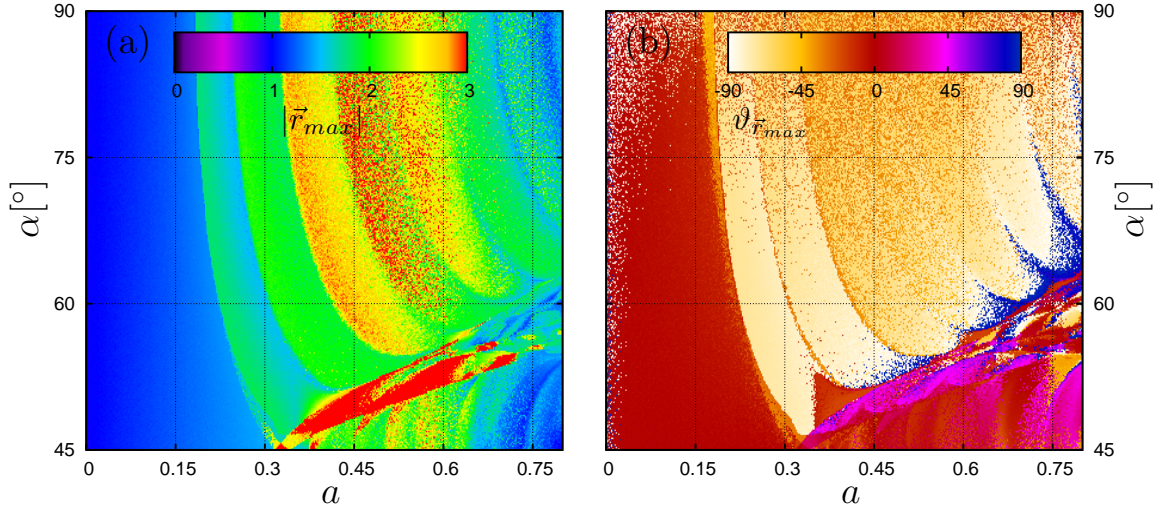


Figure 4.42: (a) $|\vec{r}_{max}|$ and (b) angle $\vartheta_{\vec{r}_{max}}$ obtained by the same method for the same dynamics and parameters as in figure 4.15, except for the potential. Instead of the Yukawa potential (4.3), a Gauss potential (4.4) with $\sigma = 0.25$ and $u = 1$ has been used. The remaining parameters have been scaled to match the dynamics with figure 4.15, i.e. $\Omega = 0.3$, and a as indicated in the figure.

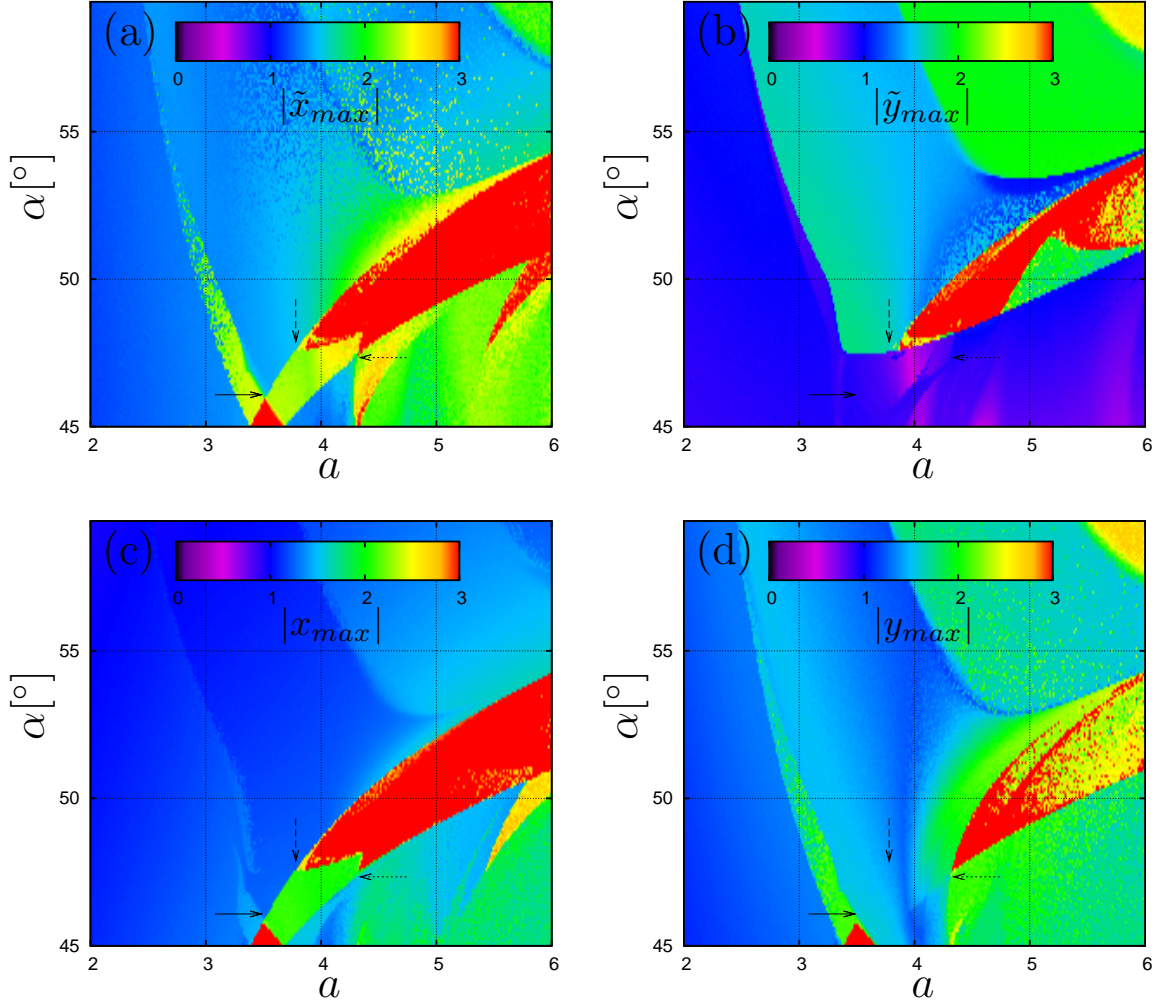


Figure 4.43: (a) $|\tilde{x}_{max}|(n) = \max_{\vec{r}_0, \vec{r}(t_0)=\vec{r}_0} |\vec{r}(nT) \cdot \vec{e}_{\tilde{x}} - \vec{r}(t_0) \cdot \vec{e}_{\tilde{x}}|$ in units of the rotated coordinate frame, i.e. multiplied by $\sqrt{2}$, and encoded in colors according to the palette which has been cutoff. $\vec{r}(t)$ is the trajectory passing through \vec{r}_0 at time t_0 and $n = 12$. 5000 random initial seeds have been samples to approximate the maximum, cf. figure 4.14. The same dynamics as in figure 4.15 are considered. (b) The same as in (a), but $\vec{e}_{\tilde{x}}$ is replaced by $\vec{e}_{\tilde{y}}$. (c) The same as in (a), but $\vec{e}_{\tilde{x}}$ is replaced by \vec{e}_x . (d) The same as in (a), but $\vec{e}_{\tilde{x}}$ is replaced by \vec{e}_y .

Chapter 5

Quenched disorder

We have considered perfectly periodic systems in chapters 3-4. We will now consider time independent (quenched) deviations from perfect periodicity, quenched disorder. Our discussion starts with a short introduction. Formally, we define our disordered system in section 5.2. Our main argument, an analogy between thermal noise and quenched disorder, will be discussed in section 5.3. For our purposes, the Golosov effect is the main qualitative difference between quenched disorder and thermal fluctuations and will be discussed in sections 5.4-5.5, along with some notes on how we calculate averages in the nonergodic disordered system. Section 5.6 contains our results, the most dramatic being “disorder induced” absolute negative mobility (ANM). We close our discussion with section 5.7 and give an outlook on inertia effects.

5.1 Introduction

The influence of thermal noise on spontaneous symmetry breaking transport (SSBT) and hence derived effects has been discussed throughout the text, see in particular sections 4.11.2 and 4.19. In experimental systems, a second important, and at first glance very different, source of fluctuations are time independent imperfections of the periodic lattice (quenched disorder), e.g. small displacements of the lattice “atoms”, inhomogeneities in their interaction with the particle such as discussed in [106, 201, 210, 217] or even completely random potentials [129, 289–293]. Quenched disorder leads to, e.g., anomalous diffusion [129], localization (Golosov effect) [294], enhancement [295] and suppression [296, 297] of chaotic diffusion, as well as enhancement of giant diffusion [217], giant transversal diffusion [219], diffusive transport [298], ratchet effects [293], friction [299], enhancement of soliton transport [300], and synchronization [301]. For our purposes, the main difference of quenched disorder and thermal noise, leading in particular to localization, is that a particle encounters the same realization of the disorder upon revisiting a particular place on the surface. Therefore, if there is a region from which it cannot escape, it will stay there indefinitely (Golosov effect) [294], suppressing transport, suppressing chaotic diffusion (if sufficiently strong) [295, 296], leading to a divergence of the diffusion coefficient [298] or quenching ratchet effects [298, 302–306].

5.2 Modelling quenched disorder

We model quenched disorder as a time independent random perturbation $\vec{\zeta}(\vec{r})$ of (4.1) (cf. the discussion of (4.1) for an explanation of the terms in (5.1)):

$$\eta \dot{\vec{r}}(t) = \vec{A}(t) + \vec{F} - \vec{\nabla}U(\vec{r}(t)) + \sqrt{2\Gamma}\vec{\xi}(t) + \vec{\zeta}(\vec{r}(t)), \quad (5.1)$$

whose statistical properties depend on the particular system we have in mind. In general, we assume that the correlation length of $\vec{\zeta}(\vec{r})$ is of the order of the spatial period of the periodic lattice. There are countless ways of modelling quenched disorder discussed in the literature. We restrict our investigations to a physically simple discrete implementation by randomizing the positions of our “atoms” in each elementary cell. I.e., we replace (4.2) by

$$U(x, y, \vec{\zeta}) = u \sum_{n,m} \tilde{U} \left(\left(x + (n + \frac{1}{2}) \cdot L, y + (m + \frac{1}{2}) \cdot L \right) + \vec{\zeta}_{nm} \right) \quad (5.2)$$

with

$$L = 1. \quad (5.3)$$

The $\vec{\zeta}_{nm}$ are independent random vectors with independent Gaussian distributed components of zero mean and variance γ^1 . This kind of disorder seems to be a natural starting point to model small imperfections in a periodic lattice. A similar approach is used in [106], and many studies focussing on random pinning in the context of vortices in superconducting devices use basically the same approach, see e.g. [23, 293] and references therein. We do not expect qualitatively different results if other parameters of the lattice are thus randomized, in particular as found in [106]². We expect our results to be robust against changes of the disorder if one considers qualitatively different types of disorder, see e.g. [217, 219] for random potentials, [304] for uncorrelated random forces³, [295, 298] for dichotomous random forces⁴, [308] for spatially correlated random forces and [129] for a review in the context of diffusion. In fact, these types of disorder, in particular those with no, or short ranged spatial correlations, seem to be even better suited with respect to the applicability of (5.7) (see below) than the physically inspired disorder considered here.

For the discussion of quenched disorder we will use a Gaussian repulsive potential:

$$\tilde{U}_{\text{Gauss}}(x, y) = u \cdot \sigma \cdot \exp\left(-\frac{r^2}{2\sigma^2}\right), \quad (5.4)$$

in (5.2), cf. (4.4). The Gaussian potential has the significant advantage of being short ranged, reducing numerical difficulties compared to the Yukawa potential used in the

¹We have cut off the Gaussian distribution such that $|\vec{e}_{x/y} \cdot \vec{\zeta}_{nm}| < 0.1$ for physical reasons. We do not expect the neglected large but rare realizations of the disorder to change our results.

²Note that the disorder considered in [106] is not fully quenched, but varies slowly. We will discuss this case in more detail below.

³Note that there is a qualitative difference between disordered force fields and disordered potentials [307].

⁴Note that in that case there is only a finite number of realizations of the disorder for each finite surface. Hence, our claim that all unbounded deterministic attractors are destroyed by disorder is not always true in this case, see section 5.4.

discussion of SSBT in chapter 4⁵, while the results are virtually identical, see figure 4.4 and section 4.14.

Our central observable will be the time and ensemble averaged normalized velocity

$$\vec{v} = v\vec{e}_\vartheta = \frac{T}{1} \left\langle \dot{\vec{r}}(t) \right\rangle = \lim_{t \rightarrow \infty} \frac{T}{1} \frac{1}{t} \int_0^\infty dt' \dot{\vec{r}}(t'), \quad (5.5)$$

where the average is over all realizations of the noise and the disorder and over time, and the last equality holds only for non-zero noise strength $\Gamma > 0$. Without thermal noise, the average velocity depends on the initial conditions, and we will comment on how we obtain the averages numerically in section 5.5.

5.3 Analogy to thermal fluctuations

We are interested in the influence of quenched disorder on phase-locked SSBT attractors with average velocity \vec{v} . Since trajectories on phase-locked SSBT attractors are transporting, they continuously visit new regions of the surface. Therefore, an analogy between weak quenched disorder and thermal fluctuations can be drawn by considering the noise and disorder free case first, and writing

$$\vec{r}(t) = \vec{r}_0 + \vec{v} \cdot t + \vec{s}(t), \quad (5.6)$$

i.e. splitting $\vec{r}(t)$ into the bounded, fluctuating part $\vec{s}(t)$ and the unbounded part $\vec{v} \cdot t$. To understand the effects of a weak quenched disorder on that trajectory, we write

$$\vec{\zeta}(t) = \vec{\zeta}(\vec{v} \cdot t + (\vec{r}_0 + \vec{s}(t))), \quad (5.7)$$

with $\vec{v} \cdot t$ linearly increasing with time. If we could neglect $\vec{s}(t)$, $\vec{\zeta}(t)$ would behave like a time dependent noise with memory, and as long as the trajectory remains transporting, the quenched disorder is a random function of time along that trajectory. In particular, we can try to apply the results about thermal noise induced metastability of these attractors. In [201] (see also [290, 292, 314]), using a similar approach, an effective temperature is defined and analyzed in a very simple two dimensional system, where both coordinates can

⁵These are as follows. In the simulations without quenched disorder, we calculate the gradient of the potential on an equally space grid, usually of about 400×400 grid points to avoid the computation of the sum in (4.2) multiple times during each iteration of the (S/O)DE solver. Alternatively, the sum can be transformed to an easier form, analogous to [309], [310, 311] in the case of magnetic bubble lattices [106] and [312, 313] in the case of vortex-vortex interactions in superconductors [203]. Obviously, both strategies rely on the periodicity of the lattice and fail in the presence of quenched disorder. Computing the full sum in (4.2) is not possible. Even after introducing a cutoff in the sum, i.e. a maximum distance (from the current particle coordinate) up to which the sum is computed, its computation remains prohibitively expensive if that cutoff is not very small. With the long ranged Yukawa interactions considered so far, this cutoff has to be chosen on the order of about 20 elementary cells, i.e. about 400 terms contribute to the sum. Using the fact that we are considering small disorder, i.e. small displacements of the atoms, we can mix both approaches, i.e. perform the summation in (5.2) using a relatively small cutoff, and compensating for the error by using a previously calculated bilinear interpolation of (4.2) with a large cutoff, including only those terms which are not accounted for in (5.2) due to the small cutoff, and neglecting the disorder for these terms. This does not change the long range of the Yukawa interaction, and therefore this approach works best for short range interaction, e.g. Gaussian interactions.

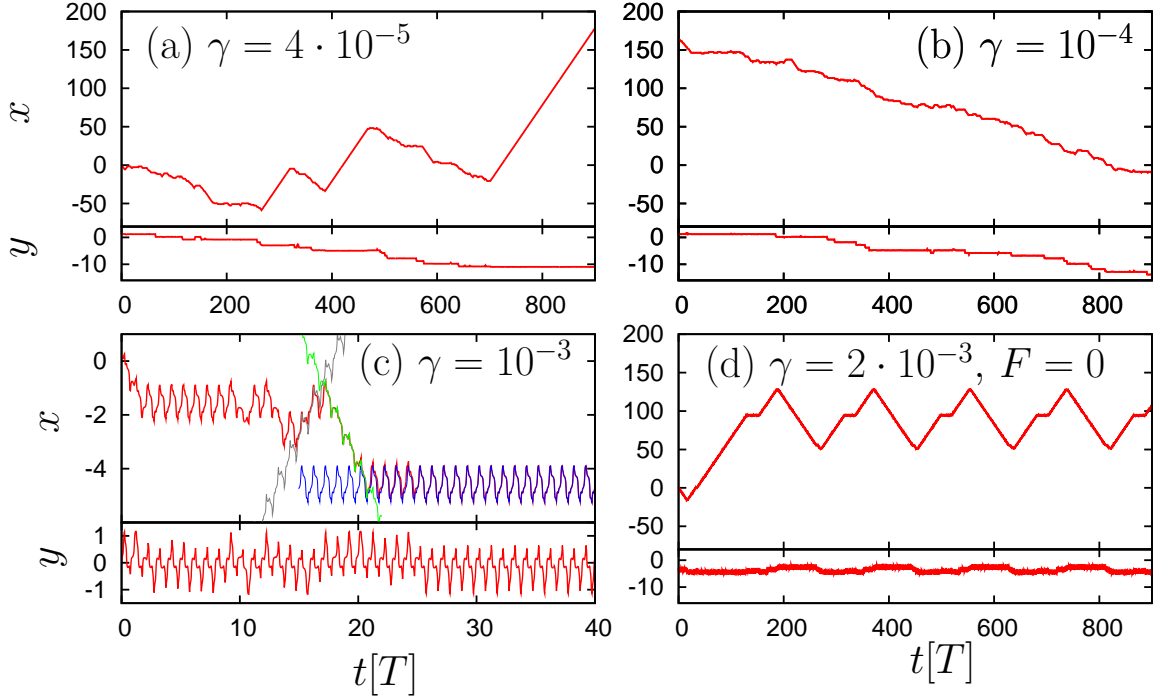


Figure 5.1: Typical trajectories for the $\Gamma = 0$ disordered dynamics (5.1) using (5.2), a repulsive Gaussian potential (5.4) ($u = 1$ and $\sigma = \frac{1}{4}$) and a square wave periodic drive (4.7) with $\alpha = 50.4^\circ$. The strength of the disorder is indicated in the panels, and the remaining parameters are (a)-(c): $\Omega = 0.328$, $a = 0.455$, $\vec{F} = 0.004 \cdot \vec{e}_x$ (corresponding to the 'x' in figure 5.2 except for \vec{F}), and (d): $\Omega = 0.4$, $a = 0.475$, $\vec{F} = 0$. In panel (c), the deterministic (i.e. $\gamma = 0$) phase space structures (periodic orbits of period 1) behind transport and trapping events are shown: the blue line corresponds to the bounded periodic orbit stable at $\Omega = 0.324$, the grey line to the transporting orbit stable at $\Omega = 0.328$, and the green line corresponds to the orbit behind ANM, stable at $\Omega = 0.33$ (in each case all remaining parameters are the same).

be decoupled, and deterministic transport in one of the components is trivial. Therefore, the dynamics are equivalent to a Langevin equation including only thermal noise of some effective temperature, as is the case in [314] for dichotomous disorder. Here, the situation is more complicated since the disorder leads to disorder induced metastability of the SSBT attractors. Once the attractor is left, the transport properties of the trajectory change, and (5.7) fails from then on.

5.4 The Golosov effect: trapping events

For our purposes, the most dramatic difference between thermal noise (i.e. time-dependent random forces) and quenched disorder are trapping events, suppressing transport for sufficiently strong disorder [295, 296, 298, 303–306, 314], termed the Golosov effect [294]. Examples of such trajectories for the systems considered here can be found in figure 5.1(c-d) (see the discussion thereof in section 5.6.4). Basically, if a trajectory subjected to quenched disorder reaches a position at which the disorder is such that it

cannot pass and the trajectory stays in that region (i.e. leaves its transporting attractor or other transporting or unbounded phase space structure, and ends up on a bounded phase space structure), it is trapped. From a mathematical point of view, this means that the trajectory is attracted by a non-transporting attractor after a (transient) time $\tau_{catch}(\vec{r}_0, \vec{\zeta})$ ⁶ has elapsed⁷. We define the average of these times for an ensemble of trajectories

$$\tau_{catch} = \frac{1}{T} \left\langle \tau_{catch}(\vec{r}_0, \vec{\zeta}) \right\rangle_{\vec{r}_0, \vec{\zeta}}, \quad (5.8)$$

averaged over all realizations of the disorder and all initial conditions according to a weight which is yet to be specified, the *catch time*. Note that we use the same symbol, τ_{catch} , but without the arguments to denote the average catch time. From a practical point of view, two main types of these events are found in the dynamics considered here.

First, quenched disorder can lead to an escape from a transporting attractor directly to a simple non-transporting attractor. The latter can either be existing in the unperturbed (disorder free) dynamics, or it may be existing for slightly different system parameters. In the latter case, the change of system parameters is “emulated” by the quenched disorder. Since the trajectory will always encounter the same realization of the disorder, with exactly the same numerical values, it will stay on this attractor indefinitely. A trapped trajectory is shown in figure 5.1(c). See [298, 306, 315] for a discussion of similar trapping events in the context of overdamped one dimensional ratchet dynamics and [305] including inertia effects.

Second, quenched disorder can lead to a transition to another transporting region of phase space (e.g. an attractor or a transient region), “deflecting” the particle. For simplicity let us consider the spatially 1D case, i.e. the disorder depends on only one coordinate. Here, the most common situation encountered is a switch from one SSBT attractor to its image under the symmetry (or what becomes thereof upon breaking the symmetry). The trajectory will then leave the region where the switch has occurred. But whenever that trajectory revisits that region, it still cannot pass, unless some other degree of freedom has changed (i.e. the phase of the drive if there is no other degree of freedom). Now, if the trajectory tends to reach said trapping region always at the same phase of the drive and all other coordinates the same, e.g. due to synchronization on a periodic

⁶Note that, in principle, we should write $\tau_{catch}(\vec{r}_0, \vec{\zeta}, t_0)$, i.e. the catch time depends on the starting time t_0 as well. This dependence can be absorbed into the starting vector. Therefore we omit this dependence and set $t_0 = 0$.

⁷Note that there are some mathematical subtleties involved in the definition of the catch times. To define such a time, one has to define a set containing the attractor. The bounded attractor’s basin of attraction is naturally excluded, since it is unbounded in general, and, even worse, the union of all basins of attraction of bounded attractors is dense in phase space (see text), and the catch time would be zero. Therefore, a suitable absorbing subset of the attractor’s basin of attraction has to be chosen, such that once a trajectory enters this set, it can be considered to be trapped. $\tau_{catch}(\vec{r}_0, \vec{\zeta})$ is then the smallest time for which a trajectory starting at \vec{r}_0 enters the set for a particular realization of the disorder. But the definition of this set is nontrivial. If the bounded attractor is chaotic and has a fractal basin boundary structure, such a set is not necessarily simple. Here, we ignore such subtleties and use an arbitrary open set containing the bounded attractor, whose distance from the attractor is sufficiently small. For the dynamics considered here, there does not seem to be a significant dependence of $\tau_{catch}(\vec{r}_0, \vec{\zeta})$ as long as the absorbing set is reasonable.

attractor, it will never pass the deflecting region, no matter how often it “tries”. This will be particularly evident for periodic attractors, and if the temporal distance between two “attempts” is large enough. If a trajectory is trapped between two such regions, it will stay there indefinitely, bouncing back and forth. An example of such a trajectory is shown in figure 5.1(d). These bounded attractors have a rather complicated structure due to their composite nature. This kind of trapping event is particularly relevant for $\vec{F} = 0$ if a pair of SSBT attractors coexists. Actually, that situation is ruled out in a periodic, spatially one dimensional overdamped dynamics (without nonanalyticities) due to the fact that deterministic trajectories cannot cross, i.e. if there is only one coordinate except for time, the asymptotic transport velocity is unique for all initial conditions due to the low dimensional nature of phase space.

The same behavior is found in spatially two dimensional systems. With more spatial dimensions, the trajectory has more options of passing the first deflecting region in another attempt. A similar behavior has also been observed in a slightly different context for diffusion in disordered media [129, 316]. E.g., if transport is along the x direction it suffices if the trajectory has a different y coordinate the next time it visits the deflecting region. With respect to synchronization (e.g. on periodic attractors), the number of transporting deterministic attractors is important in that case. If, without disorder, there is only one⁸ deterministic transporting attractor with transport in the direction considered, and this attractor leads to synchronized trajectories, the additional degrees of freedom will become synchronized. Thus, the particle will be deflected again. In contrast, if there are multiple transporting attractors with transport in the same direction, the y component can have a different value even in the presence of synchronization. If the system is periodic in the y direction, this can be due to “phase slips” of the y component⁹, such that the trajectory visits another elementary cell in that direction and thus a different “copy” of the attractor. The trajectory then encounters a different realization of the quenched disorder if it revisits the deflecting x coordinate, and will not necessarily be deflected again.

Nonetheless, unless there is a preferred direction, such as in the simpler dynamics of [201, 219], e.g. each deflection necessarily leads to a slip in the, say positive y direction (staying in the picture of transport in the x direction), it is clear that each trajectory will end up bouncing back and forth between two deflecting regions after a sufficiently long time (or on another bounded attractor), since any unbounded trajectory will eventually encounter a realization of the disorder that will trap it. The only exception to this would be if the quenched disorder is restricted such that an unbounded deterministic attractor survives for all realizations of the quenched disorder, e.g. if the disorder is bounded or there is only a finite number of realizations of the disorder on each finite sized part of surface, see e.g. [314, 315, 317–319]. Of course, such a restriction itself does not imply the existence of such an attractor.

⁸A copy of that attractor, which differs only in a coordinate not subjected to quenched disorder, e.g. time, does not count as a different attractor for obvious reasons.

⁹We are using the analogy between quenched disorder and thermal noise again. Noise induced phase slips are extensively discussed in, e.g. [37, 137] in the context of Josephson junctions. For our purpose, a phase slip is the fluctuations induced change of a periodic coordinate by an integer multiple of the period of that coordinate, with the system being in the same state before and after the transition, i.e. on the same attractor, but different copies thereof.

5.5 Averaging in the disordered dynamics

In the disordered dynamics, the disorder is tantamount to a certain averaging over phase space for transporting trajectories. But for $\Gamma = 0$, in general the latter (and all other averaged quantities) still depends on the initial condition for each realization of the disorder with the weight of the initial condition not being inherently defined.

Above discussed trapping events, see the trajectories shown in figure 5.1(c-d), represent a formidable question with respect to averaging the transport velocity in the presence of disorder: due to these, the average transport velocity obtained from a finite sample of trajectories will always be zero for asymptotically large times¹⁰. But this is not always realistic in an experiment running only for a finite time, or finite substrate sizes. Therefore, we compute the average velocity for finite but relatively large times, i.e. times for which initial transients of the ordered dynamics have died out. In a sorting experiment, this approach would correspond to starting with an ensemble of particles, subjecting them to a periodic drive for some finite time, and then collecting the particles, e.g. by means of a constant force. A different view would be to consider a finite sized sample surface with absorbing boundaries: once a trajectory has reached the edge of the surface by travelling a certain distance, it is finished, and the particle is collected. Therefore, it does not matter if the trajectory would become trapped at a later time.

If one considers large surfaces, i.e. if $\tau_{catch} \cdot \vec{v}$ is small compared to the size of the surface, most trajectories will become trapped before leaving the surface. But this limitation can be easily overcome, e.g. by slowly and periodically varying some parameter of the dynamics with a (very long) period larger than the “typical” transient times of the dynamics and of the order of τ_{catch} . Then, the bounded attractors on which trajectories are trapped are destroyed, but transporting attractors are unaffected most of the time. E.g., one could periodically apply a large constant force for a short time, and thus transport all trajectories to different regions on the surface, or one could periodically change the amplitude of the periodic drive, heat the system and so forth.

Next, the timescales on which the disorder is actually quenched are the maximum catch times. Usually, the disorder is assumed to be of such a nature, that the timescale $\tau_{disorder}$ on which it varies is much larger than all other relevant time scales. For our purposes, the relevant time scales are the “typical” transient time of the dynamics $\tau_{transient}$ and the duration of the (numerical) experiment $\tau_{experiment}$. If $\tau_{disorder} \gg \tau_{experiment}, \tau_{transient}$, the disorder is fully quenched. But the results presented in this chapter can be easily generalized if $\tau_{transient} \ll \tau_{disorder} < \tau_{experiment}$. In that case, trapping events will only be of finite duration, and trapped trajectories will become free again, once the disorder changes such that the trapping (bounded) attractor is destroyed. This will generically be the case for small disorder if there are no bounded attractors in the ordered (perfectly periodic) phase space. In contrast, if there is a bounded attractor in ordered phase space, this will only be the case if the temporal variation of the disorder is such that the bounded attractors are destabilized. E.g., slowly varying disorder is used to explain larger than expected (from the temperature alone) fluctuations in SSBT trajectories of paramagnetic colloidal particles in a magnetic-bubble lattice in [106].

Thermal fluctuations are another point to be considered. Due to the thermal fluctuations, all attractors become metastable as has been discussed in section 4.19. Therefore,

¹⁰And another averaged quantity would yield the value it has on the specific bounded attractors.

trapped trajectories are freed after a noise induced escape from the trapping (bounded) attractor. Since we are considering weak disorder, the pseudopotential depth of these attractors is small compared to the pseudopotential depths of the deterministic attractors if there are no stable bounded attractors without disorder. If one considers the disorder as a (complex) parametric variation of system parameters, e.g. one introduces a scalar prefactor (magnitude of disorder) affecting $\vec{\zeta}$ in (5.1), the pseudopotential depth of the trapping (bounded) attractors scales with the distance to the bifurcations at which these attractors are destroyed (e.g. tangent bifurcations or chaotic crises). This distance is the strength of disorder, and thus can be expected to be small.

Lastly, we address the issue of averaging. Without thermal noise, we are considering a nonergodic dynamics. In particular, the average velocity will, in general, depend on the initial conditions.

First, the choice of the initial conditions within one elementary cell may affect the value of the averages in nonergodic dynamics. The initial conditions have to be drawn according to some weight which has to be chosen according to the experiment we have in mind. E.g. if we consider a particle which is initially placed on the substrate without applying any external forces, we should choose initial conditions in the potential wells. As we are not directly trying to represent a particular experiment, we stay with a particularly simple choice for the weight of initial conditions, a uniform distribution. Thus, attractors are weighed according to the volume of their basins of attraction in the $t_0 = 0$ stroboscopic section, which is a bit arbitrary. If the strength of the quenched disorder is sufficiently strong, the disorder introduces a certain averaging for transporting phase space structures, see the trajectories shown in figure 5.1(a-b). While these trajectories are not ergodic, they closely resemble ergodic trajectories in the presence of thermal noise. Therefore, we expect (and have checked) our results to be robust against changes of the weighting of \vec{r}_0 for sufficiently strong disorder. We show the average transport velocity only if either there is only one deterministic attractor, i.e. the choice for the initial conditions does not matter for sufficiently long times, or if the disorder is strong enough to remove the dependence on the initial conditions¹¹ unless otherwise noted. We have verified this in each case manually by calculating the figures for differently distributed initial conditions.

Second, we have to average over all realizations of the disorder. In practice, it is sufficient to consider only one realization of the disorder and place all initial conditions in randomly (according to a uniform distribution) chosen elementary cells. Each trajectory starting from one of these initial conditions effectively “sees” an individual realization of the disorder since the correlation length of the disorder is of the order of the lattice spacing. To avoid trajectories “leaving” our surface, we use periodic boundary conditions and choose our surface large enough to avoid trajectories crossing the surface more than once.

¹¹In particular, we have not found any significant differences if we change the phase of the stroboscopic section by $\frac{T}{2}$, i.e. the sign of the periodic drive, in figure 5.2.

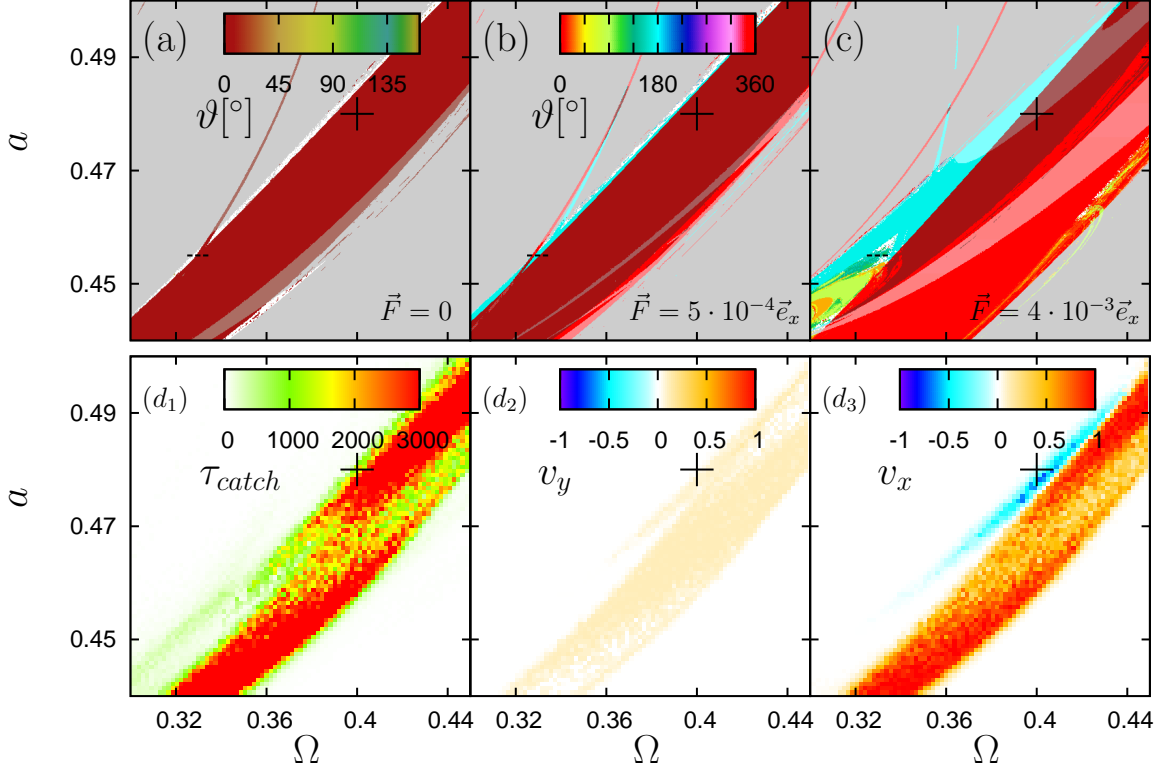


Figure 5.2: (a)-(c): deterministic phase diagram without disorder ($\Gamma = 0$ and $\gamma = 0$) for the dynamics (4.1) with a Gauss potential (4.4) ($u = 1$ and $\sigma = \frac{1}{4}$) and square wave periodic drive (4.7) with $\alpha = 50.4^\circ$. \vec{F} is indicated in the panels. (d): catch time (d_1) and average transport velocity (d_2)-(d_3) in the presence of quenched disorder ($\gamma = 10^{-3}$) for the same dynamics as in (c), but quenched disorder is accounted for by replacing (4.2) with (5.2) in (4.1). The transport velocity has been calculated from an ensemble of 20 trajectories of length 4000 drive periods T , weighting all trajectories equally. The '+' corresponds to the system parameters used in figure 5.5. Likewise, the dashed line around $\Omega \approx 0.33$ and $a = 4.55$ corresponds to the parameters considered in figure 5.4. Note that, in the large region of coexistence of the $\vartheta = 0^\circ$ transporting attractor and unbounded attractors, the average velocity depends somewhat on the initial conditions, see text. The palettes for $v_{x/y}$ and τ_{catch} have been cut off, i.e. smaller or larger values are displayed as the minimum/maximum of the palette.

5.6 Effect of quenched disorder on phase-locked SSBT attractors

5.6.1 Deterministic phase diagram

Basically, figure 5.2(a-c) shows a zoom into the largest region of parameter space exhibiting SSBT in figure 4.18, i.e. the rightmost large region of SSBT, but for a different potential, and thus different parameters. In particular, we have used $\alpha = 50.4^\circ$, as this resulted in slightly better results than $\alpha = 54^\circ$. In contrast to figure 4.18, we have also shown bounded attractors for $\vec{F} \neq 0$ in figure 5.2(b-c) by desaturation of the particular color, as these play an important role for trapping events, as has been discussed above.

Note that we have used $u = 1$ in (4.4) and not rescaled our parameters to match the Yukawa potential in (4.9), in contrast to figure 4.4. Therefore, all quantities (i.e. a , Ω , F and Γ) affected by the rescaling of u will be smaller by a factor of about 10 compared to chapter 4. With that in mind, we discover nothing “new” in figure 5.2(a-c): the behavior is the same as found in figure 4.18.

5.6.2 Disorder effects

Upon switching on the disorder, we show the average catch time τ_{catch} and transport velocity in figure 5.2(d). The average is carried out along the lines of section 5.5. Since we are mostly considering transport in the x direction, we show both components of the average velocity instead of its direction and modulus. We have used a representative choice of the bias force, $\vec{F} = 0.004\vec{e}_x$, i.e. the same parameters and view as in figure 5.2(c), and disorder strength $\gamma = 10^{-3}$. Note that in the region of parameter space where $\vartheta = 0^\circ$ transporting attractors and bounded attractors coexist, the magnitude of disorder is too low to average out the dependence of averaged quantities on the choice of initial conditions. Therefore, the observed reduction of the transport velocity is an artifact of our choice of weight for the initial conditions. In principle, the catch time is expected to be somewhat reduced for weak disorder in the presence of a stable non-transporting attractor, since then disorder only has to induce an escape from the transporting trajectory, and without the deterministically stable non-transporting attractor, the disorder has to create, or stabilize, a bounded attractor on top of inducing the escape from the transporting trajectory. Here, the disorder is too strong to observe that effect. There is no reduction of the transport velocity in the second region of coexistence of transporting and non-transporting attractors in figure 5.2(c) (to which the parameters corresponding to the ‘+’ belong): for this region of coexistence, the disorder is sufficiently strong to remove the dependence on the initial conditions.

Due to disorder, practically all regions of transport in parameter space shrink. Even more, the transport velocities are always reduced due to trapping events. This is a significant difference to thermal fluctuations which actually induce transport for certain regions of parameter space or enhance the average velocity, see section 4.19. In particular, this noise induced transport was responsible for an apparent movement of the regions of transport when the strength of thermal fluctuations was increased. This movement is practically absent from figure 5.2(d), and also if one considers weaker disorder (not shown). This absence will be further discussed in section 5.6.4.

5.6.3 Escape rates

To further understand the effect of quenched disorder on transporting attractors and the analogy to thermal fluctuations, we calculate the escape rates from deterministic transporting attractors in the presence of quenched disorder. As has been discussed in section 4.19, all deterministic attractors become metastable in the presence of thermal noise. Due to quenched disorder, only the unbounded deterministic attractors become metastable for almost all realizations of the disorder, while bounded attractors may become destabilized only for specific realizations of the disorder. Therefore, we can calculate the escape rate, or its inverse, the mean escape time, from transporting (unbounded) attractors.

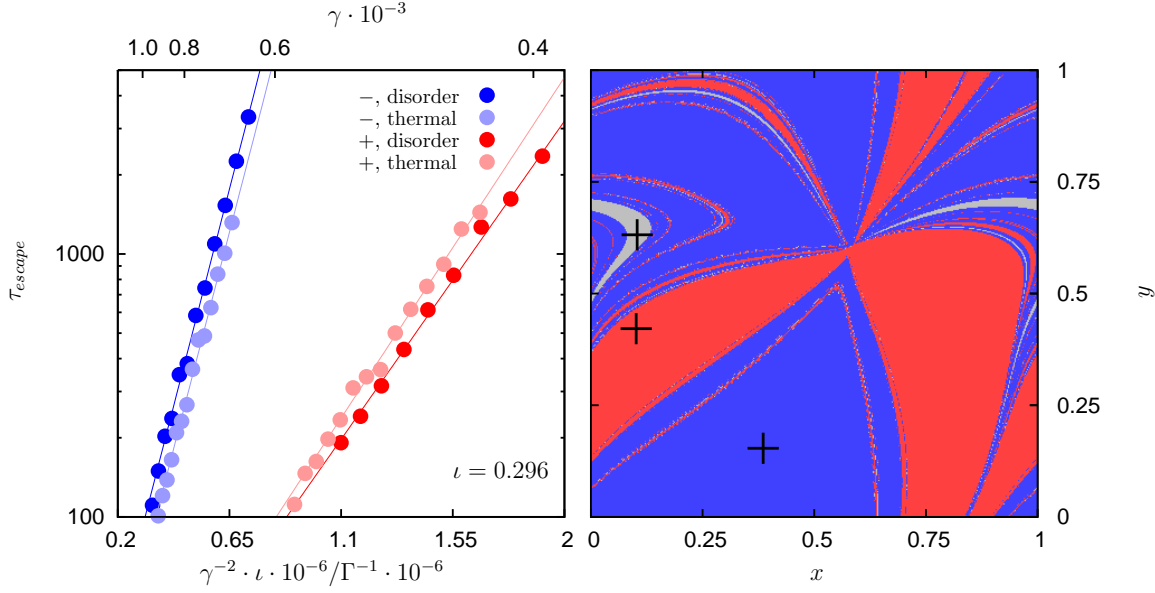


Figure 5.3: (a) mean escape times for the transporting attractors corresponding to the '+' in figure 5.2(c) in dependence of the strength of disorder γ (upper axis) and the strength of thermal fluctuations Γ (lower axis). The scales have been chosen such that the slopes of the blue lines are equal, see text. The error bars are of the order of the symbol sizes. The lines correspond to fits, see text. The attractor carrying $\vartheta = 0^\circ$ transport is labeled as '+', and the attractor carrying transport in the opposite direction as '-'. (b) basins of attraction (for $t = 0$) of the '+' attractor (red), the '-' attractor (blue), and the bounded attractor (grey). The escape rates are calculated along the lines of [2]. Symbols: the attractors (period 1 orbits).

The mean escape time is the average, over all realizations of the disorder and all initial conditions within the attractor's basin of attraction, of the time it takes a (disordered) trajectory to first leave the (immediate) basin of attraction (of the attractor) [2, 320], see [2] for a definition in the context of thermal noise. The dependence on the initial condition (within the basin of attraction) can be neglected if the perturbation is weak. In the presence of thermal noise, the dependence of the mean escape time on the temperature is given by an Arrhenius law, possibly including prefactors [2, 141, 144, 320]: $\tau \sim e^{\frac{\Delta U}{T}}$, see also section 4.19. Using the analogy between thermal noise and quenched disorder for transporting attractors, we postulate that the mean escape time from these attractors should follow an Arrhenius law in the magnitude of the disorder, if that is described by a suitable scalar quantity (depending on the particular type of the disorder). To find this for our choice of disorder, i.e. (5.2), we write $\vec{\zeta}(\vec{r}(t))$ as in (5.7). By (Taylor) expanding (5.2) in powers of ζ_{nm} , we obtain

$$\vec{\zeta}(\vec{r}(t)) \approx \left. \frac{\partial (\vec{\nabla} U)}{\partial \vec{r}} \right|_{\vec{r}(t)} \vec{\zeta}_{nm}. \quad (5.9)$$

Using $\langle \vec{\zeta}_{nm}^2 \rangle = 2\gamma^2$, we get the scaling of $\langle \vec{\zeta}(\vec{r})^2 \rangle$ with γ

$$\langle \vec{\zeta}(\vec{r})^2 \rangle \sim \gamma^2. \quad (5.10)$$

From this, we expect

$$\tau_{\text{escape}} \sim e^{\frac{\tilde{\Delta}U}{\gamma^2}} \quad (5.11)$$

and define

$$\iota = \frac{\tilde{\Delta}U}{\Delta U} \quad (5.12)$$

as the ratio of the pseudopotential depth for disorder induced escape to the pseudopotential depth for thermal noise induced escape. In general, this ratio depends on all the so far neglected contributions to the difference between quenched disorder, expressed as (5.7), and thermal noise, i.e. the specific form of the attractors, the system parameters, the type of disorder and its correlation length. Using this, we can define an effective temperature in a different way than in, e.g., [201, 290, 314].

To verify our hypothesis, we have calculated the mean escape times for the transporting attractors encountered at various choices of system parameters found in figure 5.2 and have always found an Arrhenius law with ι depending on the choice of parameters. As an example, we choose the transporting attractors found for parameters corresponding to the '+' in figure 5.2(c-d), and show the mean escape times due to both, thermal fluctuations and quenched disorder, in figure 5.3(a). Fits to straight lines $\tau_{\text{disorder}} = \tilde{D}e^{\frac{\tilde{\Delta}U}{\gamma^2}}$ and $\tau_{\text{noise}} = De^{\frac{\Delta U}{\gamma^2}}$ are included in the Arrhenius plot figure 5.3(a), and the parameters of the fits are found in table 5.1.

Attractor	$\tilde{\Delta}U \cdot 10^6$	$\Delta U \cdot 10^6$	\tilde{D}	D
+	0.92	3.32	1.88	1.82
-	2.50	8.43	1.99	1.62

Table 5.1: Parameters for the Arrhenius fits corresponding to figure 5.3(a). The attractors are labeled according to the signs of the x component of their average velocities.

As can be seen from figure 5.3(a), the Arrhenius law holds for sufficiently large escape times for the quenched disorder, and $\iota \approx 0.30$ is calculated for the '-' attractor (i.e. the attractor carrying $\vartheta = 180^\circ$ transport). In principle, we have $\iota \approx 0.28$ for the '+' attractor, but the difference is negligible. We have matched the scales of $\frac{1}{\Gamma}$ and $\frac{1}{\gamma^2}$ in figure 5.3(a), such that the slopes are identical, i.e. we have multiplied $\frac{1}{\gamma^2}$ with ι .

A different situation is found for the bounded attractor also present in phase space (its basin of attraction is shown as grey areas in figure 5.3(b)). In the presence of thermal fluctuations, its pseudopotential depth is smaller than 10^{-7} , i.e. it has no influence on the average transport properties for the noise strengths considered here. In contrast, if one were to try to calculate its pseudopotential depth in the presence of quenched disorder, one would find that the mean escape time is infinite for all strengths of the disorder. This is due to the attractor being stable for a non-zero weight subset of the realizations of the disorder, and its pseudopotential depth with respect to quenched disorder is not defined. Thus, in the case of only quenched disorder (and no thermal fluctuations), the average

transport velocity depends on the choice of initial conditions as has been discussed in section 5.5. Here, the volume of the basin of attraction of the bounded attractor is very small (as is its pseudopotential depth with respect to thermal noise), and it does not influence the average transport velocity as calculated here in the sense of section 5.5.

5.6.4 Quenched disorder induced absolute negative mobility

Quenched disorder induces escape from deterministic bounded attractors at most once for each trajectory. After a disorder induced escape from a deterministic bounded attractor (i.e., the attractor exists already without disorder) a transient follows, which can be transporting. But after that transient ends in a trapping event, the trajectory will end up on a bounded attractor, terminating transport. Therefore, disorder induced ANM, carrying significant transport velocities, will only be found close to the bifurcations leading to the disappearance of transporting ANM attractors, where the transient lengths are sufficiently long to allow a single transient to yield a significant contribution to transport. Moreover, as does thermal noise, sufficiently strong disorder is expected to reduce these transient lengths in general (in contrast, small disorder can be expected to increase the transient length under certain circumstances [147]. [295, 297] may also be a hint in that direction). We have found that transient lengths tend to zero very quickly when going away from the bifurcation in the systems and for the parameters considered here. Therefore, we conclude that the main mechanism for noise induced ANM outlined in section 4.19, coexistence of a bounded attractor and a transient ANM inducing phase space structure [63], is effectively absent from the purely disordered case without thermal fluctuations.

The situation can be remedied by considering a different situation leading to noise induced ANM, which has been discussed in [1, 2]. Basically, the reason for the absence of disorder induced ANM due to the mechanism from [63] is the failure of the analogy between thermal noise and quenched disorder for the bounded attractors considered therein. The obvious solution is to replace the bounded attractor by an unbounded attractor, e.g. a transporting attractor carrying transport in the direction of the bias force. Then, if this attractor coexists with an unstable ANM object in phase space, e.g. its region of existence is close to (but not inside) a region of existence of an ANM attractor, and the unstable ANM object dominates in the presence of fluctuations of the right magnitude, the fluctuations will induce ANM by destabilizing the transporting attractor and assigning sufficient statistical weight to the unstable ANM object. This situation has been discussed in [1, 2] for thermal noise: for certain parameters and an applied (positive) bias force, transport is in the direction of the bias force without (thermal) fluctuations. When the strength of the fluctuations is increased, the transport velocity changes to be opposite to the applied bias force. For very large (thermal) fluctuations, transport is again in the direction of the bias force. We expect the same to be true if thermal fluctuations are replaced by quenched disorder due to the analogy between thermal noise and quenched disorder for transporting trajectories (section 5.3), only that transport will vanish for large fluctuations, instead of being in the direction of the bias force. In [1, 2] this configuration of phase space was realized by choosing a pair of SSBT attractors and a small bias force. In general, the regions of existence of the SSBT attractors have numerous filaments and protrusions (in parameter space), but the SSBT attractors have very small

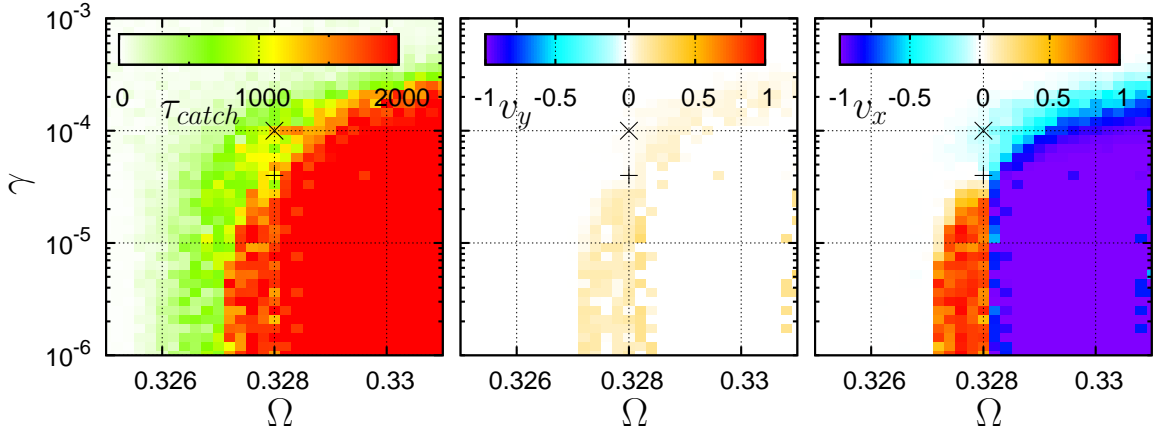


Figure 5.4: Dependence of the average transport velocity on the strength of the disorder, γ , and the frequency of the periodic drive, Ω , calculated from an ensemble of 20 trajectories of length 5000 drive periods T , weighting all trajectories equally. The parameters chosen correspond to the dashed line in figure 5.2(b), except for the addition of quenched disorder. The palettes have been cut off as in figure 5.2.

pseudopotential depths in the filaments. If we select parameters where such a filament belonging to the attractor carrying transport in the direction of the bias force meets the main “body” of the region of existence of the attractor carrying transport against the bias force, the situation described above is realized.

Considering figure 5.2(a), such a filament is readily found for $\vec{F} = 0$. Upon switching on the bias force, the regions of existence of the pair of SSBT attractors separate, yielding a parameter region where the filament of the attractor carrying transport in the direction of the bias force goes straight through the main region of existence of the ANM attractor, and where no other attractors of relevance¹² exist. At the intersection of the edge of this region and the filament, above described situation is realized, see the dashed line in figure 5.2(b). To quantify the effect, we choose $a = 4.55$ and $\vec{F} = 0.0005\vec{e}_x$ fixed and vary the frequency Ω and the strength of the disorder, see figure 5.4. The symbols correspond to $\Omega = 0.328$ (i.e. the ‘ \times ’ in figure 5.2) and $\gamma = 4 \cdot 10^{-5}$ and $\gamma = 10^{-4}$ respectively, i.e. the parameters corresponding to the trajectories in figure 5.1(a-b). There is a narrow range of parameters around $\Omega \approx 0.328$, marked with a ‘ $+$ ’ and a ‘ \times ’, for which transport is in the direction of the force for very small disorder $\gamma \lesssim 4 \cdot 10^{-5}$ (‘ $+$ ’), and against the force for larger γ (‘ \times ’). In contrast to the case of thermal noise, the transport does not return to “normal”, i.e. in the direction of the bias force, for large strengths of the disorder (at least not with a measurable velocity). As discussed above, all trajectories become trapped for strong disorder.

The trajectories shown in figure 5.1 show this behavior in more detail. (a) corresponds to a strength of the disorder where transport is still normal, but with a small transport velocity (the ‘ $+$ ’ in figure 5.4). It consists of relatively long almost periodic flights, where the particle travels in the positive x direction, broken by parts where the particle seems to diffuse chaotically in the negative x direction and occasionally travels a few length units in the y direction. When the strength of the disorder is increased further, the length

¹²I.e., such that have an appreciably large region of existence in parameter space.

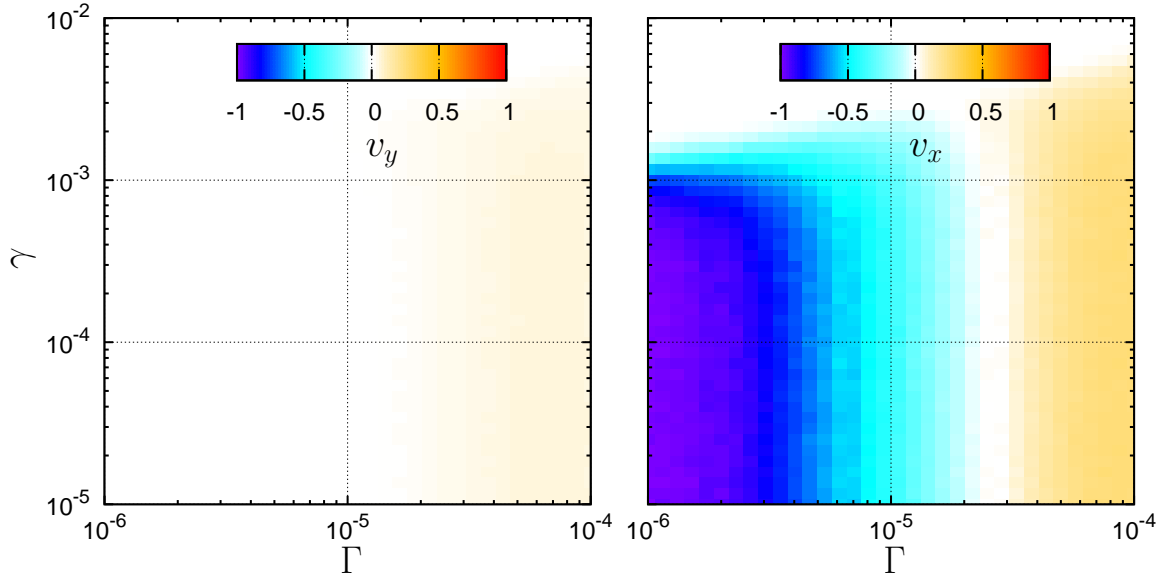


Figure 5.5: Dependence of the average transport velocity on the strength of the disorder, γ , and the strength of thermal fluctuations, Γ , calculated from an ensemble of 20 trajectories of length 5000 drive periods T , weighting all trajectories equal. Except for the addition of thermal noise and varying disorder strength, all other parameters correspond to the '+' in figure 5.2(d).

of the almost periodic flights is reduced, and the x component of the transport velocity becomes negative. At $\gamma = 10^{-4}$, the almost periodic flights have all but vanished, and only the chaotic parts, carrying transport in the $-x$ direction, remain. The transport velocity in the y direction has not changed significantly, i.e. remains small. For an even larger strength of the disorder, $\gamma = 10^{-3}$, the transport velocity is practically 0, with only short excursions to the metastable or unstable transporting structures in phase space, and trajectories are almost immediately attracted to a bounded attractor. That attractor is the stable period one orbit existing for slightly smaller values of Ω , and is stabilized locally by disorder. This behavior is shown in figure 5.1(c), where a short excursion to both transporting phase space structures (periodic orbits, grey line and green line in figure 5.1(c)) is shown, as well as the periodic bounded attractor (blue line). Indeed, the transport properties are determined by the interplay of these periodic orbits and quenched disorder. Of course, the same analysis can be applied to the other panels in figure 5.1 as well and yields identical results (with different orbits for panel (d) of course).

5.6.5 Thermal fluctuations and quenched disorder

Finally, we consider the interplay of thermal noise and quenched disorder. As has been discussed above, the main effect of weak thermal noise on the phase space structure due to quenched disorder is to destabilize the unbounded attractors, and thus to suppress trapping events. Furthermore, thermal noise has the usual effects on all other phase space structures. There is a competition between thermal noise induced and quenched disorder induced escape for all deterministic attractors of the ordered system. As has been discussed above, bounded attractors are affected only to a lesser degree to weak

quenched disorder. If the disorder is “weaker” than the thermal noise, i.e. the disorder induced escape times are much larger than the thermal noise induced escape times, the effect of thermal noise will be identical to the case without quenched disorder.

The chief consequence of thermal noise is that the asymptotic transport velocity will (almost) always have a non-zero value (unless there is an appropriate symmetry, of course). In that sense, ANM in the presence of quenched disorder is always “noise induced” if the average is calculated for infinite times. In contrast, NANM in perfectly periodic systems, as discussed in [1, 63], is noise induced for certain values of system parameters only. As has been discussed above, in most cases, this is only relevant for possibly very long times and large surfaces, and only if the strength of the quenched disorder is such that transport practically vanishes for the surface size considered.

With that in mind, we turn to figure 5.5, showing the effect of thermal noise and quenched disorder for a representative choice of system parameters corresponding to the ‘+’ in figure 5.2(c-d). First, we find exactly the effect described in above paragraph: around $\gamma = 2 \cdot 10^{-3}$, where transport vanishes without thermal noise, we find NANM: for $\Gamma = 10^{-6}$ the transport current vanishes, and for $\Gamma = 10^{-5}$ (and the same value of γ), we find transport against the applied bias force.

As can be seen from figure 5.2(c-d), the choice of parameters in figure 5.5 does not lie exactly in the center of the ANM region but slightly outside. This choice is motivated to optimize both resistivities simultaneously: from figure 4.24 we have inferred that upon increasing the noise strength, the region of parameter space in which ANM is found moves into regions previously exhibiting no transport, see section 4.19 (NANM). It turns out that, for this particular choice of parameters, ANM vanishes at about $\gamma_{max} \approx 2 \cdot 10^{-3}$ and $\Gamma_{max} \approx 2 \cdot 10^{-5}$, of which the latter is in line with what we have observed in section 4.19 if we factor in the different potentials used, i.e. the factor of 10 discussed in section 5.6.1. Going back to (5.1), both limits are not unrelated.

Using the analogy between thermal noise and quenched disorder as discussed in section 5.6.3, we can quantify this relation. To estimate the typical magnitude of $\vec{\zeta}(\vec{r}(t))$, we estimate the second order derivative of the potential, $\frac{\partial(\vec{\nabla}U)}{\partial \vec{r}} \Big|_{\vec{r}(t)}$, in (5.9): along the lines $y = 0$ and $y = x$ the potential basically looks like a sine potential with period 1 and $\sqrt{2}$ respectively, and barrier heights $\Delta U \approx 0.05$ and $\Delta U \approx 0.25$ respectively. Thus, the second order derivative will be of order 1, yielding a proportionality constant of order 1 in (5.10). Comparing with $\langle (\vec{\xi}(t))^2 \rangle = 2 \cdot \Gamma$, we obtain $\gamma^2 \sim \Gamma$ up to a factor of order 1. For this factor we can use $\frac{1}{\iota} \approx 3.4$, relating the pseudopotential depths as discussed in section 5.6.3, yielding $\frac{\gamma_{max}^2}{\iota} \approx 1.4 \cdot 10^{-5}$, which is quite close to Γ_{max} . The remaining difference can be attributed to our rough estimate, in particular using ι as proportionality constant, i.e. only the respective lifetimes of the transporting states and not taking into account transient states or trapping events.

5.7 Summary and outlook on inertia effects

We have shown that quenched disorder can be treated as thermal noise with regard to the disorder induced escape from unbounded attractors carrying ballistic transport¹³. Using this analogy, we have found quenched disorder induced ANM by a similar mechanism as NANM in [1]. At disorder strengths slightly larger than the “critical” value at which ANM vanishes for the given parameters and experiment, thermal noise again induces ANM in a somewhat less artificial way than in [1, 2, 63]. Moreover, we have estimated the threshold of disorder at which SSBT, and SSBT induced ANM, vanish using that analogy. These thresholds tend to be rather small, as can already be inferred from the thresholds with regard to thermal noise. Thus, experiments exploiting SSBT have to be well controlled with regard to disorder in the lattice. While that may seem to be discouraging at first glance, it is important to note that our analogy, and the derived thresholds, depend on the distribution of disorder. E.g., rare but large impurities of the lattice have a much different effect on the dynamics. Ultimately, they will lead to the Golosov effect, but at very different time scales than small but frequent disorder, and their effect may well be covered up by realistic thermal noise. In such a situation, the effect of quenched disorder may be much weaker than the Gaussian disorder considered in this chapter.

The observed resistivities against random perturbations can be improved by including inertia effects. If one compares the pseudopotential depths found in [1, 2] with those found here and accounts for the different potential well depths, the overdamped dynamics still have a lower threshold at which the SSBT derived effects vanish, see also section 4.19. Including inertia effects, all effects from [1, 2] are recovered trivially for e.g. $\alpha = 0^\circ$. For other values of α , there is a competition between the effects discussed so far (see also [4]), and the spatially 1D effects from [1, 2], see [183, 208] for a hint in that direction. We have found pseudopotential depths in line with those found in [1, 2] (accounting for the differences in the depth of the potential wells) if we include inertia effects in (4.1). Moreover, as was found in [1, 2] (see also [137, 183, 208, 321]), for sufficiently large inertia (or, equivalently, small damping coefficients), the behavior of the system is dominated by diffusive chaos, and bounded attractors are much less common than in the overdamped case considered above, reducing the trapping rate of disorder.

We have found that, with inertia, ANM can survive up to $\gamma \lesssim 10^{-2}$, with significant transport velocities sustained up to $\gamma \approx 10^{-3}$, which is about one order of magnitude “better” than in the overdamped case. First, this is due to the more robust mechanism of SSBT using inertia effects, as has been discussed in section 4.19. Second, the catch times are larger. First, this is due to bounded attractors being less common, i.e. it is easier to choose system parameters far away from the regions of existence of bounded attractors in parameter space, and a less probable realization of the disorder is needed to stabilize these. Second, the additional degrees of freedom increase the dimensionality of the dynamics and allow trajectories more possibilities to pass deflecting regions. Lastly, disorder induced ANM as discussed in section 5.6.4 is more common if inertia effects are included since the regions of existence of SSBT attractors tend to have more filaments in

¹³Quenched disorder may have a different influence on purely diffusive attractors. In particular, the scaling between disorder and noise strength may be different since diffusive transporting trajectories frequently revisit regions of phase space, and thus disorder.

that case.

Chapter 6

Dimers in one dimension

Contrary to the remainder of this work, we will consider interacting particles in this chapter and show that in spatially one dimensional overdamped dynamics the interaction of two monomers induces spontaneous symmetry breaking transport (SSBT) and absolute negative mobility (ANM). We introduce our minimal model in section 6.2. In section 6.3 we show analytically that the dynamics are very simple for convex interaction potentials and that SSBT and ANM are ruled out. Turning to non-convex interaction potentials, we show that SSBT induced ANM can exist for symmetric dimers in section 6.5 and also for asymmetric dimers in section 6.6.

6.1 Introduction

To find ANM, we have to consider at least three dimensional dynamical systems. So far we have considered only single particle dynamics. Spatially one dimensional systems with time and inertia were considered in chapter 3 and spatially two dimensional system with time (and without inertia) were considered in chapter 4. A three dimensional phase space can also be realized by two overdamped particles in a one dimensional periodic potential subjected to time depended forces and interacting via a coupling force, i.e. a dimer. We restrict ourselves to the case where that interaction is mediated by an interaction potential $U_{int}(y)$, where y is the distance of the monomers. Then the dimer dynamics can be mapped to the dynamics of a single particle on a two dimensional surface which is not periodic in one direction.

These systems have attracted considerable recent interest in the context of modeling friction and diffusion (mostly considering more than two monomers) [322–334], molecular motors [10, 335], in particularly in the form of dimer ratchets with harmonic interactions, both overdamped [336–346] and underdamped [347, 348] (allowing for chaos) or including more monomers [349–352] which may even lead to SSBT and SSBT induced ANM as a collective effect [38, 40–44] for a non-convex global interaction potential. Convex interaction potentials usually serve as an approximation of the “real” interaction potential around the minimum (equilibrium length) of that potential. Non-convex interaction potentials are the more general situation. First, when the distance of the monomers becomes large, the interaction forces have to vanish, which is captured by e.g. molecular inspired potentials [353, 354], such as Lennard-Jones [355–357] or Morse potentials, used to model the dynamics of weakly bound dimers [358] or chains of coupled particles [359, 360]. Second,

we will consider spatially one dimensional dynamics which are an approximation of two or higher dimensional dynamics, i.e. only one component of the monomer coordinates is kept and the other components of the monomer coordinates are neglected. Some of the effects of the neglected degrees of freedom can be captured by a modified interaction potential. In particular, a 180° rotation of the dimer can be allowed for if the interaction potential is reflection symmetric, i.e. $U_{int}(-y) = U_{int}(y)$, but that leads to a non-convex interaction potential if the dimer is to have a non-zero equilibrium length, the simplest case being a bistable interaction potential. Bistable interaction potentials, inspired by the modeling of random walkers in motor proteins [361–368] (see in particular [367, 368] for a symmetric motor protein), have been considered in dimer ratchet models [369–373] and were shown to yield a richer dynamical behavior of the ratchet. Third, more complex dimers may have several stable configurations, or the stretching process may involve additional (fast) internal degrees of freedom that lead to a non-convex interaction potential, as considered in e.g. [374]. Lastly, another possible generalization of the model is the inclusion of hydrodynamic interactions in a fluid [375, 376], and Hamiltonian transport of dimers has been considered in [333, 377, 378].

6.2 Model

We require our model dynamics to be reflection symmetric and to consist of two over-damped particles, which we will henceforth refer to as monomers, with monomer coordinates x_1 and x_2 . Furthermore, we define the “center of mass”¹

$$x = x_1 + x_2 \quad (6.1)$$

and the dimer length

$$y = x_1 - x_2. \quad (6.2)$$

Each monomer is subjected to a one dimensional periodic and symmetric potential $U_{1,2}(x_{1,2}) = U_{1,2}(x_{1,2} + L_{1,2})$ (the indices indicating to which monomer they apply) and are coupled via an interaction potential $U_{int}(x_1 - x_2) = U_{int}(y)$. Furthermore, we apply rocking, symmetric, and periodic driving forces $a_{1,2}(t)$ with periods $T_i = \frac{T}{n_i}$ with integers n_i ($\frac{T}{2}$ is the time shift of reflection symmetry, see below)², constant bias forces $F_{1,2}$ and (white noise) thermal fluctuations³ $\xi_{1,2}(t)$ with $\langle \xi_i(t) \xi_j(t') \rangle = \delta_{ij} \cdot \delta(t - t')$ with scalar prefactors $\sqrt{2\Gamma_i \eta_i}$ according to the usual fluctuation-dissipation relations [8] to each monomer. As in chapter 4, we require the periodic potential and the driving forces to be symmetric, i.e.

$$U_i(x_i) = U_i(-x_i) \quad (6.3)$$

and

$$a_i(t + \frac{T_i}{2}) = -a_i(t) \quad (6.4)$$

¹Actually, the physical center of mass is one half our “center of mass”, but we found our definition to be more convenient.

²If the periods of the two driving forces are incommensurate, reflection symmetry would always be broken, as the time shift could not be applied to change the signs of both driving forces simultaneously.

³In principle, we could use more general stochastic processes and in particular with different statistical properties for the two particles, as long as the symmetry properties are fulfilled (see below).

where trivial shifts have been set to zero [10, 379]. There are two different ways to implement reflection symmetry if $F_1 = F_2 = 0$, depending on whether the system, interpreted as a single particle in a two dimensional potential, is symmetric under an interchange of the monomer coordinates (i.e. exhibits the S_{xy} symmetry from chapter 4). This is the case if both monomers are identical, i.e. $U_1(x) = U_2(x)$, $\eta_1 = \eta_2$, $\Gamma_1 = \Gamma_2$, $a_1(t) = a_2(t)$ and we define

$$\tilde{S}_0 : (x_1, x_2, t) \rightarrow \left(-x_2, -x_1, t + \frac{T}{2} \right) \quad (6.5)$$

(corresponding to $S_0 \circ S_{xy}$ from chapter 4 but with a different physical meaning). If the two monomers are not identical, reflection symmetry can only be satisfied⁴ if the total potential $U_{total}(x_1, x_2) = U_1(x_1) + U_2(x_2) + U_{int}(x_1 - x_2)$ is reflection symmetric, i.e.

$$U_{total}(x_1, x_2) = U_{total}(-x_1 + N_1 \cdot L_1, -x_2 + N_2 \cdot L_2) \quad (6.6)$$

with integers N_1 and N_2 ⁵. But since U_{int} is, in general, not periodic (or has a different spatial period than $U_{1/2}$), it is not invariant under translations by integer multiples of the spatial periods of the coordinates. Therefore, the interaction potential has to satisfy

$$U_{int}(-x_1 + N_1 \cdot L_1 + x_2 - N_2 \cdot L_2) = U_{int}(x_1 - x_2), \quad (6.7)$$

i.e. it has to be reflection symmetric around an integer-linear combination of the spatial periods of the individual monomer potentials $U_{1/2}$. Henceforth we will set $N_1 = N_2 = 0$ for simplicity and define the reflection symmetry as

$$S_0 : (x_1, x_2, t) \rightarrow \left(-x_1, -x_2, t + \frac{T}{2} \right), \quad (6.8)$$

which is the analog of S_0 symmetry in chapter 4. In particular, this applies is the dimer is allowed to rotate by 180° , as discussed above.

We focus on the simple choices for the monomer potentials and the periodic drive

$$U_{1/2}(x) = \frac{1}{2\pi} \cos(2\pi \cdot x) \quad (6.9)$$

and

$$a_{1/2}(t) = a_{1/2} \sin(\Omega \cdot t) \quad (6.10)$$

with $T = \frac{2\pi}{\Omega}$. As in the preceding chapters, reasonable generalizations of these simple choices are not expected to qualitatively change our conclusions, as long as the symmetry properties are unchanged, and changes in the potential barrier heights and spatial periods are taken into account. Moreover, we use the same functional form for the drive protocol of the two monomers, allowing only for different amplitudes. Thus, our model reads:

$$\begin{aligned} \eta_1 \dot{x}_1(t) &= \sin(2\pi x_1(t)) - U'_{int}(x_1(t) - x_2(t)) + a_1 \sin(\Omega t) + F_1 + \sqrt{2\eta_1 \Gamma_1} \xi_1(t) \\ \eta_2 \dot{x}_2(t) &= \sin(2\pi x_2(t)) + U'_{int}(x_1(t) - x_2(t)) + a_2 \sin(\Omega t) + F_2 + \sqrt{2\eta_2 \Gamma_2} \xi_2(t). \end{aligned} \quad (6.11)$$

⁴The “proof” is obtained by evaluating the force field of the deterministic equation of motion for $(-x_1, -x_2, t + \frac{T}{2})$.

⁵Note again that we have absorbed trivial shifts of $x_{1/2}$ into the choice of the coordinate system.

For identical monomers, we can absorb the friction coefficient into the time unit and our model reads

$$\begin{aligned}\dot{x}_1(t) &= \sin(2\pi x_1(t)) - U'_{int}(x_1(t) - x_2(t)) + a \sin(\Omega t) + F + \sqrt{2\Gamma} \xi_1(t) \\ \dot{x}_2(t) &= \sin(2\pi x_2(t)) + U'_{int}(x_1(t) - x_2(t)) + a \sin(\Omega t) + F + \sqrt{2\Gamma} \xi_2(t).\end{aligned}\quad (6.12)$$

We have used the same symbols for the rescaled quantities, in particular Ω for the rescaled frequency $\Omega \cdot \eta_1$ since we will only consider the case $\eta_1 = \eta_2$ in the following.

Our central observable will be the time and ensemble averaged normalized velocity of the monomers

$$v = \frac{T}{1} \lim_{t \rightarrow \infty} \frac{1}{t} \int_0^\infty dt' \dot{x}_i(t') , i = 1, 2 \quad (6.13)$$

which will be identical for both monomers for all data presented in this chapter⁶.

6.3 Convex interaction potentials

We first consider the case that in the dynamics (6.12) the two monomers interact via a harmonic potential

$$U_{int}(y) = \frac{k}{2\pi} \cdot (y - l)^2 \quad (6.14)$$

with the equilibrium length l and interaction strength k . If l is an integer, the dynamics are S_0 symmetric, otherwise not. The dynamics are \tilde{S}_0 symmetric if the monomers are identical [285]. This system is of particular importance in the modeling of superconducting rings containing two weak links, i.e. SQUIDs [380] irradiated by microwaves in the resistively shunted junction model [7, 64, 65]. Generalizations have been used to model various SQUID ratchets [17, 285, 381, 382]. Moreover, in the limit of small displacements from the minimum, it is a reasonable approximation to all interaction potentials featuring a quadratic minimum.

A harmonic interaction potential is the simplest representative of convex interaction potentials, which we will consider in the following, i.e.

$$\frac{\partial^2}{\partial y^2} U_{int}(y) > 0 \quad (6.15)$$

for all y . This property implies that the asymptotic average velocity

$$(6.16)$$

(which we have defined in normalized units for convenience) is unique for all initial conditions already in the absence of thermal fluctuations [383–386]. The proof is as follows: consider two solutions of (6.11), $\vec{h}(t) = (h_1(t), h_2(t))$ and $\vec{g}(t) = (g_1(t), g_2(t))$ with

$$h_1(t_0) > g_1(t_0), h_2(t_0) > g_2(t_0). \quad (6.17)$$

⁶For bound interaction potentials, i.e. $U_{int}(y) \rightarrow \infty$ for $|y| \rightarrow \infty$ sufficiently fast, this is clear. For interaction potentials that become flat for large monomer distances, the average velocity of the “free” monomers will be identical if the monomers are identical (even in the absence of noise due to the low dimensional nature of phase space). The average velocities of the monomers may be different in the case of an (unphysical) periodic interaction potential or if the monomers are not identical and the interaction potential allows the dimer to dissociate. We will not consider these cases.

The physical reasoning is as follows: if the second dimer, $\vec{g}(t)$, tries to “pass” the first, $\vec{h}(t)$, at a later time, there is a time at which the positions of, e.g., the “right” monomers are identical and the relative order due to (6.17) still holds for the other monomers. Then the monotonically increasing interaction forces (due to the convexity of the interaction potential) will try to restore that order while all other forces acting on the “right” monomers will be identical. The right monomer of the second dimer will be “pulled back” if the dimers are stretched or the “right” monomer of the first dimer will be “pushed ahead” if the dimers are compressed. More formally, proceeding along the lines of [386], let

$$t^* = \inf \{t > t_0 : h_i(t^*) = g_i(t^*), i = 1, 2\} \quad (6.18)$$

and $i = 1$ without loss of generality, i.e.

$$h_1(t^*) = g_1(t^*) \quad (6.19)$$

and thus

$$h_2(t) > g_2(t) \quad \forall t_0 < t \leq t^*. \quad (6.20)$$

If such a t^* does not exist, (6.17) will hold for all t or the solutions will coincide (which is not possible due to uniqueness [387]). Using (6.15), (6.19) and (6.20) we get

$$\dot{h}_1(t^*) - \dot{g}_1(t^*) = -U'_{int}(h_1(t^*) - h_2(t^*)) + U'_{int}(g_1(t^*) - g_2(t^*)) \quad (6.21)$$

$$> -U'_{int}(h_1(t^*) - h_2(t^*)) + U'_{int}(h_1(t^*) - h_2(t^*)) \quad (6.22)$$

$$= 0. \quad (6.23)$$

Thus, (6.17) will hold for all $t > t^*$ and “the solutions cannot pass each other”. Due to the periodicity of the monomer potentials, each deterministic solution of (6.11) is straddled by two other solutions with the same average velocity, and hence, all solutions have the same the average velocity. If the order of the dimers is inversed, the proof is similar. This result is known as Middleton’s no-passing rule in the context of Frenkel-Kontorova models [383–386], mathematically proven in [388], known already in [389] (but not in a physical context) and more recently in [390, 391]. The result can be generalized to disordered (i.e. not periodic) potentials and up to infinite chains of monomers with convex interaction potentials.

Note that we have not used that the driving forces applied to the monomers are identical, i.e. the results directly apply to the stochastic dynamics (6.11) for each particular realization of the stochastic process. A second and for our purposes even more severe consequence is that we can extend the no-go theorem from [1, 2] to a dimer. Let $\vec{h}(t) = (h_1(t), h_2(t))$ be a solution to (6.11) with $F_i = H_i$, $i = 1, 2$ and the realization $\vec{\xi}(t)$ of the stochastic process and $\vec{g}(t) = (g_1(t), g_2(t))$ a solution of (6.11) for the same realization of the stochastic process but different value of the bias force $F_i = G_i$, $i = 1, 2$ and

$$H_i > G_i, \quad i = 1 \text{ and } i = 2 \quad (6.24)$$

and the same initial condition

$$\vec{h}(t_0) = \vec{g}(t_0). \quad (6.25)$$

Then

$$\dot{h}_i(t_0) - \dot{g}_i(t_0) = H_i - G_i > 0, \quad (6.26)$$

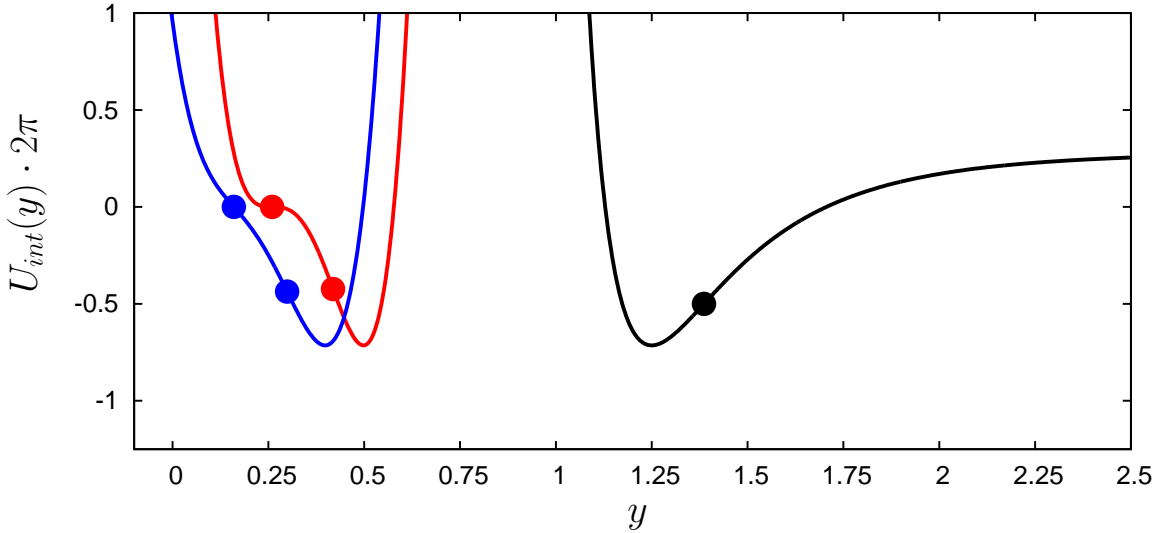


Figure 6.1: Red: interaction potential (6.32) for $d = 0$, $k = 0.357$, $l = 0.26$ and $s = 2.1$; Blue: (6.32) for $d = -3$, $k = 0.357$, $l = 0.16$ and $s = 2.1$; Black: (6.33) for $k = 1$ and $l = 1.25$. Dots indicate turning points.

i.e. the solutions separate and, assuming everything to be well behaved, we get

$$t^* = \inf \{t > t_0 : h_i(t^*) = g_i(t^*), i = 1, 2\} > t_0 \quad (6.27)$$

(it can be infinite, though). Moreover, we assume $i = 1$ without loss of generality and thus

$$h_1(t^*) = g_1(t^*) \quad (6.28)$$

$$h_2(t^*) \geq g_2(t^*). \quad (6.29)$$

Using the same arguments as to get (6.21), we get

$$\dot{h}_1(t^*) - \dot{g}_1(t^*) \geq H_1 - G_1 > 0. \quad (6.30)$$

Therefore, $\vec{g}(t)$ cannot pass $\vec{h}(t)$. Again, this is an obvious generalization to a stochastic dynamics of the results found in [383–386, 388–391].

The generalization of these results to finite (or even infinite) chains of monomers coupled by nearest neighbor convex interaction potentials is straightforward. Thus, *absolute negative mobility is ruled out for convex interaction potentials*. Moreover, SSBT requires two coexisting deterministic solutions, which is ruled out by the no-passing rule and thus *SSBT cannot be found for convex interaction potentials*.

In particular, both theorems apply to a harmonic interaction potential and thus SSBT and ANM are ruled out. As discussed below (6.14) this conclusion applies to SQUIDs.

6.4 Non-convex interaction potentials

As has been discussed in section 6.1, convex interaction potentials are only approximations of “real” interaction potentials, which are necessarily non-convex for “physical”

dimers. The question is whether the non-convexity of the interaction potential is actually “explored” by the dimer dynamics in a particular model. The no-go theorems from section 6.3 do not apply to non-convex interaction potentials, and SSBT and ANM are no longer ruled out. We will now show how we can actually get SSBT and SSBT induced ANM for dimers with non-convex interaction potentials.

6.5 Identical monomers - symmetric dimers

First, we will consider two identical monomers coupled by a non-convex interaction potential. Then, there is no simple argument for the occurrence of SSBT, apart from Curie’s principle [14] “that if a certain phenomenon is not ruled out by symmetries, then it will occur” [10] (where, of course, we have to take liberties in the interpretation of the term “symmetries”)⁷. Since we know that SSBT will occur in spatially two dimensional over-damped dynamics which are periodic in both components (chapter 4), we can reasonably expect to find SSBT. Since both monomers are now identical, we drop the indices, i.e.

$$F_i = F, a_i(t) = a(t), \eta_i = 1, \Gamma_i = \Gamma, U_i(x) = U(x). \quad (6.31)$$

As a first example of a non-convex interaction potential, we will consider the quartic potential

$$U_{int}(y) = \frac{k}{2\pi} \left(\frac{b_1(d)}{4} (s(y-l))^4 + \frac{b_2(d)}{3} (s(y-l))^3 + d(s(y-l)) \right) \quad (6.32)$$

with $b_1 = 192 \left(\frac{d}{3} + 2 \right)$ and $b_2 = -(36 \cdot d + 192)$, see figure 6.1 for an illustration. Four parameters are needed to define a quartic potential, and we have found k , s , l and d to be particularly convenient: $-5\frac{1}{3} \leq d \leq 0$ is the slope of the potential at the leftmost turning point⁸, k is the interaction strength, l the position of the leftmost turning point and s the stretching factor, which controls the distance from the minimum to the leftmost turning point. The potential (6.32) has two turning points: a turning point at $y_{tl} = l$ (which is a saddle for $d = 0$) and a second turning point at $s(y_{tr} - l) = -\frac{2b_2(d)}{3b_1(d)} = \frac{3d+16}{8d+48}$. It has a unique minimum at $y_{min} = l + \frac{1}{2s}$ with $U(y_{tl}) - U(y_{min}) = \frac{2k}{2\pi}$ matching the barrier height of the periodic monomer potential up to the factor k , and only for $d = 0$ there is a saddle point at $y = l$. Between the turning points $l < y < y_{tr}$ it is concave, and otherwise convex. The basic idea of the interaction potential (6.32) is that there exists, in addition to the stable dimer length $y = y_{min}$, another “likely” dimer configuration in the concave regime allowing for SSBT and ANM, with $y = y_{tl}$ being most “likely” in the sense that the restoring force is smallest then. Physically, this could be interpreted as a (bio-) molecule having a stretched and a compressed state, or more generally two (meta-) stable states. As has been discussed in chapter 4, a three dimensional phase space is necessary to find SSBT in the overdamped dynamics of a point particle, to which the dynamics (6.12) are equivalent. If the interaction potential is either stiff or soft compared to the monomer potentials, one variable can be eliminated from the equations of motion, ruling

⁷In particular, we do not know these “symmetries” a priori, e.g. no-go theorems.

⁸For $d > 0$, the potential has a second minimum and for $d = -5\frac{1}{3}$, the turning points coincide, i.e. the potential is convex again. For sufficiently small d , a second minimum develops.

out SSBT. Two representative examples of (6.32), matching the monomer potential (6.9) in their shape, are drawn in figure 6.1.

As a second example, we consider the Lennard-Jones potential, which is often used in molecular dynamics simulations:

$$U_{int}(y) = \frac{k}{2\pi} \left[\left(\frac{l}{y}\right)^{12} - 2 \left(\frac{l}{y}\right)^6 \right], \quad (6.33)$$

see figure 6.1. It has a unique minimum at $y = l$ with dissociation energy (well depth) $\frac{k}{2\pi}$ and a single turning point at $y_{tp} = \frac{7}{13} \cdot l \approx 1.109 \cdot l$ with $U_{lj}(y_{tp}) - U_{lj}(l) \approx 0.213 \frac{k}{2\pi}$. This potential is significantly different from (6.32) in that the dimer can dissociate. The interaction force is monotonously decreasing to 0 for $y > y_{tp}$. Thus, if the distance of the monomers becomes large enough, the monomers will become trapped by the periodic monomer potential, i.e. the slightly perturbed unique (up to translations) attractor of the uncoupled ($k = 0$) deterministic dynamics. With noise, the monomers can recombine again. We will address this issue in more detail below.

Lastly, we point out again that our dynamics will be the same if the interactions potentials are shifted by an integer-linear combination of the spatial periods of the monomer potentials, as has been noted under (6.7). In the picture of monomers with identical monomer potentials, this means that dimers that differ in their equilibrium length l by one spatial period of the monomer potential will have the same dynamics. This corresponds to a shift of the potential minimum in figure 6.1, i.e. a change of l in (6.32) or a translation of y in (6.33) respectively, and our following results directly apply to such “longer” or “shorter” dimers.

6.5.1 Bound interaction potentials

From chapter 4 we know that SSBT can be expected if “everything” is of the same order, such that the nonlinearity is not suppressed in the dynamics (6.12). From chapter 4 (see, e.g. figure 4.4) we expect that for each, not too large or small frequency a suitable drive amplitude a can be found. If we consider a cut in the direction of the “center of mass” x through the total potential U_{tot} , i.e. we fix the dimer length y , the potential looks like a sine, the amplitude of which is modulated by the dimer length⁹. For y integer, the amplitude is $\frac{1}{\pi}$, while for $y = 0.5 + n$ with $n \in \mathbb{Z}$, the amplitude is zero [336, 337]. Thus, the potential barriers for the motion of the “center of mass” are somewhat smaller than those considered in chapter 4, depending on the choice of dimer equilibrium length in the interaction potential, i.e. l (and s in case of (6.32)).

We focus first on the potential (6.32) and choose an arbitrary dimer model, avoiding any “symmetries” in the parameters

$$k = \frac{0.75}{2.1}, s = 2.1, l = 0.26, d = 0, \quad (6.34)$$

corresponding to the red curve in figure 6.1 where the value of d was chosen to get a saddle point in the interaction potential, i.e. a second but marginally stable dimer equilibrium

⁹Writing the total potential in dependence of the “center of mass” x and the dimer length y , we get $U_{tot}(x, y) = \frac{1}{\pi} \sin(\pi x) \cos(\pi y) + U_{int}(y)$.

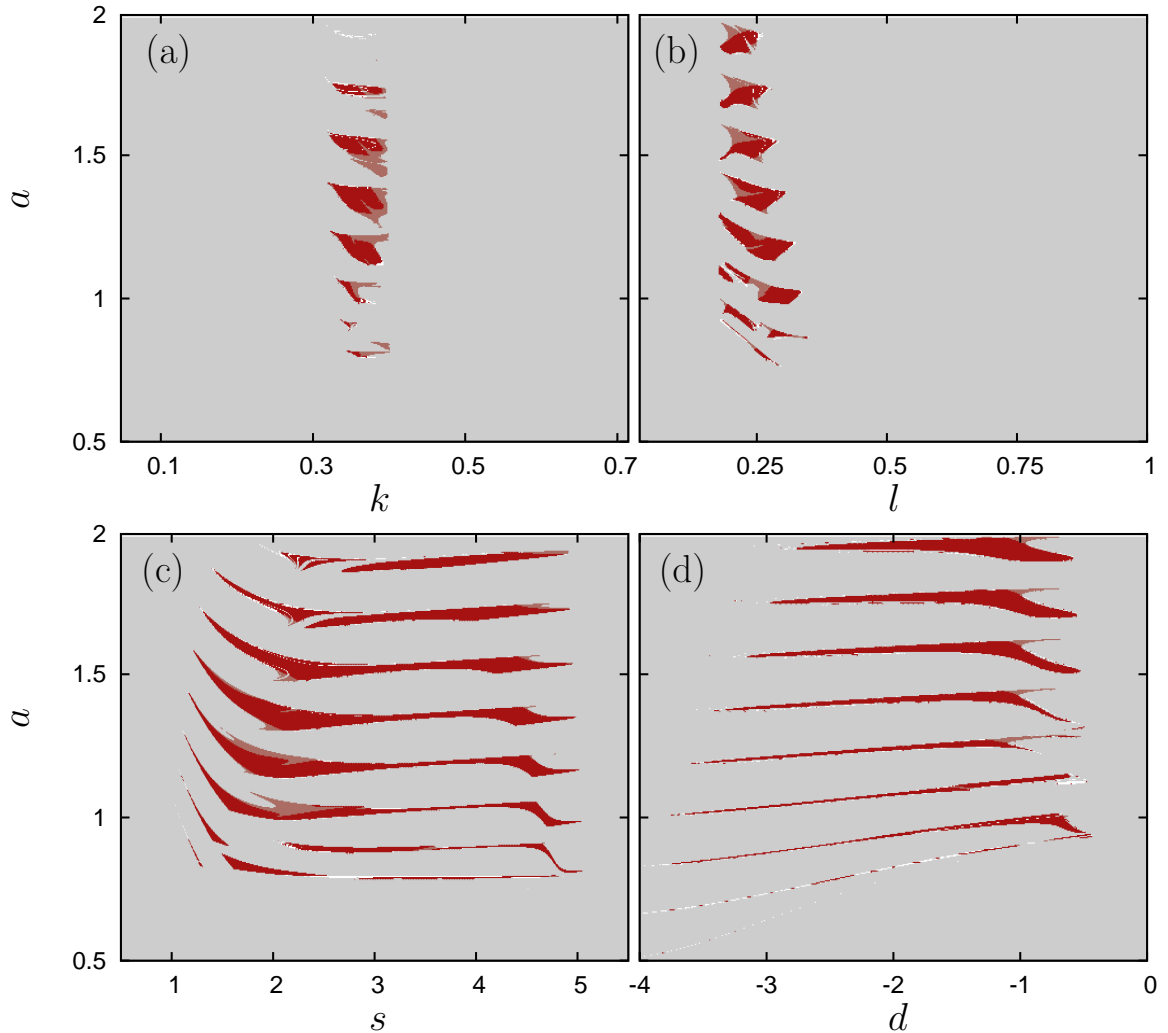


Figure 6.2: Phase diagrams for the dynamics (6.12) with $\Gamma = 0$, $F = 0$, $\Omega = 0.4$ and interaction potential (6.32) with parameters (a) $d = 0$, $l = 0.26$ and $s = 2.1$; (b) $d = 0$, $k = 0.357$ and $s = 2.1$; (c) $d = 0$, $k = 0.357 \cdot s$ and $l = 0.26$; (d) $k = 0.357$, $l = 0.16$ and $s = 2.1$. The color palette corresponds to the color palettes used in, e.g. figure 5.2 and figure 6.4, i.e. dark red indicates to a pair of SSBT attractors and no other phase-locked attractors, desaturated dark red to a pair of SSBT attractors coexisting with bounded attractor(s), grey to bounded attractors, and white to no (found) phase-locked attractors.

length. Moreover, to study SSBT we fix

$$\Gamma = 0 \text{ and } F = 0. \quad (6.35)$$

To get an idea of the SSBT parameter region of the dynamics (6.12) with the interaction potential (6.32), we have considered a number of frequencies of order 1 and calculated phase diagrams in which a and one of the interaction potential parameters k , l , s or d is varied while all remaining parameters are kept fixed at the values given by (6.34). We have found SSBT for frequencies $0.05 < \Omega < 2$, and henceforth focus on the convenient choice

$$\Omega = 0.4 \quad (6.36)$$

(i.e. neither too large or too small for the given potential), except where otherwise noted. The results are shown in figure 6.2. There are always several separate regions of SSBT, each corresponding to a “tongue” (see section 4.9.2) since we are considering a frequency well below the threshold frequency beyond which SSBT vanishes (see section 4.8 and section 4.9). The parameter regions of l (figure 6.2(b)) and k (figure 6.2(a)) are rather narrow and depend somewhat on the choice of Ω , corresponding to the subtle matching of the monomer dynamics with the interaction dynamics giving rise to SSBT, see below (section 6.5.2),

Physically interesting are the values of l for which SSBT is found, $0.16 < l < 0.35$. Since we have $y_{min} = l + 0.238$, these values correspond to equilibrium dimer lengths around $y_{min} \approx 0.5$, i.e. a significantly reduced total potential barrier height in the direction of the “center of mass” x (note that for $y_{min} = 0.5$ we would always get (possibly) unstable periodic orbits corresponding to free, i.e. with a flat monomer potential, oscillations of the dimer, which we avoid). The metastable dimer length $y = l$ is thus about a fourth of the monomer potential period corresponding to significantly larger barrier heights. Note that the same behavior will be found for l shifted by integers due to the periodicity of the monomer potentials, as has been noted above.

The range of s values for which SSBT is found for all remaining parameters fixed is rather narrow (not shown). Basically, an increase of s increases the slope of the interaction potential which becomes too stiff/soft for only moderate changes in s (see also the behavior upon changing l and k in figure 6.2(a-b)). Therefore, we scale k with s in figure 6.2(c) as

$$\tilde{k}(s) = k \cdot s, \quad (6.37)$$

i.e. we change the distance between y_{lp} and y_{min} and keep the slope at the same level. With that scaling, the region of s values for which SSBT is found is quite large, and the particular choice of s has no significant impact on the occurrence of SSBT, but there are optimum values.

With respect to the choice of d , we have not found a significant impact of that choice as long as the potential is not too close to being convex, i.e. d is not too close to $-5\frac{1}{3}$. For the model parameters (6.34) SSBT vanishes already around $d \approx -1$, and the optimum choice is $d \approx 0$ (not shown). For only slightly different values of the remaining interaction potential parameters much smaller values of d support SSBT, i.e. that SSBT is not found for $d < -1$ for our choice (6.34) is not due to the potential being “too convex” but a feature of our chosen parameters. Therefore, we consider a slightly different value for the dimer length, $l = 0.16$, to consider the influence of d on the parameter region of SSBT

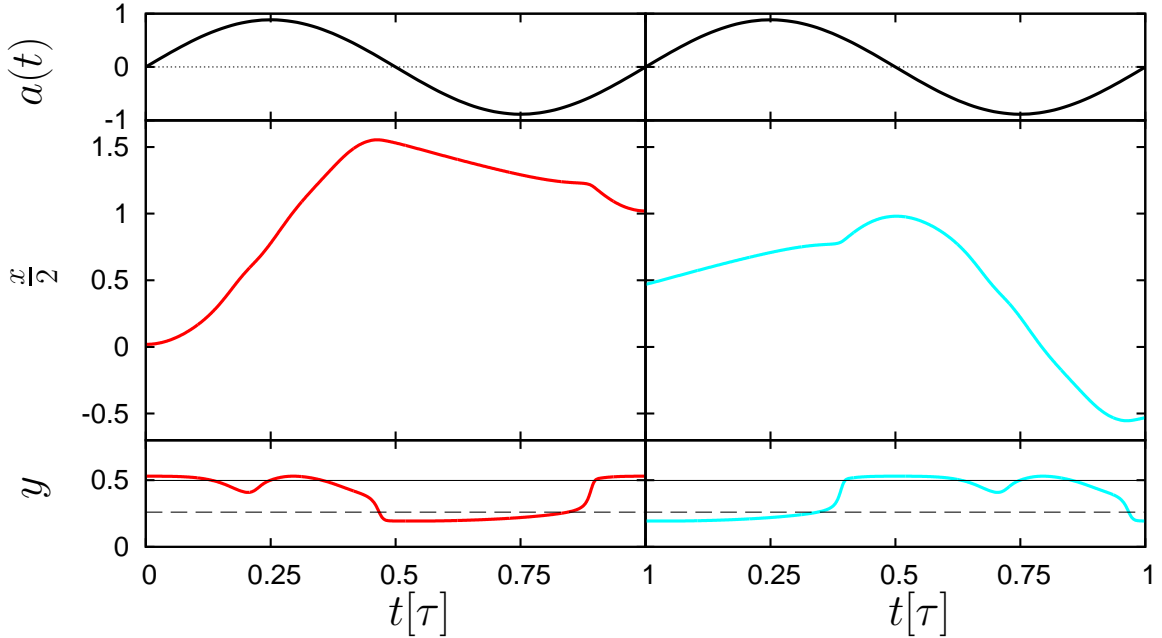


Figure 6.3: Periodic orbits corresponding to a pair of SSBT attractors found for system parameters $\Gamma = 0$, $F = 0$, $\Omega = 0.4$, $a = 0.885$, $k = 0.357$, $d = 0$, $l = 0.26$ and $s = 2.1$, i.e. the 'x' in figure 6.4(a). The right orbit $(x_r(t), y_r(t))$ is the (shifted) symmetry partner of the left orbit $(x_l(t), y_l(t))$, i.e. $(x_r(t), y_r(t)) = (-x_l(t + \frac{\tau}{2}) + 1, y_l(t + \frac{\tau}{2}))$.

and obtain figure 6.2(d). As expected, the width (in the a direction) of each separate parameter region of SSBT shrinks as d gets closer to $-5\frac{1}{3}$, i.e. the potential becomes convex. Numerically, we have found SSBT with very narrow regions of existence up to $d \lesssim -4$, cf. figure 6.2(d). We expect to be able to find SSBT (possibly unstable) for even smaller values of d , though there does not seem to be much practical use in this, as the regions of existence are very narrow in all directions in that case, resulting in a very low noise resistivity.

As discussed above, the choice of the frequency Ω is not critical for the occurrence of SSBT, and the influence is basically as in chapter 4. As an example we consider the dimer model corresponding to (6.34) yielding the expected tongue structure in figure 6.4(a). Comparing with e.g. figure 4.4 or figure 4.18(a), the same structure is recovered, only that transport is restricted to one direction due to the bound interaction potential¹⁰.

6.5.2 Mechanism of SSBT

In section 4.9 the origin and properties of SSBT orbits were discussed in detail. In short, SSBT orbits spontaneously break the reflection symmetry by dissipating the drive energy during one half period of the drive and use the drive energy during the other half period to achieve (spontaneous symmetry breaking) transport. In section 4.9 this was achieved by the coordinate of the particle position transverse to the transport direction. If the

¹⁰Considering e.g. a periodic interaction potential somewhat similar to [38], transport would be two dimensional, and we have found results basically equivalent to chapter 4 in the case of a sine interaction potential, as expected.

particle was “trapped” between potential maxima at the borders of the transporting channel, drive energy would be dissipated, and if the particle was close to the middle of the transporting channel, the drive energy could be used to achieve transport.

Basically, the same mechanism is at work here. We show a representative example of a pair of SSBT orbits in figure 6.3. Here, the parameter determining the “instantaneous dimer mobility” with respect to the driving force is the dimer length: if the dimer length is commensurate with half the spatial period of the monomer potentials, the forces due to the monomer potentials cancel, and the corresponding “instantaneous” dimer mobility is high, i.e. the dimer reacts to an applied force by moving “quickly” into the direction of that force. If the dimer length is commensurate with the spatial period of the monomer potentials, the forces due to the monomer potentials add up, and the corresponding “instantaneous” dimer mobility is low. If these states of “instantaneous” mobility are synchronized with the periodic drive such that during one drive half period, the “instantaneous” mobility is high, and it is low in the other half period, the result will be transport in the direction of the periodic drive during the high “instantaneous” mobility half period of the drive. Since it is “normal” for a nonlinear dynamics to synchronize with an externally applied periodic driving force, such a “special” synchronization not unrealistic.

That is exactly the case for the majority of SSBT attractors that we have found. An example is shown in figure 6.3: for the left orbit, carrying transport in the $+x$ direction, the dimer length is around $y \approx 0.5$, i.e. the equilibrium length, during the first half period of the periodic drive, i.e. positive forces, and the dimer advances by about one spatial period during that half period. When the driving force amplitude becomes small around the time at which the drive changes sign, the dimer is compressed to the metastable length $y = 0.26$, because both monomers “relax” towards the same monomer potential minimum. The dimer remains in this configuration for most of the second half period of the periodic drive, i.e. negative forces. Towards the end of that half period of the periodic drive, the current monomer positions “straddle” a monomer potential maximum, and when the driving force becomes smaller and changes sign, the dimer switches to the $y \approx 0.5$ length, because the monomers cannot relax towards the same monomer potential minimum.

6.5.3 Consequences of SSBT

Systematic transport being restricted to one dimension, the effects of SSBT on transport are as discussed in section 4.11, i.e. deterministic diffusion with a divergent (with $\Gamma \rightarrow 0$) diffusion coefficient, the transport properties depend sensitively on the system parameters, and ANM. We will focus on the latter, since it is absent in all other dimer models considered in the literature (to our knowledge). To discuss ANM, we proceed as in chapter 4, i.e. we consider the regions of existence of SSBT at $F = 0$ in a suitable cut through parameter space. Here we use again the Ω - a plane in order to be able to use the relation between frequency and damping coefficient to exploit the heuristic reasoning from [1, 2] and section 4.11.2.

The results are given in figure 6.4. Similar to the previously discussed overdamped SSBT induced ANM, upon switching on the bias force and breaking \tilde{S}_0 symmetry, the previously coexisting regions of existence of SSBT attractors (see figure 6.4(a)) separate. The regions of existence of attractors transporting in the direction of the bias force

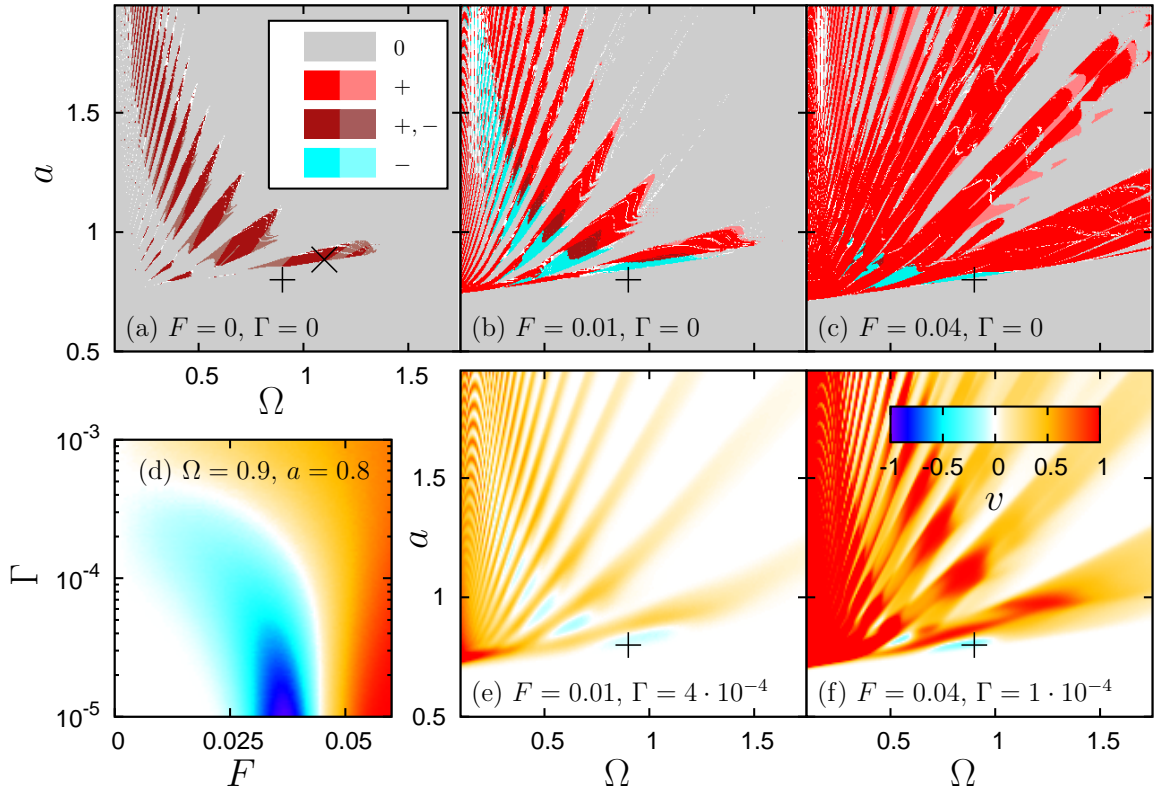


Figure 6.4: (a)-(c): phase diagrams for the dynamics (6.12) in the a - Ω parameter plane for $\Gamma = 0$ and the interaction potential (6.32) with (6.34) and various values of the force as indicated in the panels. (d-f): average velocity of one monomer. (d): depending on the force F and the noise strength Γ for parameters corresponding to the '+' in (a),(b),(c),(e),(f). (e)-(f): for the same region of parameter space as in (b)-(c), but $\Gamma = 4 \cdot 10^{-4}$ and F as indicated in the panels. The color palette used in (a)-(c) corresponds to the color palettes used in e.g. figure 5.2, see the legend in (a). Dark red corresponds to a pair of SSBT attractors and no other phase-locked attractors, light red to an attractor transporting in the direction of the bias force, blue to an attractor transporting against the direction of the bias force, grey to bounded attractors and white to no (found) phase-locked attractors. Regions of coexistence of transporting attractors and bounded attractors are shown by the color corresponding to the transporting attractors but desaturated. The desaturated colors are indicated to the right of the saturated colors in the legend. The colors in (d)-(f) are defined in the palette shown in (f). Note that the palette has been cut off at ± 1 , i.e. average velocities v larger(smaller) than $+1(-1)$ are shown as $v = +1(v = -1)$.

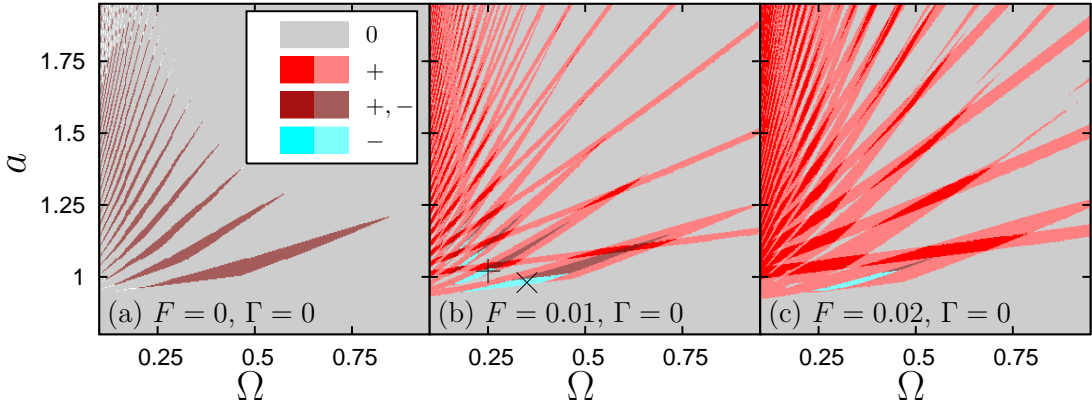


Figure 6.5: Phase diagrams of the dynamics (6.12) in the a - Ω parameter plane for $\Gamma = 0$ and the interaction potential (6.33) with $k = 1$ and $l = 1.25$ for various F as indicated in the panels. The colors correspond to figure 6.4(a-c), see also the legend in (a).

grow and move roughly towards increasing frequencies and (as in section 4.11.2) drive amplitudes, and the regions of existence of attractors transporting against the bias force shrink and move roughly towards decreasing frequencies and drive amplitudes, i.e. into the opposite direction (see figure 6.4(b,c)). The borders of the SSBT regions at $F = 0$ in the direction of decreasing frequencies and drive amplitudes are quite frequent, and ANM is readily found at these borders. The regions of existence of SSBT attractors at $F = 0$ being mostly surrounded by regions of existence of bounded attractors, the already discussed mechanism of noise induced ANM (see section 4.11.2 and section 4.19) and movement of regions of noisy ANM upon increasing the noise strength (not shown) is at work.

As already found in chapter 4, the ‘‘simplest’’ SSBT attractors survive ‘‘best’’ in the presence of noise and bias forces opposite to the transport direction, and at the considered noise strength, ANM is found for the tongues corresponding to the smallest oscillation amplitudes, i.e. smallest a and Ω . The noise resistivity of ANM is further detailed in figure 6.4(d), with a particular choice of parameters corresponding to the ‘+’ in panels (a),(b),(c),(e) and (f) exhibiting noise induced ANM due to the known mechanism [2, 63]. The maximum noise strengths and bias forces against which transport in the direction opposite to the bias force is sustained are of order $F \lesssim 0.04$ and $\Gamma \lesssim 4 \cdot 10^{-4}$, which is in line with the results from section 4.19 considering the differences in the potentials barrier heights.

6.5.4 Unbounded interaction potentials

Next, we consider our second model interaction potential, (6.33), which has only one turning point y_{tp} , i.e. is concave for $y > y_{tp}$, and convex for $y < y_{tp}$. Therefore, the potential cannot become large for large y , and the interaction forces holding together the dimer vanish with $y \rightarrow \infty$. Therefore, for $y \gg 1$ the monomers are effectively decoupled and single particle dynamics apply.

6.5.5 Uncoupled dynamics

For our purposes, the main property of the uncoupled dynamics is that all deterministic solutions for a given set of parameters have the same asymptotic average velocity. There are no unbounded solutions in the uncoupled dynamics for $F = 0$ (and $\Gamma = 0$) due to symmetry and the low dimensional phase space, i.e. the monomers are trapped. In the presence of noise, the dimers diffuse unbiased for $F = 0$, while the diffusion is biased if a constant bias force $F > 0$ is applied. In that case, the single particle dynamics features Shapiro steps, i.e. unbounded solutions locked to the periodic drive, and the diffusion may be significantly enhanced at the borders the Shapiro steps [267–269]. For small values of the bias force such Shapiro steps are found directly around the symmetry breaking bifurcations of the unbiased $F = 0$ single particle dynamics by a similar mechanism as discussed in section 4.17. In figure 6.5(b)-(c), the diagonal desaturated red stripes, corresponding to transport in the direction of the bias force, and which are not present at $F = 0$ (panel (a) of figure 6.5), are these Shapiro steps. For small values of the bias force, this enhancement of diffusion is due to the competition between the transporting phase-locked Shapiro steps and bounded solutions. Thus, around these values in parameter space, the recombination time for decoupled monomers is significantly reduced. Moreover, due to the uniqueness of the average velocity of the uncoupled dynamics, there is always only one solution (up to periodicity) due to decoupled monomers.

6.5.6 Interplay of coupled dynamics and uncoupled dynamics

Coupled monomers forming a dimer feature basically the same dynamical behavior as already discussed in section 6.5.3. At $F = 0$ (see figure 6.5(a)), the regions of existence of SSBT attractors form repeated tongues, as in figure 6.4(a), and always coexist with trapped solutions corresponding to dimers with large y , i.e. effectively decoupled monomers. At the borders of the SSBT regions towards decreasing frequency and drive amplitude, ANM results upon breaking the symmetry, cf. figure 6.5(b)-(c), as has already been discussed in section 6.5.3. Furthermore, around symmetry breaking bifurcations of the decoupled dynamics, Shapiro steps carrying transport in the direction of the bias force emerge. As has been noted above, the “new” diagonal transporting stripes in figure 6.5(b)-(c) having no corresponding transporting stripe in figure 6.5(a) are the parameter regions of these Shapiro steps.

Roughly speaking, all attractors of the coupled dynamics coexist with one attractor corresponding to effectively decoupled monomers, either transporting in the direction of the bias force or bounded. If a dimer trajectory decouples, it is trapped on an decoupled attractor until the monomers reach a partner and recombine. The time until that happens depends on the diffusion constant of the decoupled dynamics. At $F > 0$ and at certain places in parameter space, the regions of existence of coupled dynamics attractors meet the lines in parameter space where the uncoupled dynamics switch from bounded to unbounded. We expect transport to be particularly efficient around these lines if dissociated dimer states play any role at all, since decoupled monomers will have lower waiting times to reform a dimer due to the enhancement of single particle diffusion [269].

Considering an ensemble of monomers on some substrate, a straightforward application of this behavior would be to sort monomers from dimers by condensation [235].

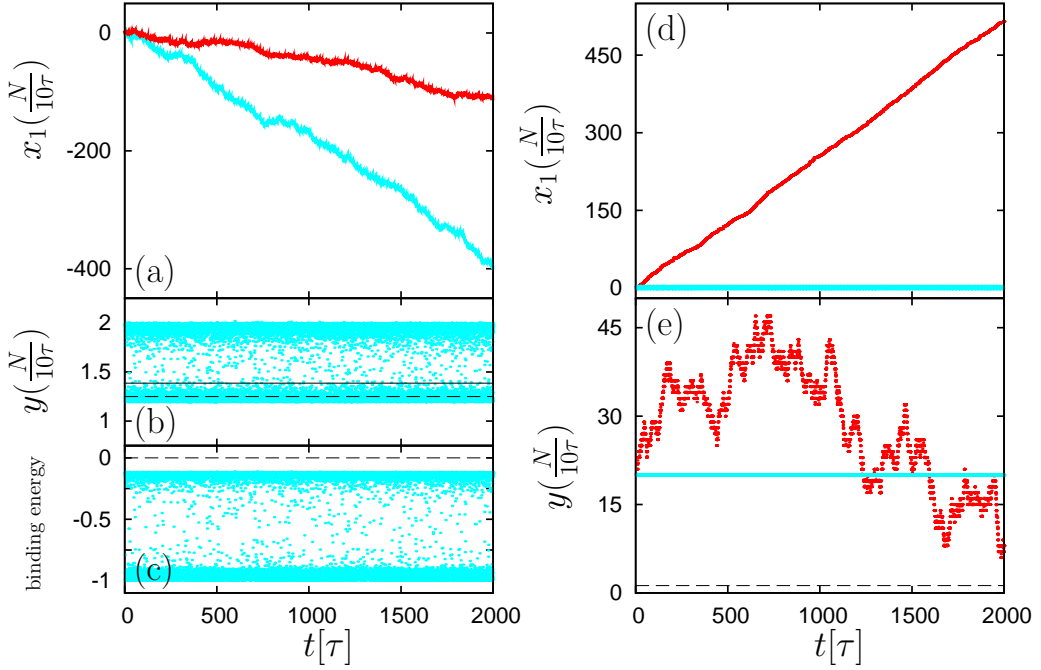


Figure 6.6: Typical noisy trajectories of the dynamics corresponding to the symbols in figure 6.5(b) but $\Gamma = 10^{-4}$. Cyan corresponds to the 'x' and red to the '+'. The left panels show trajectories with seed $y = l$ and the right panels with seed $y = 20$. Panels (a) and (d) show the x_1 component of the trajectory, and panels (b) and (e) show the dimer length and the lines correspond to $y = y_{min}$ (dashed) and $y = y_{tp}$ (solid, only in the left panels). Panel (c) shows the corresponding binding energy $U_{lj}(y(\frac{N}{10\tau})) - U_{lj}(+\infty)$ of the dimer. The trajectories are plotted at the discrete times $t = \frac{N}{10\tau}$, $N = 0, 1, \dots, 20000$.

Note that separation is only possible if the reactants can pass each other, i.e. in more than one dimension. But our results are easily generalized to that case for, e.g. effectively 1D transport channels on a substrate between which hopping is possible. Moreover, taking into account another (rotational) degree of freedom does not destroy SSBT, but only changes the parameters [5, 392], see also chapter 7. If one considers parameters such that dimers are transported against the bias force (ANM) and uncoupled monomers in the direction of the bias force (either via biased diffusion or ballistic transport on a Shapiro step), one gets an effective mechanism for separation. Moreover, if there are different dimer configurations, or different dimers, these can be separated along the lines of "normal" SSBT, i.e. the different species will typically belong to different transporting attractors and thus migrate in different directions. Using only diffusion for sorting would be possible as well by considering the unbiased $F = 0$ dynamics¹¹ and parameters such that the dimers exhibit SSBT. Then the diffusion coefficient diverges for $\Gamma \rightarrow 0$, i.e. dimers diffuse very fast for sufficiently small noise strengths.

Whether dissociation of the dimers is relevant in practice depends on the nature of the deterministic attractors and, in particular, on the noise strength. Basically, if there is a deterministic attractor corresponding to a bound¹² dimer, which usually is the case,

¹¹One can also consider the biased dynamics, of course, and use the resulting biased diffusion.

¹²In the sense of not dissociated.

thermal noise has to induce an escape from that attractor to a deterministic attractor corresponding to a dissociated dimer.

The pseudopotential barrier separating these attractors is influenced by the entire time dependent dynamics of the dimer and is rather complicated [145, 263]. In particular, it is not only due to the higher interaction potential energy of the dissociated dimer compared to the bound dimer. But, in a rough picture, the latter may be seen as an approximation of the real potential barrier which has to be overcome by noise. For our example potential (6.33) with $k = 1$ and $l = 1.25$, we have found that transporting stochastic trajectories corresponding to transporting attractors of the bound dimer typically do not extend much beyond $y = 2 \cdot l$. Therefore, the potential energy difference between the maximum length of the dimer due to the bound dynamics and the dissociated dimer is very large compared to the thermal energies at which ANM induced by SSBT vanishes. As a result, dissociation of an initially bound dimer practically does not happen. Typical trajectories for dimers initiated in the bound state at two different sets of parameters are shown in figure 6.6(a-c). Panel (c) shows the bare interaction potential difference between the current dimer length $y(t)$ and the dissociated state, the minimum energy differences being of order of 0.1 and thus much larger than the noise strength $\Gamma = 1 \cdot 10^{-4}$. That noise strength is about $\frac{1}{2}$ the maximum noise strength at which transport against the bias force vanishes for the given parameters anyhow. Panels (d)-(e) show typical trajectories when the dimer is initiated in the dissociated state. As has been noted above, if the parameters are close to a transport affecting bifurcation of the dissociated dynamics, the diffusion of the dissociated monomers is enhanced significantly, as shown by the red trajectories. In contrast, if parameters are far from such a bifurcation, the dissociated monomers do not diffuse at all during the selected time frame and noise strength. Thus a mixture of dissociated monomers and dimers would behave drastically different for the two sets of parameters despite the bound dimer dynamics being similar. I.e. for the parameters corresponding to the red curves, dissociated monomers diffuse and will eventually recombine. During diffusion the monomers migrate in the $+x_1$ direction, while dimers migrate in the $-x_1$ direction. In contrast, for parameters corresponding to the cyan curves, monomers are effectively trapped, while dimers are transported in the $-x_1$ direction. If one considers parameters for which the dissociated monomer dynamics are transporting via a Shapiro step, one has the situation of monomers migrating in the $+x_1$ direction without significant diffusion, and thus without recombining. If then the dimers exhibit ANM, one also gets separation of dimers and monomers.

6.6 Asymmetric dimers

If both monomers are identical and the interaction potential is bistable, we have observed basically the same dynamical behavior as discussed in section 6.5.1. E.g. if we replace the saddle of (6.32) with a local minimum, the dynamics are qualitatively unchanged. Therefore, we will not discuss bistable interaction potentials with identical monomers further.

The more interesting situation is found if *two different* monomers are coupled via a bistable *symmetric* interaction potential. This situation corresponds to a S_0 symmetric dynamical system. Each of the two equilibrium configurations corresponds to a state with broken reflection symmetry and thus to an effective ratchet model [393, 394], and the two

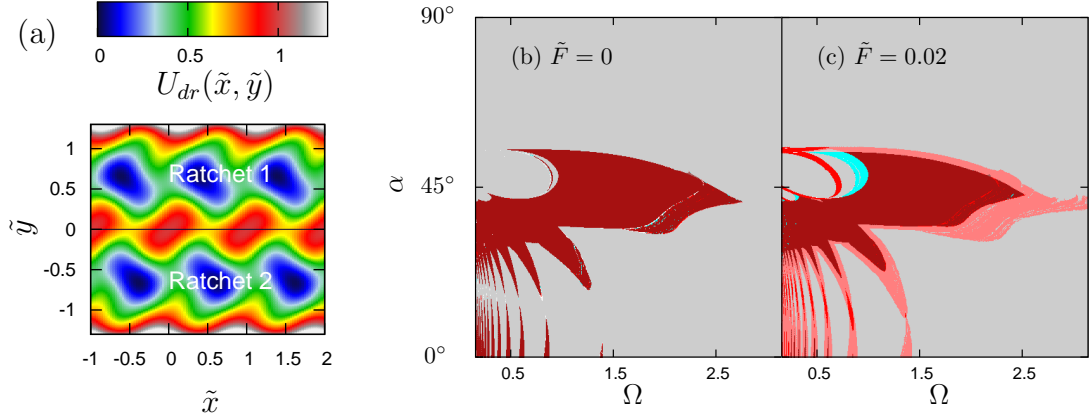


Figure 6.7: (a) Double ratchet potential (6.38) for $\tilde{l} = \frac{5}{2\pi}$. (b)-(c) phase diagram for the coupled ratchet model corresponding to the potential in (a) for $a = 2$, $\Gamma = 0$ and (b) $\tilde{F} = 0$ and (c) $\tilde{F} = 0.02$. The color palette corresponds to the one used in, e.g. figure 6.4(a).

states are images under S_0 of each other. We have found the dynamics of asymmetric dimers to be qualitatively very similar to those of a single particle in a similar, but not equivalent, 2D potential as in [393] and will now consider this situation.

The single particle potential is

$$U_{dr}(\tilde{x}, \tilde{y}) = \frac{1}{2\pi} \left(\sin(2\pi\tilde{x}) \cdot \sin(2\pi\tilde{y}) + \cos(2\pi\tilde{x}) + \cos(2\pi\tilde{y}) + \frac{1}{2\pi\tilde{l}^4} \cdot (\tilde{y}^2 - \tilde{l}^2)^2 \right) \quad (6.38)$$

with the particle position $\vec{r} = (\tilde{x}, \tilde{y})$. An example of the potential for $\tilde{l} = 0.78$ is shown in figure 6.7(a). The particle is subjected to a sinusoidal rocking driving force $\vec{A}(t) = a \sin(\Omega t) \vec{e}_\alpha$, a constant bias force $\vec{F} = F \vec{e}_{\tilde{x}}$ and Gaussian white noise of strength Γ . The equation of motion is (analogous to (4.1))

$$\dot{\vec{r}}(t) = \vec{A}(t) + \vec{F} - \vec{\nabla} U_{dr}(\vec{r}(t)) + \sqrt{2\eta\Gamma} \vec{\xi}(t) \quad (6.39)$$

with $\langle \xi_i(t) \xi_j(s) \rangle = \delta_{ij} \delta(t - s)$, and the dynamics are S_0 symmetric. Both equilibrium configurations of the quartic term in (6.38) correspond to states with broken reflection symmetry, or ‘‘transport channels’’ of the potential. SSBT is readily found for $a = 2$ and $0^\circ < \alpha \lesssim 56^\circ$ with $\alpha = 0^\circ$ corresponding to a drive in the \tilde{x} direction, see figure 6.7(b).

Upon closer inspection, SSBT at $\alpha = 0^\circ$ corresponds to spatially separated transporting attractors, each attractor ‘‘living’’ in one half (i.e. $\tilde{y} < 0$ and $\tilde{y} > 0$) of the transporting channel. If one removes e.g. the lower half \tilde{y} of the transporting channel, the attractor in the upper half is not affected. In that sense, the attractor resembles that of a one dimensional ratchet model, but the no-go theorem from [1, 2] does not apply directly. Applying a bias force $\vec{F} = \tilde{F} \vec{e}_{\tilde{x}}$ with $\tilde{F} > 0$, each ratchet shows the ‘‘normal’’ 1D response behavior. In turn, for $\tilde{F} > 0$ there are no regions around $\alpha \gtrsim 0$ where the attractor transporting against the direction of the bias force does not coexist with the attractor transporting in the direction of the bias force, cf. figure 6.7(c).

Thus, ANM is not found for the attractors corresponding to $\alpha = 0^\circ$ SSBT. The situation is different if the driving force is rotated to about $\alpha \approx 45^\circ$. Then the oscillations

imposed by the driving force destroy the quasi one dimensional two state structure. In turn, ANM is found along the lines of chapter 4. Moreover, taking into account the potential barrier heights, noise resistivity is again in line with the results from chapter 4 (for $\alpha \neq 45^\circ$), as are the maximum forces against which transport is sustained.

We have found qualitatively the same behavior for various models of overdamped single particle dynamics in globally symmetric two dimensional potentials, but which break the symmetry locally. In particular, we have considered potentials that are periodic in both directions, e.g. ratchet potentials (in the x direction) arranged with alternating x directions in the y direction, such that the potential is reflection symmetric with respect to a reflection across the origin but not with respect to a reflection across the x axis. A particularly simple example is a periodic potential whose elementary cell consists of two pairs of spatially separated Gaussian potential wells, each pair forming a ratchet (e.g. the wells have different depths), and arranged such that the total elementary cell of the potential is S_0 symmetric. These models can be constructed such (if the potential wells are arranged along lines) that for a driving force parallel to the ratchets, the lines parallel to the ratchet direction are one dimensional invariant manifolds of the dynamics. On these manifolds, the no-go theorem from [1, 2] applies in the deterministic case, yielding an analytic example where deterministic ANM is rigorously ruled out for a specific direction of the driving force despite SSBT being at work.

As noted above, we have found the same behavior for asymmetric dimers with symmetric bistable interaction potentials when considered as a single particle in a two dimensional “channel” similar to the model (6.39), in particular with respect to the direction of the driving force in the 2D potential. This implies that the monomers have to interact differently with the periodic drive such that the direction of the driving in the equivalent single particle dynamics is not a “trivial” direction.

6.7 Conclusions

We have shown that monomers interacting via convex interaction potentials do not show SSBT and ANM. Dimers with non-convex interaction potentials, or more general models of single (effectively) mass less particles in two dimensional potentials which are non-convex and bound in one direction, have a rich dynamical behavior due to SSBT. We have discovered qualitatively similar results as in chapter 4, the difference being that systematic transport is restricted to one spatial dimension. In particular, noise resistivities and maximum load forces against which transport can be sustained are of similar magnitudes.

Overdamped single particle dynamics in two dimensional potentials consisting of “alternating ratchet channels” are very similar to models of asymmetric dimers with a symmetric interaction potential in a spatially one dimensional symmetric potentials. These models are examples of systems exhibiting SSBT while ANM can be rigorously excluded (if the attractors are particularly simple), ruling out chaos and giving another hint at the close connection of SSBT induced ANM and chaos.

Our model systems are of a simple and minimal nature, the main requirement being non-convex interaction potentials¹³, symmetry, and non-equilibrium conditions. Our

¹³Actually, realistic interaction potentials should be non-convex, since the restoring force should vanish for large monomer distances, but this non-convex regime might actually correspond to a destruction of

conclusions can be extended to a broader class of systems, in particular more (spatial) degrees of freedom, finite inertia, different forms of driving, such as a flashing potential or (inherently) weakly broken spatial symmetry, and our results should apply to many different dynamics with an internal degree of freedom. Moreover, we expect our results to be applicable also to systems with more internal dynamical degrees of freedom or more complex internal dynamics, such as a droplet on a surface, a (bio-) molecule interacting only at a few specific sites with a surface onto which it is absorbed, or two linked colloids, e.g. via a DNA strand [220, 277]. The effects might be observed as, e.g., negative absolute resistance in superconducting rings containing several weak links and various forms of coupling (e.g. inductive, resistive, capacitive) [7, 107, 278, 279, 285, 381, 395–401], spontaneous transport and ANM¹⁴ in (symmetric generalizations of) motor protein models [367, 368], surface dynamics of dimers (or more complex objects) [353] or colloidal particles [375] and spontaneous, or negative, friction in nanofriction experiments [402–404]¹⁵.

the physical system and might not be covered by a simple model.

¹⁴which could be applied to sorting

¹⁵If the spring potential of the tip-sample interaction is sufficiently soft, or possibly mediated by a some sort of a linker molecule, such that the actual area of contact may move by several lattice periods independent of the cantilever position, the combined potential of the surface and the cantilever/linker correspond to a soft bound (harmonic) potential, due to the cantilever/linker, modulated by a periodic potential due to the surface (see Fig. 4 of [402]). In that picture, the bound (harmonic) potential induces a position dependent bias force, which is controlled by the position of the cantilever relative to the area of contact. If, under these circumstances, the area of contact is such that it has some sort of internal dynamics, e.g. the deformation of a nanodroplet or an atomic force microscope (AFM) tip with multiple apexes, and some sort of periodic driving, such as mechanical agitation of the sample, an applied ac electrical field [405] or modulation of the cantilever position [403, 406], is applied, our model might apply as a rough approximation. The resulting “spontaneous” movement of the contact area might manifest as “spontaneous” or negative friction in the experiment, i.e., depending on the particular response behavior of the model, the cantilever would be “spontaneously” deformed without actually moving the cantilever, the cantilever might be deflected opposite to the expected deflection due to “normal” friction if the cantilever is moved, or the area of contact might perform “spontaneous” oscillations as in [407].

Chapter 7

Chiral separation

Stereoisomers are molecules containing exactly the same constituents but arranged differently and have different chemical, biological and pharmaceutical properties but share many physical properties (such as mass). A special subclass are chiral molecules, i.e. molecules which are not identical to their mirror images, also called enantiomers. Chiral molecules share even more physical properties than general stereoisomers, e.g. volume, charge, melting temperature (dissociation energy) etc. will be exactly identical for enantiomers. Nevertheless, enantiomers may have drastically different biological and pharmaceutical properties, such as a chiral molecule having a medical use, while its chiral partner, i.e. its mirror image, is toxic [69, 70].

Several methods to separate a chiral molecule from its symmetry partner have been put forth. Commonly used are techniques employing a chiral selector [70–74], i.e. a molecule or structure which in itself is chiral (i.e. breaks reflection symmetry) and allows to separate enantiomers by interacting differently with the two partners, such as different binding affinities. Usually, chiral selectors are highly specific, and most chiral molecules require a different chiral selector. Thus, less specific methods are of great interest, and several concepts employing asymmetric devices have been put forth, mostly microfluidic flows breaking reflection symmetry. Using microfluidic vortices, spatial separation of chiral molecules was theoretically predicted in [79]. Shear flows leading to a lateral migration which is different for the chiral partners have been considered theoretically in [75–78] and experimentally in [80–83] with chiral objects of sizes from centimeters to micrometers. Asymmetric parabolic flow profiles are predicted to lead to different longitudinal migration speeds of the chiral partners in [67, 68]. Another way of breaking mirror symmetry in the device and achieving separation is to use circularly polarized light, with which the chiral partners interact differently [408], and has been considered theoretically in [409].

Using an achiral device (i.e. a device having a reflection symmetry, see [84] for some fundamental thoughts), [85] predicts chiral crystals sliding on an inclined but otherwise (reflection) symmetric surface to separate transverse to the slope, the magnitude of the effect being the main obstacle to a practical implementation. Here, we will overcome this limitation by considering a structured but symmetric inclined (i.e., a constant bias force is applied) surface. Our main idea has already been discussed in chapter 2 and can be summarized as follows. If the bias force is parallel to the reflection line of the symmetry of the surface, the dynamics of a point particle are reflection symmetric across that line.

Each path of the point particle, in a particular realization of the experiment, has the same probability as the mirror image of that path across the reflection line of the symmetry. Hence, the average velocity of a point particle sliding down the surface has to be parallel to the reflection line.

A similar reasoning applies to the dynamics of an extended molecule. The difference is that the probability of the extended molecule, sliding down the surface in a particular realization of the experiment, taking a particular path, is the same as the probability of the mirror image of that molecule taking the mirror image (with respect to the reflection line of the symmetry of the potential) of that path. Hence, the average velocity of a chiral, i.e. not identical to its mirror image, molecule, sliding down the surface, is not necessarily parallel to the reflection line of the symmetry. Rather, the average velocity of the chiral partner, is the mirror image of the average velocity of the molecule. Formally, this can be expressed by (2.27). Thus, if a chiral molecule, sliding down the surface, is, on average, displaced orthogonal (transverse) to the reflection line from its initial position, its chiral partner will be displaced, on average, in the other direction transverse to the reflection line.

Adding a time-dependent driving force, the magnitude of the effect can be enhanced dramatically, and the chiral partners can even be made to move into opposite directions. These results have been published in the following paper [5], which is the basis of our discussion in the remainder of this chapter.

7.1 Preprint of [5]

D. Speer, R. Eichhorn, and P. Reimann, Physical Review Letters **105**, 090602 (2010),
 Copyright (2010) by the American Physical Society

Exploiting lattice potentials for sorting chiral particles

David Speer¹, Ralf Eichhorn², and Peter Reimann¹

¹Universität Bielefeld, Fakultät für Physik, 33615 Bielefeld, Germany

²NORDITA, Roslagstullsbacken 23, 10691 Stockholm, Sweden

Several ways are demonstrated of how periodic potentials can be exploited for sorting molecules or other small objects which only differ by their chirality. With the help of a static bias force, the two chiral partners can be made to move along orthogonal directions. Time-periodic external forces even lead to motion into exactly opposite directions.

PACS numbers: 05.40.-a 05.60.-k, 05.45.-a

Chiral particles are extended objects which are non-superposable with their mirror image. So-called enantiomers, i.e. chemically identical molecular species with opposite chirality play a crucial role in Chemistry, Biology, and Medicine due to the omnipresence of chiral molecules in living organisms but with only one of the two chiral partners actually being present. Accordingly, enantiomers in drugs, pesticides etc. have very different effects on an organism and thus their separation is of great importance. Established methods of separating enantiomers mostly exploit some kind of chiral selector [1], i.e. some materials, structures, or ancillary molecules which themselves exhibit an intrinsic chirality. Their main disadvantage is that essentially every enantiomer species requires a different selector. Therefore, several alternative concepts have recently been put forward. A first promising direction proposes to utilize appropriate microfluidic flows, such as vortices [2] or shear flows [3, 4]. Second, photoinduced separation by means of suitably chosen electromagnetic fields has been theoretically predicted in Ref. [5]. A third approach to exploit a structure without an intrinsic chirality is due to de Gennes [6], predicting qualitatively that, according to Curie's principle [7], small chiral crystals should slide down an inclined plane along directions which slightly differ for the two chiral partners, provided thermal noise is negligible. Here, we further pursue this approach, showing that with the help of periodic potentials the two chiral partners even can be made to move into opposite directions, with remarkable persistence against thermal noise.

Apart from “true” (bio-) molecular enantiomers, we also have in mind chiral nano- and micro-particles, e.g. helically shaped nonmotile bacteria [3] and artificial flagellae [8], carbon nanotubes, chiral colloidal clusters [9], or ferromagnetic nano-propellers [10]. The periodic potentials we are proposing to utilize for sorting those chiral particles may be realized e.g. by means of crystal surfaces [11], optical lattices [12], periodic micro- and nano-structures [13], or magnetic bubble lattices [14].

Most of us are not very accustomed to think in terms of chiral symmetry and symmetry-breaking, especially in combination with the crystal symmetries of a periodic potential. For this reason only, we mainly focus on the simplest possible setup [2], namely the two-dimensional dynamics in a square lattice potential of a “minimal”

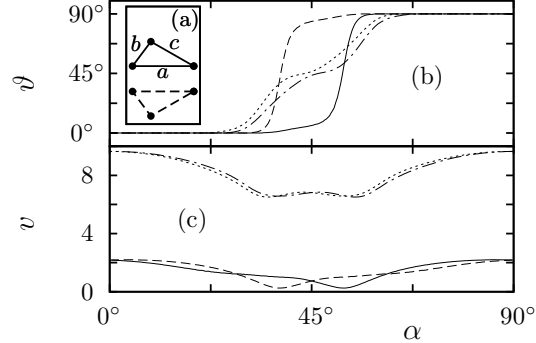


FIG. 1: (a) Solid: Triangle, specified by a , b , c . Dashed: Its chiral partner. (b) and (c): Direction ϑ and modulus v of the net velocity $\vec{v} = \vec{e}_\vartheta v$ versus the direction α of a static bias A in (5) by numerically solving (2)-(6) with parameters as specified below (6). Solid: $kT = 0.08$, $A = 3.6$, $a = 0.4$, $b = 0.23$, $c = 0.34$ (proportional to the solid triangle in (a)). Dashed: Same but for the chiral partner (dashed in (a)). Dashed-dotted and dotted: Same but for $A = 10$.

planar, chiral “molecule”, consisting of three identical, rigidly coupled “atoms” or other small objects with broken mirror symmetry, see Fig. 1a. All basic effects and mechanisms are recovered in three dimensions and also for more general lattices, but are much more cumbersome to visualize and explain. This very general validity of our main results will be exemplified for various other chiral “molecules” in the end. We thus consider the two-dimensional dynamics

$$m_i \ddot{\vec{x}}_i(t) = -\gamma_i \dot{\vec{x}}_i(t) + \vec{F}(\vec{x}_i(t), t) + \vec{f}_i + \vec{\xi}_i(t) . \quad (1)$$

Dots indicate time derivatives, $\vec{x}_i = \vec{e}_1 x_{i,1} + \vec{e}_2 x_{i,2}$ are the “atom positions” ($i = 1, 2, \dots, N$) in Cartesian coordinates \vec{e}_ν ($\nu = 1, 2$), m_i their mass, and γ_i their dissipation coefficient, e.g. due to an ambient fluid. In particular, for the triangular particles (Fig. 1a) we have $N = 3$ and i -independent γ_i and m_i . The force field $\vec{F}(\vec{x}, t)$ is partly due to a “lattice potential” (see below) and partly due to an externally applied driving, typically via electrophoresis. Under these conditions, hydrodynamic interactions are screened [15] and therefore safely negligible [2, 3]. The internal constraining

forces, maintaining e.g. the triangular shape in Fig. 1a, are represented by \vec{f}_i , and thermal fluctuations are modelled as usual by unbiased Gaussian white noise $\xi_i(t) = \vec{e}_1 \xi_{i,1}(t) + \vec{e}_2 \xi_{i,2}(t)$, satisfying the fluctuation dissipation relation $\langle \xi_{i,\mu}(s) \xi_{j,\nu}(t) \rangle = 2\gamma_i kT \delta_{ij} \delta_{\mu\nu} \delta(s-t)$ with T the ambient temperature and k Boltzmann's constant. The position of the rigid "molecule" is conveniently specified by the so-called center of friction [2] $\vec{X} := \sum_{i=1}^N \gamma_i \vec{x}_i / \sum_{i=1}^N \gamma_i$, and its orientation by the angle ϕ between the \vec{e}_1 axis and the position of "atom 1" relative to the center of friction: $\phi := \alpha(\vec{e}_1, \vec{x}_1 - \vec{X})$. Rewriting (1) in terms of \vec{X} and ϕ to get rid of the constraining forces \vec{f}_i is a basic mechanics exercise. Further, for the very small objects we have in mind, inertia effects are negligible [16, 17], yielding [2]

$$\dot{\vec{X}}(t) = \frac{\sum_{i=1}^N \vec{F}(\vec{x}_i(t), t)}{\sum_{i=1}^N \gamma_i} + \vec{\zeta}(t), \quad (2)$$

$$\dot{\phi}(t) = \frac{\vec{e}_3 \cdot \sum_{i=1}^N \vec{y}_i(t) \times \vec{F}(\vec{x}_i(t), t)}{\sum_{i=1}^N \gamma_i y_i^2} + \zeta_\phi(t), \quad (3)$$

$$\vec{x}_i(t) = \vec{X}(t) + \vec{y}_i(t), \quad \vec{y}_i(t) = \mathbf{O}(\phi(t)) \vec{y}_i(0). \quad (4)$$

In (3), vectors are temporally embedded into \mathbb{R}^3 with standard scalar and vector products \cdot and \times . In (4), $\mathbf{O}(\phi)$ is a rotation matrix with elements $O_{11} = O_{22} = \cos \phi$ and $O_{12} = -O_{21} = -\sin \phi$. Thus, $\vec{y}_i(t)$ are the particle positions relative to the center of friction with convention $\phi(0) = 0$ and with t -independent modulus $y_i := |\vec{y}_i(t)|$. Finally, $\vec{\zeta}(t)$ and $\zeta_\phi(t)$ are independent Gaussian white noises with $\langle \zeta_\mu(s) \zeta_\nu(t) \rangle = 2kT \delta_{\mu\nu} \delta(s-t) / \sum \gamma_i$ and $\langle \zeta_\phi(s) \zeta_\phi(t) \rangle = 2kT \delta(s-t) / \sum \gamma_i y_i^2$.

As already said, the force field consists of two parts,

$$\vec{F}(\vec{x}, t) = \vec{e}_\alpha A(t) - \vec{\nabla} U(\vec{x}), \quad (5)$$

namely a spatially homogeneous, externally applied force along the direction $\vec{e}_\alpha := \vec{e}_1 \cos \alpha + \vec{e}_2 \sin \alpha$ and a Gaussian square lattice potential with period L :

$$U(\vec{x}) = u \sum_{m,n=-\infty}^{\infty} \exp\left\{-\frac{(\vec{x} - [m\vec{e}_1 + n\vec{e}_2]L)^2}{2\sigma^2}\right\}. \quad (6)$$

For this potential with $u > 0$ and $u < 0$ as well as for various other potentials we always found similar results. Focusing on $u > 0$ from now on, the natural energy scale is the potential barrier $\Delta U := U(\vec{e}_1 L/2) - U((\vec{e}_1 + \vec{e}_2) L/2)$ separating adjacent potential wells. We henceforth adopt time, energy, and length units so that $\min_i \gamma_i = 1$, $\Delta U = 1$, $L = 1$, and focus on $\sigma = L/4$ [18].

The quantity of central interest is the net velocity $\vec{v} = \vec{e}_\alpha v$, obtained by averaging $\dot{\vec{X}}(t)$ over time. Obviously, rotating the force field (5) by 90° leaves the potential (6) invariant and entails a rotation of \vec{v} by 90° . Hence, it is sufficient to focus on $\alpha \in [0^\circ, 90^\circ]$. Likewise, one readily sees that $A(t) \mapsto -A(t)$ implies $\vec{v} \mapsto -\vec{v}$.

We first consider t -independent A , i.e. the force field (5) derives from a tilted periodic potential. For $A = 0$

symmetry implies $\vec{v} = \vec{0}$. For $A \neq 0$ the salient point is to realize that there exists no symmetry argument why two "molecules" of opposite chirality should travel down the tilted periodic potential with identical velocities \vec{v} . Following de Gennes [6], we thus can invoke Curie's principle to conclude [7, 16] that generically (i.e. up to parameter sets of measure zero) the velocities will indeed be different. In other words, (practically) *any tilted periodic potential can separate chiral partners* via their velocities. The main remaining problem pinpointed by De Gennes is the quantitative efficiency of the effect.

Fig. 1 provides those quantitative details in a typical case. We see that the velocities \vec{v} of the two chiral partners are indeed disappointingly similar, except around $\alpha = 45^\circ$. The explanation is as follows: For small thermal energies kT and small bias A , the particles travel extremely slowly by thermally activated hopping from one local minimum of the tilted periodic potential to the next. For any given orientation α there exists a critical tilt A in (5) at which certain local minima disappear by annihilation (collision) with saddle points, giving rise to "running solutions". For $kT = 0$ (deterministic limit), these solutions travel either parallel to \vec{e}_1 or to \vec{e}_2 , and for small $kT > 0$ still almost so. Roughly speaking, the direction "closer" to that of the static bias $\vec{e}_\alpha A$ is preferred, but due to the broken mirror symmetry, the direction actually switches already at some $\alpha < 45^\circ$ for one chiral partner and symmetrically at $\alpha > 45^\circ$ for the other (solid and dashed in Fig. 1). Since these considerations do not depend on any details of the model we can conclude that *a separation by (almost) 90° is generic for $\alpha = 45^\circ$, small kT , and A close to criticality*. Upon further increasing A , the deterministic running solutions speed up and bifurcate into new ones, "locked" [12, 17] along directions of the form $n\vec{e}_1 + m\vec{e}_2$ with increasingly large integers n and m (dashed-dotted and dotted in Fig. 1) and with $\vec{v} \rightarrow \vec{e}_\alpha A N / \sum \gamma_i$ for $A \rightarrow \infty$. Likewise, for finite kT the deterministically "sharp" bifurcations get washed out (Fig. 1) and $\vec{v} \rightarrow \vec{e}_\alpha A N / \sum \gamma_i$ for $kT \rightarrow \infty$.

Thus focusing on $\alpha = 45^\circ$, the dependence of the velocity \vec{v} on the bias A is shown in Fig. 2 (a,b). For symmetry reasons, *the velocities of the two chiral partners are now equal in modulus and symmetric about $\alpha = 45^\circ$* (see also Fig. 1). Remarkably enough, for some A -values, one triangle moves (practically) parallel to \vec{e}_1 (Fig. 2c) and thus its chiral partner parallel to \vec{e}_2 (not shown in Fig. 2), while for some different A -values it is exactly the other way round (Fig. 2d). In other words, *one and the same triangle may move along orthogonal directions for two different A -values*.

Turning to periodic $A(t)$ in (5), our so far findings quite naturally suggest the following idea: We select $\alpha = 45^\circ$ and two static bias values A_1 and A_2 with velocities $\vec{v}_1 = v_1 \vec{e}_1$ and $\vec{v}_2 = v_2 \vec{e}_2$ (e.g. $A_1 = 4$ and $A_2 = 6$ for the solid lines ($kT = 0.014$) in Fig. 2a,b) and exploit that the signs of v_1 and v_2 can be arbitrarily chosen by adjusting the signs of A_1 and A_2 (recall that $A \mapsto -A$ implies $\vec{v} \mapsto -\vec{v}$). If we now construct a time-periodic

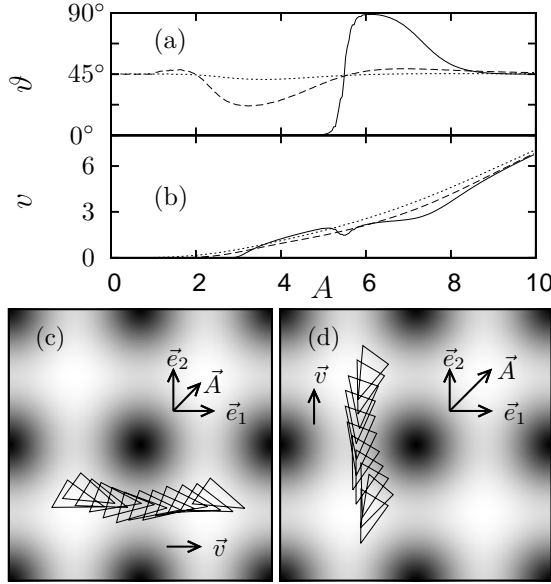


FIG. 2: (a) and (b): Direction ϑ and modulus v of the net velocity $\vec{v} = \vec{e}_\vartheta v$ for the solid triangle from Fig. 1a versus static bias A with fixed direction $\alpha = 45^\circ$. Shown are numerical solutions of (2)-(6) for $kT = 0.014$ (solid), $kT = 0.16$ (dashed), and $kT = 0.32$ (dotted). Other parameters as in Fig. 1. (c) and (d): Illustration of the triangle's motion for $A = 4$ (c) and $A = 6$ (d) at $kT = 0.014$. The static bias is indicated by $\vec{A} := \vec{e}_\alpha A$ and the periodic potential (6) as “shaded background”. The triangle motion is shown for a time-span of about 14.5 time-units in (c) and about 8.5 in (d), and then continues periodically up to noise effects (not shown).

$A(t)$ which takes the value A_1 during a fraction $p \in [0, 1]$ of its total period τ and the value A_2 during the rest of the period, the resulting time averaged velocity will be $\vec{v} = p\vec{v}_1 + (1-p)\vec{v}_2$, provided τ is so large that transient effects after each jump of $A(t)$ are negligible. Therefore, the molecule can be steered into *any* direction on the two-dimensional plane by varying p and adapting the signs of $A_{1,2}$. In particular, we will encounter a situation where \vec{v} is orthogonal to the force direction \vec{e}_α . E.g. from the solid lines in Fig. 2 we can read off that the triangle will move with such a velocity $\vec{v} \perp \vec{e}_\alpha$ if we choose $A_1 = -4$, $A_2 = 6$, and $p \approx 2/3$ to account for the difference in modulus of the corresponding velocities $\vec{v}_1 \approx -1.2 \vec{e}_1$ and $\vec{v}_2 \approx 2.4 \vec{e}_2$. The net velocity \vec{v} of the chiral partner follows from the above mentioned symmetry about $\alpha = 45^\circ$: This symmetry applies to both \vec{v}_1 and \vec{v}_2 separately, and hence also to $\vec{v} = p\vec{v}_1 + (1-p)\vec{v}_2$. Altogether, *the two chiral partners can thus be forced to move into exactly opposite directions*. Deviations due to the so far neglected transient effects after each jump of $A(t)$ are – at least for not too small τ -values – small and thus can be compensated by adjusting p and/or $A_{1,2}$.

Fig. 3 shows that these ideas indeed work out in prac-

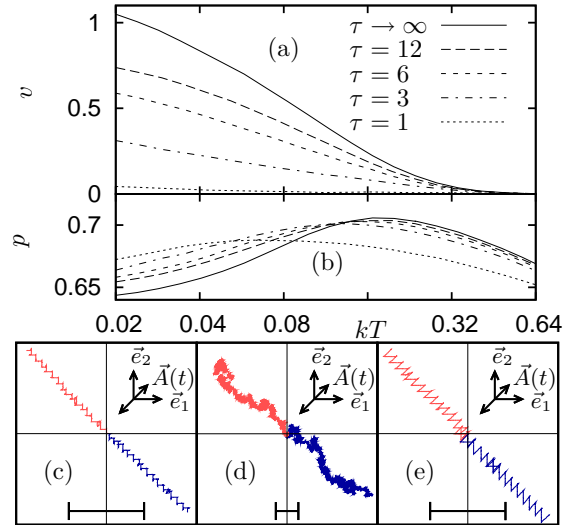


FIG. 3: (a): Absolute velocity v versus thermal energy kT (logarithmic scale) for the same system as in Fig. 1 but with a τ -periodic driving $\vec{e}_\alpha A(t)$ with $\alpha = 45^\circ$ and $A(t)$ taking the value $A_1 = -4$ during a fraction p of the period τ and the value $A_2 = 6$ during the rest of the period. (b): The corresponding p -values, adjusted as described in the main text so that the two chiral partners move into exactly opposite directions. (c) Typical single-particle trajectories $\vec{X}(t)$ for the two chiral partners (light red and dark blue) with $t \in [0, 100]$, $\vec{X}(0) = \vec{0}$, $kT = 0.02$, $p = 0.66$, and $\tau = 6$. Other parameters as in (a). The bar indicates 50 lattice periods and the double arrow the periodic driving [18]. (d) Same but for a much larger thermal energy $kT = 0.32$ and $t \in [0, 6000]$, $p = 0.69$. (e) Same as in (c) but for a very different triangle with $a = 2.5$, $b = 2.2$, $c = 1.1$ (cf. Fig. 1), and a driving with $A_1 = -7$, $A_2 = 14$, $p = 0.8$ [18].

tice, and in fact down to surprisingly small time-periods τ and up to remarkably large thermal energies kT . Note that while the velocities in Fig. 3a are long-time averages, Figs. 3c-e exemplify single-particle trajectories of moderate duration. Hence the thermal noise still leads to quite notable random fluctuations of each trajectory $\vec{X}(t)$ around the average behavior, especially in Fig. 3d. Only in Figs. 3c,e we still can see the expected “steps” of $\vec{X}(t)$ at jumps of $A(t)$.

Our above recipe for tailoring transport directions can be readily extended to arbitrary velocities \vec{v}_1 and \vec{v}_2 , provided they are not parallel to each other: Then, as before, $\vec{v} = p\vec{v}_1 + (1-p)\vec{v}_2$ can be made to point along any direction by properly choosing p and the signs of $A_{1,2}$. Intuitively and in view of Fig. 2, it is quite clear that generically one will always be able to find two bias values A_1 and A_2 with non-parallel velocities \vec{v}_1 and \vec{v}_2 . We thus can conclude that *chiral partners can (practically) always be made to move into opposite directions by means of a suitably tailored periodic driving force*. Fig. 3e exemplifies this generalized theoretical scheme for comparatively

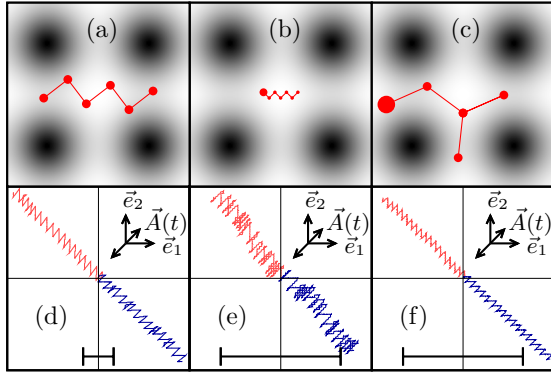


FIG. 4: (a)-(c): Further examples of chiral “molecules”. Dots indicate the constituting “atoms”, lines their rigid coupling, and the “shaded background” the periodic potential (6). Adopting units as specified below (6), $\gamma_i = 1$ for all “atoms” except for the larger dots in b and c, representing $\gamma_i = 3$. (d) Typical single-particle trajectories $\vec{X}(t)$ for the molecule from (a) and its chiral partner (light red and dark blue), obtained by numerically simulating (2)-(6) with $t \in [0, 100]$, $\vec{X}(0) = \vec{0}$, and $kT = 0.02$. Parameters of the periodic driving (see main text): $\alpha = 45^\circ$, $A_1 = 7.8$, $A_2 = -11.7$, $\tau = 6$, $p = 0.71$. The bar indicates 50 lattice periods and the double arrow the periodic driving. (e): Same but for the “molecule” from (b) and $A_1 = 7$, $A_2 = -10.5$, $p = 0.78$ [18]. (f): Same but for the “molecule” from (c) and $A_1 = 3$, $A_2 = -6$, $p = 0.85$ [18].

“large” triangular particles and Fig. 4 for a representative selection of more general chiral “molecules”. Generalizations involving more than two “static velocities” \vec{v}_i and the concomitant optimization problems point into interesting directions for future research.

In conclusion, periodic potentials can act as very effective and versatile selectors for sorting small objects which only differ by their chirality. Static bias forces make the two chiral partners move into directions which differ by up to 90° (Figs. 1,2). Appropriately chosen time-periodic forces even lead to motion into exactly opposite directions (Figs. 3,4). A major advantage compared to many other separation concepts [1] is that one and the same periodic potential may act as an efficient selector for quite different chiral particle species by suitably adapting the time-periodic driving force. Furthermore, the separation mechanisms are remarkably robust against thermal noise. The basic symmetry breaking conditions at the origin of all these effects are generically satisfied for much more general systems than in (1)-(6), including three spatial dimensions, finite inertia effects, other chiral objects and crystal potentials. An experimental proof of principle for chiral micro-particles [8–10] moving in a periodically structured microfluidic device [13] is presently under construction in the Anselmetti lab at Bielefeld University.

This work was supported by Deutsche Forschungsgemeinschaft under SFB 613 and RE1344/5-1

- [1] S. Ahuja (Editor), Chiral Separations: Applications and Technology, Amer. Chemical Soc. (1997); Chiral Separation Methods for Pharmaceutical and Biotechnological Products, Wiley (2010)
- [2] M. Kostur, M. Schindler, P. Talkner, and P. Hänggi, Phys. Rev. Lett. **96**, 014502 (2006)
- [3] Marcos, H. C. Fu, T. R. Powers, and R. Stocker, Phys. Rev. Lett. **102**, 158103 (2009)
- [4] N. Watari and R. G. Larson, Phys. Rev. Lett. **102**, 246001 (2009)
- [5] B. Spivak and A. V. Andreev, Phys. Rev. Lett. **102**, 063004 (2009)
- [6] P. G. de Gennes, Europhys. Lett. **46**, 827 (1999)
- [7] P. Curie, J. Phys. (Paris) 3. Série (théorique et appliquée) t. III (1894) 393.
- [8] L. Zhang et al, Appl. Phys. Lett. **94**, 064107 (2009)
- [9] D. Zerrouki et al, Nature **455**, 380 (2008)
- [10] A. Gosh and P. Fischer, Nano Lett. **9**, 2243 (2009)
- [11] S. Miret-Artés and E. Pollak, J. Phys. Condens. Matter **17**, S4133 (2005).
- [12] P. T. Korda, M. B. Taylor, and D. G. Grier, Phys. Rev. Lett. **89**, 128301 (2002); M. P. MacDonald, G. C. Spalding, and K. Dholakia, Nature **426**, 421 (2003); K. Xiao and D. G. Grier, Phys. Rev. Lett. **104**, 028302 (2010)
- [13] S. W. Turner et al. J. Vac. Sci. Technology B **16**, 3835 (1998) M. Carbodi et al., Electrophoresis **23**, 3496 (2002) N. Kaji et al. Anal. Chem. **76**, 15 (2004); J. Fu et al, Nature Nanotech. **2**, 121 (2007)
- [14] P. Tierno, T. H. Johansen, and T. M. Fischer, Phys. Rev. Lett. **99**, 038303 (2007); P. Tierno, A. Soba, T. H. Johansen, and F. Sagués, Appl. Phys. Lett. **93**, 214102 (2008).
- [15] D. Long, J.-L. Viovy, and A. Ajdari, Phys. Rev. Lett. **76**, 3858 (1996).
- [16] P. Reimann, Phys. Rep. **361**, 57 (2002).
- [17] C. Reichhardt and F. Nori, Phys. Rev. Lett. **82**, 414 (1999); M. Pelton, K. Ladavac, and D. G. Grier, Phys. Rev. E **70**, 031108 (2004); A. Gopinathan and D. G. Grier, Phys. Rev. Lett. **92**, 130602 (2004); A. M. Lacasta, J. M. Sancho, A. H. Romero, and K. Lindenberg, Phys. Rev. Lett. **94**, 160601 (2005); J. P. Gleeson, J. M. Sancho, A. M. Lacasta, and K. Lindenberg, Phys. Rev. E **73**, 041102 (2006); M. Balvin et al. Phys. Rev. Lett. **103**, 078301 (2009)
- [18] For example, $L \approx 1 \mu\text{m}$, $T \approx 293 \text{ K}$, and $\min_i \gamma_i \approx$ Stokes friction in water of a sphere with radius $r \approx L/10$ yields $v \approx 25 \mu\text{m/s}$ and $\tau \approx 0.1 \text{ s}$ in Fig. 3c, e and Fig. 4e, f.

7.2 Equations of motion of a rigid body

The equations of motion of an overdamped rigid object in two spatial dimensions are given by (1) of [5] but only one \mathbb{R}^2 vector and one angle are needed to describe the dynamics. Calling these the generalized coordinates, the straightforward way to obtain them from (1) of [5] is to use Itô's formula [89], i.e. the chain rule of stochastic calculus, after performing the overdamped limit $m_i \rightarrow 0$ [10]. Itô's formula for a function $p(\vec{q}(t))$ of the solution $\vec{q}(t)$ of the SDE (2.1) reads [88, 89]

$$\frac{dp}{dt}(t) = \frac{\partial p}{\partial \vec{q}} \frac{d\vec{q}}{dt}(t) + \frac{1}{2} \sum_{i,j,k} D_{ik} \frac{\partial^2 p}{\partial q_i \partial q_j}(t) D_{kj} \quad (7.1)$$

after removing all terms not needed now and with the notation of chapter 2.

As generalized coordinates we choose the center of friction [79] \vec{X} and the orientation ϕ :

$$\vec{X}(t) = \sum_{i=1}^N \frac{\gamma_i}{\gamma} \vec{x}_i(t) \quad (7.2)$$

$$\phi(t) = \phi_i(t) - \phi_i(0) = \text{atan} \left(\frac{y_{iy}(t)}{y_{ix}(t)} \right) - \phi_i(0) \quad \forall i \in [1, N] \quad (7.3)$$

$$\vec{y}_i(t) = \vec{x}_i(t) - \vec{X}(t) = \mathbf{O}(\phi(t)) \vec{y}_i(0) \quad \forall i \in [1, N] \quad (7.4)$$

$$\gamma = \sum_{i=1}^N \gamma_i \quad (7.5)$$

$$\gamma_\phi = \sum_{i=1}^N \gamma_i \vec{y}_i^2 \quad (7.6)$$

with $\mathbf{O}(\phi) = \begin{pmatrix} \cos(\phi) & -\sin(\phi) \\ \sin(\phi) & \cos(\phi) \end{pmatrix}$. Note that we use subscripts x and y to denote the x and y components of vectors, e.g. $X_{x/y} = \vec{X} \vec{e}_{x/y}$. Applying (7.1) to (7.2)-(7.3), we get the equations of motion of the generalized coordinates, (2)-(3) of [5]:

$$\dot{\vec{X}}(t) = \frac{\sum_{i=1}^N \vec{F}(\vec{x}_i(t), t)}{\gamma} + \vec{\zeta}(t), \quad (7.7)$$

$$\dot{\phi}(t) = \frac{\vec{e}_z \cdot \sum_{i=1}^N \vec{y}_i(t) \times \vec{F}(\vec{x}_i(t), t)}{\gamma_\phi} + \zeta_\phi(t) \quad (7.8)$$

with independent Gaussian white noises $\vec{\zeta}(t)$ and $\zeta_\phi(t)$: $\langle \zeta_i(s) \zeta_j(t) \rangle = 2kT\delta_{ij}\delta(s-t)/\gamma$ and $\langle \zeta_\phi(s) \zeta_\phi(t) \rangle = 2kT\delta(s-t)/\gamma_\phi$.

We now summarize the main steps of the derivation of these equations. First, we require the constraining forces to satisfy

$$\sum_i \vec{f}_i(\vec{q}) = 0 \quad (7.9)$$

$$\sum_i \vec{x}_i \times \vec{f}_i(\vec{q}) = 0, \quad (7.10)$$

i.e. there is no net internal force and no net internal torque acting on the rigid body. (7.9)-(7.10) follow immediately if we consider pair interactions for the monomers. Let

$$\vec{f}_i(\vec{q}) = \sum_{j \neq i} \vec{C}_{ij}(\vec{q}) \quad (7.11)$$

with $\vec{C}_{ij}(\vec{q}) = \frac{\vec{x}_i - \vec{x}_j}{|\vec{x}_i - \vec{x}_j|} c_{ij}(|\vec{x}_i - \vec{x}_j|)$, $c_{ij}(|\vec{x}_i - \vec{x}_j|) = c_{ji}(|\vec{x}_i - \vec{x}_j|)$ and \vec{q} is the phase space vector, i.e. all the coordinates \vec{x}_i . (7.9) is then obtained by using $\vec{C}_{ij}(\vec{q}) = -\vec{C}_{ji}(\vec{q})$, and (7.10) follows from

$$\sum_{i,j \neq i} \vec{x}_i \times \vec{C}_{ij}(\vec{q}) = \sum_{i,j \neq i} (\vec{x}_i - (\vec{x}_i - \vec{x}_j)) \times \vec{C}_{ij}(\vec{q}) = \sum_{i,j \neq i} \vec{x}_j \times \vec{C}_{ij}(\vec{q}) = - \sum_{i,j \neq i} \vec{x}_i \times \vec{C}_{ij}(\vec{q}) \quad (7.12)$$

since $(\vec{x}_i - \vec{x}_j) \times \vec{C}_{ij}(\vec{q}) = 0$.

We start with the nonstiff equations of motion, (1) of [5] and let $m_i \rightarrow 0$ (overdamped limit [10]). Applying (7.1) to (7.2), using (1) of [5] with $m_i = 0$, linearity and (7.9), we obtain (7.7) ((2) of [5]) except for the noise term:

$$\dot{\vec{X}}(t) = \frac{\sum_{i=1}^N \vec{F}(\vec{x}_i(t), t)}{\gamma} + \frac{\sum_{i=1}^N \vec{\xi}_i(t)}{\gamma}. \quad (7.13)$$

We now let the

$$\phi_i(t) = \text{atan} \left(\frac{y_{iy}(t)}{y_{ix}(t)} \right) \quad \forall i \in [1, N] \quad (7.14)$$

vary independently of each other (nonstiff coupling potential), apply (7.1) to (7.14) and use

$$\frac{\partial \phi_i}{\partial \vec{x}_j} = \frac{\left(\delta_{ij} - \frac{\gamma_j}{\gamma} \right)}{\vec{y}_i^2} (-y_{iy}, y_{ix}) \quad (7.15)$$

$$\frac{\partial^2 \phi_i}{\partial \vec{x}_{jx}^2} = \frac{2 \left(\delta_{ij} - \frac{\gamma_j}{\gamma} \right)^2 y_{ix} y_{iy}}{\vec{y}_i^2} = -\frac{\partial^2 \phi_i}{\partial \vec{x}_{jy}^2} \quad (7.16)$$

to get

$$\frac{d\phi_i}{dt}(t) = \sum_{j=1}^N \frac{d\phi_i}{d\vec{x}_j} \frac{d\vec{x}_j}{dt} = \vec{e}_z \cdot \sum_{j=1}^N \frac{\left(\frac{\delta_{ij}}{\gamma_j} - \frac{1}{\gamma} \right)}{\vec{y}_i^2} \vec{y}_i(t) \times \left(\vec{F}(\vec{x}_j, t) + \vec{f}_j(\vec{q}) + \vec{\xi}_j(t) \right). \quad (7.17)$$

Summing over all the ϕ_i , weighted to get rid of the constraining forces, we get

$$\sum_{i=1}^N \gamma_i \vec{y}_i^2(t) \frac{d\phi_i}{dt}(t) = \vec{e}_z \cdot \sum_{i,j=1}^N \left(\delta_{ij} - \frac{\gamma_i}{\gamma} \right) \vec{y}_i(t) \times \left(\vec{F}(\vec{x}_j, t) + \vec{f}_j(\vec{q}) + \vec{\xi}_j(t) \right) \quad (7.18)$$

$$= \vec{e}_z \cdot \sum_{i=1}^N \vec{y}_i(t) \times \left(\vec{F}(\vec{x}_i, t) + \vec{f}_i(\vec{q}) + \vec{\xi}_i(t) \right) \quad (7.19)$$

$$= \vec{e}_z \cdot \sum_{i=1}^N \vec{y}_i(t) \times \left(\vec{F}(\vec{x}_i, t) + \vec{\xi}_i(t) \right), \quad (7.20)$$

where we have used $\sum_{i=1}^N \frac{\gamma_i}{\gamma} \vec{y}_i = 0$ to get (7.19) and $\sum_{i=1}^N \vec{y}_i \times \vec{f}_i(\vec{q}) = \sum_{i=1}^N \vec{x}_i \times \vec{f}_i(\vec{q}) - \sum_{i=1}^N \vec{X} \times \vec{f}_i(\vec{q}) = 0$ because of (7.9)-(7.10) to get (7.20).

Now, we perform the limit of stiff coupling¹ and get

$$\phi_i(t) = \phi(t) + \phi_i(0) \text{ and } \vec{y}_i^2(t) = \vec{y}_i^2(0) \quad \forall i \in [1, N], t > 0 \quad (7.21)$$

with some arbitrary reference angle $\phi(t)$, and thus²

$$\frac{d\phi}{dt}(t) = \sum_{i=1}^N \frac{\vec{y}_i(t) \times (\vec{F}(\vec{x}_i, t) + \vec{\xi}_i(t))}{\gamma_\phi}, \quad (7.22)$$

which is (7.3) or (3) of [5] except for the noise terms. Lastly, we simplify the noise terms by using a statistically equivalent stochastic process. The easiest way to do this without hassle is to transform the system (7.13),(7.22) to a Fokker-Planck equation (and back). The system (7.13),(7.22) can be interpreted as a 3 dimensional non-autonomous SDE with a $2N$ dimensional Wiener process and multiplicative noise:

$$\frac{d\vec{q}}{dt}(t) = \vec{Q}(\vec{q}(t), t) + H(\vec{q}(t)) \vec{\Upsilon}(t) \quad (7.23)$$

with the noise process $\vec{\Upsilon}(t)^T = \frac{1}{\sqrt{2kT}} \left(\frac{1}{\sqrt{\gamma_1}} \xi_{1x}(t), \frac{1}{\sqrt{\gamma_1}} \xi_{1y}(t), \frac{1}{\sqrt{\gamma_2}} \xi_{2x}(t), \dots, \frac{1}{\sqrt{\gamma_N}} \xi_{Ny}(t) \right)$, $\langle \Upsilon_i(t) \Upsilon_j(s) \rangle = \delta_{ij} \delta(t-s)$, the phase space vector $\vec{q}(t)^T = (X_x(t), X_y(t), \phi(t))$ and

$$H(\vec{q}) = \sqrt{2kT} \begin{pmatrix} \frac{\sqrt{\gamma_1}}{\gamma} & 0 & \frac{\sqrt{\gamma_2}}{\gamma} & 0 & \dots & \frac{\sqrt{\gamma_N}}{\gamma} & 0 \\ 0 & \frac{\sqrt{\gamma_1}}{\gamma} & 0 & \frac{\sqrt{\gamma_2}}{\gamma} & \dots & 0 & \frac{\sqrt{\gamma_N}}{\gamma} \\ -\frac{\sqrt{\gamma_1}}{\gamma_\phi} y_{1y} & \frac{\sqrt{\gamma_1}}{\gamma_\phi} y_{1x} & -\frac{\sqrt{\gamma_2}}{\gamma_\phi} y_{2y} & \frac{\sqrt{\gamma_2}}{\gamma_\phi} y_{2x} & \dots & -\frac{\sqrt{\gamma_N}}{\gamma_\phi} y_{Ny} & \frac{\sqrt{\gamma_N}}{\gamma_\phi} y_{Nx} \end{pmatrix}. \quad (7.24)$$

Using $(D_{FP})_{ij} = \frac{1}{2} \sum_{k=1}^{2N} (H)_{ik} (H)_{jk}$ [90] we get the diffusion matrix of the corresponding Fokker-Planck equation:

$$D_{FP} = kT \begin{pmatrix} \frac{\sum_{i=1}^N \gamma_i}{\gamma^2} & 0 & -\frac{\sum_{i=1}^N \gamma_i y_{iy}}{\gamma \gamma_\phi} \\ 0 & \frac{\sum_{i=1}^N \gamma_i}{\gamma^2} & \frac{\sum_{i=1}^N \gamma_i y_{ix}}{\gamma \gamma_\phi} \\ -\frac{\sum_{i=1}^N \gamma_i y_{iy}}{\gamma \gamma_\phi} & \frac{\sum_{i=1}^N \gamma_i y_{ix}}{\gamma \gamma_\phi} & \frac{\sum_{i=1}^N \gamma_i (y_{iy}^2 + y_{ix}^2)}{\gamma_\phi^2} \end{pmatrix} \quad (7.25)$$

$$= \begin{pmatrix} \frac{kT}{\gamma} & 0 & 0 \\ 0 & \frac{kT}{\gamma} & 0 \\ 0 & 0 & \frac{kT}{\gamma_\phi} \end{pmatrix}, \quad (7.26)$$

from which (7.7)-(7.8), i.e. (2)-(3) of [5], follow since the deterministic part of the equation is unaffected by the transformation.

7.3 Setup

Throughout this chapter, we will consider general chiral objects which need not be “real” molecules, but we will refer to them as molecules and to their constituents as atoms.

¹We should take more care in doing so, similarly as with the overdamped limit [10].

²Actually, this step is another application of Itô’s formula, but to a linear transformation.

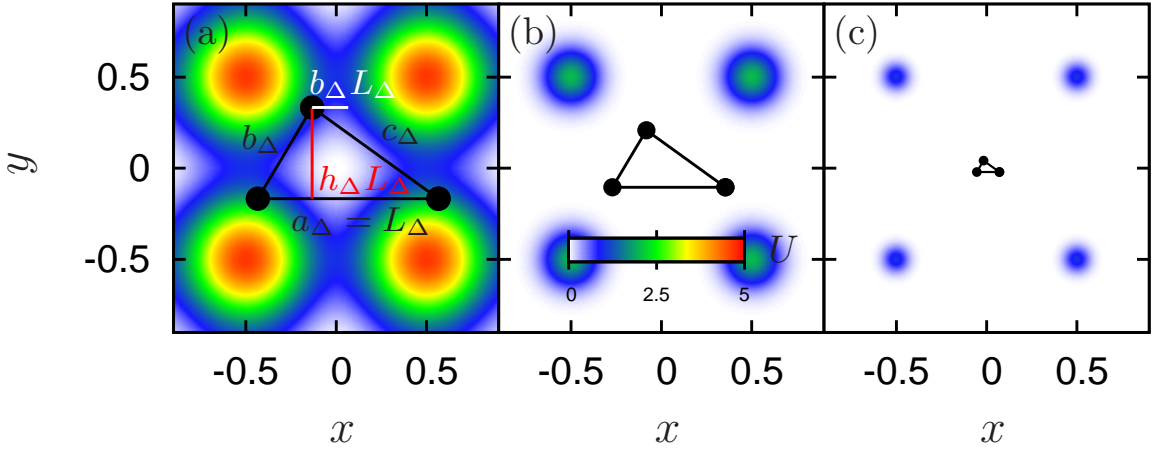


Figure 7.1: Representation of the square lattice potentials with Gaussian the lattice site potentials, i.e. (7.30)-(7.31), (a) $\sigma = 0.25$, (b) $\sigma = 0.1$ and (c) $\sigma = 0.05$. The potential height is encoded in colors according to the legend in panel (b). The molecules (triangles) correspond to our ‘‘standard’’ triangle (7.36) but the triangles in (b) have $L_\Delta = 0.25$ and (c) $L_\Delta = 0.05$. Furthermore, the parameters b_Δ (red) and h_Δ (white) are illustrated.

Moreover, we restrict ourselves to rigid objects. That restriction is not necessary as long as the dynamics are such that the configuration of the molecules is not changed (or only with vanishing probability), e.g. one chiral partner cannot change its configuration to that of its mirror image, but it makes the discussion much easier.

Our setup will be the dynamics of a molecule described by (7.2)-(7.8) in the force field

$$\vec{F}(\vec{r}, t) = -\vec{\nabla}U(\vec{r}) + A\vec{e}_\alpha + A'(t)\vec{e}_{\alpha'} \quad (7.27)$$

of a square lattice potential $U(\vec{r})$ (see below), a constant bias force $A\vec{e}_\alpha$ and the rocking driving force $A'(t)\vec{e}_{\alpha'}$. We allow the rocking driving force to have its own direction in contrast to [5], but unless otherwise noted we will use

$$\alpha = \alpha' \quad (7.28)$$

and otherwise keep the notation of [5]. Moreover, we will consider only a constant bias force, i.e.

$$A' = 0 \quad (7.29)$$

unless otherwise noted. For the potential $U(\vec{r})$, we will use (4.2) and (4.4) with $u = 20$, i.e.³

$$U(\vec{r}) = \sum_{n,m} \tilde{U} \left(x + \left(n + \frac{1}{2} \right) \cdot L, y + \left(m + \frac{1}{2} \right) \cdot L \right) \quad (7.30)$$

and

$$\tilde{U}(x, y) = 20 \cdot \sigma \cdot \exp\left(-\frac{r^2}{2\sigma^2}\right). \quad (7.31)$$

³ $\vec{r} = (x, y)$. Note that the lattice considered in [5] has been shifted by $\frac{\vec{e}_1 + \vec{e}_2}{2}$ (in the notation of [5]) for aesthetic reasons, and there is a typo in [5]: the equation following ‘‘... potential barrier’’ should read $\Delta U := U(\vec{e}_2 L/2) - U(\vec{e}_1 L/2 + \vec{e}_2 L/2)$.

Our “standard” choice for the remaining parameter will be

$$\sigma = \frac{1}{4} \quad (7.32)$$

so that the potential barrier for a point particle escaping from one potential well to the next along the x direction is approximately⁴ 1 for our standard choice, and we get the same setup as in [5] except for above mentioned minor differences in notation. We will henceforth tacitly refer to the above described dynamics, and only mention differences from these “standard” dynamics when appropriate.

Our “standard” molecule will be a trimer, parameterized as a triangle with side lengths as in [5], but we will use a more convenient way to define the side lengths:

$$a_\Delta = L_\Delta \quad (7.33)$$

$$b_\Delta = L_\Delta \sqrt{\left(\frac{1}{2} - b_\Delta\right)^2 + h_\Delta^2} \quad (7.34)$$

$$c_\Delta = L_\Delta \sqrt{\left(\frac{1}{2} + b_\Delta\right)^2 + h_\Delta^2}, \quad (7.35)$$

see figure 7.1(a) for an illustration. $L_\Delta \cdot h_\Delta$ is the height of the triangle with respect to the base $a_\Delta = L_\Delta$. $L_\Delta \cdot b_\Delta$ is a qualitative measure of the chirality of the triangle. $b_\Delta = 0$ implies a isosceles triangle and the chiral partners are obtained by changing the sign of b_Δ . Our “standard” choice for the triangle will be identical to the one shown in figure 1a of [5] and figure 7.1(a):

$$b_\Delta = 0.2, h_\Delta = 0.5, L_\Delta = 0.5, \gamma_{1,2,3} = 1. \quad (7.36)$$

At some points, we will consider “smaller” or “larger” triangles “proportional” to (7.36) in the sense that the triangles are described by (7.36), only that L_Δ is smaller/larger. Moreover, we will always consider $\gamma_{1,2,3} = 1$ unless otherwise noted.

We denote the time and ensemble averaged center of friction [5] (or spatial) transport velocity of the molecule as

$$\vec{v} = v \vec{e}_\vartheta = \left\langle \dot{\vec{X}} \right\rangle \quad (7.37)$$

with the modulus v and direction ϑ . We will add subscripts L and R to indicate that we refer to one of the chiral partners when necessary. Unless otherwise noted, L will be our standard choice and omitted. We quantify the separation efficiency by the *separation angle*

$$\vartheta_S = \vartheta_L - \vartheta_R \quad (7.38)$$

where $\vartheta_{L/R}$ denote the transport directions of the chiral partners, L denoting the considered triangle and R its mirror image, and the *separation vector*

$$\vec{v}_S = \vec{v}_L - \vec{v}_R \quad (7.39)$$

with $\vec{v}_{L/R}$ being the average velocities of the chiral partners and L and R as above.

⁴Actually, in [5] $u = \frac{1}{U(0.5,0) - U(0,0)} \approx 20.24$ is used for all computations, so that the barrier height is exactly one, but the differences are negligible.

The bare potential is \hat{S}_x , \hat{S}_y , \hat{S}_{xy} , $\hat{S}_{\frac{\pi}{2}}$ and \hat{S}_0 symmetric. The applied forces break some or all of these symmetries depending on their direction and nature. First, the bias force always breaks $\hat{S}_{\frac{\pi}{2}}$ and \hat{S}_0 . The line reflection symmetries will be broken unless the bias force is parallel to the particular reflection line, i.e. at most one of the symmetries implied by \hat{S}_x , \hat{S}_y and \hat{S}_{xy} survives in the presence of a bias force, depending on its direction. The time dependent drive breaks the reflection symmetries again unless it is parallel to the particular reflection line, or orthogonal and symmetric (see section 2.4). Moreover it always breaks $\hat{S}_{\frac{\pi}{2}}$ if chosen as in (7.27). Only a circular drive (see section 2.4) would keep the rotation symmetry. \hat{S}_0 is broken by the time dependent drive unless the drive is symmetric (see section 2.4). Lastly, a chiral molecule breaks all line reflection symmetries \hat{S}_x , \hat{S}_y and \hat{S}_{xy} , but if any of these symmetries is present in the dynamics of a point particle in the same potential (to which we will refer as “point particle dynamics”), it maps the dynamics of one chiral partner onto the other, as has been discussed in chapter 2:

$$\vec{v}_R = \hat{S} \vec{v}_L, \quad (7.40)$$

where we have called the appropriate symmetry \hat{S} , and (7.40) is equivalent to (2.27).

As was already hinted at in section 2.5.3, according to Curie’s principle [14], once all symmetries preventing transport in a given direction are broken, transport in that direction will be the generic situation. Moreover, in the same spirit, two different dynamics which are not related by symmetry will have different transport properties. Thus we are left with two setups:

1. The point particle dynamics have no reflection symmetry (across any line). Then the currents of the chiral partners will be different in general.
2. The point particle dynamics have a reflection symmetry (across a line). Then, by Curie’s principle, the current of a general chiral molecule will have a component orthogonal to that line, and the corresponding component of the current of its chiral partner will have the opposite sign. A special case of this situation is if the point particle dynamics are additionally \hat{S}_0 symmetric. Then, there is no current, but there may be diffusion, and (2.27) will then apply to the diffusion tensors.

Throughout this chapter, we will consider mainly the latter, but the former will be considered in section 7.4 (figure 7.2), section 7.6.2 (figure 7.7) and section 7.9 for a slightly different situation (namely, a locally flat potential).

7.4 “Long” molecules

Complementary to figure 1 of [5], we consider a two dimensional phase diagram of the dynamics of our standard triangle in figure 7.2(a). The deterministic dynamics of its mirror image is obtained by applying \hat{S}_{xy} symmetry and not shown, as are the dynamics for other directions of the bias force, which are obtained by using $\hat{S}_{\frac{\pi}{2}}$. For small bias forces, the triangle is in a bound state, and at some critical value of the force the triangle starts moving. Since it is easier for the triangle to move parallel to the coordinate axes due to the lower potential barriers to be overcome, this critical force is lower for forces parallel to the coordinate axes, and highest for a bias force parallel to the bisectrix,

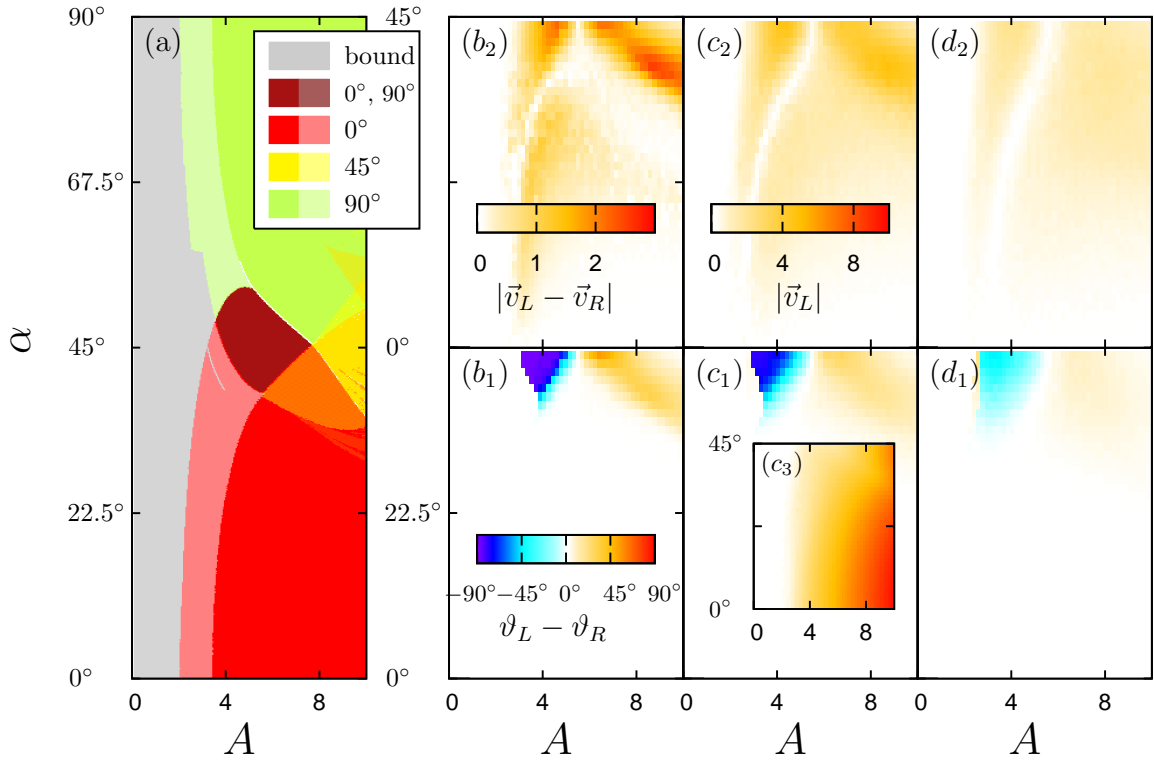


Figure 7.2: (a) Deterministic $kT = 0$ phase diagram showing only periodic attractors for the dynamics of the triangle described by (7.36) subjected only to a constant bias force $\vec{A} = A \vec{e}_\alpha$. The transport direction of the triangle, i.e. ϑ_L , is encoded in colors. The colors corresponding to the predominant transport directions are shown in the legend in panel (a). Coexistence of deterministic transporting attractors with different transport directions is indicated by hatching the corresponding colors, except for the most important attractors, see the legend in (a). The full color palette used can be found in e.g. figure 7.4(a) (the palette shown for ϑ), but colors other than those shown in the legend in (a) are practically absent in figure 7.2(a). If a transporting attractor coexists with a non-translating attractor its color is desaturated. All phase diagrams in this chapter have been calculated along the lines of section 3.9.1. (b)-(d) show the separation angle and vector of the triangle and its mirror image for (b) $kT = 0.04$, (c) $kT = 0.08$ and (d) $kT = 0.16$. The separation angle and vector for $\alpha > 45^\circ$ follow from symmetry and are not shown. b_1 shows the separation angle, i.e. $\vartheta_L - \vartheta_R$ for $\alpha \in [0^\circ, 45^\circ]$, b_2 shows the modulus of the separation vector $|\vec{v}_L - \vec{v}_R|$ for the same α range and $(c_1), (c_2), (d_1), (d_2)$ are analogous. The inset (c_3) shows the modulus of the transport velocity $|\vec{v}_L|$ for the intermediate noise strength $kT = 0.08$ considered in panels (c_i) , encoded in colors according to the palette shown in panel (c_2) . The palette has been cut off at 10, and larger velocities are shown as 10. The modulus of the transport velocity for the other noise strengths considered is not very different and not shown.

i.e. $\alpha = 45^\circ$. The triangle moves parallel to the coordinate axes if the force is parallel to either axis. Upon rotating the force away from the axis, the motion of the triangle remains locked to the direction of the axis, and this locking persists up to $\alpha = 45^\circ$ for small forces, while the triangle locks to $\vartheta = 45^\circ$ for larger forces around $\alpha = 45^\circ$ and there are some regions of coexistence of different locking regimes. Due to the broken \hat{S}_{xy} symmetry (even at $\alpha = 45^\circ$), i.e. chirality, the phase diagram is not symmetric around $\alpha = 45^\circ$. Thus, the general situation is that if the solutions locked to the coordinate axes persist up to $\alpha = 45^\circ$, they will have different properties and regions of stability, and in particular the critical forces at which they emerge from a bound solution will be different, which is clearly visible in figure 7.2(a) with the solution locked to the x direction having a smaller critical force. Moreover, due to \hat{S}_{xy} symmetry of the point particle dynamics at $\alpha = 45^\circ$ the chiral partner molecule will exhibit the same behavior with the x and y axis interchanged.

The fact that these solutions persist up to $\alpha = 45^\circ$ is due to the shape of the triangle and the potential. Imagine a very long straight “rod”. Due to the potential this rod cannot rotate and will always move parallel to one of the coordinate axes unless the bias force is very large, even if the bias force is parallel to the bisectrix. Basically this property carries over to the particular triangle we have selected, and is the basis of the 90° separation of triangles subjected to a constant bias force reported in [5]. By considering noise induced escape at small bias forces (see [5]) instead of deterministic running solutions, 90° separation can always be achieved if there are non-flat potential barriers separating adjacent potential wells, but possibly at vanishing currents. In contrast, if the potential barriers separating minima are negligible, i.e. the potential is locally flat (smaller σ , see section 7.9), this behavior is lifted, and at $\alpha = 45^\circ$ the triangle will always move parallel to the bisectrix, and we have found no separation with respect to the separation angle at $\alpha = 45^\circ$.

Including noise, we find that for our potential the separation angle is only large (in modulus) around $\alpha = 45^\circ$ and practically zero otherwise, it being largest for smaller forces. Moreover, the separation vector exhibits a similar behavior, but it is non-zero also for α far from 45° due to the transport velocities of the chiral partners differing in modulus (see also figure 1 in [5]). Furthermore, noise reduces the separation efficiency in most cases, with separation vanishing for arbitrarily large noise strengths, but there are also regions in which noise improves the separation efficiency, in particular for small bias forces where transport is noise induced and no deterministic running solutions are present [5].

We conclude that for relatively large triangles (we have found $L_\Delta \approx 0.1$ to be close to the lower limit, and the same applies to the “size”, i.e. the largest monomer-monomer distance of more generally shaped objects, cf. figure 4 of [5]) and potentials with non-flat potential barriers separating minima, separation is most efficient at

$$\alpha = 45^\circ, \quad (7.41)$$

and we will consider this situation in the following sections. Additionally the \hat{S}_{xy} symmetry of the point particle dynamics simplifies the situation drastically, allowing us to calculate the average velocity of the chiral partner by means of (2.27).

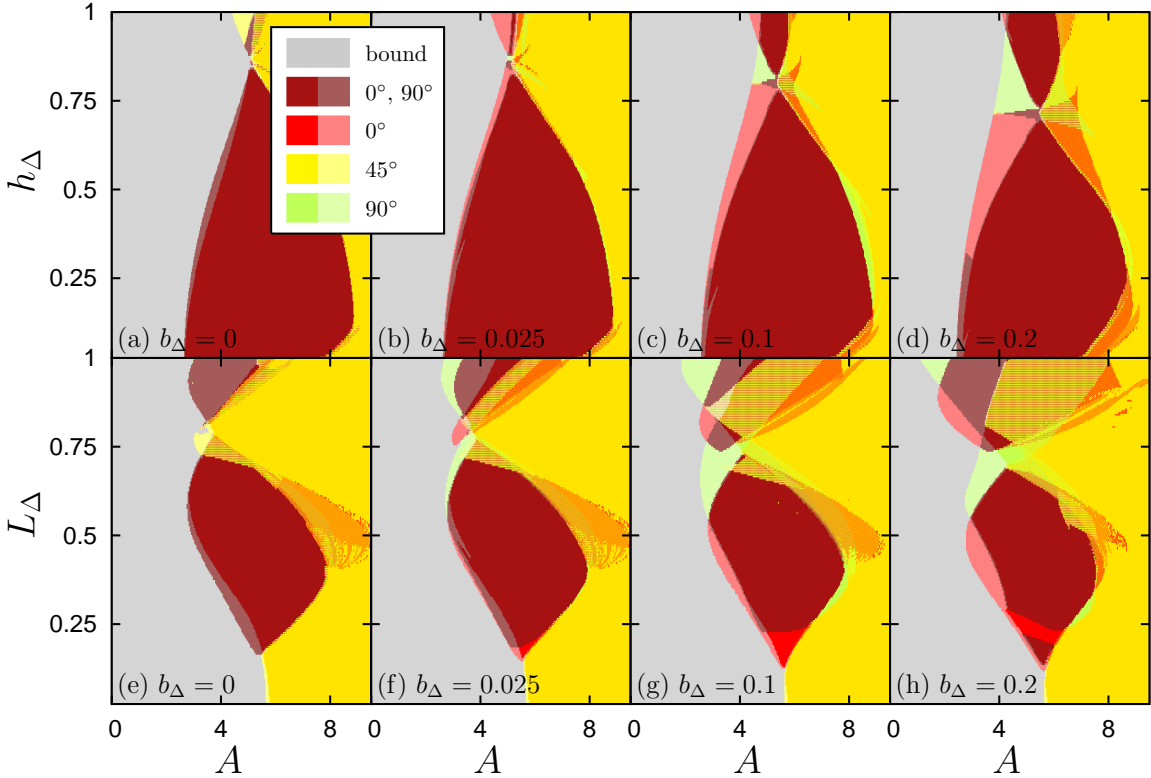


Figure 7.3: Deterministic $kT = 0$ phase diagrams as in figure 7.2(a) of the dynamics of a triangle with parameters as indicated in the panels, $L_\Delta = 0.5$ (upper row) and $h_\Delta = 0.2$ (lower row). The direction of the average transport velocity of periodic attractors, ϑ , is shown in dependence of a constant bias force $\vec{A} = A\vec{e}_\alpha$ with $\alpha = 45^\circ$ and there is no time dependent drive. The same method as in figure 7.2(a) is used to show ϑ as colors, including coexistence, see also the legend.

7.5 Spontaneous symmetry breaking transport leading to chiral separation

Figure 7.3 investigates the influence of the shape of the triangle on its deterministic static bias transport properties at $\alpha = 45^\circ$. Focusing first on $b_\Delta = 0.2$ in panels (d) and (h), i.e. a triangle of the same “chirality” as in figure 7.2 (in the sense that for all other parameters identical, the triangles are identical), we find that the shape of the triangle does not alter our main conclusion, i.e. there are running solutions locked to either coordinate axis for sufficiently small bias forces as long as the triangle is not too small ($L_\Delta \gtrsim 0.15$ for the given parameters). But, depending on the shape of the triangle, this can be either the x or the y axis. For small h_Δ , i.e. almost “rod” like triangles, as well as for small b_Δ , both chiral partners are almost identical (i.e. “less chiral”). Hence, for most parameter values for which running solutions locked to the coordinate axes are found, at least two coexist, one locked to the x axis and one to the y axis, except for a very narrow strip close to the critical value of A at which the first running solution is created. That difference scales with the “degree of chirality”.

We next focus on $b_\Delta = 0$ (panels (a) and (e)) to take a different view on chiral separation. In that case the triangle is achiral, hence the dynamics are \hat{S}_{xy} invariant with

the formal symmetry of the dynamics as discussed in section 2.5.3. Then the critical values of the bias force for which running solutions (locked to the coordinate axes) are created are identical for both coordinate axes due to the symmetry. E.g. a running solution locked to the x axis implies the existence of another running solution locked to the y axis and vice versa⁵. Therefore the regions of existence of these solutions coincide exactly. Thinking in terms of section 2.7 these solutions are actually SSBT solutions with respect to \hat{S}_{xy} symmetry. In those terms, chiral separation can now be understood as a consequence of SSBT. If we break the symmetry of the dynamics by letting $b_\Delta > 0$, the regions of existence of the two solutions no longer coincide. At the borders of their regions of existence only one of the solutions will be stable, and hence the triangle will be transported parallel to the corresponding coordinate axis for sufficiently small noise strengths. But employing the symmetry, the triangle is mapped onto its chiral partner, i.e. the symmetry can be understood to work as \hat{S}_0 works in chapters 3-4, but it inverts the sign of b_Δ instead of F . It follows that the triangle's chiral partner will be transported along the other coordinate axis. In contrast, if there is no SSBT at $b_\Delta = 0$, no deterministic chiral separation occurs (with noise, the average velocities of the chiral partners will still be different, in general).

Putting this idea to test, figure 7.4 (and figure 7.5) reveals a plot that, with colors and labels interchanged, could easily pass as belonging to chapters 3-4, cf. figure 3.1. At $b_\Delta = 0$, there is a critical value of the force around $A \approx 0.18$ at which all remaining stable and bounded solutions annihilate and become running solutions via saddle node bifurcations (see figure 7.5), creating two running solutions with transport along the coordinate axes, each solution being the image under S_{xy} of the other solution. Breaking the symmetry, these critical values of the force no longer coincide, and two lines of bifurcations in figure 7.4 with different slopes in the A - b_Δ plane of parameter space are found. The first corresponds to the creation of a running solutions carrying transport along the x axis and the second corresponds to the creation of the symmetry partner (using that the symmetry is only weakly perturbed), and, in particular, to the vanishing of the bound solution with which the first running solutions coexists. At the other border of the region of existence of SSBT attractors around $A \approx 0.4$ the order of the critical lines is the same. The running solution carrying transport along the y axis survives for larger bias forces, at which it coexists with a running solution carrying transport in the (1,1) direction, i.e. parallel to \vec{e}_{45° . Including weak noise (see figure 7.4(b-d)), the picture remains the same with noise averaging between the coexisting attractors and other phase space structures, thus uniquely determining the transport direction and chiral separation. An interesting effect is that upon increasing the bias force with all other parameters fixed, the transport direction of the triangle can be changed from $\vartheta = 0^\circ$ to $\vartheta = 90^\circ$ (for vanishing noise strength) for $b_\Delta \lesssim 0.38$, and the other way around for larger b_Δ . This effect, which is specific to our choice of the triangle (see e.g. figure 7.3), can be used to beautifully explain how to obtain 180° separation angles by using an asymmetric periodic driving force [5]. Lastly turning to the modulus of the average velocity, we find that it does not significantly depend on the choice of b_Δ and the magnitude of noise due to the nature of the running solutions, which are created via saddle node bifurcations

⁵More generally, any solution spontaneously breaking the symmetry implies the existence of a symmetry partner as discussed in section 2.6. This applies particularly for any running (i.e. SSBT) solutions whose average velocity is not parallel to \vec{e}_{45° .

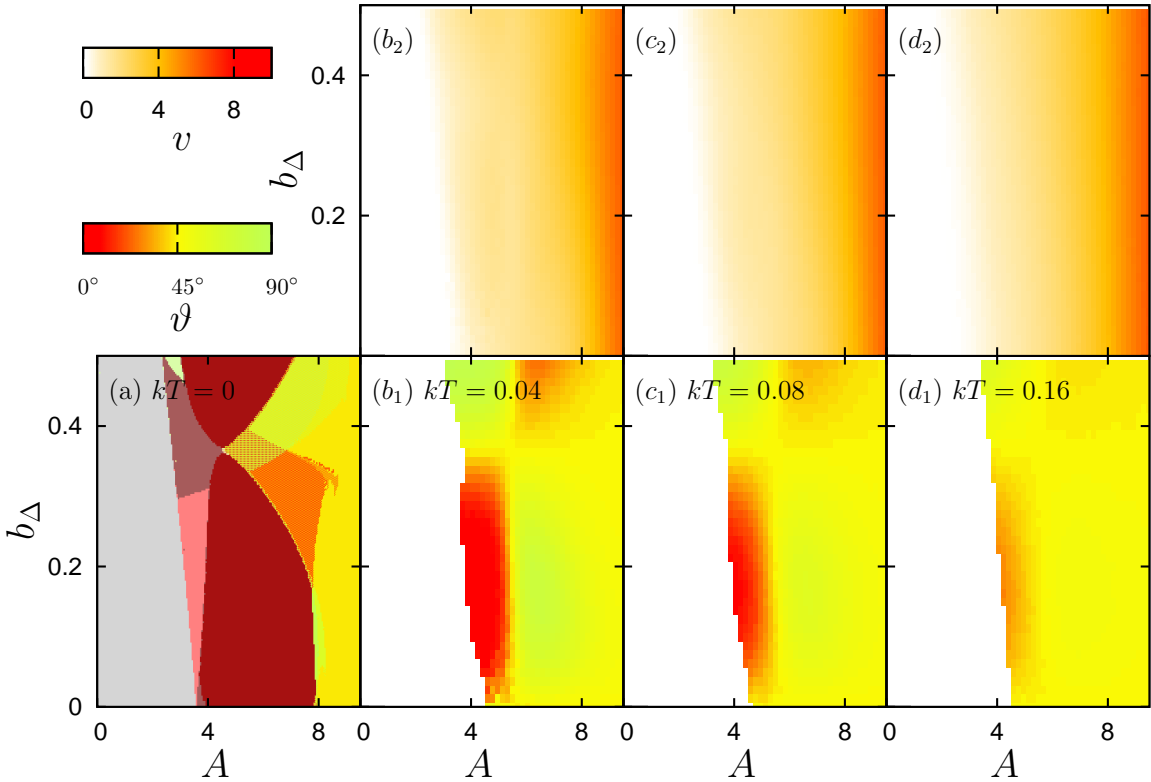


Figure 7.4: (a) Deterministic $kT = 0$ phase diagram as in figure 7.2(a) for the dynamics of the same triangle, driving forces and potential as considered in figure 7.2 except for $\alpha = 45^\circ$ and b_Δ is varied as a parameter. Due to $\alpha = 45^\circ$ the average velocity of the mirror image of the triangle follows from \hat{S}_{xy} symmetry and is not shown. The angle of the transport direction, ϑ , is shown in (a), (b₁), (b₂) and (b₃) and is encoded in colors according to the legends. In panel (a) the same method as in figure 7.2(a) is used to show coexistence of deterministic attractors with different transport directions, see the legend in figure 7.2(a). (b₁) shows ϑ in the presence of noise with kT as indicated in the panels. (b₂) shows the modulus of the transport velocity, v , according to the legend and for the same noise strength as in (b₁). The same applies to (c_{1/2}) and (d_{1/2}).

like simple running solutions of a particle in a tilted potential, in contrast to the phase locked solutions considered in chapter 4.

A more detailed account of the creation of running solutions is found in the bifurcation diagram in figure 7.5 showing the ϕ coordinates of all equilibria of the tilted force field (potential) and those of stable running solutions at the instant when they cross their Poincaré surfaces of section $X_{x/y} = n \cdot L$, n integer. At $A = 0$ and $b_\Delta = 0$ there are four stable equilibrium configurations of the triangle, separated by saddle-type equilibria due to $\hat{S}_{\frac{\pi}{2}}$ symmetry, and many more unstable equilibria, which, having the same ϕ but different \vec{X} coordinates are not all visible in figure 7.5(a). We focus on the stable equilibria and their saddles. $A > 0$ breaks \hat{S}_0 symmetry, and some of these equilibria annihilate in pitchfork and saddle node bifurcations, the former becoming also saddle node bifurcations (avoided pitchfork bifurcations) for $b_\Delta \neq 0$. Some of these saddle node

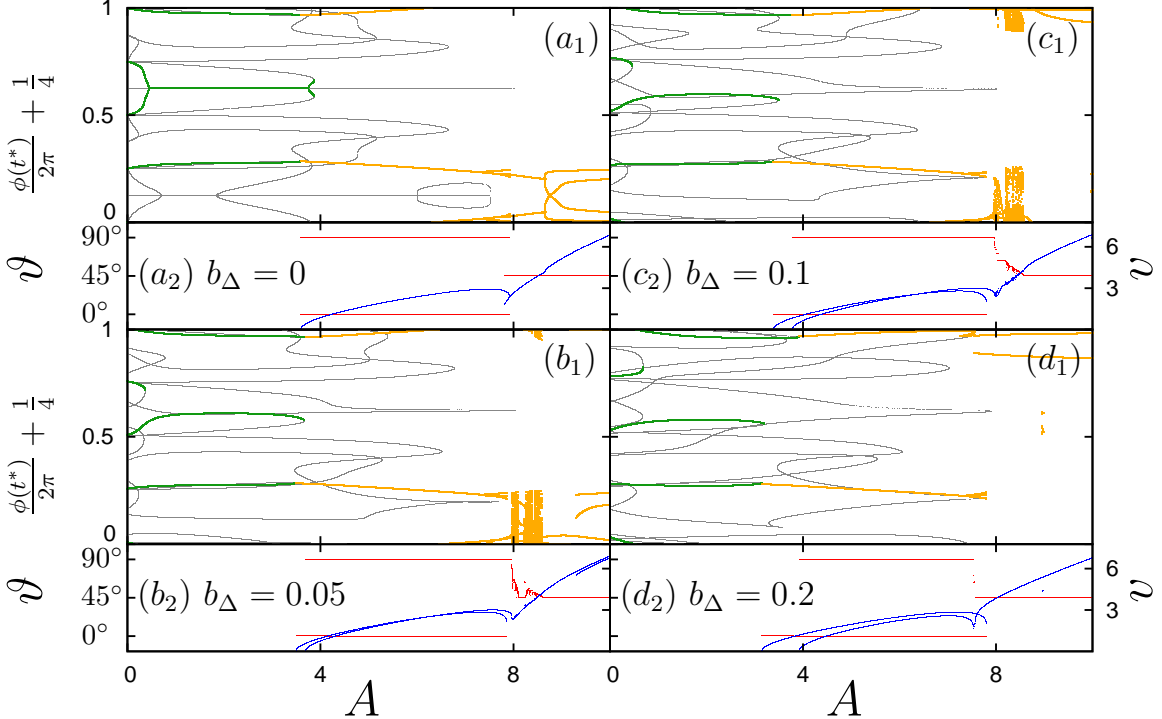


Figure 7.5: Deterministic $kT = 0$ bifurcation diagrams for the dynamics of the same triangle, driving force and parameters as considered in figure 7.4 and for specific values of b_Δ , as indicated in the panels. The modulus of the static bias force, A , is the bifurcation parameter. The upper panels, (a_1) , (b_1) , (c_1) and (d_1) , show the orientation of the triangle for stable equilibrium configurations in green, unstable equilibrium configurations in grey and stable running solutions in orange, for which the orientation is shown only for the time instant t^* at which the center of friction passes the Poincaré surface of section, i.e. $\vec{X}(t^*)\vec{e}_x = 0 + nL$ or $\vec{X}(t^*)\vec{e}_y = 0 + nL$, n integer. The lower panels, (a_2) , (b_2) , (c_2) and (d_2) , show the modulus of the concomitant average transport velocity, v , in blue and the direction, ϑ , in red.

bifurcations (but not all, depending on other saddles⁶) give rise to running solutions. In particular, the configurations of the triangle with its longest side (a_Δ) aligned parallel to one of the coordinate axes and the opposite vertex pointing in the positive direction of the other coordinate axis lead to stable running solutions of largely the same triangle orientation after colliding with their saddles (which start on the saddle of the potential at $A = 0$), see figure 2(c)-(d) in [5].

Another noteworthy feature is that the running solutions carrying transport in the (1,1) direction⁷ for large bias forces are not directly created from bifurcations of the running solutions carrying transport along the coordinate axes, as the lower resolution phase diagrams, e.g. figure 7.4, suggest but are created from saddle node bifurcations, which we have not further investigated. Thus there are regions of parameter space in which all three kinds of running solutions coexist, as one can already guess from the

⁶Transport only arises if the unstable manifolds of the saddles are connected to the stable manifolds of different copies (in different elementary cells) of the equilibria

⁷We refer to the lattice direction by (n,m), meaning the direction of $n \cdot \vec{e}_x + m \cdot \vec{e}_y$.

phase diagrams.

Lastly, the regions in which the direction of the running solutions varies continuously are not well resolved in the phase diagrams due but visible in figure 7.5. As can be inferred from figure 7.5, these regions contain devils staircase structures, period adding and quasiperiodicity [21, 26] and have a rather complicated structure depending on the symmetry of the lattice, which is mostly destroyed by noise and thus not of further interest here.

7.6 180° chiral separation by an asymmetric periodic drive

7.6.1 $\alpha = 45^\circ$

As has been detailed in [5], by applying a time dependent periodic and asymmetric drive

$$A'(t)\vec{e}_{\alpha'} = (A'_1\theta(p\tau - t) + A'_2\theta(t - p\tau))\vec{e}_{45^\circ} \quad (7.42)$$

(for $t \in [0, \tau]$ and outside that interval periodically continued with period τ) with $\alpha' = 45^\circ$, the chiral partners can almost always be made to move into opposite directions, even for relatively large noise strengths.

For our “standard” triangle, one particular chiral species can be made to move along x direction or the y direction depending only on the magnitude of the instantaneous bias force, and the explanation is particularly simple, but the mechanism requires only that the transport direction of the triangle depends on the magnitude of a constant bias force in the (1,1) direction. Then, for sufficiently slow switching, i.e. large τ ,

$$\vec{v} = p\vec{v}(A_1) + (1 - p)\vec{v}(A_2) \quad (7.43)$$

can be chosen arbitrarily if the transport velocities $\vec{v}(A_{1/2})$ belonging to the two bias force values $A_{1/2}$ are linearly independent. Therefore, \vec{v} can be made to be orthogonal to the (1,1) direction, i.e. the reflection line of \hat{S}_{xy} symmetry, and the two chiral partners will move into opposite directions. Complementary to figure 3 of [5], we investigate the robustness of the effect against thermal noise and finite switching times in more detail in figure 7.6 by showing the p dependence of the transport direction and velocity. It turns out that for large bias forces or short switching times (high frequencies), the transport direction depends sensitively on the choice of p , and the transport velocity is close to zero as already evident from figure 3a of [5]. While there is always only exactly one value of p for which the separation angle is 180° , in an experiment a smaller value may be sufficient depending on how exact p and other parameters (e.g. the magnitude of the instantaneous bias forces) can be adjusted in the experimental apparatus. The robustness of separation can be estimated from the width of the region of p values for which separation is achieved. This becomes very narrow for $kT \gtrsim 0.2$ or $\tau \lesssim \pi$, and the transport velocity at which the chiral partners are separated becomes very small. Thus, applying a time dependent drive can improve the separation angle dramatically and increases the robustness against thermal noise but does so at the expense of the speed at which the chiral partners separate (see e.g. figure 4e of [5]) and added experimental complexity.

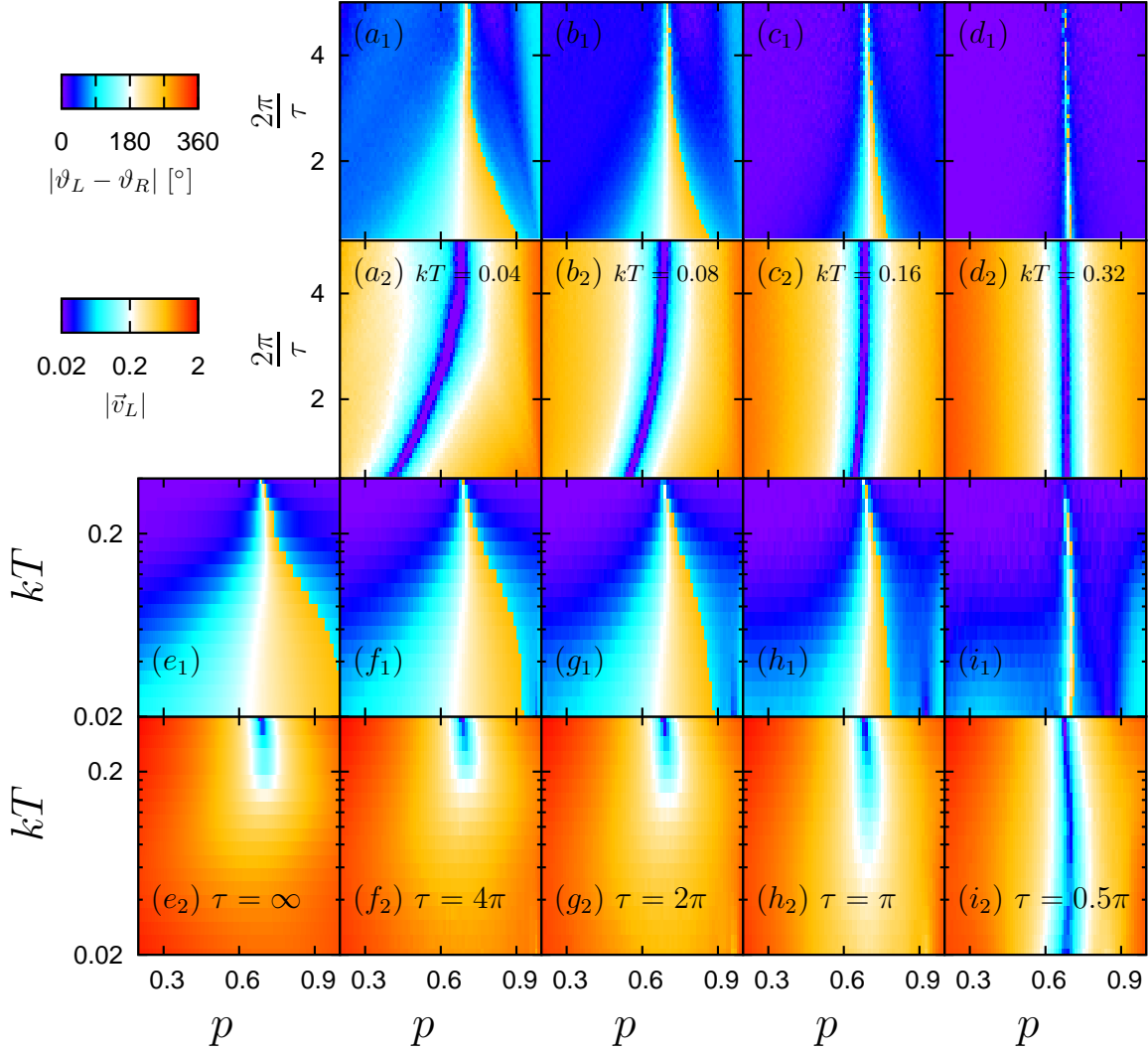


Figure 7.6: (a₁)-(i₁) separation angle $\vartheta_L - \vartheta_R$ and (a₂)-(i₂) average velocity of one of the enantiomers (the average velocity of the chiral partner is identical) for the dynamics of the triangle (7.36) in dependence of p , kT and $\frac{2\pi}{\tau}$ as indicated in the panels. An asymmetric periodic drive as described in [5], i.e. (7.42) with $\alpha' = 45^\circ$, $A'_1 = -4$, $A'_2 = 6$ and frequency $\frac{2\pi}{\tau}$, is applied to the triangle. Panel (e) is obtained by using the average velocities obtained for constant bias force directly, i.e. (7.43).

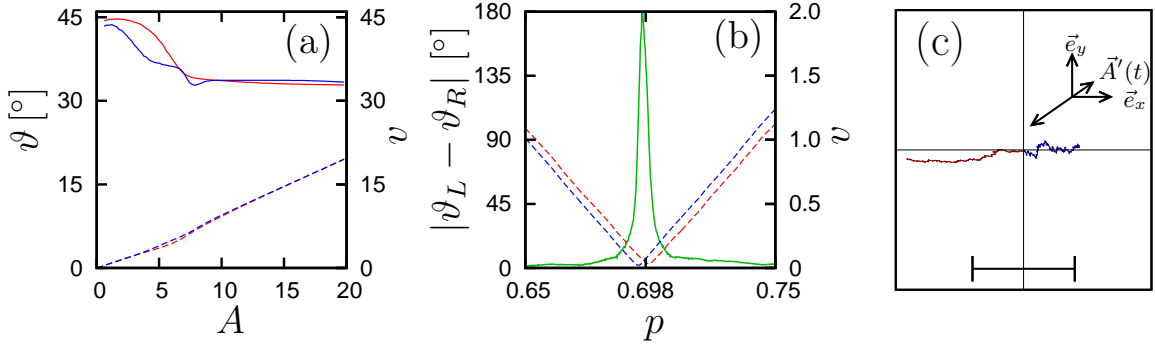


Figure 7.7: (a) Average velocity $\vec{v}_{L/R} = v_{L/R}\vec{e}_{\vartheta_{L/R}}$ for the noisy $kT = 0.002$ dynamics of the triangle and potential as considered in figure 7.13, i.e. Gaussian repulsive lattice potential with $\sigma = 0.1$ and the triangle is proportional to (7.36), but $L_\Delta = 0.25$. Only to a constant bias force $\vec{A} = A\vec{e}_\alpha$ with direction $\alpha = 32.6^\circ$ is applied. The solid red(blue) line shows $\vartheta_L(\vartheta_R)$ and the corresponding dashed lines show $v_{L/R}$. (b) Separation angle (green line) and average velocities (dashed lines as in (a)) for the same dynamics as in (a) but the constant bias force is replaced by the asymmetric periodic drive (7.42) with $\tau = 2\pi$, $A'_1 = -7.8$, $A'_2 = 16$ and p according to the x axis of the panel. (c) Example trajectories of length $3142 = 500\tau$, showing 180° separation for the same dynamics as in (b) with $p = 0.697$. The red line corresponds to the triangle proportional to (7.36) and the blue line to its mirror image. The bar shows 200 spatial periods of the potential.

7.6.2 $\alpha \neq 45^\circ$

Achieving 180° separation is more complicated if the driving forces are not in a symmetry direction of the lattice. Again using a slow asymmetric periodic drive, i.e. applying a force \vec{A}_1 for a fraction p of the very long drive period and a different force \vec{A}_2 for the remaining fraction $q = 1 - p$, one gets 4 independent instantaneous average velocities \vec{v}_{1L} , \vec{v}_{1R} , \vec{v}_{2L} and \vec{v}_{2R} , with the numeric index denoting the value of the driving force to which the velocity belongs and the index L/R referring to the chiral partners. As above, one gets

$$v_L \vec{e}_{\vartheta_L} = \vec{v}_L = p \vec{v}_{1L} + q \vec{v}_{2L} \quad (7.44)$$

for the average velocity of the first molecule in the time dependent force field, and for the second molecule the same equation with L replaced by R . Note that we would get the same equations for 2 completely different molecules, not only for chiral partners. Solving these equations for $|\vartheta_L - \vartheta_R| = 180^\circ$ means solving a quadratic equation for p , i.e. the solution may not be real since, in general, 180° separation will no longer be possible⁸. Changing q means rotating both directions ϑ_L and ϑ_R simultaneously, thus it is clear that the two directions need not become orthogonal for any choice of q . Thus, $\alpha \neq 45^\circ$ is not well suited to 180° separation. But according to section 7.9, chiral separation will be impossible under certain conditions at $\alpha = 45^\circ$. We will therefore focus on the situation described in section 7.9, and collinear \vec{A}_1 and \vec{A}_2 for experimental simplicity. Considering figure 7.13, the general situation will be that \vec{v}_{iL} and \vec{v}_{iR} , $i = 1, 2$ will differ only by a few degrees with the lengths of the vectors being proportional to the modulus of the respective

⁸If the solution is real but not in the unit interval, one can always change the sign of one of the force values and renormalize to get a solution in the unit interval.

forces. Choosing \vec{A}_1 in the first quadrant without loss of generality, we have to choose \vec{A}_2 in the third quadrant. Increasing q from zero then means rotating $\vec{v}_{L/R}$, i.e. increasing (counter clockwise rotation) or decreasing (clockwise rotation) $\vartheta_{L/R}$. If the transport directions of both chiral partners rotate in the same order, the transport directions will remain similar. But if the transport direction of one chiral partner rotates clockwise and the other counter clockwise, one will always get 180° separation since both directions have to rotate by almost 180° . At $\alpha = 45^\circ$, reflection symmetry maps the dynamics of the two chiral partners onto each other and thus 180° chiral separation actually makes use of above described mechanism (reflection inverts the order of rotation).

We conclude that 180° separation by an asymmetric drive can be obtained for the dynamics considered in section 7.9 if

$$(\vec{v}_{1L} - \vec{v}_{2L}) \cdot (\vec{v}_{1R} - \vec{v}_{2R}) < 0. \quad (7.45)$$

Considering figure 7.13, one readily finds that this situation is realized for certain combinations of parameters, in particular for the locking step transitions to the $\vartheta = 45^\circ$ step, i.e. close to the symmetric case (for which, as remarked above, the requirement for 180° separation is naturally met if separation is possible at all). An example is shown in figure 7.7 for the same triangle and potential as considered in figure 7.13 and $\alpha' = 32.6^\circ$, $A'_1 = -7.8$ and $A'_2 = 16$ for the drive and $kT = 0.002$. Furthermore, we were able to achieve 180° separation for kT one order of magnitude larger. For even larger kT we found the average velocities to be too small to reasonably achieve 180° separation.

7.7 Symmetric periodic drive

Applying a symmetric periodic drive to the trimer is theoretically of interest, corresponding to a situation with S_0 symmetry, but may also be more feasible in certain experimental situations where constant bias forces are not available for some reason or otherwise undesirable, e.g. a biased drive could lead to a drift of other constituents of the experimental setup. From chapter 4, SSBT may be expected in general and can be employed for chiral separation. In particular, there are no invariant manifolds restricting the dynamics if the drive is applied in a symmetry direction of the lattice, and the dynamics are much more complicated due to the 3+1 dimensional phase space. Therefore, we do not perform a systematic investigation of these effects but consider only a few examples. We choose as square wave of amplitude A' and period τ :

$$A'(t) = A' \operatorname{sgn} \left(\sin \left(\frac{2\pi}{\tau} t \right) \right). \quad (7.46)$$

7.7.1 Directing Brownian motion

For very small triangles approaching the limit of point particles all effects derived in chapter 4 can be applied for chiral separation. The chiral partners correspond to different particle species and will have different transport properties in general, and in particular if SSBT enhances the sensitivity of the transport properties to variations of the system parameters. Thus, using a pair of SSBT attractors to sort chiral particles is straightforward: the regions of existence of the SSBT attractors will be different for both

chiral partners, and the same applies to the transporting attractors considered in section 4.17. Thus, if parameters are such that one chiral partner is transported by a SSBT attractor and the other is not or is transported by a different attractor, separation is achieved. A particularly interesting situation can be constructed by considering a pair of SSBT attractors leading to ANM in the presence of an added constant bias force. Then, one chiral partner can be transported against the bias force, and the other in the opposite direction, achieving 180° separation. Furthermore this approach (or more generally using a pair of SSBT attractors, and lifting symmetry by a constant bias force in any direction) seems to be a reasonable method for the separation of more general stereoisomers as in [67]. We have found 180° chiral separation by ANM attractors for triangles whose longest side was of order 0.2 and found a strikingly similar structure of transporting attractors as in chapter 4, see in particular figure 4.18 for a similar direction of the external forces. Furthermore, we have found 90° separation by using the quasiperiodic attractors encountered for smaller drive amplitudes in figure 4.18. We do not present these results here, as they are very similar to those already considered in chapter 4, but focus on “novel” methods.

7.7.2 Diffusive separation

Consider first the simplest case of 90° chiral separation for a constant bias force $\vec{A} = A\vec{e}_\alpha$ in the $\alpha = 45^\circ$ (1,1) direction, e.g. $A = 3.6$ for our “standard” triangle. Then there is only one transporting attractor carrying transport along the x direction, and otherwise only non-transporting solutions. Now consider $A = -3.6$, i.e. apply \hat{S}_0 symmetry to the problem. Then there is only one attractor carrying transport along the $-x$ direction. But that attractor corresponds to a triangle rotated by 180° . Now apply a positive bias force $A = 3.6$ for a sufficiently long time $\frac{\tau}{2}$, then a negative bias force $A = -3.6$ for an equal amount of time, and then repeat the process. If the triangle is initially on the constant bias force attractor corresponding to transport along the x direction, it will be transported along the positive x direction during the first half period of the periodic drive. When the drive changes sign, the triangle has to rotate by 180° before it can be transported along the $-x$ direction. When and if this rotation occurs deterministically depends on the structure of phase space, and this waiting reduces the triangle’s velocity during the second half period of the drive. It turns out that for the considered example the rotation is even noise induced for some parameter values and does not occur at all deterministically. Thus a SSBT (exactly in the sense of chapter 4) attractor is created, carrying transport along the $+x$ direction. By S_0 symmetry, its symmetry partner carries transport along the $-x$ direction. Adding noise, and thus switching between these attractors, results in a strongly anisotropic diffusion, with diffusion along the x axis being fast, and slow along the y axis. Due to the \hat{S}_{xy} symmetry of the potential and the direction of the drive, the chiral partner will diffuse quickly in the y direction and slowly along the x direction. This in turn can be exploited to achieve chiral separation. Consider a racemic mixture of (non-interacting) triangles initially close to the center of the substrate to which this symmetric periodic drive is applied. After some time has elapsed, these initially sharp spatial distributions will evolve into ellipsoidal distributions with large eccentricities close to 1, the major axis being either the x axis or the y axis depending on the chiral partner, allowing an experimentalist to collect the sorted chiral molecules at the right/left and the

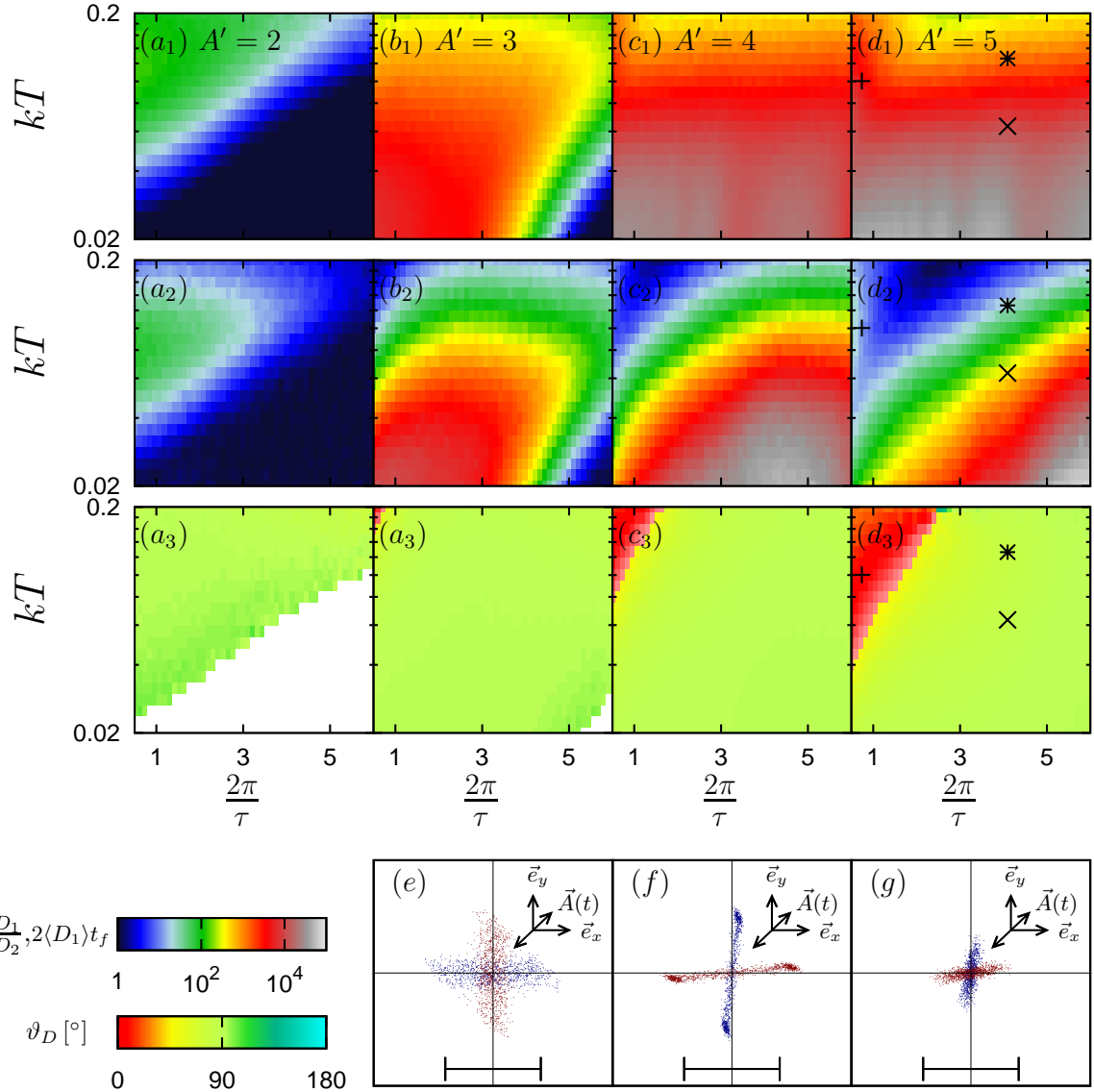


Figure 7.8: (a)-(d): Properties of the diffusion matrix (7.47) for the noisy (kT as indicated in the panels) dynamics of the triangle described by (7.36) subjected only to a symmetric periodic square wave driving force (7.46) with $\alpha = 45^\circ$ and the parameters of (7.46) as indicated in the panels. The upper row (a₁)-(d₁) shows the larger eigenvalue of the diffusion matrix, multiplied by 2 times the (temporal) length of the simulation $t_f = 4000\tau$, denoted as $2\langle D_1 \rangle t_f$, see the upper legend to the right of (e), the middle row (a₂)-(d₂) shows the anisotropy of the diffusion, i.e. the ratio of the eigenvalues of the diffusion matrix, denoted as $\frac{D_1}{D_2}$, see the upper legend to the right of (e), and the lower row (a₃)-(d₃) shows the direction of the eigenvector belonging to the larger eigenvalue, denoted ϑ_D , see the lower legend to the right of (e). (e)-(f) show the final center of friction positions after 4000 cycles of the periodic drive of an ensemble of 1000 particles initialized with coordinates in the center of the plot for the dynamics corresponding to the symbols shown in (d), (e) corresponding to the '+', (f) to the 'x' and (g) to the '*'. The bar indicates 200 lattice periods.

top/bottom of the substrate.

A bit more formally, we use the “diffusion tensor” of the center of friction:

$$\mathbf{D} = \lim_{t \rightarrow \infty} \frac{1}{2t} \cdot \quad (7.47)$$

$$= \mathbf{O}_{\vartheta_D} \begin{pmatrix} D_1 & 0 \\ 0 & D_2 \end{pmatrix} \mathbf{O}_{-\vartheta_D} \quad (7.48)$$

with the rotation matrix $\mathbf{O}_{\vartheta_D} = \begin{pmatrix} \cos(\vartheta_D) & -\sin(\vartheta_D) \\ \sin(\vartheta_D) & \cos(\vartheta_D) \end{pmatrix}$, the diffusion coefficients (eigenvalues) $D_1 > D_2$ and the main diffusion direction ϑ_D being the direction of the eigenvector of \mathbf{D} to the eigenvalue D_1 . We can quantify the effect of diffusive chiral separation by the ratio $\frac{D_1}{D_2}$, and the angle ϑ_D and get figure 7.8, finding diffusive separation for a large range of frequencies $\frac{2\pi}{\tau}$, drive amplitudes A' and noise strengths. Separation is most efficient at small noise strengths, and the dependency on the frequency is complicated. In particular, the drive periods considered are rather short, and the SSBT attractors found carry transport along the y direction, and not along the x direction as would be expected from the intuitive explanation given above and valid in the limit of slow driving. From, e.g. panel (d), we can infer that this adiabatic limit of chiral separation will be reached for lower frequencies, i.e. the particle clouds rotate, see panels (e)-(g) for a visualization. In particular, depending on the frequency and the noise strength, one species of particles can be made to diffuse along different axes, cf. panels (e) and (f), and the “green” and “red” areas in e.g. panel (d₃). A similar conclusion applies to the smaller drive amplitudes considered in (a)-(c). Moreover, the anisotropy of the diffusion can be enhanced significantly by considering different parameters, e.g. $A' = 3.6$, $\tau = 20$ and $kT = 0.02$ for diffusion as shown in panel (e), and $A' = 3.6$, $\tau = 2.5$ and $kT = 0.005$ for diffusion as shown in panel (f) (result not shown).

We have also considered the deterministic phase space structure of the synchronization of the triangle to the periodic drive and found a complex behavior including chaos, devils staircases, period adding and quasiperiodicity around the periodic SSBT attractors. In particular, the transport direction varies when the parameters are changed, i.e. the SSBT attractors are destroyed by suitable variations of the parameters, leaving behind chaotic attractors. Further variation of parameters leads to new periodic SSBT attractors with different locking directions. This applies in particular to the transition to the adiabatically driven case, with SSBT along the y axis for large frequencies, the next locking direction being the (1,1) direction, reached after a reduction of the frequency, then the (1,2) direction for an ever lower drive frequency, and so forth until SSBT is almost along the (0,1) direction in the adiabatic limit, corresponding to the intuitive explanation presented above.

7.7.3 180° separation by absolute transverse mobility

In [203] the term absolute transversal mobility is coined, corresponding to a situation in which a particle reacts to an applied constant bias force by transport orthogonal (transversal) to that force. Here we can employ such a situation to achieve 180° chiral

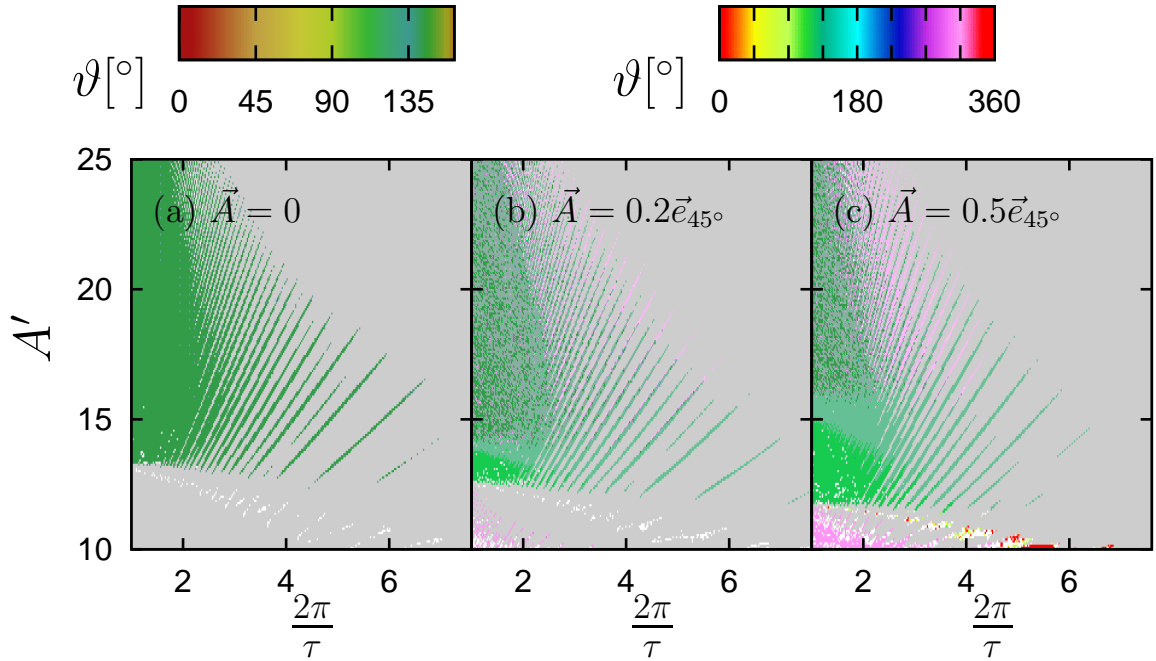


Figure 7.9: Deterministic $kT = 0$ phase diagram showing nondiffusive attractors of the dynamics of a triangle corresponding to $h_\Delta = 0.75$, $b_\Delta = 0.5$ and $L_\Delta = 0.25$ subjected to a symmetric periodic square wave drive (7.46) with direction $\alpha = 135^\circ$ in dependence of its frequency $\frac{2\pi}{\tau}$ and amplitude A' . A transverse dc bias force $\vec{A} = A\vec{e}_{45^\circ}$ is applied with A as indicated in the panels. Coexistence of nondiffusive SSBT attractors of opposite transport velocities is indicated by colors corresponding to the palette shown above (a). The transport direction of deterministic transporting attractors not coexisting with symmetry partners is shown by colors corresponding to the palette shown above (b)-(c). If a deterministic transporting attractor coexists with a non-transporting attractor, the color of the transporting attractor is shown but desaturated. Bounded attractors are shown as grey. Parameter values for which only diffusive attractors were found are drawn in white.

separation. If the dynamics (including the bias force) have a reflection symmetry, i.e. the bias is parallel to the reflection line of that symmetry, one immediately gets 180° separation. To achieve this, we apply a periodic and symmetric square wave drive (7.46) with amplitude A' , frequency $\frac{2\pi}{\tau}$ and $\alpha' = 135^\circ$ orthogonal to the \vec{e}_{45° direction in which we apply the constant bias force $\vec{A} = A\vec{e}_{45^\circ}$. As can be inferred from chapter 4, SSBT parallel to the periodic drive can be expected according to the mechanism outlined in section 4.9 for small triangles. For larger triangles, such as our ‘‘standard’’ triangle, we have found a different mechanism of achieving almost the same for somewhat larger drive amplitudes: a bounded periodic attractor collides with its corresponding saddle orbit and create a transporting quasiperiodic attractor already in the absence of a constant bias force, a situation, which we have not found for point particles. Due to \hat{S}_0 symmetry of the potential and the symmetry of the drive, this happens simultaneously for two bounded attractors⁹. Their regions of existence are shown in figure 7.9, and their quasiperiodic

⁹Due to S_0 symmetry, each bounded attractor coexists with another bounded attractor in which the molecule has been rotated by 180° .

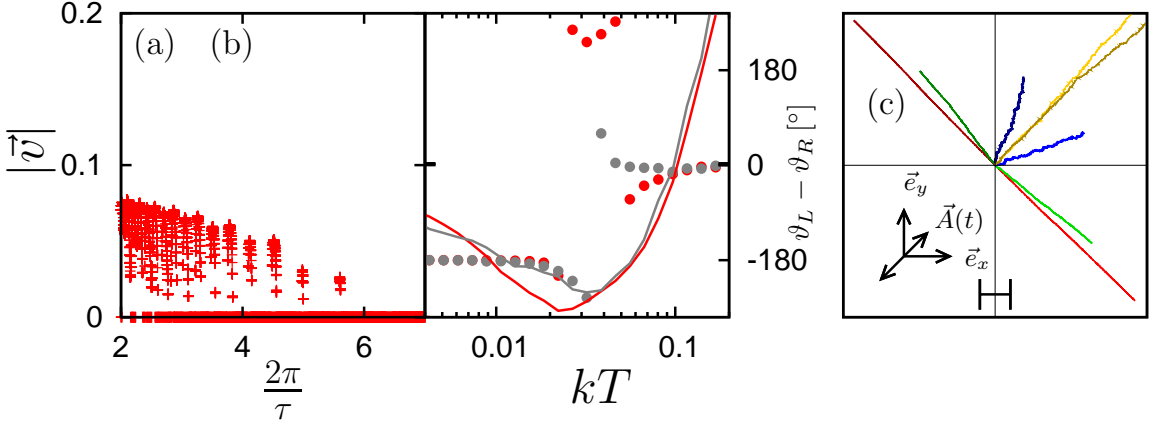


Figure 7.10: The same dynamics as in figure 7.9 are considered. (a) Modulus of the average velocity of SSBT attractors in dependence of the frequency of the periodic drive corresponding to a horizontal cut through figure 7.9 at $A' = 13.3$ and $A = 0.5$. (b) Modulus of the average velocities of the chiral species (lines, left scale) and the separation angle $\vartheta_L - \vartheta_R$ (symbols, right scale) in dependence of the noise strength kT for three values of the drive frequency: $\frac{2\pi}{\tau} = 2$ (grey) (blue) and $\frac{2\pi}{\tau} = 0.5$ (red). (c) Sample trajectories of a triangle as in figure 7.9 (bright colors) and its mirror image (dark colors) corresponding to the parameters shown in (a) with $\frac{2\pi}{\tau} = 2$ and $kT = 0.01$ (red), $kT = 0.02$ (green), $kT = 0.04$ (blue) and $kT = 0.2$ (orange). The triangles are initialized at the origin, and their center of friction position for the next 10000 cycles of the periodic drive are shown. The bar indicates 200 lattice periods. The orange trajectories are longer than the substrate sample shown in the figure.

nature is revealed from their continuously varying transport velocity in figure 7.10(a) (we have also done a careful analysis, verifying the mechanism by explicitly calculating the involved orbits and their invariant manifolds, finding them to create an invariant circle which forms the quasiperiodic attractor after the periodic orbits annihilate).

Upon switching on the constant bias force $\vec{A} = A\vec{e}_{45^\circ}$, the dynamics of an achiral molecule would remain \hat{S}_{xy} symmetric (with an appropriate symmetry of the dynamics involving a time translation). Thus applying the symmetry maps the dynamics of one chiral partner onto its mirror image. If the conditions are such that applying a constant bias force results in transverse mobility, the direction of transport is inverted as well, resulting in 180° separation, which is found for $A > 0$. The regions of existence of the pair of SSBT attractors no longer coincide, leading to absolute transverse mobility. Calculating the separation angle and the corresponding transport velocity for various frequencies in dependence of the noise strength in figure 7.10(b), we find no significant dependence on the drive frequency in the range of frequencies considered. For $kT \gtrsim 10^{-3}$, the separation angle deviates from 180° while the transport velocity decreases simultaneously. In contrast to the case of phase locked attractors, where the transport velocity is typically much larger than the asymptotic large noise transport velocity due to a small constant bias force [2], here the transport velocity increases once the deterministic structures are destroyed by noise. The reason is that the quasiperiodic attractors carry a rather slow transport velocity due to the dynamical bottleneck left behind on the invariant circle by the destroyed bounded orbits. Finally, we show some sample trajectories for

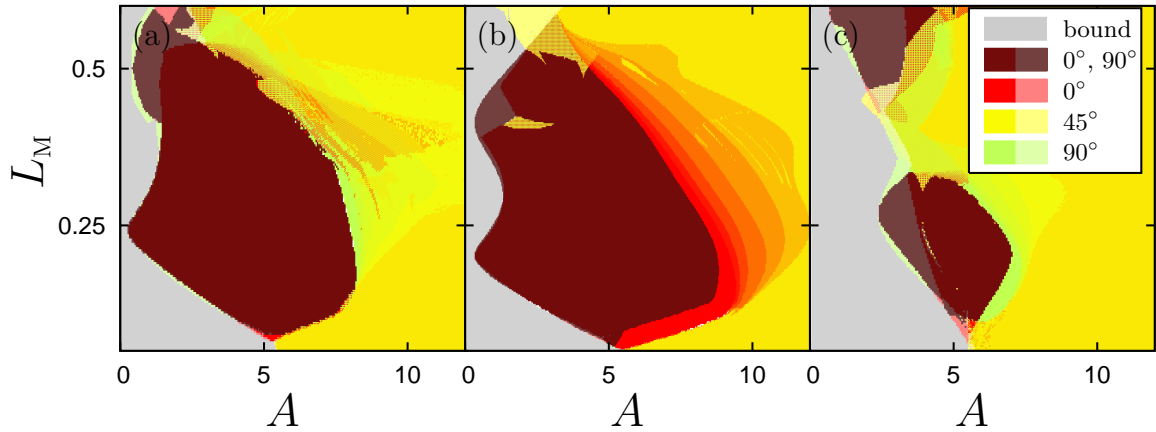


Figure 7.11: Deterministic $kT = 0$ phase diagrams showing nondiffusive attractors for the dynamics of chiral molecules proportional to those considered in figure 4 of [5] and subjected only to a constant bias force $\vec{A} = Ae_\alpha$. The panels correspond to those of figure 4 [5], i.e. (a) corresponds to the 6 vertex molecule, (b) to the 7 vertex molecule and (c) to the 5 vertex molecule in figure 4 of [5]. The parameter L_M controls the length of all lines of the molecules, i.e. the inter vertex distance and thus the size of the molecules. In [5] $L_M = 0.3$ is used in panel (a), $L_M = 0.08$ in panel (b) and $L_M = 0.44$ in panel (c). Note that due to a shortcoming of the plotting program employed (Gnuplot 4.4), the color transitions are not smooth. In particular, the transition from $\vartheta = 0^\circ$ to $\vartheta = 45^\circ$ in panel (b) should be continuous.

various noise strengths showing the 180° chiral separation in figure 7.10(c).

7.8 Differently shaped molecules and large triangles

In figure 4 of [5], three differently shaped chiral molecules are considered. Their deterministic transport behavior is further detailed in figure 7.11. A notable difference to the triangles considered so far is that the critical forces at which both running solutions (leading to $\vartheta = 0^\circ$ and $\vartheta = 90^\circ$, respectively) are created are almost identical for both axes and for all sizes of the molecules considered in panels (a) and (b), i.e. the screw like molecules. This can be explained by considering the close to critical force equilibria of these molecules, which turn out to be almost identical for both chiral partners due to the tube like shape of the molecules staying the same upon reflection. But in both cases the critical values of the bias force at which the running solutions cease to be locked to the coordinate axes, i.e. the molecules start to rotate, vary significantly for the different coordinate axes, and thus also for the statistical weights of the corresponding solutions, even in the region of coexistence. Thus, the molecules can be made to be transported almost along one of the coordinate axes for a suitable value of the bias force. Selecting this value and e.g. a very large bias force leading to $\vartheta = 45^\circ$ as the second force value in (7.43), 180° separation is obtained by using the asymmetric periodic drive protocol discussed in section 7.6. In contrast, the critical configurations at which running solutions are created for the molecule considered in figure 7.11(c) are very different for both chiral partners, since they have less similar shapes, and the transport behavior is more like that

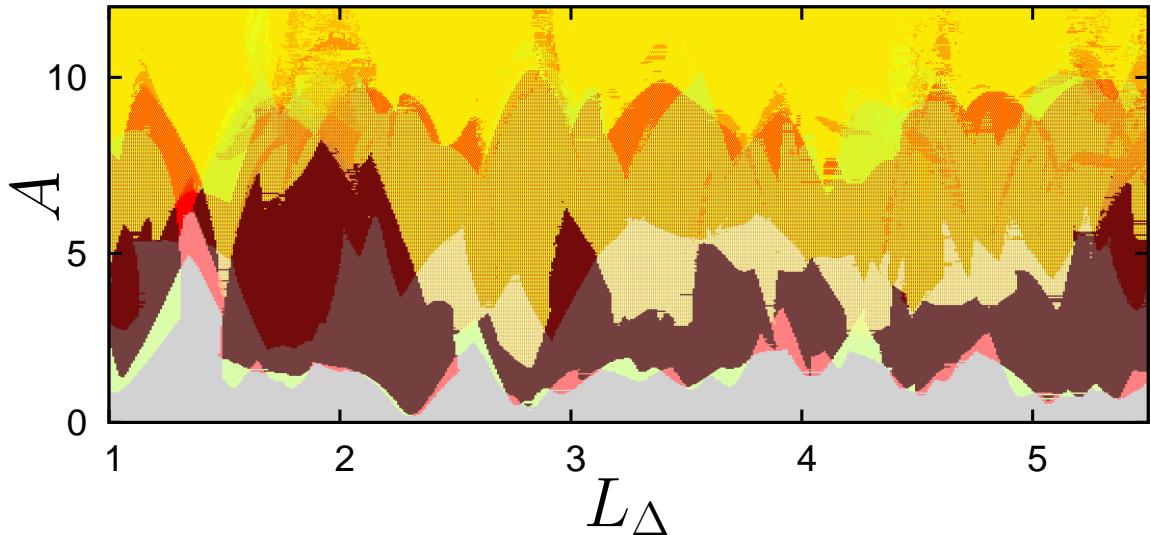


Figure 7.12: Deterministic $kT = 0$ phase diagram for the same dynamics as in figure 7.3(h), but larger values of L_Δ . Otherwise, the description of figure 7.3 applies.

of the triangular molecules.

As is evident from figure 7.11, chiral separation is possible for very different sizes of the molecules, as was found for triangular molecules. Furthermore, we have found that chiral separation is likewise possible for even more differently shaped molecules, such as 20 vertex screws, or for different angles between the vertices of the molecules in figure 4 of [5].

Figure 7.12 considers our standard triangle, but for large values of L_Δ and thus triangles extending through multiple elementary cells. As evident from figure 7.12, chiral separation of these large triangles can be obtained similarly as for smaller molecules while the structure is relatively complicated. While these large triangles might seem artificial at first glance, they may correspond to large molecules that interact only via a few binding sites with the substrate.

We conclude that chiral separation as discussed in [5] can be obtained for chiral molecules of almost any form, as long as these are not too small, i.e. point particle like, or the potential is locally flat, see section 7.9.

7.9 Small molecules and locally flat potentials

So far we have exploited a “rod” like behavior of our chiral molecules, i.e. transport locked to the coordinate axes, or SSBT upon applying a bias force in the \vec{e}_{45° direction. In contrast, we have found that for locally flat potentials¹⁰ and small molecules (on the scale of the potential), such behavior is not “typical”, e.g. for the potentials and molecules shown in figure 7.1(b,c). In particular, we have found the delocalization threshold (critical force) for these molecules and locally repulsive potentials to be practically

¹⁰We have considered Gaussian potential wells separated by flat regions and Gaussian potential hills separated by flat regions.

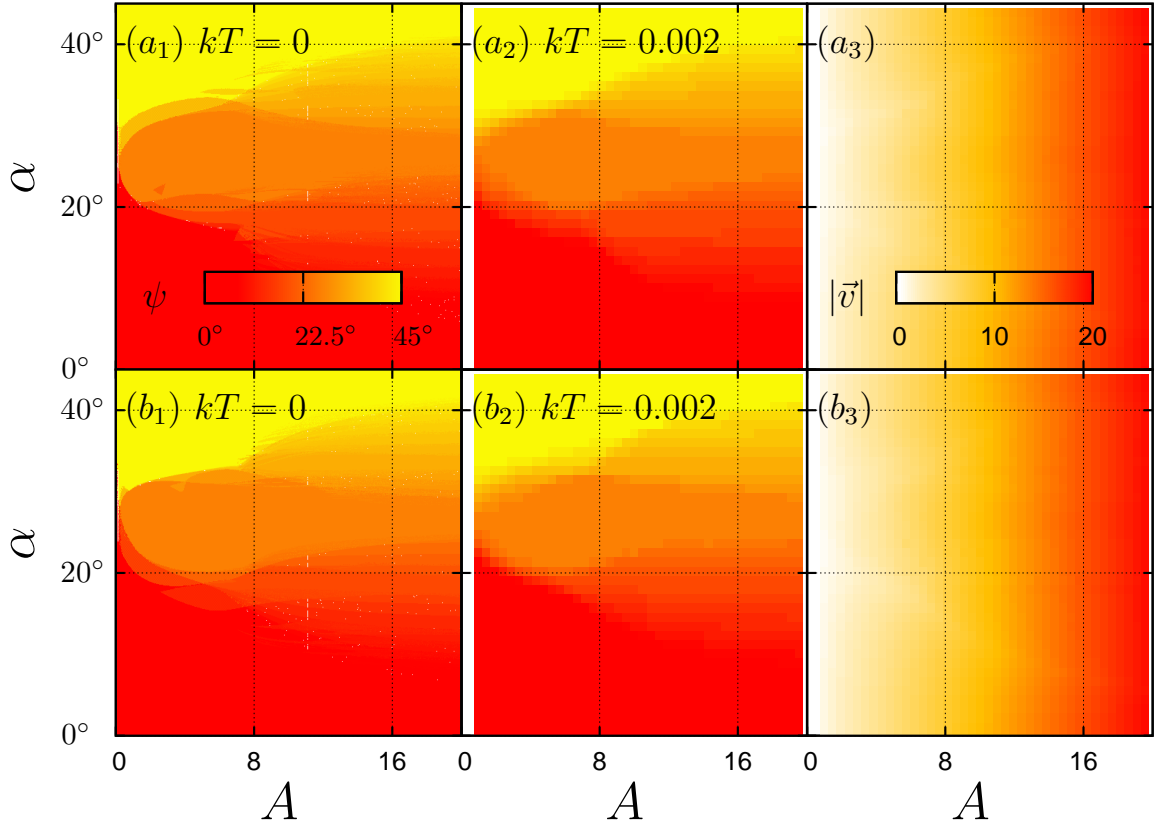


Figure 7.13: (a₁) Deterministic $kT = 0$ phase diagram of the dynamics of a triangle proportional to (7.36) but $L_\Delta = 0.25$ a square lattice of Gaussian repulsive potentials (7.31) with $\sigma = 0.1$. Only a (not too large) constant bias force $\vec{A} = A\vec{e}_\alpha$ is applied, and of which all possible (up to symmetry) orientations are considered. The transport direction, i.e. ϑ_L , of nondiffusive deterministic attractors of the triangle is encoded in colors, as indicated by the palette shown in (a₁). Coexistence of deterministic attractors with different transport directions is indicated by hatching. White is displayed if no nondiffusive attractors were found. (a₂) ϑ_L for the noisy $kT = 0.002$ counterpart of the dynamics in (a₁). The same color encoding is used, but white is used if the modulus of the numerically obtained average velocity, see (a₃), was too small to reasonably define its direction. (a₃) $|\vec{v}_L|$ for the same dynamics as in (a₂). The colors are encoded according to the legend in the panel. (b_{1,2,3}) contain the same information, but for the mirror image of the triangle considered in (a_{1,2,3}), respectively.

zero¹¹, rendering the conclusions from [5] partially inapplicable. In those situations, the molecule behaves mostly like a point particle, locking to lattice directions of the form

$$\vec{v} = n\vec{e}_x + m\vec{e}_y \quad (7.49)$$

(with integers n, m) close to the direction of the bias force as reported for point particles in e.g. [18, 20, 21, 23, 26]. In particular, locking to the coordinate axes or the (1,1) axis was found to be particularly robust. Higher order (referring to the higher periodicity of the solutions with respect to an appropriately chosen Poincaré section) locking steps are less robust (cf. figure 7.14). Thus the separation techniques relying on the bias force in the (1,1) direction considered so far are not directly applicable to this situation.

Section 7.7.1 contains some findings which are applicable to this case, as long as the potential is not too flat (cf. figure 4.40).

Another approach is to make use of the fact that the dynamics of the two chiral partners are simply different. Thus, whenever the transport properties of one chiral molecule depends sensitively on some external parameters like the bias force, we can expect its mirror image to show a different transport behavior. This in turn is the case close to critical values of the parameters, i.e. at bifurcations where the molecule changes the direction to which it locks. An example of this behavior is shown for Gaussian repulsive potentials with $\sigma = 0.1$ at each lattice site and a triangle proportional to our “standard” triangle but with $L_\Delta = 0.25$ in figure 7.13, see figure 7.1(b) for an illustration of the setup. The upper row shows the transport direction (and modulus in panel (a₃)) for one chiral partner, and the lower row the same for its mirror image. As can be seen from panels (a₁) and (b₁), there are critical lines in parameter space at which the transport direction changes abruptly, corresponding to deterministic bifurcations which are different for the two chiral partners. Including noise, these differences are washed out, but still visible, and can be employed for chiral separation. But now, the separation angles are rather small, limited by the distance of the jump of the transport direction, similar to the situation of large bias forces considered in [5]. As discussed in [5], 90° chiral separation by a constant bias force can be interpreted as one large jump as well. Turning to the modulus of the transport velocity, we find that it is practically identical for the two chiral partners for almost all directions of the bias force, and especially so in the presence of noise, and is thus an even worse tool for chiral sorting.

We show a more precise picture of the dynamics by considering a vertical cut through figure 7.13 at $A = 0.5$ in figure 7.14. There are many plateaus of the transport direction (left panel) where the molecule locks to one direction for a whole interval of bias force directions, between which more or less smooth transitions by means of devils staircase like structures (i.e. smaller plateaus) are found. In particular, there are large plateaus around the main symmetry directions, $\alpha = 0^\circ$ and $\alpha = 45^\circ$, but also e.g. a large plateau with $\vartheta \approx 26.57^\circ$ corresponding to transport locked to the (2,1) direction of the lattice. Around the edges of these plateaus the transport directions of the chiral molecule and its mirror image are different, allowing for chiral separation, while around the centers of the plateaus they are identical. This is somewhat unfortunate since the locking to the plateaus is most robust around their centers, as found for $kT > 0$, but

¹¹For Gaussian potential wells separated by flat parts of the potential, the delocalization threshold is non-zero. For bias forces larger than the delocalization threshold, we have found the same behavior as discussed in this section, i.e. as for Gaussian potential hills.

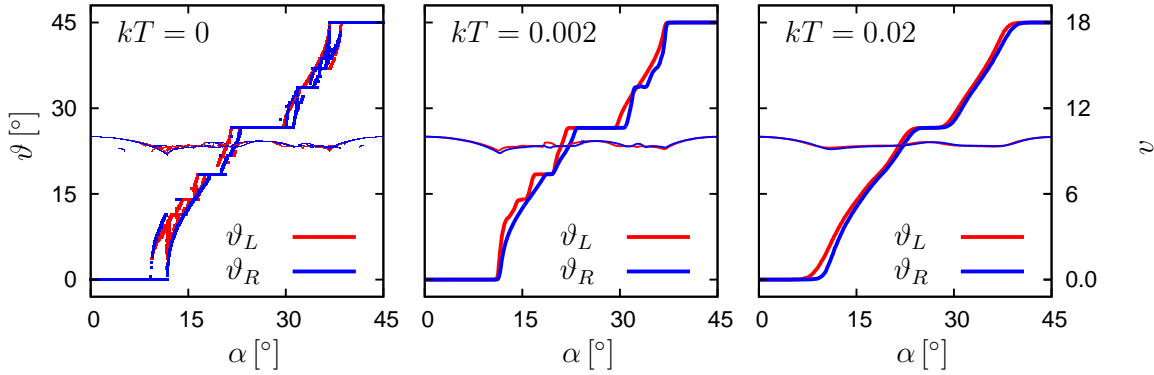


Figure 7.14: Transport direction $\vartheta_{L/R}$ (thick lines) and velocity $v_{L/R}$ (thin lines) for the same dynamics as considered in figure 7.13 but $A = 0.5$ and the noise strength is indicated in the panels. The lines with subscript L correspond to the upper row in figure 7.13 and the ones with subscript R to the lower row in figure 7.13 (mirror image).

expected since we are exploiting a sensitive dependence on parameters, which is usually accompanied by a sensitive dependence on noise, see e.g. section 4.19. Noise smoothes the transitions between the plateaus, reducing the separation angle, but separation persists up to $kT \approx 0.02$ (right panel).

Having understood the mechanism of separation, we turn to a survey of separation regimes to estimate the limits of chiral separation of “short” molecules in “locally flat” potentials as shown in figure 7.15 for the separation angle and figure 7.16 for the separation vector. Considering a triangle smaller (with smaller L_Δ) but otherwise proportional to our standard triangle (panels with indices $(i1)$ $i = 1, 2$), we find that for $\sigma = 0.05$ separation is practically impossible for the triangles considered, and also for many more that we have tried and for which results are not shown. For $\sigma = 0.1$ separation is possible as was already found in figure 7.13.

For locally flat potentials an important feature is that with all monomers of the molecule being identical there is no torque acting on the molecule in the flat regions of the potential. Thus, noise can freely rotate the molecule, reducing the effectiveness of deterministic locking significantly. In contrast, if the monomers are not identical, the molecule has at least one preferred orientation even in a homogeneous force field. We consider this situation by setting

$$\gamma_1 = 0.5, \gamma_2 = 1.0, \gamma_3 = 1.5, \quad (7.50)$$

but otherwise considering the same triangles, thus obtaining the same value for γ to get the same point particle limit for $L_\Delta = 0$. Therefore the dynamics are comparable, in particular for small molecules, i.e. small L_Δ . The results are shown in the second and fourth columns of figure 7.15 (panels with indices $(i2)$, $i = 1, 2$) and figure 7.16, showing that chiral separation is enhanced, in particular for $\sigma = 0.05$ but also for $\sigma = 0.1$. While we have not introduced a quantitative measure of chirality, the triangles with anisotropic monomers will be somewhat “more chiral” depending on that measure, making the comparison less direct. Evaluating trajectories directly (not shown) we have found that the main mechanism of enhancement is indeed the preferred orientation of the molecules in the flat part of the potential.

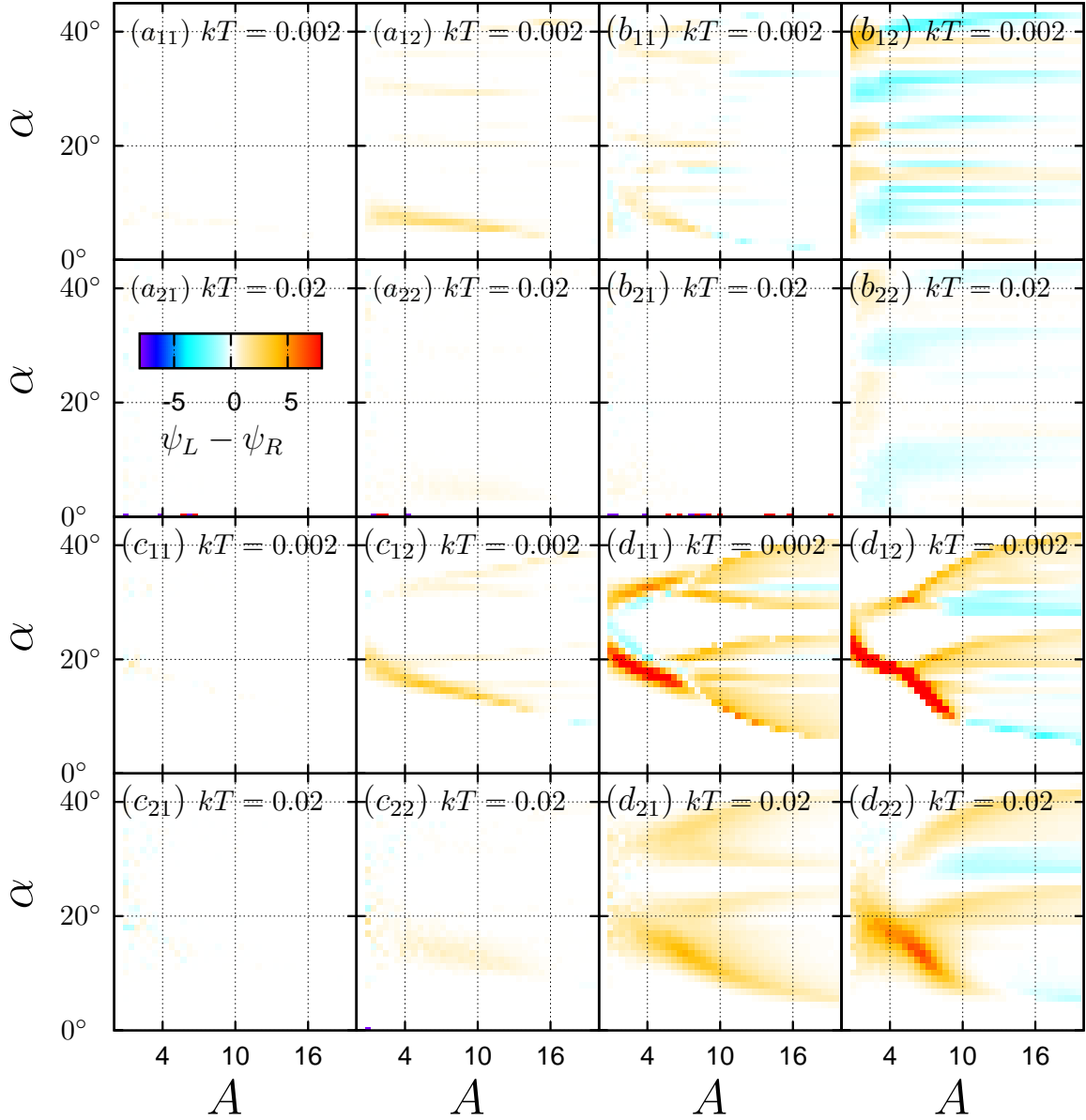


Figure 7.15: Separation angle $\vartheta_L - \vartheta_R$ according to the legend in (a_{21}) for the noisy (kT as indicated in the panels) dynamics of triangles proportional to (7.36) and their mirror images subjected only to a constant bias force $\vec{A} = A\vec{e}_\alpha$. In the two upper rows, (a_{ij}) and (b_{ij}) , $\sigma = 0.05$ is used in the potential (7.31), and $\sigma = 0.1$ in the two lower rows, (c_{ij}) and (d_{ij}) . The triangle “lengths” are $L_\Delta = 0.05$ for the two columns on the left, (a_{ij}) and (c_{ij}) , and $L_\Delta = 0.25$ for the two columns on the right, (b_{ij}) and (d_{ij}) . The triangles considered in the first column, (a_{i1}) and (c_{i1}) ($i = 1, 2$), and the third column, (b_{i1}) and (d_{i1}) ($i = 1, 2$), have $\gamma_j = 1$, $j = 1, 2, 3$, and the triangles considered in the second column, (a_{i2}) and (c_{i2}) ($i = 1, 2$), and fourth column, (b_{i2}) and (d_{i2}) ($i = 1, 2$), have $\gamma_1 = 0.5$, $\gamma_2 = 1$ and $\gamma_3 = 1.5$.

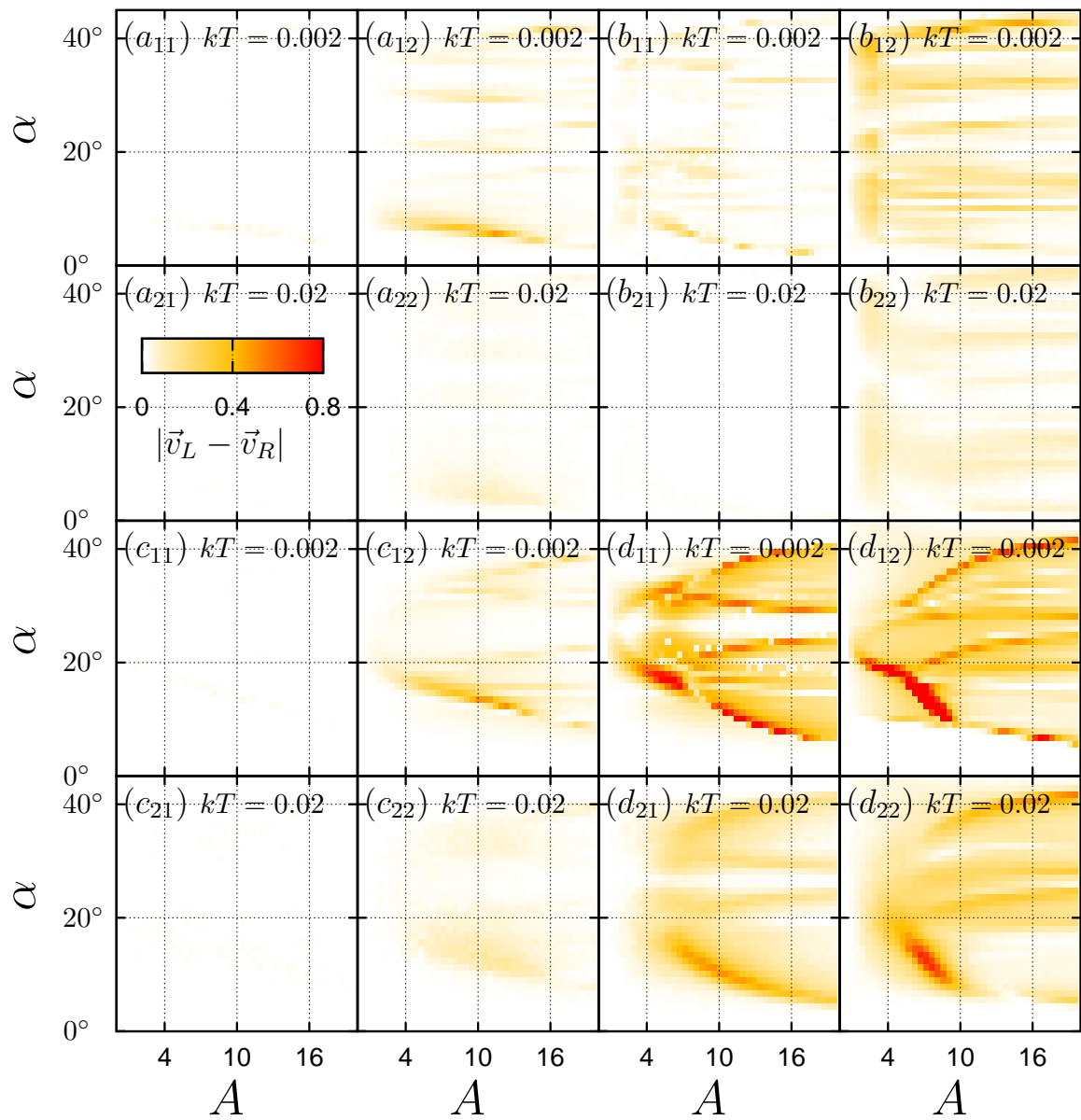


Figure 7.16: Modulus of the separation angle $|\vec{v}_L - \vec{v}_R|$ and otherwise corresponding to figure 7.15.

As a final remark we have found the behavior to be similar if we replace the Gaussian repulsive interactions at the lattice sites with attractive interactions. In that case there is a finite delocalization threshold, but that does not lead to transport parallel to the x axis for $\alpha = 45^\circ$ because, after escaping a trap, the molecule finds itself in a flat part of the potential and will subsequently move into the direction of the force. It will then be attracted by the next trap in the direction of the force. Thus, there is no chiral separation at $\alpha = 45^\circ$, while similar conclusions as above apply for $\alpha \neq 45^\circ$.

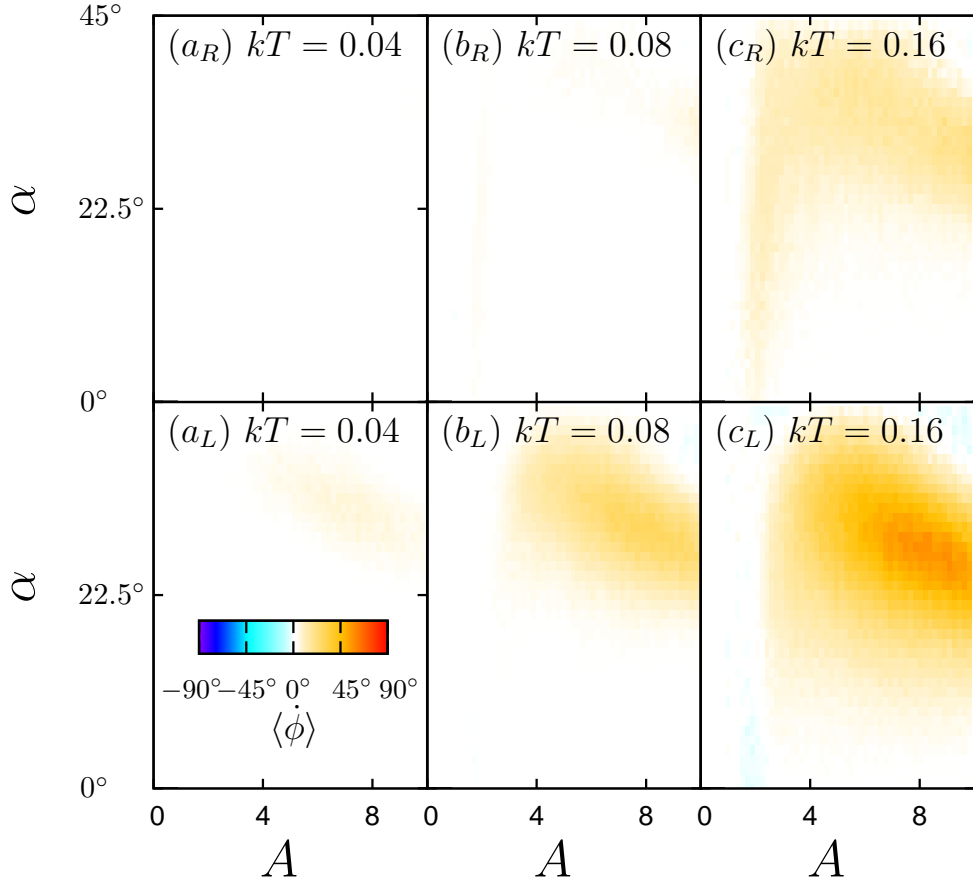


Figure 7.17: Average angular velocity $\langle \dot{\phi} \rangle$ for the noisy (kT as indicated in the panels) dynamics of the standard triangle (7.36) (lower row) and its mirror image (upper row) subjected only to a constant bias force $\vec{A} = A\vec{e}_\alpha$.

7.10 Rotation

Last, we consider the average angular velocity at the example of the triangles considered in section 7.4 and section 7.9. If the dynamics have a reflection symmetry, the angular velocity vanishes in the presence of noise, while SSBT is possible in the deterministic dynamics. Thus, considering chiral molecules, a non-zero angular velocity is expected by Curie's principle. As intuition suggests, and from figure 2 of [5], the average angular velocity of triangles with side lengths of the order of one elementary cell of the potential is rather small, and usually vanishes in the deterministic dynamics, in particular for running solutions locked to one of the coordinate axes. Due to noise, the angular velocity takes a non-zero value, see figure 7.17.

The situation changes if we consider smaller triangles (smaller L_Δ in (7.36)), see figure 7.18 for some results. We have found the angular velocity to still be zero at $kT = 0$ for the majority of parameters of the systems considered here (not shown). Noise induces a non-zero angular velocity with varying effectiveness with the smaller triangle ($L_\Delta = 0.05$) having the largest angular velocity, and the larger triangle ($L_\Delta = 0.1$) having a larger angular velocity for the $\sigma = 0.1$ potential. The latter can be explained by noting that the angular velocity will be zero for a flat potential. We conclude that, for the triangles

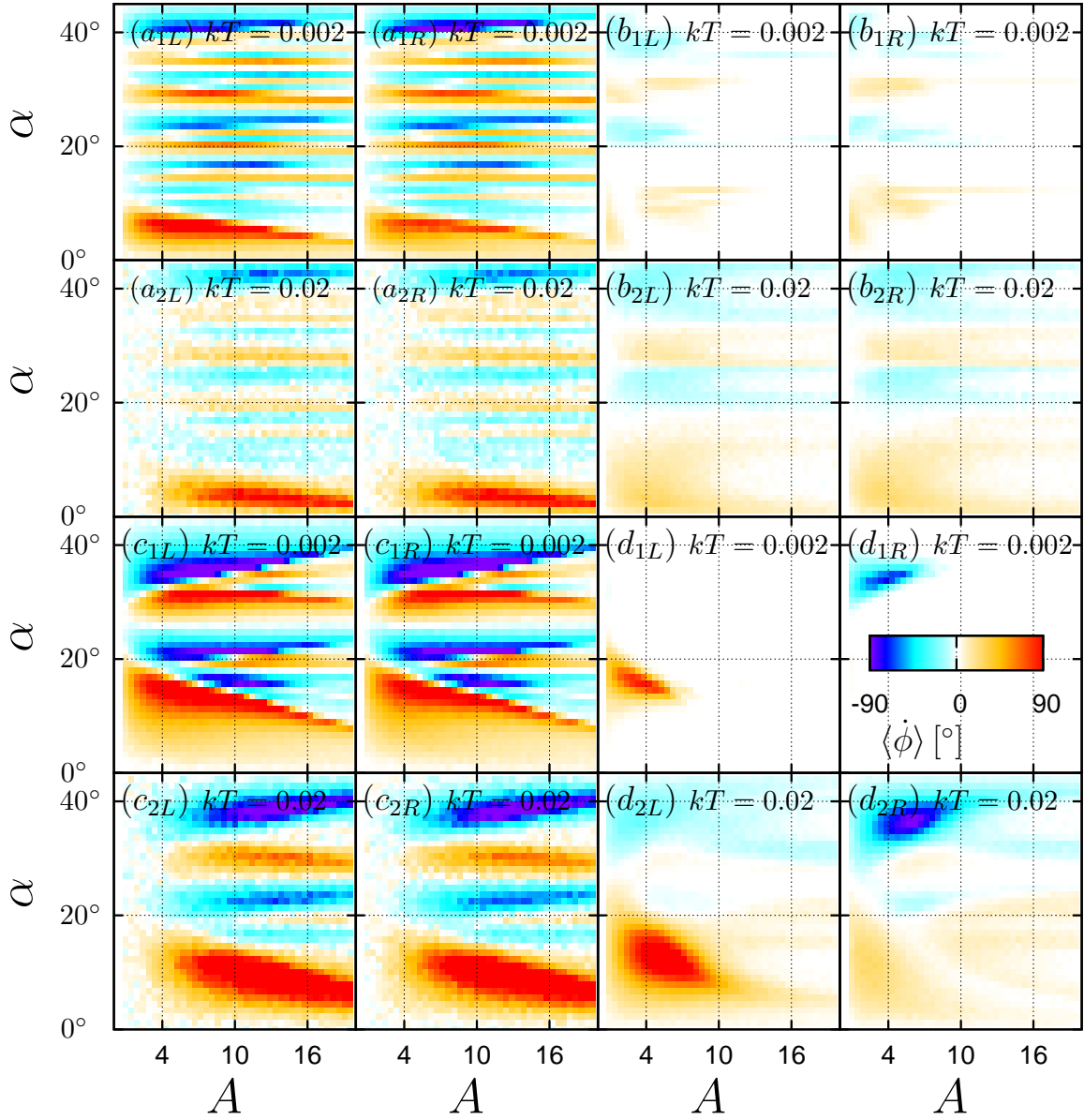


Figure 7.18: Average angular velocity $\langle \dot{\phi} \rangle$ for the noisy (kT as indicated in the panels) dynamics of triangles proportional to (7.36) (subscript L) and their mirror images (subscript R) subjected only to a constant bias force $\vec{A} = A\vec{e}_\alpha$. The parameters are (a) $L_\Delta = 0.05$ and $\sigma = 0.05$, (b) $L_\Delta = 0.1$ and $\sigma = 0.05$, (c) $L_\Delta = 0.05$ and $\sigma = 0.1$, and (d) $L_\Delta = 0.1$ and $\sigma = 0.1$. Thus, the dynamics of triangles with $\gamma_{1/2/3} = 1$ in the same potentials and noise strengths as in figure 7.15 are considered.

considered, most running solutions locked to a specific direction (which may be of higher order) do not carry an angular velocity, while (noise induced visits to) deterministically transient regions lead to a non-zero angular velocity. This can be further supported by noting that the angular velocity is usually smallest close to the center of locking steps, which is particularly visible for the smaller triangle ($L_\Delta = 0.05$) (deterministic result not shown), but also for the larger one (cf. figure 7.13(a_1) and figure 7.18(d_{1L})).

Finally, if we consider the triangles whose monomers have different friction coefficients according to (7.50) (cf. figure 7.15) with all other parameters as in figure 7.18, we find that the angular velocity is practically zero in figure 7.19. This is due to the anisotropic friction coefficients inducing a preferred orientation of the triangle in the constant bias force field. Thus we find the angular velocity to be larger in this case if the bias force is small.

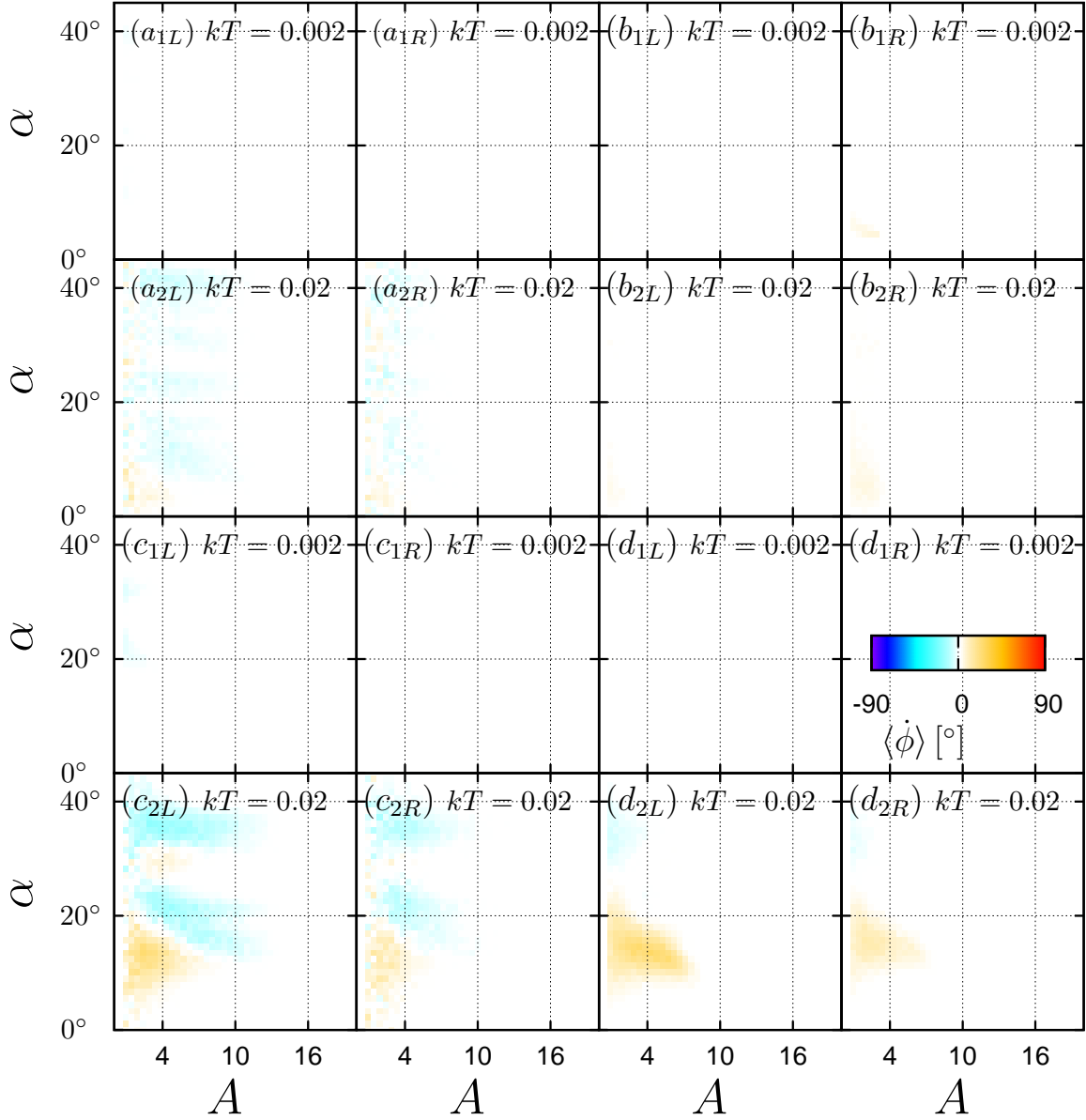


Figure 7.19: Average angular velocity $\langle \dot{\phi} \rangle$ for the noisy (kT as indicated in the panels) dynamics of triangles proportional to (7.36) (subscript L) and their mirror images (subscript R) subjected only to a constant bias force $\vec{A} = A\vec{e}_\alpha$ but the triangles have $\gamma_1 = 0.5$, $\gamma_2 = 1$ and $\gamma_3 = 1.5$. The parameters are (a) $L_\Delta = 0.05$ and $\sigma = 0.05$, (b) $L_\Delta = 0.1$ and $\sigma = 0.05$, (c) $L_\Delta = 0.05$ and $\sigma = 0.1$, and (d) $L_\Delta = 0.1$ and $\sigma = 0.1$. Thus, the dynamics of triangles with $\gamma_1 = 0.5$, $\gamma_2 = 1$ and $\gamma_3 = 1.5$ in the same potentials and noise strengths as in figure 7.15 are considered.

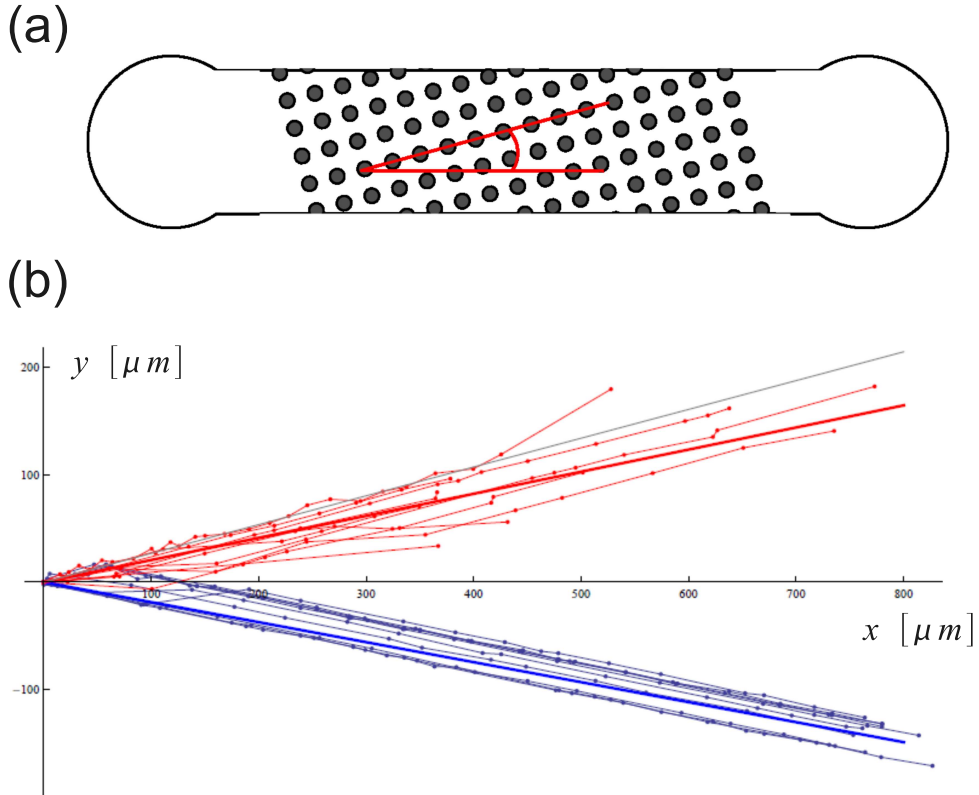


Figure 7.20: (a) Schematic representation (not to scale) of the experiment discussed in [86]. The posts are represented by grey discs. The inlet/outlet for the fluid is one the left/right. The $(1,0)$ direction of the lattice is indicated by the non-horizontal red line and the average flow direction by the horizontal line. (b) Experimental result. The red and the blue lines correspond to the spatial traces of the chiral partner molecules, and the respective thick lines indicate the average directions. The grey line indicates the $(1,0)$ direction of the lattice. The figure was provided by Jan Regtmeier, Universität Bielefeld, and is taken from [86].

7.11 Proof of principle experiment

A proof of principle experiment sorting microfabricated “L” shaped chiral particles with side lengths of several micrometers in a quasi two dimensional microfluidic periodic post array has been conducted successfully in the Anselmetti lab of Bielefeld University [86]. A schematic illustration of the experimental setup is shown in figure 7.20(a). A periodic and symmetric array of posts has been fabricated using soft lithography [86]. The posts have radii of $5\text{ }\mu\text{m}$, and the center-center distance of the posts is $L_{exp} = 22\text{ }\mu\text{m}$, i.e. the free space between posts is about $12\text{ }\mu\text{m}$ in the $(1,0)$ direction, and $17\text{ }\mu\text{m}$ in the $(1,1)$ direction of the lattice. The height of the channel is about $5.7\text{ }\mu\text{m}$. The particles are L shaped, the longer side being of length $15\text{ }\mu\text{m}$, the shorter side $9\text{ }\mu\text{m}$, and the height is about $4.6\text{ }\mu\text{m}$. Thus the particle dynamics are effectively two dimensional. Inertia effects are negligible in aqueous solution, i.e. the particle dynamics are overdamped (see also [5] and [6]). The bias forces are generated by hydrodynamic pressure using a pump, and are always parallel to the x axis. The post array is tilted, and the bias force is tilted with

respect to the lattice directions, see figure 7.20(a). Neglecting the impact of the suspended particles on the incompressible low Reynolds number flow profile, the approximate force field is the flow profile of water in the empty post array, and the maximal flow velocity can be estimated to be several $100 \frac{\mu\text{m}}{\text{s}}$. It is not constant in space, as the simple bias forces considered here are, but its effect is similar¹². Neglecting wall interactions, the generated dynamics are phase space volume preserving [246] for point particles, but it is interesting to note that the dynamics of molecules are not [79]. With wall interactions (collisions), the dynamics of point particles do not preserve phase space volume [27], and may have attractors.

To get a feeling of the experimental time scales, and in particular the noise strength, we do some hand-waving estimates, which should be correct up to one order of magnitude. The diffusion coefficient at room temperature can be estimated to be about $D \approx 0.02 \frac{\mu\text{m}^2}{\text{s}} \approx 4 \cdot 10^{-5} \frac{\text{L}_{\text{exp}}^2}{\text{s}}$ (that of a sphere of radius $10 \mu\text{m}$), and free diffusion is negligible. From the flow velocity, the “typical” velocity of the particles should be of the order of some tens of lattice periods per second. The time scale of the experiment is given by the particle velocity in first approximation since the post array generates a hard wall potential, and time can be absorbed into the unit of the applied force if thermal fluctuations are neglected. The particle velocity in the experiment is comparable (within the order of magnitude) to that of the triangles considered in figure 7.14, and the experiment corresponds to a noise strength of $kT \sim \mathcal{O}(10^{-5})$, which is much smaller than the noise strengths considered in the remainder of this chapter. Thus, thermal fluctuations should be negligible in the experiment, possibly giving rise to complications due to deterministically coexisting attractors or chaos, which would make the experiment unreliable at first glance. The experiment works reliably, but some hints of coexisting dynamical states have been found, and early simulations clearly reveal coexisting attractors [410]. In that context, quenched disorder in the form of imperfections of the post array might play an important role, leading to fluctuations of a possibly larger effective temperature (see chapter 5). This would result in a smoothing of the complicated deterministic structures. Furthermore, the complexity of the experiment, in particular the driving with microfluidic pumps¹³, the neglected z dynamics, the z structure of the post array and the structure of the particles might give rise to further stochastic or deterministic effects in the dynamics [86].

The post array “potential” is a hard wall potential, and is flat in between the posts. According to preliminary simulation results of the dynamics using L shaped particles composed of four or more circular monomers [410], chiral separation cannot be achieved for $\alpha = 45^\circ$, in agreement with our findings for locally flat potentials (see section 7.9). Chiral separation was found to work best for particles only slightly smaller than the distance between posts. Such particles barely fit through the post array [410], which is in line with section 7.9, see in particular figure 7.15 and figure 7.14. As discussed in section 7.9, chiral separation occurs at the borders of deterministic locking steps of the dynamics, and the chiral partners lock to different steps. The separation angle is bounded by the

¹²Note that an anisotropic force field leads to a preferred orientation of an extended object composed of identical monomers, as opposed to the spatially isotropic bias forces considered throughout this chapter. This should enhance enantioselectivity, see e.g. figure 7.15.

¹³E.g., a periodic modulation with a frequency of 0.1 Hz has been applied to free particles that got stuck in the post array.

angular difference of the steps onto which the chiral partners lock. Early simulation results [410] indicate that for the relatively large (in the sense that slightly larger particles would become stuck) particles considered in the experiment, the separation angle is largest for the first locking step transition, i.e. one chiral partner moves in the $(1,0)$ direction, and the other in a direction of lesser symmetry and similar to that of the force, and the experiment has been conducted accordingly. This is in line with our toy model. Comparing with figure 7.15 and figure 7.14, we find that the separation angle is indeed largest for the first locking step transition.

Achieving 180° separation with time dependent forces seems to be rather difficult in this particular experiment. Due to the hard wall interactions the magnitude of the applied forces (i.e. the fluid velocity or applied pressure) can be absorbed into the time unit, up to the negligible thermal fluctuations. Therefore, the transport direction does not depend significantly on the magnitude of the bias force (i.e. fluid velocity). Taking into account fluctuations by using a smaller driving (fluid velocity) or modifications of the driving (e.g. pulsed driving), such a dependence might be introduced. But even then, one would be left with the difficulty of applying the driving reliably and precisely (which might be challenging with pumps) to achieve 180° separation (see section 7.6). Given the complexity of the experiment, implementing a sufficiently precise simulation model is a formidable challenge, and the most direct way of getting parameters suitable for 180° separation would be measurements. Whether that is worth the effort in the current proof of principal state of the experiment is doubtful since the current separation efficiency (see figure 7.20(b)) already seems to be sufficient.

7.12 Generalizations, further experimental realizations

The effects discussed in this chapter have a very general nature, relying on the fact that the dynamics of the chiral partners is simply different for both partners [84, 85]. The main obstacle is the magnitude of the effect, as was discussed in the preceding sections. In short, we have found that the interaction of the enantiomers with a periodic potential drastically enhances enantioselectivity if the strength of thermal noise is not too large. The latter requirement can be summarized as being that purely noise induced diffusion in the absence of applied bias forces has to be small. Generalizations of the model, such as including hydrodynamic interactions [375, 376], quenched disorder or inertia effects are not expected to alter our conclusions qualitatively. Including inertia effects may even enhance the effects due to a stronger locking mechanism [1, 183, 208]. Quenched disorder was shown to be similar to thermal noise for deterministic unbounded solutions in a slightly different context in chapter 5, i.e. the predicted sorting mechanisms will survive in the presence of not too large quenched disorder¹⁴.

We have found several regimes of chiral separation. Using only a constant bias force, molecules of sizes of the order of the substrate periodicity and substrates without flat parts (accessible to the dynamics) can be sorted with a separation angle of up to 90° at

¹⁴Chiral separation may even be achieved on a purely disordered substrate. For each realization of the disorder, the molecules will be slightly deflected from the direction of the bias force, and that reflection will be different for both chiral partners. If the disorder is quenched on sufficiently large time scales, this reflection can be measured for any given sample, and thus used for chiral separation without further measurements. Of course, this is a rather complicated way of achieving chiral separation.

$\alpha = 45^\circ$. For locally flat potentials, $\alpha = 45^\circ$ does not allow for chiral separation, but deterministic locking behavior allows for chiral separation when α is between competing lattice directions, but the maximum separation angle is limited by the difference between the competing directions. Using an asymmetric periodic driving force, one can achieve up to 180° separation in both cases, but the latter is much more complicated.

With only a symmetric periodic driving force in a symmetry direction of the lattice up to 90° diffusive sorting can be reached under the same prerequisites as for 90° separation with a constant bias force. Combining a symmetric periodic driving force and a constant bias force, almost point like molecules can be sorted with separation angles of up to 180° by exploiting SSBT as described in chapter 4 and [4]. If the symmetric drive and the constant bias force are orthogonal and both point into a symmetry direction of the lattice, 180° separation can be achieved by exploiting absolute transverse mobility [203].

The periodic potentials required can be realized by optical lattices [18, 23, 24, 27, 28, 189, 190, 271–273, 273–276], crystal surfaces [182, 183, 270], micro and nanostructuring [411–414] or magnetic bubble lattices [105, 106, 185, 218, 220, 277]. The chiral molecules can be real molecules or artificial structures [78, 83, 86, 415–418]. Compared to other separation techniques, the main advantage of our method is that the same structure can be used for very differently shaped chiral particles (e.g. see figure 4 of [5]) only by adjusting the applied forces. Furthermore, no chemical additives are needed a priori.

A proof of principle experiment on a microfluidic chip using micrometer sized artificial particles in a post array has been conducted with success [86].

Generalizing our method of chiral separation to three dimensions is straightforward. The easiest way of doing so is to break reflection symmetry across the plane perpendicular to the added z direction. Consider a periodic structured surface aligned with the x - y plane. The presence of the surface already breaks reflection symmetry, and thus a chiral molecule interacting with the surface such that it is usually close to this surface can be sorted as above, if all likely orientations of the molecules to the surface are suitable, or the molecules may be aligned with respect to the surface, e.g. by an electric field or a hydrodynamic flow. Using only one surface has the disadvantage that the volume of molecules interacting with the surface is much smaller than the volume of molecules in free suspension [73]. In a truly three dimensional periodic structure reflection symmetry across the x - y plane can be broken e.g. by a force in that direction or an anisotropy of that surface, to recover above discussed effects.

Chapter 8

Conclusion

We have shown that SSBT is a common feature of the nonlinear dynamics of a Brownian particle driven out of equilibrium by a periodic driving force if the phase space of the dynamics is at least three dimensional and the dynamics are reflection symmetric. For inertial dynamics this fact is well established, as discussed in chapter 3, and our work implies a similar conclusion for overdamped dynamics with the exception of the absence of SSBT in any asymptotic limit of the drive parameters, such as the large drive power limit of inertial dynamics.

Together with a symmetry breaking perturbation, SSBT can be used to control the transport properties, and, in particular, the transport direction of a Brownian particle by varying almost any scalar parameter of the dynamics. Most naive expectations with respect to the influence of a given parameter of the dynamics are unhinged due to SSBT. E.g. an applied bias force may direct the particle against that bias force (ANM) [1–3] or, more generally, may lead to transport into almost any direction (“directing Brownian motion” [4]), an increase of the dissipation strength or a reduction of the drive power may accelerate the particle (see e.g. Fig. 6 of [2] or figure 4.24), an increase of the strength of fluctuations may direct the particle into the opposite (or, more generally, another) direction than the direction expected for very large fluctuations, or an increase of the bias force may direct the particle into the opposite direction even if the particle mobility is positive for a small bias force (see e.g. Figs. 14–15 of [2], figure 4.25 or figure 5.5). The result is that

- Brownian particles can be directed into almost any direction without changing the direction of any external force,
- and the transport direction of Brownian particles depends sensitively and often unexpectedly on almost all parameters of the dynamics.

This high selectivity of the dynamics allows efficient separation of different particle species. The differences between the particle species may be encoded in parameters of the dynamics and will lead to possibly very different transport directions. Possible applications may look like (e.g.) [62], where ANM is exploited for separation, or [185], where diffusive sorting induced by SSBT is demonstrated. If transport is restricted to be parallel to a particular direction, there are only two possible directions and the absolute transport velocities to choose from. Lifting that restriction, the response behavior

becomes much richer. In particular, if at least two spatial dimensions are available for transport, one can sort more than two particle species at once (see e.g. figure 4.27).

Another aspect is that the absolute transport velocities due to SSBT are typically much larger than those found for similar system parameters without SSBT. This in itself may be used for particle separation, and its consequence in the symmetric dynamics is particularly appealing: (deterministically) enhanced (anisotropic) diffusion due to the, either noise induced or intermittent chaotic, switching between SSBT attractors with different transport directions. The diffusion may be highly anisotropic, i.e. strong in the direction of SSBT and weak in the other. If the direction of strong diffusion is different for different particle species, this provides a tool for sorting particles without breaking the spatial symmetry, see e.g. figure 4.28 and figure 7.8.

We have unraveled the mechanisms of SSBT in overdamped dynamics of Brownian particles at three example dynamics, in chapter 4 for point particle dynamics, in chapter 6 for two coupled point particles, and in chapter 7 for the dynamics of extended “molecules” with an internal structure. The main requirement is that the time scales and the forces due to the periodic potential and the drive have to be comparable, i.e. all relevant parameters have to be of order unity in properly scaled units¹, and random fluctuations have to be sufficiently small. With respect to thermal noise, the latter means that the typical thermal energy has to be much smaller than the potential barriers separating adjacent potential wells, i.e. free thermal diffusion has to be suppressed on the relevant time scales. In chapter 5, we have shown that in the presence of SSBT quenched disorder can be treated similarly to thermal noise. Using that analogy for randomly (Gaussian) displaced lattice sites of the periodic potential, we have found that the mean square displacement has to be smaller than about $\frac{1}{1000}$ th of the spatial period. That requirement is very strong but depends heavily on the statistics of the disorder. E.g., large but rare displacements of the lattice sites are much less detrimental.

In chapter 7, we have employed SSBT with respect to chiral symmetry to enhance the chiral selectivity of a tilted two dimensional periodic potential significantly, achieving up to 90° separation, i.e. both chiral partners move into orthogonal directions. Adding an asymmetric periodic driving force, 180° separation could be achieved from the same principles. Adjusting a scalar parameter of the periodic driving force, 180° separation could be maintained for astonishingly large noise strengths, and 90° diffusive separation could be achieved for small noise strengths with a symmetric periodic driving force. The mechanism of SSBT with respect to chiral symmetry is very different to that of SSBT as discussed in chapters 3-6, but both require a sufficiently small noise strength to make use of SSBT. Our main conclusion, that the interplay of SSBT and the symmetry breaking perturbation controls transport, remains valid and is behind the large separation angles. We have found the main requirement for SSBT with respect to chiral symmetry to be that the molecule rotation is sufficiently inhibited by the potential, i.e. the size of the molecules has to be of the order of the length unit of the potential, and the potential must not have (relevant) flat parts. The latter requirement is lifted for very “long” (rod like) molecules, but further studies are needed to determine the usefulness of SSBT in that limit. Our method of sorting by use of SSBT can be considered as an extreme case of a well known locking phenomenon [21], where the molecule locks to different lattice

¹In contrast, SSBT may also be found in the high drive power limit of underdamped dynamics, but that limit restricts the possible response behavior significantly [137, 157].

directions in dependence of the direction of the (tilting) bias force [5]. By making use of the fact that the locking steps will be different for the chiral partner molecules in general, chiral separation could be achieved under conditions under which SSBT is unavailable, but the separation angles are much smaller in this case. If certain conditions are met, 180° separation could be achieved again by adding a periodic driving force, but that effect is of a less general nature than the 180° separation in the symmetric case. This method of chiral separation has been realized in a proof of principle experiment sorting artificial particles in a microfluidic post array [86]. The associated potential is locally flat, and only effectively constant bias forces are available. Hence the experiment makes use only of the nonlinear locking behavior and achieves rather small (but sufficient) separation angles.

Our findings from chapter 3 have been realized experimentally in a resistively shunted Josephson junction [3]. We have achieved remarkably good agreement between theory and experiment by means of a careful fit of the model parameters. The method could be extended along the lines of (e.g.) [172] and accelerated by using a GPU for the computations [173] (see chapter 3), such that automated and almost instantaneous characterization of Josephson junctions becomes possible.

The models considered in this work are of a very simple and general nature, and each model is minimal in the sense that the predicted effects cannot be found in simpler dynamics. Our results can be generalized to many different experimental systems featuring periodic potentials and driven out of equilibrium by a deterministic driving force. Examples are atoms or molecules on crystal surfaces [182, 183, 208, 270], molecules or artificial particles in micro and nano structures (driven by hydrodynamic flows or electromagnetic fields) [25, 59, 61, 62, 280–283, 411–414], molecules or artificial particles in optical lattices (driven by hydrodynamic flows, travelling potentials² or additional electromagnetic fields) [18, 23, 24, 27, 28, 189, 190, 271–276, 422, 423], paramagnetic particles in magnetic bubble lattices (driven by magnetic fields) [105, 106, 185, 218, 220, 277], the electrical properties of superconducting devices (driven by microwaves) [107, 278, 279], superconducting vortex lattices with or without pinning (driven by electric and magnetic fields³) [223–228, 230, 231], models of motor proteins [361–368] or mechanical pendula (driven by magnetic fields, electric fields or mechanical agitation) [138, 168–171]. Beyond the fundamental interest in such paradoxical response behavior, our main application is to control the transport properties of Brownian particles, which can be applied in many ways, e.g. sorting, stabilization of unstable states, making work available upon request or switchable resistors in the context of superconductors. Lastly, according to the methods outlined in chapter 2, our conclusions apply also to systems that are physically very different, but which can be described within the same framework of SDE's and have discrete symmetries.

²I.e., the potential moves relative to the particles [419, 420], e.g. [218, 273, 421].

³An additional driven vortex layer might also be used.

Bibliography

- [1] D. Speer, R. Eichhorn, and P. Reimann, “Brownian motion: Anomalous response due to noisy chaos,” *Europhys. Lett.*, vol. 79, p. 10005, 2007.
- [2] D. Speer, R. Eichhorn, and P. Reimann, “Transient chaos induces anomalous transport properties of an underdamped Brownian particle,” *Phys. Rev. E*, vol. 76, p. 051110, 2007.
- [3] J. Nagel, D. Speer, T. Gaber, A. Sterck, R. Eichhorn, P. Reimann, K. Ilin, M. Siegel, D. Koelle, and R. Kleiner, “Observation of negative absolute resistance in a Josephson junction,” *Phys. Rev. Lett.*, vol. 100, p. 217001, 2008.
- [4] D. Speer, R. Eichhorn, and P. Reimann, “Directing Brownian motion on a periodic surface,” *Phys. Rev. Lett.*, vol. 102, p. 124101, 2009.
- [5] D. Speer, R. Eichhorn, and P. Reimann, “Exploiting lattice potentials for sorting chiral particles,” *Phys. Rev. Lett.*, vol. 105, p. 090602, 2010.
- [6] H. Bruus, *Theoretical microfluidics*. Oxford Univ. Press, 2008.
- [7] A. Barone, *Physics and Applications of the Josephson Effect*. John Wiley and Sons, Inc., New York, 1982.
- [8] A. Einstein, “Über die von der molekularkinetischen Theorie der Wärme geforderte Bewegung von in ruhenden Flüssigkeiten suspendierten Teilchen,” *Ann. Phys.-Berlin*, vol. 17, p. 549, 1905.
- [9] P. Reimann and P. Hänggi, “Introduction to the physics of Brownian motors,” *Appl. Phys. A*, vol. 75, p. 169, 2002.
- [10] P. Reimann, “Brownian motors: noisy transport far from equilibrium,” *Phys. Rep.*, vol. 361, p. 57, 2002.
- [11] P. Hänggi and F. Marchesoni, “Artificial Brownian motors: Controlling transport on the nanoscale,” *Rev. Mod. Phys.*, vol. 81, p. 387, 2009.
- [12] A. Ashkin, “Acceleration and trapping of particles by radiation pressure,” *Phys. Rev. Lett.*, vol. 24, p. 156, 1970.
- [13] D. Eigler and E. Schweizer, “Positioning single atoms with a scanning tunneling microscope,” *Nature*, vol. 344, p. 524, 1990.

- [14] P. Curie, “Sur la symétrie dans les phénomènes physiques, symétrie d’un champ électrique et d’un champ magnétique,” *J. Phys. (Paris) Sér. 3 (théorique et appliquée) III*, p. 393, 1894.
- [15] J. Rousselet, L. Salome, A. Ajdari, and J. Prost, “Directional motion of Brownian particles induced by a periodic asymmetric potential,” *Nature*, vol. 370, p. 446, 1994.
- [16] A. D. Waele, W. Kraan, R. D. B. Ouboter, and K. Taconis, “On the d.c. voltage across a double point contact between two superconductors at zero applied d.c. current in situations in which the junction is in the resistive region due to the circulating current of flux quantization,” *Physica*, vol. 37, p. 114, 1967.
- [17] A. Sterck, R. Kleiner, and D. Koelle, “Three-junction SQUID rocking ratchet,” *Phys. Rev. Lett.*, vol. 95, p. 177006, 2005.
- [18] A. M. Lacasta, J. M. Sancho, A. H. Romero, and K. Lindenberg, “Sorting on periodic surfaces,” *Phys. Rev. Lett.*, vol. 94, p. 160601, 2005.
- [19] K. Lindenberg, A. M. Lacasta, J. M. Sancho, and A. H. Romero, “Transport and diffusion on crystalline surfaces under external forces,” *New Journal of Physics*, vol. 7, p. 29, 2005.
- [20] J. M. Sancho, M. Khouri, K. Lindenberg, and A. M. Lacasta, “Particle separation by external fields on periodic surfaces,” *Journal of Physics: Condensed Matter*, vol. 17, p. S4151, 2005.
- [21] C. Reichhardt and F. Nori, “Phase locking, devil’s staircases, Farey trees, and Arnold tongues in driven vortex lattices with periodic pinning,” *Phys. Rev. Lett.*, vol. 82, p. 414, 1999.
- [22] T. Chou and D. Lohse, “Entropy-driven pumping in zeolites and biological channels,” *Phys. Rev. Lett.*, vol. 82, p. 3552, 1999.
- [23] P. T. Korda, M. B. Taylor, and D. G. Grier, “Kinetically locked-in colloidal transport in an array of optical tweezers,” *Phys. Rev. Lett.*, vol. 89, p. 128301, 2002.
- [24] M. P. MacDonald, G. C. Spalding, and K. Dholakia, “Microfluidic sorting in an optical lattice,” *Nature*, vol. 426, p. 421, 2003.
- [25] L. R. Huang, E. C. Cox, R. H. Austin, and J. C. Sturm, “Continuous Particle Separation Through Deterministic Lateral Displacement,” *Science*, vol. 304, p. 987, 2004.
- [26] A. Gopinathan and D. G. Grier, “Statistically locked-in transport through periodic potential landscapes,” *Phys. Rev. Lett.*, vol. 92, p. 130602, 2004.
- [27] M. Balvin, E. Sohn, T. Iracki, G. Drazer, and J. Frechette, “Directional locking and the role of irreversible interactions in deterministic hydrodynamics separations in microfluidic devices,” *Phys. Rev. Lett.*, vol. 103, p. 078301, 2009.

- [28] K. Xiao and D. G. Grier, “Multidimensional optical fractionation of colloidal particles with holographic verification,” *Phys. Rev. Lett.*, vol. 104, p. 028302, 2010.
- [29] F. Jülicher and J. Prost, “Cooperative molecular motors,” *Phys. Rev. Lett.*, vol. 75, p. 2618, 1995.
- [30] T. J. Banis, Y. K. Pozhela, and I. V. Parshelyunas, “Absolutely negative-resistance of gallium-arsenide in a strong microwave field,” *Sov. Phys. Semicond.*, vol. 5, p. 1727, 1972.
- [31] R. A. Höpfel, J. Shah, P. A. Wolff, and A. C. Gossard, “Negative absolute mobility of minority electrons in GaAs quantum wells,” *Phys. Rev. Lett.*, vol. 56, p. 2736, 1986.
- [32] B. J. Keay, S. Zeuner, S. J. Allen, K. D. Maranowski, A. C. Gossard, U. Bhattacharya, and M. J. W. Rodwell, “Dynamic localization, absolute negative conductance, and stimulated, multiphoton emission in sequential resonant-tunneling semiconductor superlattices,” *Phys. Rev. Lett.*, vol. 75, p. 4102, 1995.
- [33] E. H. Cannon, F. V. Kusmartsev, K. N. Alekseev, and D. K. Campbell, “Absolute negative conductivity and spontaneous current generation in semiconductor superlattices with hot electrons,” *Phys. Rev. Lett.*, vol. 85, p. 1302, 2000.
- [34] K. N. Alekseev, E. H. Cannon, J. C. McKinney, F. V. Kusmartsev, and D. K. Campbell, “Spontaneous dc current generation in a resistively shunted semiconductor superlattice driven by a terahertz field,” *Phys. Rev. Lett.*, vol. 80, p. 2669, 1998.
- [35] H. S. J. van der Zant, E. Slot, S. V. Zaitsev-Zotov, and S. N. Artemenko, “Negative resistance and local charge-density-wave dynamics,” *Phys. Rev. Lett.*, vol. 87, p. 126401, 2001.
- [36] N. F. Pedersen, O. H. Soerensen, B. Dueholm, and J. Mygind, “Half-harmonic parametric oscillations in Josephson junctions,” *J. Low. Temp. Phys.*, vol. 38, p. 1, 1980.
- [37] C. Noeldeke, R. Gross, M. Bauer, G. Reiner, and H. Seifert, “Experimental survey of chaos in the Josephson effect,” *J. Low. Temp. Phys.*, vol. 64, p. 235, 1986.
- [38] P. Reimann, R. Kawai, C. Van den Broeck, and P. Hänggi, “Coupled Brownian motors: Anomalous hysteresis and zero-bias negative conductance,” *Europhys. Lett.*, vol. 45, p. 545, 1999.
- [39] P. Reimann, C. Van den Broeck, and R. Kawai, “Nonequilibrium noise in coupled phase oscillators,” *Phys. Rev. E*, vol. 60, p. 6402, 1999.
- [40] C. Van den Broeck, I. Bena, P. Reimann, and J. Lehmann, “Coupled Brownian motors on a tilted washboard,” *Ann. Phys.-Berlin*, vol. 9, p. 713, 2000.

- [41] J. Buceta, J. M. Parrondo, C. Van den Broeck, and F. J. de la Rubia, “Negative resistance and anomalous hysteresis in a collective molecular motor,” *Phys. Rev. E*, vol. 61, p. 6287, 2000.
- [42] S. E. Mangioni, R. R. Deza, and H. S. Wio, “Transition from anomalous to normal hysteresis in a system of coupled Brownian motors: A mean-field approach,” *Phys. Rev. E*, vol. 63, p. 041115, 2001.
- [43] B. Cleuren and C. Van den Broeck, “Ising model for a Brownian donkey,” *Europhys. Lett.*, vol. 54, p. 1, 2001.
- [44] C. Van den Broeck, B. Cleuren, R. Kawai, and M. Kambon, “A trio of Brownian donkeys,” *Int. J. Mod. Phys. C*, vol. 13, p. 1195, 2002.
- [45] G. P. Harmer and D. Abbott, “Game theory - Losing strategies can win by Parrondo’s paradox,” *Nature*, vol. 402, p. 864, 1999.
- [46] J. M. R. Parrondo, G. P. Harmer, and D. Abbott, “New paradoxical games based on Brownian ratchets,” *Phys. Rev. Lett.*, vol. 85, p. 5226, 2000.
- [47] R. Eichhorn, P. Reimann, and P. Hänggi, “Brownian motion exhibiting absolute negative mobility,” *Phys. Rev. Lett.*, vol. 88, p. 190601, 2002.
- [48] R. Eichhorn, P. Reimann, and P. Hänggi, “Paradoxical motion of a single Brownian particle: Absolute negative mobility,” *Phys. Rev. E*, vol. 66, p. 066132, 2002.
- [49] R. Eichhorn, P. Reimann, and P. Hänggi, “Absolute negative mobility and current reversals of a meandering Brownian particle,” *Physica A*, vol. 325, p. 101, 2003.
- [50] R. Eichhorn and P. Reimann, “Meandering Brownian donkeys,” *Acta Phys. Pol. B*, vol. 35, p. 1407, 2004.
- [51] R. Eichhorn, P. Reimann, B. Cleuren, and C. Van den Broeck, “Moving backward noisily,” *Chaos*, vol. 15, p. 026113, 2005.
- [52] R. Eichhorn, J. Regtmeier, D. Anselmetti, and P. Reimann, “Negative mobility and sorting of colloidal particles,” *Soft Matter*, vol. 6, p. 1858, 2010.
- [53] R. Eichhorn and P. Reimann, “Paradoxical nonlinear response of a Brownian particle,” *Phys. Rev. E*, vol. 70, p. 035106, 2004.
- [54] R. Eichhorn and P. Reimann, “Paradoxical directed diffusion due to temperature anisotropies,” *Europhys. Lett.*, vol. 69, p. 517, 2005.
- [55] P. Hänggi, F. Marchesoni, S. Savel’ev, and G. Schmid, “Asymmetry in shape causing absolute negative mobility,” *Phys. Rev. E*, vol. 82, p. 041121, 2010.
- [56] B. J. de Cisneros, P. Reimann, and J. M. R. Parrondo, “Non-cooperative Brownian donkeys: A solvable 1D model,” *Europhys. Lett.*, vol. 64, p. 599, 2003.

- [57] A. Haljas, R. Mankin, A. Sauga, and E. Reiter, “Anomalous mobility of Brownian particles in a tilted symmetric sawtooth potential,” *Phys. Rev. E*, vol. 70, p. 041107, 2004.
- [58] B. Cleuren and C. Van den Broeck, “Brownian motion with absolute negative mobility,” *Phys. Rev. E*, vol. 67, p. 055101, 2003.
- [59] A. Ros, R. Eichhorn, J. Regtmeier, T. T. Duong, P. Reimann, and D. Anselmetti, “Brownian motion - absolute negative particle mobility,” *Nature*, vol. 436, p. 928, 2005.
- [60] R. Eichhorn, A. Ros, J. Regtmeier, T. T. Duong, P. Reimann, and D. Anselmetti, “Paradoxical Brownian motion in a microfluidic device: Absolute negative mobility,” *Eur. Phys. J.-Spec. Top.*, vol. 143, p. 159, 2007.
- [61] J. Regtmeier, S. Grauwin, R. Eichhorn, P. Reimann, D. Anselmetti, and A. Ros, “Acceleration of absolute negative mobility,” *J. Sep. Sci.*, vol. 30, p. 1461, 2007.
- [62] J. Regtmeier, R. Eichhorn, T. T. Duong, P. Reimann, D. Anselmetti, and A. Ros, “Pulsed-field separation of particles in a microfluidic device,” *Eur. Phys. J. E*, vol. 22, p. 335, 2007.
- [63] L. Machura, M. Kostur, P. Talkner, J. Łuczka, and P. Hänggi, “Absolute negative mobility induced by thermal equilibrium fluctuations,” *Phys. Rev. Lett.*, vol. 98, p. 040601, 2007.
- [64] W. Stewart, “Current-voltage characteristics of Josephson junctions,” *Appl. Phys. Lett.*, vol. 12, p. 277, 1968.
- [65] D. E. McCumber, “Effect of ac impedance on dc voltage-current characteristics of superconductor weak-link junctions,” *J. Appl. Phys.*, vol. 39, p. 3113, 1968.
- [66] L. Bogunovic, private communication. 2010.
- [67] R. Eichhorn, “Microfluidic sorting of stereoisomers,” *Phys. Rev. Lett.*, vol. 105, p. 034502, 2010.
- [68] R. Eichhorn, “Enantioseparation in microfluidic channels,” *Chem. Phys.*, vol. 375, p. 568, 2010.
- [69] E. J. Ariëns, “Stereochemistry, a basis for sophisticated nonsense in pharmacokinetics and clinical pharmacology,” *Eur. J. Clin. Pharmacol.*, vol. 26, p. 663, 1984.
- [70] M. Eichelbaum, B. Testa, and A. Somogyi, *Stereochemical Aspects of Drug Action and Disposition*. Handbook of experimental pharmacology, v. 153, Springer, Berlin London, 2003.
- [71] G. Gubitz and M. G. Schmid, “Chiral separation principles in chromatographic and electromigration techniques,” *Mol. Biotechnol.*, vol. 32, p. 159, 2006.

- [72] D. Belder and M. Ludwig, “Microchip electrophoresis for chiral separations,” *Electrophoresis*, vol. 24, p. 2422, 2003.
- [73] R. Bielski and M. Tencer, “Absolute enantioselective separation: Optical activity ex machina,” *J. Sep. Sci.*, vol. 28, p. 2325, 2005.
- [74] T. J. Ward and B. A. Baker, “Chiral separations,” *Analytical Chemistry*, vol. 80, p. 4363, 2008.
- [75] Y. J. Kim and W. J. Rae, “Separation of screw-sensed particles in a homogeneous shear field,” *Int. J. Multiph. Flow*, vol. 17, p. 717, 1991.
- [76] M. Makino and M. Doi, “Migration of twisted ribbon-like particles in simple shear flow,” *Phys. Fluids*, vol. 17, p. 103605, 2005.
- [77] N. Watari and R. G. Larson, “Shear-induced chiral migration of particles with anisotropic rigidity,” *Phys. Rev. Lett.*, vol. 102, p. 246001, 2009.
- [78] C. I. Mendoza, C. M. Marques, and F. Thalmann, “Enhanced shear separation for chiral magnetic colloidal aggregates,” *Phys. Rev. E*, vol. 82, p. 060401, 2010.
- [79] M. Kostur, M. Schindler, P. Talkner, and P. Hänggi, “Chiral separation in microflows,” *Phys. Rev. Lett.*, vol. 96, p. 014502, 2006.
- [80] D. W. Howard, E. N. Lightfoot, and J. O. Hirschfelder, “Hydrodynamic resolution of optical isomers,” *AICHE J.*, vol. 22, p. 794, 1976.
- [81] P. Chen and C.-H. Chao, “Lift forces of screws in shear flows,” *Phys. Fluids*, vol. 19, p. 017108, 2007.
- [82] M. Makino, L. Arai, and M. Doi, “Shear migration of chiral particle in parallel-disk,” *Journal of the Physical Society of Japan*, vol. 77, p. 064404, 2008.
- [83] Marcos, H. C. Fu, T. R. Powers, and R. Stocker, “Separation of microscale chiral objects by shear flow,” *Phys. Rev. Lett.*, vol. 102, p. 158103, 2009.
- [84] C. J. Welch, “Some thoughts concerning the separation of enantiomers without the use of enantioenriched materials or forces,” *Enantiomer*, vol. 3, p. 275, 1998.
- [85] P. G. de Gennes, “Mechanical selection of chiral crystals,” *Europhys. Lett.*, vol. 46, p. 827, 1999.
- [86] S. Wegener, *Bachelor Arbeit: Kontinuierliche Trennung chiraler Objekte ohne chemische Selektoren*. Universität Bielefeld, 2010.
- [87] E. Ott, *Chaos in dynamical Systems*. Cambridge University Press, 2002.
- [88] W. Paul and J. Baschnagel, *Stochastic processes*. Springer, Berlin, 1999.
- [89] P. E. Kloeden and E. Platen, *Numerical solution of stochastic differential equations*. Springer, Berlin, 1995.

- [90] H. Risken, *The Fokker-Planck equation*. Springer, Berlin, 1996.
- [91] S. Denisov, P. Hänggi, and J. L. Mateos, “AC-driven Brownian motors: A Fokker-Planck treatment,” *Am. J. Phys.*, vol. 77, p. 602, 2009.
- [92] B.-q. Ai and L.-g. Liu, “Facilitated movement of inertial Brownian motors driven by a load under an asymmetric potential,” *Phys. Rev. E*, vol. 76, p. 042103, 2007.
- [93] F. R. Alatriste and J. L. Mateos, “Anomalous mobility and current reversals in inertial deterministic ratchets,” *Physica A*, vol. 384, p. 223, 2007.
- [94] L. Jing-hui, “Current reversal and negative conductance for a super-conducting junctions device,” *Commun. Theor. Phys.*, vol. 51, p. 853, 2009.
- [95] L. Jing-hui and J. Luczka, “Thermal-inertial ratchet effects: Negative mobility, resonant activation, noise-enhanced stability, and noise-weakened stability,” *Phys. Rev. E*, vol. 82, p. 041104, 2010.
- [96] F. Lorenz, *Lineare Algebra I*. Spektrum Akademischer Verlag, Heidelberg, 1993.
- [97] S. Denisov, Y. Zolotaryuk, S. Flach, and O. Yevtushenko, “Vortex and translational currents due to broken time-space symmetries,” *Phys. Rev. Lett.*, vol. 100, p. 224102, 2008.
- [98] P. Reimann, “Supersymmetric ratchets,” *Phys. Rev. Lett.*, vol. 86, p. 4992, 2001.
- [99] A. Vanderbauwhede, *Local bifurcation and symmetry*. Pitman Advanced Publishing Program, Boston, 1982.
- [100] P. Chossat and R. Lauterbach, *Methods in Equivariant Bifurcations and Dynamical Systems*. World Scientific, Singapore, 2000.
- [101] N. H. Ibragimov, *Elementary Lie Group Analysis and Ordinary Differential Equations*. John Wiley Sons, New York, 1999.
- [102] F. Lorenz, *Lineare Algebra II*. Spektrum Akademischer Verlag, Heidelberg, 1996.
- [103] C. Kittel and S. Hunklinger, *Einführung in die Festkörperphysik*. Oldenbourg, München, 2006.
- [104] C. Reichhardt, C. J. O. Reichhardt, and M. B. Hastings, “Nonlinear dynamics, rectification, and phase locking for particles on symmetrical two-dimensional periodic substrates with dc and circular ac drives,” *Phys. Rev. E*, vol. 69, p. 056115, 2004.
- [105] P. Tierno, T. H. Johansen, and T. M. Fischer, “Localized and delocalized motion of colloidal particles on a magnetic bubble lattice,” *Phys. Rev. Lett.*, vol. 99, p. 038303, 2007.
- [106] A. Soba, P. Tierno, T. M. Fischer, and F. Saguès, “Dynamics of a paramagnetic colloidal particle driven on a magnetic-bubble lattice,” *Phys. Rev. E*, vol. 77, p. 060401, 2008.

- [107] U. Geigenmüller, “Dynamics of a ring with three Josephson junctions,” *J. Appl. Phys.*, vol. 80, p. 3934, 1996.
- [108] S. Denisov, S. Flach, A. A. Ovchinnikov, O. Yevtushenko, and Y. Zolotaryuk, “Broken space-time symmetries and mechanisms of rectification of ac fields by nonlinear (non)adiabatic response,” *Phys. Rev. E*, vol. 66, p. 041104, 2002.
- [109] S. Flach, O. Yevtushenko, and Y. Zolotaryuk, “Directed current due to broken time-space symmetry,” *Phys. Rev. Lett.*, vol. 84, p. 2358, 2000.
- [110] S. Denisov, S. Flach, and P. Hänggi, “Stationary Hamiltonian transport with dc bias,” *Europhys. Lett.*, vol. 74, p. 588, 2006.
- [111] A. B. Buda, T. A. Dereeyde, and K. Moslow, “On quantifying chirality,” *Angew. Chem.-Int. Edit. Engl.*, vol. 31, p. 989, 1992.
- [112] H. Zabrodsky and D. Avnir, “Continuous symmetry measures .4. chirality,” *J. Am. Chem. Soc.*, vol. 117, p. 462, 1995.
- [113] M. Petitjean, “Chirality and symemtry measures: A transdisciplinary review,” *Entropy*, vol. 5, p. 271, 2003.
- [114] H. Goldstein, C. P. P. jr., and J. Safko, *Klassische Mechanik*. Wiley, New York, 2006.
- [115] S. H. Strogatz, *Nonlinear dynamics and chaos*. Perseus Books, Reading, Mass., 1998.
- [116] E. A. Coddington and N. Levinson, *Theory of ordinary differential equations*. McGraw-Hill Book Company, New York, 1955.
- [117] T. S. Parker and L. O. Chua, *Practical numerical algorithms for chaotic systems*. Springer, New York, 1989.
- [118] H. G. Solari, M. A. Natiello, and G. B. Mindlin, *Nonlinear dynamics : A two-way trip from physics to math*. Institute of Physics Publishing, Bristol, 1995.
- [119] K. Königsberger, *Analysis/1*. Springer, Berlin, 1999.
- [120] K. Königsberger, *Analysis/2*. Springer, Berlin, 2002.
- [121] M. J. Feigenbaum, “Quantitative universality for a class of non-linear transformations,” *J. Stat. Phys.*, vol. 19, p. 25, 1978.
- [122] M. J. Feigenbaum, “The universal metric properties of nonlinear transformations,” *J. Stat. Phys.*, vol. 21, p. 669, 1979.
- [123] C. Grebogi, E. Ott, and J. A. Yorke, “Chaotic attractors in crisis,” *Phys. Rev. Lett.*, vol. 48, p. 1507, 1982.
- [124] C. Grebogi, E. Ott, and J. A. Yorke, “Crises, sudden changes in chaotic attractors, and transient chaos,” *Physica D*, vol. 7, p. 181, 1983.

- [125] C. Grebogi, E. Ott, and J. A. Yorke, “Critical exponent of chaotic transients in nonlinear dynamical systems,” *Phys. Rev. Lett.*, vol. 57, p. 1284, 1986.
- [126] T. Tél, “Transient chaos,” *Directions in Chaos*, vol. 3, p. 149, 1990.
- [127] J. W. Swift and K. Wiesenfeld, “Suppression of period doubling in symmetric systems,” *Phys. Rev. Lett.*, vol. 52, p. 705, 1984.
- [128] F. Cecconi, M. Cencini, M. Falcioni, and A. Vulpiani, “Brownian motion and diffusion: From stochastic processes to chaos and beyond,” *Chaos*, vol. 15, p. 026102, 2005.
- [129] J.-P. Bouchaud and A. Georges, “Anomalous diffusion in disordered media: Statistical mechanisms, models and physical applications,” *Phys. Rep.*, vol. 195, p. 127, 1990.
- [130] T. Geisel and J. Nierwetberg, “Onset of diffusion and universal scaling in chaotic systems,” *Phys. Rev. Lett.*, vol. 48, p. 7, 1982.
- [131] M. Schell, S. Fraser, and R. Kapral, “Diffusive dynamics in systems with translational symmetry - a one-dimensional-map model,” *Phys. Rev. A*, vol. 26, p. 504, 1982.
- [132] E. G. Gwinn and R. M. Westervelt, “Fractal basin boundaries and intermittency in the driven damped pendulum,” *Phys. Rev. A*, vol. 33, p. 4143, 1986.
- [133] T. Geisel, J. Nierwetberg, and A. Zacherl, “Accelerated diffusion in Josephson junctions and related chaotic systems,” *Phys. Rev. Lett.*, vol. 54, p. 616, 1985.
- [134] H. Fujisaka and S. Grossmann, “Chaos-induced diffusion in non-linear discrete dynamics,” *Z. Phys. B-Condens. Mat.*, vol. 48, p. 261, 1982.
- [135] J. A. Blackburn and N. Grønbech-Jensen, “Phase diffusion in a chaotic pendulum,” *Phys. Rev. E*, vol. 53, p. 3068, 1996.
- [136] R. Harish, S. Rajasekar, and K. P. N. Murthy, “Diffusion in a periodically driven damped and undamped pendulum,” *Phys. Rev. E*, vol. 65, p. 046214, 2002.
- [137] R. L. Kautz, “Noise, chaos, and the Josephson voltage standard,” *Rep. Prog. Phys.*, vol. 59, p. 935, 1996.
- [138] D. van der Meer, P. Reimann, K. van der Weele, and D. Lohse, “Spontaneous ratchet effect in a granular gas,” *Phys. Rev. Lett.*, vol. 92, p. 184301, 2004.
- [139] K.-H. Ahn, H. C. Park, J. Wiersig, and J. Hong, “Current rectification by spontaneous symmetry breaking in coupled nanomechanical shuttles,” *Phys. Rev. Lett.*, vol. 97, p. 216804, 2006.
- [140] C. Kim, J. Park, and R. H. Blick, “Spontaneous symmetry breaking in two coupled nanomechanical electron shuttles,” *Phys. Rev. Lett.*, vol. 105, p. 067204, 2010.

- [141] M. I. Freidlin and A. D. Wentzell, *Random perturbations of dynamical systems*. Springer, New York, 1984.
- [142] R. L. Kautz, “Thermally induced escape: The principle of minimum available noise energy,” *Phys. Rev. A*, vol. 38, p. 2066, 1988.
- [143] R. L. Kautz, “Quasipotential and the stability of phase lock in nonhysteretic Josephson junctions,” *J. Appl. Phys.*, vol. 76, p. 5538, 1994.
- [144] J. Lehmann, P. Reimann, and P. Hänggi, “Activated escape over oscillating barriers: The case of many dimensions,” *Phys. Status Solidi B*, vol. 237, p. 53, 2003.
- [145] S. Getfert and P. Reimann, “Suppression of thermally activated escape by heating,” *Phys. Rev. E*, vol. 80, p. 030101, 2009.
- [146] C. Grebogi, E. Ott, F. Romeiras, and J. A. Yorke, “Critical exponents for crisis-induced intermittency,” *Phys. Rev. A*, vol. 36, p. 5365, 1987.
- [147] P. Reimann, “Stabilization of transient chaos by noise,” *Helv. Phys. Acta*, vol. 67, p. 235, 1994.
- [148] M. Kostur, L. Machura, P. Talkner, P. Hänggi, and J. Łuczka, “Anomalous transport in biased ac-driven josephson junctions: Negative conductances,” *Phys. Rev. B*, vol. 77, p. 104509, 2008.
- [149] M. Kostur, L. Machura, J. Łuczka, P. Talkner, and P. Hänggi, “Negative conductance in driven Josephson junctions,” *Acta Phys. Pol. B*, vol. 39, p. 1115, 2008.
- [150] L. Machura, M. Kostur, P. Talkner, P. Hänggi, and J. Łuczka, “Negative conductances of Josephson junctions: Voltage fluctuations and energetics,” *Physica E*, vol. 42, p. 590, 2010.
- [151] M. Kostur, J. Łuczka, and P. Hänggi, “Negative mobility induced by colored thermal fluctuations,” *Phys. Rev. E*, vol. 80, 2009.
- [152] D. N. Langenberg, D. J. Scalapino, B. N. Taylor, and R. E. Eck, “Microwave-induced d.c. voltages across Josephson junctions,” *Phys. Lett.*, vol. 20, p. 563, 1966.
- [153] J. T. Chen, R. J. Todd, and Y. W. Kim, “Investigation of microwave-induced dc voltages across unbiased Josephson tunnel junctions,” *Phys. Rev. B*, vol. 5, p. 1843, 1972.
- [154] S. Shapiro, A. R. Janus, and S. Holly, “Effect of microwaves on Josephson currents in superconducting tunneling,” *Rev. Mod. Phys.*, vol. 36, p. 223, 1993.
- [155] M. T. Levinsen, R. Y. Chiao, M. J. Feldmann, and B. A. Tucker, “An inverse ac Josephson effect voltage standard,” *Appl. Phys. Lett.*, vol. 31, p. 776, 1977.
- [156] L. Machura, M. Kostur, P. Talkner, J. Łuczka, F. Marchesoni, and P. Hänggi, “Brownian motors: Current fluctuations and rectification efficiency,” *Phys. Rev. E*, vol. 70, p. 061105, 2004.

- [157] D. Speer, *Diplomarbeit*. Universität Bielefeld, 2006.
- [158] R. L. Kautz, “Global stability of phase lock near a chaotic crisis in the rf-biased Josephson junction,” *J. Appl. Phys.*, vol. 62, p. 198, 1987.
- [159] B. Y. Shapiro, I. Dayan, M. Gitterman, and G. H. Weiss, “Exact calculation of Shapiro step sizes for pulse-driven Josephson junctions,” *Phys. Rev. B*, vol. 46, p. 8349, 1992.
- [160] S. Maggi, “Step width enhancement in a pulse-driven Josephson junction,” *J. Appl. Phys.*, vol. 79, p. 7860, 1996.
- [161] J. Kim, A. Sosso, and A. F. Clark, “Dynamics of overdamped Josephson junctions driven by a square-wave pulse,” *J. Appl. Phys.*, vol. 83, p. 3225, 1998.
- [162] J. Isohätälä, K. N. Alekseev, L. T. Kurki, and P. Pietiläinen, “Symmetry breaking in a driven and strongly damped pendulum,” *Phys. Rev. E*, vol. 71, p. 066206, 2005.
- [163] J. Isohätälä and K. N. Alekseev, “Stability properties of periodically driven overdamped pendula and their implications to physics of semiconductor superlattices and Josephson junctions,” *Chaos*, vol. 20, 2010.
- [164] Y. Mizugaki, J. Chen, S. Nishikata, K. Sugi, K. Nakajima, and T. Yamashita, “Zero-crossing Shapiro step in a three-junction SQUID magnetically coupled with two phase-shifted rf signals,” *IEEE Trans. Appl. Supercon.*, vol. 13, p. 926, 2003.
- [165] Y. Mizugaki and K. Katoh, “Zero-crossing Shapiro step generated in an asymmetric and nonhysteretic rf-current-driven two-junction superconducting quantum interference device,” *J. Appl. Phys.*, vol. 100, p. 064503, 2006.
- [166] R. L. Kautz, “The ac Josephson effect in hysteretic junctions: Range and stability of phase lock,” *J. Appl. Phys.*, vol. 52, p. 3528, 1981.
- [167] R. L. Kautz and R. Monaco, “Survey of chaos in the rf-biased Josephson junction,” *J. Appl. Phys.*, vol. 57, p. 875, 1984.
- [168] D. B. Sullivan and J. E. Zimmermann, “Mechanical analogs of time dependent Josephson phenomena,” *Am. J. Phys.*, vol. 39, p. 1504, 1971.
- [169] J. A. Blackburn, S. Vik, B. R. Wu, and H. J. T. Smith, “Driven pendulum for studying chaos,” *Rev. Sci. Instrum.*, vol. 60, p. 422, 1989.
- [170] H. J. T. Smith and J. A. Blackburn, “Experimental-study of an inverted pendulum,” *Am. J. Phys.*, vol. 60, p. 909, 1992.
- [171] H. J. T. Smith and J. A. Blackburn, “Multiperiodic orbits in a pendulum with a vertically oscillating pivot,” *Phys. Rev. E*, vol. 50, p. 539, 1994.
- [172] J. C. W. Locke, A. J. Millar, and M. S. Turner, “Modelling genetic networks with noisy and varied experimental data: the circadian clock in *Arabidopsis thaliana*,” *J. Theor. Biol.*, vol. 234, p. 383, 2005.

- [173] M. Januszewski and M. Kostur, “Accelerating numerical solution of stochastic differential equations with CUDA,” *Comput. Phys. Commun.*, vol. 181, p. 183, 2010.
- [174] L. Dematte and D. Prandi, “GPU computing for systems biology,” *Brief. Bioinf.*, vol. 11, p. 323, 2010.
- [175] L. Machura, M. Kostur, and J. Luczka, “Inertial Brownian motors driven by biharmonic signals,” *Chem. Phys.*, vol. 375, p. 445, 2010.
- [176] *ATI Stream Computing User Guide 1.4(beta)*. Advance Micro Devices, Inc., Sunnyvale, California, Apr. 2009.
- [177] *NVIDIA CUDA C Programming Guide*. NVIDIA Corp., Santa Clara, California, Nov. 2010.
- [178] *Intel 64 and IA-32 Architectures Software Developer’s Manual, volume 1: Basic Architecture*. INTEL Corp., 2010.
- [179] Wikipedia, “Comparison of AMD graphics processing units.” http://en.wikipedia.org/wiki/Comparison_of_AMD_graphics_processing_units, Dec. 2010.
- [180] A. Rößler, “Runge-Kutta methods for Itô stochastic differential equations with scalar noise,” *Bit*, vol. 46, p. 97, 2006.
- [181] A. Roessler, “Second order Runge-Kutta methods for Stratonovich stochastic differential equations,” *Bit*, vol. 47, p. 657, 2007.
- [182] R. Guantes, J. L. Vega, and S. Miret-Artés, “Chaos and anomalous diffusion of adatoms on solid surfaces,” *Phys. Rev. B*, vol. 64, p. 245415, 2001.
- [183] R. Guantes and S. Miret-Artés, “Chaotic transport of particles in two-dimensional periodic potentials driven by ac forces,” *Phys. Rev. E*, vol. 67, p. 046212, 2003.
- [184] R. Chacón and A. M. Lacasta, “Controlling chaotic transport in two-dimensional periodic potentials,” *Phys. Rev. E*, vol. 82, p. 046207, 2010.
- [185] P. Tierno, A. Soba, T. H. Johansen, and F. Saguès, “Dynamic colloidal sorting on a magnetic bubble lattice,” *Applied Physics Letters*, vol. 93, p. 214102, 2008.
- [186] W. H. Press, S. A. Teukolsky, W. T. Vetterling, and B. P. Flannery, *Numerical recipes in C*. Cambridge Univ. Press, Cambridge, 1994.
- [187] G. L. Baker and J. A. Blackburn, *The pendulum - A case study in physics*. Oxford University Press Inc., New York, 2005.
- [188] M. V. Bartuccelli, G. Gentile, and . K. V. Georgiou, “On the dynamics of a vertically driven damped planar pendulum,” *Proc. R. Soc. Lond. A*, vol. 457, p. 3007, 2001.
- [189] M. Pelton, K. Ladavac, and D. G. Grier, “Transport and fractionation in periodic potential-energy landscapes,” *Phys. Rev. E*, vol. 70, p. 031108, 2004.

- [190] G. Milne, D. Rhodes, M. MacDonald, and K. Dholakia, “Fractionation of polydisperse colloid with acousto-optically generated potential energy landscapes,” *Opt. Lett.*, vol. 32, p. 1144, 2007.
- [191] Y. Roichman, V. Wong, and D. G. Grier, “Colloidal transport through optical tweezer arrays,” *Phys. Rev. E*, vol. 75, p. 011407, 2007.
- [192] M. Vélez, J. Martín, J. Villegas, A. Hoffmann, E. González, J. Vicent, and I. K. Schuller, “Superconducting vortex pinning with artificial magnetic nanostructures,” *J. Magn. Magn. Mater.*, vol. 320, p. 2547, 2008.
- [193] J. P. Gleeson, J. M. Sancho, A. M. Lacasta, and K. Lindenberg, “Analytical approach to sorting in periodic and random potentials,” *Phys. Rev. E*, vol. 73, p. 041102, 2006.
- [194] J. Herrmann, M. Karweit, and G. Drazer, “Separation of suspended particles in microfluidic systems by directional locking in periodic fields,” *Phys. Rev. E*, vol. 79, p. 061404, 2009.
- [195] T. A. J. Duke and R. H. Austin, “Microfabricated sieve for the continuous sorting of macromolecules,” *Phys. Rev. Lett.*, vol. 80, p. 1552, 1998.
- [196] D. Ertaş, “Lateral separation of macromolecules and polyelectrolytes in microlithographic arrays,” *Phys. Rev. Lett.*, vol. 80, p. 1548, 1998.
- [197] A. van Oudenaarden and S. G. Boxer, “Brownian ratchets: Molecular separations in lipid bilayers supported on patterned arrays,” *Science*, vol. 285, p. 1046, 1999.
- [198] M. Bier, M. Kostur, I. Derényi, and R. D. Astumian, “Nonlinearly coupled flows,” *Phys. Rev. E*, vol. 61, p. 7184, 2000.
- [199] M. Kostur and L. Schimansky-Geier, “Numerical study of diffusion induced transport in 2D systems,” *Phys. Lett. A*, vol. 265, p. 337, 2000.
- [200] C. Keller, F. Marquardt, and C. Bruder, “Separation quality of a geometric ratchet,” *Phys. Rev. E*, vol. 65, p. 041927, 2002.
- [201] A. B. Kolton, “Transverse rectification of disorder-induced fluctuations in a driven system,” *Phys. Rev. B*, vol. 75, p. 020201, 2007.
- [202] C. Reichhardt, C. J. Olson, and M. B. Hastings, “Rectification and phase locking for particles on symmetric two-dimensional periodic substrates,” *Phys. Rev. Lett.*, vol. 89, p. 024101, 2002.
- [203] C. Reichhardt and C. J. Olson Reichhardt, “Absolute transverse mobility and ratchet effect on periodic two-dimensional symmetric substrates,” *Phys. Rev. E*, vol. 68, p. 046102, 2003.
- [204] C. Reichhardt and C. J. Olson, “Transverse phase locking for vortex motion in square and triangular pinning arrays,” *Phys. Rev. B*, vol. 65, p. 174523, 2002.

- [205] C. Reichhardt and C. J. Olson Reichhardt, “Dynamic regimes and spontaneous symmetry breaking for driven colloids on triangular substrates,” *Europhys. Lett.*, vol. 68, p. 303, 2004.
- [206] C. Reichhardt and C. J. Olson Reichhardt, “Directional locking effects and dynamics for particles driven through a colloidal lattice,” *Phys. Rev. E*, vol. 69, p. 041405, 2004.
- [207] C. Reichhardt and C. J. O. Reichhardt, “Moving vortex phases, dynamical symmetry breaking, and jamming for vortices in honeycomb pinning arrays,” *Phys. Rev. B*, vol. 78, p. 224511, 2008.
- [208] S. Sengupta, R. Guantes, S. Miret-Artés, and P. Hänggi, “Controlling directed transport in two-dimensional periodic structures under crossed electric fields,” *Physica A*, vol. 338, p. 406, 2004.
- [209] T. M. Squires and S. R. Quake, “Microfluidics: Fluid physics at the nanoliter scale,” *Rev. Mod. Phys.*, vol. 77, p. 977, 2005.
- [210] S.-H. Lee and D. G. Grier, “Giant colloidal diffusivity on corrugated optical vortices,” *Phys. Rev. Lett.*, vol. 96, p. 190601, 2006.
- [211] V. Bickle, T. Speck, U. Seifert, and C. Bechinger, “Characterizing potentials by a generalized boltzmann factor,” *Phys. Rev. E*, vol. 75, p. 060101, 2007.
- [212] M. Evstigneev, O. Zvyagolskaya, S. Bleil, R. Eichhorn, C. Bechinger, and P. Reimann, “Diffusion of colloidal particles in a tilted periodic potential: Theory versus experiment,” *Phys. Rev. E*, vol. 77, p. 041107, 2008.
- [213] G. Costantini and F. Marchesoni, “Threshold diffusion in a tilted washboard potential,” *Europhys. Lett.*, vol. 48, p. 491, 1999.
- [214] P. Reimann, C. Van den Broeck, H. Linke, P. Hänggi, J. M. Rubi, and A. Pérez-Madrid, “Giant acceleration of free diffusion by use of tilted periodic potentials,” *Phys. Rev. Lett.*, vol. 87, p. 010602, 2001.
- [215] P. Reimann, C. Van den Broeck, H. Linke, P. Hänggi, J. M. Rubi, and A. Pérez-Madrid, “Diffusion in tilted periodic potentials: Enhancement, universality, and scaling,” *Phys. Rev. E*, vol. 65, p. 031104, 2002.
- [216] P. E. Parris, M. Kuš, D. H. Dunlap, and V. M. Kenkre, “Nonlinear response theory: Transport coefficients for driving fields of arbitrary magnitude,” *Phys. Rev. E*, vol. 56, p. 5295, 1997.
- [217] P. Reimann and R. Eichhorn, “Weak disorder strongly improves the selective enhancement of diffusion in a tilted periodic potential,” *Phys. Rev. Lett.*, vol. 101, p. 180601, 2008.
- [218] P. Tierno, T. H. Johansen, and F. Saguès, “Dynamical regimes of a paramagnetic particle circulating a magnetic bubble domain,” *Phys. Rev. E*, vol. 80, p. 052401, 2009.

- [219] P. Tierno, P. Reimann, T. H. Johansen, and F. Sagués, “Giant transversal particle diffusion in a longitudinal magnetic ratchet,” *Phys. Rev. Lett.*, vol. 105, p. 230602, 2010.
- [220] P. Tierno, F. Saguès, T. H. Johansen, and T. M. Fischer, “Colloidal transport on magnetic garnet films,” *Phys. Chem. Chem. Phys.*, vol. 11, p. 9615, 2009.
- [221] C. Reichhardt and C. J. Olson, “Vortex pinball under crossed ac drives in superconductors with periodic pinning arrays,” *Phys. Rev. B*, vol. 65, p. 100501, 2002.
- [222] R. Eichhorn and P. Reimann, “Analytic theory of absolute negative mobility in a microfluidic device,” *Acta Phys. Pol. B*, vol. 37, p. 1491, 2006.
- [223] W. Gillijns, A. V. Silhanek, V. V. Moshchalkov, C. J. O. Reichhardt, and C. Reichhardt, “Origin of reversed vortex ratchet motion,” *Phys. Rev. Lett.*, vol. 99, p. 247002, 2007.
- [224] S. Ooi, S. Savel’ev, M. B. Gaifullin, T. Mochiku, K. Hirata, and F. Nori, “Nonlinear nanodevices using magnetic flux quanta,” *Phys. Rev. Lett.*, vol. 99, p. 207003, 2007.
- [225] H. Hilgenkamp, V. V. Moshchalkov, and P. Kes, “Flux quanta on the move,” *Science*, vol. 302, p. 1159, 2003.
- [226] J. E. Villegas, S. Savel’ev, F. Nori, E. M. Gonzalez, J. V. Anguita, R. Garca, and J. L. Vicent, “A superconducting reversible rectifier that controls the motion of magnetic flux quanta,” *Science*, vol. 302, p. 1188, 2003.
- [227] Y. Togawa, K. Harada, T. Akashi, H. Kasai, T. Matsuda, F. Nori, A. Maeda, and A. Tonomura, “Direct observation of rectified motion of vortices in a Niobium superconductor,” *Phys. Rev. Lett.*, vol. 95, p. 087002, 2005.
- [228] J. van de Vondel, C. C. de Souza Silva, B. Y. Zhu, M. Morelle, and V. V. Moshchalkov, “Vortex-rectification effects in films with periodic asymmetric pinning,” *Phys. Rev. Lett.*, vol. 94, p. 057003, 2005.
- [229] C. Mennerat-Robilliard, D. Lucas, S. Guibal, J. Tabosa, C. Jurczak, J.-Y. Courtois, and G. Grynberg, “Ratchet for cold Rubidium atoms: The asymmetric optical lattice,” *Phys. Rev. Lett.*, vol. 82, p. 851, 1999.
- [230] S. Savel’ev and F. Nori, “Experimentally realizable devices for controlling the motion of magnetic flux quanta in anisotropic superconductors,” *Nat. Mater.*, vol. 1, p. 179, 2002.
- [231] D. Cole, S. Bending, S. Savel’ev, A. Grigorenko, T. Tamegai, and F. Nori, “Ratchet without spatial asymmetry for controlling the motion of magnetic flux quanta using time-asymmetric drives,” *Nat. Mater.*, vol. 5, p. 305, 2006.
- [232] B. B. Jin, B. Y. Zhu, R. Wördenweber, C. C. de Souza Silva, P. H. Wu, and V. V. Moshchalkov, “High-frequency vortex ratchet effect in a superconducting film with a nanoengineered array of asymmetric pinning sites,” *Phys. Rev. B*, vol. 81, p. 174505, 2010.

- [233] C. C. de Souza Silva, A. V. Silhanek, J. van de Vondel, W. Gillijns, V. Metlushko, B. Ilic, and V. V. Moshchalkov, “Dipole-induced vortex ratchets in superconducting films with arrays of micromagnets,” *Phys. Rev. Lett.*, vol. 98, p. 117005, 2007.
- [234] L. Dinis, D. P. de Lara, E. M. Gonzalez, J. V. Anguita, J. M. R. Parrondo, and J. L. Vicent, “Transverse ratchet effect and superconducting vortices: simulation and experiment,” *New Journal of Physics*, vol. 11, p. 073046, 2009.
- [235] S. Savel’ev, F. Marchesoni, and F. Nori, “Interacting particles on a rocked ratchet: Rectification by condensation,” *Phys. Rev. E*, vol. 71, p. 011107, 2005.
- [236] V. I. Marconi, “Rocking ratchets in two-dimensional josephson networks: Collective effects and current reversal,” *Phys. Rev. Lett.*, vol. 98, p. 047006, 2007.
- [237] I. Derényi and R. Dean Astumian, “Ac separation of particles by biased Brownian motion in a two-dimensional sieve,” *Phys. Rev. E*, vol. 58, p. 7781, 1998.
- [238] S. Savel’ev, V. Misko, F. Marchesoni, and F. Nori, “Separating particles according to their physical properties: Transverse drift of underdamped and overdamped interacting particles diffusing through two-dimensional ratchets,” *Phys. Rev. B*, vol. 71, p. 214303, 2005.
- [239] E. M. Gonzalez, N. O. Nunez, J. V. Anguita, and J. L. Vicent, “Transverse rectification in superconducting thin films with arrays of asymmetric defects,” *Appl. Phys. Lett.*, vol. 91, p. 062505, 2007.
- [240] C. Reichhardt and C. J. Olson Reichhardt, “Pinning and dynamics of colloids on one-dimensional periodic potentials,” *Phys. Rev. E*, vol. 72, p. 032401, 2005.
- [241] S. Bleil, H. von Grünberg, J. Dobnikar, R. Castaeda-Priego, and C. Bechinger, “Strain-induced domain formation in two-dimensional colloidal systems,” *Europhys. Lett.*, vol. 73, p. 450, 2006.
- [242] K. Ladavac, K. Kasza, and D. G. Grier, “Sorting mesoscopic objects with periodic potential landscapes: Optical fractionation,” *Phys. Rev. E*, vol. 70, p. 010901, 2004.
- [243] R. L. Kautz, “Activation energy for thermally induced escape from a basin of attraction,” *Phys. Lett. A*, vol. 125, p. 315, 1987.
- [244] D. G. Zarlenga, H. A. Larrondo, C. M. Arizmendi, and F. Family, “Complex synchronization structure of an overdamped ratchet with discontinuous periodic forcing,” *Phys. Rev. E*, vol. 80, p. 011127, 2009.
- [245] G. Iooss, *Elementary stability and bifurcation theory*. Springer, New York, 1990.
- [246] J. Argyris, G. Faust, and M. Haase, *Die Erforschung des Chaos*. Friedr. Vieweg und Sohn Verlagsgesellschaft, Braunschweig, 1994.
- [247] D. Reguera, G. Schmid, P. S. Burada, J. M. Rubí, P. Reimann, and P. Hänggi, “Entropic transport: Kinetics, scaling, and control mechanisms,” *Phys. Rev. Lett.*, vol. 96, p. 130603, 2006.

- [248] P. S. Burada, P. Hänggi, F. Marchesoni, G. Schmid, and P. Talkner, “Diffusion in confined geometries,” *ChemPhysChem*, vol. 10, p. 45, 2009.
- [249] P. S. Burada, G. Schmid, P. Talkner, P. Hänggi, D. Reguera, and J. M. Rubi, “Entropic particle transport in periodic channels,” *Biosystems*, vol. 93, p. 16, 2008.
- [250] P. S. Burada, G. Schmid, Y. Li, and P. Hänggi, “Controlling diffusive transport in confined geometries,” *Acta. Phys. Pol. B*, vol. 41, p. 935, 2010.
- [251] Y. He and B.-q. Ai, “Enhancement of the longitudinal transport by a weakly transversal drive,” *Phys. Rev. E*, vol. 81, p. 021110, 2010.
- [252] M. Galassi, J. Davies, J. Theiler, B. Gough, G. Jungman, M. Booth, and F. Rossi, *GNU Scientific Library Reference Manual*. Published by Network Theory Ltd, 2006.
- [253] J. E. Hirsch, B. A. Huberman, and D. J. Scalapino, “Theory of intermittency,” *Phys. Rev. A*, vol. 25, p. 519, 1982.
- [254] E. Ben-Jacob, I. Goldhirsch, Y. Imry, and S. Fishman, “Intermittent chaos in Josephson junctions,” *Phys. Rev. Lett.*, vol. 49, p. 1599, 1982.
- [255] B. R. Hunt, E. Ott, and J. A. Yorke, “Fractal dimensions of chaotic saddles of dynamical systems,” *Phys. Rev. E*, vol. 54, p. 4819, 1996.
- [256] T. Geisel and J. Nierwetberg, “Statistical properties of intermittent diffusion in chaotic systems,” *Z. Phys. B-Condens. Mat.*, vol. 56, p. 59, 1984.
- [257] E. G. Gwinn and R. M. Westervelt, “Intermittent chaos and low-frequency noise in the driven damped pendulum,” *Phys. Rev. Lett.*, vol. 54, p. 1613, 1985.
- [258] P. Reimann, “Suppression of deterministic diffusion by noise,” *Phys. Rev. E*, vol. 50, p. 727, 1994.
- [259] T. Geisel, A. Zacherl, and G. Radons, “Chaotic diffusion and 1/f-noise of particles in two-dimensional solids,” *Z. Phys. B-Condens. Mat.*, vol. 71, p. 117, 1988.
- [260] J. Wagenhuber, T. Geisel, P. Niebauer, and G. Obermair, “Chaos and anomalous diffusion of ballistic electrons in lateral surface superlattices,” *Phys. Rev. B*, vol. 45, p. 4372, 1992.
- [261] V. Latora, A. Rapisarda, and S. Ruffo, “Superdiffusion and out-of-equilibrium chaotic dynamics with many degrees of freedoms,” *Phys. Rev. Lett.*, vol. 83, p. 2104, 1999.
- [262] O. Yevtushenko, S. Flach, and K. Richter, “Ac-driven phase-dependent directed diffusion,” *Phys. Rev. E*, vol. 61, p. 7215, 2000.
- [263] J. Lehmann, P. Reimann, and P. Hänggi, “Surmounting oscillating barriers: Path-integral approach for weak noise,” *Phys. Rev. E*, vol. 62, p. 6282, 2000.
- [264] T. Tél and Y.-C. Lai, “Quasipotential approach to critical scaling in noise-induced chaos,” *Phys. Rev. E*, vol. 81, p. 056208, 2010.

- [265] M. Franaszek, “Influence of noise on mean lifetime of chaotic transients,” *Phys. Rev. A*, vol. 44, p. 4065, 1991.
- [266] Y. Pomeau and P. Manneville, “Intermittent transition to turbulence in dissipative dynamical-systems,” *Commun. Math. Phys.*, vol. 74, p. 189, 1980.
- [267] H. Gang, A. Daffertshofer, and H. Haken, “Diffusion of periodically forced Brownian particles moving in space-periodic potentials,” *Phys. Rev. Lett.*, vol. 76, p. 4874, 1996.
- [268] M. Schreier, P. Reimann, P. Hänggi, and E. Pollak, “Giant enhancement of diffusion and particle selection in rocked periodic potentials,” *Europhys. Lett.*, vol. 44, p. 416, 1998.
- [269] D. Reguera, P. Reimann, P. Hänggi, and J. M. Rubi, “Interplay of frequency-synchronization with noise: Current resonances, giant diffusion and diffusion-crests,” *Europhys. Lett.*, vol. 57, p. 644, 2002.
- [270] S. Miret-Artés and E. Pollak, “The dynamics of activated surface diffusion,” *Journal of Physics: Condensed Matter*, vol. 17, p. S4133, 2005.
- [271] P. T. Korda, G. C. Spalding, and D. G. Grier, “Evolution of a colloidal critical state in an optical pinning potential landscape,” *Phys. Rev. B*, vol. 66, p. 024504, 2002.
- [272] K. Mangold, P. Leiderer, and C. Bechinger, “Phase transitions of colloidal monolayers in periodic pinning arrays,” *Phys. Rev. Lett.*, vol. 90, p. 158302, 2003.
- [273] S.-H. Lee and D. G. Grier, “Flux reversal in a two-state symmetric optical thermal ratchet,” *Phys. Rev. E*, vol. 71, p. 060102, 2005.
- [274] T. c. v. Čižmár, M. Šiler, M. Šerý, P. Zemánek, V. Garcés-Chávez, and K. Dholakia, “Optical sorting and detection of submicrometer objects in a motional standing wave,” *Phys. Rev. B*, vol. 74, p. 035105, 2006.
- [275] S. Bleil, P. Reimann, and C. Bechinger, “Directing Brownian motion by oscillating barriers,” *Phys. Rev. E*, vol. 75, p. 031117, 2007.
- [276] B. Sun, Y. Roichman, and D. G. Grier, “Theory of holographic optical trapping,” *Opt. Express*, vol. 16, p. 15765, 2008.
- [277] P. Tierno, S. V. Reddy, M. G. Roper, T. H. Johansen, and T. M. Fischer, “Transport and separation of biomolecular cargo on paramagnetic colloidal particles in a magnetic ratchet,” *J. Phys. Chem. B*, vol. 112, p. 3833, 2008.
- [278] J. Blackburn, N. Grønbech-Jensen, and H. Smith, “Harmonic synchronization in resistively coupled Josephson-junctions,” *J. Appl. Phys.*, vol. 75, p. 3668, 1994.
- [279] J. A. Blackburn, G. L. Baker, and H. J. T. Smith, “Intermittent synchronization of resistively coupled chaotic Josephson junctions,” *Phys. Rev. B*, vol. 62, p. 5931, 2000.

[280] E. B. Cummings and A. K. Singh, “Dielectrophoresis in microchips containing arrays of insulating posts: Theoretical and experimental results,” *Anal. Chem.*, vol. 75, p. 4724, 2003.

[281] M. Baba, T. Sano, N. Iguchi, K. Iida, T. Sakamoto, and H. Kawaura, “DNA size separation using artificially nanostructured matrix,” *App. Phys. Lett.*, vol. 83, p. 1468, 2003.

[282] L. R. Huang, J. O. Tegenfeldt, J. J. Kraeft, J. C. Sturm, R. H. Austin, and E. C. Cox, “A DNA prism for high-speed continuous fractionation of large DNA molecules,” *Nat. Biotechnol.*, vol. 20, p. 1048, 2002.

[283] J. Regtmeier, T. T. Duong, R. Eichhorn, D. Anselmetti, and A. Ros, “Dielectrophoretic manipulation of DNA: Separation and polarizability,” *Anal. Chem.*, vol. 79, p. 3925, 2007.

[284] J. Nagel, private communication. 2009.

[285] A. Sterck, S. Weiss, and D. Koelle, “SQUID ratchets: basics and experiments,” *Appl. Phys. A-Mater.*, vol. 75, p. 253, 2002.

[286] M. Khouri, J. P. Gleeson, J. M. Sancho, A. M. Lacasta, and K. Lindenberg, “Diffusion coefficient in periodic and random potentials,” *Phys. Rev. E*, vol. 80, p. 021123, 2009.

[287] M. Abramowitz, ed., *Handbook of mathematical functions*. U.S. Gov. Print. Off., Washington, D.C., 1972.

[288] I. N. Bronstein and K. A. Semendjajew, *Taschenbuch der Mathematik*. Verlag Harri Deutsch, Zürich und Frankfurt/M., 1968.

[289] A. B. Kolton, D. Domínguez, and N. Grønbech-Jensen, “Hall noise and transverse freezing in driven vortex lattices,” *Phys. Rev. Lett.*, vol. 83, p. 3061, 1999.

[290] A. B. Kolton, R. Exartier, L. F. Cugliandolo, D. Domínguez, and N. Grønbech-Jensen, “Effective temperature in driven vortex lattices with random pinning,” *Phys. Rev. Lett.*, vol. 89, p. 227001, 2002.

[291] A. B. Kolton, D. Domínguez, and N. Grønbech-Jensen, “Mode locking in driven vortex lattices with transverse ac drive and random pinning,” *Phys. Rev. B*, vol. 65, p. 184508, 2002.

[292] A. B. Kolton, “Pinning induced fluctuations on driven vortices,” *Physica C: Superconductivity*, vol. 437-438, p. 153, 2006. Proceedings of the Fourth International Conference on Vortex Matter in Nanostructured Superconductors VORTEX IV.

[293] C. Reichhardt and C. J. Olson Reichhardt, “Ratchet effect and nonlinear transport for particles on random substrates with crossed ac drives,” *Phys. Rev. E*, vol. 73, p. 011102, 2006.

- [294] A. O. Golosov, “Localization of random-walks in one-dimensional random environments,” *Commun. Math. Phys.*, vol. 92, p. 491, 1984.
- [295] M. N. Popescu, Y. Braiman, F. Family, and H. G. E. Hentschel, “Quenched disorder enhances chaotic diffusion,” *Phys. Rev. E*, vol. 58, p. R4057, 1998.
- [296] G. Radons, “Suppression of chaotic diffusion by quenched disorder,” *Phys. Rev. Lett.*, vol. 77, p. 4748, 1996.
- [297] R. Klages, “Suppression and enhancement of diffusion in disordered dynamical systems,” *Phys. Rev. E*, vol. 65, p. 055203, 2002.
- [298] M. N. Popescu, C. M. Arizmendi, A. L. Salas-Brito, and F. Family, “Disorder induced diffusive transport in ratchets,” *Phys. Rev. Lett.*, vol. 85, p. 3321, 2000.
- [299] Y. Braiman, H. G. E. Hentschel, F. Family, C. Mak, and J. Krim, “Tuning friction with noise and disorder,” *Phys. Rev. E*, vol. 59, p. R4737, 1999.
- [300] P. J. Martínez and R. Chacón, “Disorder induced control of discrete soliton ratchets,” *Phys. Rev. Lett.*, vol. 100, p. 144101, 2008.
- [301] S. F. Brandt, B. K. Dellen, and R. Wessel, “Synchronization from disordered driving forces in arrays of coupled oscillators,” *Phys. Rev. Lett.*, vol. 96, p. 034104, 2006.
- [302] T. Harms and R. Lipowsky, “Driven ratchets with disordered tracks,” *Phys. Rev. Lett.*, vol. 79, p. 2895, 1997.
- [303] F. Marchesoni, “Transport properties in disordered ratchet potentials,” *Phys. Rev. E*, vol. 56, p. 2492, 1997.
- [304] C. M. Arizmendi, F. Family, and A. L. Salas-Brito, “Quenched disorder effects on deterministic inertia ratchets,” *Phys. Rev. E*, vol. 63, p. 061104, 2001.
- [305] F. Family, H. A. Larrondo, D. G. Zarlenga, and C. M. Arizmendi, “Chaotic dynamics and control of deterministic ratchets,” *Journal of Physics: Condensed Matter*, vol. 17, p. S3719, 2005.
- [306] D. G. Zarlenga, H. A. Larrondo, C. M. Arizmendi, and F. Family, “Trapping mechanism in overdamped ratchets with quenched noise,” *Phys. Rev. E*, vol. 75, p. 051101, 2007.
- [307] C. Aslangul, N. Pottier, and D. Saint-James, “One-dimensional motion in a biased random medium: Random potential versus random force,” *Physica A: Statistical and Theoretical Physics*, vol. 174, p. 272, 1991.
- [308] L. Gao, X. Luo, S. Zhu, and B. Hu, “Dispersive anomalous diffusive transport in ratchets with long-range correlated spatial disorder,” *Phys. Rev. E*, vol. 67, p. 062104, 2003.
- [309] H. Takemoto, T. Ohyama, and A. Tohsaki, “Direct sum of coulomb potential without ambiguities of conditionally convergent series,” *Progress of Theoretical Physics*, vol. 109, p. 563, 2003.

- [310] W. F. Druyvesteyn, J. W. Dorleijn, and D. L. A. Tjaden, “Calculation of stray field of a magnetic bubble, with application to some bubble problems,” *Philips Research Reports*, vol. 27, p. 7, 1972.
- [311] C. J. Hegedus and E. Della Torre, “On the efficient calculation of magnetic bubble functions,” *J. Appl. Phys.*, vol. 49, p. 942, 1978.
- [312] N. Grønbech-Jensen, “Summation of logarithmic interactions in periodic media,” *Int. J. Mod. Phys. C*, vol. 7, p. 873, 1996.
- [313] N. Grønbech-Jensen, “Summation of logarithmic interactions in nonrectangular periodic media,” *Computer Physics Communications*, vol. 119, p. 115, 1999.
- [314] S. I. Denisov, M. Kostur, E. S. Denisova, and P. Hänggi, “Analytically solvable model of a driven system with quenched dichotomous disorder,” *Phys. Rev. E*, vol. 75, p. 061123, 2007.
- [315] S. I. Denisov, T. V. Lyutyy, E. S. Denisova, P. Hänggi, and H. Kantz, “Directed transport in periodically rocked random sawtooth potentials,” *Phys. Rev. E*, vol. 79, p. 051102, 2009.
- [316] J. P. Bouchaud, A. Comtet, A. Georges, and P. Le Doussal, “Anomalous diffusion in random media of any dimensionality,” *J. Phys. France*, vol. 48, p. 1445, 1987.
- [317] S. I. Denisov, M. Kostur, E. S. Denisova, and P. Hänggi, “Arrival time distribution for a driven system containing quenched dichotomous disorder,” *Phys. Rev. E*, vol. 76, p. 031101, 2007.
- [318] S. I. Denisov and H. Kantz, “Anomalous biased diffusion in a randomly layered medium,” *Phys. Rev. E*, vol. 81, p. 021117, 2010.
- [319] S. I. Denisov, E. S. Denisova, and H. Kantz, “Biased diffusion in a piecewise linear random potential,” *Eur. J. Phys. B*, vol. 76, p. 1, 2010.
- [320] P. Hänggi, P. Talkner, and M. Borkovec, “Reaction-rate theory - 50 years after Kramers,” *Rev. Mod. Phys.*, vol. 62, p. 251, 1990.
- [321] D. Hennig, A. Burbanks, and A. Osbaldestin, “Directing particle transport in a two-dimensional periodic potential landscape,” *Chemical Physics*, vol. 375, p. 492, 2010.
- [322] H. D. Vollmer, “Two particle model for the diffusion of interacting particles in periodic potentials,” *Z. Phys. B Con. Mat.*, vol. 33, p. 103, 1979.
- [323] F. Family, H. G. E. Hentschel, and Y. Braiman, “Friction at the nanoscale,” *J. Phys. Chem. B*, vol. 104, p. 3984, 2000.
- [324] A. E. Filippov, J. Klafter, and M. Urbakh, “Friction through dynamical formation and rupture of molecular bonds,” *Phys. Rev. Lett.*, vol. 92, p. 135503, 2004.

- [325] S. Maier, Y. Sang, T. Filleter, M. Grant, R. Bennewitz, E. Gnecco, and E. Meyer, “Fluctuations and jump dynamics in atomic friction experiments,” *Phys. Rev. B*, vol. 72, p. 245418, 2005.
- [326] O. M. Braun, R. Ferrando, and G. E. Tommei, “Stimulated diffusion of an adsorbed dimer,” *Phys. Rev. E*, vol. 68, p. 051101, 2003.
- [327] S. Gonçalves, V. M. Kenkre, and A. R. Bishop, “Nonlinear friction of a damped dimer sliding on a periodic substrate,” *Phys. Rev. B*, vol. 70, p. 195415, 2004.
- [328] S. Gonçalves, C. Fusco, A. R. Bishop, and V. M. Kenkre, “Bistability and hysteresis in the sliding friction of a dimer,” *Phys. Rev. B*, vol. 72, p. 195418, 2005.
- [329] E. Heinsalu, M. Patriarca, and F. Marchesoni, “Dimer diffusion in a washboard potential,” *Phys. Rev. E*, vol. 77, p. 021129, 2008.
- [330] M. Tiwari, S. Gonçalves, and V. M. Kenkre, “Generalization of a nonlinear friction relation for a dimer sliding on a periodic substrate,” *Eur. Phys. J. B*, vol. 62, p. 459, 2008.
- [331] A. H. Romero, A. M. Lacasta, and J. M. Sancho, “Modelization of surface diffusion of a molecular dimer,” *Phys. Rev. E*, vol. 69, p. 051105, 2004.
- [332] C. Fusco and A. Fasolino, “Nonlinear dynamics and surface diffusion of diatomic molecules,” *ChemPhysChem*, vol. 6, p. 1749, 2005.
- [333] C. Fusco and A. Fasolino, “Microscopic mechanisms of thermal and driven diffusion of non rigid molecules on surfaces,” *Thin Solid Films*, vol. 428, p. 34, 2003. Proceedings of Symposium J on Growth and Evolution of Ultrathin Films: Surface and Interface Geometric and Electronic Structure, of the E-MRS Spring Conference.
- [334] C. Fusco, A. Fasolino, and T. Janssen, “Nonlinear dynamics of dimers on periodic substrates,” *Eur. Phys. J. B*, vol. 31, p. 95, 2003.
- [335] F. Jülicher, A. Ajdari, and J. Prost, “Modeling molecular motors,” *Rev. Mod. Phys.*, vol. 69, p. 1269, 1997.
- [336] S. von Gehlen, M. Evstigneev, and P. Reimann, “Dynamics of a dimer in a symmetric potential: Ratchet effect generated by an internal degree of freedom,” *Phys. Rev. E*, vol. 77, p. 031136, 2008.
- [337] S. von Gehlen, M. Evstigneev, and P. Reimann, “Ratchet effect of a dimer with broken friction symmetry in a symmetric potential,” *Phys. Rev. E*, vol. 79, p. 031114, 2009.
- [338] M. Evstigneev, S. von Gehlen, and P. Reimann, “Interaction-controlled Brownian motion in a tilted periodic potential,” *Phys. Rev. E*, vol. 79, p. 011116, 2009.
- [339] S. Cilla and L. M. Floría, “Internal degrees of freedom in a thermodynamical model for intracell biological transport,” *Physica D*, vol. 113, p. 157, 1998. Proceedings of the Conference on Fluctuations, Nonlinearity and Disorder in Condensed Matter and Biological Physics.

- [340] S. Cilla, F. Falo, and L. M. Floría, “Mirror symmetry breaking through an internal degree of freedom leading to directional motion,” *Phys. Rev. E*, vol. 63, p. 031110, 2001.
- [341] S. Klumpp, A. Mielke, and C. Wald, “Noise-induced transport of two coupled particles,” *Phys. Rev. E*, vol. 63, p. 031914, 2001.
- [342] A. Pototsky, F. Marchesoni, and S. E. Savel’ev, “Ratcheting of neutral elastic dimers on a charged filament,” *Phys. Rev. E*, vol. 81, p. 031114, 2010.
- [343] J. A. Fornes, “Hydrodynamic interactions induce movement against an external load in a ratchet dimer Brownian motor,” *J. Colloid Interf. Sci.*, vol. 341, p. 376, 2010.
- [344] H. S. Wright, M. R. Swift, and P. J. King, “Migration of an asymmetric dimer in oscillatory fluid flow,” *Phys. Rev. E*, vol. 78, p. 036311, 2008.
- [345] D. Dan, A. M. Jayannavar, and G. I. Menon, “A biologically inspired ratchet model of two coupled Brownian motors,” *Physica A*, vol. 318, p. 40, 2003.
- [346] Y. A. Makhnovskii, V. M. Rozenbaum, D.-Y. Yang, and S. H. Lin, “Net transport due to noise-induced internal reciprocating motion,” *The Journal of Chemical Physics*, vol. 130, p. 164101, 2009.
- [347] U. E. Vincent, O. I. Olusola, D. Mayer, and P. V. E. McClintock, “Controlling current reversals in synchronized underdamped ratchets,” *J. Phys. A-Math. Theor.*, vol. 43, p. 165101, 2010.
- [348] U. E. Vincent, A. Kenfack, D. V. Senthilkumar, D. Mayer, and J. Kurths, “Current reversals and synchronization in coupled ratchets,” *Phys. Rev. E*, vol. 82, p. 046208, 2010.
- [349] M. Porto, M. Urbakh, and J. Klafter, “Atomic scale engines: Cars and wheels,” *Phys. Rev. Lett.*, vol. 84, p. 6058, 2000.
- [350] A. Igarashi, S. Tsukamoto, and H. Goko, “Transport properties and efficiency of elastically coupled Brownian motors,” *Phys. Rev. E*, vol. 64, p. 051908, 2001.
- [351] M. T. Downton, M. J. Zuckermann, E. M. Craig, M. Plischke, and H. Linke, “Single-polymer Brownian motor: A simulation study,” *Phys. Rev. E*, vol. 73, p. 011909, 2006.
- [352] H. Chen, Q. Wang, and Z. Zheng, “Deterministic directed transport of inertial particles in a flashing ratchet potential,” *Phys. Rev. E*, vol. 71, p. 031102, 2005.
- [353] X. R. Qin, B. S. Swartzentruber, and M. G. Lagally, “Diffusional kinetics of SiGe dimers on Si(100) using atom-tracking scanning tunneling microscopy,” *Phys. Rev. Lett.*, vol. 85, p. 3660, 2000.

[354] R. Bukowski, K. Szalewicz, G. Groenenboom, and A. van der Avoird, “Interaction potential for water dimer from symmetry-adapted perturbation theory based on density functional description of monomers,” *J. Chem. Phys.*, vol. 125, p. 044301, 2006.

[355] M. Bishop, M. Derosa, and J. Lalli, “Molecular-dynamics simulations of one-dimensional Lennard-Jones systems,” *J. Stat. Phys.*, vol. 25, p. 229, 1981.

[356] A. M. Bazhenov and D. M. Heyes, “Dynamical properties and transport-coefficients of one-dimensional Lennard-Jones fluids - a molecular-dynamics study,” *J. Chem. Phys.*, vol. 92, p. 1106, 1990.

[357] S. Lepri, P. Sandri, and A. Politi, “The one-dimensional Lennard-Jones system: collective fluctuations and breakdown of hydrodynamics,” *Eur. Phys. J. B*, vol. 47, p. 549, 2005.

[358] E. Pijper and A. Fasolino, “Mechanisms for correlated surface diffusion of weakly bonded dimers,” *Phys. Rev. B*, vol. 72, p. 165328, 2005.

[359] E. M. Craig, M. J. Zuckermann, and H. Linke, “Mechanical coupling in flashing ratchets,” *Phys. Rev. E*, vol. 73, p. 051106, 2006.

[360] S. Martens, D. Hennig, S. Fugmann, and L. Schimansky-Geier, “Resonancelike phenomena in the mobility of a chain of nonlinear coupled oscillators in a two-dimensional periodic potential,” *Phys. Rev. E*, vol. 78, p. 041121, 2008.

[361] U. Henningsen and M. Schliwa, “Reversal in the direction of movement of a molecular motor,” *Nature*, vol. 389, p. 93, 1997.

[362] I. Derényi and T. Vicsek, “The kinesin walk: A dynamic model with elastically coupled heads,” *Proc. Natl. Acad. Sci. U. S. A.*, vol. 93, p. 6775, 1996.

[363] S. Rice, A. Lin, D. Safer, C. Hart, N. Naber, B. Carragher, S. Cain, E. Pechatnikova, E. Wilson-Kubalek, M. Whittaker, E. Pate, R. Cooke, E. Taylor, R. Milligan, and R. Vale, “A structural change in the kinesin motor protein that drives motility,” *Nature*, vol. 402, p. 778, 1999.

[364] C. L. Asbury, A. N. Fehr, and S. M. Block, “Kinesin moves by an asymmetric hand-over-hand mechanism,” *Science*, vol. 302, p. 2130, 2003.

[365] A. Yildiz, M. Tomishige, R. D. Vale, and P. R. Selvin, “Kinesin walks hand-over-hand,” *Science*, vol. 303, p. 676, 2004.

[366] A. Hendricks, B. Epureanu, and E. Meyhöfer, “Mechanistic mathematical model of kinesin under time and space fluctuating loads,” *Nonlinear Dynam.*, vol. 53, p. 303, 2008.

[367] S. A. Endow and H. Higuchi, “A mutant of the motor protein kinesin that moves in both directions on microtubules,” *Nature*, vol. 406, p. 913, 2000.

- [368] M. Badoual, F. Julicher, and J. Prost, “Bidirectional cooperative motion of molecular motors,” *Proc. Natl. Acad. Sci. U. S. A.*, vol. 99, p. 6696, 2002.
- [369] J. Mateos, “Walking on ratchets with two Brownian motors,” *Fluct. Noise Lett.*, vol. 4, p. L161, 2004.
- [370] J. Mateos, “A random walker on a ratchet,” *Physica A*, vol. 351, p. 79, 2005.
- [371] J. Menche and L. Schimansky-Geier, “Two particles with bistable coupling on a ratchet,” *Phys. Lett. A*, vol. 359, p. 90, 2006.
- [372] R. Retkute and J. P. Gleeson, “Role of interaction on noise-induced transport of two coupled particles in Brownian ratchet devices,” *Fluct. Noise Lett.*, vol. 6, p. L263, 2006.
- [373] A. Pototsky, N. B. Janson, F. Marchesoni, and S. Savel’ev, “Dipole rectification in an oscillating electric field,” *Europhys. Lett.*, vol. 88, p. 30003, 2009.
- [374] S. Denisov, “Particle with internal dynamical asymmetry: chaotic self-propulsion and turning,” *Phys. Lett. A*, vol. 296, p. 197, 2002.
- [375] C. Lutz, M. Reichert, H. Stark, and C. Bechinger, “Surmounting barriers: The benefit of hydrodynamic interactions,” *Europhys. Lett.*, vol. 74, p. 719, 2006.
- [376] J. Bammert, S. Schreiber, and W. Zimmermann, “Dumbbell diffusion in a spatially periodic potential,” *Phys. Rev. E*, vol. 77, p. 042102, 2008.
- [377] D. Hennig, A. D. Burbanks, and A. H. Osbaldestin, “Directed transport of two interacting particles in a washboard potential,” *Physica D*, vol. 238, p. 2273, 2009.
- [378] D. Hennig, S. Martens, and S. Fugmann, “Transition between locked and running states for dimer motion induced by periodic external driving,” *Phys. Rev. E*, vol. 78, p. 011104, 2008.
- [379] A. Ajdari, D. Mukamel, L. Peliti, and J. Prost, “Rectified motion-induced by ac forces in periodic structures,” *J. Phys. I*, vol. 4, p. 1551, 1994.
- [380] J. Clarke and A. Braginski, *The SQUID Handbook*. Wiley-VCH, Berlin, 2004.
- [381] I. Zapata, R. Bartussek, F. Sols, and P. Hänggi, “Voltage rectification by a SQUID ratchet,” *Phys. Rev. Lett.*, vol. 77, p. 2292, 1996.
- [382] A. Sterck, D. Koelle, and R. Kleiner, “Rectification in a stochastically driven three-junction SQUID rocking ratchet,” *Phys. Rev. Lett.*, vol. 103, p. 047001, 2009.
- [383] A. A. Middleton and D. S. Fisher, “Critical behavior of pinned charge-density waves below the threshold for sliding,” *Phys. Rev. Lett.*, vol. 66, p. 92, 1991.
- [384] A. A. Middleton, “Asymptotic uniqueness of the sliding state for charge-density waves,” *Phys. Rev. Lett.*, vol. 68, p. 670, 1992.

- [385] A. A. Middleton and D. S. Fisher, “Critical behavior of charge-density waves below threshold: Numerical and scaling analysis,” *Phys. Rev. B*, vol. 47, p. 3530, 1993.
- [386] L. M. Floría and J. J. Mazo, “Dissipative dynamics of the Frenkel-Kontorova model,” *Adv. Phys.*, vol. 45, p. 505, 1996.
- [387] B. Aulbach, *Gewöhnliche Differentialgleichungen*. Spektrum Akademischer Verlag GmbH, Heidelberg, 1997.
- [388] C. Baesens and R. S. MacKay, “Gradient dynamics of tilted Frenkel-Kontorova models,” *Nonlinearity*, vol. 11, p. 949, 1998.
- [389] E. Kamke, “Zur Theorie der Systeme gewöhnlicher Differentialgleichungen,” *J. Reine Angew. Math.*, vol. 1929, p. 194, 1929.
- [390] M. W. Hirsch, “Systems of differential equations which are competitive or cooperative I: Limit sets,” *SIAM J. Math. Anal.*, vol. 13, p. 167, 1982.
- [391] M. W. Hirsch, “Systems of differential equations that are competitive or cooperative II: Convergence almost everywhere,” *SIAM J. Math. Anal.*, vol. 16, p. 423, 1985.
- [392] R. Wittmaack, *Bachelor Arbeit*. Universität Bielefeld, 2009.
- [393] M.-A. Assmann, *Bachelor Arbeit*. Universität Bielefeld, 2008.
- [394] B. Cleuren and C. Van den Broeck, “Brownian motion with absolute negative mobility,” *Phys. Rev. E*, vol. 67, p. 055101, 2003.
- [395] S. Das, S. Datta, M. Dutta, S. Jain, and D. Sahdev, “The dynamical response of a three-junction network I. Phase variables,” *Physica D*, vol. 91, p. 278, 1996.
- [396] S. Das, S. Datta, D. Sahdev, M. K. Verma, and R. Mehrotra, “The dynamical response of a three-junction network II. Vortices,” *Physica D*, vol. 91, p. 292, 1996.
- [397] J. Kim, W. G. Choe, S. Kim, and H. J. Lee, “Dynamics of Josephson-junction ladders,” *Phys. Rev. B*, vol. 49, p. 459, 1994.
- [398] J. A. Blackburn, H. J. T. Smith, and N. Grønbech-Jensen, “Chaos and thermal noise in a Josephson junction coupled to a resonant tank,” *Phys. Rev. B*, vol. 53, p. 14546, 1996.
- [399] F. Ichikawa, T. Aomine, and S. Hosogi, “Dynamics of a triangular loop containing 3 Josephson-junctions with zero capacitance,” *J. Appl. Phys.*, vol. 63, p. 1636, 1988.
- [400] M. A. H. Nerenberg, J. H. Baskey, and J. A. Blackburn, “Chaotic behavior in an array of coupled Josephson weak links,” *Phys. Rev. B*, vol. 36, p. 8333, 1987.
- [401] K. Saitoh and T. Nishino, “Phase locking in a double junction of Josephson weak links,” *Phys. Rev. B*, vol. 44, p. 7070, 1991.

- [402] H. Hölscher, A. Schirmeisen, and U. D. Schwarz, “Principles of atomic friction: from sticking atoms to superlubric sliding,” *Proc. R. Soc. A*, vol. 366, p. 1383, 2008.
- [403] A. Socoliuc, E. Gnecco, S. Maier, O. Pfeiffer, A. Baratoff, R. Bennewitz, and E. Meyer, “Atomic-Scale Control of Friction by Actuation of Nanometer-Sized Contacts,” *Science*, vol. 313, p. 207, 2006.
- [404] M. Evstigneev, A. Schirmeisen, L. Jansen, H. Fuchs, and P. Reimann, “Force dependence of transition rates in atomic friction,” *Phys. Rev. Lett.*, vol. 97, p. 240601, 2006.
- [405] J. Y. Park, D. F. Ogletree, P. A. Thiel, and M. Salmeron, “Electronic Control of Friction in Silicon pn Junctions,” *Science*, vol. 313, p. 186, 2006.
- [406] R. W. Carpick, “Controlling Friction,” *Science*, vol. 313, p. 184, 2006.
- [407] F. Jülicher and J. Prost, “Spontaneous oscillations of collective molecular motors,” *Phys. Rev. Lett.*, vol. 78, p. 4510, 1997.
- [408] A. Ghosh and P. Fischer, “Chiral molecules split light: Reflection and refraction in a chiral liquid,” *Phys. Rev. Lett.*, vol. 97, p. 173002, 2006.
- [409] B. Spivak and A. V. Andreev, “Photoinduced separation of chiral isomers in a classical buffer gas,” *Phys. Rev. Lett.*, vol. 102, p. 063004, 2009.
- [410] M. Fliedner, private communication. 2010.
- [411] M. Cabodi, Y. F. Chen, S. W. P. Turner, H. G. Craighead, and R. H. Austin, “Continuous separation of biomolecules by the laterally asymmetric diffusion array with out-of-plane sample injection,” *Electrophoresis*, vol. 23, p. 3496, 2002.
- [412] S. W. Turner, A. M. Perez, A. Lopez, and H. G. Craighead, “Monolithic nanofluidic sieving structures for DNA manipulation,” *Papers from the 42nd international conference on electron, ion, and photon beam technology and nanofabrication*, vol. 16, p. 3835, 1998.
- [413] N. Kaji, Y. Tezuka, Y. Takamura, M. Ueda, T. Nishimoto, H. Nakanishi, Y. Horiike, and Y. Baba, “Separation of long DNA molecules by quartz nanopillar chips under a direct current electric field,” *Analytical Chemistry*, vol. 76, p. 15, 2004.
- [414] J. Fu, R. B. Schoch, A. L. Stevens, S. R. Tannenbaum, and J. Han, “A patterned anisotropic nanofluidic sieving structure for continuous-flow separation of DNA and proteins,” *Nat. Nanotechnol.*, vol. 2, p. 121, 2007.
- [415] A. Ghosh and P. Fischer, “Controlled propulsion of artificial magnetic nanostructured propellers,” *Nano Lett.*, vol. 9, p. 2243, 2009.
- [416] D. Zerrouki, J. Baudry, D. Pine, P. Chaikin, and J. Bibette, “Chiral colloidal clusters,” *Nature*, vol. 455, p. 380, 2008.

- [417] L. Zhang, J. J. Abbott, L. Dong, B. E. Kratochvil, D. Bell, and B. J. Nelson, “Artificial bacterial flagella: Fabrication and magnetic control,” *Applied Physics Letters*, vol. 94, p. 064107, 2009.
- [418] E. Ercolini, F. Valle, J. Adamcik, G. Witz, R. Metzler, P. De Los Rios, J. Roca, and G. Dietler, “Fractal dimension and localization of DNA knots,” *Phys. Rev. Lett.*, vol. 98, p. 058102, 2007.
- [419] L. P. Faucheux, G. Stolovitzky, and A. Libchaber, “Periodic forcing of a Brownian particle,” *Phys. Rev. E*, vol. 51, p. 5239, 1995.
- [420] M. Borromeo and F. Marchesoni, “Brownian surfers,” *Physics Letters A*, vol. 249, p. 199, 1998.
- [421] V. Bickle, T. Speck, C. Lutz, U. Seifert, and C. Bechinger, “Einstein relation generalized to nonequilibrium,” *Phys. Rev. Lett.*, vol. 98, p. 210601, 2007.
- [422] G. Grynberg and C. Robilliard, “Cold atoms in dissipative optical lattices,” *Phys. Rep.*, vol. 355, p. 335, 2001.
- [423] R. Gommers, S. Bergamini, and F. Renzoni, “Dissipation-induced symmetry breaking in a driven optical lattice,” *Phys. Rev. Lett.*, vol. 95, p. 073003, 2005.

Danksagung

Zunächst möchte ich Prof. Dr. Peter Reimann und Prof. Dr. Ralf Eichhorn für die umfangreiche Betreuung und Unterstützung bei diesem Projekt und dem Schreiben dieser Arbeit danken. Viele der in dieser Arbeit umgesetzten Ideen gehen auf sie zurück.

Prof. Dr. Jürgen Schnack und Prof. Dr. Peter Reimann danke ich für das Lesen und Begutachten dieser Arbeit.

Prof. Dr. Ralf Eichhorn und Jan-Philipp Knoop danke ich für das sorgfältige Korrekturlesen dieser umfangreichen Arbeit.

Joachim Nagel, Dr. Albert Sterck, Prof. Dr. Reinhold Kleiner und Prof. Dr. Dieter Koelle danke ich für anregende Diskussionen über Josephson Kontakte, die Durchführung des Experiments und die bereit gestellten Messdaten.

Marc Fliedner danke ich für viele anregende Diskussionen zur chiralen Trennung und das Gegenrechnen einiger Ergebnisse.

Lukas Bogunovic und Dr. Jan Regtmeier danke ich für die Einblicke in die Mikrofluiddik, die sie mir gewährt haben, und die Abbildungen, die sie bereit gestellt haben.

Der Arbeitsgruppe Theorie der kondensierten Materie danke ich für die freundliche Atmosphäre und das gute Arbeitsklima. Und dabei danke ich auch nicht zuletzt Hanne Litschewsky die sich immer perfekt um alles praktische gekümmert hat.

Mein persönlicher Dank gilt meiner Frau Ruth und meinem Sohn Jamin, die mich unterstützt, ertragen, geliebt, mit mir gelitten, und mich mit einem freudigen “Baba!” begrüßt haben, und nicht zuletzt meinen Eltern.